Failure Behaviour of Fasteners in Timber Connections

Testing Approaches for Laterally Loaded Dowel-Type Fasteners

Zur Erlangung des akademischen Grades einer

DOKTORIN DER INGENIEURWISSENSCHAFTEN (Dr.-Ing.)

von der KIT Fakultät für
Bauingenieur-, Geo- und Umweltwissenschaften
des Karlsruher Instituts für Technologie (KIT)

genehmigte

DISSERTATION

von

Elisabet Kuck, M.Sc.
geb. in Mutlangen

Tag der mündlichen Prüfung:	16.01.2026
Hauptreferent:	Prof. Dr.-Ing. Hans Joachim Blaß
Korreferent:	Prof. Dr.-Ing. Thomas K. Bader

Karlsruhe 2026

Abstract

Changes, challenges and potentials arise with the increasing use of hardwoods in timber construction. High stiffness and strength of hardwoods place higher mechanical demands on fasteners. Hardwoods with its higher density subject fasteners to complex multiaxial stress states not fully represented in current design, i.e. *European Yield Model*, which mainly consider fastener bending and timber embedment, while only partially accounting for axial resistance from rope effects. As a result, fasteners may fail at the shear plane or at plastic hinges under combined loading, indicating that the load-bearing capacity of the fastener's cross-section under such multiaxial stress states remains largely unconsidered. To address this, insights from related disciplines, particularly steel design, are combined with newly developed testing and measurement approaches to improve the understanding of cross-sectional failure and interaction mechanisms. These investigations form the basis for a comprehensive understanding of the behaviour, design and application of fasteners in hardwood connections.

A design concept requires knowledge of both the loads acting on the fastener and its capacity to resist them, and this work investigates both aspects through a holistic experimental and analytical programme. To investigate these phenomena, novel test setups are developed to study the behaviour of dowel-type fasteners under lateral, axial, and combined loading. Embedded strain gauges in fully threaded screws and digital image correlation on exposed fasteners quantify local strains, critical stress concentrations, and elastic re-deformation. These measurements focus on capturing plastic hinge formation and strain distribution within the fastener. Bending angles, plastic hinge positions, and strain distributions are determined for aluminium and steel fasteners, allowing assessment of material strength effects across different connection types and timber densities. Timber-to-timber connections are dominated by plastic hinge formation, whereas timber-to-steel connections exhibit more pronounced shear-plane yielding.

To study the effect of combined loading, a selected interaction between normal and shear forces, which can lead to failure of the fastener in the shear plane, is investigated using a dedicated combined-loading setup for screws and bolts. Fully threaded screws show a reduction of maximum load, corresponding to changes in the tensile-to-shear force ratio, with interaction curves approximated by elliptical or super elliptical functions. Round fastener sections, such as smooth shanks of partially threaded screws and bolts, are effectively represented by bilinear models, constant under tension-dominated and linear under shear-dominated conditions.

Practical insights for hardwood connections highlight that careful installation, flush fitting, predrilling, and adequate spacing are essential to achieve full load-bearing capacity and ductile behaviour. Loads and deformations are evaluated at different relative displacement stages, enabling meaningful comparison between softwood and hardwood with increasing displacement. Larger spacing of fasteners in grain direction improves ductility.

Overall, fastener type, cross-section, timber density, and connection configuration strongly influence failure mechanisms, load distribution, and ductility of connections. The measured bending angles, plastic hinge positions, and interaction models provide reference values for modelling and support extended, safe design approaches for hardwood connections in structural timber engineering. The new understanding, together with the quantified differences between softwood and hardwood, allows defining thresholds for fastener cross-sectional failure and identifying cases that require further investigation. Furthermore, recommendations are given on how to address critical cases and account for potential fastener failures.

Kurzfassung

Mit der zunehmenden Verwendung von Laubholz als tragendem Werkstoff im Ingenieurholzbau verändern sich die Beanspruchungen und Anforderungen an Verbindungsmittel. Laubholz setzt diese Verbindungsmittel vermehrt multiaxialen Spannungszuständen aus, die von den derzeitigen Bemessungsmodellen, basierend auf dem *European Yield Model*, nicht vollständig erfasst werden. Diese Modelle berücksichtigen vorwiegend das Biegeverhalten der Verbindungsmittel sowie die Lochleibung im Holz und nur teilweise axiale Widerstände durch den Seileffekt. Infolgedessen können Verbindungsmittel in der Scherfuge oder in Fließgelenken unter kombinierter Beanspruchung versagen, was darauf hinweist, dass die Tragfähigkeit des Verbindungsmittelquerschnitts unter solchen Bedingungen maßgebend werden kann und das Versagen des Verbindungsmittelquerschnitts derzeit nicht berücksichtigt wird. Erkenntnisse aus verwandten Disziplinen, insbesondere dem Stahlbau, werden daher zusammen mit neu entwickelten Prüf- und Messmethoden kombiniert, um das Querschnittsversagen und Interaktionsmechanismen der Schnittgrößen in Verbindungsmitteln besser zu verstehen. Dadurch entsteht ein umfassendes Verständnis von Verhalten, Anwendung und Auslegung von Laubholzverbindungen.

Ein belastbares Bemessungskonzept erfordert Kenntnisse über die auf das Verbindungsmittel wirkenden Lasten und dessen Widerstandskraft. Diese Arbeit untersucht beide Aspekte in einem ganzheitlichen experimentellen und analytischen Rahmen. Dazu werden neuartige Versuchsaufbauten und -methoden entwickelt, um das Verhalten von Verbindungsmitteln unter lateraler, axialer und kombinierter Belastung zu untersuchen. In Vollgewindeschrauben eingeklebte Dehnmessstreifen und digitale Bildkorrelation an außenliegenden, sichtbaren Verbindungsmitteln quantifizieren lokale Dehnungen, kritische Spannungsbereiche und die elastische Rückverformung von Verbindungen. Eine direkte Beobachtung von Fließgelenkbildung und Dehnungsverteilung im Verbindungsmittel unter Last ist möglich. Biegewinkel, Fließgelenkpositionen und Dehnungsverteilungen werden für Aluminium- und Stahlverbindungsmittel analysiert und der Einfluss der Festigkeit auf verschiedene Verbindungstypen unter

Verwendung verschiedener Holzrohdichten bewertet. In Holz-Holz-Verbindungen dominiert die Fließgelenkbildung, während in Holz-Stahl-Verbindungen die Querkräfte stärker ins Gewicht fallen und vermehrtes Plastizieren in der Scherfuge auftritt.

Aus den möglichen Interaktionen wird in dieser Arbeit die kombinierte Wirkung von Normal- und Scherkräften explizit betrachtet, die zum Versagen des Verbindungsmittels in der Scherfuge führen kann. Experimentell wird dies an Schrauben und Bolzen in einem speziell entwickelten Zug-Scherprüfstand untersucht. Vollgewindeschrauben zeigen eine Abnahme der maximalen Traglast mit zunehmendem Scheranteil, wobei sich bei der Beschreibung des Zug-Scherverhaltens Näherungskurven mit elliptischen oder superelliptischen Funktionen ergeben. Runde Querschnitte, wie glatte Schaftbereiche von Teilgewindeschrauben und Bolzen, lassen sich durch bilineare Beziehungen beschreiben: konstant im zugdominierten Bereich und linear im scherbeanspruchten Bereich.

Praktische Erkenntnisse für Laubholzverbindungen zeigen, dass eine sorgfältige Montage, bündiges Anlegen der Schraubenköpfe, Vorbohren und ausreichende Abstände entscheidend sind, um die volle Tragfähigkeit und ein duktiles Verbindungsverhalten zu gewährleisten. Lasten und Verformungen der Verbindungsmittel werden schrittweise bei zunehmenden Relativverschiebungen ausgewertet, um einen Vergleich zwischen Nadel- und Laubholzverbindungen zu ziehen.

Insgesamt beeinflussen Verbindungsmitteltyp, Querschnitt, Holzrohdichte und Konfiguration maßgeblich die Versagensmechanismen, Lastverteilung und Duktilität. Die ermittelten Biegewinkel, Fließgelenkpositionen und Interaktionsmodelle liefern Referenzwerte für Modellierungen und unterstützen erweiterte, sichere Bemessungsansätze für Laubholzverbindungen im Ingenieurholzbau. Mit dem neuen Verständnis und den quantifizierten Unterschieden zwischen Nadel- und Laubholz lassen sich nun Grenzen bestimmen, ab wann ein Querschnittsversagen von Verbindungsmitteln zu erwarten ist und wann eine gesonderte Untersuchung erforderlich wird. Darüber hinaus werden Empfehlungen gegeben, wie mit kritischen Fällen umgegangen und das mögliche Versagen in der Bemessung berücksichtigt werden kann.

Acknowledgement

Die vorliegende Arbeit entstand während meiner Tätigkeit als wissenschaftliche Mitarbeiterin am Lehrstuhl für Holzbau und Baukonstruktion der Versuchsanstalt für Stahl, Holz und Steine des Karlsruher Instituts für Technologie (KIT). Teile der Thesis sind in einem Artikel [1] und in Konferenzbeiträgen [2, 3, 4] veröffentlicht.

Ohne unterstützende Gesten, offene Ohren, kritische Stimmen, kontroverse Diskussionen, reflektierende Gespräche, zugetragene Impulse, spontane Flurgespräche und wohlwollende Wegbereitende wäre diese Arbeit nicht entstanden.

Mein erster Dank gilt meinem Kollegium am Lehrstuhl für Holzbau und Baukonstruktion; allen voran Carmen Sandhaas für ihre allzeit unterstützende Art, ihre wertvollen Hinweise zur richtigen Zeit und ihr umfassendes wissenschaftliches Know-how, mit dem sie mir bei Fragen zur Seite stand und mich auf meinem Weg begleitet hat. Ebenso danke ich dem Team des Lehrstuhls für sechs prägende Jahre voller Austausch und Inspiration.

Ein Lächeln am Morgen beim Betreten der Laborräume und die Bereitschaft sich mit mir auf neue Ideen oder spontane Einfälle einzulassen, haben mir immer wieder vor Augen geführt, wie wertvoll das menschliche Miteinander und die Zusammenarbeit beim experimtentellen Forschen ist. Danke, dass ich von den Mitarbeitenden des Karl-Möhler-Holzbaulaboratoriums lernen durfte und bei Bedarf auf tatkräftige Unterstützung setzen konnte.

Die initiale thematische Ausrichtung verdanke ich meinem Hauptreferenten, Herrn Prof. Hans Joachim Blaß, der mir nicht nur wertvolle Impulse und Freiräume zur Entwicklung eigener Ideen gab, sondern auch durch die mir gegebene Zeit am Lehrstuhl, den fachlichen Austausch und seine Bereitschaft zu konstruktiven Gesprächen maßgeblich zum Gelingen dieser Arbeit beitrug.

Ein besonderer Dank gilt meinem Korreferenten, Herrn Prof. Thomas K. Bader, für die Übernahme des Korreferats, den inspirierenden dreimonatigen Forschungsaufenthalt an der LNU in Växjö, der mir einen Blick über den Tellerrand hinaus schenkte und

mir viele neue Eindrücke der dortigen Forschungsthemen und tolle Begegnungen ermöglichte.

Mein Dank gilt zudem Herrn Prof. Philipp Dietsch für seine Unterstützung, das mir entgegengebrachte Vertrauen und die Möglichkeit, eigenständig zu forschen und gemeinsam zu lehren – eine Erfahrung, an der ich mit der Zeit große Freude gefunden habe.

Ich danke Björn Burzlaff, Carla Meiertoberend, Elena Bäumle, Jonas Scheidt und Julia Wodtke für die Durchführung von Versuchen, gewissenhafte Dokumentation und sorgfältige Niederschrift im Rahmen ihrer Abschlussarbeiten.

Mein Dank geht zudem an das Karlsruhe House of Young Scientists für die Bewilligung eines Research Travel Grant, das meinen Forschungsaufenthalt in Schweden ermöglichte.

Allen mir nahestehenden Personen kann ich nicht genug danken – für ihren Zuspruch, die Ratschläge, Rückhalt und dass sie mich manchmal meinem Ziel näher gesehen haben als ich selbst.

Karlsruhe, 2025
Elisabet Kuck

Table of Contents

Nomenclature

Abbreviations

Beech LVL	Beech laminated veneer lumber
COS	Coordinate system
COV	Coefficient of variation
DVW	Densified Veneer Wood
DIC	Digital image correlation
EDM	Electrical Discharge Machining
EYM	European yield model
glulam	Glued laminated timber
HAZ	Heat-affected zone
LVDT	Linear Variable Differential Transformer
PH	Plastic hinge
T-S	Timber-to-steel connection
T-T	Timber-to-timber connection

Parameter

A	Area
a	Depth
$a_{i,c/t}$	Distance or spacing of fasteners
b	Width of specimen or Intersection point with ordinate
β	Exponent
c	Chord length of circle
Δ	Difference

d	Diameter
d_1	Core diameter of threaded part
d_h	Head diameter
d_{hole}	Diameter of predrilled hole
d_{nom}	Nominal diameter
d_s	Shank diameter
ε	Strain
$\varepsilon_{0°/45°/90°}$	Normal strain in different directions acc. to local coordinate system
ε_e	Engineering strain
ε_t	True strain
ε_x	Normal strain in x-direction
ε_{xy}	Tensor shear strain (half the engineering shear strain γ_{xy})
ε_y	Normal strain in y-direction
ε_v	Equivalent (von Mises) Strain
E	Young's Modulus
F_{5mm}	Load at 5 mm displacement (10, 15, 25 respectively)
F_{ax}	Withdrawal resistance
f_{ax}	Withdrawal parameter
f_h	Embedment strength
F_{head}	Head pull-through resistance
f_{head}	Head pull-through parameter
F_{max}	Maximum load
F_{shear}	Shear capacity
f_{shear}	Shear strength
F_{tens}	Tensile capacity
f_{tens}	Tensile strength used for fasteners in timber design
f_u	Tensile strength used for fasteners in steel design
f_y	Yield strength
G	Shear Modulus
l_d	Insertion depth

ℓ	Length
L_0	Original length
M	Bending moment
MNV	Interaction of internal forces N, V and bending moment M
MN	Interaction of internal force N and bending moment M
MV	Interaction of internal force V and bending moment M
M_y	Yield moment
m	Slope
N	Normal force
μ	Coefficient of static friction
NV	Interaction of internal force N and V
p	Thread pitch
r	Radius
ρ	Density
R^2	Coefficient of determination
$R_{p,0.2}$	Yield strength for screws at 0.2% strain
s_e	End stiffness in plastic section
s_i	Initial stiffness in linear elastic section
t	Thickness
τ	Shear stress
τ_R	Shear strength
u	Moisture content
u	Displacement
V	Shear force
σ	Stress
ν	Poisson's ratio
$x/y/z$	Directions of coordinate system
y_{def}	Deformation in y-direction
y_s	Distance circle centre to centre point of segment

Indices

0°/11.25°...90°	Directions acc. to coordinate system or angles to load
α	Angle to grain or angle to load direction
Ed	Design value on action side
el	Elastic
fric	Friction
mean	Mean value
np	Non predrilled
p	Predrilled
pl	Plastic
R	Resistance
red	Reduced
remain	Remaining value
Rd	Design value on resistance side
c	Compression or Circular
shear	Shear
sp	Shear plane
tens	Tension
w	Withdrawal
y	Yield

1 Introduction

1.1 Problem Definition

In science, as in everyday life, solutions are often shaped by the tools at hand. A hammer may be an excellent instrument for driving nails, but it is hardly suitable for a screw that must be carefully driven into timber. In such a situation, the limitation lies not in the task itself, but in the choice of tool. Reaching for a screwdriver or a power drill, devices developed for a different purpose, can transform the approach and lead to a more appropriate outcome.

Research follows a similar principle. Fields that become highly specialised may grow accustomed to established concepts and methods, applying them even to problems that require new perspectives. True innovation, however, rarely emerges in isolation. It often arises in dialogue, between disciplines, between methods, and between ways of thinking that challenge conventional boundaries. In the field of timber engineering, such openness to alternative viewpoints can lead to a deeper understanding of long-established phenomena. Timber connections combine two fundamentally different materials: timber and steel. Both play a crucial role in the mechanical behaviour of a connection and therefore deserve careful consideration. Despite their critical role, fasteners are frequently underestimated in timber connection design, particularly regarding their behaviour under multiaxial stress states. Current design models, such as the European Yield Model (EYM), primarily focus on the bending behaviour of fasteners, while also accounting for the tensile capacity and other axial resistances in the context of the rope effect. They further consider the embedment strength of the surrounding timber. Nevertheless, these models generally do not consider the stress state or potential failure of the fastener cross-section itself. However, the load-bearing capacity of connections can be limited by the cross-sectional capacity of the fastener, particularly when the fastener is subjected to combined stresses beyond simple bending. This design gap introduces uncertainty regarding the safety of timber structures, especially when the fasteners are critical to the connection performance.

This issue becomes particularly relevant with the increased use of hardwoods in recent years. Compared to softwoods, the higher densities and mechanical properties of hardwoods lead to increased stresses in the fasteners. Engineered hardwood products, such as laminated veneer lumber made of beech, represent a significant advancement in timber construction, offering strength and stiffness far beyond conventional softwoods. While these materials expand the possibilities for timber structures, they also require detailed knowledge of their connection behaviour and the limitations of existing design models. Investigations on softwood connections have shown that failure typically involves a combination of plastic hinge formation and timber embedment [1]. In hardwood connections, however, additional failure modes can emerge, such as rupture of the fastener cross-section even at relatively small displacements [67], which current models do not capture. Fig. 1.1 provides representative examples of such failures, illustrating the need for targeted investigations of fastener behaviour under the higher stresses induced by hardwoods.

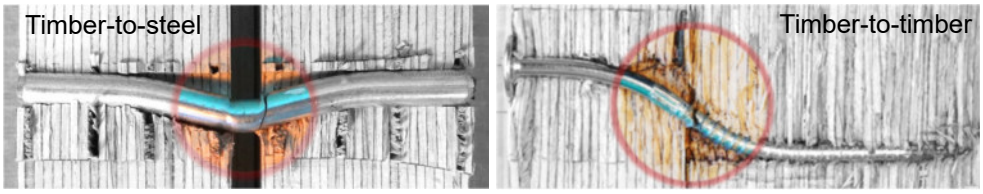

a. Timber-to-steel connection with dowel. b. Timber-to-timber connection with partially threaded screw.

Fig. 1.1: Exemplary fastener failure in shear planes of connections.

The relevance of these considerations is supported by numerous experimental studies that reveal the stress conditions in fasteners in hardwood connections. Observations by Sandhaas [81] demonstrate the influence of dowel strength on connection behaviour, for example in beech and azobé. Kobel [56], Kobel et al. [57] observed dowel failure in beech LVL, while Franke and Franke [35] reported similar findings for beech glulam, both occurring at large displacements. Comparable observations for mild steel dowels in beech LVL were made by Misconel et al. [69]. Furthermore, Blaß et al. [15], Meyer [67], and Goossens [41] initiated discussions on the origins of fastener failure by examining interaction criteria in individual cases. A study on screws by Kuck and Sandhaas [1] reported screw failure at deformations of around 13 mm. In contrast, investigations by Choquette [22] and Meyer [67] on nails in steel-to-timber connections revealed failures occurring even earlier. These findings indicate that fasteners in hardwoods are subjected to considerably higher stresses than those in softwoods, and that fastener failure is a realistic possibility.

Increased embedment strengths lead to larger bending angles and smaller bending radii, and inclined fastener sections experience significantly higher axial forces due to withdrawal and head pull-through resistance. In some cases, these stress combinations result in failure of the fastener cross-section by tearing or shearing, which can occur at relative displacements as small as 3–4 mm (e.g. steel-to-hardwood connections with profiled nails in Meyer [67]). Such fastener failure becomes critical if it occurs at small relative displacements before the connections have reached the calculated load carrying capacity. In contrast, similar failures in softwood connections only appear at much larger relative displacements, far beyond those typically encountered in service conditions [43]. The occurrence of such fastener failure poses a critical challenge for the design and safety of timber connections made of high-density timber products. Although recent studies have identified this as a potential failure mode, it has not yet been systematically investigated nor taken into account in existing design rules.

These observations highlight the need for a deeper understanding of the mechanisms leading to fastener failure in high-density timber products, forming the basis for the motivation of this work. Therefore, design models should include the assessment of cross-sectional failure of fasteners under combined stresses, such as the induced normal stresses generated by the developing rope effect.

1.2 Motivation

The challenges outlined above underline the need to advance our understanding of fastener behaviour in high-density timber products. Although current knowledge captures some aspects of connection performance, it does not fully explain the combined effects of normal, shear, and bending stresses in the fastener cross-section. As a result, the conditions leading to brittle rupture remain poorly understood.

The motivation for this work arises from this gap in understanding. Normal, shear, and bending stresses are not only individually important, but their interaction also plays a crucial role in fastener behaviour. In particular, the rope effect has a positive influence by increasing the overall load-carrying capacity of the connection, but it also has a negative effect by locally increasing the stresses in the fastener. To achieve a holistic understanding, it is therefore essential to determine *when* and *why* cross-sectional failures occur, and under which circumstances these stress interactions govern the overall behaviour of the connection.

By investigating these mechanisms systematically, this work aims to provide a fundamental understanding of fastener failure in high-density timber products. Such knowledge will clarify the critical stress interactions that trigger failure and, as a consequence, provide a scientific basis for the eventual improvement of timber connection design and the development of safe connections.

1.3 Aims

The primary aim of this thesis is to improve the understanding of fastener behaviour in laterally loaded hardwood connections through a combination of experimental and analytical approaches. The study seeks to describe deformation patterns, stress distributions, and mechanisms of failure in fasteners. It aims to make previously unknown phenomena visible and to critically assess common assumptions in connection design. Special attention is given to the effects of connection configuration, fastener geometry, timber density, and differences between hardwood and softwood connections. The work explicitly addresses cross-sectional failure and the interaction of internal forces within fasteners, including bending moments, normal forces, and shear forces, to provide a holistic understanding of failure mechanisms.

Furthermore, the thesis aims to determine previously unquantified strength parameters of fasteners, such as shear capacity and load-bearing behaviour under combined stresses. Particular focus is placed on identifying *when* and *why* cross-sectional failure occurs, and under which conditions it becomes critical for the overall connection behaviour. Based on these findings, an analytical framework is developed to extend conventional design approaches, such as the EYM, by incorporating aspects currently not captured, providing a scientific basis for improved and reliable timber connection design. On this basis, the following research questions (RQ) are formulated and addressed throughout the thesis:

- **RQ1: Is the current understanding of fastener behaviour suitable for high density hardwood, and how does it differ from softwood?**
- **RQ2: Which factors influence fastener failure under combined bending, normal, and shear forces occurring in the fastener?**
- **RQ3: When and why does cross-sectional fastener failure occur?**

- **RQ4: How can experiments and analysis contribute to a holistic understanding of fastener behaviour under lateral loading?**
- **RQ5: How can the findings extend design approaches for new failure modes and material behaviour?**

1.4 Structure of the Thesis

To address the research questions and achieve the objectives described above, the thesis is structured as shown in Fig. 1.2.

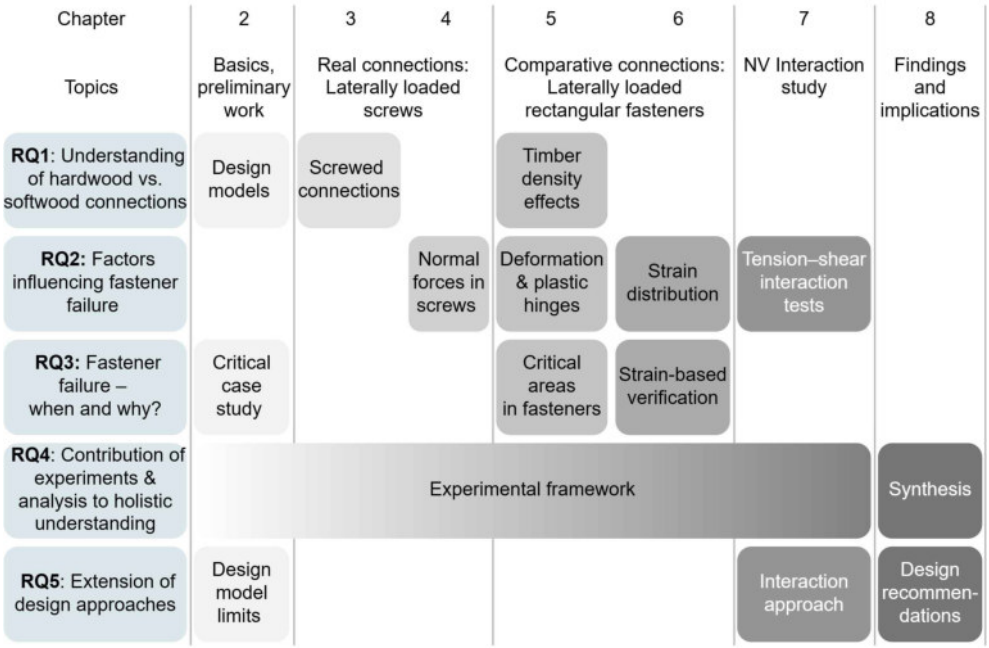

Fig. 1.2: Flowchart for content.

Chapter 2 provides a review of current design models for laterally loaded fasteners, highlighting their limitations and identifying gaps in knowledge. This chapter also introduces fundamental principles of steel design, which are later referenced to transfer insights to fasteners in timber connections. Preliminary investigations are

included to illustrate the problem more clearly and to establish the starting point of the present work in relation to existing engineering knowledge.

Chapters 3 and 4 focus on typical connections using partially and fully threaded screws. They examine general differences in connection behaviour between softwoods and hardwoods, as well as the deformation behaviour of the fasteners themselves, which is affected by the higher stresses in hardwood. Chapter 3 presents experimental investigations on standard connections using partially threaded screws in spruce, birch, and beech, considering both mechanical performance and practical aspects of assembly, such as predrilling, spacing, and stiffness. Tests include single-screw connections as well as screw rows and groups. Chapter 4 addresses the measurement of strains in fully threaded screws using embedded cylindrical strain gauges. This novel method for laterally loaded fasteners is evaluated in terms of its applicability. By positioning the gauges at different locations along the fastener, the study provides insights into the distribution of normal forces and their development with increasing load.

Chapters 5 and 6 present a comparative study of rectangular fasteners. The aim is to visualise deformations and strains in the fastener during connection loading and to identify highly stressed regions depending on the timber product used. Chapter 5 focuses on the deformation behaviour and the influence of connection parameters, such as timber density, fastener strength, and the distinction between timber-to-timber and timber-to-steel connections. The analysis includes the development of bending angles and the position of plastic hinges during progressive loading. Chapter 6 presents the results of strain measurements, which support the identification of critical regions and demonstrate how higher timber density can alter the stress state in fasteners, potentially leading to cross-sectional failure.

Chapter 7 introduces the experimental setup for assessing the interaction between tensile and shear forces in fasteners, presenting results for fully threaded screws, partially threaded screw shanks, and bolts. The chapter proposes a method to incorporate this type of interaction into design considerations, addressing a gap in existing knowledge regarding interaction parameters for typical timber fasteners.

Chapter 8 synthesises the results and highlights the significance of the findings and insights from Chapters 2 to 7. Recommendations for accounting for fastener failure in the design of connections are presented.

Finally, the outlook presents further experimental ideas for other interactions that may occur in fasteners, serving as inspiration for future investigations and extensions of the present work.

2 Background and Preliminary Work

2.1 Laterally Loaded Fasteners in Timber Structures – State of the Art

An outline of the fundamental equations used for connection design in timber engineering is presented at the beginning of this thesis to provide a conceptual introduction. This is the design model, of which the validity and applicability to hardwood connections is questioned and examined in the course of the work. In addition, in the end, this model is provided with supplementary suggestions based on the results and findings of the investigations. This overview also serves as a reference for later calculations and comparisons. The fundamental assumptions and design concepts for determining the load-bearing capacity of timber connections and individual fasteners are, in both the current Eurocode 5 [118] and the new draft version [128], derived from the Johansen equations [50] and additions concerning the rope effect. These provide the basis for calculating the dowel-effect contribution per shear plane [128]:

$$F_{\mathrm{D,k}} = \min \begin{cases} f_{\mathrm{h,1,k}}\, t_{\mathrm{h1}}\, d & \text{(a)} \\ f_{\mathrm{h,2,k}}\, t_{\mathrm{h2}}\, d & \text{(b)} \\ \dfrac{f_{\mathrm{h,1,k}}\, t_{\mathrm{h1}}\, d}{1+\beta}\left[\sqrt{\beta + 2\beta^2\left[1+\dfrac{t_{\mathrm{h2}}}{t_{\mathrm{h1}}}+\left(\dfrac{t_{\mathrm{h2}}}{t_{\mathrm{h1}}}\right)^2\right]+\beta^3\left(\dfrac{t_{\mathrm{h2}}}{t_{\mathrm{h1}}}\right)^2}-\beta\left(1+\dfrac{t_{\mathrm{h2}}}{t_{\mathrm{h1}}}\right)\right] & \text{(c)} \\ 1.05\,\dfrac{f_{\mathrm{h,1,k}}\, t_{\mathrm{h1}}\, d}{2+\beta}\left[\sqrt{2\beta(1+\beta)+\dfrac{4\beta(2+\beta)M_{\mathrm{y,k}}}{f_{\mathrm{h,1,k}} d t_{\mathrm{h1}}^2}}-\beta\right] & \text{(d)} \\ 1.05\,\dfrac{f_{\mathrm{h,1,k}}\, t_{\mathrm{h2}}\, d}{1+2\beta}\left[\sqrt{2\beta^2(1+\beta)+\dfrac{4\beta(1+2\beta)M_{\mathrm{y,k}}}{f_{\mathrm{h,1,k}} d t_{\mathrm{h2}}^2}}-\beta\right] & \text{(e)} \\ 1.15\sqrt{\dfrac{2\beta}{1+\beta}}\,\sqrt{2M_{\mathrm{y,k}} f_{\mathrm{h,1,k}} d} & \text{(f)} \end{cases} \tag{2.1}$$

with

- $F_{D,k}$ Characteristic value of the dowel-effect contribution per shear plane
- $f_{h,i,k}$ Characteristic embedment strength of timber part *i*
- $t_{h,i}$ Embedment depths of members *i*
- d Diameter of the dowel
- $M_{y,k}$ Characteristic yield moment
- β Ratio of the characteristic embedment strengths $f_{h,2,k}/f_{h,1,k}$

For a design value a rope-effect contribution can be added for failure modes (c–f) in Eq. 2.1 [128]:

$$F_{rp,d} = \min \begin{cases} k_{rp,1}\, F_{ax,t,d} \\ k_{rp,2}\, F_{D,d} \end{cases} \tag{2.2}$$

with

- $k_{rp,1}$ Factor for the rope effect (0.25 general)
- $F_{ax,t,d}$ Design tensile resistance (minimum of head pull-through, withdrawal and tensile resistance)
- $k_{rp,2}$ Limitation factor for the rope effect (e.g. 0 for dowels, 1.0 for screws)
- $F_{D,d}$ Design dowel-effect contribution determined with Eq. 2.1

Although differences exist between the code versions, such as the unification of equations for timber-to-timber and timber-to-steel connections, the equations acc. to Johansen [50] still form the basis for the design of connections. When neglecting conversion factors (1.05 and 1.15) as well as the reference factor β, the two key design parameters remain the embedment strength $f_{h,i,k}$ and the yield moment $M_{y,k}$. These reflect the dominant mechanisms considered in the design model and the associated failure modes: embedding and deformation in the timber, and bending failure, i.e. plastic hinge formation, of the fastener. Within the scope of the rope effect, the axially acting resistances are also taken into account. This includes the resistances acting between timber and fastener, i.e. head pull-through and withdrawal, as well as the tensile capacity of the fastener itself. These resistances create friction in the shear plane. Consequently, the components of the connection are designed for the individual stresses and forces acting on them; however, a comprehensive consideration of the multiaxial stress state of the fastener is not yet included in current design approaches.

The following section will therefore provide an introduction to these stress states and present possible methods for describing the occurring fastener stress states.

2.2 Plastic Design of Steel Structures – State of the Art

2.2.1 Historical Outline of Elastic and Plastic Design Approaches - Yield Criteria

The development of plastic design methods for structural systems originates from early concepts of *plastic hinges* and *collapse mechanisms* [52, 53]. These ideas enabled the determination of the maximum load capacity of statically indeterminate systems by considering material yielding and the redistribution of internal forces.

Before the emergence of plastic design concepts, the assessment of load-carrying capacity was dominated by elasticity-based approaches that relied on Hooke's law and allowable-stress design. Pioneering works by Engesser [34] and Timoshenko [100] gradually relaxed these assumptions by considering elastic-plastic effects and e.g. shear deformations in beams. Their analyses revealed that structural members are capable of sustaining additional loads beyond the elastic limit, thus motivating later research on plastic redistribution and collapse mechanisms.

The first systematic plastic design approach was introduced by Kazinczy [53] in 1914 for continuous beams. He emphasised that, when determining the true capacity of statically indeterminate structures, permanent deformation of the steel must be considered. His assumptions included an idealised stress-strain curve of the material, that the cross-section remains plane during deformation, and that yielding gradually progresses from the outer fibres toward the neutral axis. The concept of a plastic hinge implies theoretically infinite curvature (i.e. unrestricted rotation at constant moment) at the plastic hinge location, which is of course an idealisation, since the material strains remain finite.

Hill [45, 46] formulated a general theory of plastic flow for anisotropic materials, extending the isotropic von Mises yield criterion [104]. His work demonstrated that yielding depends on the combined action of all stress components, meaning that the presence of one component influences the critical value of others. Although Hill

did not explicitly analyse combined stress cases such as bending-shear or tension-bending interaction, his framework implies that such stress combinations are critical for yielding and influence the formation and location of plastic zones (later influencing generalised yield criteria such as Drucker-Prager [29]).

Plastic Hinge and Limit Theorems
The concept of plastic hinge theory states that the load-bearing capacity of a statically determinate system is reached once a single plastic hinge forms and the cross-sectional reserves are fully utilised. In statically indeterminate systems, additional capacity is mobilised by the formation of further plastic hinges until the structure becomes a mechanism and the ultimate load is reached. This concept assumes that the cross-sectional load-bearing capacity is determined by the fully plastic moment M_{pl}, corresponding to a rectangular stress distribution [26].

Ultimate Load – Plastic Limit State
The ultimate load method aims to determine the maximum load a structure can sustain before collapse. In first-order theory, the ultimate load defines the plastic limit state, which satisfies the following conditions:

- Equilibrium,
- Material condition $|M| \leq |M_{\text{pl}}|$,
- Kinematic mechanism reached,
- Positive dissipation work $D > 0$.

When all four conditions are met, the ultimate load has been attained [26]. This state represents the transition from a statically stable to a kinematically unstable configuration.

Lower Bound – Static Limit State
A statically admissible equilibrium state can exist as long as no kinematic mechanism has formed. Such a state may be entirely elastic or may include local plastic hinges, as long as these do not form a complete mechanism that would cause collapse. The following conditions apply:

- Equilibrium,
- Material condition $|M| \leq |M_{\text{pl}}|$.

Any state fulfilling these two requirements represents a lower bound to the true collapse load and is therefore equal to or smaller than the ultimate load [26]. In other words, the lower-bound theorem yields a safe estimation of the collapse load: as long as these conditions hold, the structure remains stable.

Upper Bound – Kinematic Limit State
If the applied load exceeds the true load-bearing capacity, a kinematic chain (mechanism) must develop, accompanied by positive dissipation work. Because equilibrium is not necessarily satisfied, local bending moments may temporarily exceed M_{pl}. According to Greenberg and Prager [30] an upper limit of the load is obtained when the following conditions are satisfied:

- Kinematic mechanism reached,
- Positive dissipation work $D > 0$.

All states fulfilling these three requirements are kinematically admissible, and the corresponding load represents an upper bound to the true load-bearing capacity. Thus, the upper-bound theorem provides an unsafe estimation: it overpredicts the actual collapse load if the assumed mechanism does not fully represent reality. Comprehensive formulations and applications of these theorems for structural systems are given by Chen and Han [20].

Experimental validation was provided by Roderick [80] and Horne [47]. Roderick [80] investigated pure bending and found that the simple plastic hinge theory provides accurate predictions under typical transverse loading, since shear effects are generally small. At that time, it was assumed that shear stresses in ordinary structural members were significantly lower than the magnitudes required to affect collapse behaviour. He suggested, however, that under very high shear the yield load is slightly reduced, whereas the collapse load remains almost unaffected.

Horne [47] extended this work and referred explicitly to Roderick's findings. He showed that the simple plastic hinge theory yields accurate stress distributions except near fully plastic regions in beams subjected to combined bending moments and shear forces. Shear slightly reduces the full plastic moment, but this effect is generally negligible except in very short beams. For illustrative rectangular or I-shaped sections, a reduction in moment capacity was observed for length-to-depth ratios below 0.456 (depth is height if member/beam). Below this limit, the entire cross-section yields, and no clear separation of bending and shear plastic zones occurs. The reduction in

capacity is more pronounced for I-sections than for rectangular ones, although the difference becomes significant only for length-to-depth ratios less than 4.

Drucker [28] applied similar principles to specific structural problems, studying the effect of shear on plastic bending and the stability of plastic flow in beams. A comprehensive consolidation of the theory, including yield criteria, flow rules, and limit analysis methods for structural systems, was later provided by Prager and Neal [73]. Prager's work remains a standard reference for understanding plastic hinges, collapse mechanisms, and ultimate load analysis in engineering structures.

The theoretical foundations of plasticity, from the early work of Drucker et al. [30] and Prager and Neal [73], provide the basis for modern limit analysis and plastic design in engineering. The general Drucker-Prager yield function accounts for hydrostatic and deviatoric stresses and is therefore applicable to materials with pressure-dependent yielding, such as soils or concrete.

In structural steel members, however, the material behaviour under typical loading is nearly pressure-independent. As a result, the von Mises yield criterion suffices for practical design. Plastic cross-section capacities under combined bending, normal force, and shear (*MNV*) are determined using this approach. Design rules and interaction formulas are implemented in standards such as DIN 18800-1 [113] and Eurocode 3 [116], often in the form of reduced moment capacities or interaction tables that account for the effects of shear and normal force on the plastic moment.

For connection elements (bolts, screws), the dominant stress components are normal and shear forces (*NV*), while bending is usually negligible. Interaction formulas are used to prevent shear or tensile failure, sometimes including minor bending effects for slender fasteners. While the theoretical foundation is general, the practical implementation differs between structural levels. For cross-sections, an *MNV* interaction following the von Mises criterion and plastic design principles as defined in the relevant standards is adopted. In contrast, the design of connections relies on simplified plastic analyses considering primarily the dominant *NV* interaction.

This illustrates how historical plasticity theory has evolved into current steel design practices, linking classical limit theorems with modern regulations and computational methods for safe and efficient structural design.

2.2.2 Internal Forces and Moments in Circular Cross-sections

Simultaneously acting internal forces and moments influence each other. The moment resistance M_{pl} of a cross-section is strongly influenced by large normal forces N. The shear forces V present in common structural components have a comparatively small influence on the maximum bending strength M_{pl}, see Dinkler [26]. However, they can also result in a reduction of plastic moments. Assuming the cross-section is perpendicular to the neutral axis, simultaneous bending moment M and normal force N produce a linear strain distribution and corresponding stress distribution across the section.

The progression of stress distributions with linear strain distribution for a circular cross-section is shown in Fig. 2.1. If the ratio of moment M to normal force N remains constant during the transition from elastic to plastic limit state, the position of the zero strain line shifts due to the changes in stiffness in the section during plasticising. However, the effect on the overall load bearing behaviour of the structure is estimated to be negligible [20, 26].

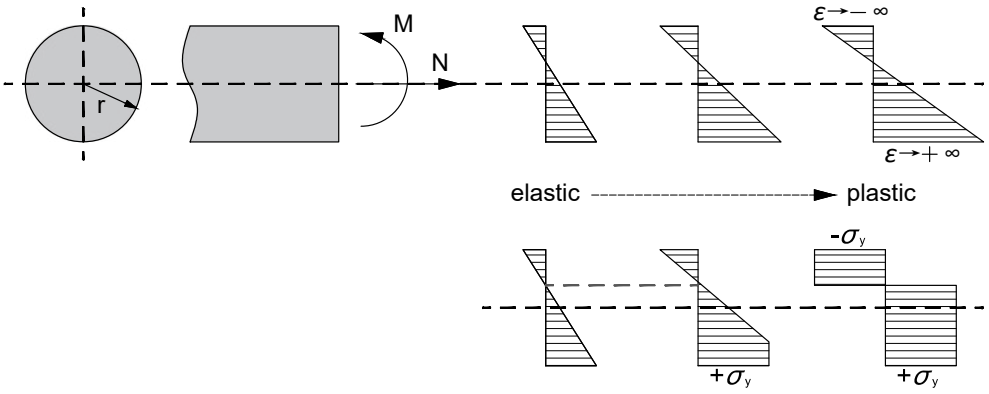

Fig. 2.1: Linear strain and stress distributions for a circular cross-section.

Stresses caused by the normal force and the bending moment can be assigned to separate parts of the cross-section in the stage of complete plasticity. The outer areas are assigned to the bending moment, as only there are the necessary compressive and tensile stresses to generate a corresponding bending moment. The stresses in the area of the beam axis, on the other hand, are assigned to the normal force

[26]. With a yield condition, the relation between the normal force and the associated bending moment can be described.

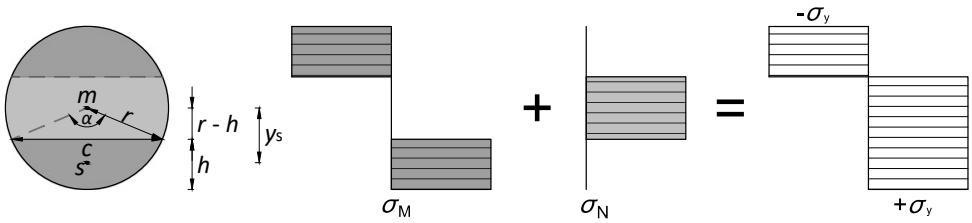

Fig. 2.2: Fully plasticised circular cross-section with stress distribution and division into moment and normal force components.

with

$c = 2\ r \cdot sin(\frac{\alpha}{2})$	Chord length
$y_s = \frac{c^3}{12 \cdot A}$	Center of the circle segment
$A = \frac{r^2}{2} \cdot (\alpha - sin(\alpha))$	Area of circle segment

Possible acting and plastic variables bearable for the circular cross-section are:

Bending moment
$$M_{y,c} = \text{area} \cdot \text{lever arm} \cdot \sigma_y = 2 \cdot A \cdot y_s \cdot \sigma_y = 2 \cdot \frac{A \cdot c^3}{12 \cdot A} \cdot \sigma_y = \frac{c^3}{6} \cdot \sigma_y \quad (2.3)$$

Normal force
$$N_{y,c} = \text{area} \cdot \sigma_y = (\pi r^2 - 2A) \cdot \sigma_y = r^2 \cdot [\pi - (\alpha - \sin(\alpha))] \cdot \sigma_y \quad (2.4)$$

Plastic bending moment
$$M_{y,c,pl} = \frac{d^3}{6} \cdot \sigma_y \quad \text{with circle diameter } d \quad (2.5)$$

Plastic normal force
$$N_{y,c,pl} = \pi r^2 \cdot \sigma_y \quad (2.6)$$

In order to derive the yield condition for the circular cross-section, the occurring elastic variables are each set in relation to their corresponding plastic limit values.

$$\frac{M_{\mathrm{y,c}}}{M_{\mathrm{y,c,pl}}} = \left[\sin\left(\frac{\alpha}{2}\right)\right]^3 \tag{2.7}$$

$$\frac{N_{\mathrm{y,c}}}{N_{\mathrm{y,c,pl}}} = 1 - \frac{\alpha - \sin(\alpha)}{\pi} \tag{2.8}$$

Thereby, the blue marked α is to be used in radians. Considering simultaneously acting moment and normal force leads to an interaction criterion assuming a full exploitation of the cross-section. It can be formulated as:

$$\left[\frac{M_{\mathrm{y,c}}}{M_{\mathrm{y,c,pl}}}\right]^x + \left[\frac{N_{\mathrm{y,c}}}{N_{\mathrm{y,c,pl}}}\right]^y \leq 1.0 \tag{2.9}$$

The exponents are given by variables x and y as they may be chosen individually. To demonstrate the dependency of the two terms, they are visualised in Fig. 2.3. Thereby, an angle α of 180° equals a full exploitation of the cross-section by a bending moment without an acting normal force (in blue) and vice versa for an angle α of 0° (in grey). These separately illustrated ratios can be combined acc. to equation 2.9.

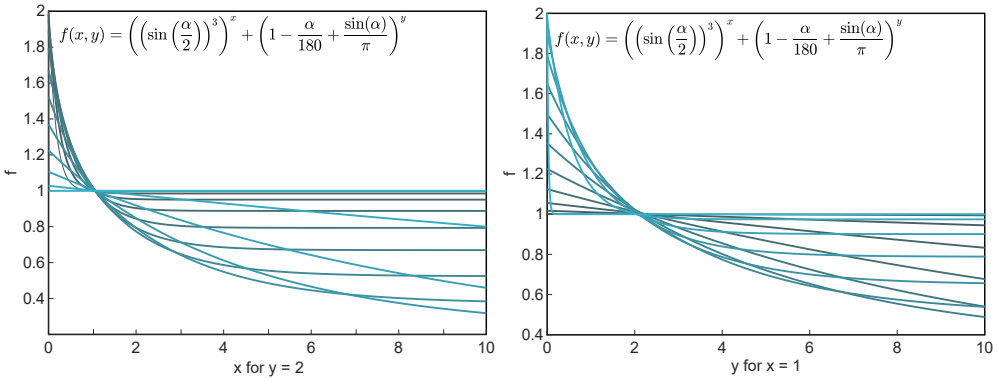

a. Function over exponent x.

b. Function over exponent y.

Fig. 2.3: Illustration considering different exploitations of a circular cross-section. α is to be used in degrees.

2.2.3 Implicit Formulation

For a circular cross-section under combined bending moment *M* and normal force *N*, the fully plastic stress distribution allows the derivation of an implicit relation *M(N)*. The basic geometric and material parameters are the circle radius *r* and the yield stress σ_y. Assuming a linear strain distribution over the cross-section, the proportion of the circular segment under compression or tension is defined by the angle α, which depends on the applied normal force *N*. The implicit relation between α and *N* is given by

$$\alpha - \sin\alpha = \pi \left(1 - \frac{N}{N_{pl}}\right), \tag{2.10}$$

where $N_{pl} = \pi r^2 f_y$ denotes the plastic normal force of the full cross-section. Eq. (2.10) generally cannot be solved analytically, and α must be determined numerically for a given *N*. Once $\alpha(N)$ is known, the corresponding bending moment is obtained from

$$M(N) = \frac{4}{3} r^3 f_y \sin^3\left(\frac{\alpha(N)}{2}\right), \tag{2.11}$$

which represents the moment capacity of the section as a function of the axial load. A similar approach is outlined by Pyykkö and Svensson [74], but the assumptions differ. Due to a different definition of the angle α, the formula differs, but remains mathematically identical.

Special Cases

- For $N = 0$, the full cross-section contributes to bending, giving $\alpha = \pi$ and $M = M_{pl}$.
- For $N = N_{pl}$, the entire section is in tension or compression, implying $\alpha = 0$ and $M = 0$.

In practice, $\alpha(N)$ is obtained by solving Eq. 2.10 numerically for each value of *N*, e.g. using a root-finding algorithm. This procedure yields a smooth curve *M(N)* that can be used for interaction diagrams or comparison with approximate analytical expressions of the form

$$\left(\frac{M}{M_{pl}}\right)^x + \left(\frac{N}{N_{pl}}\right)^y = 1.0 \tag{2.12}$$

where the exponents x and y are chosen to best fit the numerical solution. This approach allows a direct visualisation of the bending-normal force interaction, see Fig. 2.4.

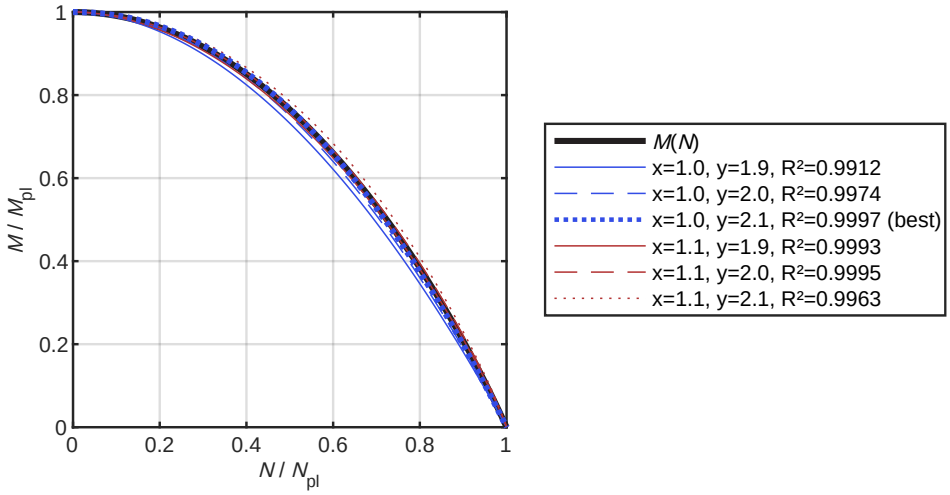

Fig. 2.4: Illustration and best fit for $M(N)$.

A slightly better fit for the normal force could be achieved with $y \approx 2.1$, but for simplicity and consistency, $y = 2$ is adopted. The implicit *M(N)* curve visualises the full exploitation of the circular cross-section under combined bending and normal force, providing the basis for 3D interaction surfaces including shear V.

Remarks

- The implicit formulation captures the plastic behaviour of the circular cross-section, avoiding approximations inherent in power-law interaction formulas.
- The curve *M(N)* corresponds to the numerical solution plotted in the previous figures and is used as reference for fitting analytical expressions with adjustable exponents.
- This formulation assumes a full plastic utilisation of the cross-section and neglects local effects such as partial yielding, shear lag, or stress concentrations.

During an interaction, different internal forces and moments can be related to each other in different ways. In Fig. 2.5a all three components contribute fully to the plastic limit surface, which is described by

$$\frac{M}{M_{\mathrm{pl}}} + \left(\frac{N}{N_{\mathrm{pl}}}\right)^2 + \left(\frac{V}{V_{\mathrm{pl}}}\right)^2 = 1.0. \tag{2.13}$$

Bending enters linearly, while normal and shear contributions are quadratic, reflecting the dominant influence of bending.

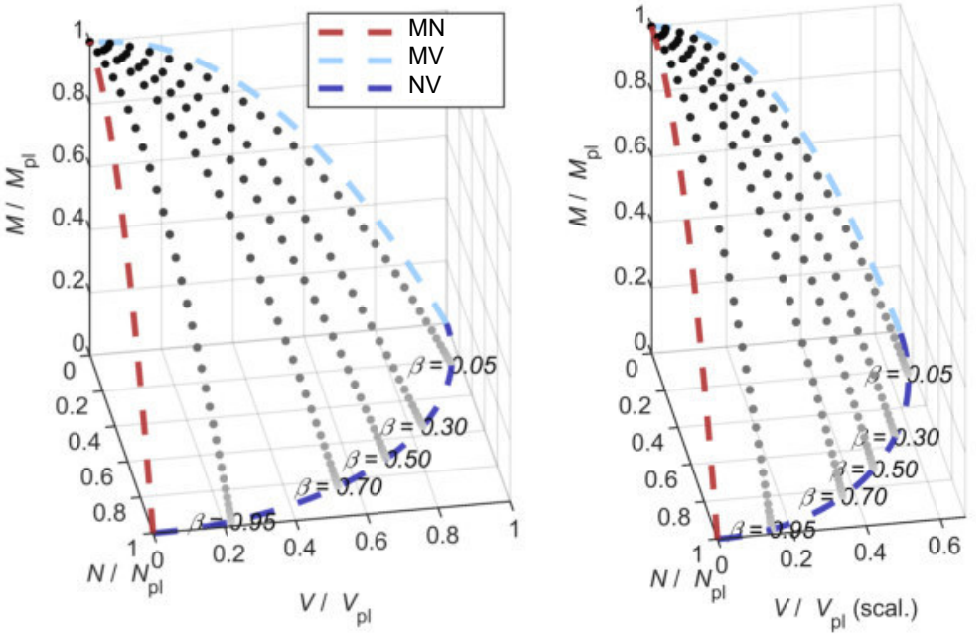

a. Full contribution to plastic limit surface, k = 1.0.

b. Scaled shear component with k = 2/3.

Fig. 2.5: Illustration of interaction for a circular cross-section acc. to Eq. 2.13, surface approximates the plastic limit state.

The 3D illustration in Fig. 2.5 visualises the combined interaction of bending moment M, normal force N, and shear force V. The parameter β_1 defines the proportion between normal and shear components,

$$\beta_1 = \frac{N^2}{N^2 + V^2}, \tag{2.14}$$

and shifts the points along the *NV* plane: Low β values correspond to higher shear contributions, while high β indicate dominant normal contributions. The squares in Eq. (2.13) reflect that the normal and shear components contribute independently to the overall interaction in that case. In Fig. 2.5b, the shear component is scaled by the factor k to account for reduced plastic shear capacity: k = 2/3 for Tresca, $k \approx 0.577$ for von Mises, and $k = 1.0$ for the idealised case. Scaling by k compresses the surface along the *V*-axis, slightly reducing the attainable bending moment under combined *N* and *V*. Overall, the surface represents a *MNV* interaction criterion, illustrating the combined effect of bending, normal and shear forces on the plastic load-bearing capacity and the admissible internal force combinations within the fully plastic range. However, a more conservative assumption, in the form of

$$\frac{M}{M_{\mathrm{pl}}} + \left(\frac{N}{N_{\mathrm{pl}}} + \frac{V}{V_{\mathrm{pl}}} \right)^2 = 1.0, \tag{2.15}$$

is frequently applied in practice [117]. Accordingly, a modified formulation arises, as illustrated in Fig. 2.6.

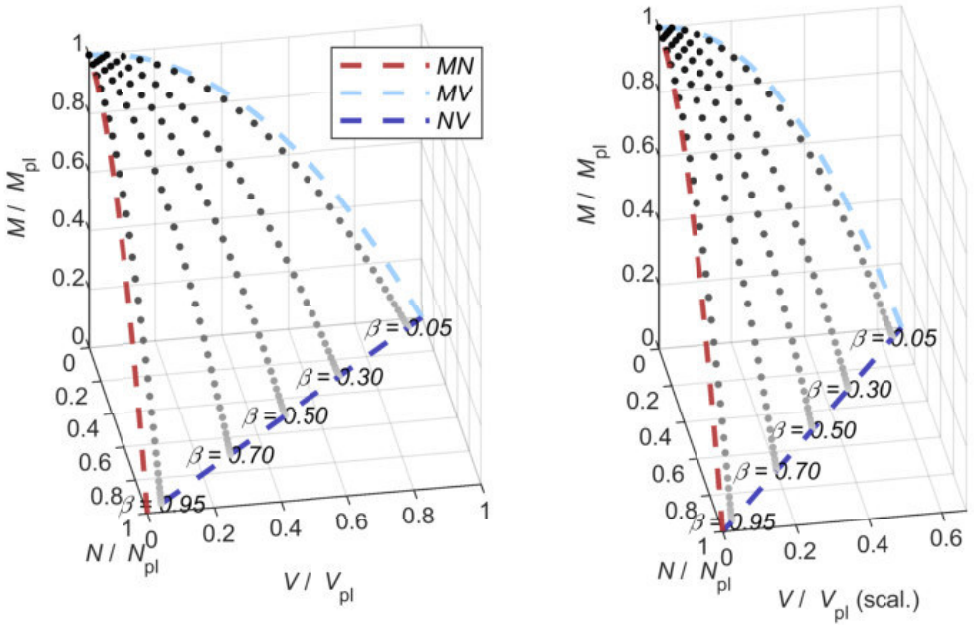

a. Full contribution to plastic limit surface, k = 1.0.

b. Scaled shear component with k = 2/3.

Fig. 2.6: Illustration of interaction for a circular cross-section acc. to Eq. 2.15, surface approximates the plastic limit state.

In this framework, the contribution of the normal and shear forces is described by the load share parameter β_2, defined as

$$\beta_2 = \frac{N}{N+V}, \tag{2.16}$$

where N and V denote the normalized axial and shear components, respectively. The principles of combined bending, normal and shear interactions in steel cross-sections provide a basis for understanding the load-bearing behaviour of fasteners in timber connections, as discussed in the following section.

2.3 Transfer of Interaction Mechanisms to Fasteners in Timber Connections

Building on the understanding of internal force interactions in steel cross-sections, similar principles can be applied to dowel-type fasteners in timber connections. Current design rules according to Eurocode 5 [118] provide guidelines for softwood and hardwood connections, taking into account the density or other input parameters such as embedment, withdrawal, and head pull-through resistances. These differences result in higher stresses in the fasteners and require careful consideration when transferring interaction concepts from steel to timber fasteners. The following section explores this transfer in detail.

Softwoods and hardwoods differ primarily in density, fibre structure, and mechanical properties, which significantly affect the load-bearing behaviour of fasteners in timber connections. Hardwood typically exhibits higher density and strength due to a larger proportion of latewood and thicker cell walls, whereas softwood is generally less dense and has comparably lower strength. These differences influence embedment, withdrawal, and head pull-through resistances, as well as overall connection behaviour. Consequently, the induced internal forces and stress distributions in the fastener cross-section are affected, resulting in significantly higher stresses for fasteners in hardwood compared to softwood. Consequently, understanding the material-specific response is essential for applying the interaction principles of internal forces and moments previously discussed for steel cross-sections to timber fasteners, as will be elaborated in the next section.

To describe the stresses on fasteners in timber connections, a dowel-type fastener is considered as a beam component subjected to stresses perpendicular and parallel to its axis. Normal forces and bending moments induce normal stresses in the cross-section, while shear forces generate shear stresses. For typical steel cross-sections, e.g. I-sections, additional effects such as warping torsion and primary or secondary moments appear. These are neglected here in the simplified analysis of a round solid cross-section. In plasticity calculations, a distinction is made between a critical load leading to the yield strength and a load corresponding to the ultimate capacity. Plastic yielding is generally avoided in typical timber structures, except when intended to activate the load-bearing mechanism, e.g. via formation of plastic hinges or embedment deformations in timber fasteners. A clear definition of plastic load-bearing capacity is challenging. Early approaches by Drucker et al. [30] considered ideal-plastic materials, leading to the *lower-bound theorem* [28] which identifies equilibrium stress states that do not violate the yield condition, see Section 2.2.1. Kindmann and Frickel [54] summarise studies on ultimate loads and limitations from simultaneous internal force interactions. Material hardening further complicates experimental verification, especially at large strains [102]. A common simplification is the reduction of the yield strength f_y to account for combined stresses [62]. Assuming a constant shear stress τ over the cross-section, the von Mises equivalent stress $\sigma_v = f_y$ is converted to the normal stress σ_x as:

$$f_{y,red} = \sigma_x = f_y \cdot \sqrt{1 - \left(\frac{\tau}{\tau_R}\right)^2} \qquad [62] \qquad (2.17)$$

with

$f_{y,red}$ Reduced yield strength
f_y Yield strength
τ Shear stress
τ_R Shear strength

Eq. 2.17 represents current practice and is used, e.g. in elastic analyses of steel cross-sections. Plastic cross-section analyses are commonly limited to the yield strength according to Eurocode 3 Part 1-1 [116]. A different approach can be found for steel construction fasteners. The load-bearing capacity of fasteners is determined using shear and tensile design values, $F_{v,Rd}$ and $F_{t,Rd}$, according to Eurocode 3 Part 1-8 [117]. Combined shear and tensile loads are checked as:

$$\frac{F_{\text{v,Ed}}}{F_{\text{v,Rd}}} + \frac{F_{\text{t,Ed}}}{1.4 \cdot F_{\text{t,Rd}}} \leq 1.0 \tag{2.18}$$

with

$F_{\text{v,Ed}}$ Design shear force
$F_{\text{v,Rd}}$ Design shear capacity
$F_{\text{t,Ed}}$ Design normal force
$F_{\text{t,Rd}}$ Design tensile capacity

Bending stresses in the fasteners are neglected, as dowel-type fasteners are embedded in steel plates along their entire length. A key difference between Eurocode 3 [116] and Eurocode 5 [118] is the material property basis: steel design uses yield strength, whereas timber fasteners rely on ultimate strength parameters such as f_{u} and yield moment M_{y} determined in plastic states. Non-homogeneous strength distributions across the fastener cross-section further complicate detailed analyses [78], and timber fasteners generally lack a well-defined yield strength [81]. Failure of the fastener cross-section can be described using an interaction of internal forces, considering plastic or ultimate strengths rather than conventional yield criteria. The bending moment M, shear force V, and normal force N interact, as illustrated in Fig. 2.7. Each internal force is assigned a proportionate cross-section area (method of partial internal forces, see [54]). Full cross-section utilisation corresponds to the case that every fibre reaches the yield strength f_{y}, i.e. the load-bearing capacity for steel cross-sections. The underlying assumption is ideal plastic behaviour of the material. Simultaneous action of forces can reduce the cross-section capacity.

For timber connections, the rope effect, caused by inclined fasteners or inclined fastener sections, increases the load-bearing capacity through additional friction and force components [13]. Eurocode 5 [118] specifies typical values, but actual normal forces, especially in the shear plane of laterally loaded fasteners, may be significantly higher [12]. Normal forces of arbitrary magnitude are conceivable under combinations

of internal forces according to the lower-bound theorem. These can be described and checked for circular fasteners using the following interaction term [15]:

Interaction term

$$\frac{M}{M_y} + \left(\frac{N}{F_{tens}} + \frac{V}{F_{shear}}\right)^2 \leq 1.0 \tag{2.19}$$

with

M	Occurring bending moment
M_y	Yield moment
N	Occurring normal force
F_{tens}	Tensile capacity
V	Occurring shear force
F_{shear}	Shear capacity

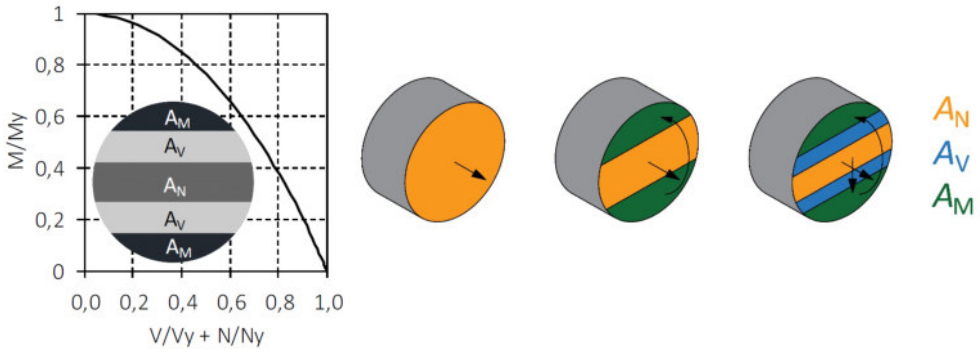

a. Interaction diagram from Blaß et al. [15].

b. Allocation of internal forces in cross-section.

Fig. 2.7: Interaction of internal forces *M*, *N* and *V*, and allocation of partial cross-section areas in a circular fastener depending on the occurring forces and moments.

To illustrate the application to fasteners, two cases are presented here that highlight the critical points. The interaction of internal forces is demonstrated using the example of double-shear steel-to-timber connections (see Fig. 2.8).

For failure mode in Fig. 2.8a, the embedment strength f_h is achieved over the entire middle timber thickness. The moment in the shear plane M_{sp} is smaller than the yield moment M_y of the fastener. Consequently, only elastic deformations of the fastener

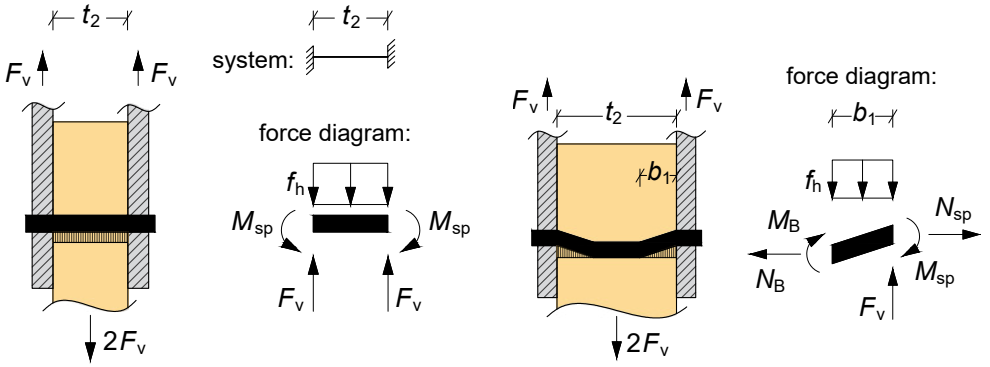

a. Embedment failure in middle timber.

b. Formation of two plastic hinges.

Fig. 2.8: Force diagrams of investigated connections with outer steel plates. Deformed connections and acting internal forces and moments.

can occur. In the shear plane, there is an internal force interaction between shear force V (= load-bearing capacity per shear plane F_v) and moment M_{sp}, assuming that the fastener is clamped in the steel plate on both sides. The second failure mode in Fig. 2.8b shows the failure of the connection with the formation of two plastic hinges per shear plane, i.e. M_y has been reached and the embedment strength f_h has been reached in the inclined section of the fastener. The force diagram only considers the inclined section of length b_1 between the two plastic hinges. Due to the inclined position of the fastener, additional normal forces arise here, which differ between the inner plastic hinge in the centre timber, N_B, and in the shear plane, N_{sp}. The equilibrium can now be formed at the force diagram of failure mode a:

Equilibrium of forces:
$$F_v = 0.5 \cdot f_h \cdot d \cdot t_2 \tag{2.20}$$

Equilibrium of moments:
$$M_{sp} = \frac{f_h \cdot d \cdot {t_2}^2}{12} \tag{2.21}$$

with

F_v Load per shear plane in N

f_h Embedment strength in N/mm²

d Dowel diameter in mm

t_2 Middle timber thickness in mm

M_{sp} Bending moment in shear plane in Nmm

Based on the defined interaction term in Eq. 2.19, a limit for the highest bearable shear force V can be formulated, which corresponds to the load-bearing capacity per shear plane F_v (with F_{shear} = shear capacity and M_y = yield moment of the fastener). Thereby, the normal force component is neglected as it is assumed to be zero.

$$\frac{M_{sp}}{M_y} + \left(\frac{F_v}{F_{shear}}\right)^2 \leq 1.0 \qquad \Leftrightarrow \qquad F_v \leq F_{shear} \cdot \sqrt{1 - \frac{f_h \cdot d \cdot {t_2}^2}{12 \cdot M_y}} \tag{2.22}$$

In preliminary studies, see [4], the applicability of the interaction equation given in Eq. 2.19 is examined by means of experimental tests. Failure modes shown in Fig. 2.8 are investigated by enforcing an *MNV* and an *MV* interaction acc. to Eq. 2.19.

2.4 Fastener Failure: Initial Findings

The aim of the executed test programme is to investigate fastener failure in connections with laterally loaded dowels. A key focus is on the influence of the interaction between bending moments, normal forces, and shear forces within the fastener, and how this interaction affects the overall load-bearing capacity of the connection. The study builds on the previously defined steel-to-timber connections (see Fig. 2.8) and examines different failure modes, including embedment and the formation of one or two plastic hinges per shear plane. In addition, fastener failure is intentionally induced in order to identify the conditions under which it occurs. Ultimately, the unknown forces and the knowledge of the deformation behaviour are considered essential for selecting suitable analytical models, including appropriate load-displacement relationships, assumptions regarding the fastener system, and the expected magnitude of internal forces.

2.4.1 Material and Methods

Copper, aluminium, C15 steel, and silver steel dowels with a nominal diameter of $d = 6$ mm are used. The outer steel plates each have a thickness of $t_s = 10$ mm. The middle timber element of the connections consists of either beech laminated veneer lumber (beech LVL) or densified veneer wood (DVW), with varying timber thicknesses to achieve the intended failure modes. The mean densities were in the range of 833 kg/m^3 for beech LVL and 1367 kg/m^3 for DVW.

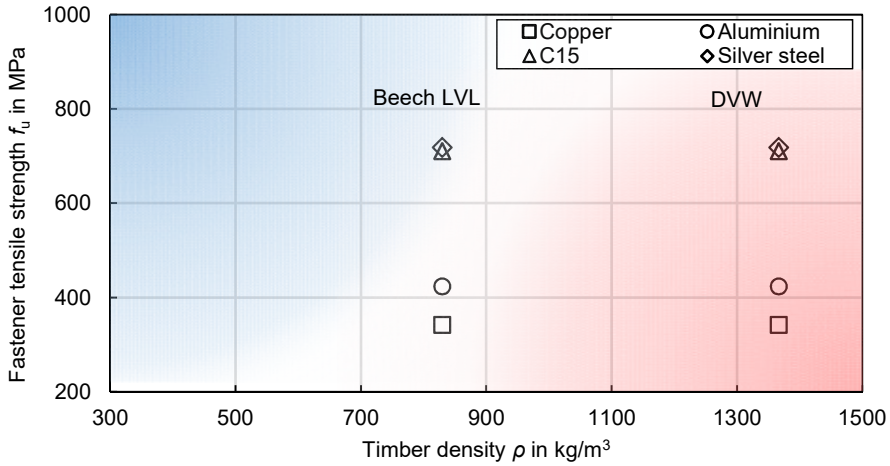

Fig. 2.9: Combination of connection members, sorted by tensile strength of the fastener and density of the timber. Common (blue) and unusual (red) combination of fastener and timber.

The variation in fastener strength and timber density is used methodically to test different configurations and to explore transitions between failure modes. Fig. 2.9 shows the tested combinations. The blue regions correspond to configurations typical for construction practice, whereas the red regions represent connections that are rare or unlikely in reality and are therefore of exemplary character.

2.4.2 Test Setup and Programme

Tailor-made tests investigating the influence of an interaction of internal forces and moments on the load-bearing capacity of connections with laterally loaded fasteners are carried out. By varying two high density timber products, the fastener material as well as the timber thickness, a cross-sectional failure of the dowels is specifically

induced and analysed. The main test programme includes double-shear steel-to-timber connections with thick outer steel plates as shown in Fig. 2.10. The thickness of the timber varies between 20–60 mm. Spacers that generate a gap of 0.5 mm in the shear planes are used to avoid friction between timber and the outer steel plates.

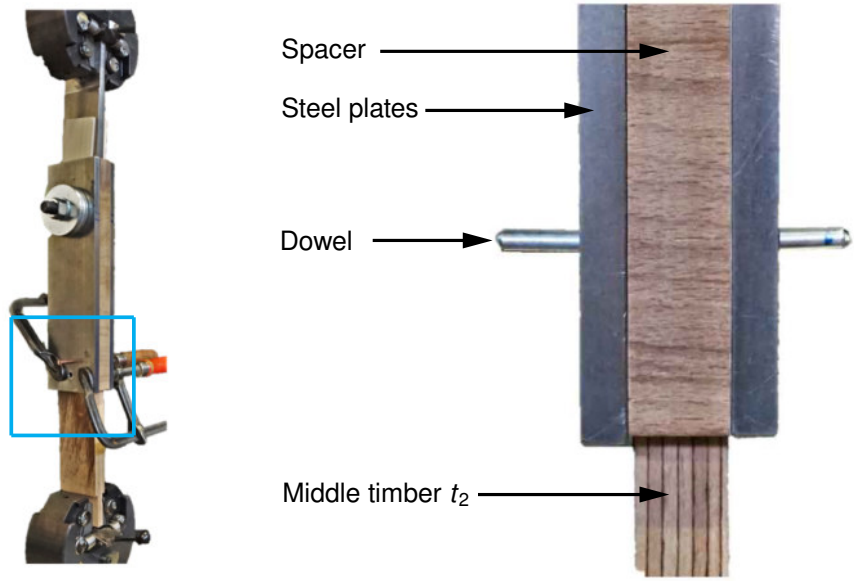

a. Whole test setup.

b. Detail of tested connection with $t_{spacer} > t_2$.

Fig. 2.10: Test setup for double-shear tests with dowels.

For the failure modes studied, Fig. 2.8 provides assumptions and force diagrams with corresponding internal forces and moments acting in the shear plane.

The different possible connection failure modes are:

a) Straight fastener: timber failure due to embedment or timber splitting or a fastener shear failure

b) Inclined fastener: formation of two plastic hinges per shear plane (with simultaneous embedment failure in inclined areas) and a secondary fastener failure in the shear plane

As long as the fastener axis is straight, no normal force develops and an *MV* interaction prevails in the shear plane. With increasing middle timber thickness, a transition to the failure mechanism with plastic hinges is expected. Due to the inclined fastener

axis, normal forces occur that lead to an *MNV* interaction in the shear plane. Hence, the influence of different interactions are investigated.

Two fundamental failure modes are considered for the connections (see Fig. 2.8). In the first failure mode, the fastener remains elastic as the shear plane moment M_{sp} is below the yield moment M_y, and the embedment strength f_h is fully mobilised across the timber thickness. The interaction of bending moment and shear force governs, see Eq. 2.22. In the second mode, Fig. 2.8b, plastic hinges form in the shear plane, reaching both M_y and f_h in the inclined fastener section, generating additional normal forces due to the inclination. The interaction of bending moment, shear force, and normal force governs the equilibrium and the resulting calculation is given in Eq. 2.19.

Tested configurations are listed in Tab. 2.1. Additionally, the shear capacity F_{shear}, tensile capacity F_{tens} and yield moment M_y of the dowels are determined experimentally with ten samples each.

Table 2.1: Test programme.

Number of tests	Beech LVL			DVW		
Timber thickness [mm]	20	30	60	15	30	60
Copper	3	2	1	2	1	
Aluminium	2	1	1	1	1	
Steel C15			2	1	3	1
Silversteel			3	1	2	2

2.4.3 Results

Tab. 2.2 provides the results for material properties determined experimentally. The ratio of F_{shear}/F_{tens} varies from 58–76% for tested metals, whereas a ratio for steel is 58%, i.e. a factor of $1/\sqrt{3}$, see Eurocode 3 [116]. No metals tested showed a distinct yield zone during tensile tests. The yield moment is evaluated at a bending angle of $\alpha = 45°$. Results of the connection tests as well as their failure modes and maximum loads reached in the tests are given in Tab. 2.3 for each specimen.

Fig. 2.11 shows exemplary deformed fasteners in opened specimens. All fasteners failed in the shear plane, but in different ways. The recorded load-machine displacement

Table 2.2: Material properties of tested dowels.

	F_{shear} kN	F_{tens} kN	f_u N/mm^2	M_y (45°)* Nm	F_{shear}/F_{tens} %
Copper	5.62	9.70	342	13.0	58.0
Aluminium	7.40	12.0	424	16.5	61.6
Steel C15	12.6	20.1	711	27.5	62.5
Silversteel	15.5	20.3	719	29.5	76.1

evaluated at a bending angle of 45°

curves are given in the diagrams, see Fig. 2.12, where the initial slip of the machine is eliminated and the curves start at 0.25 kN on the ordinate. To compare the loads achieved in the double-shear connection tests with the shear capacity of the dowels, the results of the shear tests on the dowels are included with grey dots. In DVW, all dowels failed due to shear and for some connections, the maximum loads reach the shear capacity of the dowels. Even higher loads than the pure shear capacity are observed for dowels made of steel C15. However, loads exceeding the shear capacity can be reached if additional friction develops in the shear planes, which suggests that some level of contact must have occurred due to embedment deformation taking place out-of-plane of the shear plane. Another explanation for the higher loads is the inclination of the fastener itself, which leads to vertical force components contributing to the capacity of the connection. A representative example of this phenomenon is a DVW connection with C15 dowels, see Fig. 2.11g, where deformed timber fibres close the gap and thereby generate contact between steel plate and timber surface. This additional contact likely enhances the connection's overall load-bearing capacity. However, these specific tests will not be addressed any further in this study.

In general, lower load-bearing capacities are reached for connections with beech LVL compared to DVW. A peculiarity of some connections with copper and aluminium dowels is the splitting of the test specimens in grain direction, even with increased end grain distances. This only occurred for a timber thickness of 20 mm and is marked with orange dashed lines in Fig. 2.12. In case of fastener inclination, the dominant failure is embedment failure occurring simultaneously with the formation of plastic hinges. Depending on the displacement of the connection and the ratio of embedment strength to fastener strength, fastener failure in the shear plane follows at a later stage (e.g. beech LVL connections in Fig. 2.11). A straight fastener axis, as seen in the DVW connection with copper or aluminium, only allows for embedment failure and/or fastener failure in the shear plane without additional deformation effects. In that case,

Table 2.3: Load-bearing capacities and failure modes.

	t_2 in mm	Copper	Alu	Steel C15	Silversteel	Failure mode
Beech LVL	20	5.22				Timber splitting, fastener failure
		5.57				Slight plastic hinges, fastener failure
		5.34				
			4.93			Splitting of timber
			4.94			
	30	5.07				Plastic hinges, fastener failure
		5.25				
			6.00			
	60	5.42				
			5.78			
				11.3		Plastic hinges, pull-in of fastener at large deformations
				11.3		
					12.2	
					15.0	
					13.3	
DVW	15	5.42				Shear failure fastener
		5.46				
			7.11			Slight plastic hinges, fastener failure
				13.2		
					15.8	Plastic hinges, pull-in of fastener
	30	5.77				Shear failure fastener
			7.40			
				13.8		Plastic hinges, fastener failure
				13.5		
				12.7		
					15.9	
					15.2	
	60			14.3		
					14.0	
					15.3	

the load-bearing capacity per shear plane more or less corresponds directly to the fasteners' shear capacity F_{shear}.

The results show a lower load-bearing capacity for connections with inclined fasteners when compared to those with straight fasteners. Copper dowels in beech LVL, for example, exhibit distinct plastic behaviour with a transition from elastic to plastic connection behaviour at lower loads compared to the shear tests. The behaviour of copper in DVW connections, instead, is quite similar to that observed in a shear test comparable to a conventional steel-to-steel connection, where pure shear failure of the fasteners is observed. The ultimate load of these connections then corresponds directly to the shear capacity of the dowels, as indicated with grey dots in Fig. 2.12. However, a lower embedment strength of beech LVL compared to DVW results in an inclined axis of the copper fasteners. Hence, a rope effect develops and consequently results in the yield limit being reached prematurely. For the other metals tested, this effect is amplified.

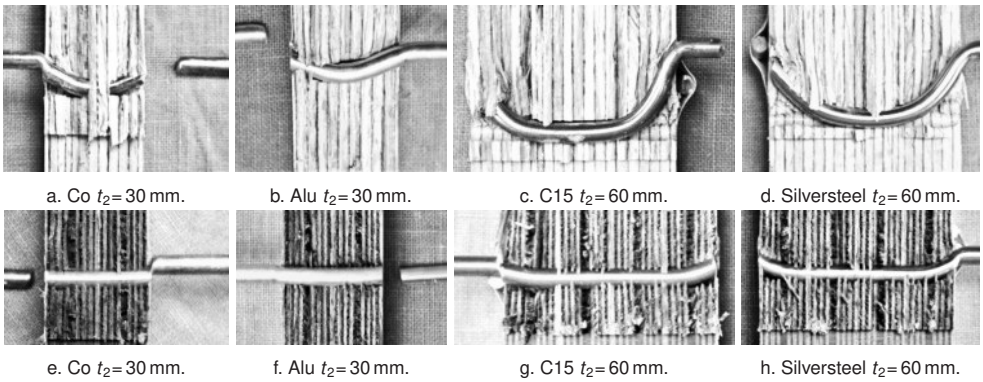

Fig. 2.11: Exemplary deformed fasteners for different dowels in beech LVL (a–d) and DVW (e–h).

2.4.4 Discussion

Different fastener deformations observed lead to different internal forces and moments occurring in the fastener. To apply the interaction criterion presented in Eq. 2.19, an analytical approach for the failure mode acc. to Fig. 2.8a is explained in the following. For calculations, mean values are used.
As a first step, the load-bearing capacity is calculated acc. to Eurocode 5 [118] for all tested connections for the failure modes shown in Fig. 2.8, i.e. embedment failure

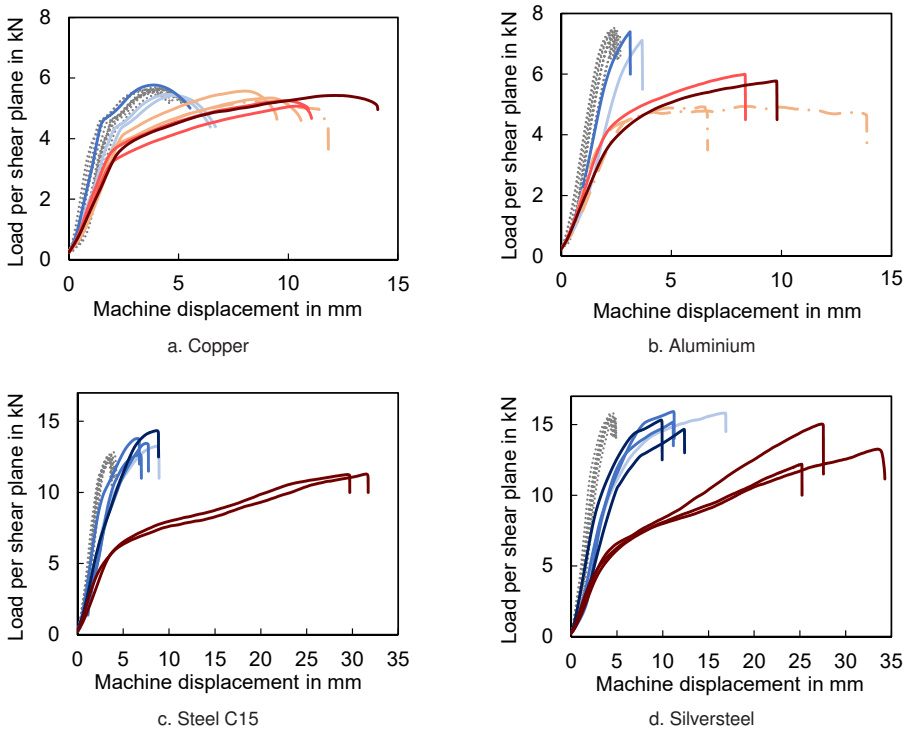

Fig. 2.12: Load-machine displacement curves for different dowels. Results of shear tests on dowels and connection tests with beech LVL and timber thickness of 20 mm, 30 mm, 60 mm and with DVW and timber thickness of 20 mm, 30 mm, 60 mm.

of the middle timber or failure with two plastic hinges per shear plane. Here, mean values are used, see also Tab. 2.2. Exemplary calculations for aluminium (timber thickness 30 mm) are shown in Fig. 2.13.

Ellipses included in the diagram mark the test results, if more than one test is conducted. The minor axis of the ellipse marks the min/max load reached, which stands for typical possible scattering, whereas the major axis marks the range of possible calculated embedment strengths depending on density variations, both with a certain assumed scattering. Aluminium in beech LVL develops two plastic hinges per shear plane and fails due to shear afterwards, see Fig. 2.11b. The test results in a load of 6 kN per shear plane, which is similar to the calculated load-bearing capacity $F_{v,R}$ acc. to Eurocode 5 [118] without preliminary factors and based on average values. Because of the inclined fastener sections between the plastic hinges in beech LVL, an additional line with an included rope effect is given in the diagrams, see dashed

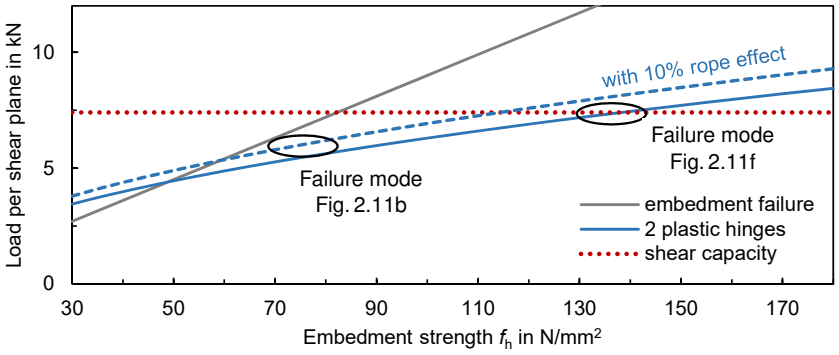

Fig. 2.13: Dependency of different failure modes for aluminium dowels with 30 mm timber thickness.

blue line. For this purpose, the load per shear plane is calculated as 1.1 x $F_{v,R}$. In contrast to this, the axis of the fastener in DVW stays almost straight and a clear shear failure occurs, see Fig. 2.11f. The load reached in the test is exactly the same as the shear capacity of the aluminium dowel, see red line in Fig. 2.13. If the load-bearing capacity is calculated acc. to Eurocode 5 [118], the load per shear plane exceeds the shear capacity as soon as the embedment strength is higher than 140 N/mm^2 (failure mode with two plastic hinges per shear plane). Thus, the shear capacity F_{shear} can be taken as an upper limit of the load-bearing capacity of the investigated connections. For a straight fastener axis, i.e. embedment failure acc. to Fig. 2.8a and Fig. 2.11f, an interaction of bending moment and shear force can be formulated. Assuming the dowel to be clamped in the outer steel plates, the moment in the shear plane can be calculated with Eq. 2.21. When inserted into the reduced interaction criterion, the remaining shear force V_{remain} can be calculated acc. to Eq. 2.22.

As soon as the embedment stress exceeds 39 N/mm^2, see Fig. 2.14, the remaining shear capacity V_{remain} would be reduced to 0 kN. This reduction is significant and leads to comparably low remaining shear capacities V_{remain}. Hence, for that case, Eq. 2.22 is not useful to calculate the remaining shear capacity because a load approximately equal to the shear capacity is reached in the test. At the same time, the question can be raised of whether the assumptions made are suitable. The occurring moment in the shear plane could be overestimated with the assumption of a fully clamped dowel in the outer steel plates. As a more appropriate assumption, something in between a rigid and an elastic restraint in the steel plates could be discussed. In addition, the assumption of a uniformly distributed embedment stress along the fastener axis is to be questioned. To verify that hypothesis, an exemplary calculation, again exemplarily

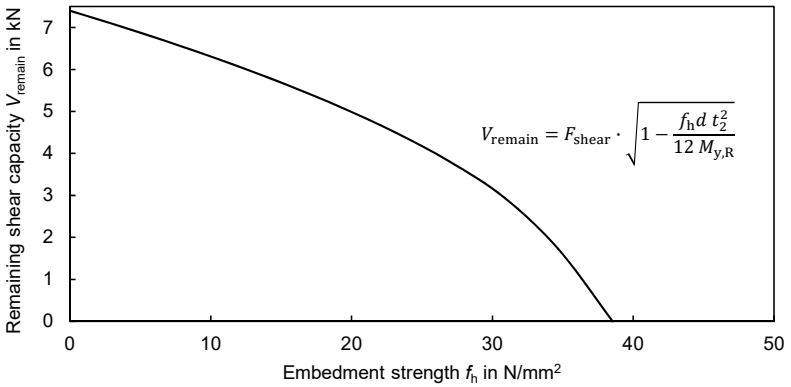

Fig. 2.14: Decrease of remaining shear capacity V_{remain} with higher embedment stress for an aluminium dowel and 30 mm timber thickness. Constant embedment stress distribution assumed.

on the aluminium fastener, follows. The shear capacity and load per shear plane reached in the test are equal and amount to 7.4 kN. In order to calculate the load-bearing capacity with an embedment failure, the load per shear plane F_{sp} is calculated with

$$F_{sp} = \frac{f_h \cdot d \cdot {t_2}^2}{12} = 7.40\,\text{kN} \tag{2.23}$$

With a dowel diameter of 6 mm and a timber thickness of 30 mm, an embedment stress of 82.2 N/mm² needs to be reached to fulfil the condition of Eq. 2.23. The magnitude of the embedment stress in DVW initially appears realistic. However, when calculating the bending moment in the shear plane with Eq. 2.21, it results in $M_{sp} = 37.0$ Nm. It becomes obvious that it exceeds the yield moment of the aluminium dowel by far ($M_{y,45°} = 16.5$ Nm, see test results in Tab. 2.2). Even if a lower clamping effect of the dowel in the steel plates is taken into account, the bending moments along the fastener axis are too high and still exceed $M_{y,45°}$.

Considering the deformed fastener in Fig. 2.11f, a slight bending of the fastener can be detected. Thus, the embedment stress must be distributed similarly to a failure mechanism with two plastic hinges per shear plane. The difference is that the bending moment does not reach the amount of the yield moment at any point along the fastener axis. This leads to the assumption that the state of full plastic bending is not yet reached.

Generally speaking, the higher the strength of the timber material, the higher the embedment stresses in the area of the shear plane. And, the areas with high embedment stress become progressively smaller and have a decisive effect on the magnitude of the shear force acting in the fastener in the shear plane. This becomes clearer when comparing the distributions in Fig. 6. The embedment stresses $\sigma_{h,1}$ and $\sigma_{h,2}$ shown are defined to be $\sigma_{h,1} > \sigma_{h,2}$ for each case to show how they differ from one another. For the case shown on the left, it is assumed that the embedment strength is achieved in certain areas near the shear plane, see partially constant stresses $\sigma_{h,1}$, and, in the centre part the stress $\sigma_{h,2}$ is below the embedment strength. For the case shown on the right, by contrast, the embedment stresses are assumed to remain below the embedment strength across the entire timber thickness.

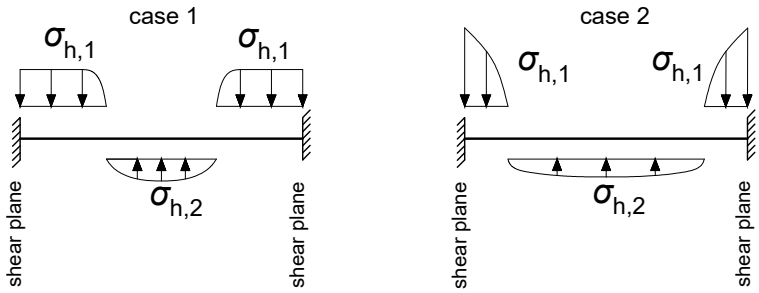

Fig. 2.15: Exemplary embedment stresses for high density timber material on the left (case 1) and very high density timber on the right (case 2).

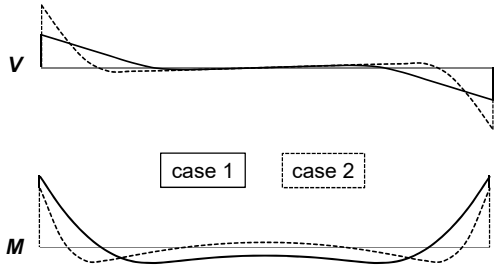

Fig. 2.16: Qualitative distributions for shear force *V* and bending moment *M* for high density timber material (case 1) marked with continuos line and very high density timber (case 2) marked with dashed line. Remarks: maximum of $\sigma_{h,1}$ is 2.5x higher in case 2 than in case 1; $\sigma_{h,2}$ is 4x lower in case 2 than in case 1

The left case stands for a typical steel-to-timber connection, where the bending moments reach the yield moment and plastic hinges develop. Increasing the embedment

strength leads to higher stresses in a smaller area close to the shear plane, eventually causing higher shear forces and lower bending moments acting in the shear planes, see Fig. 2.15 on the right. As no clear plastic hinge is visible in the exemplary connection, see Fig. 2.11f, the bending moment does not reach the yield moment. Considering the test results no reduction in shear capacity due to the bending moment can be observed as the connection capacity is equal to the dowel's shear capacity F_{shear}.

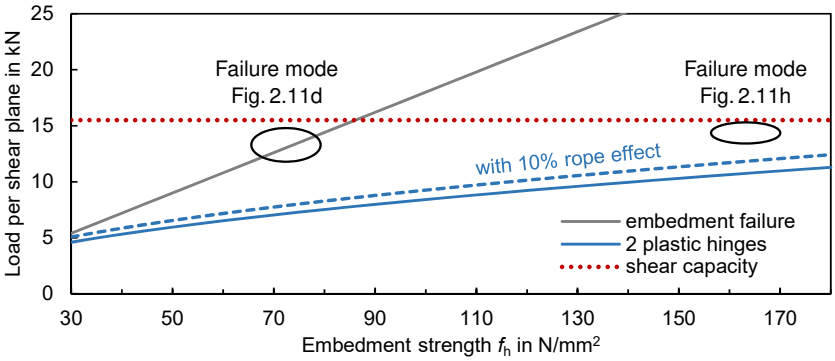

Fig. 2.17: Dependency of different failure modes for silversteel dowels with 60 mm timber thickness.

Consequently, this means that in Fig. 2.15 on the right, the occurring bending moment M is so small that there is no influence of the interaction on the shear capacity. This goes along with former findings about the ultimate load being more or less unaffected by the interaction of shear and bending [80]. If other failure modes, as shown in Fig. 2.11b, d and h, are also considered, it becomes clear that the distributions shown in Fig. 2.15 are nevertheless only partially appropriate. There is a smooth transition between the two shown distributions and corresponding failures. When plastic hinges are visible, and bending in the fastener dominates, the moments increase from the elastic to the plastic range. Only the left case can be used then. In contrast, the inclined orientation of the fasteners between the plastic hinges generates a normal force, which has not yet been taken into account, e.g. Johansen [50] and Meyer [66]. The normal force causes an increase in the connection load-bearing capacity due to the rope effect, whereas the effects on the fastener itself have not been investigated further. However, the results shown here indicate which effects are possible. The normal force creates additional normal stress components in the fastener. These, together with the components from the bending moment and the shear stresses caused by the shear force, can lead to failure in the shear plane before the shear capacity is reached, see Fig. 2.11 and 2.17. A comparison of the reached load-bearing

capacities shows the magnitude of the reduction. For aluminium in beech LVL, a load-bearing capacity of approx. 80% of F_{shear} is reached, see Fig. 2.13. The results for silversteel dowels scatter and result in a load-bearing capacity in the range of 79–97% of the shear capacity. It could be assumed that a more inclined position of the fastener would result in higher normal forces and thus, leading to a greater reduction in load-bearing capacity. Therefore, the impact of normal forces on the interaction between internal forces and moments in fasteners subjected to lateral loads is a crucial aspect to consider. Normal forces are particularly important because, in the case of pure normal stress, the cross-section does not have any plastic reserve. This means that all fibres in the cross-section will reach the yield strength simultaneously, assuming a uniform strength distribution across the cross-section. As a result, the behaviour of a laterally-loaded fastener becomes more complex, and understanding how these normal forces interact is essential for an accurate calculation of the load-bearing capacity of a connection. Simultaneously, increased inclination of fasteners and normal forces enhance the rope effect and lead to an increased load-bearing-capacity of a connection, see Fig. 2.11c and d. However, the tests carried out could not rule out the possibility of frictional effects. Higher loads than the shear capacity can be achieved with additional friction in the shear planes or by the contribution of the vertical force components due to the inclination of the fastener.

Thus, there must have been contact in the shear plane due to embedment deformation out-of-plane of the timber. This effect occurred with steel C15 and silversteel in DVW. The magnitudes of the normal forces acting in laterally loaded fasteners remain uncertain. Understanding their exact magnitudes is essential for accurately predicting the load-bearing capacity of connections.

The experimental series conducted on dowels have length-to-diameter ratios of approximately five or greater. According to Horne [47], a significant reduction of the plastic moment due to shear effects occurs only for very short beams with L/d < 4. Therefore, the influence of shear on the observed *MV* interaction in these tests can be considered minor. The results obtained here fit well with the known findings by Horne, confirming that shear effects play only a subordinate role for members with moderate or large slenderness ratios.

2.4.5 Conclusion

Tailor-made tests investigating the effect of an interaction between internal forces and moments in fasteners on the load-bearing capacity of connections with laterally loaded fasteners are carried out. These tests lead to different conclusions for two possible types of interaction, namely *MV* interaction and *MNV* interaction, highlighting their distinct influence on connection performance. A constant distribution of embedment stress across the fastener applies only in the case of a particularly stiff fastener embedded in comparatively soft timber. However, this condition is not fulfilled for any of the cases investigated in this study.

Based on the test results, the interaction between bending moment and shear force has only a minor influence on the overall load-bearing capacity, but it affects the onset of yielding. In contrast, normal forces must be present when fasteners are inclined, and ultimately, the *MNV* interaction leads to a reduced load-bearing capacity. This raises the question of how normal forces influence the interaction between internal forces and moments in laterally loaded fasteners.

For an extreme case, such as copper dowels in DVW, the opposite scenario is observed: a very soft fastener embedded in a high-strength timber material behaves similarly to a typical steel-to-steel connection, where the fastener ultimately fails due to pure shear without significant embedment effects. Higher connection capacities than the shear capacity of the fasteners are occasionally observed in tests and are attributed to an additional frictional component developing between the timber and the steel plate. The magnitude of this frictional contribution remains uncertain and cannot be precisely quantified based on the conducted experiments.

Normal forces are particularly critical since, under pure normal stress conditions, no plastic cross-sectional reserve exists, meaning that all fibres in the fastener reach the yield point simultaneously, assuming a uniform strength distribution across the cross-section. The exact magnitudes of the normal forces acting in laterally loaded fasteners remain unknown. Given their crucial role in influencing the load-bearing behaviour, these forces should be investigated further to improve the understanding of their contribution to the load-bearing capacities of connections and their failure mechanisms.

The selection of suitable assumptions depends significantly on the unknown normal forces and on the knowledge of the deformation behaviour of laterally loaded fasteners. This includes choosing appropriate embedment distributions, making assumptions

about the fastener system, and estimating the magnitude of internal forces. A precise understanding of these factors is essential to ensure accurate modelling and reliable structural analysis.

These findings highlight the relevance of the key questions driving this thesis, which concern the deformation behaviour of fasteners and the stress and strain distributions along fastener axes. The following chapters address these individual topics, first for typical screwed connections and afterwards in a comparative study including external fasteners in an individually adapted test setup.

3 Load-Deformation Behaviour of Partially Threaded Screw Connections

To understand potential fastener failure in hardwood connections, it is useful to first investigate the fundamental differences between softwood and hardwood connections. This chapter focuses on partially threaded screws, one of the most widely used fasteners in timber construction. With the growing use of engineered hardwood products such as beech LVL, it becomes necessary to question whether design assumptions derived mainly from softwood remain valid. The chapter presents a direct comparison of screwed connections in softwood and hardwood, focusing on their behaviour under increasing load and deformation, with particular attention to the deformation of the fasteners themselves. The results reveal distinct deformation and failure characteristics in hardwood, providing practical insights for connection design.

3.1 Introduction

As one of the most widely used fasteners in timber construction, partially threaded screws form the focus of the first main chapter of this work. Their application in hardwoods is steadily increasing, driven by the growing use of engineered hardwood products such as beech LVL in building practice [56, 64]. Connections in beech LVL have therefore been the focus of several recent research projects, most of which studied axially loaded fasteners. Other dowel-type fasteners, such as glued-in rods, have also been investigated, typically under axial loading conditions [33, 67]. Despite the widespread use of partially threaded screws, the understanding of their load-displacement behaviour, particularly in laterally loaded connections with hardwood, remains incomplete. Many studies focus on individual parameters, such as strength properties of birch glulam and cross laminated timber, embedment strength or withdrawal resistance for specific birch products and fasteners, [17, 49, 105]. However, the interaction of these parameters and their experimental determination

for specific connection configurations are crucial to accurately predict connection behaviour and to calculate the load-bearing capacity of connections. The relevance of knowing these basic parameters was shown early by Larsen [61] or Jorissen [51] and more recently by Sandhaas [82]. However, in the case of hardwoods, not only do the individual input parameters change, but also the connection behaviour, i.e. the interaction of the mechanisms involved is different compared to softwood. This motivates a closer investigation of hardwood connection behaviour. The investigation dives into incremental deformation behaviour, aiming to link load levels to the onset of plastic connection behaviour. The key questions include: at which load does yielding or plastic hinge formation in the fastener begin, how plastic deformations of the fastener be distinguished from deformations of the surrounded timber, and how the higher density of hardwood as compared to softwood influences these mechanisms. The investigations centre on the load-displacement behaviour, with particular attention to the deformations of the fasteners themselves as highlighted in the introductory sections. Some of the results discussed in this chapter are published in [1]; here, they are presented in a broader context focusing on the incremental deformation of fasteners and extended by additional findings and comparisons to softwood connections. To describe the interaction of the governing mechanisms in laterally loaded fasteners, basic tests are carried out on two different screw types, including embedment tests, head pull-through tests, and withdrawal tests. This is the first part of the chapter. In addition, a broad test programme for hardwood and softwood connections is carried out. By explicitly examining the individual deformation and stiffness sections of the load-displacement curves, the deformation process of single-shear timber-to-timber connections is clarified. Since screws can be inserted into both predrilled and non-predrilled members, and especially because hardwood increases the risk of splitting and potential fastener failure, dedicated investigations are carried out on both predrilled and non-predrilled specimens with various configurations. The findings are subsequently extended to rows and groups of screws.

3.2 Materials and Methods

3.2.1 Material Properties and Input Parameters

Laminated beech veneer lumber (BauBuche ETA-14/0354 [125]) type S with only parallel layers (*Fagus sylvatica*), birch glulam (according to ETA-19/0031 [126]) made

from boards with brown heartwood (*Betula pendula*), and spruce glulam (*Picea abies*) were used. Both glulam products made of birch and spruce were stored in a standard climate of 20 °C temperature and 65% relative humidity prior to testing. The beech LVL members were mostly used directly after delivery. This resulted in low moisture contents, as beech LVL is produced in a very dry state, as described in ETA-14/0354 [125]. The moisture content of the veneers during gluing was $5 \pm 3\%$. The mean density ρ_{mean} was specified as $\geq$800 kg/m^3. For beech LVL cross-sections, the density varies over the height of the element. Local densities are higher in the area of secondary glue lines between individual panels of laminated veneer lumber due to the manufacturing process and applied pressure, as shown by Frese [37]. The boards used to produce the birch glulam contained a considerable amount of heartwood (brown core). Piths were often visible, with radial cracks appearing around them. The width of the annual rings varied considerably. According to the manufacturer, the boards had a moisture content of $11 \pm 2\%$ and a density of 600 kg/m^3, see ETA-19/0031 [126].

3.2.1.1 Basic Input Parameters

Partially threaded screws consist of a smooth shank and a threaded section, which differ in design-relevant properties. Accordingly, all necessary parameters were determined for both sections. In this study, two different partially threaded screw types were tested to determine embedment strength, withdrawal, and head pull-through parameters. These tests were conducted within the scope of a bachelor thesis by Meiertoberend [65]. The screws were tested in beech LVL and in birch solid wood or birch glulam. Screws were installed at an angle of 90° in beech LVL, and in birch, the angle between the screw axis and the grain direction was also 90°. Finally, tensile capacities and yield moments of the partially threaded screws were determined to complete the set of required parameters. The screw types used are shown in Fig. 3.1.

3.2.1.2 Test Programme

The test programme for the basic tests is listed in Tab. 3.1. All tests were carried out according to test standards DIN EN 383:2007 [119], DIN EN 1382:2016 [114] and DIN EN 1383:2016 [115]. Due to the geometric differences between the shank and threaded sections of partially threaded screws, the embedment strength f_{h} was determined for both areas. All timber test specimens were cut randomly rather than

a. Type 1: screw 8x160/100 mm, washer head, non predrilled (np), shank diameter $d_S = 6.5$ mm, core diameter $d_1 = 6.1$ mm.

b. Type 2: screw 8x160/80 mm, countersunk head, presunk, predrilled (p) with $d_{hole} = 6$ mm, shank diameter $d_S = 5.8$ mm, core diameter $d_1 = 5.4$ mm.

Fig. 3.1: Screw types used.

in series to capture a range of properties representative of real conditions. After testing, the density and moisture content of each specimen were measured. A timber thickness of 15 mm was chosen for the embedment tests.

Table 3.1: Experimental test programme and number of tests in beech LVL and Birch glulam.

Type of test	Load-grain-angle	Screw type 1		Screw type 2	
		Shank	Thread	Shank	Thread
Embedment	0°	10	10	10	10
Withdrawal	90°	20		20	
Head pull-through	90°	20		20	
Tensile tests		10		10	
Yield moment		10		10	

When installing non-predrilled screws, an additional glued-on thin steel plate was applied to prevent splitting. The embedment depth of the partially threaded screws for determining the withdrawal parameters was $l_d = 6d = 48$ mm in all cases, which deviated from the recommendations of the test standard. For withdrawal tests in birch, a distinction was made between the radial and tangential directions. For the head pull-through tests, a timber thickness of 40 mm was used. Due to differences in load-deformation behaviour, the head pull-through parameters were determined consistently at a machine displacement of 15 mm. The parameters are calculated

according to the following equations:

Embedment strength

$$f_{\mathrm{h}} = \frac{F_{\mathrm{max}}}{d \cdot t} \quad \text{in N/mm}^2 \tag{3.1}$$

with

F_{max}	Max. load until 5 mm displacement in N
d	Nominal diameter of fastener in mm
t	Thickness of specimen in mm

Withdrawal parameter

$$f_{\mathrm{ax}} = \frac{F_{\mathrm{max}}}{d \cdot l_{\mathrm{d}}} \quad \text{in N/mm}^2 \tag{3.2}$$

with

F_{max}	Max. load during test in N
d	Nominal diameter of fastener in mm
l_{d}	Insertion depth of thread incl. tip in mm

Head pull-through parameter

$$f_{\mathrm{head}} = \frac{F_{\mathrm{15mm}}}{{d_{\mathrm{h}}}^2} \quad \text{in N/mm}^2 \tag{3.3}$$

with

$F_{\mathrm{15\,mm}}$	Max. load until 15 mm displacement in N
d_{h}	Head diameter of fastener in mm

3.2.2 Methodology for Single-Screw Connections Tests

The load-deformation behaviour of laterally loaded screwed connections is analysed using compression tests. Particular attention is given to the different connection stiffness ranges and their effect on the overall connection response. Fig. 3.2 illustrates a representative load-deformation curve of a connection with partially threaded screws, divided into three characteristic sections. Sections 2 and 3 display the typical elastic-plastic behaviour of dowel-type fasteners under lateral loading. Section 1, however, shows an unusual high initial stiffness. Because the deformations remain extremely

small until the curve detaches from the ordinate axis, this range is referred to as *initial adhesion*. The initial adhesion is the maximum machine load reached at the point where the curve detaches from the ordinate and also marks the onset of the elastic behaviour in section 2. The visible kink at approximately 13 mm displacement results from the switch of the testing machine from force control to displacement control. The individual test speed is selected so that the test specimens each achieve a relative displacement of at least 10 mm in the force-controlled range. The speeds are listed in Tab. 3.2. These loads apply for one specimen, i.e. for two screws. The unloading was not recorded.

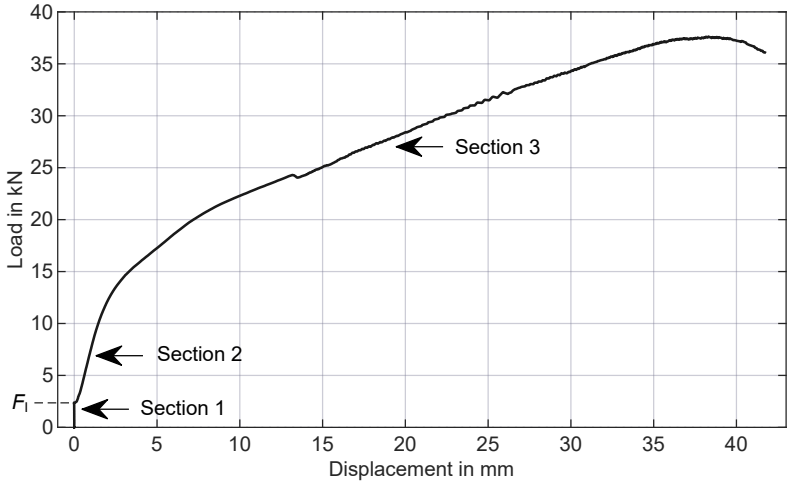

Fig. 3.2: Exemplary load-displacement behaviour of a screwed connection.
Section 1: Vertical curve section until initial adhesion is reached
Section 2: Elastic connection behaviour
Section 3: Plastic connection behaviour

The reasons for the occurrence and magnitude of the initial adhesion are analysed. A typical screw insertion suggests that, when the screw head is tightened, the two members of the connection are pressed together, generating compression forces in the shear plane at the beginning of the load application. These compression forces act as adhesive forces when the connection is loaded laterally. In the load-deformation curve, they appear as the initial adhesion. It is therefore assumed that the magnitude of the initial adhesion correlates with both the initial adhesive force and the coefficient of friction between the timber surfaces, as expressed in Eq. 3.4.

$$F_{\mathrm{I}} = F_{\mathrm{adhesion}} \cdot \mu_{\mathrm{adhesion}} \tag{3.4}$$

with

F_{I}	Initial adhesion in kN
F_{adhesion}	Occurring compression force in shear plane in kN
μ_{adhesion}	Coefficient of static friction of timber surfaces [-]

Table 3.2: Test parameters for different screw types and timber materials. All values refer to one specimen (two screws).

Material	Screw	Load control	Up to load	Displacement control
Beech LVL	Type 1	10 kN/min	30 kN	5 mm/min
	Type 2	5 kN/min	25 kN	5 mm/min
Birch glulam	Type 1	5 kN/min	20 kN	5 mm/min
	Type 2	3.5 kN/min	14 kN	5 mm/min
Spruce glulam	Type 1	4 kN/min	10 kN	5 mm/min
	Type 2	3.5 kN/min	7 kN	3 mm/min

Using an experimentally determined static friction coefficient of 0.41 between wide beech LVL surfaces [108], the compression forces acting in the shear plane can be estimated. This raises the question of whether, and to what extent, the overall load-bearing behaviour of screwed connections is influenced by the initial adhesion. Several factors may affect the magnitude of these forces. The machining or cutting process of the specimens influences the surface roughness, which in turn depends on wood moisture. Increased moisture can cause surface fibres to swell, thereby increasing roughness. The influence of initial adhesion is investigated using connection configurations in beech LVL and spruce glulam, with screw insertion either predrilled or non-predrilled. All screws were inserted in a standard manner, with the head flush with the timber surface. In additional tests, some screws were deliberately overtightened or slightly unscrewed. Furthermore, selected displacement stages of the load-deformation curve were targeted: the tests were stopped before maximum load, and the specimens are opened. This allows incremental analysis of screw deformation and, in particular, observation of plastic hinge formation. This method of stopping the test prematurely leads to the name of the so called *multi-stage tests*. Edge distances for the predrilled screws differ from those of the non-predrilled configuration.

Side member thicknesses are chosen according to the screw shank length. The resulting geometries are listed in Tab. 3.3. Following preliminary tests with minimum edge distances acc. to Eurocode 5 [118], the edge distances were increased to prevent premature splitting failures.

Table 3.3: Test configurations with partially threaded screws 8 x 160 mm.

Dimension in mm		Screw type 2		Screw type 1	
		Shank	Thread	Shank	Thread
Length	ℓ	80	80	60	100
Diameter of shank or core	d_i	5.8	5.4	6.5	6.1
Thread pitch	p	5.6		4.0	
Angle of flank	α	–		40°	
Thickness side timber	t_1	80		60	
Thickness middle timber	t_2	170		210	
Distances	$a_{3,c}$	24		56	
	$a_{4,c}$	80		120	
	$a_{4,t}$	140		180	

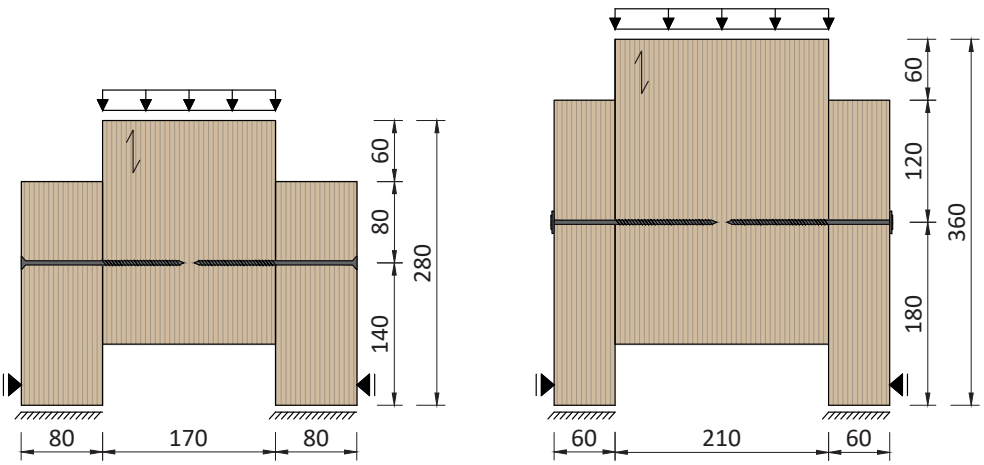

Fig. 3.3: Schemes of test configurations: predrilled on the left and non predrilled screw on the right, exemplarily in beech LVL, dimensions in mm.

Fig. 3.3 illustrates the geometries of the analysed predrilled and non-predrilled timber-to-timber connections. All fasteners are loaded in single shear. Specimens made of beech LVL, spruce and birch glulam of identical geometry are tested for comparison. The screws are inserted at 90° to both the timber surface and the fibre direction in all configurations. The tests are conducted on an electromechanical testing machine. Surface deformations are continuously measured using a digital image correlation (DIC) system. The test setup permits a slight rotation of the middle member around the screw axes due to the resulting kinematics. The analysis focuses on relatively small displacements, for which DIC measurement is particularly suitable. Fig. 3.4 shows a representative test and measurement setup. Because the DIC system does not provide real-time displacement output, additional displacement transducers are installed. They serve only to monitor the current displacement and to stop the test at the predefined displacement stages.

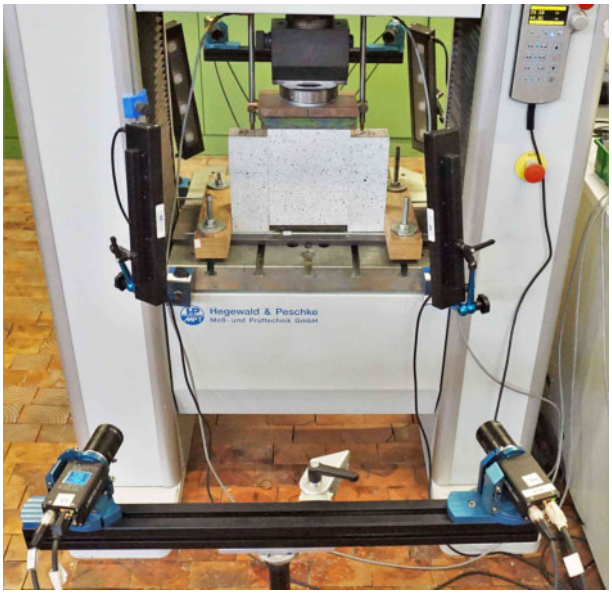

Fig. 3.4: Test setup and measurement via DIC for compression tests.

3.2.2.1 Stops of Multi-stage Tests

To analyse the progressive plastic deformation of the fasteners, tests are interrupted at defined relative displacements and opened afterwards. Openings at displacements

below 5 mm are omitted, as the transition from elastic to plastic connection behaviour is expected within this range. It is therefore assumed that only negligible irreversible deformations occur below this threshold. Each opening stage is labelled according to the relative displacement reached in the shear plane. The selected opening stages for observing incremental deformation are illustrated in Fig. 3.5 and are as follows: 5 mm, 10 mm, 25 mm and after failure.

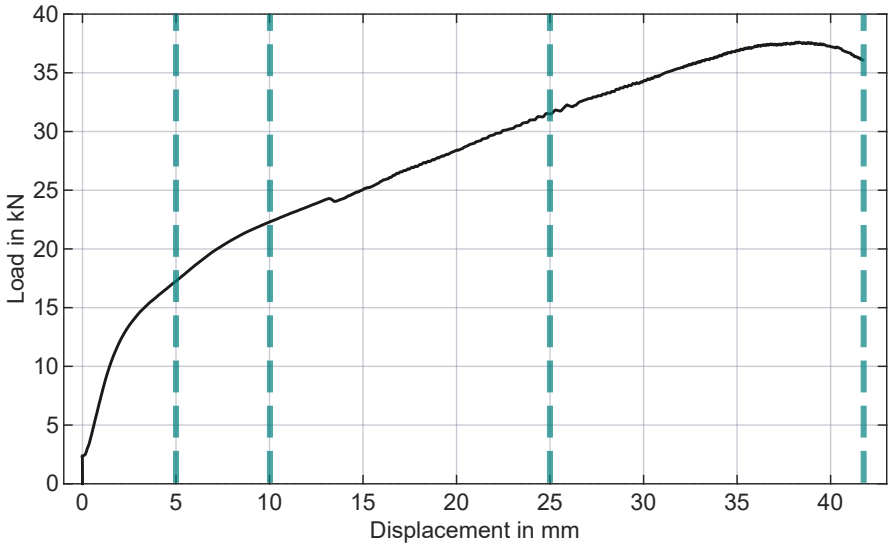

Fig. 3.5: Opening stages of specimens at 5 mm, 10 mm, 25 mm and at failure.

3.2.2.2 Screw Insertion

Screws are first inserted in the standard manner until the heads are flush with the timber surface. The even contact is verified visually at the end of insertion. To analyse the magnitude and influence of the initial adhesion, the screws are then rotated either further in or slightly back, resulting in intentionally sunk or protruding screw heads, see Tab. 3.4. The values given in the table refer to the additional rotation angle applied after the regular fit, where one full rotation corresponds to 360°.

It should be noted that the two screw types tested have different thread pitches (see p in Tab. 3.3), so that an additional rotation leads to different axial movements of the screws. Overtightening of the washer-head screws (type 1) is critical and was stopped

Table 3.4: Type of installation of the partially threaded screws.

Type	Image	Description
Regular		Flush insertion, head of countersunk screw is flush with timber surface, washer head is fitted tightly
+ 90°/+ 180°		Screw 90° or 180° overturned, screw head is sunk-in
- 90°/- 180°	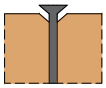	Screw 90° or 180° turned backwards, screw head protrudes

Table 3.5: Number of tests for each type of installation.

No. tests/ Type of installation	Screw type 2		Screw type 1	
	Beech LVL	Spruce glulam	Beech LVL	Spruce glulam
Regular	10	8	10	2
+ 90°	4		1	
+ 180°	2			
- 90°	3		3	
- 180°			2	
Total	19	8	16	2

after a few trials, as resuming the insertion of non-predrilled screws immediately after installation requires very high torque. In several cases, this led to screw failure due to exceeding the torsional capacity. A further limitation is the screw rebound after the applied torsional loading, which cannot be measured exactly and is therefore not considered in the evaluation.

3.2.3 Methodology for Multi-Screw Connection Tests

To investigate possible row and group effects, test results from previous studies [67, 103] are analysed and test configurations are adapted for this study. Earlier investigations frequently show early and brittle splitting of screwed connections in

beech LVL before reaching 10 mm displacement. For instance, with a side member thickness of 5 d and a spacing of $a_1 = 7\,d$, Meyer [67] reports an average maximum displacement of 9.06 mm for rows of screws inserted into the wide face of beech LVL. Vedovelli [103] observed maximum displacements of 7.2 mm in similar configurations. These results indicate that the EAD 130118-01-0603 requirement [127], to reach at least 10 mm displacement before the load drops below 80% of the maximum, is not fulfilled. However, it is also important to consider the load-bearing capacities achieved, as premature brittle failure may result in the calculated load-bearing capacities not being achieved. Consequently, the applicability of this regulation for hardwood connections requires reconsideration. In the present study, displacement criteria and minimum spacing regulations are reviewed in a new test series. The aim is to draw conclusions about the limits of plasticity and to evaluate different connection test setups. Tension tests are conducted on screwed connections in beech LVL type S and birch glulam. The load-grain angle and screw insertion angle are chosen analogously to the compression tests described in Section 3.2.2. Dimensions, distances, and spacings of the fasteners are mainly selected according to the minimum nail distances listed in Eurocode 5, Tab. 8.2 [118]. Modifications are applied to prevent early splitting along the fibre direction. Specifically, the distance between fasteners in grain direction a_1 in the predrilled configuration is adjusted. A complete list of fastener spacings and insertion depths is provided in Tab. 3.6. Different test setups are used depending on the applied load and the type of connection. For groups of screws, a double-symmetrical configuration is used due to the high loads involved. For rows of screws, either a single-symmetrical or an eccentric configuration is used. Schematic drawings of the symmetrical setups are shown in Figs. 3.6 and 3.7, while the actual test setups are illustrated in Fig. 3.8.

Table 3.6: Geometry of tension test specimens in beech LVL and birch glulam.

Dimensions	Predrilled		Non-predrilled	
		in mm		in mm
a_1	8 d	64	15 d	120
a_2	3 d	24	7 d	56
$a_{3,t}$	12 d	96	20 d	160
$a_{4,c}$	3 d	24	7 d	56
t_1	10 d	80	7.5 d	60
t_2	10 d	80	12.5 d	100

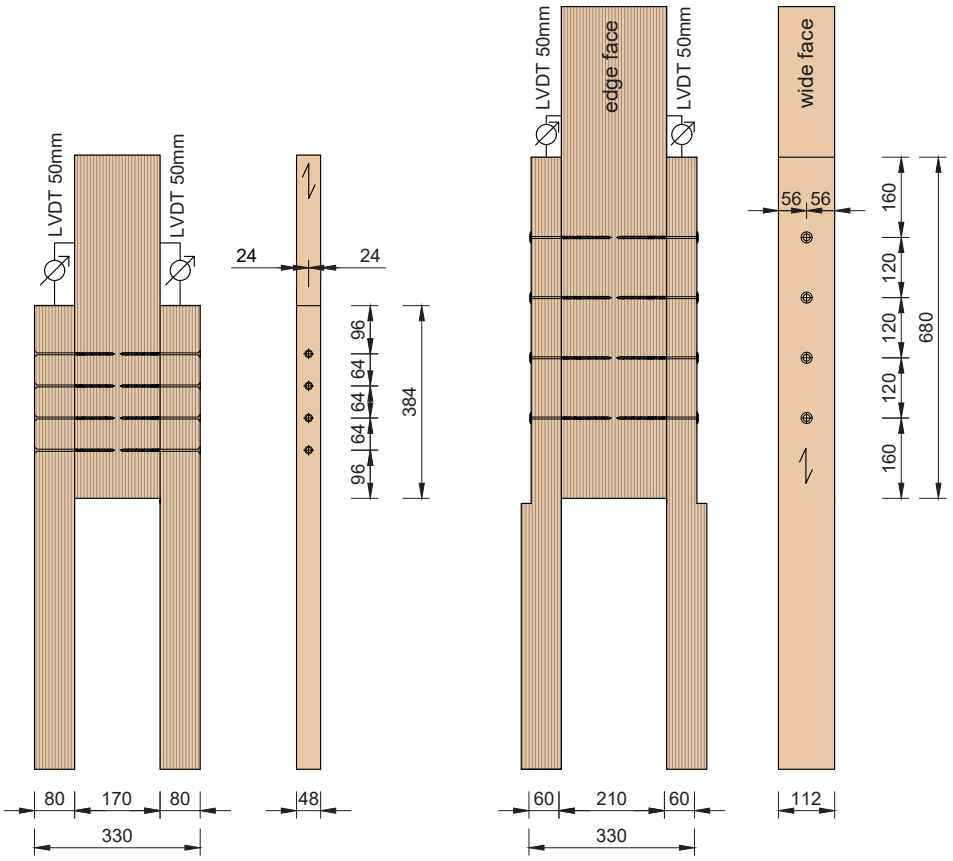

a. Specimen for predrilled screws.

b. Specimen for non-predrilled screws.

Fig. 3.6: Schematic drawing of specimens for rows of screws, dimensions in mm.

The load is applied from above using outer rough steel plates and a bolted connection. In the double-symmetrical configuration, the bottom fixation is carried out in the same manner. For the single-symmetrical configuration in Fig. 3.6, the two side members are connected to a block via steel L-profiles and bolts, with the block anchored to the ground. Individual side members are tested by clamping and loading them directly in a clamping jaw. This simple test configuration focuses on evaluating the influence of eccentricity on the test results. Displacements are recorded for all series and group tests using transducers (LVDTs = Linear Variable Differential Transformer) with a 50 mm measuring length. Each connection is measured separately, with the transducers positioned on the end-grain surfaces of the side members.

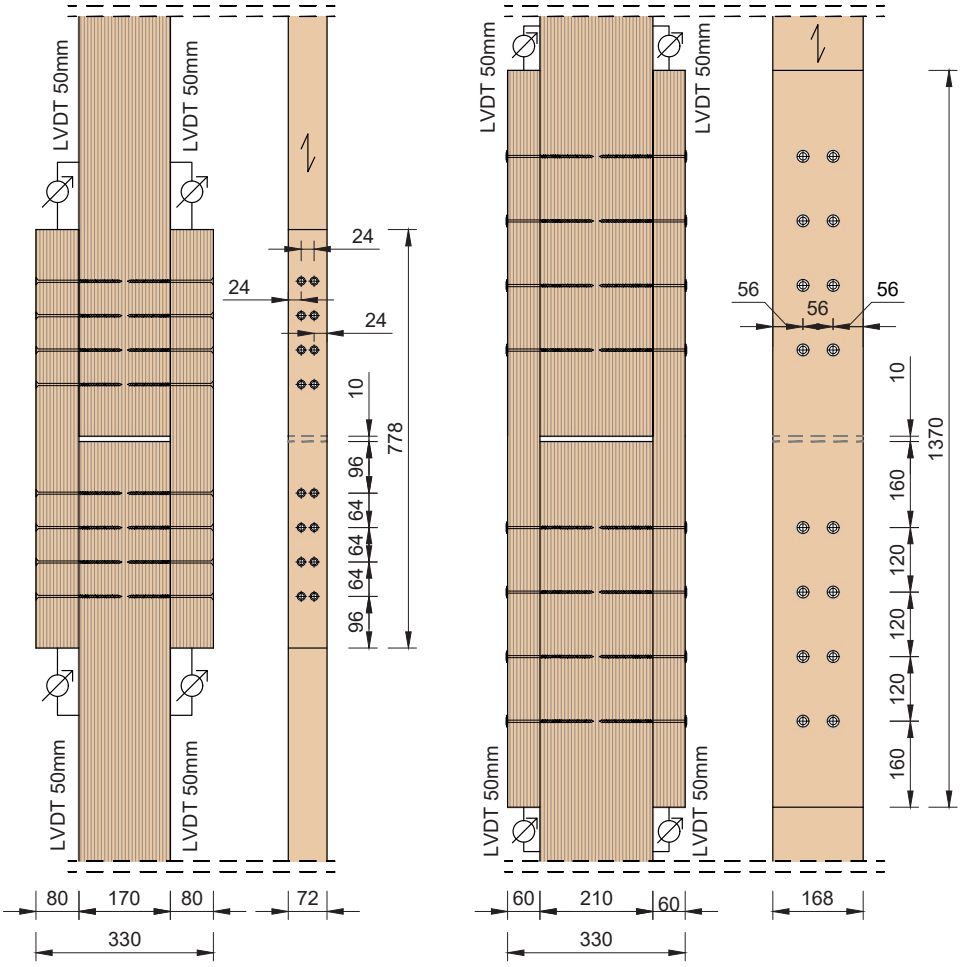

a. Specimen for predrilled screws.

b. Specimen for non-predrilled screws.

Fig. 3.7: Schematic drawing of specimens for groups of screws, dimensions in mm.

Screws are inserted in the same way as described for the multi-stage tests on single screws. All type 1 countersunk-head screws are installed in pre-sunk (cone shape of the head), predrilled timber ($d_{predrilled}$= 6 mm) until the head is flush with the timber surface. Non-predrilled washer-head screws are inserted using a screwing aid at 90° to the grain and timber surface, ensuring the heads are firmly seated. A minimum standing time of 24 hours is maintained between assembly and testing for all specimens.

a. Groups of screws np. b. Rows of screws np. c. Rows of screws, eccentric.

Fig. 3.8: Exemplary images of the test setups for investigated configurations.

3.2.4 Test Programme

Tab. 3.7 provides an overview of all test series, including the installation types and the corresponding number of tests. A total of 65 compression tests (multi-stage tests) are conducted on single screws, and 26 tension tests are performed on rows or groups of screws. For the eccentric non-predrilled side member, only three screws are inserted due to the geometry, i.e. limited height, of the anchoring block.

Table 3.7: Test series of connection tests, gl = glulam.

No. of tests/ Configuration		Type 1 screw np			Type 2 screw p		
		Beech LVL	Spruce gl	Birch gl	Beech LVL	Spruce gl	Birch gl
Compression Single screw	Regular	10	2	4	10	8	4
	+90	1			4		
	+180				2		
	-90	3			3		
	-180	2					
Tension Several screws	Row 1x4	3		3	3		3
	Row[a] 1x4				2		
	Row[b] 1x4	1			1		
	Row[c] 1x4				2		
	Group 2x4	2		2	2		2
	Total	25	2	12	35	8	12

[a] Middle and side members are predrilled in separate working steps
[b] Eccentric testing, single side timber tested
[c] Only side timber predrilled with spacings according to the np configuration

3.3 Basic Input Parameters

For a better understanding of the differences between timber species, used products, and screw types, the first results focus on the basic input parameters before discussing the connection outcomes. Understanding these basic input parameters is fundamental, as special behaviors can already be observed at this stage.

3.3.1 Results

The embedment strengths are determined with a reference diameter of 8 mm. The differences in the obtained results are due to the varying shank and core diameters, as well as the type of insertion, predrilled or non-predrilled. In general, higher embedment forces occur in the threaded area than in the shank area, as a larger area is engaged. With a predrilled screw, only the outer thread penetrates the timber. In contrast, a type 1 screw displaces wood fibres when non-predrilled, causing predamage to the surrounding wood. In this observation, the tendency of type 2 screws to exhibit higher embedment strength in birch compared to type 1 screws should be emphasised, despite their smaller geometric dimensions. Brittle splitting of the test specimens occurs when inserting non-predrilled screws in beech LVL and birch. A glued-on steel reinforcement plate prevents this in subsequent specimens. Mean embedment strengths of screw type 1 reach 58.6 N/mm^2/72.4 N/mm^2 (shank/thread) in beech LVL and 23.7 N/mm^2/31.7 N/mm^2 (shank/thread) in birch. Type 2 screws show lower values in beech LVL (55.5 N/mm^2/63.1 N/mm^2) and slightly higher in birch (27.4 N/mm^2/32.5 N/mm^2), see Fig. 3.9. Tab. A.1 gives the complete list of results in Appendix A.1.

The withdrawal tests are conducted on specimens of beech LVL and birch glued laminated timber due to the required specimen size. Results are listed in Tab. A.2 and visualised against density in Fig. 3.10. For birch glulam, the evaluation distinguishes between radial and tangential directions, which is discussed in [1]. But without this distinction, type 1 screws reach a mean value of 27.8 N/mm^2 with a coefficient of variation of 14.9 %. Type 2 screws show a mean of 23.7 N/mm^2 (CoV = 21.0 %) when considering all withdrawal tests. In general, withdrawal parameters in birch glulam show high scatter. In contrast, beech LVL exhibits only slight variability due to its highly homogenised structure, with mean withdrawal parameters of 51.6 N/mm^2 for type 1 and 39.3 N/mm^2 for type 2 screws.

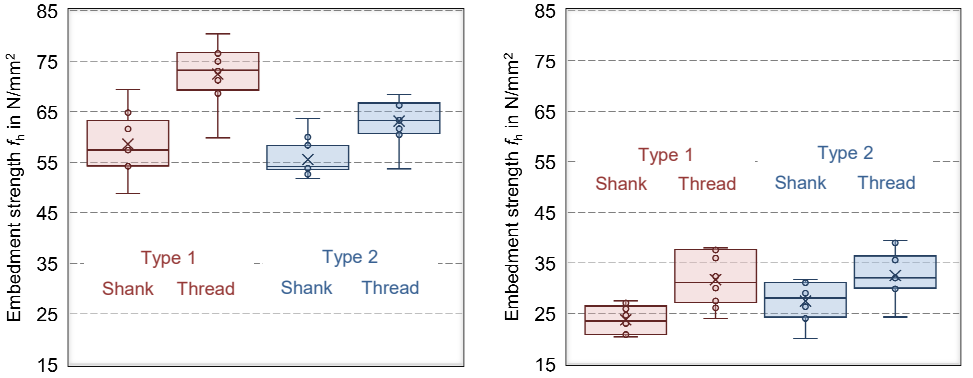

a. Beech LVL type S.

b. Birch solid wood.

Fig. 3.9: Results of determined embedment strengths.

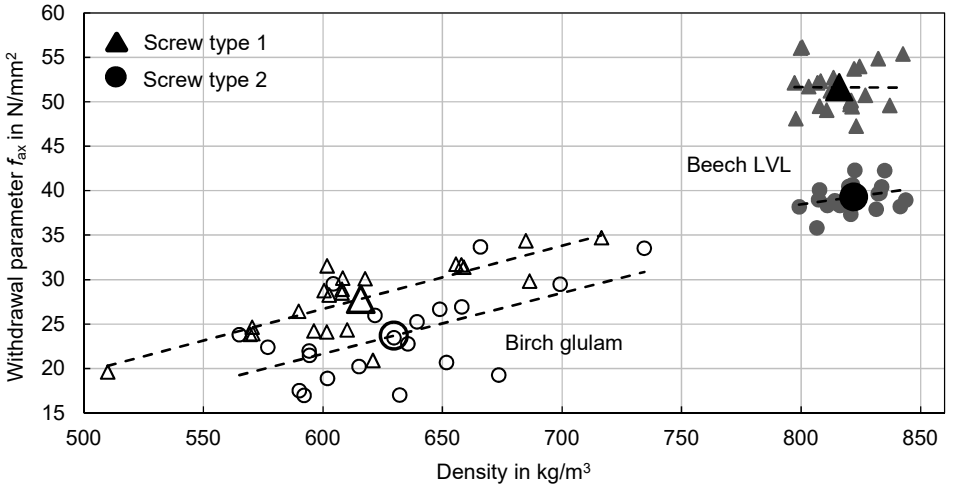

Fig. 3.10: Dependency of determined withdrawal parameters on density.

The head diameters are measured and mean values over a sample of ten screws are calculated. The evaluation of the head pull-through parameters is therefore based on the following head diameters:

Screw type 1 $d_h = 21.4$ mm
Screw type 2 $d_h = 15.0$ mm

To determine the head pull-through parameters, the machine load is recorded at a displacement limit of 15 mm. In tests with beech LVL, type 1 screws reach an average

maximum load of 31.4 kN, while the load at the displacement limit averages 24.5 kN. Type 2 screws reach mean maximum resistance of 18.4 kN, with 15.4 kN measured at 15 mm displacement. In birch solid wood, average maximum loads are 17.2 kN (type 1) and 7.80 kN (type 2), whereas the mean loads at the displacement limit are 12.4 kN (type 1) and 6.43 kN (type 2). This evaluation point at 15 mm is justified by the significantly smaller head pull-through distances in common timber connections, which are typically a few millimetres. Maximum loads during testing occur at approximately 20–30 mm displacement. In some tests, the tensile capacity of the washer-head screws is reached, so failure is no longer exclusively characterised by head pull-through. For comparability and to exclude brittle tensile failure, all evaluations are therefore carried out at the defined displacement.

a. Deformations after head pull-through test in birch solid wood.

b. Crack in fibre direction in test specimen made of birch solid wood.

Fig. 3.11: Details of head pull-through test specimens.

Mean head pull-through parameters in beech LVL are 53.4 N/mm^2 for type 1 and 68.6 N/mm^2 for type 2, and in birch 27.2 and 28.6 N/mm^2, respectively. The higher values are attributed to the larger head diameter. Section A.1 lists the head pull-through results in Tab. A.3, while Fig. 3.11 shows exemplary deformations and a brittle splitting failure.

Additional key input parameters include steel properties, such as the tensile capacities and yield moments of the fasteners. The tensile capacities of both screw types are measured, with type 2 screws reaching a mean of 24.7 kN (CoV 0.95%) and type 1 screws 34.2 kN (CoV 0.50%). To characterise the different behaviour of the screws in the smooth shank and profiled thread areas, the yield moments are determined in both sections with respect to the bending angle. The transition sections with reverse

threads or shank mills are also analysed. Results are shown in Fig. 3.12. Ten fasteners are tested in the transition area and three in each of the threaded and shank sections.

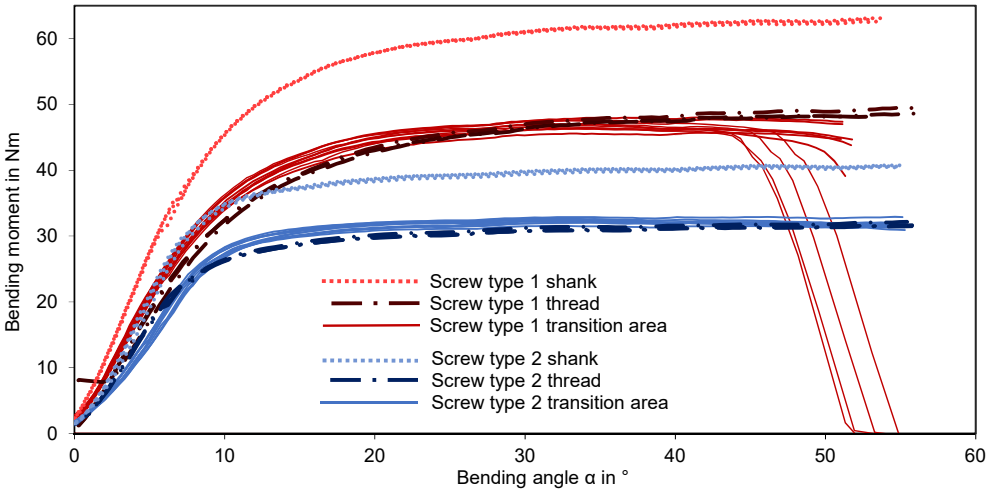

Fig. 3.12: Bending moments as a function of the bending angle of both screw types.

Large differences are observed between the shank and thread areas, which can be attributed to the varying shank and core diameters. The type 2 screws used in the tests have a shank diameter of $d_s = 5.8$ mm and a core diameter of $d_1 = 5.4$ mm. In comparison, type 1 screws have a shank diameter of $d_s = 6.5$ mm and a core diameter of $d_1 = 6.1$ mm. The yield moment curves of the transition areas from shank to thread show a behaviour very similar, both qualitatively and quantitatively, to that of the threaded sections of the partially threaded screws.

3.3.2 Discussion

The variation in the parameters can be attributed to multiple factors, including differences in the material. Structurally, the heartwood of birch is particularly important, as it is clearly distinguishable from the rest of the wood by colour and may contain structural differences affecting mechanical properties. In birch, annual rings are often significantly thicker near the pith, indicating juvenile wood with lower density and, consequently, lower strength. This partly explains the observed variation in birch determined properties. Clear physical differences between juvenile and mature hardwood are previously described by Fukazawa [39]. In birch species such as *Betula*

maximowicziana and *Betula ermanii*, density increases radially from pith to bark. Within the juvenile wood, density rises rapidly and remains relatively constant in mature wood sections. Fukazawa [39] visually illustrated the increased thickness of cell walls in mature cells, contributing to higher densities. Similarly, Schwab et al. [90] confirmed comparable properties in European birch species, including *Betula pendula*, *Betula pubescens*, and *Maximowicz's birch*. The proportion of juvenile wood in the birch boards used lead to lower densities in some specimens, in line with the observations of Fukazawa [39], Schwab et al. [90], and the contemporary investigations by Dobrowolska et al. [27].

Fig. 3.13: Specimen cross-section of a non-predrilled group connection test: Birch glulam with heartwood that can be distinguished by colour and wide annual ring widths in the pith area.

Other influencing factors in this study are the different screw geometries, which also influence the different parameters. The different head shapes, countersunk head and washer head, do not show any major differences in the magnitude of the scatter when subjected to head pull-through. On the other hand, lower scatter is observed for higher mean values of screw type 1 than for screw type 2 with lower mean values when subjected to withdrawal loads. The insertion mode, non-predrilled and predrilled, could have an influence here. A comparison with the analysed material parameters in beech LVL should be considered with regard to the different types of failure that occurred in some cases. Birch wood was generally rather brittle at the time of failure, whereas beech LVL revealed a certain ductility. This might be structurally justified, as the wood rays present in beech LVL act as reinforcement for the material.

3.3.3 Conclusion

In general, higher material property values are observed for beech LVL and type 1 screws. This can be attributed both to the higher density and to the geometric differences between the two screw types. For embedment strength, higher values are achieved in birch with predrilled type 2 screws, indicating that the installation mode affects the screw behaviour under embedment stress. Non-predrilled insertion causes predamage and densification of the surrounding wood, leading to lower embedment strength in birch solid wood. Whether this effect also occurs in connections will be discussed later. In head pull-through tests, birch boards exhibit rather brittle failure with cracking. The low scatter of parameters in beech LVL is explained by the highly homogenised material structure.

3.4 Load-Displacement Behaviour

In the following section, the results of the multi-stage tests are presented, considering the different types of wood and engineered wood products used. The plastic deformation behaviour of the screws, the load-bearing capacities of individual screws, and the initial adhesion are analysed in detail. This is followed by a comparison with the results of the tests on rows and groups of screws dealing with the effective number of fasteners.

3.4.1 Beech LVL

3.4.1.1 Predrilled Screws in Beech LVL

This section first presents an overview of all test results, highlighting general trends and differences between configurations, before discussing specific details of the load-deformation behaviour for individual test series. For the multi-stage tests, the load per screw is plotted against the relative displacement, given as the mean value of all four installed transducers. For row and group tests, the values represent the mean of the left and right connections. In Fig. 3.14, the grey dotted curves represent the results from the multi-stage tests on single screws, which serve as reference tests. Maximum displacements of nearly 40 mm are reached at failure. Various test configurations are

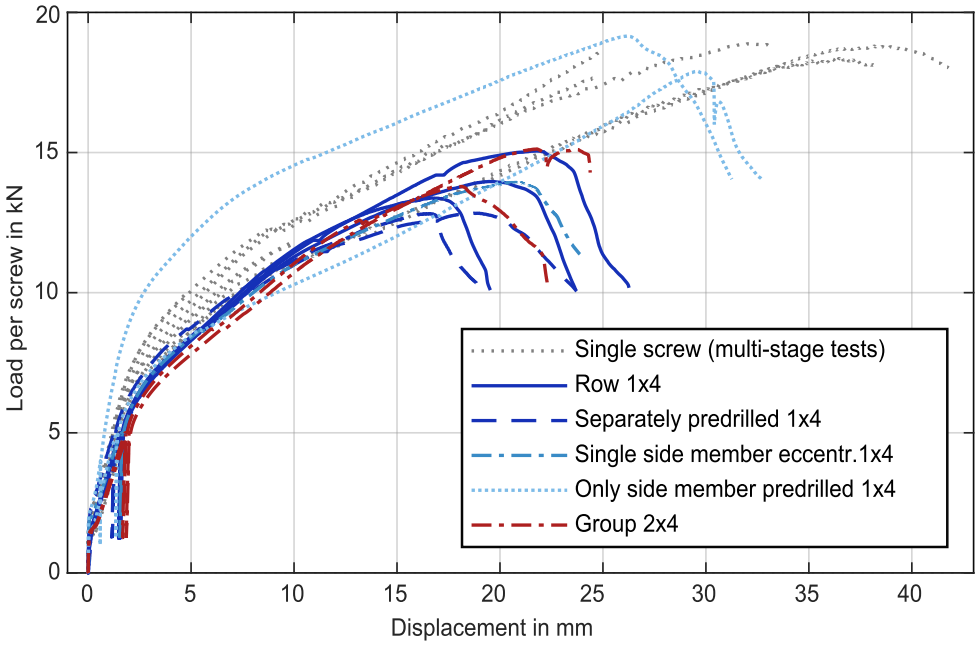

Fig. 3.14: Load-displacement curves of predrilled type 2 screws in beech LVL.

examined, including different installation types, predrilling of both timber components in one step or separately each, i.e. side timber and middle timber, and an eccentric test with a single side member. One test curve, corresponding to the configuration in which only the side timber is predrilled and pre-sunk, but the middle timber is not, shows significant deviations. In this case, three out of eight screws failed during installation. Consequently, the load-bearing capacity is calculated based on the five remaining intact screws. The deviations observed in the upper dash-dotted curve can be attributed to the contribution of the remaining screw stubs, resulting in a higher apparent load-bearing capacity. The behaviour of the eccentrically tested single side member is comparable to the symmetrically tested connections for predrilled screws in that case. All other series and group tests show only minor deviations compared to the reference tests, which can be explained by natural scatter in timber density and stiffness. Load capacities, as well as selected values of loads and stiffnesses from the recorded load–displacement curves shown in Fig. 3.14, are summarised in Tab. 3.8. Maximum loads F_{max} and the corresponding displacements $u(F_{max})$ are reported only for tests carried to failure.

The loads at defined displacements $F_{5\,mm}$, $F_{10\,mm}$, and $F_{15\,mm}$ are mean values from all multi-stage tests that reached the respective displacement; consequently, fewer data points contribute to $F_{15\,mm}$ than to $F_{10\,mm}$. Single screws show the highest maximum load and initial stiffness, while screw rows and groups exhibit lower F_{max} per screw.

Table 3.8: Results for predrilled type 2 screws. Mean values in beech LVL per screw.

Configuration	F_{max}	$u(F_{max})$	$F_{5\,mm}$	$F_{10\,mm}$	$F_{15\,mm}$	s_i	s_e	s_i/s_e
	kN	mm	kN	kN	kN	kN/mm		
Single screw (multi-stage)	18.6	31.3	9.33	12.0	13.8	2.92	0.382	7.64
Row 1x4	14.1	19.3	8.42	11.4	13.3	2.51	0.450	5.61
Row 1x4 sep. predrilled	12.8	17.6	8.55	11.1	12.5	2.49	0.345	7.22
Group 2x4	14.5	19.9	7.98	10.9	13.0	2.32	0.497	4.67

$F_{X\,mm}$ Load when achieving a mean displacement of X mm
s_i Stiffness of connection in linear elastic section: u = 0.5–1.0 mm
s_e Stiffness of connection in plastic section: u = 7–15 mm

The initial stiffness s_i characterises the response in the linear-elastic range (0.5–1.0 mm), and the effective stiffness s_e describes behaviour under larger displacements (7–15 mm). The ratio s_i/s_e indicates how much of the connection's resistance is mobilised at small displacements. These results highlight that not only maximum load but also the stiffness and the load at small displacements are crucial when comparing the behaviour of multi-screw with single-screw connections. The test results for individual screws in the multi-stage tests refer exclusively to regularly assembled connections that are tested until failure. The configurations with the eccentrically tested side member and the configuration with only predrilled side members are not considered further, since the results are not directly comparable. The maximum load F_{max} is given for completeness but occurs at different displacements in the individual configurations. The load capacities determined at the specified displacement levels are therefore more suitable for comparison. On average, the compression tests (multi-stage tests) reach a load of 12 kN at a displacement of 10 mm, which is about 10 % higher than the load per screw in the tested groups. The calculated initial stiffness s_i in the range of elastic connection behaviour is also slightly higher for the single screws. This effect is shown in Fig. 3.15. Differences in the initial behaviour occur for specimens with separately predrilled timber members. Depending on the fitting accuracy of the timber members and drilled holes, initial slip or increased tightening of the screws may

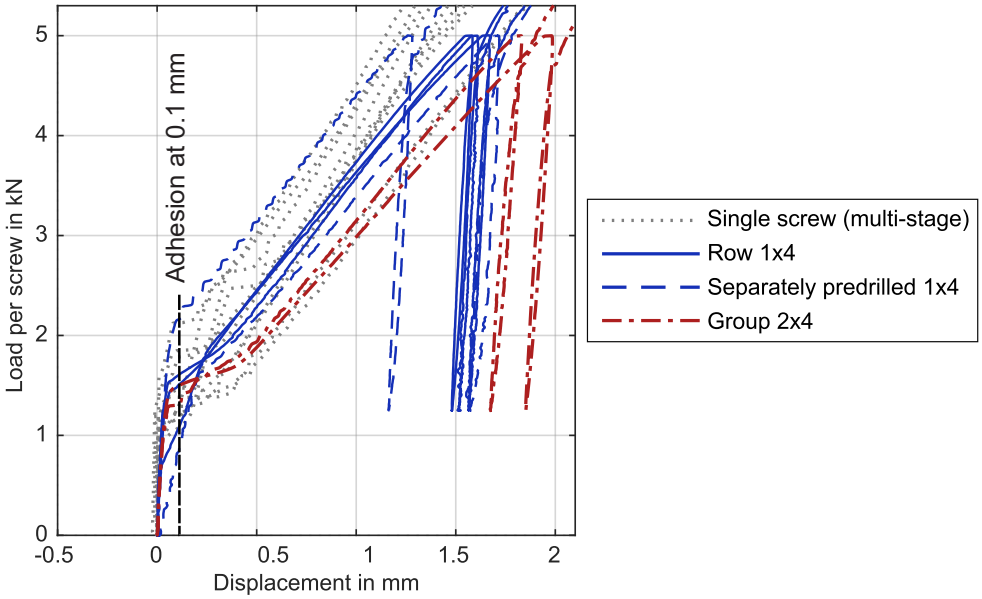

Fig. 3.15: Initial range of load-displacement curves of predrilled type 2 screws in beech LVL.

occur, which delays the detachment of the curve from the ordinate. The detachment point is defined at a deformation of 0.1 mm, where the loads are determined to allow a consistent comparison between the tests. The initial adhesion for all tests is 1–2 kN per screw (≈ 8–18 % of the ultimate load) and similar values are measured for groups of screws. With an increasing number of screws, the activated contact area within the shear plane becomes larger compared to a single-screw connection. At the same time, the resulting total normal force increases. Consequently, the overall frictional resistance in the shear plane increases, meaning that screw rows and groups require higher absolute loads to overcome static friction. However, the mean initial adhesion per screw amounts to 1.47 kN for groups, 1.56 kN for rows, and 1.66 kN for single screws in the multi-stage tests. This indicates that the friction-activating contact area does not increase linearly on a per-screw basis. To investigate and influence the initial adhesion, the type of screw insertion is varied as described in section 3.2.2.2. Sinking the screw heads presses the specimen components more tightly together and increases the initial adhesion in the shear plane. Loosening the screws by a quarter turn has the opposite effect, so that no vertical increase appears at the beginning of the load–displacement curves. The corresponding curves are shown in Fig. 3.16. The average initial adhesion of screws overtightened by 180° is 2.3 kN

per screw, and 1.7 kN for screws overtightened by 90°. Loosened screws behave differently, as their heads contact the timber later and the rope effect is activated with delay. This produces a wavelike curve with a subsequent increase in stiffness. The initial adhesion of screws turned back by 90° is nearly zero. Tab. 3.9 lists selected load stages and stiffnesses of the connections. The first row differs from Tab. 3.8, as the evaluation range for stiffness is chosen larger. The load-bearing capacity of the analysed connections increases with additional screw tightening due to higher friction in the shear plane. Turning back the screws, however, reduces the load-bearing capacity up to a displacement of at least 15 mm. Beyond this point, these specimens reach maximum capacities similar to regularly flush-fitted screws. In practice, small displacements of only a few millimetres are most relevant for serviceability, as they affect deflection limits and overall structure stability. The results therefore indicate that proper flush screw insertion is essential to achieve the load-bearing capacities determined in design.

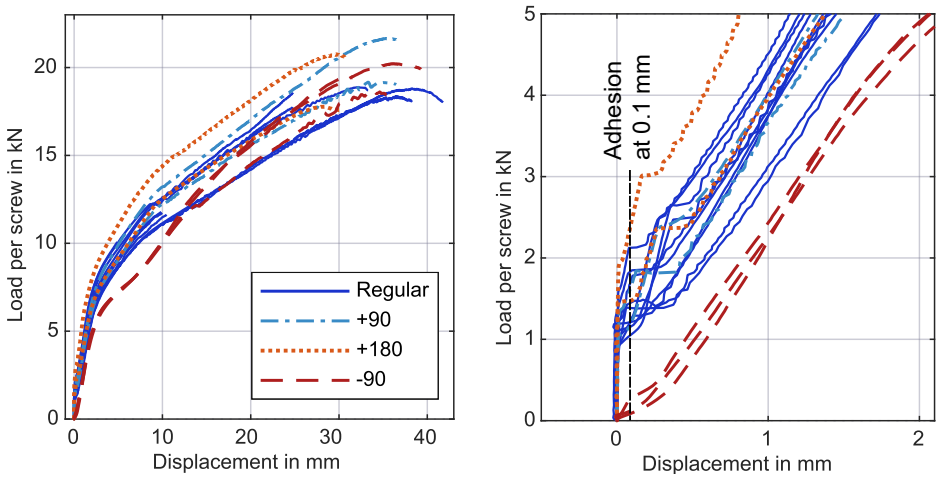

a. Total load-displacement behaviour.

b. Initial range from 0 - 5 kN focussing the initial adhesion.

Fig. 3.16: Load-displacement behaviour of predrilled type 2 screws in beech LVL, results of modified screw insertion.

Tab. 3.9 presents the load-bearing capacities and stiffnesses of connections with predrilled type 2 screws for different screw insertions. The maximum load F_{max} and the corresponding displacement $u(F_{max})$ are reported only for tests carried out until failure. The initial stiffness s_i is determined in the linear-elastic range (0.5–1.5 mm), while the stiffness s_e is evaluated in the plastic range (15–25 mm). Both stiffnesses

provide insight into the connection behaviour: s_i characterizes the initial resistance to small displacements, whereas s_e reflects the capacity under larger deformations. The ratio s_i/s_e indicates how much of the connection's resistance is mobilized in the early loading phase. These stiffness measures are therefore essential for understanding the performance of connections under service conditions, not just their maximum load.

Table 3.9: Results for predrilled type 2 screws. Mean values in beech LVL per screw considering the modified screw insertion.

Configuration	F_{max}	$u(F_{max})$	$F_{5\,mm}$	$F_{10\,mm}$	$F_{15\,mm}$	s_i	s_e	s_i/s_e
	kN	mm	kN	kN	kN	kN/mm		
Regular	18.6	31.3	9.33	12.0	13.8	2.94	0.336	8.85
+ 90°	20.5	34.4	9.60	12.8	14.5	2.75	0.347	7.95
+ 180°	19.3	28.8	10.2	13.5	15.3	3.07	0.334	9.21
- 90°	19.5	33.7	7.37	10.2	13.1	2.79	0.413	6.77

$F_{X\,mm}$ Load when achieving a mean displacement of X mm
s_i Stiffness of connection in linear elastic section: $u = 0.5$–1.5 mm
s_e Stiffness of connection in plastic section: $u = 15$–25 mm

3.4.1.2 Non-Predrilled Screws in Beech LVL

The resulting load-displacement curves for the non-predrilled washer-head screws are shown in Fig. 3.17. The results of multi-stage tests are shown for single screws, four screws arranged in a row, eight screws in a group, and an eccentrically loaded single side member with three screws.

Considering the eccentrical test setup with a single side member, it is evident that the geometry of the test affects the load-displacement behaviour. A slight inclination of the side member leads to edge pressure and increases friction in the shear plane, resulting in higher stiffness and early splitting of the side timber. Following this observation, no further eccentric tests are conducted, as the test setup is not assessed as a proper way to investigate the connection behaviour. Nevertheless, it is a helpful insight for the evaluation and the assessment of the possible scatter of load-deformation behaviour in general. The results for the screw rows in the simple symmetrical setup

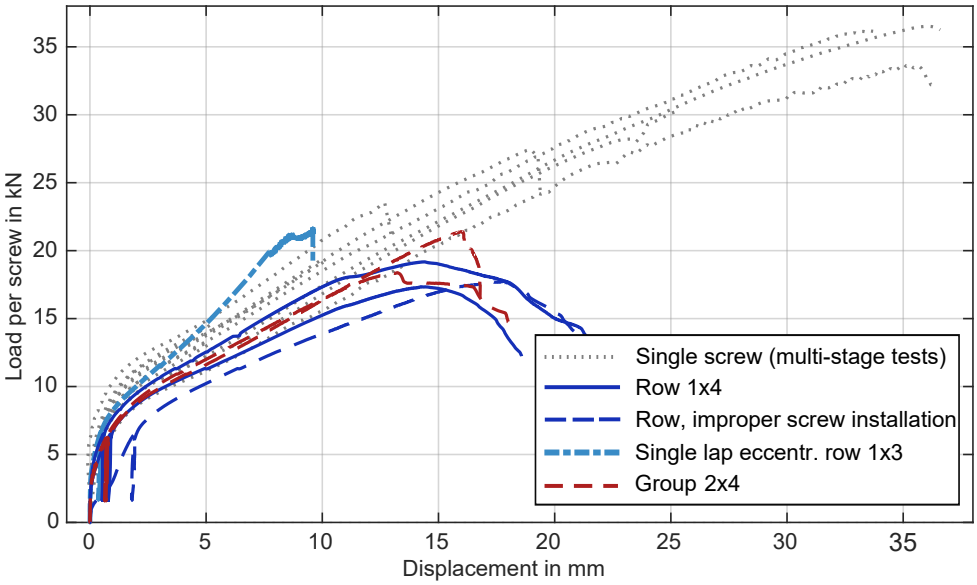

Fig. 3.17: Load-displacement curves of non predrilled type 1 screws in beech LVL.

Table 3.10: Results for non predrilled type 1 screws in beech LVL.

Configuration	F_{max}	$u(F_{max})$	$F_{5\,mm}$	$F_{10\,mm}$	$F_{15\,mm}$	s_i	s_e	s_i/s_e
	kN	mm	kN	kN	kN	kN/mm		
Single screw (multi-stage)	32.7	29.2	13.5	18.5	22.5	6.24	0.750	8.33
Row 1x4	18.1	15.4	11.4	15.5	17.7	4.21	0.844	4.99
Group 2x4	19.9	14.5	11.8	16.4	19.2	5.07	0.917	5.53

$F_{X\,mm}$ Load when achieving a mean displacement of X mm
s_i Stiffness of connection in linear elastic section: $u = 0.2$–0.4 mm
s_e Stiffness of connection in plastic section: $u = 5$–8.7 mm

(blue continuous lines) are comparable to the multi-stage compression tests up to a displacement of approximately 10 mm. Beyond this point, the test specimens exhibit a load drop and failure of the side members due to splitting. Screw failure is possible and visible in the load-displacement curves as a sudden drop in load, for example at approximately 13 mm and 19 mm displacement. The dashed blue line in Figs. 3.17 and 3.18 represents an exception: it is shifted to the right, so that the maximum load is reached at larger relative displacements. Examination of the initial load-displacement

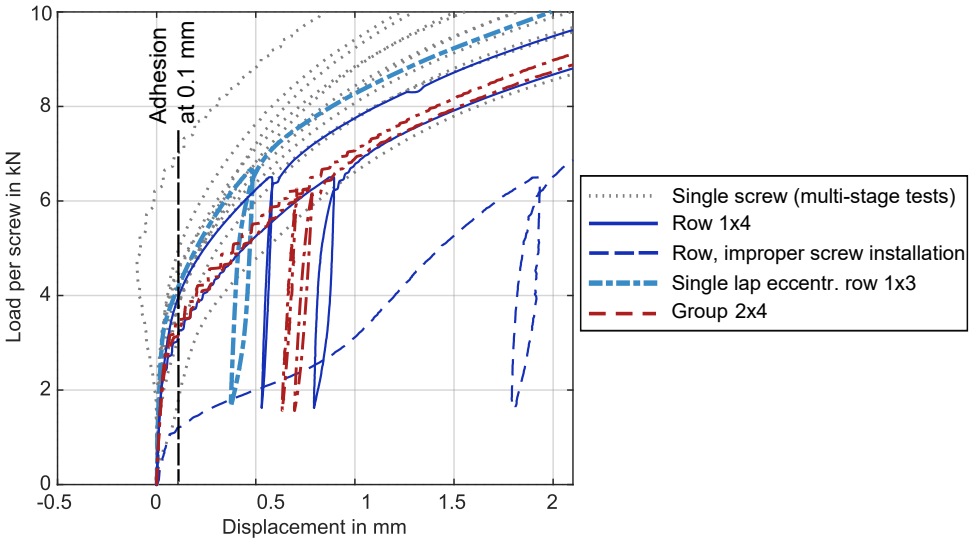

Fig. 3.18: Initial range of load-displacement curves of non predrilled type 1 screws in beech LVL.

behaviour shows an early detachment from the ordinate, see Fig. 3.18, indicating slip in the connection. The different connection behaviour results from improper screw insertion, see Fig. 3.19. During insertion of screw no. 3, the screw head was damaged, causing the bit to spin in the head and preventing firm, flush attachment to the timber surface.

3.4.1.3 Comparison of Connections in Beech LVL

The results for predrilled and non-predrilled screws in beech LVL reveal distinct differences in connection behaviour. Non-predrilled screws reach considerably higher maximum loads than predrilled screws, with single screws achieving 32.7 kN compared to 18.6 kN for predrilled single screws. Maximum relative displacements are similar for both screw types, generally between 14–31 mm, indicating ductile performance. For predrilled screws, load at selected displacement stages increases more gradually from single screws to rows and groups, whereas non-predrilled screws maintain higher loads at small displacements, reflecting stiffer initial behaviour under service-relevant conditions. Initial stiffness s_i is notably higher for non-predrilled single screws (6.24 kN/mm) than for predrilled ones (2.92 kN/mm), while end stiffness s_e is also higher, demonstrating that non-predrilled screws resist larger deformations more

Fig. 3.19: Improper screw insertion: Protruding screw head no. 3.

effectively. The ratio s_i/s_e is similar for both types in single screws, but decreases for rows and groups of non-predrilled screws, suggesting that load resistance is mobilised over a wider displacement range. Overall, predrilled screws provide moderate initial stiffness and lower maximum loads, whereas non-predrilled screws combine high initial stiffness with high ultimate load-carrying capacity.

3.4.1.4 Observed Failure Modes in Beech LVL

Maximum loads are reached at widely varying displacements and lead to different failures, see Fig. 3.20. Single screws often exhibit very large displacements, with failure occurring due to splitting of the timber test specimens. In some cases, failure occurs earlier due to fastener failure, i.e. steel failure, in the shear plane or in the plastic hinge. Representative images of failed screws are shown in Fig. 3.21. This failure is only observed in single-screw tests. For rows and groups of screws, the primary failure occurs due to splitting of the timber either between screws or at the end grain, with secondary, enlarged cracks appearing along the screw rows on all specimens. A crack in the screw tip line is also observed, see Fig. 3.20c.

a. Deformation of predrilled screwed connection (type 2), opened specimen.

b. Deformation of non-predrilled screwed connection (type 1), opened specimen.

c. Crack in screw tip line.

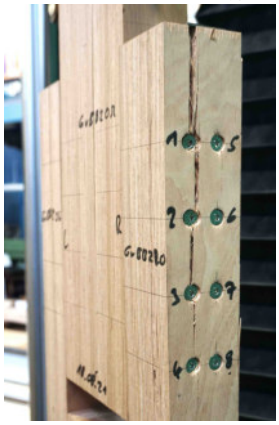

d. Splitting of timber (type 2).

e. Splitting of timber (type 1).

Fig. 3.20: Different deformation and timber failures in single-screw and multi-screw connections in beech LVL.

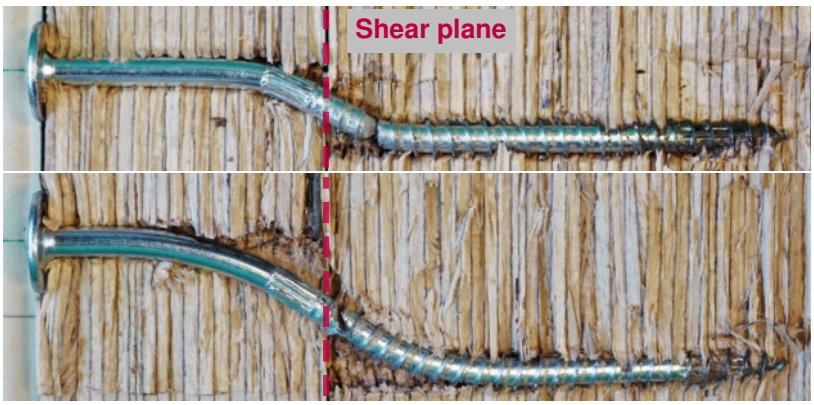

Fig. 3.21: Fastener failure of non-predrilled (type 1) single screws in connection tests: Failure in plastic hinge of the middle timber at the top. Failure in the shear plane at the bottom.

3.4.2 Birch Glulam

3.4.2.1 Predrilled Screws in Birch Glulam

Compared to beech, birch has a lower density, of approximately 600 kg/m^3. This results in lower load-bearing capacities and connection stiffness, which the tests confirm. Estimated maximum loads are adjusted between separate tests, which explains the variation in loop sizes in Fig. 3.22 and leads to different ranges for the stiffness evaluation of $s_{i,row}$ and $s_{i,group}$ in Tab. 3.11. In one of the row tests, the transducer stopped at around 18 mm relative displacement, so the curve ends at that point. Maximum machine loads are still recorded and included in the evaluation. Deformations when reaching failure loads are comparable for rows and groups with the fastener spacings used. Overall, very large displacements are reached, with a maximum relative displacement of nearly 40 mm, indicating ductile behaviour of the connections. Considerable variations in the initial stiffness s_i are observed between the tested series. A possible explanation is the settlement of the connection elements: due to predrilling, the screws have a limited tolerance before they are firmly seated in the borehole and the embedment stresses are fully activated.

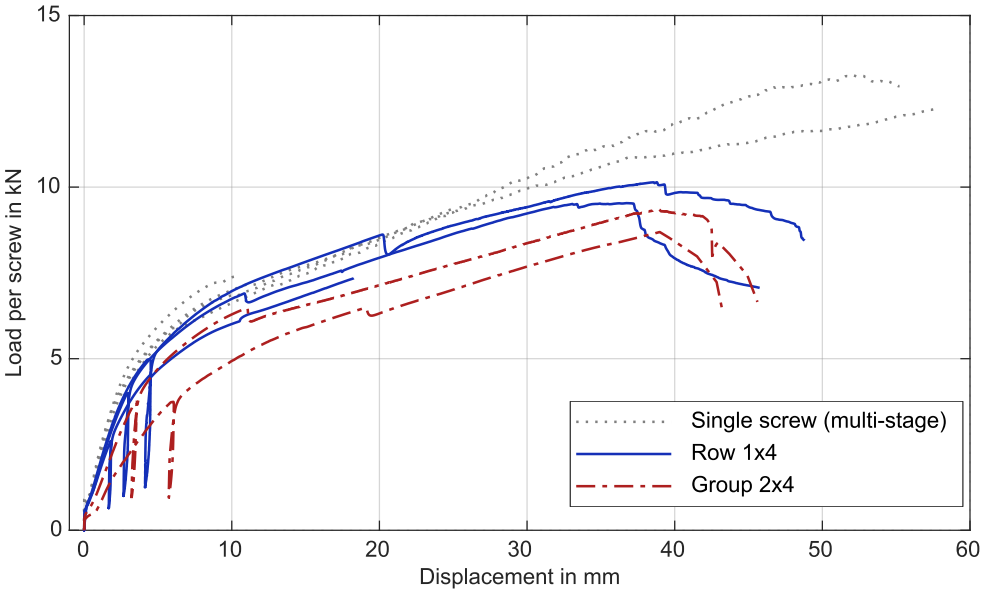

Fig. 3.22: Load-displacement curves of predrilled type 2 screws in birch glulam.

Table 3.11: Results for predrilled type 2 screws in birch glulam.

Configuration	F_{max}	$u(F_{max})$	$F_{5\,mm}$	$F_{10\,mm}$	$F_{15\,mm}$	s_i	s_e	s_i/s_e
	kN	mm	kN	kN	kN	kN/mm		
Single screw (multi-stage)	12.8	54.7	5.74	7.02	7.64	1.63	0.118	13.8
Row 1x4	9.93	37.8	5.07	6.59	7.31	1.38	0.150	9.24
Group 2x4	9.03	38.9	4.05	5.63	6.25	0.908	0.138	6.56

$F_{X\,mm}$ Load when achieving a mean displacement of X mm
$s_{i,row}$ Rows: Stiffness of connection in linear elastic section: $u = 0.5$–1.5 mm
$s_{i,group}$ Groups: Stiffness of connection in linear elastic section: $u = 1$–3 mm
s_e Stiffness of connection in plastic section: $u = 12$–17 mm

3.4.2.2 Non-Predrilled Screws in Birch Glulam

The resulting stiffnesses of single screws, rows, and groups behave very similarly, with no outliers observed, see Fig. 3.23. Elastic stiffnesses at the beginning show little scatter, whereas the end stiffness in section 3 decreases from single screws to rows and then to groups, as reflected by the end stiffness s_e in Tab. 3.12.

Table 3.12: Results for non predrilled type 1 screws in birch glulam.

Configuration	F_{max}	$u(F_{max})$	$F_{5\,mm}$	$F_{10\,mm}$	$F_{15\,mm}$	s_i	s_e	s_i/s_e
	kN	mm	kN	kN	kN	kN/mm		
Single screw (multi-stage)	21.5	52.6	6.74	8.73	10.3	1.53	0.313	4.88
Row 1x4	14.2	24.0	6.70	8.77	10.1	1.39	0.203	6.83
Group 2x4	11.5	34.2	6.11	8.03	8.92	1.43	0.159	9.00

$F_{X\,mm}$ Load when achieving a mean displacement of X mm
s_i Stiffness of connection in linear elastic section: $u = 0.5$–1.5 mm
s_e Stiffness of connection in plastic section: $u = 15$–22 mm

Maximum loads per screw of screw groups are lower than those of rows. Single screws and rows behave similarly in terms of load-deformation behaviour when

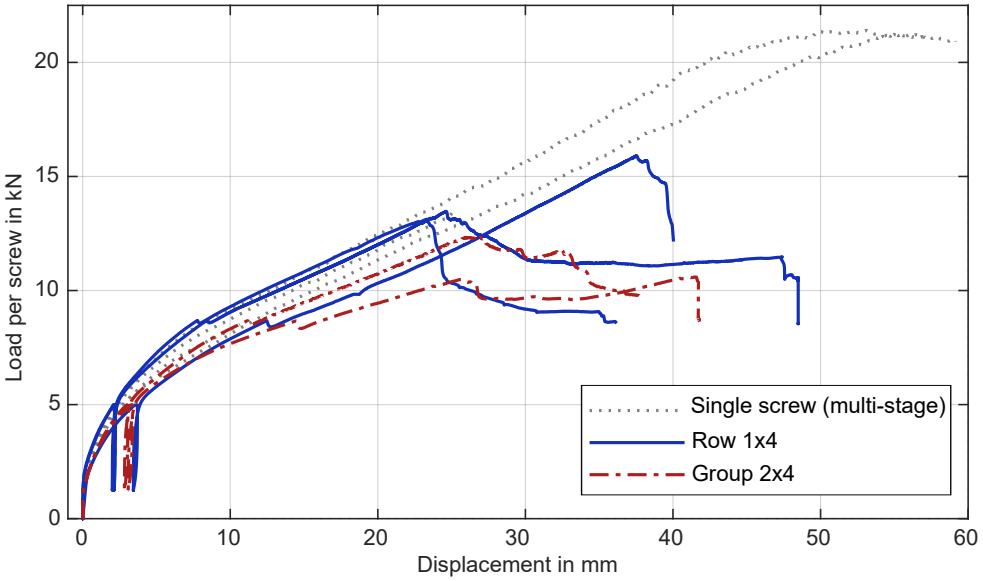

Fig. 3.23: Load-displacement curves of non predrilled type 1 screws in birch glulam.

considering loads achieved at selected displacement stages. Non-predrilled screw groups, however, show a reduction in load of approximately 90 % compared to the single screws tested. Additional diagrams for the initial behaviour of connections in birch glulam are given in Appendix A.2.

3.4.2.3 Comparison of Connections in Birch Glulam

The results for predrilled and non-predrilled screws in birch glulam show clear differences in load-bearing behaviour. Non-predrilled screws achieve higher maximum loads across all configurations compared to predrilled screws, with single screws reaching 21.5 kN versus 12.8 kN for predrilled single screws. Maximum relative displacements are similar for both screw types, ranging from approximately 35–55 mm for single screws, indicating ductile behaviour, which is due to the large end distances. Considering loads at selected displacement stages, non-predrilled screws generally carry higher loads at small displacements, particularly for single screws and rows, which is important for serviceability. Initial stiffness s_i of single screws is slightly higher for predrilled screws (1.63 kN/mm) than for non-predrilled screws (1.53 kN/mm), whereas rows and groups show similar values for both types. In contrast, end stiffness s_e is

considerably higher for non-predrilled screws, reflecting stiffer behaviour under larger deformations. As a result, the ratio s_i/s_e is larger for predrilled screws, indicating that a higher proportion of their ultimate resistance is mobilised at small displacements, while non-predrilled screws mobilise resistance more gradually over the deformation range. Overall, predrilled screws provide higher initial stiffness relative to their ultimate load, whereas non-predrilled screws offer higher maximum loads and greater stiffness under large displacements.

3.4.2.4 Observed Failure Modes in Birch Glulam

As a common observation, all connections in birch glulam show a fairly ductile behaviour and large displacements are achieved with the chosen spacings and end distances. For some of the multi-stage tests represented with the gray dashed lines there is no failure of the connection until almost 60 mm displacement. Nevertheless deformations are visible as e.g. pull-in of the screw head into the side timber, see Fig. 3.24 and 3.25. Observed failure modes of rows and groups of screws are splitting of the timber between the screws or tensile failure of the middle timber in the axis of symmetry due to induced tensile forces perpendicular to the grain. This was followed by a block shear failure of the specimen in the area of the lowest screw, see Fig. 3.26.

Fig. 3.24: Exemplary head pull-in of non-predrilled screws (type 1) in birch glulam and inclination in side timber at large displacements.

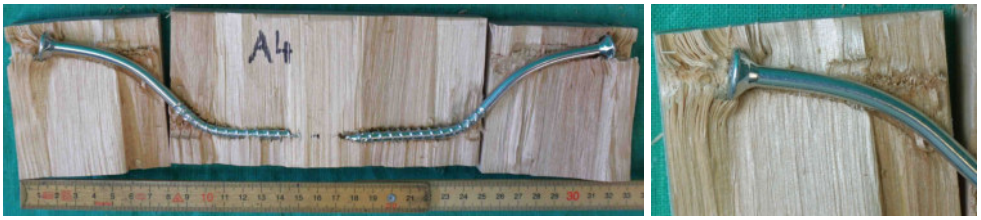

Fig. 3.25: Exemplary head pull-in of predrilled screws (type 2) in birch glulam.

Fig. 3.26: Splitting in grain direction on the left and secondary block shear failure of predrilled screws in birch glulam.

3.4.3 Spruce Glulam

As a reference, specimens made of spruce glulam are tested to point out the differences between softwood and hardwood connections. Results are presented in Fig 3.27 and Tab. 3.13.

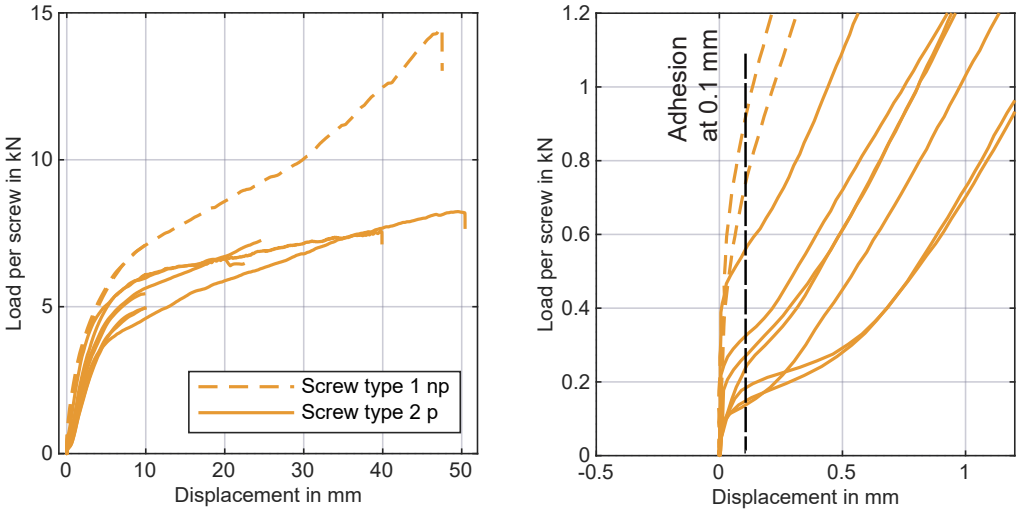

a. Complete load-displacement curves

b. Initial range of load-displacement curves .

Fig. 3.27: Load-displacement curves for screws in spruce glulam.

Table 3.13: Results for predrilled and non predrilled screws in spruce glulam, only multi-stage tests.

Configuration	F_{max}	$u(F_{max})$	$F_{5\,mm}$	$F_{10\,mm}$	$F_{15\,mm}$	s_i	s_e	s_i/s_e
	kN	mm	kN	kN	kN	kN/mm		
Screw type 1 np	14.5	47.4	5.72	7.15	7.88	1.43	0.0121	119
Screw type 2 p	7.49	36.2	4.42	5.48	6.08	1.25	0.0056	226

$F_{X\,mm}$ Load when achieving a mean displacement of X mm
s_i Stiffness of connection in linear elastic section: $u = 0.5$–1.5 mm
s_e Stiffness of connection in plastic section: $u = 15$–24.5 mm

Considering the initial adhesion, screwed connections in spruce glulam show only minor adhesional forces at the beginning. For predrilled screws, a mean initial adhesion of 0.571 kN is determined. One of the plotted continuous curves is excluded from this evaluation, as it reaches a detachment point of almost 1 kN. In this case, the screws are inserted without presinking the heads into the timber surface and thus leads to higher initial adhesion. The two tested non-predrilled screws behave similarly, as their curves are nearly identical until one test is stopped at 10 mm displacement. In general, the connections in spruce show ductile behaviour and reach large displacements. Due to knots and density variations in the connection area, a considerable scatter in stiffness is observed between specimens. Non-predrilled screws reach clearly higher maximum loads than the predrilled screws, with almost twice the capacity. This difference is also visible at selected displacements of 5, 10 and 15 mm. However, the corresponding displacements at the maximum loads are higher for the non-predrilled screws, indicating a more ductile behaviour. The ratio of initial to end stiffness shows a significant difference between the two screw types. Predrilled screws have a considerably higher ratio, which means that the relative reduction in stiffness from the elastic to the plastic range is larger. Overall, the non predrilled screws combine higher capacities with a more gradual stiffness decrease.

3.4.3.1 Observed Failure Modes in Spruce Glulam

In spruce glulam, the deformation failure modes of the single-screw connections are characterised by the development of one or two plastic hinges per shear plane, see

Fig. 3.28. In addition, embedment failure of the softwood is visible on the opened specimens. There was no cross-sectional failure of the fastener.

a. Deformation of non-predrilled screwed connection (type 1).

b. Deformation of predrilled screwed connection (type 2).

Fig. 3.28: Exemplary deformation failure modes of screws in spruce glulam.

The predrilled screws form two plastic hinges, whereas the non-predrilled screws, due to their larger core diameter and higher bending resistance, form only a single plastic hinge in the middle timber. The thickness of the side members is insufficient to develop a second plastic hinge.

3.5 Incremental Deformation Analysis

The incremental plasticising of the fasteners is examined by means of the multi-stage tests. The results of the predrilled configuration at defined displacement stages are presented as an example. Additionally, the effect of modified screw installation is analysed. Fig. 3.29 shows the load-displacement curves of regularly installed screws, terminated at displacements of 5 mm, 10 mm and 25 mm and some conducted until failure. The corresponding progressive displacement and the associated plastic deformations in the timber and fasteners are visible on the opened test specimens, see Fig. 3.30. It is important to note, however, that due to elastic recovery of both the screw and the timber during unloading, the condition of the opened specimens does not exactly correspond to their state under load.

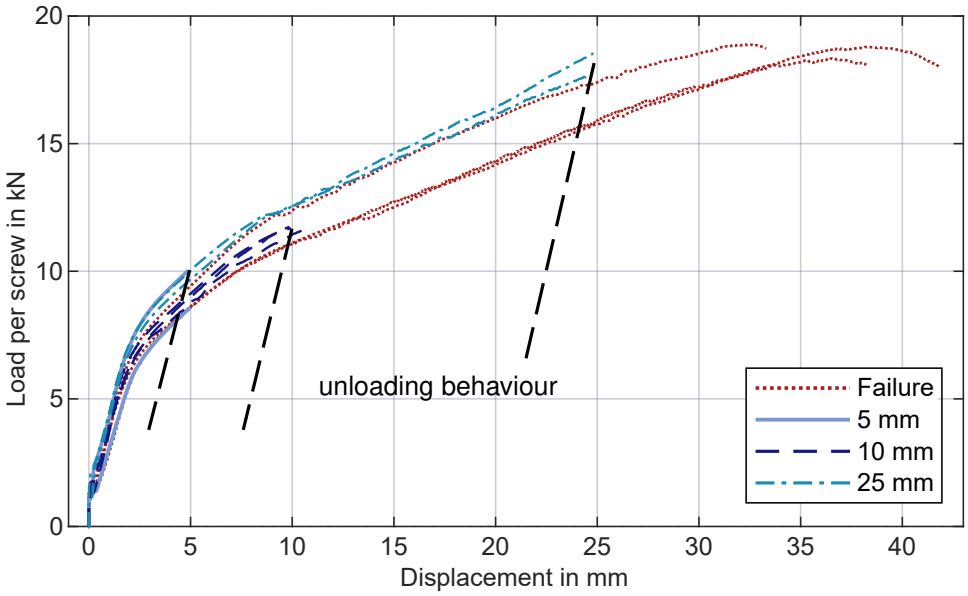

Fig. 3.29: Load-displacement curves for predrilled configurations in beech LVL with stops at predefined deformation stages.

Table 3.14: Mean values for measured geometry corresponding to deformed screws in Fig. 3.30, displacement u, embedment length b_i, bending radius R and bending angle α_{remain}.

Specimen	u_{max}	u_{remain}	b_1	b_2	R_1	R_2	α_{remain} in °	
	in mm	in mm	shank	thread	shank	thread	shank	thread
A4	5	1.84	15.1	10.1	316	163	4.00	4.50
A3	10	6.53	16.0	11.7	69.9	56.9	13.5	14.0
A8	25	19.0	16.9	11.3	42.7	31.9	34.0	33.5
A2	Fail*	32.2	18.8	14.2	52.6	27.4	45.5	44.0

* Splitting failure of the specimen at $u_{max} = 42$ mm

A geometric analysis of the deformed configurations is conducted exemplarily. From a qualitative perspective, initial irreversible deformations are visible at the first opening stage of 5 mm, although they remain minor. Incipient embedment failure occurs near the shear plane. At 10 mm displacement, distinct plastic hinges form in the fastener, which intensify further with increasing displacement up to $u = 25$ mm. Due to the softer behaviour of countersunk head screws in head pull-in compared to thread withdrawal,

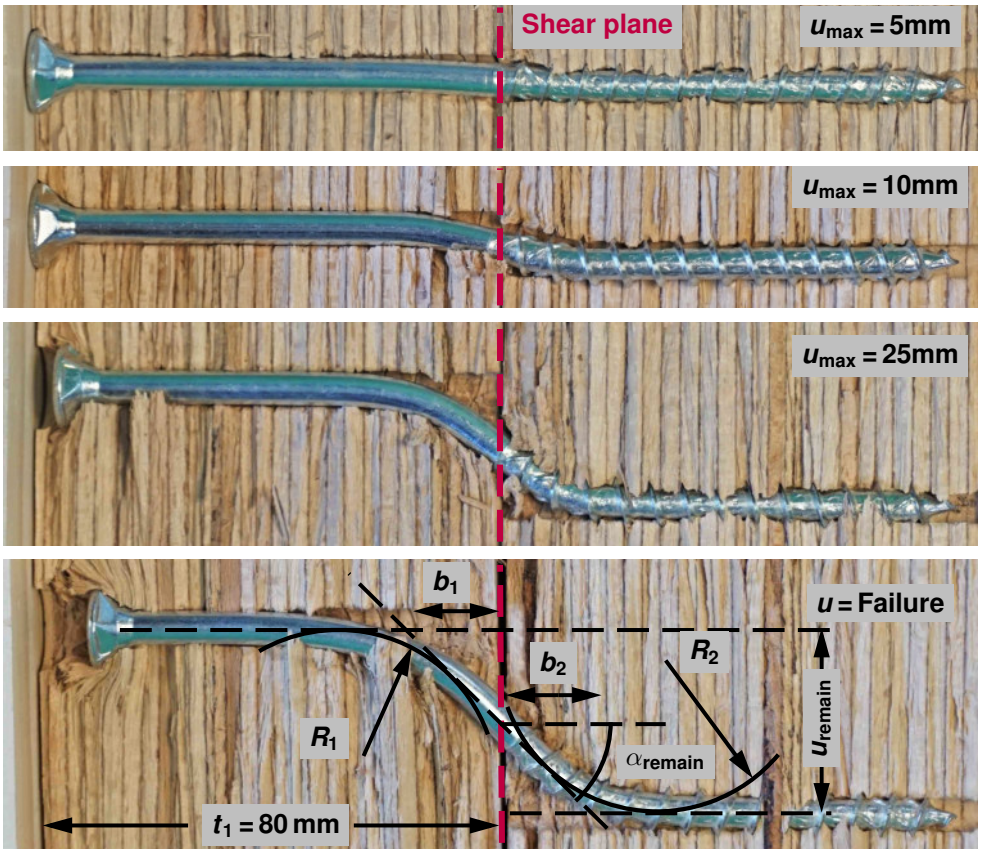

Fig. 3.30: Incremental deformation at opening stages 5 mm, 10 mm, 25 mm and failure.

the screw head is pulled progressively deeper into the side member, resulting in an increasing asymmetric connection.

Comparing the bending radii reveals a difference between shank and thread sections. The radius in the threaded sections is significantly smaller than in the shank, as the bending resistance is different due to geometric differences. In addition, the developing normal force in the fastener tends to straighten the shank. The threaded section to the right of the plastic hinge remains firmly embedded in the central member. At time of failure, the screw head is fully pulled into the side timber. The reduced embedment length of the fastener eventually leads to splitting of the side timber. For comparison of the opening stages, the remaining geometries and deformation parameters are measured, evaluated and listed in Tab. 3.14. The mean values given are the average

between the two screws of each opened specimen. Three sections that are mostly straight are defined: in the shank section close to the head, the firmly anchored part close to the screw tip and the inclined section in the shear plane. For each of those sections, an axis is determined and a line is drawn.

The remaining displacement u_{remain} is taken as the vertical distance between the intersection points of the screw axis lines. The embedment lengths b_1 and b_2 are determined as a horizontal distance between the intersection points and the shear plane. In addition, two bending angles, for the shank and threaded sections, are measured. Another observation mentioned is the different characteristics of the bending radii in shank and thread. The deformed yield sections are therefore approximated by circles, with the diameter marked with three lines and a circle set as a tangent using a three-point definition. Individual results for each screw and an exemplary geometrical evaluation are shown in Appendix A.4. As the images show the state after test completion and after opening of the specimens, they do not directly represent the situation at the moment of failure. Elastic contributions to a reverse deformation from the bending of the fastener and the embedment of the timber must be considered. The difference between the maximum displacement measured between the timber members and the remaining irreversible deformation increases when larger deformations are reached. In the case of small deformations, the reverse deformations mainly consist of an elastic embedment component. As the maximum deformation increases, the reverse deformation resulting from the bending of the screw itself becomes more significant. The elastic bending angle is approximately $\alpha_{\text{el}} = 6°$ according to the yield moment curves, see Fig. 3.12. For larger relative displacements, the elastic contribution from fastener rebound increases due to geometric conditions, whereas the contribution due to embedment stresses remains nearly constant and is relatively minor, with a magnitude below 1 mm. Consequently, the measured irreversible displacements differ a lot from the actual displacements present at failure. The lengths with achieved embedment strength, b_1 and b_2, increase with greater deformation. They increase evenly in the shank and thread sections. However, there are general differences in magnitude between the shank and thread sections. The length of achieved embedment strength is consistently smaller in the thread section. This is due to the reduced diameter and smaller effective cross-section of the thread sections. This determines not only the magnitude of the yield moment, but also the position of the forming plastic hinge and, consequently, b_2. It should be noted that reliable measurements of the determined bending radii are not possible, especially in the case of small deformations, as it is difficult to exactly determine the plastic hinge or the yield zone. Nevertheless, at least trends for the deformations examined can be identified. The bending radii become

smaller with increasing deformation, even if this is not consistently evident in the shank section. This may be due to the individual test specimen and should be investigated in a wider study. In addition, a difference in magnitude can be seen, whereby larger radii, i.e. larger yield zones, generally occur in the shank section than in the thread section. In this analysis, only qualitative comparisons are possible, as the geometry of the screw section and material properties have a major influence on the deformation behaviour and, in particular, on the bending behaviour. Another geometric parameter is the remaining irreversible bending angle α, which, due to the geometric correlation with u_{remain} and b_i, shows a similar increase with larger deformations.

However, significant differences exist even between the two screws within a single test specimen. One factor not taken into account is the load distribution. It cannot be assumed that the load is distributed equally across the two shear planes, which consequently leads to different deformations.

The measured bending angles show that bending moments in the range of the plastic yield moment are reached from displacements of approximately 10 mm onwards in beech LVL.

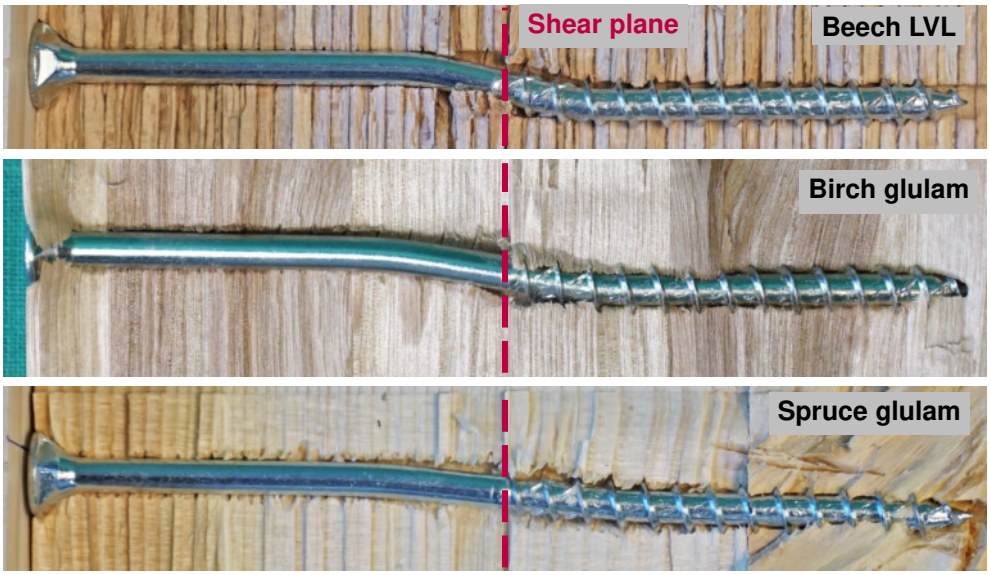

Fig. 3.31: Comparison of opening stage at 10 mm displacement in beech LVL, birch glulam and spruce glulam.

The influence of the used timber product and therefore the influence of density is shown in Fig. 3.31. Irreversible deformations at an opening stage of 10 mm for beech LVL, birch glulam and spruce glulam are presented. In hardwood, and in particular in beech LVL, distinct plastic hinges are already formed at this stage, whereas in softwood only initial plastic deformations of the screws are visible. Nevertheless, zones of embedment failure can be observed around the shear plane, indicating that significant bending angles are already present under load. When comparing the reached loads at this displacement stage, i.e. 12 kN in beech LVL, 7.02 kN in birch glulam and 5.5 kN in spruce glulam, the relation becomes clearer. In relation to spruce, this results in an increase with a factor of 1.28 for birch and a factor of 2.18 for beech LVL. An overview with exemplary opened specimens for all tested configurations and deformation stages can be found in Appendix A.4.

3.6 Discussion

This section interprets the deformation behaviour of screws observed in the multi-stage tests and the groups of screws, focusing on differences between timber species, screw types, and the influence of initial adhesion. The aim is to relate the observed load-displacement behaviour to underlying mechanisms and to derive practical implications for design.

3.6.1 Comparison of Load-Displacement Behaviour

The multi-stage tests reach relatively large displacements, which results from the large end distances of the screws in grain direction. All specimens meet the displacement requirement of 10 mm according to EAD 130118-01-0603 [127]. Comparisons with literature show that even a small increase in screw spacing leads to larger deformations and fulfils the ductility criterion for the investigated connections, see [1] and [67, 103]. The loads evaluated at 10 and 15 mm relative displacement are suitable for a direct comparison between multi-stage and row or group tests, as discussed in [1]. Comparable tests conducted by Meyer [67] and Vedovelli [103] with a distance $a_1 = 7\,d$ resulted in failure at relative displacements of 9.1 mm and 7.2 mm, respectively. The positive effect of increasing the screw spacing in grain direction by $\Delta a_1 = 1\,d$ should be noted, as it leads to significantly larger deformations and fulfills the ductility criterion for the investigated connections.

Analyses of the measured bending angles show that the plastic yield moment is approached from approximately 10 mm displacement in beech LVL. Therefore, the plastic hinge theory according to Johansen applies only beyond this displacement, as the yield moment serves as the governing design parameter for the connection. At this level of deformation, head pull-in gradually begins to occur. The Johansen equations are therefore only applicable in situations where head pull-in is minimal and the embedment length of the screw in the side timber is not significantly reduced. Using the input parameters determined, see Section 3.3 for Johansen's model, the calculated load-bearing capacity for a predrilled single-shear connection is 9.7 kN for beech LVL and 5.7 kN for birch glulam. These results include a rope effect of the minimum of $F_{ax}/4$ and the basic Johansen part, which amounts 5.8 kN for beech LVL and 4.0 kN in birch glulam. In the tests, loads of around 12 kN and 7.02 kN (and 5.5 kN in spruce glulam) respectively are reached at a displacement of 10 mm; however, this value includes an initial adhesion of approximately 1.7 kN for beech LVL and 0.5–1.0 kN for birch glulam. Considering the initial adhesion being more or less a testing phenomenon, as it is discussed shortly afterwards in Section 3.6.5, it could be conservatively substracted from the maximum loads reached. Therefore, the reduced loads amount to 10.3 kN in beech LVL and around 6–6.5 kN in birch glulam. These loads are slightly higher than the calculated loads. This indicates sufficient ductility of the connection. Secondly, the 10 mm stage marks the point at which the screws and the timber reach plasticity and yield models can be applied to all tested timber products. Whether the initial adhesion is substracted or not, the reached loads are higher than the calculated load-bearing capacity.

A complete overview of all results of the individual screw connection tests with both screw types can be found in Fig. 3.32. The significant differences in load-deformation behaviour and the differences in stiffness become clear in direct comparison. Beech LVL connections reach smaller overall deformations at the onset of failure. This also varies greatly from splitting and cross-sectional failure of the screws to typical plastic hinge formation with embedment failure. The early failures can be easily recognised by the load drops in Fig. 3.32a. Birch and spruce glulam, on the other hand, show a much more ductile behaviour. The hardwood screw with the washer head has a more pronounced rope effect than the pre-drilled screw.

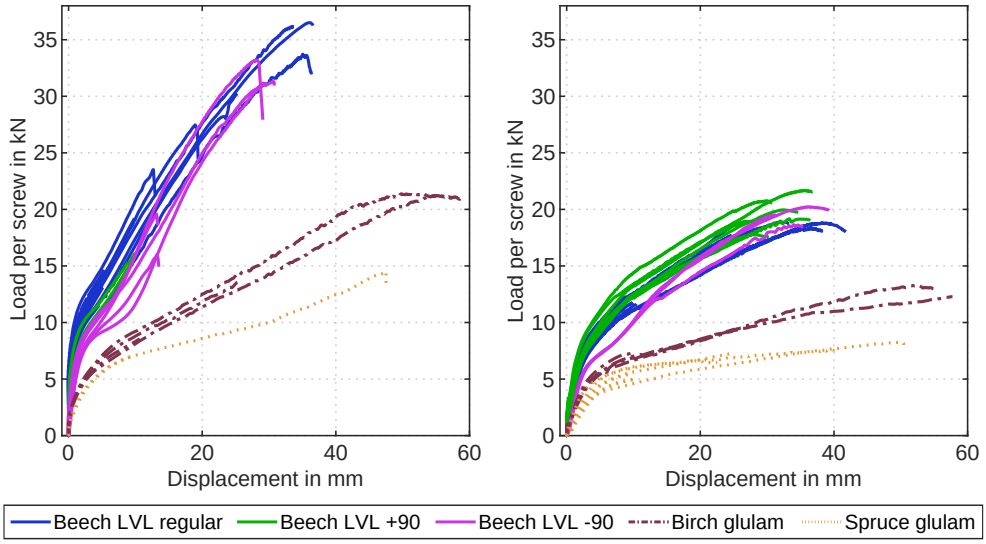

a. Screw type 1 non-predrilled. b. Screw type 2 predrilled.

Fig. 3.32: Overview: Load-displacement curves of single-screw connections with both screw types.

3.6.2 Influence of Screw Installation

The screw insertion technique significantly affects the initial adhesion and the load-displacement behaviour. Over-tightened screws (+90°, +180°) exhibit higher initial adhesion and reach higher ultimate loads, indicating that partially threaded screws can be effectively prestressed in beech LVL. Screws turned back by 90° show initial slip and a delayed activation of the rope effect, with lower loads up to approximately 13 mm relative displacement. The load at a relative displacement of 0.1 mm quantifies the initial adhesive force. Predrilled screws reach about 1.6 kN per screw, non-predrilled screws about 4.1 kN in beech LVL. In birch, predrilled connections reach 0.5–1.0 kN per screw, whereas non-predrilled screws reach 1.5–1.7 kN. Spruce connections show almost no initial adhesion. Proper screw assembly and firm application of the screw head are prerequisites for the activation of initial adhesion. The effect remains stable over three weeks under laboratory conditions, but it may decrease in real structures due to timber shrinkage and hygroscopic effects. During testing, one screw could not be fully inserted due to a turning bit in the screw head, resulting in a protruding screw head and reduced initial adhesion. This leads to increased slip and delayed activation of the rope effect. Comparable challenges with screw insertion in beech LVL are reported by Schiro et al. [89]. Such observations underline the importance of

proper assembly quality for achieving the expected load-bearing capacity. Fasteners subjected to over-tightening (+90°, +180°) show higher initial adhesion, resulting in an increase in ultimate load. This indicates that partially threaded screws can be effectively prestressed in beech LVL. Conversely, screws turned 90° back show no initial adhesion and a slight initial slip. In particular, turned-back screws exhibit a distinct load–deformation behaviour in relation to gradients. The screw head presses against the wood surface later, i.e. at larger displacements, activating the full potential of the rope effect. Up to a relative displacement of approximately 13 mm, the loads observed for turned-back screws remain below those for screws inserted regularly.

3.6.3 Influence of Material Properties

The wood species and the timber product affect both ductility and stiffness. Hardwoods (beech LVL, birch glulam) form distinct plastic hinges at smaller displacements, whereas softwoods such as spruce show gradual yielding. Initial stiffness and maximum loads are generally higher in hardwoods due to higher density, whereas softwoods exhibit higher variability due to knots and juvenile wood content. Birch in particular shows relatively low densities in the present tests, likely due to the amount of juvenile wood in the boards. The maximum loads reached reflect these material characteristics. This highlights the importance of material selection when designing for high-capacity connections. A comparison of irreversible deformations at 10 mm displacement shows that beech LVL forms distinct plastic hinges, whereas spruce glulam only exhibits slight plastic deformations. Embedment failure zones are observed in both cases, highlighting differences in ductility and the influence of timber species on load-bearing behaviour.

3.6.4 Failure Mechanisms

Primary failure mechanisms include splitting between screws or towards the end grain, and tensile failure perpendicular to the grain of the middle members in screw groups due to the activation of large normal forces. This results in cracks in the plane of the screw tips. Krenn [58, 59] investigated how this failure could be prevented in the case of an inclined screw arrangement, for example. He recommended overlapping the screw tips by 4 d, which would also be advisable for the present test configurations with the screws arranged at 90° to the surface. Secondary failure mechanisms include

progressive splitting and block shear failure, particularly observed in birch glued laminated timber. Comparing hardwood (beech LVL) and softwood (spruce glulam), distinct differences in ductility and stiffness are noted. Progressive splitting is more pronounced in birch glulam, while spruce shows more ductile failure with gradual crack development. In birch, block shear failures of the screw groups could potentially be prevented by adjusting the screw layout, for example by overlapping screw tips to reduce stress concentrations perpendicular to the grain. The observed failure patterns confirm that screw type and timber quality strongly influence the load-bearing behaviour. These differences highlight the necessity of tailoring connection design to the specific material characteristic.

3.6.5 Influence of Initial Adhesion and Preload

Initial adhesion significantly shapes the load-displacement curves, especially for predrilled countersunk screws, where a clear separation from the ordinate and a linear elastic section are visible. Non-predrilled screws with washer heads show a smoother transition. While the initial adhesion can be observed consistently under laboratory conditions, the axial preload depends on whether the shear plane remains closed in service. Timber shrinkage can reduce this effect and thus decrease the anticipated increase in load-bearing capacity. Swelling does not seem critical, as wet specimens show no reduction in load capacity or significant variation in connection stiffness, as investigated in [1]. However, under changing environmental conditions, the initial adhesion may decrease. Therefore, the load-bearing capacity could be reduced by the amount of initial adhesion when used for design. The calculated rope effect is consistent with the results obtained when considering the loads achieved without initial adhesion. In order to quantify these effects, the load at a relative displacement of 0.1 mm is taken as the initial adhesive force. This results in values of 1.6 kN for predrilled screws and 4.1 kN for non-predrilled screws in beech LVL. For predrilled connections in birch, initial adhesion values of 0.5–1.0 kN per screw are obtained, whereas non-predrilled screws reach higher initial adhesion, around 1.5–1.7 kN per screw. Compared to beech LVL, birch is softer and has significantly lower resistance to head pull-through. In spruce connections, minimal prestressing forces are observed in the screws and initial adhesion is close to zero. A prerequisite for the activation of the initial adhesion is a correct screw assembly and a firm application of the screw head. The visualised results represent only specimens evaluated 24 hours after assembly. After three weeks, the initial adhesion values remain unchanged as an exemplary

test revealed. Similar effects of initial adhesion can be observed in other studies, e.g. from Schiro et al. [89], where some load-displacement curves of screwed connections show an initial vertical section or friction is enforced, see [70]. At a displacement of 10 mm, the loads observed in the tests include an initial adhesion of approximately 1.7 kN. This contribution of initial adhesion to the measured load demonstrates its significance for small-displacement resistance, particularly in hardwood connections.

3.7 Conclusion

This chapter provides a comprehensive comparison between the connection behaviour of softwood and hardwood. The study offers practical insights and design recommendations for screwed timber connections, particularly when using hardwood. Proper screw installation, ensuring flush fitting and predrilling in one step (without separately predrilled timber elements), is essential to achieve the intended load-bearing capacities and to prevent initial slip. Increased screw spacing along the grain enhances ductility and allows for larger deformations. Maintaining a relative displacement limit of 10 mm is crucial to fully mobilise plastic hinges and to ensure that the calculated load-bearing capacity according to EAD 130118-01-0603 [127] is reached.

Experimental results show that single screws exhibit the highest maximum load and stiffness, whereas screw rows and groups demonstrate lower F_{max} and delayed force mobilisation due to increased friction surfaces and load distribution effects. Evaluating loads at defined displacements, such as $F_{5,mm}$, $F_{10,mm}$, and $F_{15,mm}$, provides a more meaningful comparison between configurations than F_{max}, which occurs at varying displacements. The initial stiffness, s_i, characterises the connection response in the linear-elastic range, whereas the end stiffness, s_e, reflects the behaviour under larger deformations. The ratio s_i/s_e indicates the proportion of resistance mobilised at small displacements. Minor specimen deviations are primarily attributed to variations in timber density, while carefully fitted predrilled setups show highly reproducible behaviour. Small displacements, up to approximately 10 mm, are most relevant for serviceability, as they influence deflection limits and overall connection performance under practical conditions.

Failure mechanisms differ between timber species. In hardwoods such as beech LVL, failure is dominated by distinct plastic hinges, whereas in softwoods, embedment failure typically occurs at small displacements, with minimal visible screw bending. In softwood, the investigated predrilled screws usually form two plastic hinges per

shear plane, whereas non-predrilled screws form only one due to their larger core diameter and, consequently, higher bending resistance, as well as the thinner timber side member. Improper insertion, eccentric loading, or reduced accuracy in predrilled holes shift the load-displacement curves, cause early slip, and may lead to premature timber splitting.

The failure of the non-predrilled screw connections highlights the high stresses acting on the fasteners. Failure of the screw cross-sections occurs at relative displacements between 12.8 and 18.8 mm. Although the ductility criterion defined by EAD 130118-01-0603 [127] is not violated, this early brittle failure remains noteworthy due to its unexpected occurrence. Given the relatively small test scope, further investigations into this failure behaviour are recommended. A certain degree of load distribution already appears to prevent this failure, as all screws in the row and group tests remain intact during loading.

From a design perspective, a flush and firm screw installation is vital to avoid early slip, while maintaining the 10 mm displacement limit ensures ductile behaviour and full plastic hinge formation. Minimum spacing must be observed to prevent premature brittle failure along the grain. In this study, a screw spacing of 8 d as a_1 does not lead to early splitting. The side member thicknesses are 10 d in the predrilled configuration and 7.5 d in the non-predrilled setup. Increasing the screw spacing along the grain improves ductility and allows greater deformation capacity. However, this study does not include reinforcement perpendicular to the grain or variations in screw diameter. Overlapping screw tips should be always considered as they effectively prevent brittle failures perpendicular to the grain.

Screw type, diameter, and thread length should be carefully selected for both predrilled and non-predrilled applications, especially in hardwoods. Accurate input parameters enable the EYM to predict connection capacity. Further research is required to optimise non-predrilled screw insertion for feasible and reliable onsite assembly, particularly for less commonly used timber species such as birch. Overall, this study emphasises that both assembly quality and the evaluation of load at service-relevant displacements are key to assessing connection performance. For design purposes, multi-screw connections demand careful consideration of friction, load distribution, and initial adhesion to ensure the expected stiffness and load-bearing capacity under service conditions.

4 Strains in Fully Threaded Screws

Investigations of connections with laterally loaded fasteners often focus on achieved loads, load–displacement behaviour, stiffness, and failure modes. However, what happens within the fastener itself during loading remains largely unknown. This becomes particularly relevant when addressing the occasional failure of the fastener. This chapter therefore examines the normal forces that may develop in screws under lateral loading. It introduces a method to investigate and measure these forces and provides initial insights into their magnitude and their role in force interaction.

4.1 Introduction

Connections with fully threaded screws are widely used in timber engineering due to their high load-bearing capacity, ductile behaviour, and suitability for hardwood applications. Understanding the internal forces developing within these fasteners under lateral loading is essential for safe design. Previous studies on dowel-type fasteners with strain gauges [93] have shown that local normal forces can be measured between plastic hinges. However, dowels generally develop only small normal forces, as their smooth surface limits interaction to friction between the surrounding timber and the dowel, as well as geometric effects from bending and hinge formation.

This raises the question of whether the methods and observations by Schweigler et al. [93] can also be applied to fasteners with profiled surfaces or threads, such as screws or profiled nails, which are capable of activating larger normal force components. For these types of fasteners, early failure at small relative displacements is often observed [1] and [22, 67]. This type of failure is caused by the considerably higher stress in the fasteners in hardwood connections compared to commonly used softwoods. Early failure at small relative displacements is therefore critical, as observed by Meyer [67], for example.

The internal forces acting in the fastener cross-section under lateral loading, namely bending moment *M*, normal force *N*, and shear force *V*, must be considered. Their interaction (*MN*, *NV*, or *MNV*) and utilisation vary along the fastener axis, depend on the connection geometry, fastener dimensions, and material properties of both the fastener and the timber product. While the distributions of bending moment and shear force are generally assumed to be known, the normal force distribution remains unknown, which limits the practical application of interaction criteria.

The use of strain gauges offers a means to analyse these normal forces, as recorded strains can be converted into internal forces. To minimise bending influence, the gauges are placed in the fastener core. For this purpose, screws are centrally drilled or eroded, and a cylindrical strain gauge is bonded into the borehole. The instrumented screws are installed in beech LVL specimens, allowing selective measurement of screw strains and calculation of the resulting normal forces under lateral loading. The gauges are positioned in screw sections that remain approximately straight according to the expected deformation line of the fastener.

The aim of the present study is to assess the feasibility and applicability of strain gauges bonded into screws to determine local normal forces, and to quantify the magnitude of the normal forces acting under lateral loading. Furthermore, the study seeks to evaluate the interaction between bending, normal and shear components within the screw, and to establish a method for deriving internal force distributions and their influence on the fastener's load-bearing behaviour.

4.2 Material

4.2.1 Screwed Connections

The test specimens consist of beech LVL type S with a mean density of 810 kg/m^3 (CoV 1.99 %) and a mean moisture content of 7.70 % (CoV 3.91 %). The test programme includes single-shear and double-shear connections, as shown in Fig. 4.1. Fully threaded screws with a nominal diameter of $d = 8$ mm and a length of $l = 180$ mm are used. Dimensions are given in Fig. A.13 and Tab. A.5.

The screw holes are predrilled with $d_{\text{predrill}} = 6$ mm. A centred hole with an inner diameter of $d_i = 2$ mm is drilled into the screws to accommodate the strain gauges. Some of these holes are produced using hardened metal drills to a depth of 26 mm,

measured from the top of the screw head. For greater depths, however, a centred position cannot be guaranteed by drilling alone. Consequently, screws with deeper strain gauge positions are machined using a wire erosion process. Fig. 4.3 presents the different screw modifications and a sectioned eroded screw. Examination of the hole eccentricity reveals only minor deviations in isolated areas. The strain gauge position within the screw is selected at a defined distance from the (theoretically) developing plastic hinges, as shown in Fig. 4.2. This configuration minimises the influence of bending moments in the screw on the measured strain.

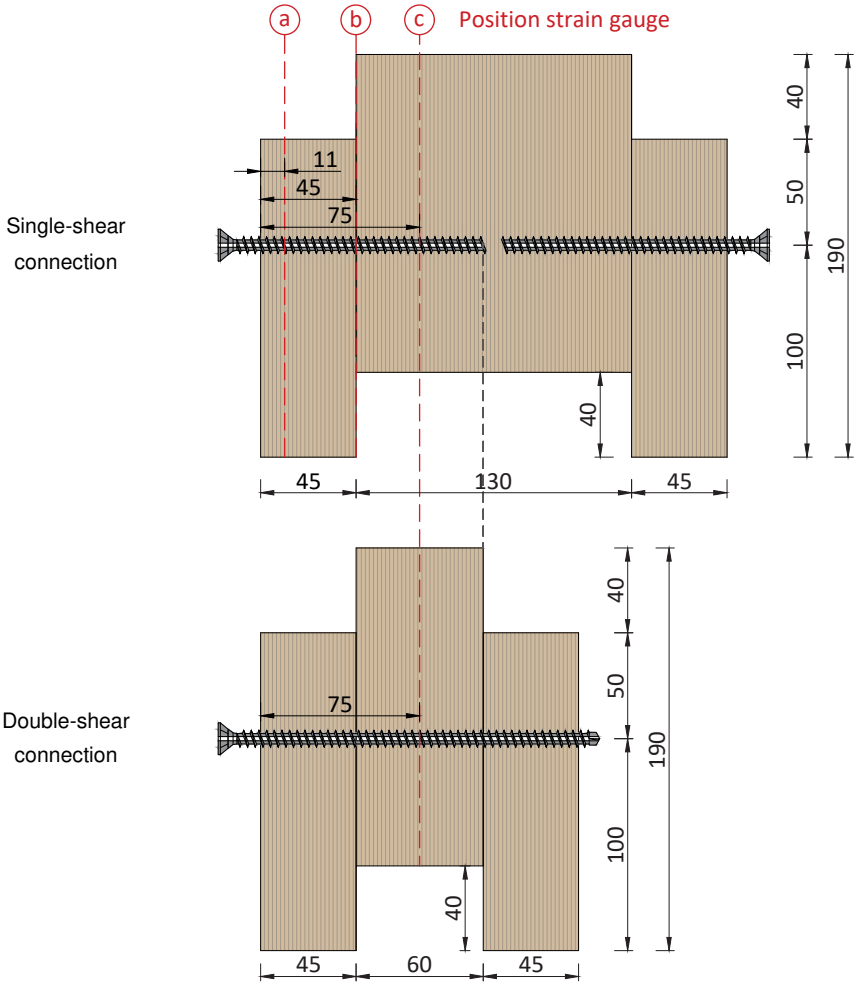

Fig. 4.1: Specimens with single-shear and double-shear screwed connection in mm.

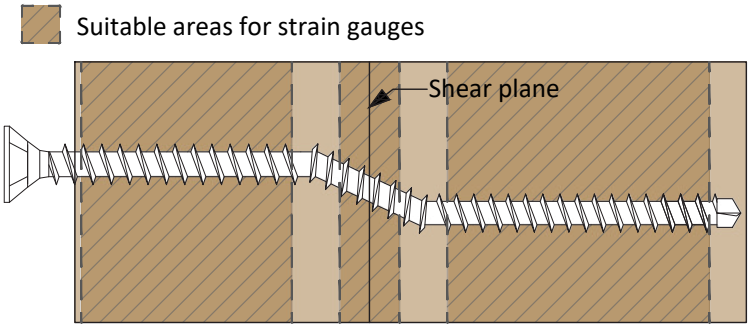

Fig. 4.2: Suitable areas for the application of strain gauges for a deformed screw with failure mode two plastic hinges per shear plane.

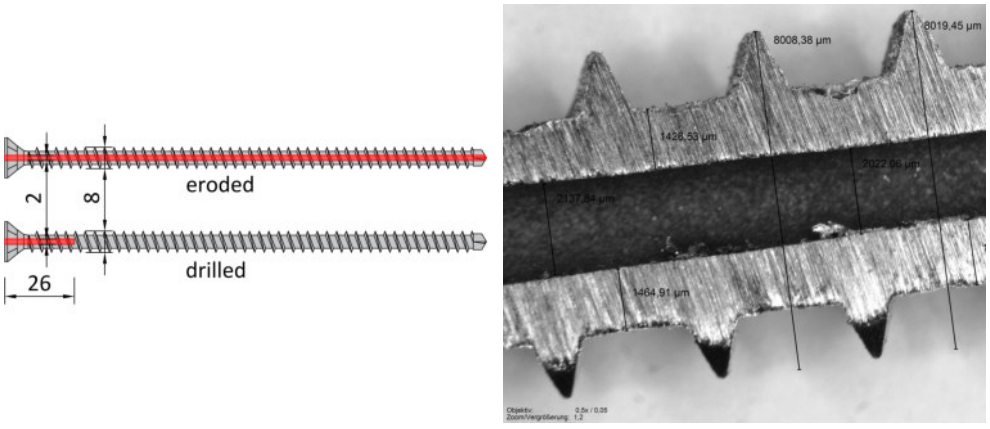

a. Modified screw types, dimensions in mm.

b. Exemplary eroded screw, radial section.

Fig. 4.3: Pre-machined screws for strain gauge application.

4.2.2 Strain Gauges

The strain gauges used by KYOWA are uniaxial strain gauges with a cylindrical carrier foil. To glue in the strain gauges an epoxy resin two-component adhesive is used. The diameter of the cylindrical strain gauges is 1.9 mm, see Fig. 4.4.

Specifications:
KYOWA Model KFB-3-120-C20-11 N5C2 (Lot No. Y4015F, Batch No. 160A)

Gauge factor:	2.04 ± 1.0 %
Resistance:	119.6 Ω ± 0.4 %
Strain gauge length:	3 mm
Self-compensating for:	Steel
Adhesive:	EP-370

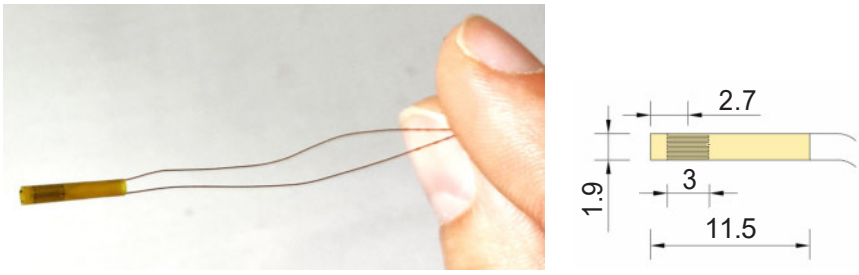

a. Picture of a strain gauge. b. Schematic drawing, in mm.

Fig. 4.4: Cylindrical strain gauges used.

4.3 Methodology

4.3.1 Manufacture and Use of Measuring Screws

The manufacturing process of the measuring screws involves several stages and requires a high level of diligence and precision. The preparation of the centred holes with a diameter of $d = 2$ mm represents the initial step. Some measuring screws are produced with a hole drilled to a depth of 26 mm from the top of the screw head. For this purpose, the screws are inserted into wooden blocks to provide secure fixation. The drilling process is carried out in several stages within an oil bath. The commercially available carbide drill bits employed remain intact throughout the process. To guarantee a centred position of the borehole, only holes with shallow depths are drilled, whereas deeper holes are produced by electrical discharge machining (EDM). EDM is a process that removes material through electrical discharges between a workpiece and an electrode, typically made of brass or copper. Several EDM techniques are commonly applied in metal machining.

Wire EDM, a specific application of sink erosion, uses electrical impulses transmitted through a fine EDM wire. The process takes place within an insulating dielectric medium by bringing a brass or copper electrode (the tool) close to the workpiece. A spark discharge generates a strong electric field that melts and vaporises the material. The electrode removes the molten material and is automatically repositioned according to its wear state. The removed particles are carried away by the dielectric, which also protects the workpiece from thermal stress. This process enables the production of holes and complex geometries regardless of the hardness or strength of the workpiece material.

A properly functioning bond between the strain gauge and the borehole surface requires the thorough removal of dirt and oil residues by mechanical cleaning using nylon wire brushes, an ultrasonic bath, and rinsing with acetone. Inspection with a new nylon brush frequently reveals remaining contamination or discolouration on the inner wall. Therefore, several cleaning cycles are carried out until only minimal staining is visible on the brush. Typically, at least ten cleaning cycles are required. One cleaning cycle includes inserting the nylon brush through the borehole, applying acetone at the upper opening until the brush is saturated, then gripping the brush at the lower end with pliers and pulling it through. Subsequently, the brush is wiped with a white cloth, and any remaining residues are evaluated, see Fig. 4.5.

a. Cleaning tools.

b. Detail with nylon wire brush.

Fig. 4.5: Preparation of boreholes by cleaning.

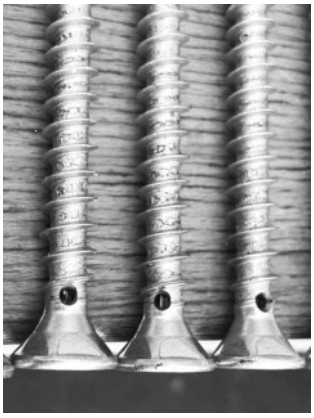

a. Variant 1: Additional borehole sideways below screw head.

b. Variant 2: Borehole in centre of screw head.

c. Nut and bit with hole.

Fig. 4.6: Possible wire exits for cable connection of the glued-in strain gauges.

Various cable management configurations are possible when using fully threaded screws. The wires of a bonded strain gauge can be routed either sideways below the screw head (variant 1) or centrally through the bit recess of the screw head (variant 2), see Fig. 4.6.

Variant 1: The lateral wire exit below the head allows conventional screw insertion using a standard bit. During testing, the screw head protrudes beyond the timber surface. However, the screw cross-section is weakened directly below the head. When inserting the screws, particularly in cases without predrilling, the insertion torque may exceed the torsional strength of the weakened screw section.

Variant 2: A modified bit with an attached nut is required for installation to prevent damage or bending of the wires at the exit point. Both the bit and the nut are provided with a hole larger than 2 mm to ensure that the wire ends emerging from the head are not kinked. The central hole within the screw maintains a symmetrical cross-section, provided that the manufacturing process is carried out with sufficient precision.

Routing the wires laterally out of the screw is challenging. Even very small amounts of adhesive can cause the wires to adhere to the inner wall. This may occur, for example, when the cannula touches the wall of the borehole during the bonding process as it is withdrawn. The wires must therefore either be protected from adhesive contamination, for instance by an additional thin protective sheath, or be routed through the central

head opening. Installing the screws using drilled bits has proven to be an effective solution and is therefore preferred.

To prevent kinking of the wires at the head exit, shrink tubing is applied as a protective measure. Additionally, strain relief can be provided by attaching the wires to the screw head using soldered support points. The configuration with the protruding head is maintained. Although a flush installation of the screw head would be possible in variant 2, such a configuration would result in threaded engagement only within the side timber. Hence, the influence of the protruding head is considered negligible.

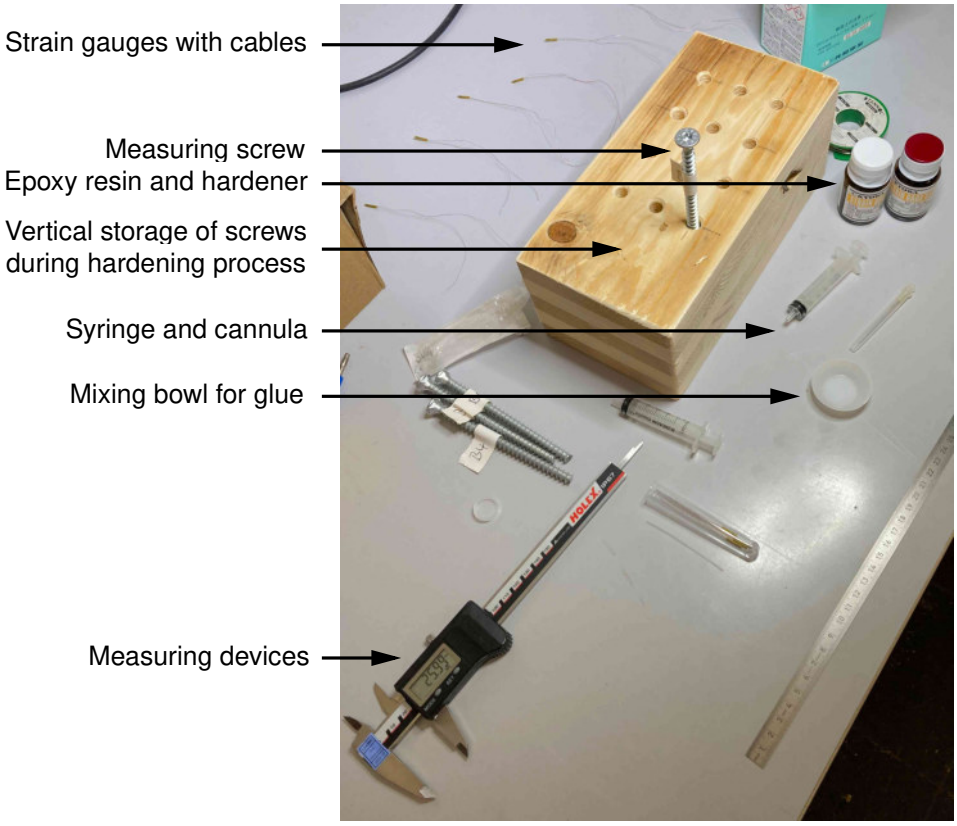

Fig. 4.7: Equipment needed to manufacture the bond.

Producing a reliable bond represents the most critical stage in the manufacture of the measuring screws. Various tools and devices are required to bond the strain gauges, see Fig. 4.7. In drilled screws, the position of the strain gauges is predetermined by

sliding them to the bottom of the borehole. In eroded screws, however, short copper wires are inserted from the screw tip to define the intended position. The strain gauges are then pushed in from the head side until they come into contact with the copper wire. The hole is subsequently filled with a two-component epoxy adhesive (type EP-370) using a cannula to ensure the deepest possible injection and to minimise the formation of air bubbles within the adhesive. Once the strain gauge is inserted, the adhesive is allowed to cure. A detailed description of the bonding procedure is given below.

Step 1: Preparation of eroded screws

First, copper wires (referred to as distance wires) are cut to the required length corresponding to the desired strain gauge position within the screw, measured from the screw head. The distance wire is inserted from the head side. Another copper wire is then inserted from the screw tip until it makes contact with the distance wire. The lower copper wire is bonded to the screw tip using a small drop of instant adhesive and is left to dry briefly. The protruding end at the tip is then cut off, and the upper distance wire is removed from the head side using pliers, see Fig. 4.8.

a. Distance wire to ensure intended depth of strain gauge.

b. Distance and bonded wire.

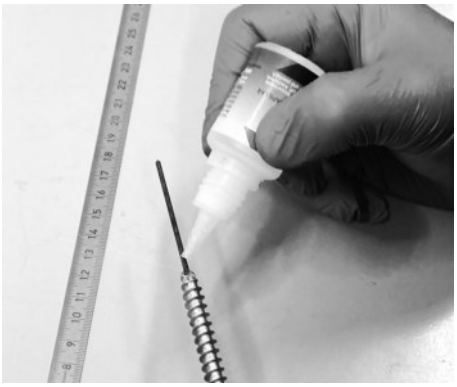

c. Bonding the copper wire on the bottom.

Fig. 4.8: Step 1 of bonding process.

Step 2: Mixing the adhesive

The two components of the epoxy adhesive are weighed into a mixing bowl using pipettes. A precision scale is employed to ensure accurate measurement. The mixing ratio is determined by weight, typically 100:9–10, in accordance with the adhesive manufacturer's instructions. The resin and hardener are thoroughly stirred, for example

with a toothpick. In this procedure, the open time of the adhesive is 30 minutes, so the mixture is occasionally stirred again to maintain homogeneity.

The adhesive is then drawn into a syringe, and any entrapped air bubbles are removed as far as possible. The adhesive is injected through the cannula until the entire system is filled.

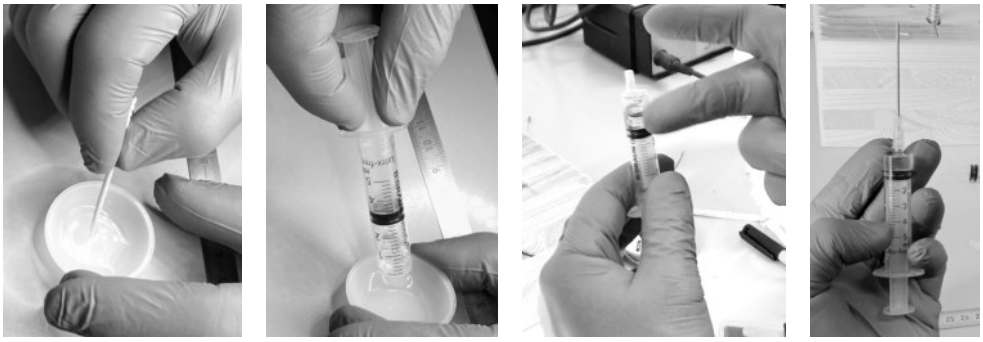

a. Mixing the adhesive. b. Filling the syringe. c. Removing air bubbles. d. Filled system.

Fig. 4.9: Step 2 of bonding process.

Step 3: Filling the borehole

The quantity of adhesive required per screw is calculated so that the strain gauge is fully embedded along its entire length, while ensuring that the borehole is not completely filled. The borehole bottom is then carefully filled with adhesive. During this process, the cannula is withdrawn slowly, and the adhesive is applied in such a way that minimal material spreads onto the interior wall of the borehole. The strain gauge is then gently inserted into position. It is recommended to verify the correct depth of insertion. In the present procedure, this is achieved by marking the lead wires; the mark should align with the upper edge of the screw head once the strain gauge is correctly positioned.

Step 4: Curing of the adhesive

Fully bonded screws are allowed to rest at room temperature for at least 24 hours, in accordance with the adhesive manufacturer's instructions, and are subsequently cured in an oven for a minimum of 5 hours at 80 °C. The curing process may vary depending on the type of adhesive and the specifications provided by the adhesive manufacturer.

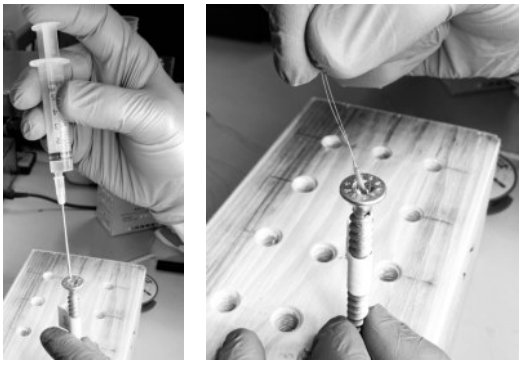

a. Filling the bore hole. b. Inserting the strain gauge.

Fig. 4.10: Step 3 of bonding process.

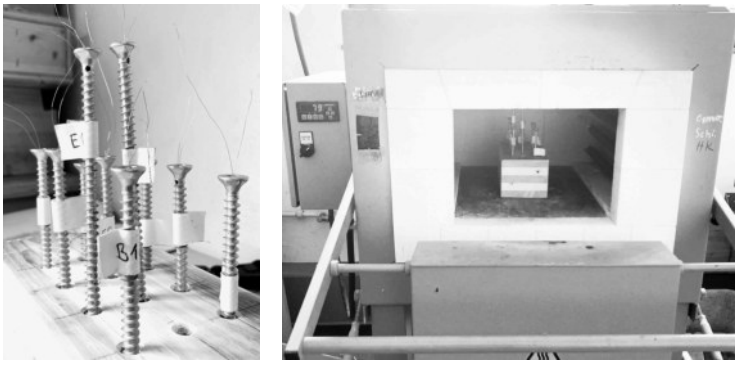

a. Completed bonding. b. Hardening in the oven.

Fig. 4.11: Step 4 of bonding process.

All measuring screws are tested and calibrated to verify a properly functioning and defect-free bond. For this purpose, the measuring screws are subjected to repeated tensile loading, ranging from 0.2 kN to 5 kN, with interim hold periods of 30 seconds, see Fig. 4.12a. This procedure produces a linear machine load-strain relationship for all manufactured measuring screws, which is subsequently used to calculate the normal forces from the measured strains.

Fig. 4.12c illustrates the calibration test setup. The screw is inserted into a round plastic profile to anchor it in the clamping jaws. The screw head is anchored in a steel plate, which contains a milled recess to accommodate the head.

Calibration results

The curve section corresponding to the final load increase of the calibration cycles is

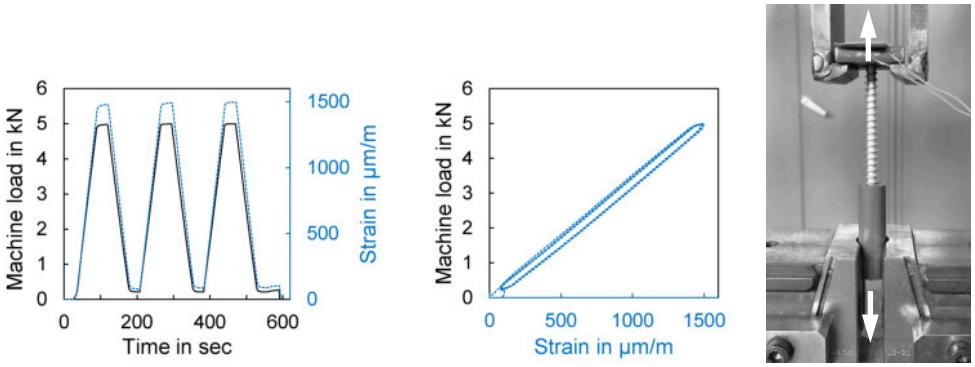

a. Load cycles for calibration. b. Load-strain relation, exemplarily. c. Calibration setup.

Fig. 4.12: Exemplary calibration of measuring screws: calibration curves and test setup.

used to evaluate the calibration. Eq. 4.1 therefore provides the results presented in Tab. 4.1, where D denotes a drilled screw and E denotes an eroded screw.

$$y = m \cdot x + b \quad \text{in kN} \tag{4.1}$$

with

- y Machine load in kN
- x Measured strain in µm/m
- b Intersection point with ordinate in kN

Table 4.1: Calibration results.

	m	b	R^2
D1	0.00352	0.0825	1.0000
D4	0.00356	0.2191	1.0000
D5	0.00363	0.1596	0.9999
D6	0.00343	-0.0013	1.0000
E1	0.00360	0.1883	0.9999
E2	0.00373	0.1659	1.0000
E3	0.00359	0.2312	0.9999
E4	0.00361	0.1286	0.9999
E5	0.00348	0.1871	1.0000
E6	0.00376	0.0679	1.0000

4.3.2 Test Programme

The test programme comprises eight shear specimens subjected to compression. Each specimen consists of either two single-shear or one double-shear connection, see Fig. 4.1. One specimen of each type is tested with unweakened screws as a reference. Loads on each shear plane are measured by placing the side timbers on separate load cells. Relative displacements in the shear plane are recorded at four locations using displacement transducers, while screw strains are measured via the bonded strain gauges. The test setup is shown in Fig. 4.13.

The position x of the strain gauge is defined as the distance from the specimen's outer surface, always referring to the centre of the measuring grid (Fig. 4.14). The deepest measurement in a single-shear connection corresponds to the axis of symmetry of the double-shear connection, as illustrated in Figs. 4.1 and 4.14. All screws are designated according to their production method: D for drilled, E for eroded, and R for reference (unweakened) screws. Single-shear and double-shear specimens are indicated by SiS and DoS, respectively.

Specimens are loaded according to DIN EN 26891 [122], including an unloading loop. Tab. 4.2 summarises the tests conducted.

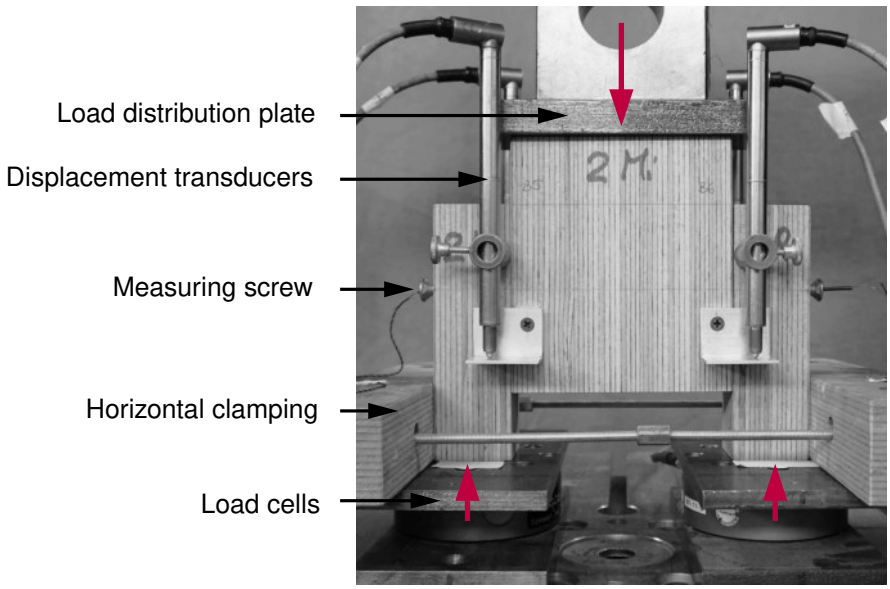

Fig. 4.13: Exemplary test setup with single-shear connections.

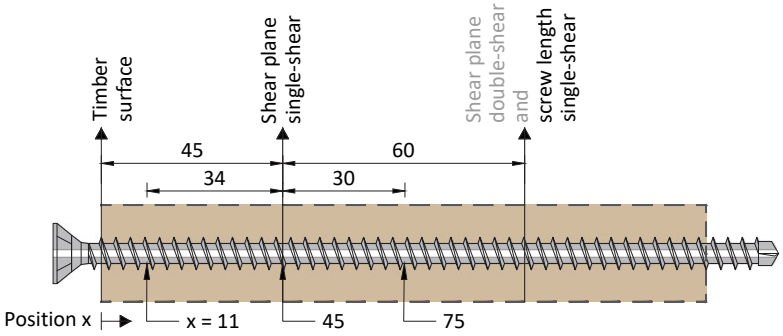

Fig. 4.14: Chosen positions *x* for strain gauges, in mm.

Table 4.2: Test programme. Number of screws with one strain gauge each. Position *x* refers to Fig. 4.14.

Type of connection *	Strain gauge position *x*			
	none	11 mm	45 mm	75 mm
Single-shear SiS	2	4	2	2
Double-shear DoS	1	-	-	2

*A test specimen contains either one double-shear or two single-shear loaded screws.

4.4 Results

Overviews of the recorded and analysed results are presented in Fig. 4.15 and 4.16, as well as in Tab. 4.3, for single-shear (SiS) connections. Correspondingly, Fig. 4.17 and 4.18, together with Tab. 4.4, show the results for double-shear (DoS) connections.

Load-displacement curves for each shear plane (mean value of two displacement transducers) and the corresponding calculated normal force at the marked point *x* are shown for the single-shear connections. Each specimen includes two measuring screws. Screws 1&2, 3&4, 5&6, and 7&8 are each installed in one specimen. For the double-shear connections, the load is presented as the mean of both shear planes in black, while the individual loads of the separate load cells are shown in gray. The strain gauge is always positioned along the axis of symmetry of the specimen. One screw per specimen is installed.

Strains are recorded for all screws until the connection fails. The normal force in the screws generally increases with increasing load and, as expected, reaches its maximum at the maximum applied load. Some exceptions are observed at the beginning

of tests no. 2 and 8 in Fig. 4.15, where brief compressive forces occur in the screws. Although compressive forces in screws subjected to shear are not expected, they are explainable. One explanation is a slight inclination of the screws due to assembly inaccuracies. An alternative explanation is that, in the beginning of the loading process, and within the elastic range, the axis of the screw remains largely straight (see also findings from Chapter 3). If a minimal gap exists in the shear plane during the assembly of the connection, which can occasionally occur with fully threaded screws, this gap is initially closed under load. This behaviour can be attributed to the test setup and the applied compressive load. As a result, initial compression forces can develop in the screws, which may be relatively high within the shear plane. Once plastic behaviour and the formation of the plastic hinges begin, however, the screw develops tensile forces that then increase further until the maximum load is reached.

The failure of the connections with drilled screws is characterised by reaching the withdrawal capacity in the side timber, as indicated by the pull-in of the screw head in Fig. 4.16 (left) and the formation of two plastic hinges per shear plane. In contrast, the eroded screws exhibit a cross-section failure in the region of the plastic hinges, occurring at comparatively smaller relative displacements.

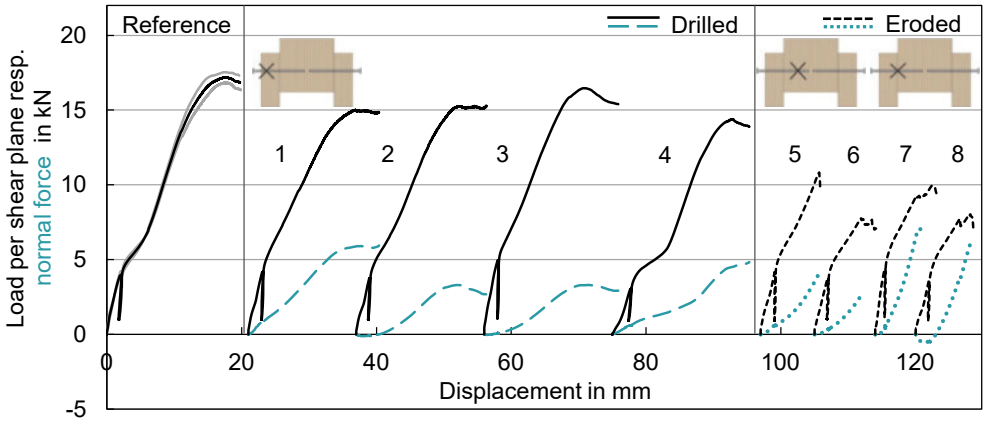

Fig. 4.15: Results single-shear connections: loads and normal forces.

It is noted that the initial stiffnesses of the connections are similar. For all connections, the calculated failure mode with two plastic hinges per shear plane is reached before either the withdrawal capacity or a screw cross-section failure limits the load capacity.

Table 4.3: Results single-shear connections: load per shear plane F, normal force N and relative displacement in shear plane u.

	Position x	F_{max}	$u(F_{max})$	$N(F_{max})$	N_{max}	$u(N_{max})$	$F(N_{max})$
	mm	kN	mm	kN	kN	mm	kN
R-SiS		17.2	17.6				
D-SiS1	11 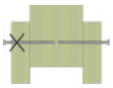	15.0	15.9	5.88	5.90	16.8	14.9
D-SiS2		15.3	17.6	2.94	3.30	15.1	15.2
D-SiS3		16.5	14.7	3.29	3.30	15.5	16.4
D-SiS4		14.4	17.8	4.51	4.77	20.1	13.9
Mean		**15.3**	**16.5**	**4.15**	**4.32**	**16.9**	**15.1**
E-SiS5	75 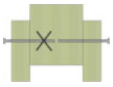	10.8	8.69	4.06	4.08	8.73	10.6
E-SiS6		7.76	6.93	-	2.54	6.81	7.72
Mean		**9.29**	**7.81**		**3.31**	**7.77**	**9.15**
E-SiS7	45 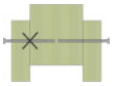	9.95	8.47	-	6.90	6.73	9.21
E-SiS8		8.03	8.13	6.12	6.12	8.13	8.03
Mean		**9.17**	**8.01**		**6.51**	**7.43**	**8.62**

Screw cross-section failure is accompanied by a failure of the strain gauge connection wires or by exceeding the maximum measurable strains of the strain gauges. Consequently, the measurement terminates at this point.

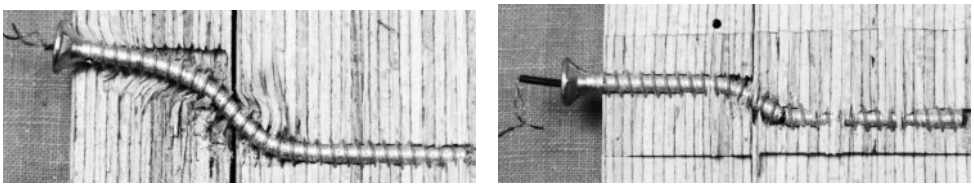

a. Failure of drilled screw.

b. Failure of eroded screw.

Fig. 4.16: Opened specimens of single-shear connections.

The load-displacement behaviour of the double-shear connections is generally comparable to that of single-shear connections. Normal forces increase up to 7.2 kN along the axis of symmetry (test E-DoS2), whereas the load-bearing capacity of the connection per shear plane amounts to 8.1 kN. Negative strains, i.e. compressive

forces in the screw, are also observed at this strain gauge position at the beginning of test E-DoS1. Fig. 4.18 shows opened specimens and the different failure modes of an unweakened (reference) and an eroded screw.

In general, the highest normal forces are measured at the strain gauge position within the shear plane, as seen in tests E-SiS7 and E-SiS8 in Fig. 4.15 and Tab. 4.3. On average, the maximum normal forces in the shear plane determined are 6.5 kN, corresponding to the failure of the connections. The progression of the curves clearly demonstrates that normal forces vary considerably with the strain gauge position. The shape of the normal force curves differs markedly between positions outside the plastic hinge regions and those located between them. The steepest gradient of normal forces occurs within the shear plane.

Considering the position $x = 75$ mm, the curves and magnitudes of the normal forces are not directly comparable between single-shear and double-shear connections. Due to the different loading conditions, double-shear connections exhibit average normal forces of 6.4 kN instead of 3.3 kN for single-shear connections, representing an increase of 94 %.

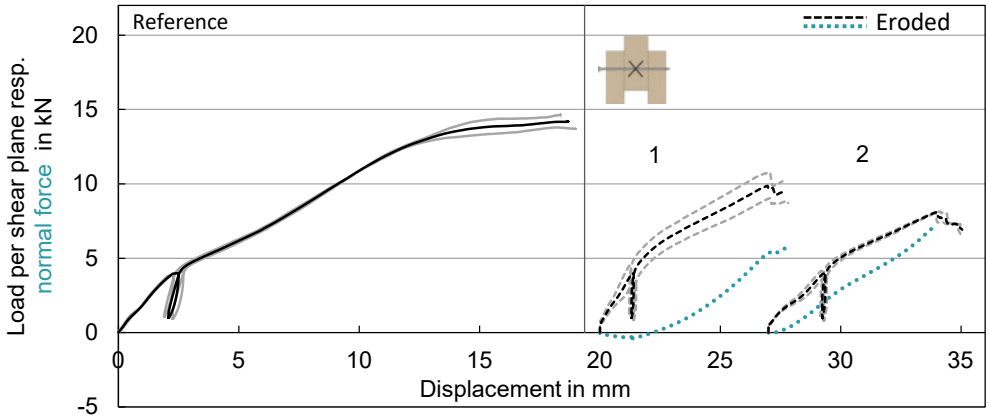

Fig. 4.17: Results double-shear connections: loads and normal forces. Mean values in black, values per shear plane in grey.

Table 4.4: Results double-shear connections: load per shear plane F, normal force N and relative displacement in shear plane u.

	Position x	F_{max}	$u(F_{max})$	$N(F_{max})$	N_{max}	$u(N_{max})$	$F(N_{max})$
	mm	kN	mm	kN	kN	mm	kN
R-DoS		14.3	18.7				
E-DoS1	75 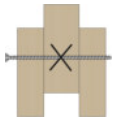	9.04	7.07	5.33	5.49	7.81	8.72
		10.8	7.05			7.58	10.2
E-DoS2		8.07	6.93	-	7.17	6.86	8.05
		8.14	7.06			6.97	8.08
Mean		**9.00**	**7.03**		**6.33**	**7.31**	**8.75**

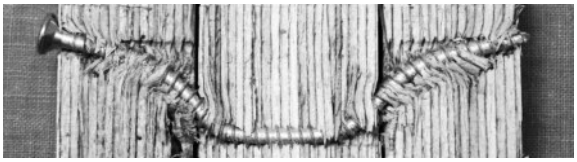

a. Failure of unweakened reference screw.

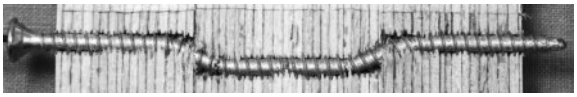

b. Failure of eroded screw.

c. Detail of failed eroded screw in plastic hinge.

Fig. 4.18: Opened specimen of double-shear connections.

4.5 Discussion

4.5.1 Effect of Electrical Discharge Machining

The longitudinal electrical discharge machining (EDM) of a highly hardened screw transforms the solid cross-section into a thick-walled cylinder. For a screw with outer radius R_{out} = 2.5 mm and inner radius R_{in} = 1 mm, the wall thickness is $t \approx 1.5$ mm and the effective axial cross-sectional area reduces from approximately 19.6 mm^2 to 15.7 mm^2, leading to an increase in nominal stress of roughly 25% under the same axial load.

The EDM process produces a heat-affected zone (HAZ) typically in the range of 0.01–0.2 mm thickness. Relative to the wall thickness, the HAZ occupies approximately

1–13% of the material adjacent to the inner surface. In high-carbon steels, the local microstructure within the HAZ can transform martensitically, increasing hardness and local brittleness, and thereby facilitating microcrack initiation [42].

Despite this local microstructural alteration, the overall plasticity of the screw is primarily governed by the reduced cross-section and the stress concentration at the longitudinal hole rather than the EDM-induced HAZ. The HAZ may slightly reduce local ductility at the inner wall, but its influence on the global axial plastic strain is minor, typically below 5%. In highly hardened steels, which are inherently brittle, EDM-induced microstructural changes serve mainly as potential crack initiation sites rather than significantly altering the load-bearing capacity.

Under bending loads, the maximum tensile stress occurs at the outer radius on the tension side, consequently, for wall thicknesses exceeding approximately 1 mm, the EDM-induced HAZ has a negligible effect on global bending or axial capacity, with premature failure dominated by the hole geometry and the HAZ influencing primarily local crack initiation only when the wall thickness approaches the order of the HAZ.

4.5.2 Connection Behaviour and Normal Forces

The observations and measurements allow for a critical discussion of the following aspects. The weakening of the cross-section due to the inner hole of $d_{\text{borehole}} = 2$ mm in a screw with a nominal diameter of 8 mm causes a premature failure. This effect is not unexpected. Until the weakened screws reach a cross-section failure, the connections behave similarly and consistently form two plastic hinges per shear plane. Assuming that the outer cross-section areas are stressed first under bending, the weakening in the area of the neutral fibre only has an effect in the fully plastic state.

The weakening of the cross-section can be approximated using a circular profile. Control tests are employed to determine the yield moment of eroded screw sections. The unweakened (reference) screws achieve a yield moment M_y according to EAD 130118-01-0603 [127] of 25.3 Nm at a plastic bending angle of $\alpha = 45/d^{0.7}$ and are therefore approximately 8 % higher than the weakened screws (23.4 Nm), see material properties in Tab. 4.5 and results in Fig. 4.19. A list of all bending test results is provided in Appendix A.3.

In addition, the weakened screws fail at bending angles of 26–48° in bending tests, which approximately coincides with the bending angles observed in the opened test

Table 4.5: Material properties of fully threaded screws used. Assumptions: core diameter of screws $d_{core} = 5.05\,mm$ and borehole diameter $d_i = 2\,mm$. $F_{shear} = \frac{F_{tens}}{\sqrt{3}}$.

	Measured		n	Calculated			
Intact	f_u	= 1088 Mpa	10				
Intact	M_y	= 25.3 Nm	10	F_{tens}	= 21.8 kN	F_{shear}	= 12.6 kN
Weakened	$M_{y,weak}$	= 23.4 Nm	4	$F_{tens,weak}$	= 18.4 kN	$F_{shear,weak}$	= 10.6 kN

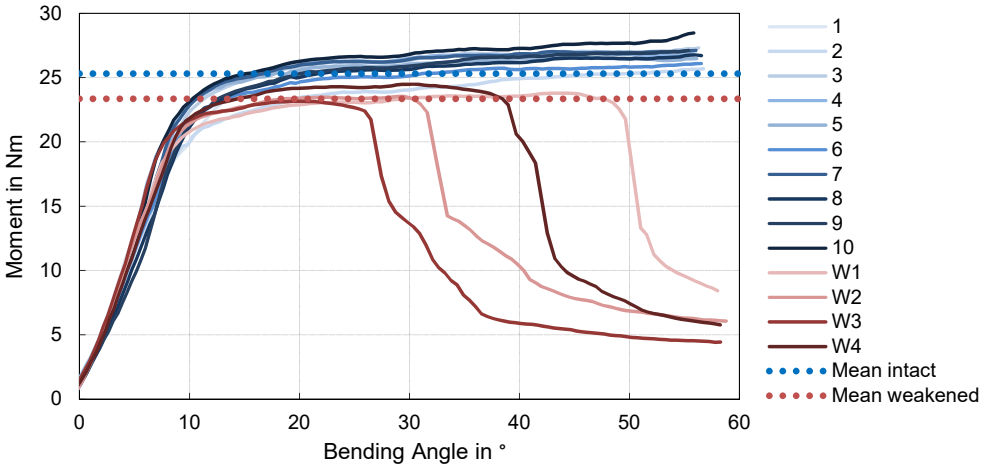

Fig. 4.19: Results and comparison of yield moments of ten intact and four weakened screws.

specimens. Slightly lower load-bearing capacities of the double-shear connections can be attributed to the higher prevailing normal forces in the middle timber. However, the natural variability of the wood properties and the limited number of tests must also be considered. Given the identical geometry of the side timbers, it is assumed that comparable normal forces occur in the side timber subjected to both single- and double-shear stresses.

In contrast to single-shear stress, where the normal force reaches its maximum within the shear plane, the normal force in double-shear stress increases up to the symmetry axis of the connection. Therefore, in the context of possible interactions of internal forces, the screw section in the middle timber is at a greater risk of early failure, potentially failing before the screw section in the side timber. All screws in the opened test specimens exhibit cracks at the plastic hinges. This hypothesis warrants further investigation.

The arrangement of the test specimens on two separate load cells demonstrates that the load per shear plane is not evenly distributed. No calotte was installed during the tests in order to minimise rotation of the middle timber. The separate load measurement allows an exact allocation of the loads per shear plane and the corresponding normal force in the screw for single-shear connections. Consequently, large load differences are sometimes recorded within a single specimen. For example, the loads of screws 3&4, installed in the same specimen, or the single-shear reference specimen R-SiS (loads of the right and left shear planes in grey, mean value in black) vary, see Fig. 4.15. Differences in load are also observed for some double-shear connections, e.g. screw E-DoS1 and the reference test in Fig. 4.17.

A qualitative distribution of the internal forces in a single-shear connection is presented in Fig. 4.20. Points based on simplified assumptions, moment M in the plastic hinge corresponds to the yield moment M_y, and shear force V in the shear plane corresponds to the load-bearing capacity F_v with friction contribution, are marked with blue circles. Previously unknown and newly measured points of the normal force distribution are marked with orange circles.

The internal forces can be superimposed and interaction terms applied using the distributions illustrated in Fig. 4.20. However, the inclined fastener axis at the state of failure (assumed α = 25°) and additional friction components (assumed μ = 0.3) between the shear surfaces must be taken into account. A force diagram is presented in Fig. 4.21.

The normal force in the shear plane, determined using strain gauges, has a horizontal component that increases the friction of the shear surfaces and contributes directly to the load-bearing capacity via its vertical component. The shear force must also be decomposed according to its components. In the intersection area, there is a difference between the horizontal forces V_H and N_H, which corresponds to the contact force of the shear surfaces, H_{fric}. The unknown variables can be determined using equilibrium conditions.

The equilibrium of internal forces within the shear plane is determined iteratively. Initially, the normal force is decomposed into vertical and horizontal components, and the horizontal component is assumed to contribute solely to friction. Based on this assumption, the shear force and its horizontal component are evaluated. The frictional contribution is then updated, and the process is repeated until the values converge.

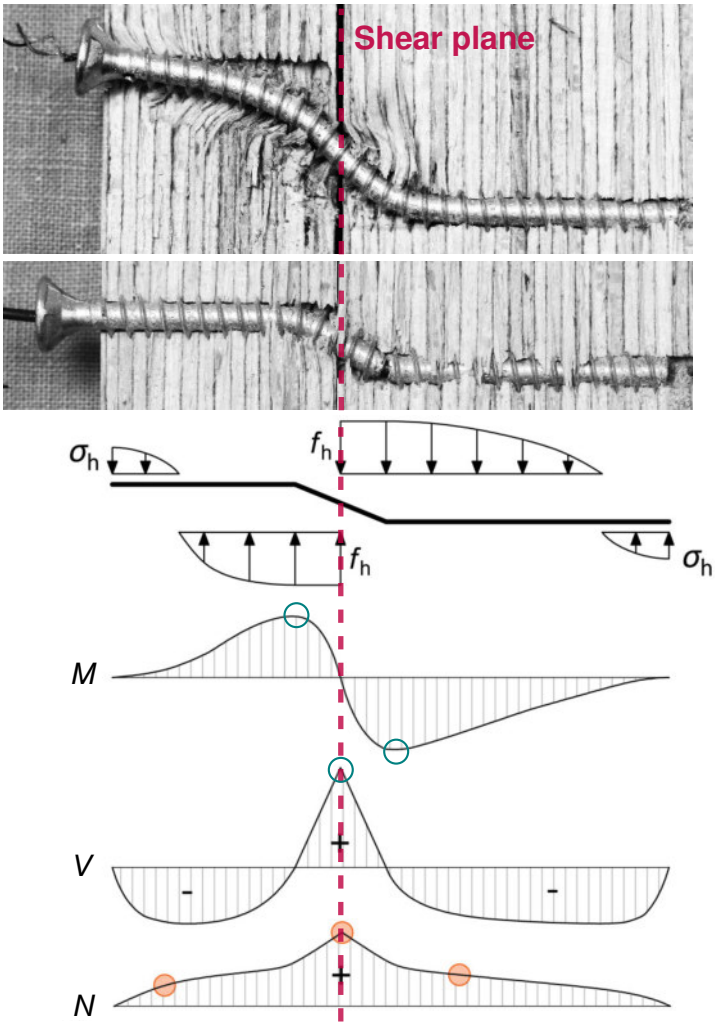

Fig. 4.20: Qualitative distributions of internal forces and moments of a single-shear connection. Deformed and opened connections on top and corresponding distributions below. Embedment stress σ_h < embedment strength f_h. Locations of measured points are marked with orange circles.

The distribution of internal forces within the shear plane is determined iteratively. Initially, the normal force N_{SG} evaluated with the strain gauge (SG) is decomposed into its vertical and horizontal components:

$$N_v = N_{SG} \cdot \sin \alpha, \tag{4.2}$$

$$N_h = N_{SG} \cdot \cos \alpha, \tag{4.3}$$

where α denotes the angle of the shear plane relative to the horizontal. The horizontal component N_h contributes initially to the frictional resistance V_{fric}:

$$V_{fric} = \mu \, N_h, \tag{4.4}$$

with μ representing the coefficient of friction.

Based on N_v and V_{fric}, the vertical component of the shear force is evaluated as

$$V_v = F_v - N_v - V_{fric}, \tag{4.5}$$

from which the total shear force along the plane is obtained:

$$V = \frac{V_v}{\cos \alpha}. \tag{4.6}$$

The horizontal component of the shear force is then given by

$$V_h = V \cdot \sin \alpha. \tag{4.7}$$

The friction is subsequently updated based on the new horizontal component:

$$V_{fric}^{new} = \mu \cdot (N_h - V_h), \tag{4.8}$$

and the calculation of the forces is repeated iteratively until convergence is achieved.

To assess the combined loading, an interaction factor η is defined, which compares the normal and shear forces relative to their respective allowable limits f_{tens} and f_{shear}:

$$\eta = \sqrt{\left(\frac{N}{F_{tens}} + \frac{V}{F_{shear}} \right)^2}. \tag{4.9}$$

This procedure provides a consistent determination of the force distribution within the shear plane, accounting for friction, and ensures that the interaction between normal and shear forces is accurately represented.

At the time of failure of screw E-SiS7, the interaction term in the shear plane, using Eq. 4.10 and assuming the moment M in the shear plane to be zero, is given as follows:

$$\eta = \left(\frac{N}{F_{\text{tens,weak}}} + \frac{V}{F_{\text{shear,weak}}} \right)^2 = \left(\frac{6.90}{18.4} + \frac{5.65}{10.6} \right)^2 = 0.825 \qquad (4.10)$$

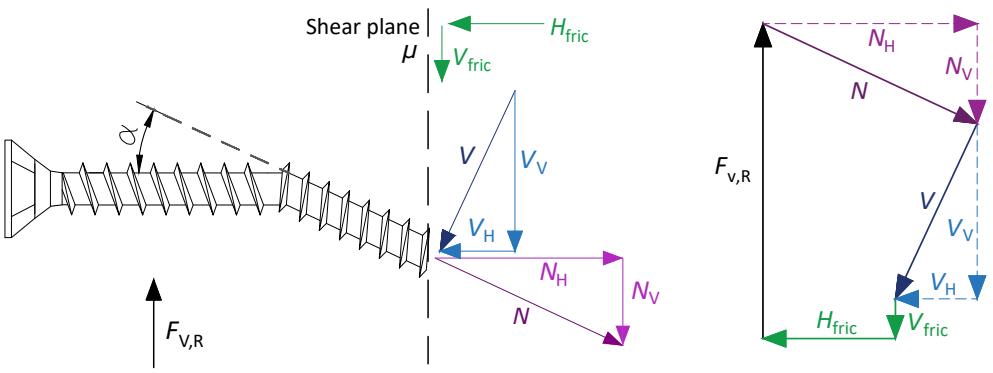

Fig. 4.21: Forces in shear plane for a single- or double-shear connection and closed force polygon: Normal force in purple, shear force in blue, friction forces acting on shear surface in green.

For screw S8, this results in a corresponding utilisation of $\eta = 0.62$ in the shear plane. A utilisation $\eta < 1.0$ appears to be plausible, as both screw cross-sections remained intact in the shear plane.

Slightly lower normal forces of 6.33 kN are obtained along the axis of symmetry of the double-shear connections compared to the 45 mm position, i.e. the shear plane of the single-shear connections (6.51 kN). In principle, the normal forces are expected to increase towards the axis of symmetry. However, no measurable normal forces are detected in the shear plane for the double-shear configuration. Given the limited number of tests, the slightly lower values can be attributed to experimental scatter. A comparison of the variability of N_{max} for position x = 11 mm yields a coefficient of variation of 29.3 %, suggesting that a larger sample size might have produced the anticipated higher normal forces.

Additional assumptions and simplifications are therefore required to enable the use of the interaction terms within the plastic hinge. This application is more complex, as no normal forces can be measured at this location and the bending resistance is reduced according to the remaining yield moment in the plastic hinge, $M_{\text{remain,ph}}$:

$$M_{\text{remain,ph}} = M_{\text{y,weak}} \cdot \left[1 - \left(\frac{N}{F_{\text{tens,weak}}}\right)^2\right] \tag{4.11}$$

If a linear progression of the normal force between the two points in the shear plane ($x = 45$ mm) and beyond the plastic hinges recorded using strain gauges is assumed for the single-shear connection, this results in a normal force of approx. 5.16 kN in the plastic hinge. The remaining bearable yield moment in the plastic hinge $M_{\text{remain,ph}}$ is then calculated to be 21.6 Nm and is thus reduced to approx. 93.3 % of $M_{\text{y,weak}}$.

For the double-shear connection, the mean value between the measured values in the shear plane (single-shear) and the values in the symmetry axis (double-shear) is assumed as a possible acting normal force. This amounts to 6.42 kN. This reduces the bearable yield moment $M_{\text{remain,ph}}$ to 20.6 Nm, which corresponds to 87.8 % of $M_{\text{y,weak}}$.

Table 4.6: Calculated load-bearing capacities based on mean values with reference, weakened, and additionally reduced yield moments.

	M_{y}	$M_{\text{y,i}}/M_{\text{y,ref}}$	$M_{\text{y,i}}/M_{\text{y,weak}}$	$F_{\text{v,R}}$	$F_{\text{v,R,i}}/F_{\text{v,R,ref}}$	$F_{\text{v,R,i}}/F_{\text{v,R,weak}}$
Reference	25.3	1.00		8.59	1.00	
Weakened	23.4	0.923	1.00	8.39	0.977	1.00
SiS	21.6	0.854	0.925	8.21	0.955	0.978
DoS	20.6	0.814	0.882	8.10	0.943	0.965

A direct comparison of the load-bearing capacities is not possible due to the different failure modes occurring at varying relative displacements. However, when calculating the capacity of a regular screw connection, i.e. based on an unweakened cross-section acc. to [118], a load of 8.59 kN per shear plane is obtained, including the rope effect, see Tab. 4.6. Starting from this load, further calculations can be carried out using the correspondingly weakened and reduced yield moments, also given in the table.

When the interaction is taken into account, the resulting load-bearing capacities are reduced to 97.8 % and 96.5 % of the weakened cross-sections. The single-shear connections reach a maximum load corresponding to the maximum normal force, $F(N_{max})$, of 8.89 kN on average, while the double-shear connections reach 8.75 kN. Although these values still exceed the calculated load-bearing capacity, there are also lower outliers, for instance screw E-SiS6.

This exemplary calculation is presented to illustrate the order of magnitude of the moment reduction caused by the normal force. However, due to the significant cross-sectional weakening in the tested geometry, resulting from the hole and bonded strain gauge, as well as the premature failure of the eroded screws, a conclusive assessment of the reduction in load-bearing capacity cannot be made.

4.6 Conclusion

The study confirms the feasibility and applicability of strain gauges bonded into screws when subjected to lateral loading under controlled conditions. The measurements provide valuable insights into the locally occurring normal forces within screws and their influence on fastener failure. The magnitudes of the normal forces evaluated in this study appear plausible but require further validation. The extent to which shear stresses and a slightly eccentric position of the strain gauge within the fastener affect the results remains uncertain. Verifying any potential eccentricity is therefore recommended and should be considered in future investigations. Although this verification was not part of the present tests, an elastic four-point bending test performed in two directions, with a 90° rotation of the measuring screw for each test, is suggested. This approach would allow any eccentric position to be identified and incorporated into subsequent evaluations.

Both single-shear and double-shear connections exhibit comparable load-displacement behaviour but differ in the distribution of normal forces along the screw axis. In double-shear connections, the normal force increases towards the symmetry axis, indicating that the screw section within the middle timber is at greater risk of premature failure compared to the side timber. Moreover, the load per shear plane is not evenly distributed within individual specimens, underscoring the importance of separate load measurements for accurately determining shear-plane forces.

The iterative procedure developed to calculate internal forces and the interaction between shear and normal components enables a consistent evaluation of forces within the shear plane while accounting for frictional effects. The applied interaction terms and the resulting reduced yield moments demonstrate that normal forces can significantly diminish the remaining bearable bending moment in the plastic hinge. For single-shear connections, the remaining yield moment amounts to approximately 93 % of the weakened screw's yield moment, whereas for double-shear connections it is reduced to about 88 % under the given assumptions. Whether this magnitude applies to full cross-sections requires further verification.

The slightly lower load-bearing capacities of double-shear connections at smaller displacements can be attributed to higher normal forces in the middle timber. However, the natural scatter of timber properties and the limited number of tests must also be considered. Despite the reduction in yield moments, the measured load-bearing capacities generally exceed the calculated mean values, though occasional lower outliers highlight the need for further experimental validation.

The fastener type and screw dimensions used in this study should be modified to minimise the significant cross-sectional weakening caused by the hole for the strain gauge, which can lead to premature failure. For practical applications or transfer of results to other connection types, these factors must be addressed, such as through adjustments to screw geometry or by employing larger diameters in future investigations.

Overall, this study emphasises the importance of considering geometric and material influences, as well as the interaction between normal and shear forces, in the design and analysis of screw connections. While the exemplary calculations illustrate the order of magnitude of moment reduction due to normal forces, a definitive assessment of the resulting reduction in load-bearing capacity remains difficult due to experimental scatter, cross-sectional weakening, and the premature failure of eroded screws. Further studies with larger sample sizes and optimised screw geometries are therefore recommended to validate and extend these findings.

5 Load-Deformation Behaviour of Rectangular Fastener Connections

This chapter builds on the previously introduced question of how applied load relates directly to fastener deformation. In conventional timber connections, fasteners are fully embedded, hiding their deformation and load transfer mechanisms. By conceptually splitting the connection at mid-depth and exposing the fasteners, their behaviour under load can be observed directly. This approach allows not only the examination of bending angles and plastic hinge positions, but also the comparison of connections across timbers of increasing density, making density-related differences in deformation and load transfer evident. Overall, the investigations provide fundamental insights into fastener behaviour, link load to deformation, and establish reference data for future analyses and simulation validation.

5.1 A Comparative Qualitative Study on Deformations

A test configuration is developed to investigate critical aspects of connections with laterally loaded dowel-type fasteners that are typically concealed in conventional setups. In such connections, the fasteners are fully embedded in the surrounding timber, which makes it difficult to directly observe their deformation and the mechanisms of load transfer during loading. This limitation raises fundamental questions: how and where load transfer occurs, at what point plastic deformations of the fastener begin, and how these processes can be measured and better understood.

To address these questions, an experimental setup conceptually exposes the fastener by cutting and unfolding the connection, enabling direct observation of its deformation behaviour and interaction with the timber. This visibility allows the use of optical measurement techniques, such as digital image correlation (DIC), to record high-resolution data on local strains and the development of plasticity.

The test series investigates variations in material combinations and connection types, including timber-to-timber and timber-to-steel configurations, to study the influence of material strength and density on deformation behaviour, failure mechanisms, and overall fastener performance. Although the geometry differs from conventional connections, the setup provides meaningful insights that can be transferred to practical applications. Most tests are conducted as part of a master's thesis [18], while the evaluation and processing of the experimental data are performed by the author.

5.2 Material

The connection behaviour is studied for different fastener and timber strength combinations. The variation of fasteners includes aluminium and steel S235 hot-rolled. Timber properties are varied by using spruce glulam, beech LVL and DVW. The range of timber densities used is approximately 400 - 1300 kg/m^3.

Table 5.1: Material properties for fasteners and timber products: Density ρ_{mean} in kg/m^3 and moisture content u_{mean} in %.

Fastener tensile properties		
in MPa	$R_{p,0,2}$	f_u
Aluminium	167	203
Steel	328	504

Timber density and moisture content			
	Spruce glulam	Beech LVL	DVW
ρ_{mean}	437	816	~1300
u_{mean}	11.6	7.76	–

Tensile tests on 10 or 11 fasteners each give results about the steel tensile strength. Results are shown in Tab. 5.1 and Fig. 5.1. In addition, mean values for density and moisture content of the timber are given, which are determined on samples taken from the test specimens, see also results in Tab. A.16. DVW density was only determined by weighing several specimen parts. The cross-section dimensions of the rectangular fasteners used is 20 mm x 15 mm and the length varied according to the type of connection tested.

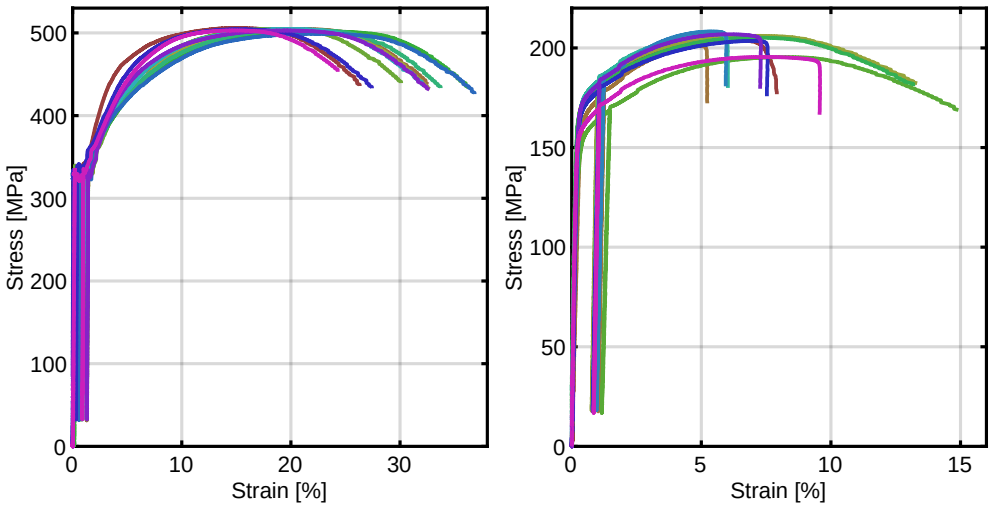

a. Steel: n = 11, $f_{u,mean}$ = 504 MPa, COV = 0.36%.

b. Aluminium: n = 10, $f_{u,mean}$ = 203 MPa, COV = 2.15%.

Fig. 5.1: Fastener material properties from tensile tests.

5.3 Methodology

A new experimental approach is developed to investigate internal mechanisms within timber connections that are typically concealed in conventional connections. In these conventional configurations, fasteners are embedded within the timber, making it difficult to observe, measure or analyse internal load paths and failure processes. The experimental concept simulates a longitudinal cross-section of a conventional connection. The two halves of the connection are conceptually folded open, bringing the previously internal fastener to the exterior, see Fig. 5.2. In a figurative sense, the outer specimen surfaces correspond to the mirror plane within a conventional connection. This configuration allows direct observation and measurement of fastener deformation while maintaining timber support on three sides. The exposed surface enables detailed analysis of strain responses and load redistribution using DIC.

Several series of tests are conducted, systematically varying timber density, fastener material, and connection type. Both timber-to-timber and timber-to-steel connections are examined. The combinations of fastener and timber materials produce different ratios of fastener tensile strength to timber density, see Tab. 5.1. The combination of DVW with aluminium was excluded, as it does not represent realistic strength ratios for typical timber structures. By exploring these material combinations, the

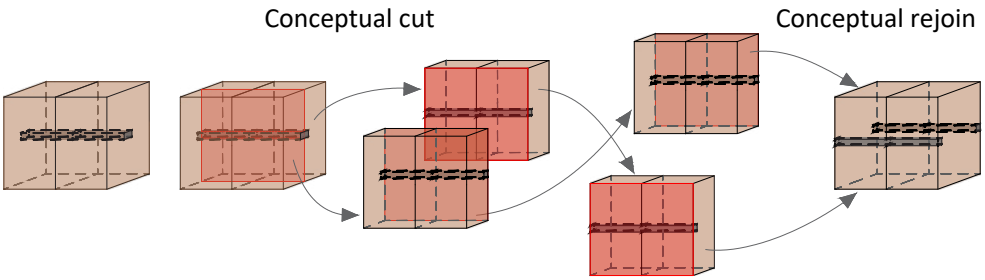

Fig. 5.2: Schematic illustration of specimen concept: Transfer of a single-shear timber-to-timber connection with an inner fastener (left) to outward facing fasteners (right).

study assesses how strength ratios and material interactions influence load transfer, deformation modes, and failure mechanisms. This structured approach provides quantitative insights into the mechanical performance of dowel-type connections under lateral loading.

5.3.1 Test Specimens

The test specimens are double-shear connections, assembled using either three timber members or two timber members and an inner steel plate. The timber thickness is uniformly set to 160 mm to ensure that the failure mode involves two plastic hinges per shear plane in each configuration. The inner steel plate has a thickness of 30 mm and is made of S355. To investigate the influence of the rope effect, an additional specimen with a head is included for each material combination. These configurations feature an anchor plate at both ends of the fastener, serving a similar function to a bolt head, as illustrated in Fig. 5.3. Inner threads are prefabricated at both ends of the fastener, allowing insertion of an M8 steel screw. The total width of the timber-to-timber connections is 480 mm, while the width of timber-to-steel connections is 350 mm, equivalent to the fastener length.

The configurations use external rectangular fasteners that are visible. The rectangular shape prevents slippage during testing, as might occur for semicircular cross-sections, and ensures that the fastener remains securely positioned, enabling accurate observation of its deformation. A key objective of this approach is to visualise fastener deformation under lateral loading. This is achieved using DIC, an advanced optical measurement technique that tracks surface deformations precisely. DIC measures deformation and strain distribution on the fastener surface, providing detailed insights

into its behaviour under lateral loading. To validate the DIC measurements, local strain gauges are applied to the fasteners. These gauges provide direct measurements at specific points, and strain values from DIC are compared with those from the gauges to cross-validate the methods, supporting accuracy and reliability. Including specimens with and without a head allows investigation of the rope effect, that is, the influence of normal forces in the fastener. The anchor plates introduce additional normal forces, which may significantly affect deformation behaviour and failure mechanisms. Comparing configurations with and without the anchor plates provides insights into the role of normal forces in the performance of dowel-type fasteners within timber connections. Horizontal clamping at the lower end prevents gaps in the shear planes and guarantees vertical movement, see Fig. 5.7. Clamping is realised by steel profiles, with wooden distance blocks added for timber-to-steel connections, pulled together by threaded rods. One steel profile is anchored in the testing machine, and the load is applied displacement-controlled via a spherical seat on the middle member. To avoid early shear failure of the specimens, fully threaded screws are inserted perpendicular to the fastener.

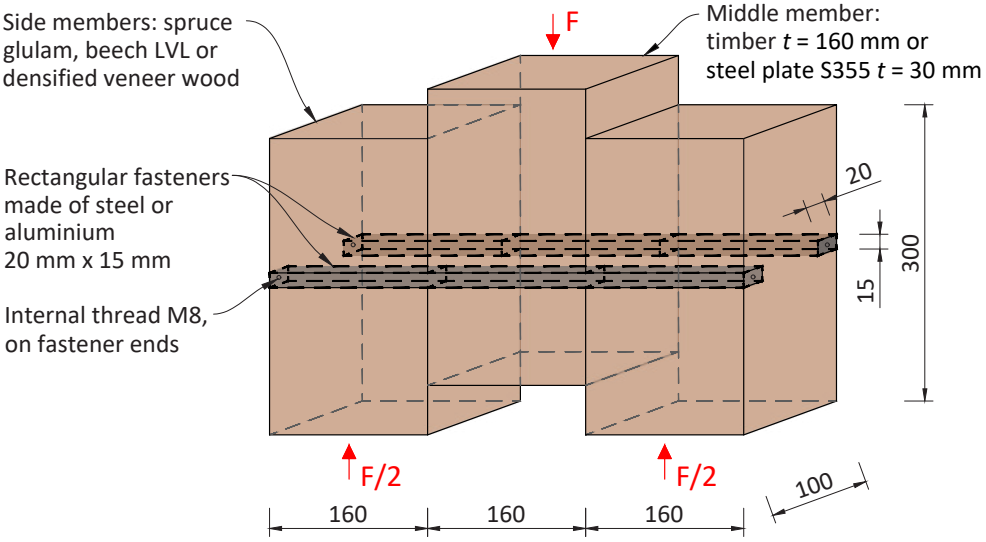

Fig. 5.3: Scheme of test specimen of an exemplary timber-to-timber connection with external rectangular fasteners, in mm.

5.3.2 Test Programme

Embedment tests

As the selected test configurations with the modified geometry are only comparable to typical connections to a limited extent, there are no corresponding input parameters with which to describe and calculate the connection behaviour. In particular, the embedment behaviour is unknown due to the fasteners' outward-facing arrangement, their three-sided embedment in the timber, and their rectangular cross-section. To address this knowledge gap, a test setup tailored for this purpose was developed to determine the embedment properties, and the corresponding tests are carried out. The test setup was designed based on the fundamental, existing normative regulations and adapted to the given context. Sandhaas et al. [87] discuss the differences between several available test and evaluation methods for embedment properties of dowel-type fasteners in timber. The methods, for instance, given in [111, 119, 129] propose full-hole or half-hole tests and different evaluations depending on the test setup. Deformation behaviour is influenced as well as the stiffness. Stiffness differences may be large between the different test and evaluation methods and is discussed in Franke and Magnière [36]. To realise a test setup that is comparable to the later connection test setup, the known setups are adapted to rectangular fasteners and to a test setup, that allows two external fasteners to be tested at the same time, see schematic drawings in Fig. 5.4 and corresponding realised test setups in Fig. 5.5.

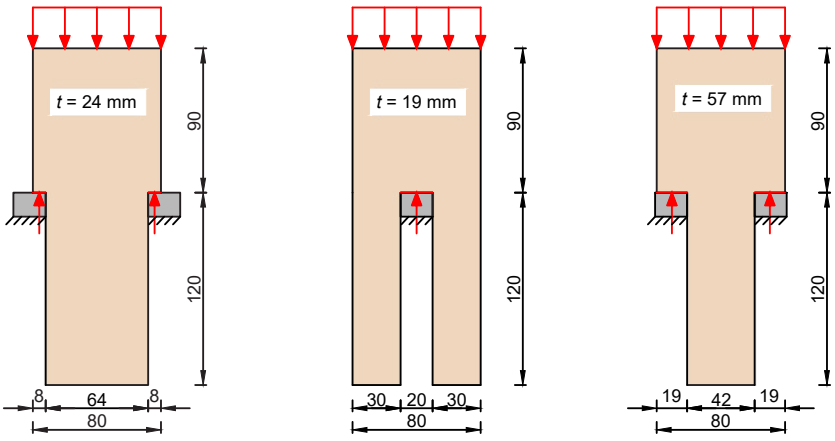

a. Series 1. b. Series 2. c. Series 3.

Fig. 5.4: Schematic embedment test setups with external and internal rectangular fasteners, in mm.

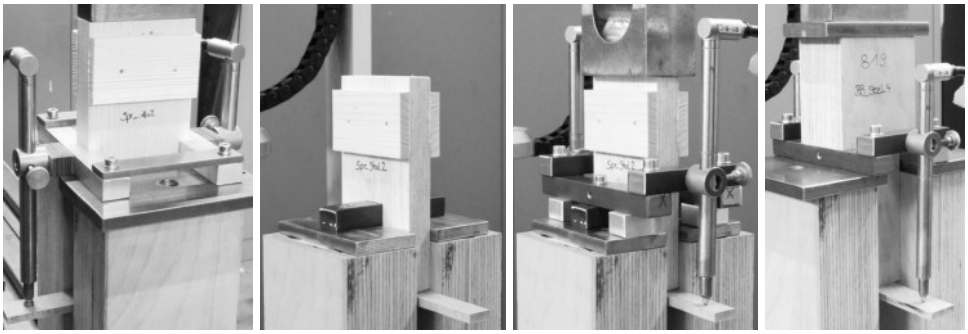

a. Series 1. b. Series 2, specimen. c. Series 2. d. Series 3.

Fig. 5.5: Test setups: embedment tests with external and internal rectangular fasteners.

For series 1, recesses are prefabricated in the timber on both sides and form rectangular surfaces with an area of 8 x 24 mm^2, that each lie on rectangular fasteners. To prevent splitting a reinforcement plate is glued on the timber surfaces for series 1 and 3 with spruce and beech LVL. In addition to series 1, two reference series are part of the programme, which are intended to investigate the difference to an internal fastener, i.e. series 2, see Fig. 5.5b and c, and a potentially existing size effect of the stressed area, i.e. series 3, see Fig. 5.5d. For series 3, the depth of the embedment area equals the depth in the connection tests, i.e. a = 19 mm. The corresponding width t is chosen in accordance to series 1 in a ratio of a/t of 1/3. The size of the contact surface for series 2 is chosen equally to series 1. The given embedment areas in Tab. 5.2–5.4 refer to one side of the test specimen for series 1 and 3, and for series 2 this corresponds to the total area subjected to embedment stress.

Table 5.2: Test programme embedment tests series 1.

Fastener position	Embedment area a in mm	t in mm	Timber product	Fastener	No.
External	8	24	Spruce glulam	Steel	3
				Alu	3
			Beech LVL	Steel	3
				Alu	3
			DVW	Steel	3

Table 5.3: Test programme embedment tests series 2.

Fastener position	Embedment area a in mm	t in mm	Timber product	Fastener	No.
Internal	20	19	Spruce glulam	Steel	3
				Alu	3
			Beech LVL	Steel	3
				Alu	3
			DVW	Steel	3

Table 5.4: Test programme embedment tests series 3.

Fastener position	Embedment area a in mm	t in mm	Timber product	Fastener	No.
External	19	57	Spruce glulam	Steel	3
			Beech LVL	Steel	3

Connection tests

Connection types, i.e. timber-to-timber and timber-to-steel connections, fastener types, i.e. smooth rectangular fastener with and without anchor plates as heads, fastener and timber material are varied and combined to assemble different specimens. The test programme given in Tab. 5.5 is carried out for a series with timber-to-timber connections and timber-to-steel connections. The different types of tested connections are schematically illustrated in Fig. 5.6. The initial loading speed was chosen to be between 1 and 2.5 mm/min. Due to the geometry of the tests, the maximum deformation of the specimens was limited to 50 mm. To maximise the potential of the tests, it was decided during the test whether an increase in the loading speed was necessary. The maximum loading speed was 8 mm/min.

5.3.3 Measuring Method

Great benefits of using digital image correlation (DIC) are the measuring without any contact to the specimens and an evaluation of different parameters afterwards. The used software is ISTRA 4D from Dantec Dynamics [25]. Thereby, deformations in all spatial directions and strains can be subsequently extracted and analysed from the

Table 5.5: Test programme for timber-to-timber and timber-to-steel connections: combination of used timber and fasteners.

Timber used	Fastener made of	Number of tests	
		with head	no head
Spruce glulam	Aluminium	1	1
	Steel	1	1
Beech LVL	Aluminium	1	1
	Steel	1	1
Densified veneer wood	Steel	1	1

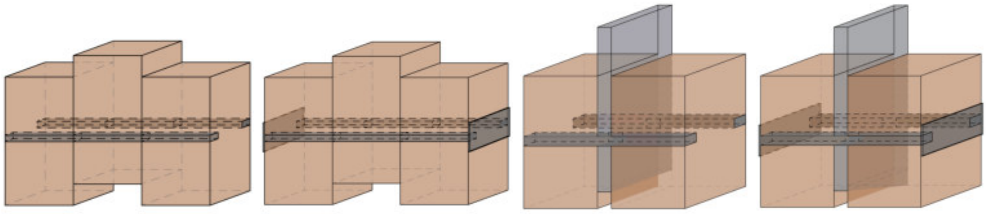

a. Timber-to-timber. b. Timber-to-timber, with head. c. Timber-to-steel. d. Timber-to-steel, with head.

Fig. 5.6: Types of tested connections.

image recordings. Images are recorded with a frequency of 1 Hz. The test setup and measuring devices are shown in Fig. 5.7. Two cameras are installed on both sides with a minimum angle in between of 15°. To use DIC, the specimen surface needs to be prepared. First of all, the surface needs to be clean and even. Steel fasteners are sandblasted to remove any residues of the tinder layer. A speckle pattern is necessary on the surfaces that are measured and evaluated. This pattern is applied by using adhesive foil, which is printed beforehand with speckles in a size depending on the test setup and camera distance. Adhesive foil is recommended when larger strains of the measured surface are expected during the test. A foil behaves elastic to some extent and can give results for large strains where colouring of the surfaces would be limited due to cracks. Previous research results from Sutton [99] and own experiences showed that the perfect speckle size is around 3 – 7 pixels to measure deformations.

Depending on the size of the measuring area (Region of interest, ROI) and camera resolution (4112 x 2176 px) in the tests, the speckle size can be adjusted and printed on the adhesive foil accordingly. For the chosen test setup, a speckle size of 1.1 mm

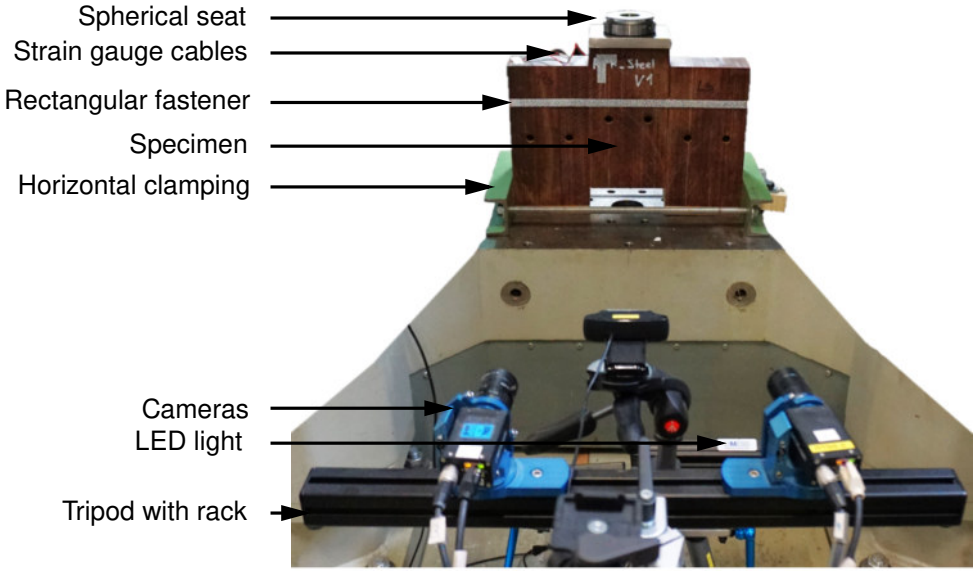

Fig. 5.7: Exemplary test setup of a timber-to-timber connection. Measuring cameras in the front, specimen with calotte and horizontal clamping on the bottom in the back.

is determined by:

$$d_{\text{speckle}} = \frac{\text{specimen width}}{\text{width ROI}} \cdot \text{speckle size in pixels} = \frac{480}{2200} \cdot 5 = 1.1\,\text{mm} \qquad (5.1)$$

To generate the speckle pattern, the software Speckle Pattern Generator from Correlated Solutions [24] is used. The density, i.e. number of point, is chosen to 80% and the variation to 99%, i.e. the random distribution of points. The quality of a pattern can be described by determining a mean intensity gradient (MIG) acc. to Pan et al. [71]. The MIG, as a statistical characteristic of the speckle pattern, influences the displacement measurement error of DIC when the subset size is fixed. Therefore, it can be used as an effective global parameter to evaluate the overall quality of the speckle pattern. It considers the sharpness of the edges and the clarity of the pattern within a change of brightness intensity. With the pattern used a MIG of 45 is calculated. A MIG larger than 20 marks a good quality pattern [71, 75]. A prepared specimen surface with the speckle pattern glued on the fastener is shown in Fig. 5.8.

Fig. 5.8: Detail of speckle pattern.

5.3.4 Coordinate Systems

To describe the deformations of the fasteners, different coordinate systems (COS) are used, see Fig. 5.9. A COS can be static, in which case it is fixed in space for all steps, even if the object moves. In the dynamic case, the COS is attached to the object and moves with the object. Each step can therefore have a different orientation of the axes. The global COS is set as static while dynamic COS are used to evaluate the strains and compare them to the strains measured with the glued on strain gauges. The x-axis of the global COS is located in the centre line of the fastener and starts at the left end of it. The local COS is either located in the shear plane for timber-to-timber connections or between shear plane and plastic hinge for timber-to-steel connections. By placing the origin of the local COS in the position of the strain gauge, the measured strains are comparable. Thus, the local COS is rotating according to the inclination of the fastener.

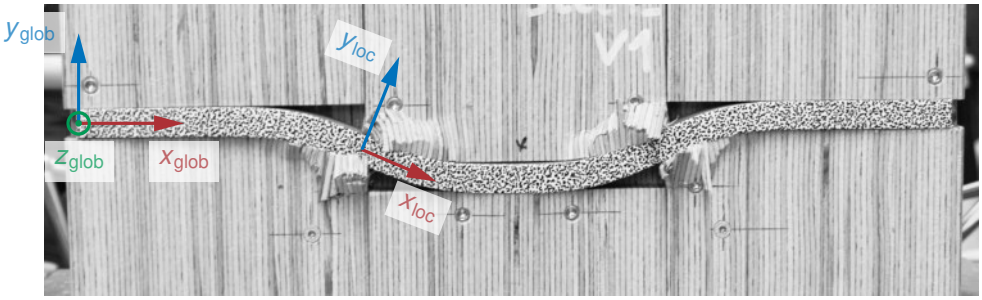

Fig. 5.9: Coordinate systems on deformed fastener after testing. Exemplary local coordinate system in the left shear plane of a timber-to-timber connection.

5.4 Results and Discussion

As the test programme included embedment tests and connection tests, results are presented below starting with the embedment behaviour since the results are necessary to later discuss the connection behaviour. The sections present a detailed evaluation of the results obtained for each individual specimen and comparisons of several connections. The correlation parameters for DIC evaluation used can be taken from Appendix A.4. Various performance parameters are assessed to gain insight into the structural behaviour and failure characteristics of the tested connections. The evaluated parameters include:

- Embedment behaviour of rectangular fasteners
- Load–displacement behaviour of connections
- Incremental deformations of rectangular fasteners
- Location of plastic hinge
- Bending angles
- Failure mechanisms

Deformations are recorded in all three mentioned global directions, compare Fig. 5.9, and can be evaluated separately or as a total deformation. To simplify the illustrations of the fastener deformation, the centre line, i.e. the axis of gravity of the rectangular fasteners, is evaluated. Each parameter is discussed systematically to highlight the observed trends, differences among specimens, and implications for structural performance. The results are first presented and visually assessed in a qualitative and comparative manner, but are then also quantitatively evaluated later in the chapter.

5.4.1 Embedment Behaviour

When studying connections in general, and particularly their load-deformation behaviour, the embedment behaviour plays a central role. Knowledge of embedment strength is required for determining failure modes and calculating load-bearing capacities. This embedment strength is discussed separately in this section as an input parameter for subsequent connection analyses. Results from the embedment tests carried out are listed in Tab. 5.6. Corresponding densities and moisture contents of

the specimens are given in Tab. 5.7. The tests aim to investigate the general embedment behaviour of the timber with rectangular fasteners at different positions. The embedment strengths are calculated by taking the maximum load achieved in relation to the corresponding contact area between timber and fastener. The magnitude of the calculated strengths is in the order of the longitudinal compressive strengths. For comparison, exemplary values for compression in longitudinal direction for spruce glulam and beech glulam can be found in [33], which coincide with the evaluated results.

Table 5.6: Embedment results with rectangular fasteners: Mean strength values per series* in N/mm^2.

Series	Fastener	Position	Spruce	Beech LVL	DVW
1	Alu	External	46.4	74.2	–
	Steel		49.5	86.6	229
2	Alu	Internal	42.3	83.6	–
	Steel		41.2	84.4	208
3	Steel	External	41.6	78.7	–

* Individual results are listed in Appendix A.5

Table 5.7: Moisture content u and density ρ: Results for samples of embedment test specimens.

	Spruce			Beech LVL			DVW		
	Mean	SD	COV	**Mean**	SD	COV	**Mean**	SD	COV
u in %	**10.9**	0.501	4.60	**6.87**	0.327	4.76	**1.46**	0.160	10,9
ρ in kg/m^3	**461**	32.9	7.13	**826**	32.8	3.97	**1328**	12.5	0.940

The results in Tab. 5.6 show differences between the external and internal position. For spruce and DVW, the internal position leads to lower strengths, whereas for beech LVL the trend is not clearly present. However, the densities and specimen lay-up also need to be considered. Any secondary glue lines in the beech LVL significantly influence the results and are one reason for the low strength value of beech LVL when used with aluminium fasteners. In this case, fewer specimens with secondary glue lines are tested. Fig. 5.10 illustrates these differences in maximum loads. In addition, the shown behaviour reveals a first peak for all specimens, which correlates with the compression strength in grain direction. Afterwards, the load drops, then reaches a plateau or sometimes even increases again at larger displacements. In

general, therefore, a lower strength is determined for the internal fasteners. Different load distributions are possible for the two geometries, internal and external. For the internal fasteners, the load can generally distribute in two directions, left and right, whereas the external fasteners can only distribute the load inwards into the test specimen. However, due to the external positioning two different areas of the specimen are stressed and often quite different displacements are observed between the two transducers mounted. This might be a sign for a non equally distributed load on both fasteners. In contrast, the internal fastener and the stressed timber is subjected to the total load applied in that case. In addition, the different specimen width t of 24 mm for external fasteners, and 19 mm for internal fasteners respectively, may influence the results, too.

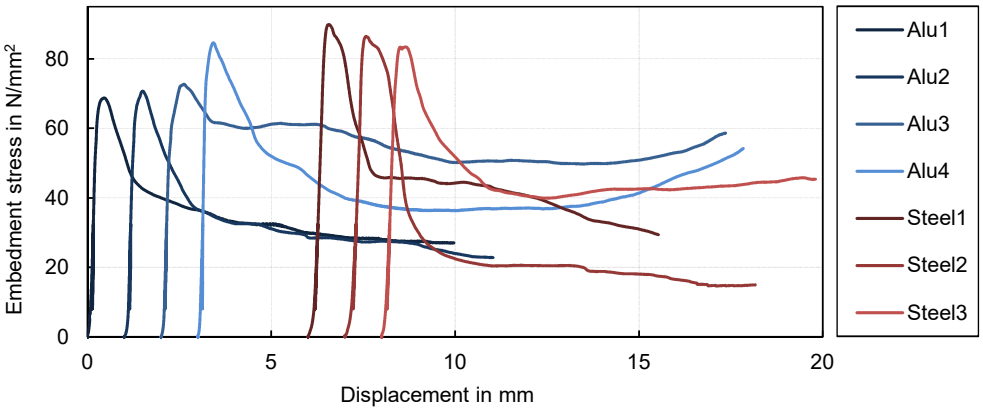

Fig. 5.10: Results of series 1 in beech LVL: Embedment behaviour of external rectangular fasteners.

For comparison, Fig. 5.11 shows the embedment behaviour of the other two series in beech LVL. For series 2, a distinct difference in behaviour can be observed after reaching the longitudinal compression strength, i.e. the first peak. Although a drop in load also occurs, it is significantly smaller than for series 1. Subsequently, a higher load plateau is reached; however, the load does not remain constant but exhibits fluctuations. Therefore, the term residual load-bearing capacity appears more appropriate in this context. This residual load-bearing capacity is lower due to the altered stress state at the outer position and continues to decrease over time rather than remaining at a constant level (see also the results of series 3 in Fig. 5.11b). The reason for this can be attributed to differences in stress distribution. In the case of an external fastener arrangement, the specimen can expand freely in three directions. After the first failure due to longitudinal compression, typically accompanied by a

tension or shear crack propagating upwards from the fastener corner, the fibres move outwards in all three directions. In contrast, in the internal arrangement, the material is restrained on at least two sides, meaning that splitting does not lead to evasion or lateral displacement of the stressed zone.

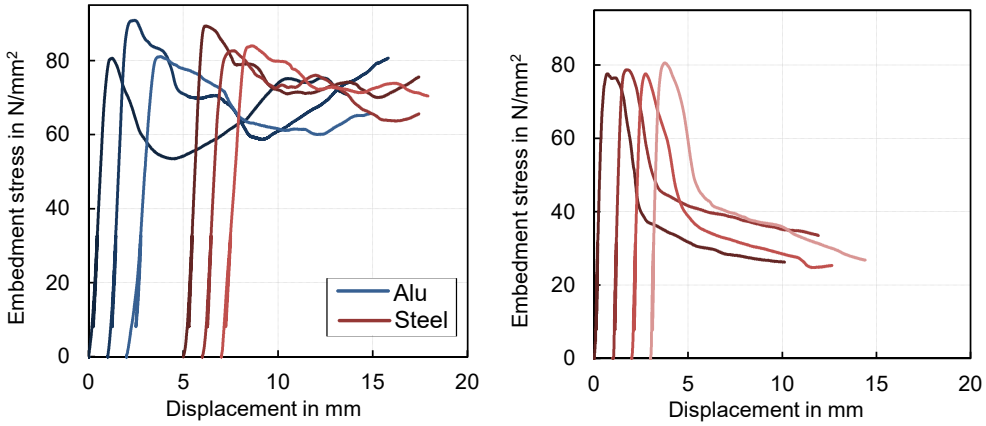

a. Series 2. b. Series 3.

Fig. 5.11: Results of series 2 and 3 in beech LVL: Embedment behaviour of internal and external rectangular fasteners.

The tendency towards lower values for series 3 could potentially be influenced by a size or volume effect. The load distribution effect is stronger for series 1 than for series 3. For beech LVL, an existing secondary glue line has a greater effect on the narrow test specimen with a thickness of 24 mm than on series 3, i.e. the wide specimens with a thickness of 57 mm. For spruce glulam, in contrast, there is no significant difference from series 2 to series 3, but a reduction to 84% is evaluated from series 1 to the larger volume in series 3.

For the subsequent analysis, the embedment strength is defined as the embedment stress corresponding to the maximum stress reached, and is therefore comparable to a compressive strength in the longitudinal direction. For spruce and beech LVL, the values from series 3 are used, i.e., 42 N/mm^2 and 79 N/mm^2, respectively. For DVW, an embedment strength of 220 N/mm^2 is assumed, which is between those of series 1 and 2. Due to the high level of homogenisation of this product, low scatter and no significant size effect is expected as a result. These values are subsequently employed in the analytical calculations presented in the following sections.

5.4.2 Load-Deformation Behaviour of Connections

The load-deformation behaviour provides valuable insight into the performance of the connection. Not only does the comparison of maximum loads or loads at several deformation steps serve as an indicator of load-bearing capacity, but the shape of the load-deformation curves also highlights characteristic differences between the individual connection configurations. Deformation steps mainly evaluated are 5, 10 and 15 mm and are marked in Fig. 5.12.

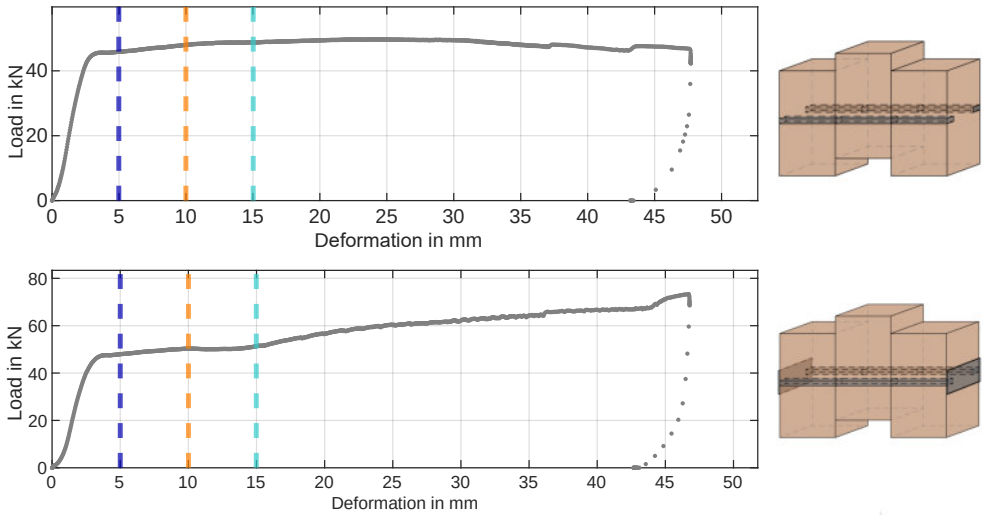

Fig. 5.12: Exemplary load-deformation curves for front connections without and with head made of spruce glulam and steel fasteners.

The illustration also shows the difference of the configurations with and without head with a rope effect developing for the bottom case. Tab. 5.8 provides an overview and lists the maximum loads achieved during the tests. The corresponding load-deformation curves are shown in Figs. 5.13 and 5.14 for all tested connections. Although the maximum loads are achieved at different stages of deformation and the results for individual tests are limited by external factors, clear trends can be seen. Higher material properties in timber and fasteners increase the loads. This is an expected development, which is further specified and verified in the following. In the timber-to-timber connection with beech LVL and steel fasteners with head, the measurement was interrupted by technical problems, with the recording covering a deformation of up to around 28 mm. An increase in load was still recorded at this

point. The geometry of the connection configurations is designed in such a way that the failure mechanism is two plastic hinges per shear plane. This results in two basic equations for calculating load-bearing capacities, which are based on Johansen [50]. The equations have been slightly adjusted to take into account the embedment depth *a* of the rectangular fastener instead of the diameter of a circular fastener. For timber-to-timber connections:

$$F_{v,R} = \sqrt{2 \cdot M_{y,R} \cdot f_h \cdot a} \tag{5.2}$$

with

$F_{v,R}$	Load in N
$M_{y,R}$	Bending moment in Nmm
f_h	Embedment strength in N/mm^2
a	Embedment depth in mm

and for timber-to-steel connections:

$$F_{v,R} = 2 \cdot \sqrt{M_{y,R} \cdot f_h \cdot a} \tag{5.3}$$

Table 5.8: Maximum loads per specimen reached in tests, in kN. Note: the displacement varies considerably when the maximum load is reached.

Connection	Timber product	Fastener		Fastener	
		Steel	Aluminium	Steel	Aluminium
					
T-T	DVW	325	-	376	-
	Beech LVL	133	110	187	163
	Spruce glulam	99.4	77.6	147	104
					
T-S	DVW	410	-	421	-
	Beech LVL	227	128	279	152
	Spruce glulam	162	106	211	137

T-T = Timber-to-timber connection, T-S = Timber-to-steel connection

Table 5.9: Loads at 15 mm fastener deformation per specimen reached in tests, in kN.

Connection	Timber product	Fastener		Fastener	
		Steel	Aluminium	Steel	Aluminium
					
T-T	DVW	320	-	375	-
	Beech LVL	131	109	150	119
	Spruce glulam	97.5	76.1	103	88.6
					
T-S	DVW	409	-	421	-
	Beech LVL	196	128	214	149
	Spruce glulam	137	94	149	105

T-T = Timber-to-timber connection, T-S = Timber-to-steel connection

The plastic bending moments $M_{y,R}$ of the fasteners are calculated based on the achieved tensile test results with

$$M_{y,R} = f_y \cdot W_{pl} \tag{5.4}$$

to 188 Nm for aluminium and 369 Nm for steel. Eqs. 5.2 and 5.3 can be extended with a corresponding term to account for the rope effect $F_{ax}/4$ according to the European Yield Model (EYM) [118]. The rope effect is influenced differently for the connections examined here. For connections without a head, only the inclined area can cause an increase in the axial forces in the fastener and the friction component in the shear plane. For connections with heads, failure of the anchoring screw, M8 8.8, pulling-out of the screw from the fastener end, or head pull-in resp. compression failure perp. to grain of the timber under the head plate is possible. The use of different timber products also results in different types of failure. The results from Section 5.4.1 of the embedment tests are used for the calculations. The embedment curves show an initial peak, which corresponds to the longitudinal compressive strength of the stressed area. If this maximum value and the actual embedment depth a of the fasteners of 19 mm are used for the calculation, the resulting loads in Tab. 5.10 are obtained. The

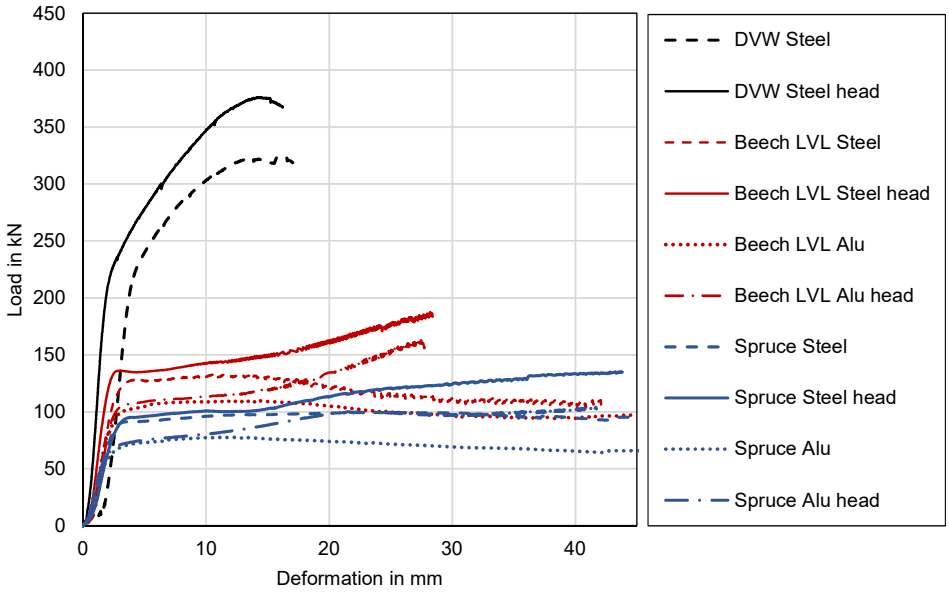

Fig. 5.13: Load-deformation curves for timber-to-timber connections.

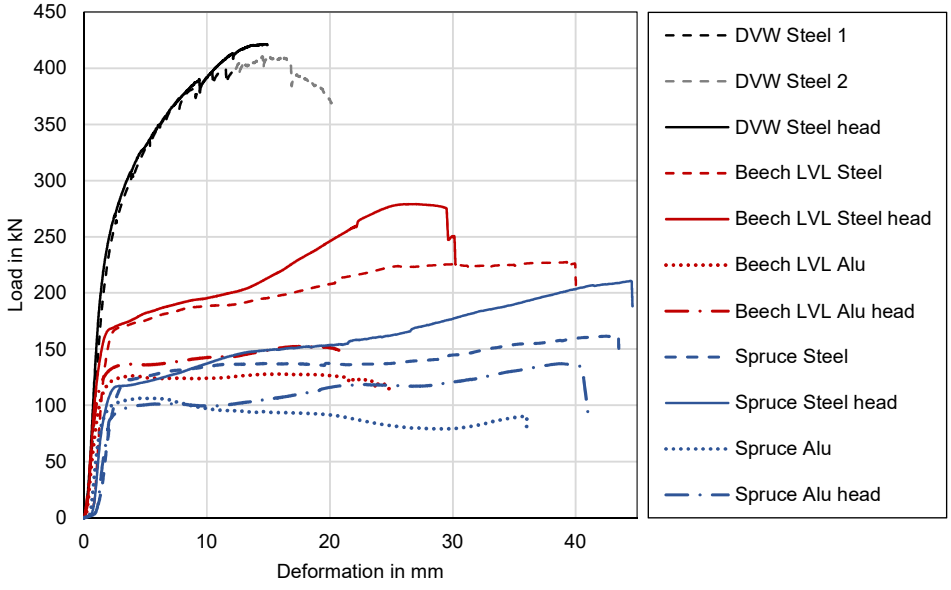

Fig. 5.14: Load-deformation curves for timber-to-steel connections.

loads for configurations with a head are consistently calculated using a rope effect of $0.25 \times F_{v,R}$.

Table 5.10: Calculated loads per specimen acc. to Johansen and EYM, in kN.

Connection	Timber product	Fastener		Fastener	
		Steel	Aluminium	Steel	Aluminium
					
T-T	DVW	222	-	278	-
	Beech LVL	133	95.0	167	119
	Spruce glulam	97.1	69.3	121	86.6
					
T-S	DVW	314	-	370	-
	Beech LVL	188	134	235	168
	Spruce glulam	137	98.0	172	122

T-T = Timber-to-timber connection, T-S = Timber-to-steel connection

An initial comparison shows that there is no comprehensive correlation with the maximum loads achieved in the test. However, closer analysis of the curve progression reveals that the loads determined based on the Johansen Eq. 5.2 and 5.3, i.e. without rope effect, correspond to the transition points from elastic to plastic connection behaviour. The kink in the curves can therefore be explained by the onset of plastic timber behaviour, i.e. the point of reaching the compressive strength of timber in-between the simultaneously forming plastic hinges. Since wood failure is the decisive factor in this case and is reached at relatively small deformations, there is hardly any difference between configurations with or without a head. The rope effect is activated by larger deformations, and the greater the inclination, the more the effect is increased. The following load-deformation behaviour after the kink is highly dependent on other factors such as wood type, the existing head in the context of compressive strength perpendicular to the grain under the head plates, or type of connection. However, it must be mentioned that for the timber-to-steel connections in DVW, no pronounced kink is visible that could indicate the transition from elastic to plastic connection behaviour. It is rather a smooth transition. Due to the varying magnitudes of maximum

deformations achieved in the tests, the maximum load given in Tab. 5.8 cannot be directly compared with the calculated results in Tab. 5.10. However, qualitative differences between the individual configurations and the effect of the head, i.e., the activation of the rope effect due to inclination, are always clearly visible compared to the specimens without a head. The connection behaviour in general is closely linked to the embedment behaviour. At larger deformations, a plateau or a region with only a slight increase or decrease in load is observed in embedment tests and also in the connection response. This correlates with the embedment behaviour after the longitudinal compressive strength is reached, the subsequent drop, and the varying residual load-bearing capacity depending on the degree of fibre damage.

5.4.3 Fastener Deformations in Y-Direction

To assess the deformation of the fasteners in the different tested connections, several deformation steps are chosen and evaluated. In general, three steps at 5, 10 and 15 mm deformation will be shown and addressed with individual exceptions, which are pointed out accordingly. The deformation refers to the deformation of the fastener in global y-direction. So in case of a 5 mm deformation, the evaluated step is the one, when the first point of the fastener surface has moved 5 mm in y-direction related to the global coordinate system, see Fig. 5.15 for an exemplary illustration. The deformations shown are consistent with the load-deformation curves shown earlier in Figs. 5.13 and 5.14.

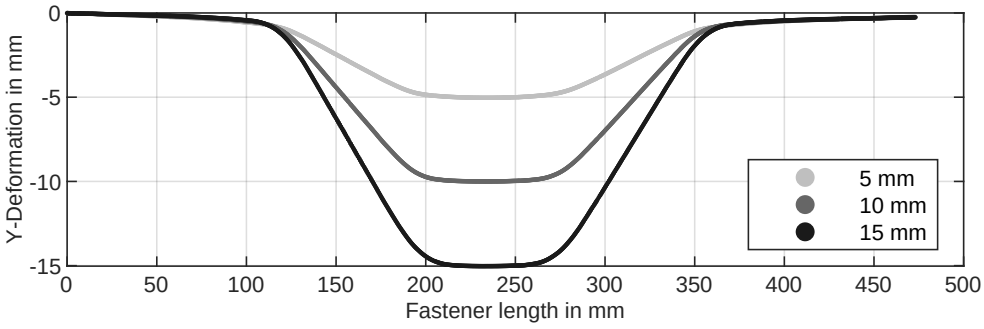

Fig. 5.15: Deformations in global y-direction for a timber-to-timber connection with spruce glulam and steel fastener.

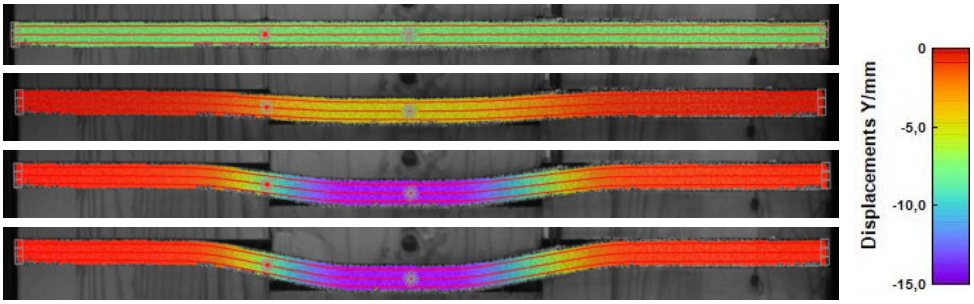

Fig. 5.16: Deformation steps 0, 5, 10, 15 mm in global y-direction for a timber-to-timber connection with spruce glulam and steel fastener. Evaluation lines are included.

The deformation lines shown in Fig. 5.15 originate from the evaluation of the y-deformations of the centre line of the fastener. The reference step is the unloaded state at the beginning. An illustrated example of the individual exaggerated curves in Fig. 5.15 is shown in Fig. 5.16. For reasons of simplicity and clarity, only the centre of gravity lines of the fasteners are shown and used in the following evaluations. The deformation examples shown in Fig. 5.15 illustrate the three stages of evaluated deformations of test specimens made of spruce glulam with steel fasteners. The lines, therefore, show the deformation that the fastener has developed since the beginning of the test. The reference state, i.e. the undeformed condition, is the starting point for all deformations analysed. It corresponds to the unloaded test specimen prior to the application of any load and remains consistent throughout. A vertical deformation of the right fastener end is visible, which means, that the fastener end dropped in y-direction. This translational component of deformation originates from initial slip and is observed for all of the investigated fasteners in different magnitudes. To understand the reasons for this translational component, the behaviour right at the beginning of the test needs to be investigated. Slip can be caused by uneven bottom planes of the specimen or a gap between the fasteners and the prefabricated recesses in the timber. To illustrate this initial slip, Fig. 5.17 shows the y-deformation of the fastener for small deformation steps up until 2.5 mm. On the right fastener end, a y-slip of around 0.2 mm occurred before bending of the fastener starts. This happens at y-deformations up until 1 mm, and, afterwards, the fastener end stays in its y-position. In contrast, the left fastener end undergoes minor y-slip and starts bending earlier, see also darkest line.

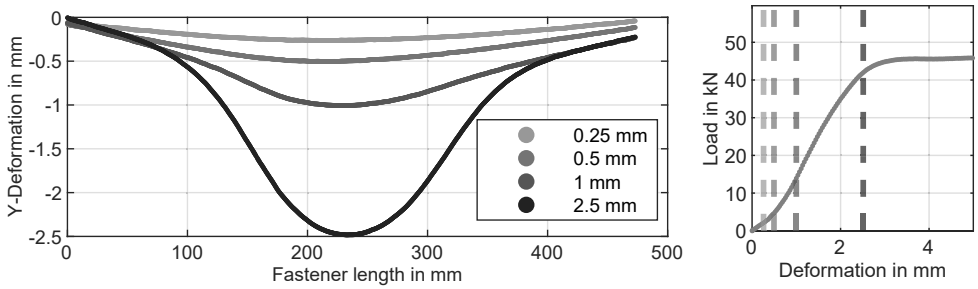

Fig. 5.17: Initial deformation steps for exemplary imber-to-timber connection with spruce glulam and steel fastener.

5.4.3.1 Influence of Timber Density

The three different timber materials used, spruce glulam, beech LVL and densified veneer wood, cover a wide range of densities. Thus, a significant influence on the connection behaviour can be expected, simply by changing the timber, while keeping all other parameters the same.

For a comparison, the connections with steel fasteners without heads are chosen. Fig. 5.18 illustrates differences occurring at 15 mm y-deformation. Apart from unintended y-direction deformations at the fastener ends, the deformation lines align with expectations. The locations of plastic hinge formation vary, and the spacing between the plastic hinges increases as the density of the surrounding material decreases - that is, the plastic hinges form at greater distances from the shear plane. Consequently, a larger plastic hinge spacing is associated with a smaller bending angle. If, instead of the total y-deformation, the evaluation is based on the relative displacements between the timber members, the results show consistently slightly larger deformations of the fasteners. This is mainly due to initial gaps being closed and the fasteners gradually settling tightly into the timber recesses. In other words, manufacturing tolerances are compensated during loading, which increases the measured deformation. These effects cannot be precisely quantified. And they vary from specimen to specimen, so the evaluation is based on the deformation of the fastener itself, as previously shown and described. With this method, as shown in Fig. 5.18, the slip deformations are not eliminated and are visible in the vertical displacement of the fastener ends, but it represents the actual recorded deformation state, which was not subsequently changed by shifting the curves. The described effects due to changes of the timber are comparable to other configurations as well.

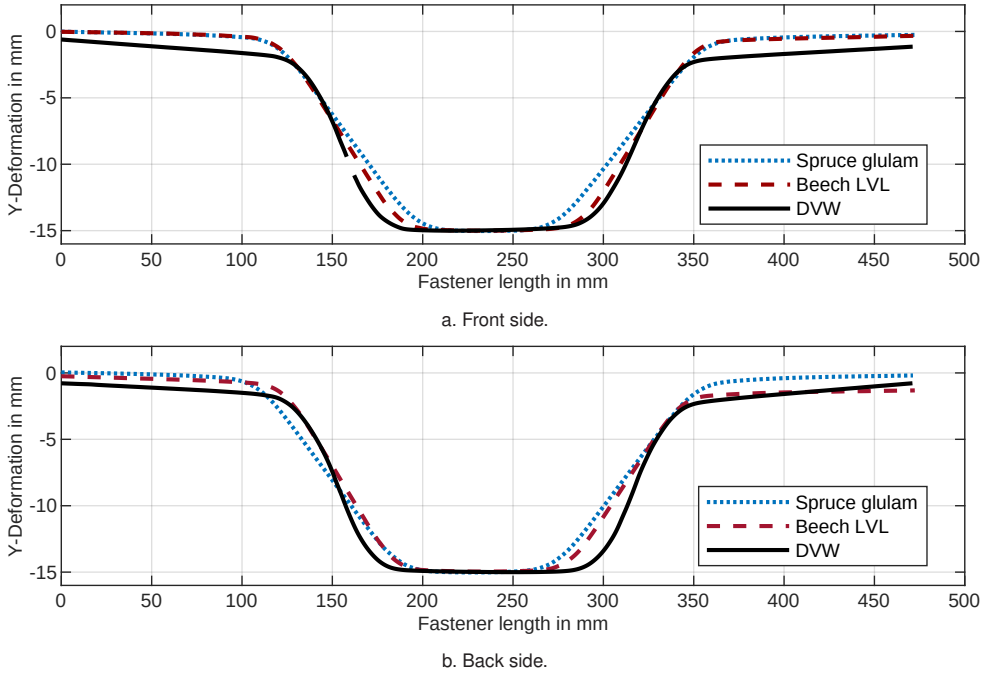

a. Front side.

b. Back side.

Fig. 5.18: Comparison of timber-to-timber connections with steel fasteners at a y-deformation of 15 mm.

5.4.3.2 Influence of Fastener Material

According to the material properties of the fastener, different deformations emerge. The weaker the fastener material, the steeper the inclination between the plastic hinges. As a result, for weaker fastener materials, the plastic hinges are spaced more closely and are located nearer to the shear plane. This effect is shown in Fig. 5.19. A comparison of the deformations between beech LVL in Fig. 5.19a and spruce glulam in Fig. 5.19b shows that a similar influence of the fastener material can be observed across the range of timber used. Hence, the influence of the fastener material is similar for all different timbers used, but in varying magnitude considering different embedment and bending stresses acting on the fasteners and their bending resistance.

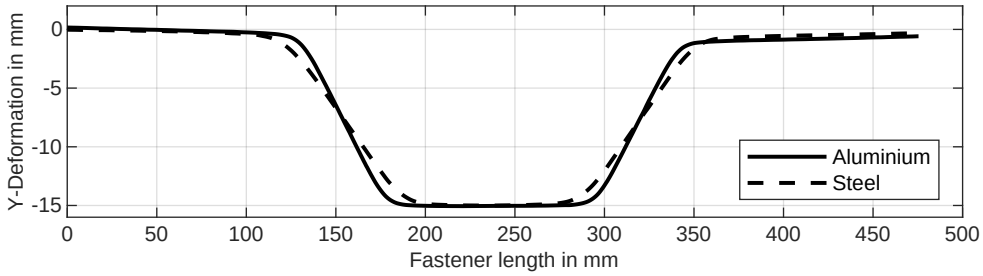

a. Timber-to-timber connection with beech LVL.

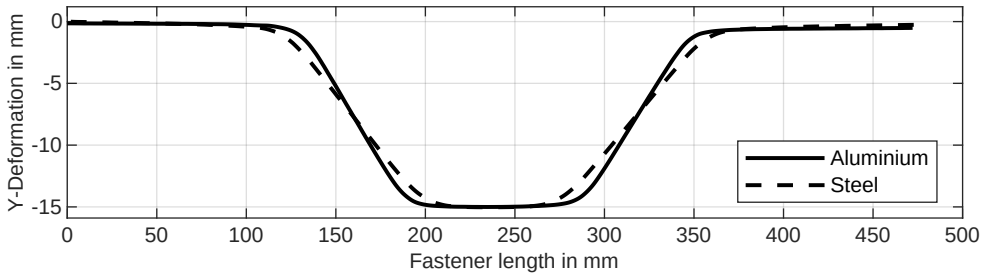

b. Timber-to-timber connection with spruce glulam.

Fig. 5.19: Comparison of different fastener material, front side connection is shown.

5.4.3.3 Influence of Connection Type

The types of connections analysed include connections with and without heads as well as timber-to-timber and timber-to-steel connections. The hypothesis for the heads is that the load-bearing capacity of the connection increases due to the activation of a occurring and/or possibly increased rope effect compared to specimens without heads, and that additional axial forces are applied to the fastener. In terms of deformation behaviour, this means that the bending angles may change slightly, as well as axial deformations, as will be discussed in the following sections. The free pull-through of the fastener ends is hindered. The differentiation of the type of connection between timber-to-timber and timber-to-steel changes the overall deformation behaviour of the fastener, the load-bearing capacity of the connection and therefore requires a more detailed evaluation.

5.4.4 Fastener Deformations in X-Direction

Deformations in the global x-direction describe the movement of the fastener along its original axial alignment. This indicates whether the resistance provided by the surrounding timber to the fastener's movement, i.e. friction, has been overcome. It also offers insight into the extent of head or fastener end pull-in into the timber. Consequently, it becomes apparent which parts of the fastener remain more or less in the same position. It is reasonable to hypothesise that the symmetry point of the connection remains fixed, i.e., all fastener parts tend to move towards or be drawn into the centre. This behaviour is evident in the exemplary deformation distributions shown in Fig. 5.20.

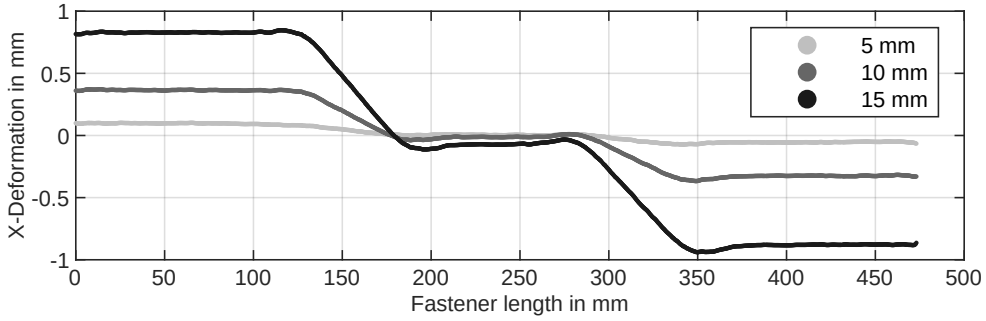

Fig. 5.20: Exemplary deformations in global x-direction for timber-to-timber connection with spruce glulam and steel fastener.

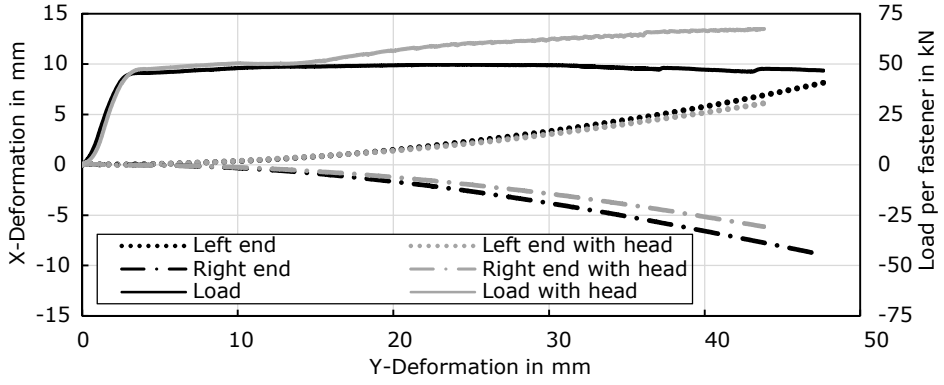

Fig. 5.21: X-deformations of fastener ends over y-deformation in timber-to-timber connection with spruce glulam and steel fastener with and without head.

The region between the inner plastic hinges remains relatively stable in position; however, beyond this region, towards the outer plastic hinges, deformations in x-direction increase. The outer portions of the fasteners, which remain nearly straight, exhibit a relatively uniform x-deformation. However, the diagram in Fig. 5.20 only shows the status quo at the defined deformation stages. It is worth considering the x-deformation change over time during the test, or over y-deformation, as the magnitude of the x-deformations increases even after the analysed deformation stages. When the x-deformations occurring at 15 mm y-deformation are compared, a head pull-in of less than 1 mm can be seen in both diagrams shown in Fig. 5.20 and Fig. 5.21. However, a progressive development can be seen, i.e. an increased head pull-in only occurs with large y-deformations. The difference between the configurations with head and without head also only becomes visible with larger deformations, although this depends on various factors such as the timber used or the firm or less firm tightening of the head plate screws.

5.4.5 Fastener Deformations in Z-Direction

Due to the rectangular fastener shape and the one sided opening a deformation out of the original plane is possible during loading, as illustrated by the exemplary distributions in Fig. 5.22. Deformations in the global z-direction describe the extent to which the fastener moves out of its initial x-y-plane relative to its original position at the beginning of the test. As a result of the end constraints applied to the fasteners in the 'with head' test configuration, the deformation of the fastener ends in the z-direction related to the timber specimen is reduced. However, in the central region of the fasteners, no such constraints are present, allowing for a free deflection out of the plane. It should also be noted, however, that the test specimen as a whole was able to undergo slight settling, for instance, in cases where the side members are not perfectly matched in height, or where minor unevenness occurred in the support surfaces. Therefore, slight movement in the z-direction cannot be entirely ruled out. This initial settling and slip behaviour can be observed when analysing the early stages of deformation in the test, see Fig. 5.23 with deformation steps referring to Fig. 5.17. When the z-direction deformations are compared, it becomes apparent that the fastener exhibits a spatial inclination already at the onset of loading, meaning at small deformation levels. The darkest curve in Fig. 5.23 shows extreme values at the ends of the fastener that are very close to, or even comparable with, those observed at a deformation of 5 mm in Fig. 5.22. Consequently, the z-deformation in Fig. 5.22

can be interpreted as a cumulative effect of multiple factors: the initial slip-related effects, the closing of pre-existing gaps and additional deformation contributions, such as plastic deformations and progressive out of plane movement of regions around plastic hinges, particularly at higher deformation levels. This complex interaction of mechanical effects highlights the need for careful interpretation of out-of-plane deformation results, especially when evaluating the initial stiffness and overall load-bearing behaviour of the connections, as such deformations can locally or even over a larger area reduce the effective embedment depth of the fastener. By examining the resulting curves listed in Appendix A.5, the various z-deformation curves for the different connection configurations can be assessed.

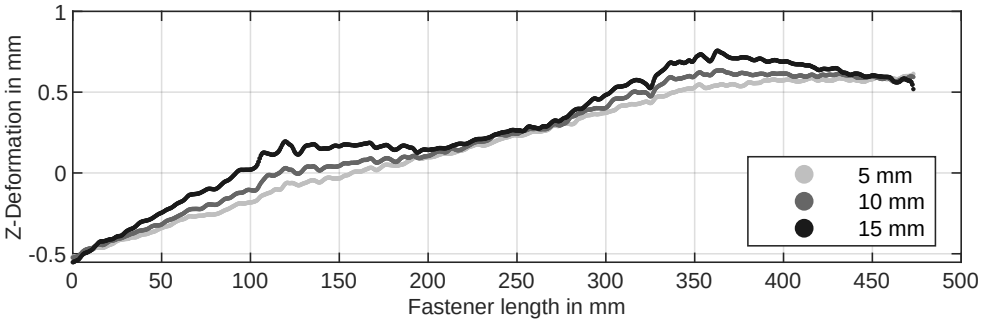

Fig. 5.22: Exemplary deformations in global z-direction for timber-to-timber connection with spruce glulam and steel fastener.

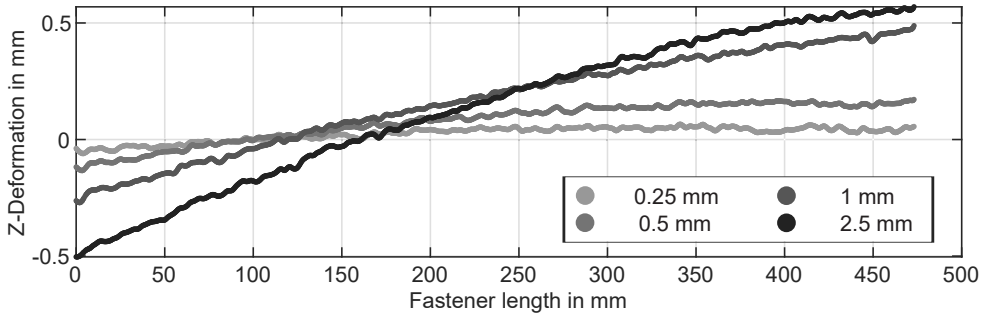

Fig. 5.23: Exemplary small deformations in global z-direction for timber-to-timber connection with spruce glulam and steel fastener.

As a general rule, the deformations in the z-direction are negligible for timber-to-steel connections, as the fasteners are held in the steel sheet by the groove. This means that timber-to-timber connections are the more critical in respect of out-of-plane

movement of the fasteners. The deformations that occur after the initial settling must be considered in order to assess whether the fastener moves critically out of the prefabricated recess. The initial deformations that lead to the inclined position of the curve shown in the diagrams in Fig. 5.23 and 5.22 are deformations that the entire test specimen undergoes as well. This becomes apparent when, for example, the z-deformation of the ends of the fasteners on the front and rear of the test specimen are compared. These deformations are opposing for all test specimens, so that it can be assumed that the settling of the fasteners only takes place in the y direction, but not in the z direction. For most fasteners, the additional deformation after initial settling is small and amounts to < 1 mm. Occasionally, however, higher deformations in the z-direction occur from about 15 mm y-deformation onwards, especially in the regions of the outer plastic hinges in combinations with higher densities, see exemplary curves in Fig. A.52 or A.62. This should be taken into account when recalculating or comparing with a reduced embedment depth.

5.4.6 Bending Angles and Location of Plastic Hinges

Although the deformation figures can be compared visually, there are no key values for the individual configurations for a quantitative comparison. As an indication of the individual influencing parameters such as material, head or no head, type of connection, an individual bending angle of the fastener results, which can be measured or calculated based on the test results. However, no generalised significance can be attributed to the individual factors; rather, different effects occur at different times when applying a continuously increasing load. For example, the rope effect is more strongly activated if a head is present, but this activation only occurs as soon as the fastener end moves in axial direction to the centre of the test specimen. Thus, the bending angle is used below as a key value and for quantitative analysis of the test results. When comparing configurations with and without head, apparent differences are difficult to identify. The example shown in Fig. 5.24 reveals minor apparent differences in the deformation behaviour of fasteners with and without heads even at larger deformations of 25 mm. This is valid for most of the recorded deformation lines.

The differences between the configurations with and without head are thus difficult to assess without closer examination. The hypothesis is, that connections with a head tend to show somewhat larger bending angles since the induced axial force leads to a straightening of the fastener axis. At which time, or at what deformation step the axial force component is activated, and leads to a rope effect, is not known and depends

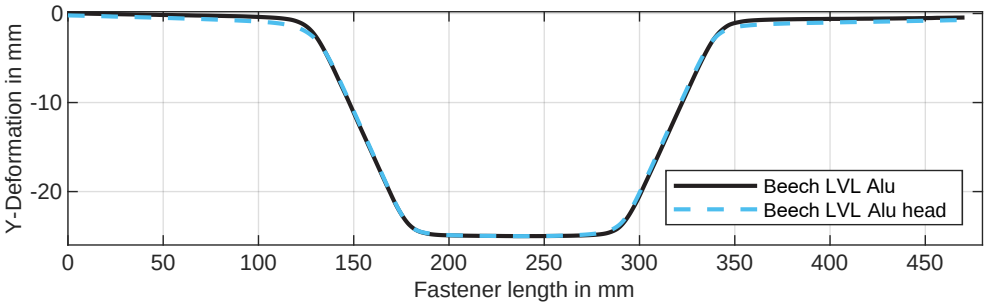

Fig. 5.24: Deformations in global y-direction for a timber-to-timber connection with beech LVL and aluminium fastener at a y-deformation of 25 mm.

on the timber used and tightening of the head plate. When comparing the deformation lines at 5 mm and 25 mm y-deformation of a connection with beech LVL and steel fasteners, see Fig. 5.25, the hypothesis seems to be valid. Bending angles are larger for the configuration with head, and, the bending radius seems to be larger, too.

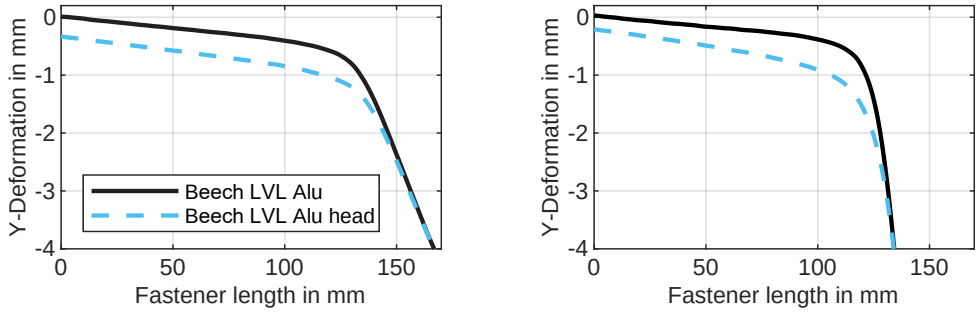

a. Deformation line at 5 mm y-deformation.

b. Deformation line at 25 mm y-deformation.

Fig. 5.25: Detail of y-deformation lines for timber-to-timber connections with beech LVL and aluminium fastener.

However, the effect of head or no head is not equally pronounced in all connection configurations, but highlights the need for a closer look at this issue. Therefore, the differences of deformations and bending angles will be discussed using selected examples. To evaluate bending angles of the fasteners, a fitting of linear sections was done for the deformation lines, see Fig. 5.26. For each dataset, the x and y coordinates representing the deformation curve of the fastener are extracted and plotted. Five linear sections are fitted to each curve using least squares regression over the comparable ranges as in the example with $x \in [30, 80]$, $x \in [145, 170]$,

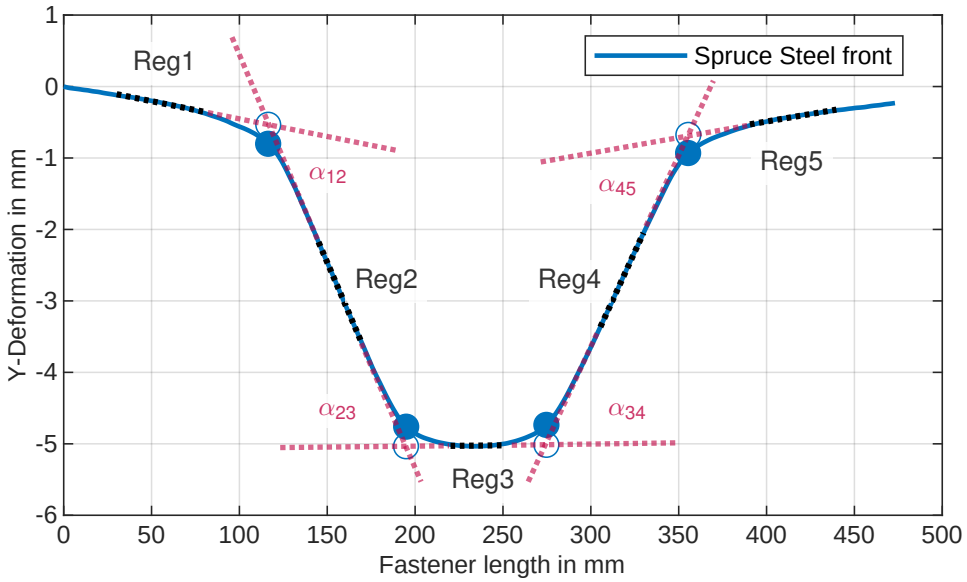

Fig. 5.26: Fastener line at 5 mm global deformation in y-direction for front fastener of the spruce glulam connection with steel fastener. Empty symbols: intersection points, filled symbols: assumed location for plastic hinges. Elongation of regression lines and bending angles.

$x \in [230, 250]$, $x \in [305, 330]$, and $x \in [390, 440]$ in mm for the timber-to-timber connections. For timber-to-steel connections the ranges change to $\approx x \in [20, 50]$, $x \in [120, 140]$, $x \in [167, 172]$, $x \in [200, 220]$, and $x \in [295, 325]$. Fig. 5.26 shows an exemplary plot for the front steel fastener in spruce glulam and the included regression sections with black dots.

The method of least squares determines the best-fitting straight line by minimising the sum of the squared vertical distances between the data points and the line. For a set of n data points (x_i, y_i), this corresponds to solving the minimisation problem:

$$\min_{m,b} \sum_{i=1}^{n} (y_i - (mx_i + b))^2, \tag{5.5}$$

where m is the slope and b the intercept of the line with the ordinate. Each linear fit takes the form:

$$y = m_k x + b_k, \tag{5.6}$$

where *k* indexes the fitted sections from 1 to 5. For each pair of adjacent regression lines, the angle α between them is calculated as:

$$\alpha = \arctan\left(\left|\frac{m_{k+1} - m_k}{1 + m_k m_{k+1}}\right|\right) \cdot \frac{180}{\pi}, \tag{5.7}$$

giving the result for the bending angle in degrees. An alternative to this method of determining the bending angle would be to derive the deformation curve.

The intersection point (x_{int}, y_{int}) of each line pair is obtained by solving the corresponding system of equations:

$$\begin{cases} m_k x + b_k = y, \\ m_{k+1} x + b_{k+1} = y. \end{cases} \tag{5.8}$$

This point is displayed with empty symbols on the exemplary plot. To associate this theoretical intersection with the empirical data, the closest point on the original measured curve is determined. This is done by computing the Euclidean distance between the intersection point (x_s, y_s) and each point (x_i, y_i) on the curve:

$$d_i = \sqrt{(x_i - x_s)^2 + (y_i - y_s)^2} \tag{5.9}$$

The point minimising this distance is selected as the nearest point to the intersection, which is defined as the location of the plastic hinge in the following. This point is highlighted with filled symbols in the exemplary plot and its coordinates, together with the intersection and angle, are listed in Tab. 5.11. The x/y coordinates of the intersections and nearest points are only given to the first decimal due to the accuracy of the results. Due to the exaggerated visualisation of the deformation, the nearest point in the plot is not shown appropriately in Fig. 5.26. There it deceptively looks as if the nearest point is directly below or above. In a non exaggerated and realistic visualisation as given in Fig. 5.27 the selection of the nearest point to the intersection point becomes clearer.

Within the individual three result tables, a certain scattering of the bending angles can be identified. This is nothing unexpected, as even small variations in density or knots, particularly in glulam, can influence the local bending behaviour. Furthermore, the manufacturing-related gaps mentioned above may also become decisive here, impacting the bending angle. Comparing the change in bending angle with increasing

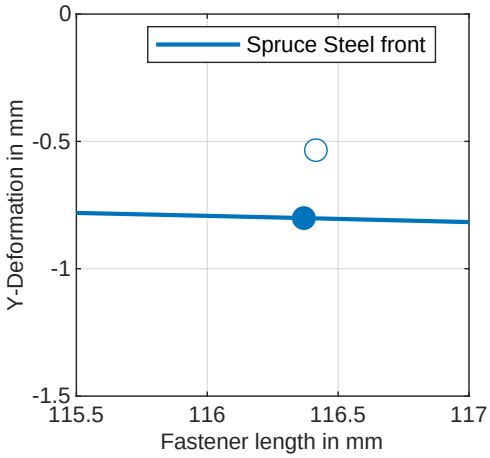

Fig. 5.27: Non exaggerated visualisation: Nearest point (filled symbol) on the deformation line equals the plastic hinge.

Table 5.11: Steel fastener in spruce glulam, y-deformation = 5 mm: Regression parameters, bending angles and coordinates in mm for intersection points and plastic hinges for plotted deformation in Fig. 5.26.

Regression	m	b	Angle	in °	x_{intsec}	y_{intsec}	$x_{\text{nextpoint}}$	$y_{\text{nextpoint}}$
Reg1	-0.00495	0.042						
			α_{12}	3.00	116.4	-0.5	116.4	-0.8
Reg2	-0.05740	6.148						
			α_{23}	3.30	194.8	-5.0	194.9	-4.8
Reg3	0.00025	-5.085						
			α_{34}	3.06	274.7	-5.0	274.7	-4.7
Reg4	0.05372	-19.77						
			α_{45}	2.84	355.5	-0.7	355.4	-0.9
Reg5	0.00419	-2.164						

Table 5.12: Steel fastener in spruce glulam, y-deformation = 10 mm: Regression parameters, bending angles and coordinates in mm for intersection points and plastic hinges.

Regression	*m*	*b*	Angle	in °	x_{intsec}	y_{intsec}	$x_{nextpoint}$	$y_{nextpoint}$
Reg1	-0.00415	0.034						
			α_{12}	6.84	118.1	-0.5	117.9	-0.9
Reg2	-0.12409	14.20						
			α_{23}	7.10	195.1	-10.0	195.0	-9.5
Reg3	0.00038	-10.08						
			α_{34}	6.62	274.3	-10.0	274.4	-9.5
Reg4	0.11652	-41.94						
			α_{45}	6.45	354.6	-0.6	354.6	-1.1
Reg5	0.00344	-1.844						

Table 5.13: Steel fastener in spruce glulam, y-deformation = 15 mm: Regression parameters, bending angles and coordinates in mm for intersection points and plastic hinges.

Regression	*m*	*b*	Angle	in °	x_{intsec}	y_{intsec}	$x_{nextpoint}$	$y_{nextpoint}$
Reg1	-0.00356	0.024						
			α_{12}	10.3	118.3	-0.4	118.4	-1.2
Reg2	-0.18485	21.47						
			α_{23}	10.5	197.5	-15.0	197.6	-14.2
Reg3	0.00027	-15.08						
			α_{34}	9.84	273.2	-15.0	273.1	-14.3
Reg4	0.17381	-62.50						
			α_{45}	9.66	356.1	-0.6	356.0	-1.3
Reg5	0.00343	-1.825						

deformation results in an increasing mean bending angle α from 3.05° to 6.75° to 10.1°. This corresponds to a scale factor of 2.2 or 3.3 in relation to the smallest analysed angle α at 5 mm y-deformation. The position of the plastic hinges is also influenced by the rope effect being activated by the formation of the plastic hinge. This means that the end of the fastener can move freely towards the centre without end anchoring/head. Thus, the position of the plastic hinge changes with increasing load and deformation. The shear planes are located approximately at x = 160 mm and x = 320 mm. Of the three deformation stages shown so far, the following direction of movement of the plastic hinges results: the outer plastic hinge on the left moves towards the shear plane (x-values increase), the inner plastic hinges move away from the shear plane, i.e. move towards the axis of symmetry of the test specimen, and the outer plastic hinge on the right initially moves towards the shear plane (comparison 5 mm to 10 mm), but then changes direction (comparison 10 mm to 15 mm). In order

to investigate this effect in more detail, a further deformation is analysed, at 25 mm y-deformation, see Tab. 5.14. If these results are taken into account, there is a tendency for the direction of movement of all plastic hinges: In the case of smaller deformations, the outer plastic hinges first move towards the shear plane and then reverse direction. The inner plastic hinges, on the other hand, constantly increase their distance to their respective shear plane. An influencing factor in this case is the possibility of a slight inclination of the outer fastener sections and the fact that the centre section is kept straight. In addition, it is possible for the outer fastener section to move significantly more towards the axis of symmetry. This means that the conditions for the formation of the plastic hinges are not identical on the inner and outer parts.

Table 5.14: Fastener y-deformation 25 mm: Regression parameters, bending angles and coordinates in mm for intersection points and plastic hinges.

Regression	m	b	Angle	in °	x_{intsec}	y_{intsec}	$x_{\text{nextpoint}}$	$y_{\text{nextpoint}}$
Reg1	-0.00350	0.051						
			α_{12}	15.9	116.4	-0.4	116.4	-1.6
Reg2	-0.28931	33.31						
			α_{23}	16.2	201.6	-25.0	201.7	-23.7
Reg3	0.00073	-25.16						
			α_{34}	15.3	271.8	-25.0	271.8	-23.6
Reg4	0.27452	-99.58						
			α_{45}	15.1	360.6	-0.6	360.8	-1.8
Reg5	0.00412	-2.078						

5.4.6.1 Influence of Head

For the selected configuration, spruce glulam with steel fastener, a comparison is made below to investigate the influence of an end anchorage of the fastener, i.e. a head. In comparison, there are differences expected for the configuration with head, which can be attributed to the increased activation of the rope effect. Due to the normal force component applied in the axial direction, the fastener is bent and deformed in the direction of the load with increasing deformations, but it is straightened due to the anchoring at the same time. The hypothesis is therefore that the bending angles are flatter, i.e. smaller, in connection configurations with a head. In addition, it is to be investigated whether the position of the theoretical plastic hinges can also be influenced by the existing head. The selected deformation steps for comparison are chosen at 5, 15 and 25 mm and can be taken from Tab. 5.15–5.17. Various aspects

demonstrate the different deformation behaviour. When the regression parameters and the magnitude of the slopes *m* are compared for the largest deformation step of 25 mm, it becomes clear that regressions Reg1 and Reg5, i.e. the outer sections, have considerably higher slope values for the configuration with head. Conversely, this means that the outer sections of the fasteners move significantly further out of the horizontal position and have a greater inclination. The mean bending angle achieved at 25 mm deformation is 15.6° without head and 15.2° with head. This tendency also applies to the other deformation steps shown in Tab. 5.15 and 5.16.

5.4.6.2 Movement along Fastener Axis

A further comparison of the position of the plastic hinges confirms the movement of their position in the previous test without the head. In this case too, the position and directional movement of the outer plastic hinges is influenced by the slight inclination of the outer sections. The inner plastic hinges increase their distance from the shear plane as the deformation increases. However, as this investigation only involves a theoretical position of the plastic hinge based on the regression sections, it must not be assumed that the actual fastener section reverses its direction of movement. From a global perspective, all fastener sections move in the x-direction towards the axis of symmetry of the test specimens, i.e. the centre. The ‘jumping’ of the outer plastic hinges is therefore rather related to the different mechanisms of the load application and deformation history of the fastener. Assuming that the fastener already begins to deform plastically at 5 mm deformation, a plastic hinge could be determined using the method presented. In reality, this is a yield zone. This yield zone drawn into the centre of the test specimen during further deformation.

Accordingly, formerly straight sections are drawn from the outer section into the yield zone and increasingly subjected to bending, and parts of the initially formed yield zone are drawn into the more straight section between the plastic hinges, which in turn is less subjected to bending. In order to investigate this effect of the moving plastic hinge, the global movements in this area can be analysed. The points of the theoretical plastic hinge position are selected as evaluation points according to Tab. 5.15. If the x/y curve of the points at x = 117, 201, 283 and 357 mm is plotted over time, see Fig. 5.28, different curves are obtained for the outer and inner plastic hinges. The outer points, points 117 and 357, show substantially larger x-displacements compared to their y-displacements. From the beginning to the end of the test, these points shift by up to 7 mm in the x-direction and the shape of the curve shows a

Table 5.15: Fastener with head, y-deformation 5 mm: Regression parameters, bending angles and coordinates in mm for intersection points and plastic hinges.

Regression	m	b	Angle	in °	x_{intsec}	y_{intsec}	$x_{\text{nextpoint}}$	$y_{\text{nextpoint}}$
Reg1	-0.00474	-0.096						
			α_{12}	2.68	116.9	-0.6	116.9	-0.9
Reg2	-0.05161	5.385						
			α_{23}	2.95	201.0	-5.0	201.0	-4.7
Reg3	-0.00012	-4.968						
			α_{34}	3.21	282.5	-5.0	282.3	-4.7
Reg4	0.05604	-20.83						
			α_{45}	2.92	356.5	-0.9	356.4	-1.1
Reg5	0.00498	-2.632						

Table 5.16: Fastener with head, y-deformation 15 mm: Regression parameters, bending angles and coordinates in mm for intersection points and plastic hinges.

Regression	m	b	Angle	in °	x_{intsec}	y_{intsec}	$x_{\text{nextpoint}}$	$y_{\text{nextpoint}}$
Reg1	-0.00415	-0.061						
			α_{12}	9.58	118.8	-0.6	118.6	-1.3
Reg2	-0.17306	20.01						
			α_{23}	9.83	202.5	-15.0	202.3	-14.2
Reg3	0.00023	-15.07						
			α_{34}	10.3	276.3	-15.0	276.4	-14.2
Reg4	0.18249	-65.42						
			α_{45}	10.1	354.1	-0.8	354.4	-1.5
Reg5	0.00460	-2.434						

Table 5.17: Fastener with head, y-deformation 25 mm: Regression parameters, bending angles and coordinates in mm for intersection points and plastic hinges.

Regression	m	b	Angle	in °	x_{intsec}	y_{intsec}	$x_{\text{nextpoint}}$	$y_{\text{nextpoint}}$
Reg1	-0.00611	0.142						
			α_{12}	14.7	115.2	-0.6	115.0	-1.9
Reg2	-0.26832	30.35						
			α_{23}	15.0	206.2	-25.0	206.3	-23.6
Reg3	0.00023	-25.02						
			α_{34}	15.8	270.5	-25.0	270.5	-23.5
Reg4	0.28252	-101.4						
			α_{45}	15.4	356.2	-0.8	356.4	-2.0
Reg5	0.00633	-3.014						

slightly progressive course. This means that the y-components of the deformation increase with the duration of the test. In comparison, there is hardly any deformation in the x-direction at points 201 and 283, the inner plastic hinges. These amount to less than 1 mm. The deformations in the y-direction are dominant at these points. The curves shown for the theoretical plastic hinge positions confirm the aspects described above and support the hypothesis that the outer plastic hinges are moving along the fastener. In other words: the yield zone of the outer plastic hinges shifts towards the outer section with increasing load and further areas of the outer section are activated by bending. This effect can also be visualised in the recorded strain distributions and is discussed later in Chapter 6.

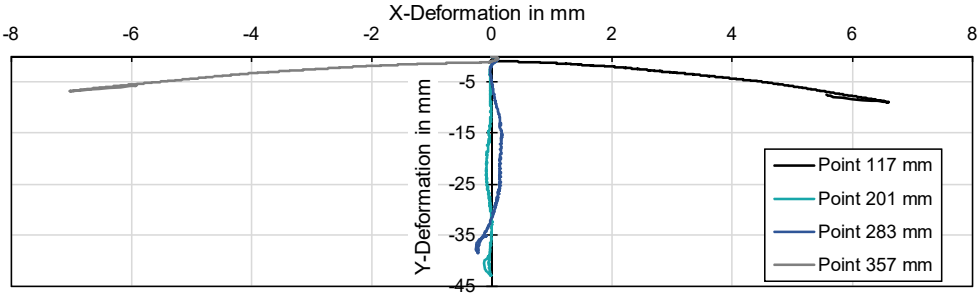

Fig. 5.28: Displacement of points related to plastic hinge location in first deformation step in Tab. 5.15 for timber-to-timber connection with spruce glulam and steel fastener with head.

5.4.6.3 Influence of Timber Density

Increasing the density of the timber used compared to the previously considered connection with spruce glulam leads to different bending angles of the fastener and to plastic hinges that are located closer to each other. Fig. 5.29 visualises three deformation lines for a steel fastener in spruce glulam, beech LVL and DVW. Differences are noticeable both in terms of the bending angles and the position of the plastic hinges. It is noticeable that the plastic hinges with higher density move closer to the shear planes. The differences are particularly apparent in the area of the outer plastic hinges. In the area of the inner plastic hinges, on the other hand, possible scattering, especially in spruce glulam, can ensure that the plastic hinges do not always have the same distance from the centre or the axis of symmetry of the specimen. Nevertheless, the clear tendency of the gradation of the three timber materials used is recognisable there. The bending angle is suitable for quantifying what is visible. Mean values of

10.2° for spruce, 12.2° for beech LVL and 18.4° for DVW are evaluated and can be taken from Tab. 5.18–5.20. This corresponds to a magnification factor of 1.2 from spruce glulam to beech LVL and a factor of 1.8 to DVW.

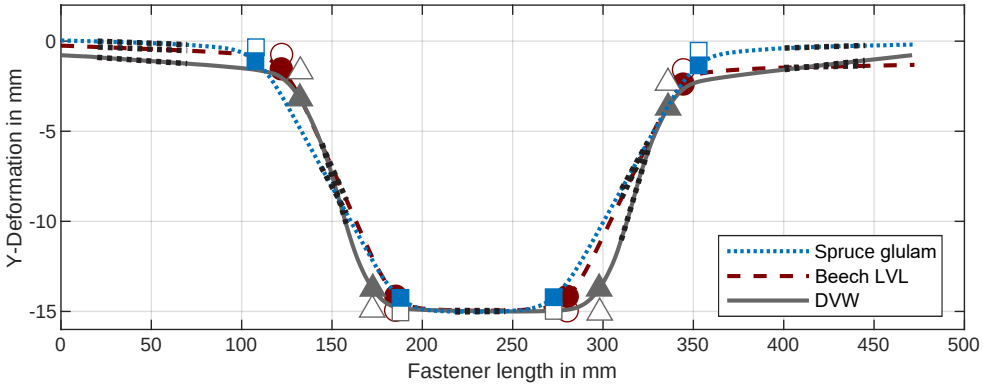

Fig. 5.29: Comparison of deformation lines and bending angles for different timber materials.

In general, it should be noted that the bending angles are slightly underestimated in this analysis. This is due to the fact that the prefabricated recesses had slightly larger gaps to allow the fastener to be inserted from the side, particularly in DVW. Accordingly, the accuracy of the assembly fit for these connections is not as high as for the other two. As a result, the fastener is more inclined in the outer sections, which of course also affects the resulting bending angle. A comparison of the inner and outer bending angles emphasises this. The inner bending angles α_{23} and α_{34} are consistently larger than the outer bending angles α_{12} and α_{45}.

Table 5.18: Steel fastener in spruce glulam, y-deformation 15 mm: Regression parameters, bending angles and coordinates in mm for intersection points and plastic hinges.

Regression	m	b	Angle	in °	x_{intsec}	y_{intsec}	$x_{\text{nextpoint}}$	$y_{\text{nextpoint}}$
Reg1	-0.00383	0.076						
			α_{12}	10.2	107.9	-0.3	107.6	-1.1
Reg2	-0.18420	19.55						
			α_{23}	10.5	187.7	-15.0	187.9	-14.2
Reg3	0.00050	-15.13						
			α_{34}	10.2	272.6	-15.0	272.7	-14.2
Reg4	0.17993	-64.04						
			α_{45}	10.0	353.0	-0.5	353.1	-1.3
Reg5	0.00306	-1.605						

Table 5.19: Steel fastener in beech LVL, y-deformation 15 mm: Regression parameters, bending angles and coordinates in mm for intersection points and plastic hinges.

Regression	m	b	Angle	in °	x_{intsec}	y_{intsec}	$x_{nextpoint}$	$y_{nextpoint}$
Reg1	-0.00402	-0.244						
			α_{12}	12.5	122.2	-0.7	121.9	-1.5
Reg2	-0.22554	26.82						
			α_{23}	12.7	185.1	-14.9	185.3	-14.2
Reg3	-0.00071	-14.79						
			α_{34}	11.8	280.1	-15.0	280.2	-14.2
Reg4	0.20811	-73.28						
			α_{45}	11.6	344.5	-1.6	344.3	-2.4
Reg5	0.00216	-2.327						

Table 5.20: Steel fastener in DVW, y-deformation 15 mm: Regression parameters, bending angles and coordinates in mm for intersection points and plastic hinges.

Regression	m	b	Angle	in °	x_{intsec}	y_{intsec}	$x_{nextpoint}$	$y_{nextpoint}$
Reg1	-0.00694	-0.761						
			α_{12}	18.2	132.8	-1.7	132.5	-3.2
Reg2	-0.33716	43.08						
			α_{23}	18.6	172.0	-14.9	172.0	-13.7
Reg3	-0.00141	-14.66						
			α_{34}	18.7	298.1	-15.1	297.9	-13.7
Reg4	0.33766	-115.7						
			α_{45}	18.0	335.9	-2.3	336.0	-3.7
Reg5	0.01141	-6.150						

As the centre area cannot be arranged symmetrically for all bending lines assessed, the distances between the respective plastic hinges per shear plane are used for a comparison of the plastic hinge position. From the results in Tab. 5.18–5.20 the following distances in x-direction between the plastic hinges can be evaluated: in spruce glulam 80.4 and 80.3 mm, in beech LVL 63.4 and 64.1 mm and in DVW 39.5 and 38.1 mm. This is equivalent to a reduction factor of 0.79 from spruce glulam to beech LVL and 0.48 to DVW.

5.4.6.4 Influence of Connection Type

Substantial changes are to be expected if a timber-to-steel connection is considered instead of a timber-to-timber connection. The formation of the plastic hinges moves

towards each other and the bending angles also become larger. Therefore, the same connection configuration as in the previous section is selected for a proper comparison. However, since the timber-to-steel connection in DVW could only be carried out up to a y-deformation of 12.3 mm, only the two configurations in spruce glulam and beech LVL are compared here. Fig. 5.30 shows the deformation lines at 15 mm y-deformation and the corresponding results for regressions and bending angles are listed in Tab. 5.21 and 5.22. The position of the inner plastic hinge remains more or less fixed due to the clamp in the steel plate and only the outer plastic hinges or the distance between them and the shear plane are considered. Mean bending angles of 12.7° for spruce glulam and 14.9° for beech LVL are evaluated. This corresponds to a magnification factor of 1.17 from spruce glulam to beech LVL, which is comparable to the enlargement of the bending angles in timber-to-timber connections. The x-distances between the inner and outer plastic hinges amount to 58.7 and 63.5 mm in spruce glulam and 55.1 and 53.7 mm in beech LVL. This is equivalent to a reduction factor of 0.89 from spruce glulam to beech LVL. Comparing the bending angles shown here with those of the timber-to-timber connections, another effect can be seen. The bending angles on the right and left form in different orders of magnitude. This is due to the clamping effect in the steel sheet. The fastener cannot create any equalisation in the centre area and the bending angle is only determined by the side timber. With timber-to-timber connections, on the other hand, a difference could be seen between the inner and outer plastic hinge, but not between the left and right shear plane.

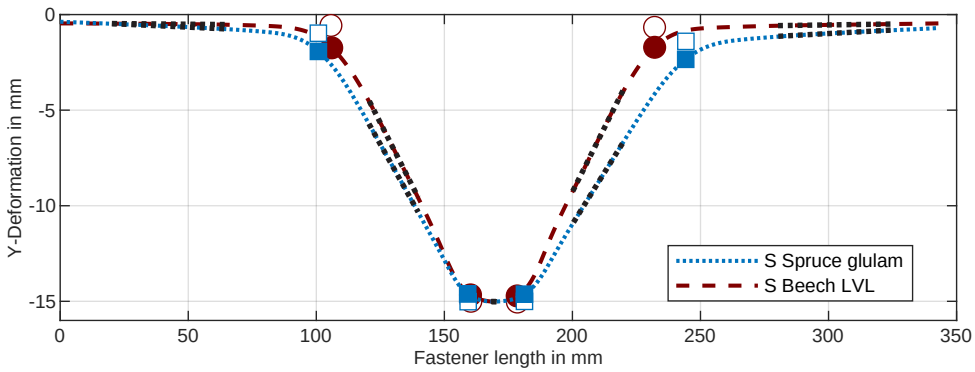

Fig. 5.30: Comparison of deformation lines and bending angles for different timber materials.

Table 5.21: Timber-to-steel connection, steel fastener in spruce glulam, y-deformation 15 mm: Regression parameters, bending angles and coordinates in mm for intersection points and plastic hinges.

Regression	m	b	Angle	in °	x_{intsec}	y_{intsec}	$x_{nextpoint}$	$y_{nextpoint}$
Reg1	-0.00573	-0.364	α_{12}	13.2	100.7	-0.9	100.4	-1.9
Reg2	-0.24011	23.23	α_{23}	13.5	159.2	-15.0	159.1	-14.6
Reg3	-0.00035	-14.95	α_{34}	12.2	181.2	-15.0	181.3	-14.6
Reg4	0.21578	-54.12	α_{45}	11.8	244.4	-1.4	244.8	-2.3
Reg5	0.00694	-3.070						

Table 5.22: Timber-to-steel connection, steel fastener in beech LVL, y-deformation 15 mm: Regression parameters, bending angles and coordinates in mm for intersection points and plastic hinges.

Regression	m	b	Angle	in °	x_{intsec}	y_{intsec}	$x_{nextpoint}$	$y_{nextpoint}$
Reg1	-0.00090	-0.456	α_{12}	14.7	105.6	-0.6	105.1	-1.6
Reg2	-0.26402	27.34	α_{23}	14.7	160.3	-15.0	160.2	-14.7
Reg3	-0.00240	-14.61	α_{34}	15.2	178.5	-15.0	178.4	-14.7
Reg4	0.26828	-62.93	α_{45}	14.9	232.1	-0.7	232.1	-1.7
Reg5	0.00176	-1.068						

5.4.7 Failure Modes

For all connections, the expected and calculated failure occurred due to the formation of two plastic hinges per shear plane. Some peculiarities and deviations from this are explained below. For some test configurations with head plates, normal forces increased to such an extent during the test that the anchor bolt reached its tensile capacity and failed, compare specimen beech LVL with steel fastener with head in Fig. 5.31b and c. In one case the anchoring screw was pulled out of the aluminium fastener, compare specimen beech LVL with aluminium fastener with head, see Fig. 5.31a. Both of these effects are characterised by a drop in load followed by residual load-bearing capacity of the connection. However, due to the resulting asymmetry, the fastener was tilted under further load and moved further and further out of recess in the test specimen. The tests are then stopped.

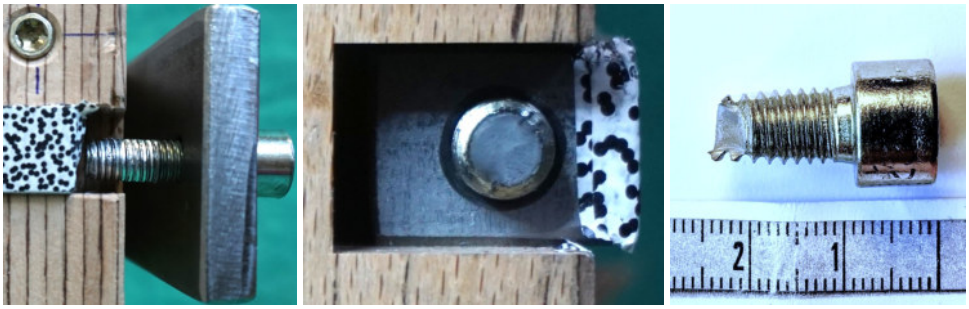

a. Pull-out of screw. b. Remaining screw stub. c. Remaining screw head.

Fig. 5.31: Failures of fastener anchoring: Screw pull-out and tensile failure. Pictures from B. Burzlaff [18].

Another type of failure is the cross-sectional failure of the fastener itself. This occurred in the timber-to-steel connections. No direct indication of this could be observed during the test. However, the deformation behaviour was characterised by severe indentations caused by the steel plate, and a subsequent analysis of the deformation lines revealed a further hint. If the deformation lines shown in Fig. 5.32 are compared, it can be seen that the area between the plastic hinges is not straight but shows a further kink. This kink indicates the plastic behaviour of the fastener in the shear plane and the local cross-sectional weakening caused by the indentation of the steel plate edges. As a result, the fastener is more inclined in the shear plane area, and the separate sections are used as shown to determine the plastic hinge locations. As the test continues, the fastener cross-section fails in this area. This unusual deformation behaviour was observed in connections with Beech LVL and aluminium fasteners and in connections made of DVW and steel fasteners. The deformation lines in Fig. 5.32 correspond to the failure scenario shown in Fig. 5.33a. It shows the failure which occurs when the deformation is increased beyond the previously shown reference at 15 mm. Fig. 5.33b shows the failure scenario for the same connection with a head. The failure is similar, but occurs at comparatively smaller deformations than without a head.

Taking a closer look at the locally occurring failure as shown in Fig. 5.34, protruding wood fibres can be seen, which slowly pushed their way over the fastener during the test. This is a combination of embedment failure and compression failure, with the fibres buckling out of the plane. This effect and this type of failure does not occur in a typical connection, but is caused by the external arrangement of the fastener. To address this effect and take it into account in calculations, embedment tests are carried out that accurately represent the chosen arrangement. In addition, the fastener

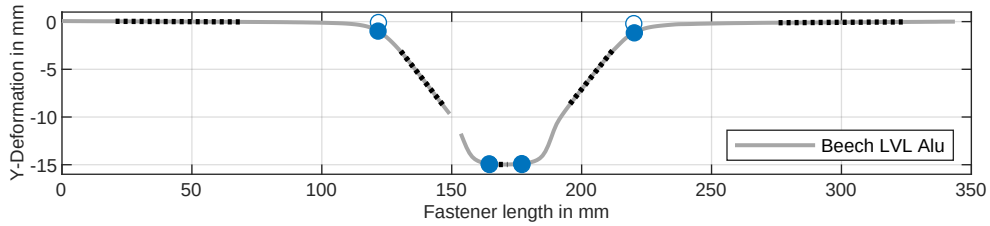

a. Regression sections for outer plastic hinges.

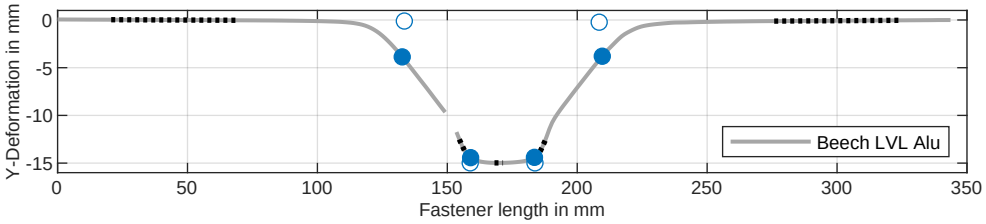

b. Regression sections for inner plastic hinges.

Fig. 5.32: Deformation behaviour of a timber-to-steel connection with an aluminium fastener in beech LVL, front side fastener at 15 mm y-deformation: individual regression sections, calculated position of plastic hinges and unusual bending behaviour between plastic hinges.

a. Aluminium fastener in beech LVL.

b. Aluminium fastener with head in beech LVL.

Fig. 5.33: Exemplary fastener failures in right shear planes.

was not inserted flush to the timber surface, but protrudes 1 mm from it. During the tests, this resulted in the timber fibres pushing over the fastener with a delay, thus allowing for a longer measurement period.

Fig. 5.34: Detail of failure near the shear planes.

5.4.8 Unloading of Connections

For a subset of the connections, testing and data acquisition are continued beyond the maximum load or even until failure, allowing the unloading behaviour to be recorded. This demonstrates the influence that unloading has on deformation behaviour and highlights the magnitude of the potential underestimation when the deformation of an opened test specimen is related to the maximum load achieved.

To illustrate this effect, an exemplary specimen, i.e. a steel fastener in spruce glulam, and its behaviour during unloading is briefly discussed in the following. Resulting elastic recoveries during unloading are shown in Fig. 5.35. The unloading is also shown in Fig. 5.12. Corresponding values are given in Tab. 5.23. The focus lies on the elastic recovery in the y-direction, as this accounts for the largest proportion of the total deformation. The two remaining deformation components in x- and z-direction are comparatively small during unloading. The maximum elastic recovery in the y-direction occurs approximately at the mid-span and accounts for about 10% of the remaining deformation, i.e. 4.33 mm. The load at the moment of unloading is 84.5 kN and corresponds to a maximum y-direction deformation of 47.8 mm. The resulting residual deformation is therefore 43.4 mm. In the x-direction, elastic recovery primarily occurs in the outer regions, which means that the ends of the fasteners each move outward again. In the z-direction, hardly any elastic recovery can be observed, as there are no acting forces that would push the displaced fastener back into its recess.

These findings clearly demonstrate that elastic recovery constitutes a significant proportion of the total deformation and directly influences the bending angle. When comparing the deformation of opened test specimens, as exemplarily carried out in

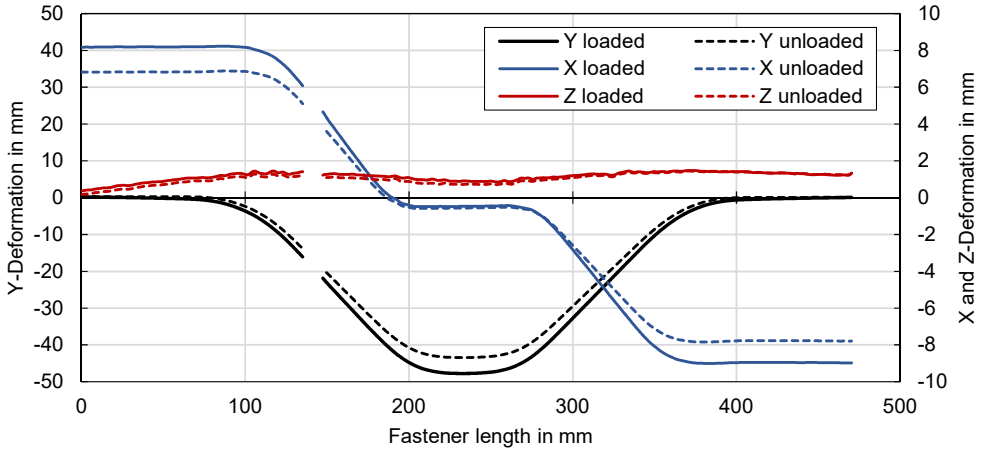

Fig. 5.35: Elastic recovery of exemplary steel fastener in spruce glulam during unloading.

Table 5.23: Elastic recovery of steel fastener in spruce glulam.

	Y	X	Z	Load
		in mm		in kN
Loaded	-47.8	-9.01	0.370	84.5
Unloaded	-43.4	-7.84	0.178	0
Δ	4.33	1.17	0.192	

Section 3.5, with the applied load, the contribution of elastic recovery is not accounted for, leading to a systematic underestimation of the actual maximum deformation. Elastic recovery must be taken into account to accurately interpret experimental deformation measurements and to validate numerical models, particularly in the context of bending angle and residual displacement assessments.

5.5 Summary of Results

In summary, the bending angles and the distance between the plastic hinges are useful parameters for comparing the results. These two parameters combine the influences of the deformation behaviour described above, making them suitable for comparing the test series. There is no clear tendency towards a smaller bending angle for fasteners with heads compared to fasteners without heads, see Tab. 5.24.

It is assumed that the influence of the head is superimposed by other influences such as local variations in density or embedment behaviour. At a y-deformation of 15 mm, the head is not yet sufficiently activated to have a significant influence on the bending angle for the investigated connections. As the head plate screws are only tightened by hand, a separate investigation into the influence of variously tightened heads on load-bearing behaviour and deformation lines is recommended. For the timber-to-steel connections beech LVL with aluminium fastener and DVW with steel fastener, only the outer bending angles are used to calculate the mean value. Since two of the test specimens did not reach the 15 mm limit, the mean bending angles at 10 mm deformation are given instead in order to complete the dataset.

Table 5.24: Mean bending angles of fasteners in ° at $y_{def} = 15$ mm.

Type	Timber	Aluminium		Steel	
		no head	with head	no head	with head
Timber-to-timber	Spruce glulam	13.7	14.2	10.1	10.1
	Beech LVL	16.9	16.9	12.2	12.6
	DVW	-	-	17.9	21.1
Timber-to-steel	Spruce glulam	17.3	16.0	12.3	12.9
	Beech LVL	19.3	18.5	14.8	15.0
	DVW	-	-	10.9*	10.5*

*Evaluation at $y_{def} = 10$ mm

According to DIN EN 409 [120], the bending angle of fasteners can be adjusted to account for the characteristic density of the timber, ρ_k, using

$$\alpha = \alpha_1 \left(\frac{2.78\,\rho_k}{f_t} \right)^{0.44} + \alpha_2 \tag{5.10}$$

with

- α Bending angle used to determine the yield moment, in degrees
- α_1 Reference bending angle according to the standard, in degrees
- α_2 10° for nails, staples and screws, 0° for dowels and bolts
- ρ_k Characteristic density of the timber, in kg/m^3
- f_t Tensile strength of the fastener, in N/mm^2

Applying this formulation to the timber types investigated, higher densities correspond to larger bending angles, consistent with the experimental results in Tab. 5.24. As an example, the mean timber densities of the tested specimens are used rather than the

characteristic values specified in the standard. For an 8 mm screw with $f_t = 1000$ MPa, the predicted bending angle for beech LVL ($\rho_{mean} = 816$ kg/m^3) is approximately 34.7°, compared to 28.7° for spruce glulam ($\rho_{mean} = 437$ kg/m^3), giving a ratio of 1.21. Although the absolute values of the predicted bending angles are not directly comparable to those of the rectangular fasteners tested here, the relative trends between timber types and densities can still be evaluated.

The ratio of 1.21 matches the ratio of the mean bending angles in Tab. 5.24 observed at 15 mm displacement in the timber-to-timber connections, confirming the relevance of density effects for the evaluation of fastener bending resistance and ductility. However, for timber-to-steel connections, the increase in bending angle from spruce glulam to beech LVL is lower on average and amounts to 1.16.

As different methods for determining the yield moment are based on varying assumptions and evaluation procedures [14] and [121, 127], these investigations raise the question of whether it is advisable to distinguish the evaluation method depending on timber density. If the yield moment is determined within an already plastic region of the moment-angle curve, using higher timber densities would not result in a substantial increase in the yield moment for most fasteners. However, differences in material properties, such as hardness, have so far been sparsely investigated, and further studies are recommended to assess whether the formula in EN 409 [120] is truly applicable and valid for all timber species, fastener types and connection types.

Overall, these results support the relevance of timber density for bending behaviour, while highlighting the need for further validation across different fastener and connection types.

The evaluated distances between the plastic hinges in Tab. 5.25 provide an overview of the relationships between the individual test series, beyond the bending angles. The complete list of individual results can be found in Appendix A.5. The results show a clear tendency towards smaller plastic hinge distances with increasing density of the timber material. A distinction between with head and without head was made throughout, but as described above, no significant influence can be seen here either. The differences between without head and with head are mostly minor and lie within the standard deviation. This leads to the conclusion that the series can also be considered as a unit in this respect. Individual connections such as timber-to-timber DVW with steel and timber-to-steel spruce glulam with steel show a comparatively high scatter, which may be due, among other things, to manufacturing tolerances

and the initial inclination of the fastener in the recess. Local differences in density in spruce glulam also play a role and influence the distance between the plastic hinges.

Table 5.25: Mean horizontal distances Δx_{PH} between evaluated plastic hinges in mm and corresponding COV in % at $y_{def} = 15$ mm.

Type	Timber	Aluminium				Steel			
		no head		with head		no head		with head	
		Δx_{PH}	COV	Δx_{PH}	COV	Δx_{PH}	COV	Δx_{PH}	COV
T-T	Spruce glulam	60.3	3.41	57.7	2.35	81.0	2.01	79.3	6.00
	Beech LVL	47.0	2.50	46.7	4.28	65.2	2.94	65.2	1.17
	DVW		-			39.9	6.66	38.2	7.38
T-S steel	Spruce glulam	47.1	2.61	48.8	3.45	62.4	7.75	61.2	1.72
	Beech LVL	36.0	3.40	35.8	3.32	54.3	3.20	55.2	3.73
	DVW		-			30.6*	2.73	32.1*	5.14

*Evaluation at $y_{def} = 10$ mm, T-T = Timber-to-timber, T-S = Timber-to-steel

5.6 Conclusion

The investigations in this chapter serve to analyse fundamental assumptions and to dissolve assumptions that are commonly taken for granted. In this respect, fundamental qualitative knowledge of the deformation behaviour of laterally loaded fasteners is quantitatively substantiated and demonstrated by a range of investigated connection configurations. The investigations show the general deformation behaviour of fasteners under load and analyse the deformation lines using regression equations. This enables a previously impossible description of the deformation state of fasteners under load. Detailed information on bending angles and the positions of the plastic hinges are a gain in knowledge and can be used in a variety of ways. The position of the plastic hinges plays a particularly important role when building with engineered wood products. Especially in the case of an inhomogeneous layer structure of the products, it is also relevant where and in which layer the plastic hinges form and which parts of the timber reach the embedment strength. Therefore, this study provides some basic reference values. The results also represent an important milestone in creating a benchmark for the validation of simulations. Current deformation shapes always include a proportion of re-deformation due to the unloading of the connections.

With the present findings, the deformation of the fastener and load can be directly linked.

6 Strains on Rectangular Fasteners

This chapter builds directly on the previous one and uses the same experimental basis, while introducing a new level of evaluation focused on surface strain distribution in rectangular fasteners under load. Extending the earlier analysis of global deformation behaviour, the investigation now shifts to local strain states along the fastener surface, with particular attention to regions of higher strain and their position along the fastener axis. Furthermore, different material densities are considered to assess their influence on strain magnitude and distribution. This enables a more detailed understanding of how material properties affect local load transfer mechanisms within the same experimental framework.

6.1 A Comparative Qualitative Study on Strains

As described in section 5.1, the analysed connection configurations represent a qualitative comparative study. Nevertheless, meaningful comparisons can be drawn between the configurations to gain insight into the connection behaviour under load, the formation of plastic hinges, and the development of yield zones, which together indicate the onset of plastic fastener behaviour. The subsequent strain analysis along the fastener axis and its height is intended to provide further understanding of the transition from elastic to plastic behaviour and to quantify the strain magnitudes that may occur in timber-to-timber and timber-to-steel connections, revealing the influence of timber density, fastener material, and connection type on strain distributions and their magnitudes. In particular, these investigations are expected to highlight how plasticity develops and redistributes stresses within the fastener, allowing the current load on a connection to be directly correlated with the actual stress state of the fastener itself.

6.2 Introduction of Strain Types Used

In materials science and engineering, two primary types of strain are distinguished, which are engineering strain and true strain. Both describe the relative change in length of a specimen under tensile or compressive loading, but they differ in their definitions and accuracy, especially at larger deformations, see Callister and Rethwisch [19] and Meyers and Chawla [68].

Engineering Strain

The engineering strain is based on the original length L_0 of the specimen and is defined as:

$$\varepsilon_{\mathsf{e}} = \frac{\Delta L}{L_0} = \frac{L - L_0}{L_0} \tag{6.1}$$

This simple calculation is widely used in the linear-elastic region and provides sufficiently accurate results for small strains, which typically are less than 10% [68].

True Strain

The true strain accounts for the instantaneous length L during deformation and is defined as the integral of infinitesimal length changes relative to the current length:

$$\varepsilon_t = \int_{L_0}^{L} \frac{dL}{L} = \ln \frac{L}{L_0} \tag{6.2}$$

This strain measure is more accurate for large strains, especially in the plastic deformation range, as it continuously considers the changing geometry of the specimen [19]. While engineering strain offers simplicity and suffices for small deformations, true strain provides a more precise description at higher strains and is preferred for detailed analyses of material behaviour [19, 68]. To illustrate the difference, consider an engineering strain of 5%. The corresponding true strain is calculated as:

$$\varepsilon_{\mathsf{t}} = \ln(1 + \varepsilon_{\mathsf{e}}) = \ln(1 + 0.05) \approx 0.04879 \tag{6.3}$$

This results in a deviation of approximately 2.4% between the two measures:

$$\frac{\varepsilon_{\mathrm{e}} - \varepsilon_{\mathrm{t}}}{\varepsilon_{\mathrm{t}}} \times 100 \approx \frac{0.05 - 0.04879}{0.04879} \times 100 \approx 2.48\% \tag{6.4}$$

For strains greater than 10%, this difference becomes more pronounced. Therefore, true strain should be preferred for plastic deformation analysis.

The strains analysed in this study are mostly below the limit of 10%. Therefore, engineering strains are predominantly used. If true strains were investigated or analysed, this is explicitly noted in the following chapter.

6.3 Measuring Methods

Two different methods are used to measure strains on the fasteners. The aim is twofold: to check both measurement methods and to ensure the results are reliable. Digital Image Correlation (DIC), described in Section 5.3.3, records displacements on the surface of the fasteners, which can be used to calculate strain components and be visualised. This allows to see how strains develop and stresses redistribute along the fastener from elastic to plastic behaviour. In addition, triaxial strain gauge rosettes are glued to the fasteners at specific points to measure strains in three directions: 0°, 45°, and 90°. The gauges are stacked types from KYOWA (KFGS-2-120-D17-11 for steel, KFGS-2-120-D17-23 for aluminium). Each measuring grid is 1.2 × 2 mm and mounted on a carrier foil of 8 mm diameter. Strain gauges work by detecting tiny changes in electrical resistance when the material stretches or compresses. These changes are measured using a Wheatstone bridge setup, which converts them into readable strain values. On all fasteners, the strain gauges are positioned in the area between the plastic hinges. For timber-to-timber connections, they are positioned right in the shear plane, see Fig. 6.1, while for timber-to-steel connections, they are placed at a distance *a* from the shear plane, see Fig. 6.2. Together, the DIC and strain gauges provide complementary information, linking the current load on a fastener directly to its local strain state, helping to identify where and how plasticity starts to develop, and allowing a comparison between the measuring methods.

The distance *a* differs for the various types of timber and fastener used, as the plastic hinge distances depend on both of these parameters. As no embedment strengths

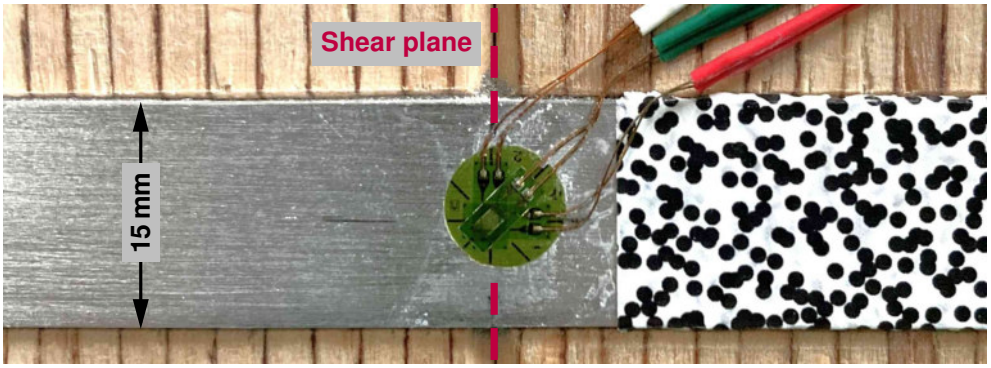

Fig. 6.1: Exemplary strain gauge glued on an aluminium fastener in the shear plane of a timber-to-timber connection with beech LVL.

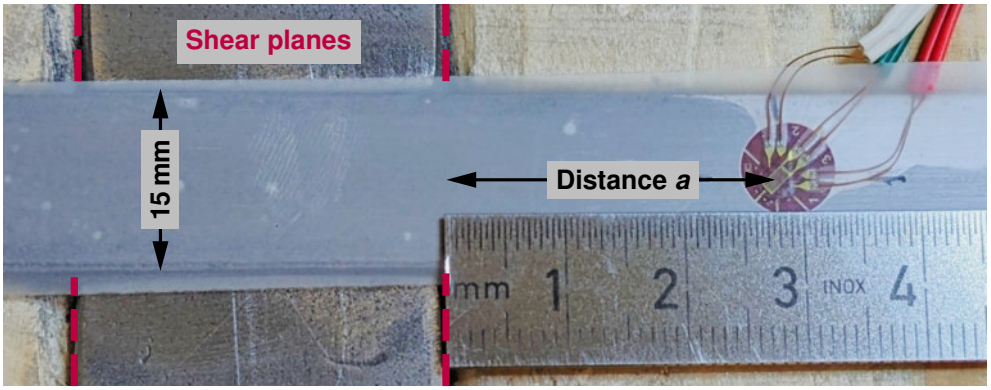

Fig. 6.2: Exemplary strain gauge glued on a steel fastener in distance a = 28 mm from the shear plane of a timber-to-steel connection with spruce glulam.

were known at the time of dimensioning and assessments were necessary, corresponding assumptions are made in order to determine the location of the strain gauges. The following assumptions regarding mean densities ρ_{mean} are based on individual samples: spruce glulam 385 kg/m^3, beech LVL 770 kg/m^3, and DVW 1350 kg/m^3. Based on these values, the embedment strengths are calculated as follows:

$$f_{\text{h,mean}} = 0.082 \cdot (1 - 0.01 \cdot d) \cdot \rho_{\text{mean}} \tag{6.5}$$

Here, d represents the embedment depth of the fastener and is equal to 19 mm. The embedment strength $f_{\text{h,mean}}$ is required to determine the spacing of the plastic hinges

and, consequently, the distance between the strain gauge and the shear plane. The spacing l_{ph} of the plastic hinges is calculated as follows:

$$l_{\text{ph}} = \sqrt{\frac{M_{\text{y}}}{f_{\text{h,mean}} \cdot d}} \tag{6.6}$$

The distances *a* are then taken as the half of the plastic hinge spacing l_{ph} and are listed in Tab. 6.1.

Table 6.1: Location of strain gauges of timber-to-steel connections depending on the timber and fastener material: Distances *a* to shear plane in mm.

Timber/Fastener	Spruce glulam	Beech LVL	DVW
Aluminium	21	14	-
Steel	28	20	15

6.4 Evaluation using DIC and Strain Gauges

The software used, ISTRA 4D [25], is a DIC software developed by Dantec Dynamics. It enables full-field, non-contact measurement of 2D and 3D surface deformations. By analysing speckle patterns on the specimen surface via stereo imaging, ISTRA 4D computes displacement and strain fields with high spatial resolution.

The primary output strains in 2D mode are:

- ε_{x} Normal strain in x-direction,
- ε_{y} Normal strain in y-direction,
- $\varepsilon_{\text{xy}} = \gamma_{\text{xy}}/2$ Tensor shear strain (half the engineering shear strain).

6.4.1 Strains

Strain gauge rosettes with orientations at 0°, 45°, and 90° measure only the normal strains $\varepsilon_{0°}$, $\varepsilon_{45°}$ and $\varepsilon_{90°}$.

The engineering shear strain γ_{xy} is then calculated from these values using:

$$\gamma_{xy} = 2 \cdot \left(\varepsilon_{45^\circ} - \frac{\varepsilon_{0^\circ} + \varepsilon_{90^\circ}}{2} \right) \tag{6.7}$$

This expression arises from the transformation of normal strains under rotation by 45°.

That means the strain gauges do not measure shear strain directly but allow γ_{xy} to be calculated from the measured normal strains as shown above. To enable comparisons, all shear quantities must be expressed using consistent conventions, preferably converting strain gauge-based γ_{xy} to $\varepsilon_{xy} = \gamma_{xy}/2$ for compatibility with results from ISTRA 4D.

Table 6.2: Comparison of strain outputs from ISTRA 4D and strain gauge (0°/45°/90°).

Strain Type	ISTRA 4D	Strain Gauge	Relation
Normal 0°	ε_x	ε_{0°	$\varepsilon_x = \varepsilon_{0^\circ}$
Normal 90°	ε_y	ε_{90°	$\varepsilon_y = \varepsilon_{90^\circ}$
Normal 45°	–	ε_{45°	Used to calc. γ_{xy}
Shear	$\varepsilon_{xy} = \gamma_{xy}/2$	γ_{xy} calculated	$\gamma_{xy} = 2 \cdot \left(\varepsilon_{45^\circ} - \frac{\varepsilon_{0^\circ}+\varepsilon_{90^\circ}}{2}\right)$
Principal	from ε_x, ε_y, ε_{xy}	after γ_{xy} conversion	See Eq. 6.8

Principal Strains

Once the strain components are unified ($\varepsilon_{xy} = \gamma_{xy}/2$), principal strains are calculated as:

$$\varepsilon_{1,2} = \frac{\varepsilon_x + \varepsilon_y}{2} \pm \sqrt{\left(\frac{\varepsilon_x - \varepsilon_y}{2} \right)^2 + \varepsilon_{xy}^2} \tag{6.8}$$

An exemplary illustration referring to the calculations above is given in Fig. 6.3.

Equivalent (von Mises) Strain

The equivalent strain according to von Mises provides a scalar measure of the deformation state in plane stress and can be calculated in two mathematically equivalent ways, depending on the shear strain representation:

- If the engineering shear strain γ_{xy} (as commonly used in strain gauge evaluation) is known:

$$\varepsilon_v = \sqrt{\varepsilon_x^2 - \varepsilon_x \varepsilon_y + \varepsilon_y^2 + \frac{3}{4} \cdot \gamma_{xy}^2} \tag{6.9}$$

- If the tensorial shear strain $\varepsilon_{xy} = \gamma_{xy}/2$ (as given in ISTRA 4D output) is used:

$$\varepsilon_v = \sqrt{\frac{1}{2}\left[(\varepsilon_x - \varepsilon_y)^2 + \varepsilon_x^2 + \varepsilon_y^2 + 6 \cdot \varepsilon_{xy}^2\right]} \tag{6.10}$$

Both formulas are mathematically equivalent and yield the same result, provided that the correct form of the shear strain is used in each case.

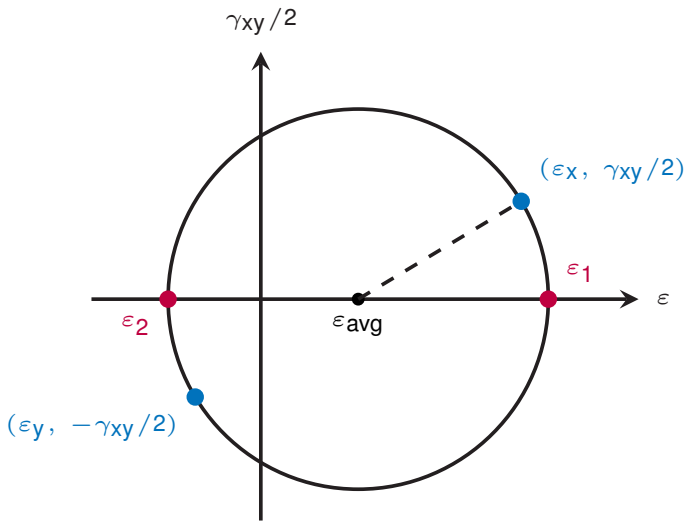

Fig. 6.3: Mohr's circle of strain for exemplary strains of $\varepsilon_x = 0.4\%$, $\varepsilon_y = -0.1\%$, $\gamma_{xy} = 0.3\%$

6.4.2 Stresses

For a stress calculation from the measured strains an assumption for the stress condition is necessary. Plane stress conditions are typical for:

- Thin components (e.g. metal sheets)
- Loading within the plane of the component (x-y plane)
- Negligible stress perpendicular to the plane: $\sigma_z = 0$

Assumptions:

- $\sigma_z = 0$, but $\varepsilon_z \neq 0$ due to Poisson's effect
- Strains in x, y, and z directions can be computed using Hooke's law (elasticity)

The points mentioned above are mostly valid and although not all of the points are fully appropriate for the present case, the evaluation is performed based on the assumption of a plane stress state.

For calculating elastic stresses with strain gauge results, the following entries are required:

- ε_x, ε_y, γ_{xy} (engineering shear strain calculated with strain gauge results)
- Young's modulus: $E_{\text{Steel}} = 210{,}000\,\text{N/mm}^2$, $E_{\text{Aluminium}} = 70{,}000\,\text{N/mm}^2$
- Poisson's ratio ν: $\nu_{\text{Steel}} = 0.3$, $\nu_{\text{Aluminium}} = 0.33$

The elastic stresses are calculated as:

$$\sigma_x = \frac{E}{1-\nu^2}\left(\varepsilon_x + \nu\varepsilon_y\right) \tag{6.11}$$

$$\sigma_y = \frac{E}{1-\nu^2}\left(\varepsilon_y + \nu\varepsilon_x\right) \tag{6.12}$$

$$\tau_{xy} = \frac{E}{2(1+\nu)} \cdot \gamma_{xy} \tag{6.13}$$

For calculating elastic stresses with ISTRA 4D results, the following changes are necessary. If instead the tensorial shear strain $\varepsilon_{xy} = \frac{\gamma_{xy}}{2}$ is given (e.g. from ISTRA 4D), the shear stress is calculated as:

$$\tau_{xy} = 2G \cdot \varepsilon_{xy} = \frac{E}{1+\nu} \cdot \varepsilon_{xy} \tag{6.14}$$

where

$$G = \frac{E}{2(1+\nu)} \tag{6.15}$$

is the shear modulus.

The principal stresses and equivalent stresses can be calculated based on the above formulae as follows:

$$\sigma_1 = \frac{\sigma_x + \sigma_y}{2} + \sqrt{\left(\frac{\sigma_x - \sigma_y}{2}\right)^2 + \tau_{xy}^2} \tag{6.16}$$

$$\sigma_2 = \frac{\sigma_x + \sigma_y}{2} - \sqrt{\left(\frac{\sigma_x - \sigma_y}{2}\right)^2 + \tau_{xy}^2} \tag{6.17}$$

$$\sigma_v = \sqrt{\sigma_x^2 - \sigma_x\sigma_y + \sigma_y^2 + 3\tau_{xy}^2} \tag{6.18}$$

6.5 Results

6.5.1 Evaluation

Strains in relation to the global coordinate system:
Since strains are recorded over the entire visible surface of the fastener, a suitable selection must first be made for evaluation. One of the main goals is to investigate the plastic behaviour of the fasteners. For this purpose, it is useful to focus on the equivalent strains. To study relevant points along the fastener axis, the strains are often presented along this axis in the following sections. The undeformed fastener's

centre of gravity line serves as a reference for this evaluation. To describe the stress state of the fasteners in detail during loading, it is also necessary to consider the individual strain components. The separate components, longitudinal (x), transverse (y), and shear, are visualised and analysed accordingly. All visualisations along the fastener axis refer to the global coordinate system, where the x-axis aligns with the fastener's longitudinal axis. This approach allows a clear picture of how strains develop and distribute both along and across the fastener.

Strains in relation to the local coordinate system:
A comparison of the recorded results from the strain gauges with the strains from ISTRA 4D is only possible using a local coordinate system, which rotates or inclines according to the deformation of the fastener. This local system ensures that the strains are evaluated relative to the changing fastener geometry itself, avoiding distortions that would arise from using a global coordinate system and allowing a more accurate comparison with the strain gauge measurements. To enable a comparison of the results of the strain gauges and DIC, an evaluation geometry first had to be defined at the corresponding point in ISTRA 4D. An investigation into the influence of the evaluation geometry in ISTRA 4D shows that surface evaluations of rectangular shapes the size of the measuring grids, point evaluations at the theoretical centre of the strain gauge, and mean values over a circle with a diameter of 2 mm yield comparable results, see exemplary visualisation in Fig. 6.4. In order to make an appropriate assessment, the standard deviations or the uncertainty of the measured values are taken into account. The standard deviation associated with the strains is illustrated in Fig. 6.5. The point evaluation exhibits the lowest standard deviation, which can be explained by the comparatively smaller size of the measuring geometry. However, since the strain gauges measure over a certain surface with their stacked grids, the circular area better represents the actual measurement process and provides a more realistic comparison between strain gauge and DIC.

Uncertainty of strains:
The previous assessment is legitimate, as this type of test specimen, i.e. a steel fastener in DVW, experiences large strains on the fastener that exceed yield stresses by far. The situation differs, however, in cases of small strains, which can be illustrated by the connection of an aluminium fastener in spruce glulam. This combination represents a typical example of low-stress conditions in timber-to-timber connections. Fig. 6.6 shows the von Mises strains and the standard deviation along the fastener axis for y-deformation stages of 5 and 10 mm. The standard deviation remains almost constant during these deformation stages, while significant strain peaks appear,

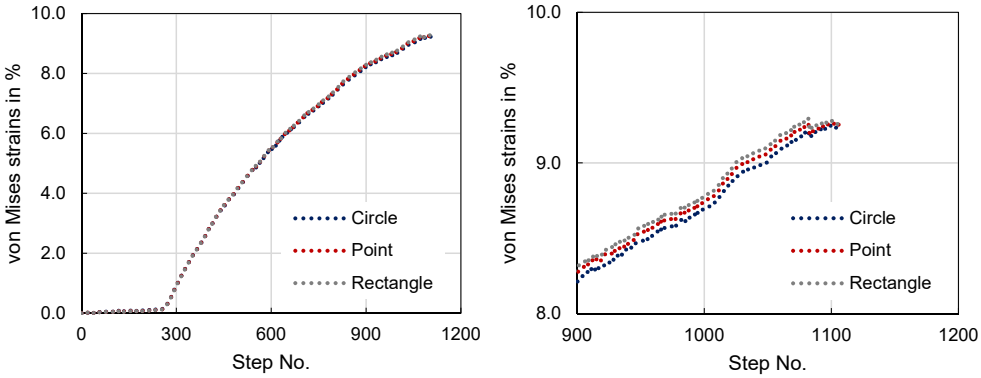

a. Complete curve.

b. Detail at higher strain rates.

Fig. 6.4: Comparison of von Mises strains for different evaluation geometries, exemplary connection: steel fastener in DVW.

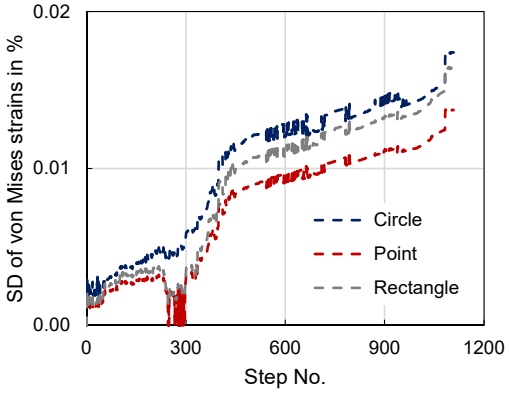

Fig. 6.5: Uncertainty of von Mises strains for different evaluation geometries, exemplary connection: steel fastener in DVW.

particularly near the plastic hinges. In other sections, the strains exhibit a certain degree of scatter. The standard deviation increases notably towards the ends of the fasteners, which can be attributed to limitations in the DIC measurement: capturing the entire fastener requires a relatively broad camera image, and areas closer to the image edges are therefore subject to higher measurement uncertainty. These observations also highlight the importance of the chosen evaluation geometry, as discussed previously, especially when interpreting small-strain behaviour. Overall, the figure illustrates how measurement uncertainty varies along the fastener and how local strain concentrations can be reliably identified despite these limitations.

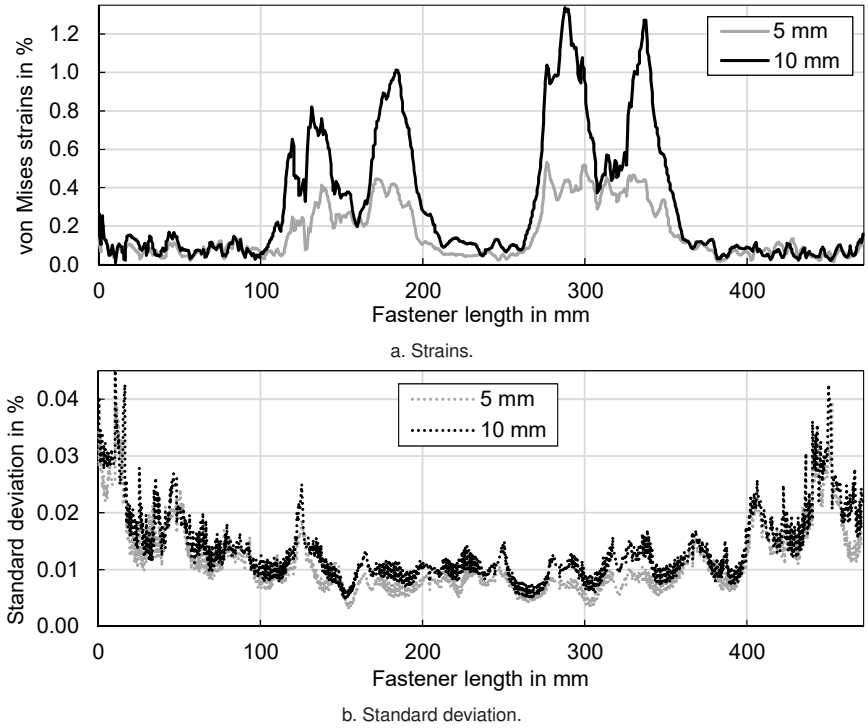

Fig. 6.6: Strains and standard deviation along fastener axis, aluminium fastener in spruce glulam.

The observed data scatter or jittering of the strains in the ranges 0–100 mm, 370–470 mm, and also in the central area is mainly related to the design of the speckle pattern. This pattern largely determines the achievable resolution of the strain measurements. The selected speckle size is defined by the fastener length, the image size, and the required camera distance and angle, and is optimised for capturing the overall deformations. However, this imposes a limitation: the chosen image size does not allow for very high resolution, meaning that small strains cannot be captured accurately. This limitation is addressed by using different strain measurement methods. The attached strain gauge is specifically designed for small strains, while DIC reliably records strains of around 1% or higher. This is based on a measured uncertainty of at least 0.01% (excluding edge areas), which corresponds to a practical measurement accuracy of about 1% for strains above 1%. To measure smaller strains with DIC, a significantly finer speckle pattern and a correspondingly smaller image field would be necessary. This, however, would restrict the measurement to only part of the test specimen rather than capturing its entire width.

6.5.2 Timber-to-Timber Connections: Strains Along Fastener Axis

6.5.2.1 Von Mises Strains

The von Mises strain, often called equivalent strain, is a scalar measure that represents the overall deformation under multiaxial loading. It reduces complex strain states to a single value, making them comparable to simple uniaxial test results. The tensile tests reveal the yield strength, tensile strength and strain limits. According to the stress-strain curves determined, see Fig. 5.1 in section 5.2, a yield point corresponding to less than $\varepsilon_{y,steel} = 1.0\%$ can be derived. Since aluminium does not exhibit a yield plateau, the yield point is taken as the kink after the elastic section, which provides a practical definition of the yield point and also corresponds to an elongation of under $\varepsilon_{y,alu} = 1.0\%$. The strains corresponding to reaching the tensile strength scatter more widely. For steel, these range between 15 and 26%, and for aluminium between approximately 5 and 8%, reflecting the variation across the tested specimens rather than inherent material properties. These threshold values are important for the subsequent analysis and assessment of which sections of the fasteners have already reached plastic behaviour. Exemplary distributions of the von Mises strains across the fastener surface are shown in Fig. 6.7. Timber-to-timber connections with steel fasteners are depicted in all three types of timber used. The upper and lower edges of the fasteners show continuously increased strains (light blue edges), which represent a misleading evaluation result at the mask edges and need to be neglected. It is therefore not taken into account further. Two things emerge: On the one hand, the strains of spruce over beech LVL to DVW increase in the area of the shear planes and plastic hinges. The areas coloured red indicate higher strains, while blue or violet areas indicate lower strains. The red zones become larger, whereby the chosen maximum strain in this case is set at 5% for reasons of comparability between the different timber materials. On the other hand, the middle image shows the effects of wood fibres starting to push over the fastener edges, which severely disturbs the strain distribution locally. These illustrations provide an overview, and the development of the plastic zones as well as the influence of timber type will be analysed in more detail below. A visualisation of the von Mises strains along the axis of the fastener, as shown in Fig. 6.8, highlights the differences in magnitude that occur. In accordance with the evaluation parameters, the line is illustrated with a minimum influence height of 4 mm. From spruce to beech LVL, there is a slight increase in strain, whereas for DVW a pronounced change in the strain distribution occurs in the shear planes. For spruce glulam, the most significant peaks

are located in the area of the plastic hinges, whereas for beech LVL and DVW, peaks also develop in the shear plane regions, at fastener lengths of approximately 155 and 315 mm.

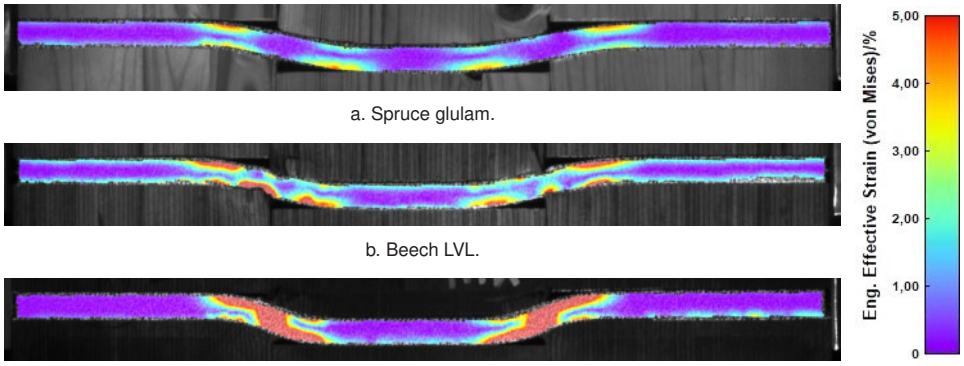

a. Spruce glulam.

b. Beech LVL.

c. DVW.

Fig. 6.7: Von Mises strains on surfaces of steel fasteners with head at a deformation of 15 mm.

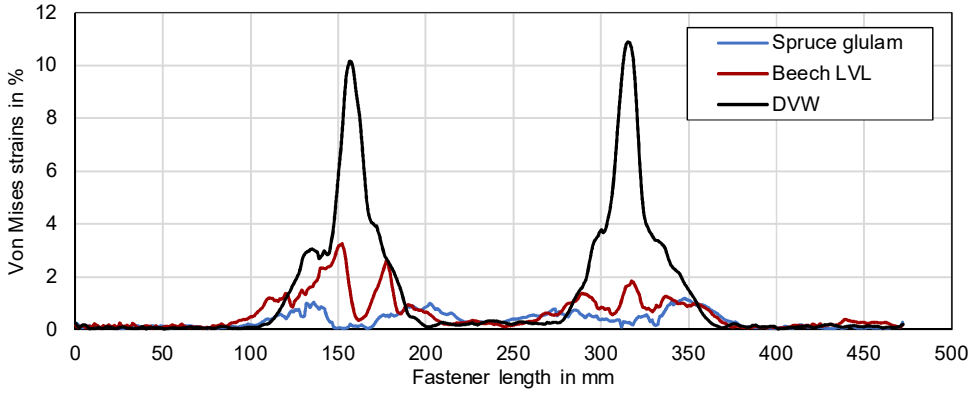

Fig. 6.8: Von Mises strains along centre line of steel fasteners with head at a deformation of 15 mm.

Another effect visible in the progression of von Mises strains is the initial formation of plastic hinges and the subsequent *movement of plastic hinges* along the fastener axis. This has already been identified on the basis of the deformations in section 5.4.6 and can also be visualised in the strain progression. The movement of the plastic hinges occurs as the fastener is pulled towards the axis of symmetry of the connection, beginning with the inclination of fastener sections inbetween plastic hinges. On one hand, this pulling causes areas of the fastener that were previously subjected to lower

stresses to enter the yield zone from the regions beside of it. The plastic hinge thus shifts along the fastener, while it is pulled inwards. Fig. 6.9 and Fig. 6.10 illustrate this effect for spruce glulam and beech LVL. As deformation increases, peaks form further on the outside of the outer plastic hinges, whereas the inner plastic hinges move inwards, causing the central area to plasticise progressively. The effect of shear plane strains in beech LVL is also visible. A notable observation is the appearance of two sharp peaks in the region of the left plastic hinge in beech LVL in Fig. 6.10, which should be ignored as they are caused by local disturbances from timber fibres pushing over the fastener.

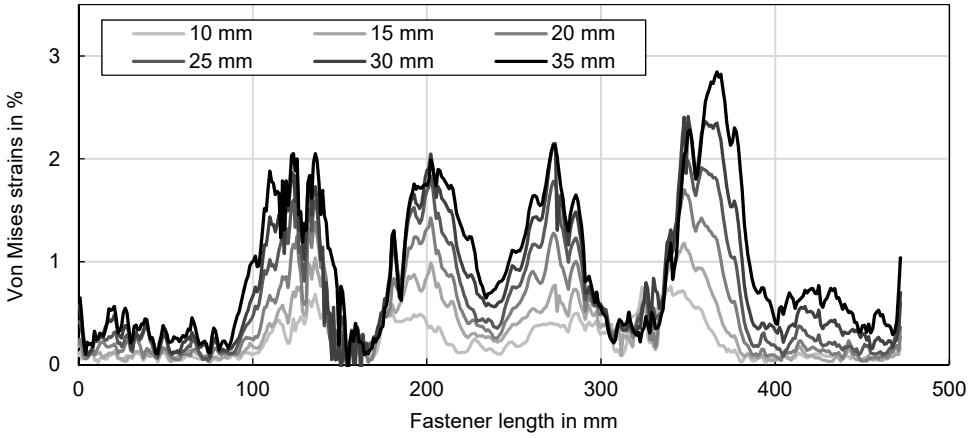

Fig. 6.9: Von Mises strains along centre line of steel fasteners with head in spruce glulam at different deformation stages.

In contrast to these progression patterns, peaks form early in the shear plane area in DVW, see Fig. 6.11. Even at 5 mm deformation, the strains at these points are well above 1%, i.e. the yield plateau is exceeded. The smaller peaks adjacent to these points indicate the plastic hinges of the fastener. The maximum strains reach around 10% at a y-deformation of just 10 mm and then increase only slightly afterwards. This magnitude corresponds to strains in the range of the tensile strength.

These observations raise the question of which strains cause the individual peaks and which of them has such a significant influence that the von Mises strains exceed the strain levels in the plastic hinges and form the additional peak in the shear plane. The individual strain contributions are therefore examined separately in the following section.

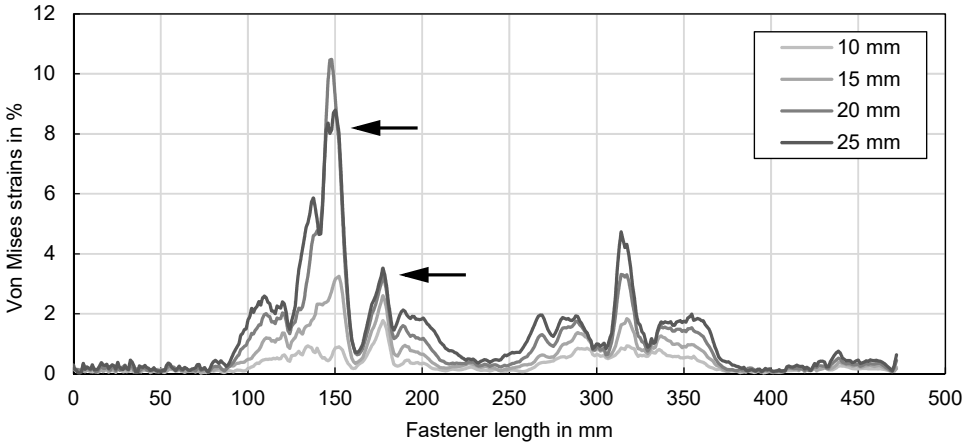

Fig. 6.10: Von Mises strains along centre line of steel fasteners with head in beech LVL. Arrows mark the unusual peaks due to interfering timber fibres.

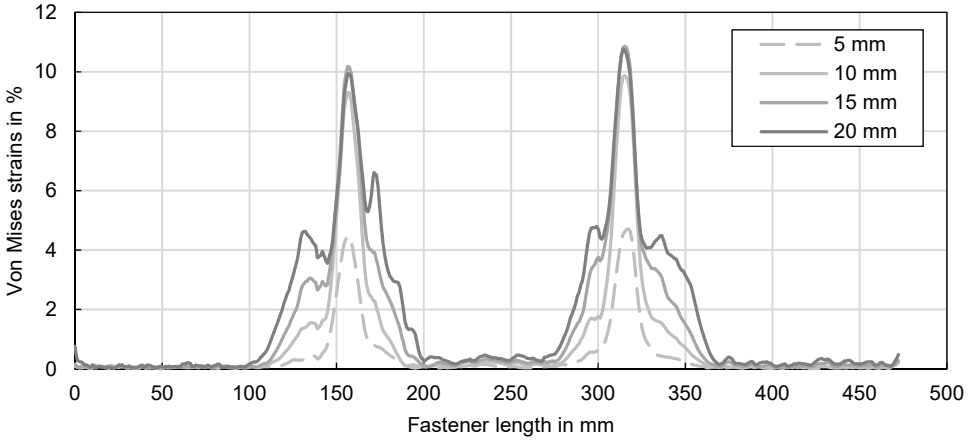

Fig. 6.11: Von Mises strains along centre line of steel fasteners with head in DVW.

6.5.2.2 Strains in X-Direction

Strains in the x-direction indicate the stress acting on the fastener along its axial direction. If the fastener inclines under increasing load, the coordinate system rotates accordingly, and the x-strains always refer to the axial direction. Fig. 6.12 shows the distributions for the three different types of timber. Limits for the exemplary visualisation are set to -3 to 3% x-strains, resulting in different areas reaching this limit. For spruce glulam, the axial stress in the area of the plastic hinge is clearly visible, with tension

and compression zones distinctly formed. In beech LVL, these zones move closer together. As a result, the areas marked in red and blue expand correspondingly. In DVW, the tensile areas appear as a continuous tensile zone, indicating that the shear plane is also subject to tensile strain. These axial strains correlate with the previously discussed von Mises strain distributions and highlight the localisation of tensile and compressive regions along the fastener. This effect appears to a lesser degree in beech LVL and even less in spruce glulam, especially when the limits of the strain visualisation are reduced or larger deformations are considered.

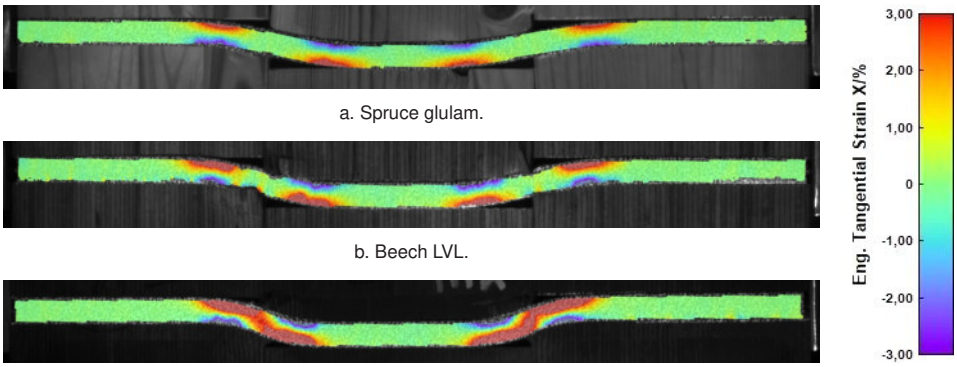

a. Spruce glulam.

b. Beech LVL.

c. DVW.

Fig. 6.12: Strains in x-direction on surfaces of steel fasteners with head at a deformation of 15 mm.

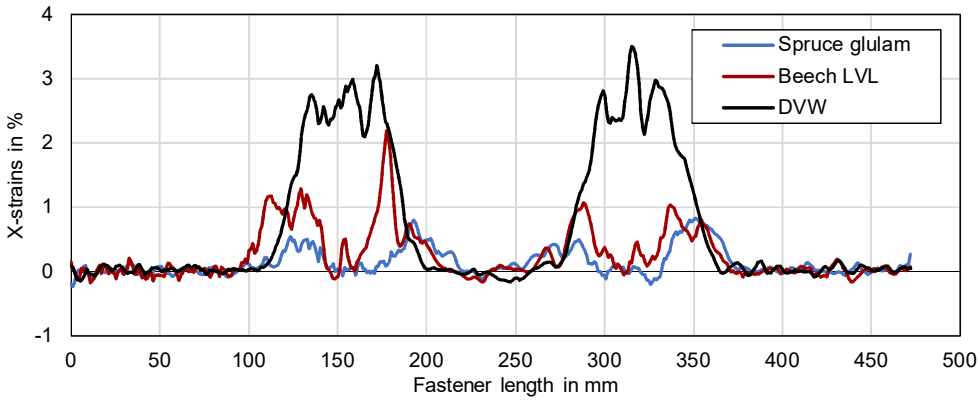

Fig. 6.13: X-strains along centre line of steel fasteners with head at a deformation of 15 mm.

Although the connections with heads are shown in these examples, no significant x-strains are recorded in the remaining fastener areas. The head only activates x-strains

to a certain extent, and only when the fastener forms inclined sections. However, these are far below the x-strains in the shear plane and plastic hinge areas. This only applies to the connections examined, though. For fasteners with continuous profiling, comparable to screws, different patterns would be expected. An evaluation of the x-strains along the centre line of the fastener in Fig. 6.13 illustrates the differences in magnitude of the surface results from Fig. 6.12. The main difference is that the fastener in DVW not only forms the two peaks in the area of the plastic hinges, but also shows comparable strains or an additional peak in between, in the area of the shear planes. In this case, the fastener is consistently subjected to high axial stress between the plastic hinges. The two tension zones are visually connected. This, in turn, means that the axial components are anchored by friction or deflection caused by the angle of inclination. The curve shown for beech LVL shows only a local increase on the right-hand shear plane at the deformation of 15 mm shown. At significantly larger deformations, higher strains also occur in the shear plane area. This effect could not be observed for spruce glulam, and the strains between the plastic hinges remain low. These observations confirm the hypothesis that, as the density increases, the normal stress components in the inclined section of the fastener increase significantly. This also shows that in DVW, the interaction of different strain contributions causes the fastener to enter the plastic behaviour earlier and more extensively.

6.5.2.3 Strains in Y-Direction

To emphasise the function of y-strains (90° strains), a simple tensile test can serve as an example: as the specimen elongates in the 0° direction, it contracts perpendicularly in the 90° direction. The y-strain therefore represents the transverse deformation, which in more complex loading situations corresponds to the strain normal to the chosen reference axis. In this study, the y-strains are defined relative to the reference state at the start in a vertical direction. They thus describe the strains in the thickness direction of the fastener, i.e. perpendicular to its longitudinal axis. Fig. 6.14 illustrates the y-strains for the previously analysed cases. For spruce glulam, only slight variations are visible within the chosen scale of -2 to 2% strain. Small nuances appear mainly near the plastic hinges, indicating transverse strains as the outer fibres of the fastener begin to yield. For beech LVL, these y-strains are more pronounced in the tensile zones of the plastic hinges than in compression zones. Blue regions visible in the shear plane area result from wood fibres pushing over the fastener and do not reflect actual strains. These areas need to be excluded from the analysis. The defects are evident,

for example, in indentations of the evaluation mask contour. In general, evaluations along the fastener axis provide a clearer picture. Such plots reveal defective areas, allowing verification of expected strain magnitudes and the positions of peaks, due to interfering wood fibres or real strain peaks, along the fastener. For instance, in beech LVL, a peak appears at around 150 mm in Fig. 6.15, slightly short of the shear plane at 155 mm due to the slightly reduced evaluation length relative to the real fastener length. This confirms the plausibility of the measurements,helps find disturbed areas and highlights the location of significant y-strains.

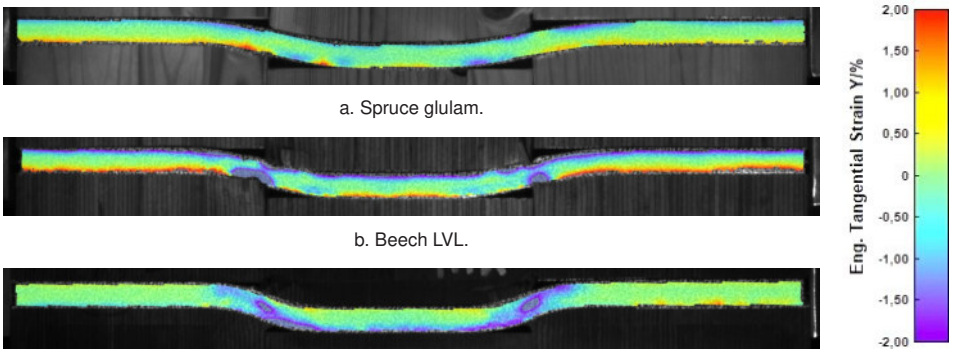

a. Spruce glulam.

b. Beech LVL.

c. DVW.

Fig. 6.14: Strains in y-direction on surfaces of steel fasteners with head at a deformation of 15 mm.

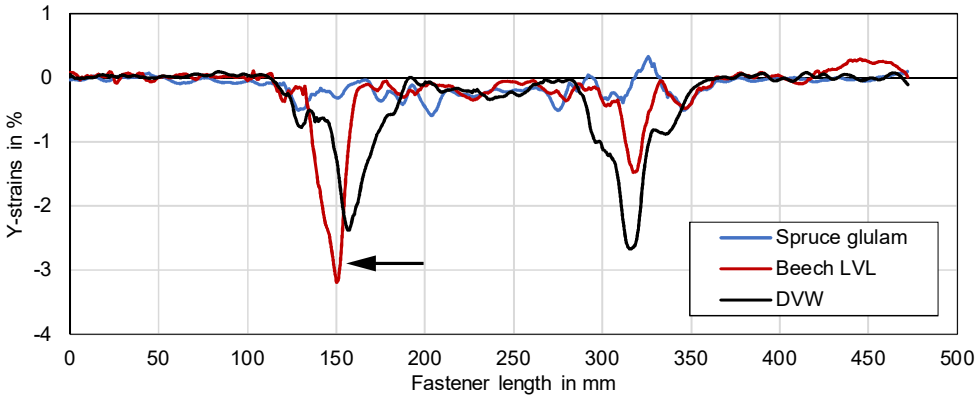

Fig. 6.15: Y-strains along centre line of steel fasteners with head at a deformation of 15 mm. Arrow marks the unusual peak due to interfering timber fibres

6.5.2.4 Shear Strains

Shear strains can be understood by considering a simple shear test. When a specimen is subjected to pure shear loading, it does not elongate, but instead becomes distorted, causing originally orthogonal lines to become skewed. The shear strain is therefore a way to quantify this angular distortion, and in complex loading states, it provides essential information on the material's deviation from purely normal deformations. These types of strains are particularly interesting in regions of the fastener where large shear forces act, i.e. in the area of the shear plane. And considering the plotted results across the surface of the fasteners in Fig. 6.16, this area in particular stands out.

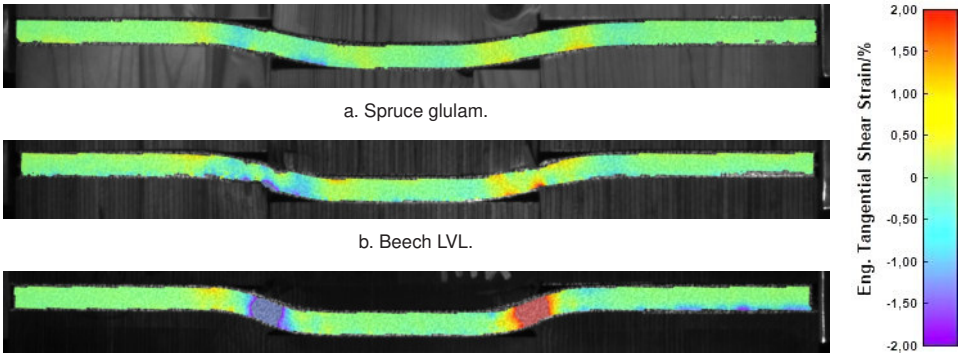

a. Spruce glulam.

b. Beech LVL.

c. DVW.

Fig. 6.16: Shear strains on surfaces of steel fasteners with head at a deformation of 15 mm.

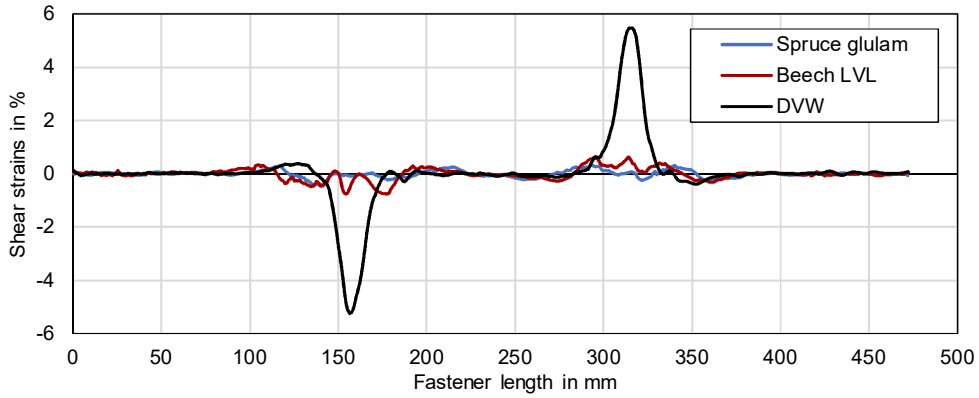

Fig. 6.17: Shear strains along centre line of steel fasteners with head at a deformation of 15 mm.

It can be noted that in spruce glulam and beech LVL, two areas, or at least a broader area, between the plastic hinges show increased shear strains, whereas in DVW this area narrows further, resulting in high shear strains around the entire shear plane. Fig. 6.17 demonstrates the differences in magnitude of the shear strains. These illustrations clearly show the significant difference between connections made from spruce glulam or beech LVL and DVW. As the density increases, the fasteners are no longer predominantly subjected to bending stresses, but instead experience increased shear stresses. This shift from bending- to shear-dominated loading is important for understanding the onset and development of plastic behaviour in the fastener. In particular, it explains why the x-strains, y-strains, and von Mises strains show higher values in the shear plane for DVW: the fastener reaches the yield limit earlier and over a broader area mainly due to high shear strains.

6.5.3 Timber-to-Steel Connections: Strains Along Fastener Axis

For timber-to-steel connections, higher loads, and consequently larger strains, are generally expected in critical regions of the fastener, such as the shear plane and areas prone to plastic hinge formation, compared to timber-to-timber connections. Many fundamental effects were already observed in timber-to-timber connections (see section 6.5.2), so this section focuses on the key differences and additional insights specific to timber-to-steel connections. Due to overlapping wood fibres in some locations, not all fasteners provide ideal measurement conditions and results. For consistency with the previously illustrated results, this section considers steel fasteners with a head, focusing on the front fastener in beech LVL and rear fasteners for spruce glulam and DVW. For beech LVL, the region containing the glued-on strain gauge (around 210–220 mm along the fastener) is thus included in the comparisons but should be disregarded in the analysis since the DIC measurement above the strain gauge area leads to local disturbances. The following analysis aims to reveal how the load increase on timber-to-steel connections affects the onset and development of plastic behaviour in the fastener.

6.5.3.1 Von Mises Strains

The illustration of the von Mises strains along the fastener axis in Fig. 6.18 highlights the most critical and highly stressed sections. It is evident that the strains in the shear

planes, at approximately 155 and 190 mm fastener length, by far exceed those in the outer plastic hinges. These high values arise from the combined effects of direct shear, bending and axial loading, which are more pronounced in timber-to-steel connections than in timber-to-timber connections. The stiffer steel interface changes how the load is transferred to the fastener, concentrating stresses locally. The measured equivalent strains surpass the reference strains from uniaxial tensile tests by roughly 20% at the point of reaching the ultimate tensile strength. This indicates that the fastener material in the shear planes has exceeded both the yield and ultimate limits, causing significant stress redistribution. Consequently, the recorded values should be evaluated as true strains rather than engineering strains. But to keep comparability with results from timber-to-timber connections, engineering strains are illustrated but can be recalculated using Eq. 6.3. Maximum von Mises strains in the shear planes reach 7% for spruce glulam, 14.2% for beech LVL, and 47.8% for DVW. Comparing these results with timber-to-timber connections, see section 6.5.2.1, confirms that the strains are substantially higher, reflecting the increased plastic deformation of the fastener. The entire surface distributions, shown in Fig. 6.19, underline the significant localisation of strains in the shear planes. These findings also highlight the transition from predominantly bending-dominated to shear-dominated loading as the density of the timber increases, which is essential for assessing which sections of the fastener have already entered plastic deformation.

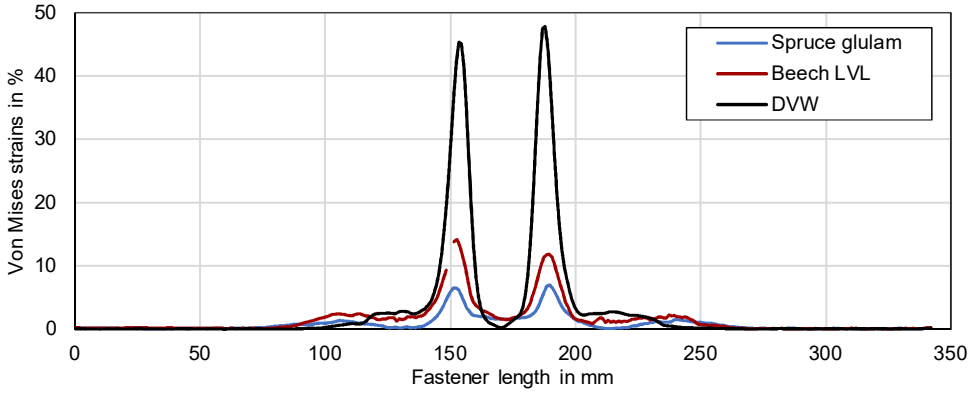

Fig. 6.18: Von Mises strains along centre line of steel fasteners with head at a deformation of 15 mm.

Because small strain values in the diagrams are difficult to discern but can still have a significant local effect, an additional example is considered. Fig. 6.20 shows connections with aluminium fasteners in spruce glulam and beech LVL. Owing to

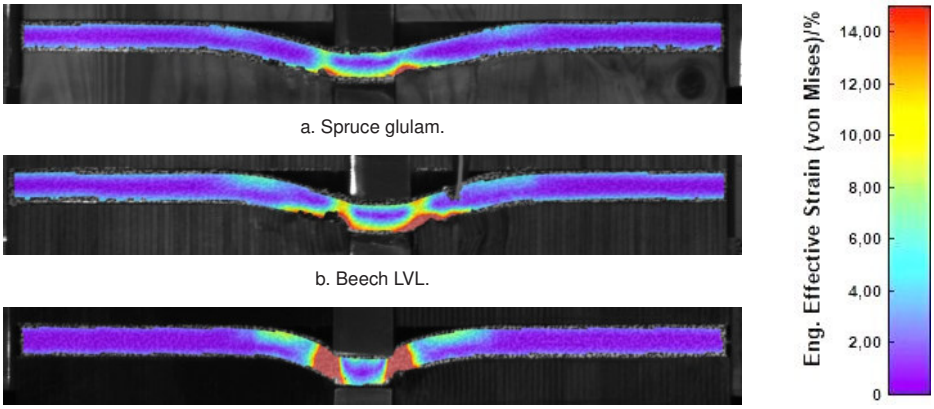

Fig. 6.19: Von Mises strains on surfaces of steel fasteners with head at a deformation of 15 mm.

the lower strength of aluminium compared to steel, yielding initiates earlier, resulting in broader and more pronounced strain distributions. Consequently, the shear-plane strains increase significantly: in beech LVL, for instance, the maximum strain rises from approximately 12–14% with steel fasteners to 30–34% with aluminium fasteners. This clearly demonstrates the more ductile behaviour of aluminium fasteners and highlights how the choice of fastener material directly influences the load-deformation behaviour of the connection.

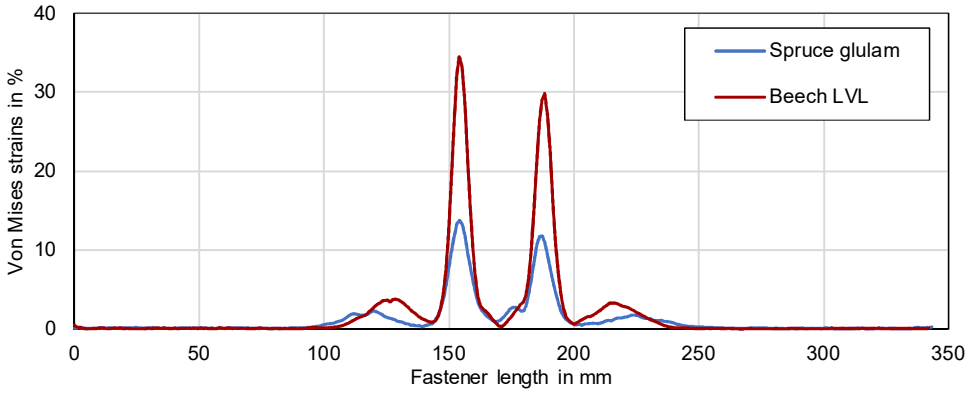

Fig. 6.20: Von Mises strains along centre line of aluminium fasteners at a deformation of 15 mm.

It must be emphasised that the strain levels observed in the aluminium fastener in beech LVL, reaching up to 30–34%, and in the steel fastener in DVW, reaching up

to 45–48%, clearly fall within the nonlinear range of the material behaviour. As a result, these measurements can no longer be interpreted using purely linear-elastic assumptions. In this case, the stress-strain relationship becomes strongly non-linear, and additional mechanisms, such as strain hardening of the fastener material, local crushing or damage in the surrounding timber, and the progressive yielding and redistribution of stresses within the fastener, -make a significant contribution to the overall load-bearing behaviour.

6.5.3.2 Individual Strain Contributions

An analysis of the individual contributions to the von Mises strains, derived from the measured x-, y-, and shear-strain components, reveals pronounced peaks for all three components within the shear plane, see Fig. 6.21.

This finding highlights that the elevated von Mises strains in this region are not the result of a single dominant component but of a combined multiaxial strain state, underlining the severity of the local strain condition. A closer look at the distribution of the x-strain component reveals a further detail: the position of the plastic hinge can be identified by the location of its strain peak. This peak shifts from roughly 105 mm in spruce glulam to about 115 mm in beech LVL and to 130 mm in DVW, indicating that the plastic hinge forms progressively closer to the shear plane as the timber density increases. The occurrence of positive x-strains in this region shows that, at this stage of deformation, the tensile zone has already propagated beyond the fastener's centre line.

6.5.4 Strains Near the Shear Planes

The shear plane is analysed in more detail, as it represents the key area of load transfer in connections and is expected to experience very high or even the highest stresses in timber-to-timber and timber-to-steel connections. For this purpose, the strains are evaluated over the height of the fastener and strain gauge results are also included in this analysis because they are located directly in or near the shear plane. In a first analysis, the strains in the shear planes are evaluated over the fastener height, and the resulting variations and trends are visualised. The evaluation line for DIC is defined vertically along the shear plane in the undeformed state. Since not the entire fastener surface is available, i.e., the edges cannot be evaluated, a

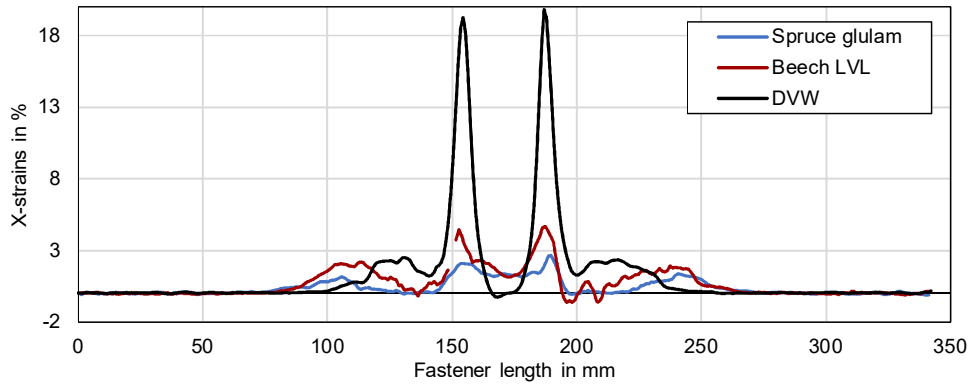

a. X-strains.

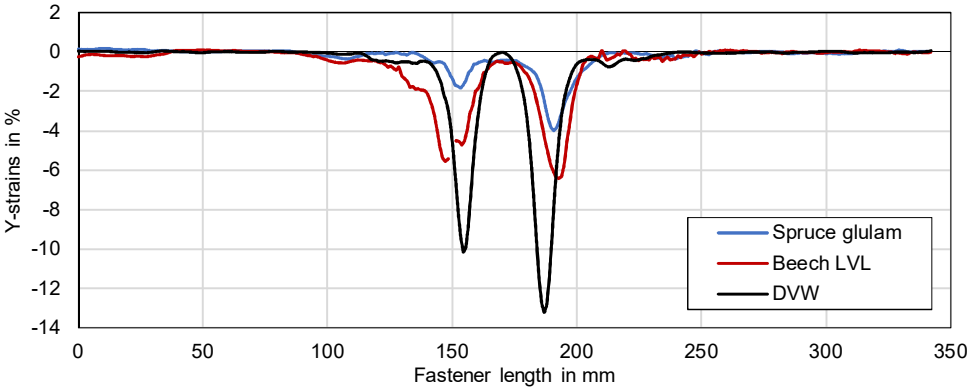

b. Y-strains.

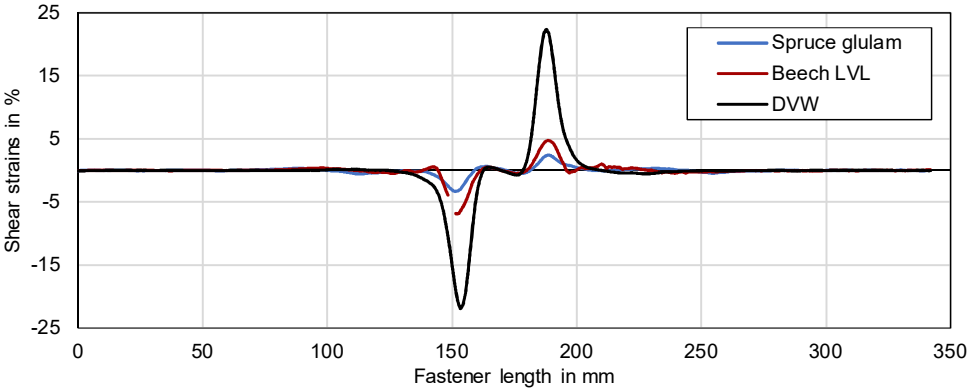

c. Shear strains.

Fig. 6.21: Strain contributions along centre line of steel fasteners with head at a y-deformation of 15 mm.

uniform evaluation height of 10 mm is chosen. According to the global COS in the fastener axis, the evaluation range is y = [-5, 5]. The strains are evaluated based on the global coordinate system. Two examples are presented in this section first: aluminium fasteners in spruce glulam and in beech LVL. The Figs. 6.22 and 6.23 show the respective strain contributions as well as the von Mises strain. Since larger strains appear, true strains are used for visualisation. A consistent strain scale has been applied to all plots in order to make the differences visible. Firstly, it is observed that the left and right shear planes are comparable in terms of both the magnitude and the shape of the strain contributions. It is reasonable to conclude, based on the following assessment, that the shape of the curves is plausible. The disparity in the shear strains, which are negative on the left side and positive on the right side, can be explained by the definition of the global coordinate system. As illustrated in Fig. 6.22, the X-strains demonstrate an approximate linear distribution, showing compressive strains in the upper region (negative values) and tensile strains in the lower region (positive values) of the cross-section. The resulting von Mises strain distribution at the evaluated step of 15 mm is parabolic, with higher strains occurring in the outer regions. This finding indicates that bending effects predominate, consistent with the observed behaviour in the area of plastic hinge formation.

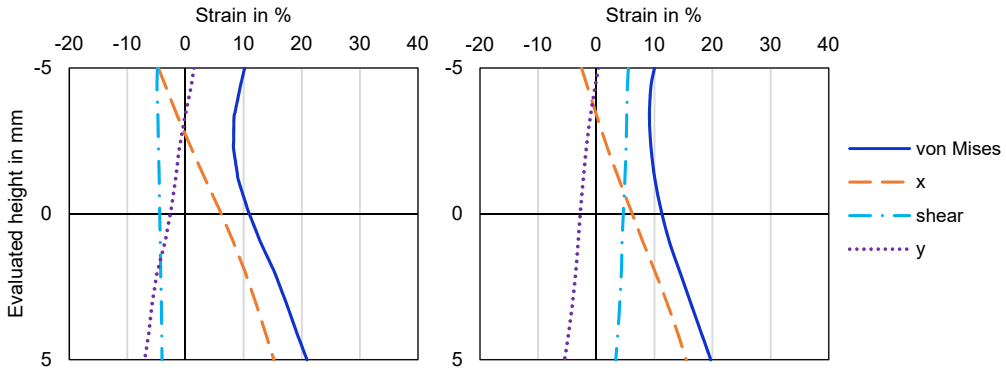

a. Left shear plane.

b. Right shear plane.

Fig. 6.22: True strain distributions over aluminium fastener height at y-deformation of 15 mm in spruce glulam.

A comparison with the distributions observed in beech LVL specimens, see Fig. 6.23, shows, on the one hand, the generally higher magnitudes of strains and, on the other hand, slight differences in the shape of the distributions. It can be noted that the x-strains are predominantly positive, indicating that the entire fastener cross-section

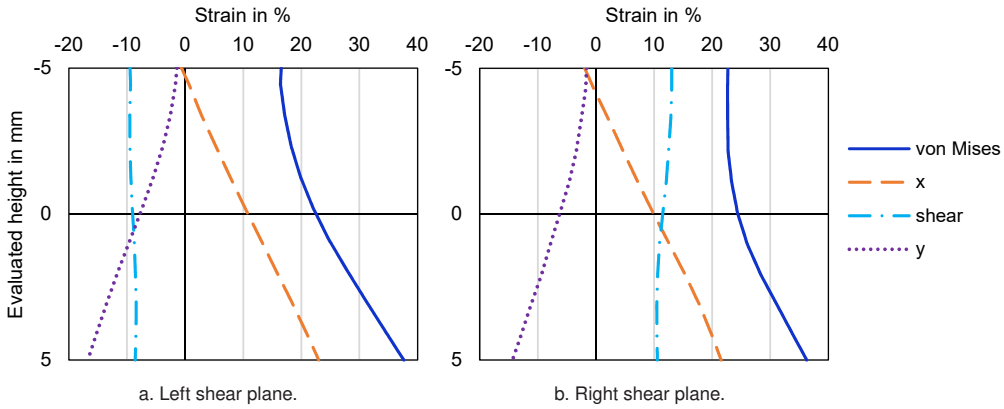

Fig. 6.23: True strain distributions over aluminium fastener height at y-deformation of 15 mm in beech LVL.

is under tension. This comparatively large tensile contribution has a strong effect on the von Mises strain distribution, which, although still parabolic in shape, does not exhibit a pronounced peak near the top face. Conversely, the strains increase from the upper to the lower region, with a progressive intensification in the lower region. Changing the fastener from aluminium to steel leads to correspondingly smaller strain components when comparing the same deformation stage of 15 mm y-deformation. The corresponding plots of the true strain results are shown in Figs. 6.24 and 6.25.

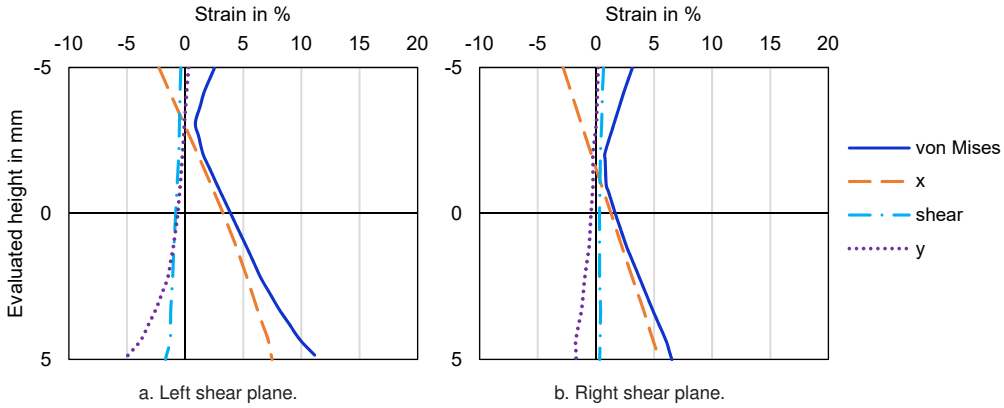

Fig. 6.24: True strain distributions over steel fastener height at y-deformation of 15 mm in spruce glulam.

Extending the analysis to other connection configurations reveals that the results for steel fasteners in DVW differ. For DVW, however, a strain state is observed in the

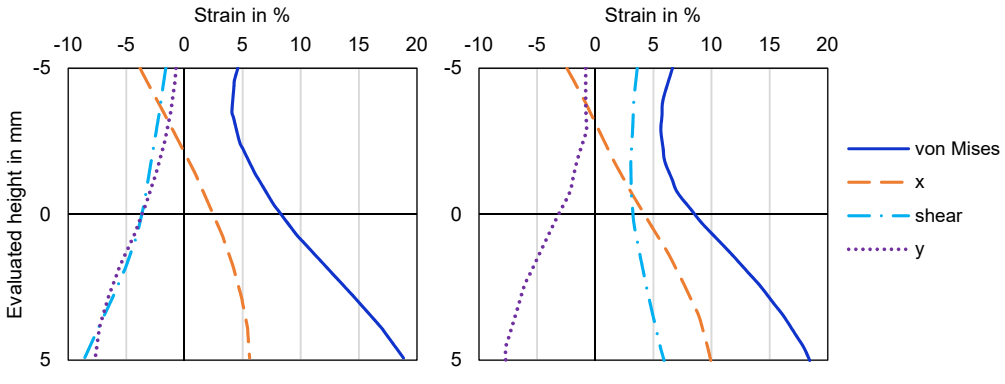

a. Left shear plane. b. Right shear plane.

Fig. 6.25: True strain distributions over steel fastener height at y-deformation of 15 mm in beech LVL.

shear plane area that does not allow a straightforward comparison of the individual shear planes. The strains change rapidly locally and a certain asymmetry is noticeable in the surface strain distribution, see Fig. 6.26. This suggests, for example, that not both shear planes transfer the same load or that the indentation by the steel plate is stronger on one side, leading to localised strain peaks. For the evaluation, this means that the evaluation line initially located in the shear plane is now in places with varying strain levels. Even a shift of the evaluation line of just one millimetre results in a noticeably different strain curve.

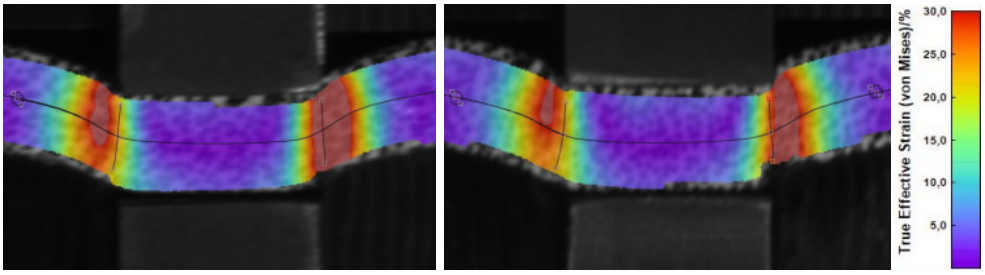

a. Front side. b. Rear side.

Fig. 6.26: Von Mises strains on surfaces of steel fasteners with head at a deformation of 15 mm including evaluation lines.

A particular observation in the shear plane is the failure of the fastener cross-section occurring at large deformations, which is analysed in more detail below. For the connection with aluminium fasteners in beech LVL, for example, such a failure can be identified on the rear side of the connection at approximately 25 mm deformation in

y-direction (around step no. 1000, see Appendix A.5 with specimen results on p. 382 - 386). The progression of von Mises strains in the shear plane indicates the beginning of the fastener failure, see Fig. 6.27. The curves mark the von Mises strains from beginning, light blue, through to the end of the test, dark blue. The increase in strain in the lower part of the fastener, even at an early stage of loading, is an important contributing factor to cross-sectional failure of the fastener. The tension zone of the plastic hinge in the shear plane begins to yield early, initiating a redistribution of stresses from this location. In addition, the steel plate pressing from above, owing to its higher strength compared to the aluminium fastener, causes localised indentation, which further reduces the effective cross-section in this highly stressed region and enhances the stress concentration. These indentations become particularly visible after the removal of the fasteners from the specimen, i.e. after the completion of the test. For the described aluminium fastener in beech LVL, the removed fastener is shown in Fig. 6.30. Further images of the removed fasteners are provided in Appendix A.5. In this case, the von Mises strains are evaluated using engineering strains. However, for such large strains it is essential to use true strains, as the calculation error becomes becomes non-negligible. This is because the true strain relates the elongation to the current length, thus accounting for the fact that the specimen has already elongated. For very small strains ($< 1\%$) the difference is negligible, as discussed in the beginning of the chapter. An evaluation based on true strains therefore yields comparable results for the first evaluation steps, but reveals slightly different results for later steps, see Fig. 6.28.

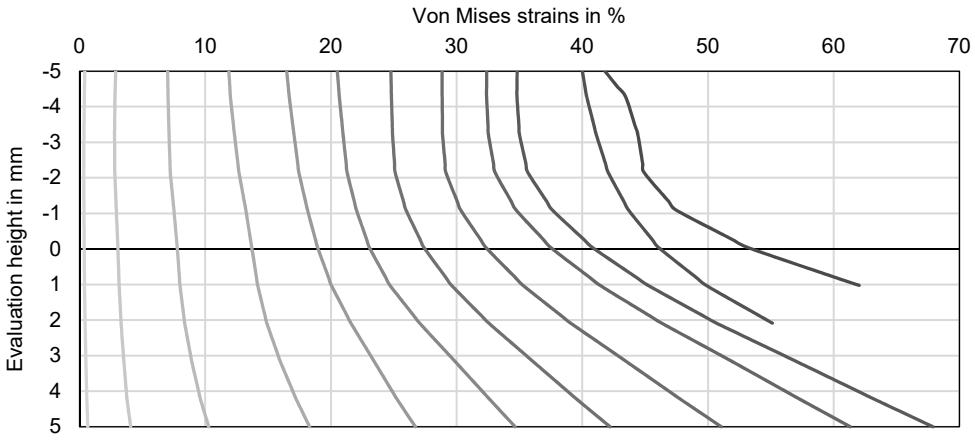

Fig. 6.27: Progression of engineering strains over height of aluminium fastener in right shear plane.

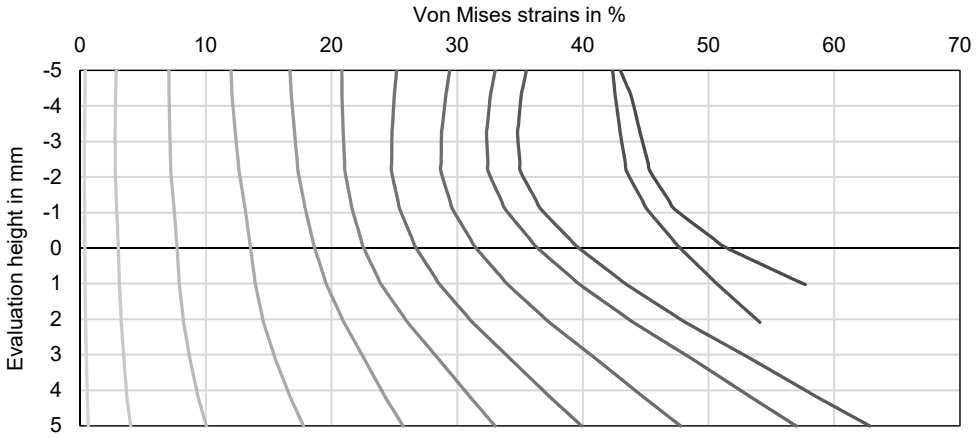

Fig. 6.28: Progression of true strains over height of aluminium fastener in right shear plane.

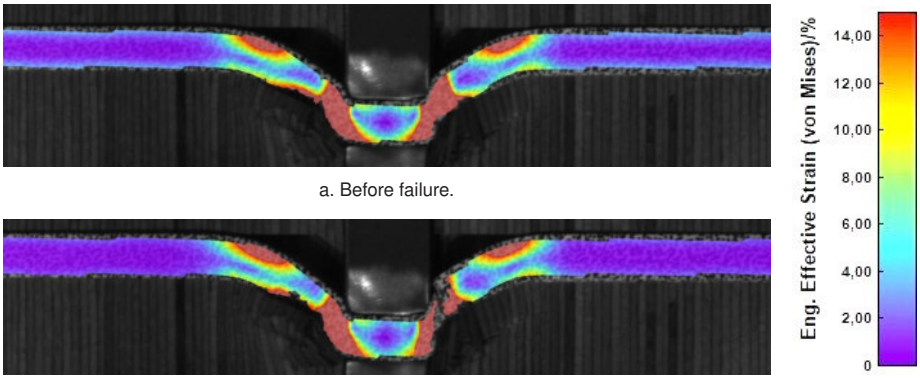

a. Before failure.

b. After failure.

Fig. 6.29: Von Mises strains on surface of aluminium fastener with failure in right shear plane.

To put the presented strains and their distributions into context, they can be compared with typical cases such as pure bending, or bending combined with shear, and the onset of local plasticity. In the elastic range and under bending-dominated loading, the distribution of von Mises strain across the fastener cross-section is expected to follow an approximately linear trend. This results from the superposition of normal strains due to bending—which vary linearly over the cross-section—and relatively small shear strains that do not significantly alter the overall shape. In this case, the linear distribution provides a valid approximation for interpreting the initial elastic behaviour of the fastener. At larger deformations, however, additional effects such as local indentation from the steel plate or plastic yielding of the fastener lead to deviations

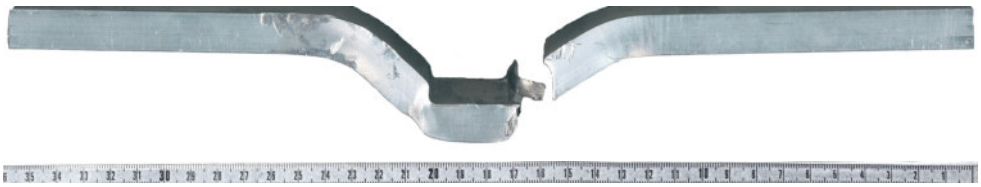

Fig. 6.30: Removed fastener after testing: back side of aluminium fastener in beech LVL.

from this simple linear distribution. The von Mises strain evolves towards a parabolic distribution, which is a characteristic of plastic hinge formation: the outer regions of the cross-section reach the yield strain first and maintain approximately constant stress, while the inner regions continue to deform plastically. This redistribution indicates a transition from elastic bending to the full plastic moment capacity of the fastener and strongly influences the ultimate load-carrying behaviour of a connection. This can be characterised, for example, by the flattening of the load-deformation curve, which is of course also influenced by the onset of plastic behaviour in the timber.

As noted at the beginning of this section, the results from the strain gauges are also presented. Fig. 6.31 shows strain measurements from four positions, focusing initially on the previously discussed case of aluminium fasteners in beech LVL. Graphs 1 and 2 correspond to the fastener on the front side of the specimen, while Graphs 3 and 4 correspond to the rear fastener. Graphs 1 and 3 show the left shear planes, whereas Graphs 2 and 4 show the right shear planes, all viewed from the respective specimen surface.

Originally, one strain gauge was intended for each specimen in shear plane no. 2. In this particular case, however, two strain gauges were unintentionally applied: one in shear plane 1 at $a = 14$ mm from the shear plane, and another at $a = 21$ mm from shear plane 2. The two lower graphs present the results obtained via DIC evaluation for the position $a = 14$ mm, shown as a mean value over a circular area of 2 mm diameter. Initial observations indicate that the strain gauges exhibit a smoother trend than the DIC results. This behaviour is attributed to the speckle size and the corresponding spatial resolution. The second graph shows a sudden drop in shear strains, and consequently in the von Mises strains. Since strain gauge 2 was unintentionally placed at a greater distance than planned, and thus within the developing plastic hinge region, its position and the resulting higher local strains may explain the premature drop in the measured signal. However, a random loss of signal cannot be completely ruled out. In any case, it is evident that the measured strains increase with distance from the shear plane, which is also related to the altered strain state in the plastic hinge region. For example,

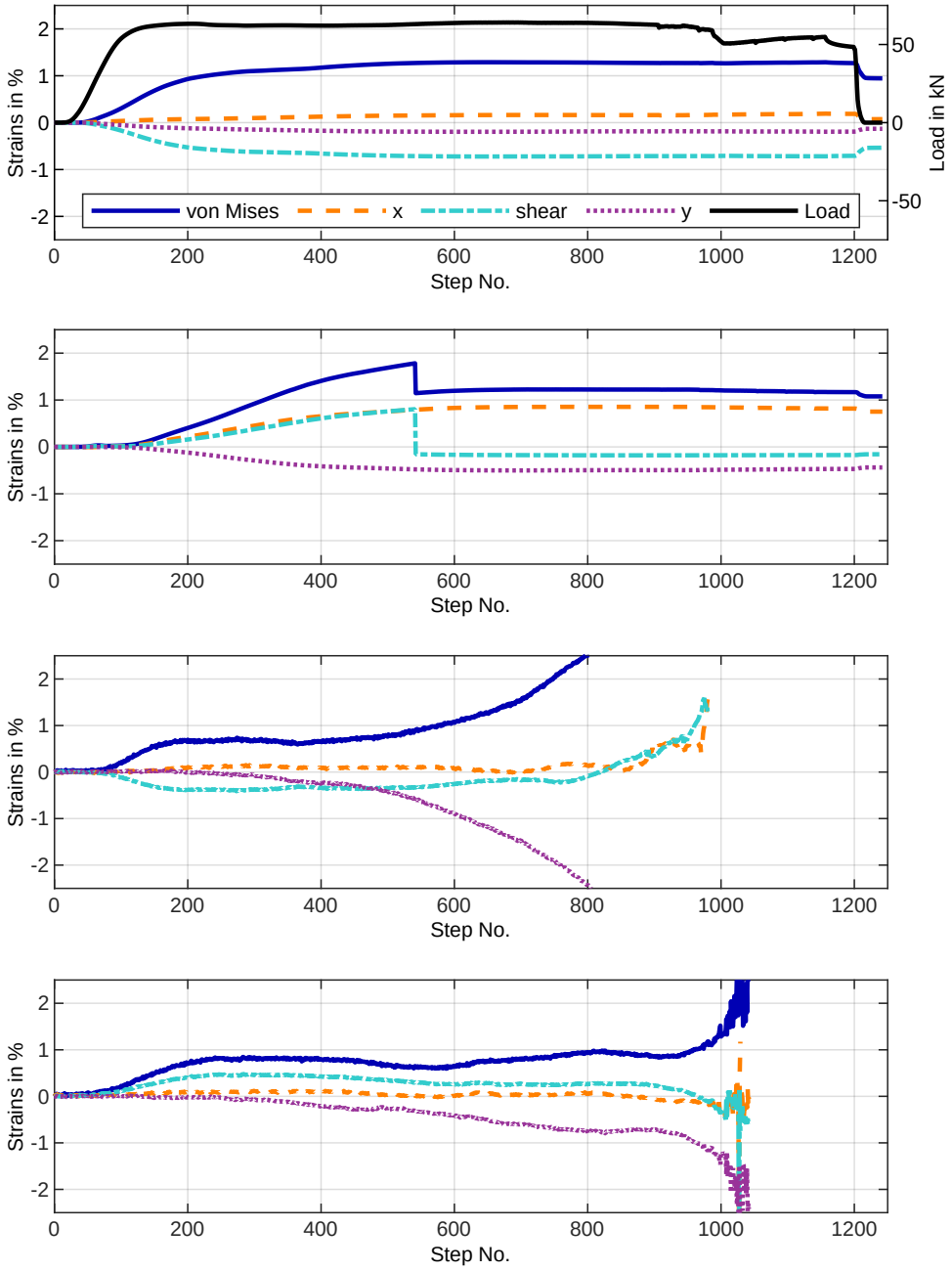

Fig. 6.31: Strains measured by strain gauges or DIC with position $a = 14$ mm, except for second graph at $a = 21$ mm: Timber-to-steel connection with aluminium fastener in beech LVL.

the tensile zone extends beyond the central axis of the fastener, which accounts for the significantly higher x-strains of almost 1%. In contrast, a comparison of graphs 1, 3 and 4, evaluated at comparable positions along the fastener axis, reveals similar strain magnitudes. However, this consistency only holds up to approximately step 500 for position 3 and step 900 for position 4. Position 3 shows a significant increase in y-strain, which, upon inspection of the image data, can be linked to the onset of overlapping wood fibres. Accordingly, the y- and von Mises strains for this case should not be interpreted as reliable measurements. Furthermore, Graph 4 shows a significant increase in strain from approximately step 900 onwards. Two factors may account for this behaviour. Firstly, minor disturbances due to wood fibres at the fastener edge, which have not yet crossed the fastener, contribute slightly. Secondly, the indentations caused by the steel plate pressing from above become pronounced enough that the cross-section in the right shear plane is locally reduced, resulting in noticeable necking and indicating the approaching failure as described earlier.

6.6 Discussion

6.6.1 Limits of Measuring Methods

When using DIC, the question generally arises as to how a speckle pattern is applied to the surface being measured. Currently, common methods involve first applying a base coat of white paint, followed by the speckle pattern using spray cans or specialised rolling tools with dots. One limitation to the use of this method is the effect of time. As the paint dries out, it gradually becomes more brittle and is more prone to cracking when subjected to significant amounts of elongation. An alternative method is to apply the speckle pattern using adhesive foil, as it was done in this case. Although the strain behaviour of the foil is not time-dependent, there are certain limit strains beyond which cracks may develop in the foil. Due to the multi-stage preparation process of the test specimens, such as sawing and fitting the timber parts, inserting the fasteners, gluing on the strain gauges and applying the speckle pattern, the use of foil was chosen. The main reason was that it was not time-dependent as both methods can lead to cracks at large deformations. The limits of measurability with the applied foil are shown in Fig. 6.32. Cracks and wrinkles begin to develop at different deformation stages during loading.

Fig. 6.32: Cracks in the tension zone and wrinkles in the compression zone of an aluminium fastener in beech LVL under large deformations.

The strain gauges were applied at locations experiencing relatively small strains and are thus suitable for capturing strains within the linear or moderately non-linear range. Their accuracy decreases when local deformations become large, as the adhesive layer may yield, the gauge may slip, or strain concentrations may exceed the elastic limit of the sensor. For very large strains, up to 50 %, the DIC measurement system is used. This technique is capable of tracking such large deformations, provided that the surface quality and speckle pattern meet the required criteria: the surface must be flat or lightly textured, well-prepared and painted, and the speckle pattern must have sufficient contrast and randomness for reliable correlation. Even under these conditions, uncertainties related to the tracking algorithm, surface reflections, or minor defects in the speckle pattern may introduce measurement artefacts. It should be noted that uncertainties inherent to the DIC method, such as interpolation errors, subset size selection, lighting conditions, and speckle quality, can influence the accuracy of the measured strains, particularly in regions of large deformation or steep strain gradients.

Because these high strain levels clearly lie within the non-linear range of material behaviour, any interpretation based solely on linear-elastic assumptions would be misleading. Non-linear effects, including strain hardening, local timber damage, and progressive yielding of the fastener, play a significant role. To obtain a physically consistent interpretation and to validate the experimental results, it is therefore proposed to complement the measurements with non-linear finite-element simulations or advanced material models capable of describing plasticity and damage evolution. Such modelling may provide a more realistic prediction of stress redistribution, connection ductility, and potential failure modes, and serves as a crucial step in confirming the plausibility of the measured strain levels.

6.6.2 Transfer to Circular Fasteners

As already described in the chapter on deformations, see chapter 5, the behaviour of external rectangular fasteners is not identical to that of conventional internal fasteners. The differences lie not only in the geometry, but also in the material properties, since the manufacturing processes can lead to inhomogeneity in circular cross-sections, whereas the thermally treated, hot-rolled rectangular fastener is more uniform. However, the focus of the study is not on precisely replicating typical fasteners, but rather on a broad parameter study that provides important insights into the various factors influencing connection behaviour. Nevertheless, the question arises as to the extent to which the results also apply to circular fasteners that are surrounded and fully embedded in wood. Due to the one-sided opening, the rectangular fasteners do not behave like circular fasteners relative to the specimen side plane, as one-sided movement is possible to a limited extent. However, it has been shown that the movement of the fastener in the z-direction only reaches significant magnitudes at larger deformations, and the results considered in the study mostly concern smaller deformation stages of 5–15 mm. The measured strains on the surface must therefore also be interpreted with regard to this movement. To investigate this question, it is assumed that the strain distribution remains consistent across the thickness of the fastener. Since the fasteners are mainly subjected to vertical loads, perpendicular to their axis and with increasing deformation along the axial direction due to the rope-effect, there are no components that apply stress to the fastener in the depth direction.

Based on the methodology and the conceptual cut through the interior of the connection, the results can nevertheless be used as qualitative comparative values. In any case, the qualitative strain distributions and highly stressed areas can be transferred to the axis of symmetry of circular fasteners and serve as reference values for further investigations and modelling or assist in the validation of numerical simulations.

6.7 Conclusion

Overall, the study demonstrates that fastener and also connection behaviour is strongly influenced by timber density, fastener material, and connection type. Although this phenomenon is well known, the study succeeded in breaking down these assumptions and contributing to an assessment outlining **how** the behaviour is influenced.

The present study on strains along the fastener axis has revealed clear differences between timber-to-timber and timber-to-steel connections, as well as the significant influence of fastener and timber material properties on the connection behaviour. Strain distributions evaluated in the global coordinate system provide an overall picture of the stress state, but a more accurate comparison with strain gauge measurements and DIC evaluations requires analysis in the local, deformation-aligned coordinate system. Circular evaluation areas offer a practical compromise, capturing the representative strain of the gauge region while maintaining sufficient spatial resolution.

Measurement uncertainty becomes particularly relevant for small strains below approximately 1%, especially near fastener ends where the camera field edges are approached. While DIC yields reliable results for larger strains, strain gauges remain indispensable for capturing small deformations with high accuracy. Analysis of von Mises strain distributions shows that timber-to-timber connections develop strain peaks at plastic hinges and, in high density timber products such as DVW, also in the shear planes. In contrast, timber-to-steel connections exhibit markedly higher strains in the shear planes, often exceeding yield and tensile limits, indicating pronounced plasticising. While the plastic hinge formation governs timber-to-timber connections, timber-to-steel connections are dominated by shear-plane yielding.

An examination of individual strain components reveals that axial strains dominate regions under tension, particularly between plastic hinges in high density timber products. Transverse strains, in y-direction, are generally small but highlight local compression or tension and are strongly influenced by timber fibres touching or pushing over the fastener surface in this study. Shear strains concentrate in the shear planes and increase with timber density, reflecting a transition from bending-dominated to shear-dominated fastener stress states. The material of the fastener also plays a critical role: aluminium fasteners yield earlier and develop higher local strains, demonstrating more ductile behaviour, whereas steel fasteners in high density timber products such as DVW reach very high local strains, emphasising the need to consider non-linear material behaviour and true strain for accurate assessment.

Von Mises strains in the shear planes of timber-to-steel connections generally follow a parabolic distribution along the fastener height under large deformations, characteristic of plastic hinge formation. Local effects such as steel plate indentation and timber fibre interference can create asymmetry in the evaluated strain distribution. Capturing true strains is therefore essential to fully describe strain magnitude and distributions at large deformations. Accurate assessment of strain therefore requires both global and local analysis, with careful consideration of measurement uncertainty, especially for

small deformations. These insights provide a deeper understanding of load transfer mechanisms and of failure modes including cross-section failure of the fastener.

From these findings, it can be concluded that connections made with higher-density timber may exhibit failure modes not accounted for by current design models. The EYM is based on plastic hinge formation, i.e. predominantly bending behaviour, and does not account for additional plastic failure mechanisms of the fastener. In fact, the current design model considers indeed the tensile capacity of the fastener within the framework of the rope effect calculation, while the complex stress state of the fastener itself is not taken into account. The increasing shear and axial force components acting on the fasteners when using higher-density timber therefore represent a type of loading that must be explicitly considered in the design of such connections. Connection failure resulting from this multiaxial loading must, under all circumstances, be prevented.

7 Fastener parameters

This chapter builds on the findings of the previous analyses, which have identified the critical regions governing potential fastener failure. With this understanding of where failure is most likely to occur, the next step is to clarify how such failure can be described in a quantitative way. Although the internal force distribution within fasteners can be determined, a consistent description of their behaviour under combined loading requires corresponding resistance values, which have not been sufficiently available so far. The present study therefore focuses on the systematic determination of interaction resistances for fasteners under combined normal and shear loading. By evaluating fully threaded screws, shanks of partially threaded screws, and bolts under varying inclination angles, characteristic load-bearing capacities are derived. These results provide previously unavailable reference values for NV interaction behaviour.

7.1 Introduction

7.1.1 Background

Previous investigations into stress distributions along fastener axes and the resulting potential failure locations show findings of clear practical relevance. While qualitative knowledge of critical zones and their respective loadings is available, the key question is how this knowledge can be effectively applied in design. New failure scenarios may arise. In particular, when comparing softwoods to hardwoods, different stress patterns appear, with shear and tensile components in the fasteners increasing significantly. Bending moment contributions are of a similar order of magnitude in both softwoods and hardwoods. However, in hardwoods, plastic hinges tend to develop earlier and at different positions along the fastener axis.

Two fundamental requirements therefore emerge for the design of connections. First, a clear understanding of the actual internal forces and moments acting within fasteners is needed, ideally described in terms of their distribution along the fastener axis. Second, appropriate resistance values must be established in order to be compared with the applied actions. While information on actions is partly available or may be assumed using existing prediction models, reliable resistance values under combined loading conditions are still lacking. At present, timber engineering has no comprehensive parameters that adequately describe the resistance of fasteners subjected to simultaneous load components.

Tension–Shear (*NV*) interaction can occur in sections of a laterally loaded fastener where the bending moment approaches zero. This situation may occur, for example, in partially threaded screws between two plastic hinges as the tension-stressed area of the fastener changes from one side of the shear plane to the other. In such cases, the normal forces and shear forces act together without significant influence from bending. This may lead to a critical loading condition. Observations of failed timber-to-timber connections show that screws can fail in the region of the shear planes where the bending moment is minimal, see Fig. 7.1a and 7.1b. This suggests that *NV* interaction plays an important role in the failure mechanism and underlines the need for a more detailed understanding of fastener behaviour under combined loading of normal and shear forces. In the worst case, this region can also be the weakest part of a fastener. Tensile tests show that, compared to other parts of the fastener, the shank-to-thread transition has a lower tensile capacity. The manufacturing process and the change of geometry are the main reasons for this reduction in strength.

To better understand the interaction between tensile and shear forces, tests are carried out under combined loading conditions. These experiments help to analyse failure mechanisms and improve understanding of fastener behaviour under idealised loading scenarios.

This chapter therefore focuses on the resistance side of one specific interaction: the combined action of tension and shear. A methodology and test setup for determining suitable parameters is presented, together with possible models for describing structural behaviour. These models may serve as a basis for the development of design approaches.

a. Partially threaded screw failed in shear plane with diameter d = 8 mm.

b. Fully threaded screw failed in shear plane with diameter d = 6 mm.

Fig. 7.1: Exemplary failures of screws in shear planes.

7.1.2 Relevant Connection Parameters

Accurate prediction of the behaviour and capacity of connections requires a sound understanding of the governing parameters. Numerous studies highlight the importance of these parameters; however, the scope and depth of existing investigations vary considerably. Some parameters are well established, while others remain insufficiently explored.

To address this, the following section classifies connection parameters into three groups, reviews existing knowledge, and outlines gaps that are addressed through new experimental approaches. These groups are:

- **Timber–fastener resistances**, e.g. embedment strength f_{h}, withdrawal parameter f_{ax}, head pull-through parameter f_{head}
- **Single resistances of fasteners**, e.g. tensile capacity F_{tens} or yield moment M_{y}
- **Combined resistances of fasteners**, e.g. reduced shear capacity $F_{\mathrm{shear,red}}$ under simultaneous action of normal force or preload

Each group is discussed in more detail below. Particular emphasis is placed on combined resistances, where this work presents new approaches and experimental results alongside the current state of research.

7.1.2.1 Timber–Fastener Resistances

The interaction between timber and fasteners has been studied extensively. Key parameters include withdrawal capacity, head pull-through resistance, embedment strength, friction in the shear plane, and timber properties such as density and moisture content. Reliable knowledge of these parameters is essential for accurate design and predictive modelling. The more precisely influencing factors are quantified, the more reliably the connection behaviour can be predicted.

Withdrawal and head pull-through capacities depend on density, moisture, screw geometry, thread type, steel grade, surface treatment, insertion method, and local wood features. Sandhaas and Blaß [85] demonstrated strong effects of wood species and moisture content, with considerable variation in hardwoods such as beech and oak. Frese [37] highlighted density variations in beech LVL, while Ringhofer [78] and Frese et al. [38] provided large datasets and regression models that capture the influence of embedment depth, screw diameter, and density. Brandner [16], Brandner et al. [17] extended these analyses to hardwoods, considering anatomy, thread-grain angle, predrilling, and group effects, and developed generic models for solid and laminated timber.

Westermayr and van de Kuilen [106] proposed a conceptual model for screws parallel to the grain in beech, ash, and spruce. The model incorporates species-specific mechanical properties, screw geometry, and insertion parameters, providing a predictive tool to improve design accuracy. Head pull-through studies [84] confirmed that geometry, insertion angle, and density strongly influence capacity, with deviations and low-density timber reducing resistance. Despite this progress, considerable scatter remains due to unquantified local factors, underlining the need for representative testing and standardised procedures [114, 115].

Embedment behaviour has also been widely investigated [32, 48, 88, 107]. Results show that stiffness and ultimate load depend strongly on density, moisture, fastener diameter, thread type, and load-to-grain angle. Methodology plays an important role, as specimen geometry, loading configuration, and evaluation procedures can influence outcomes [36]. Recent studies [86, 92, 91] further emphasise the variability caused by species, fibre orientation, fastener type, and loading direction. Overall, embedment is well documented and provides a solid basis for design.

In summary, timber–fastener interactions are quite well understood, and the effects of key parameters on connection performance are documented. This supports the

development of predictive models, while recognising that scatter from complex and partly unquantifiable factors remains. The next sections address fastener properties such as tensile strength and yield moment, and then move on to combined loading effects where significant research gaps persist.

7.1.2.2 Single Resistances

Fastener properties such as tensile capacity F_{tens} (or tensile strength f_{tens}) and yield moment M_y are well established. Shear capacity F_{shear}, in contrast, has only recently been investigated in detail, [4] and [9, 41].

The tensile strength and yield moment of self-tapping screws have been analysed recently using a large database [83]. Variability within series is low (below 5%), but differences between series are more pronounced: 12% for carbon steel screws and up to 28% for stainless steel screws with a nominal diameter of 8 mm. These variations indicate that, for detailed investigations or the determination of new parameters, the properties of screws need to be considered separately depending on manufacturing and material.

Sandhaas and Blaß [83] highlight several aspects that are particularly important when determining screw properties. Special attention should be paid to the free test length and the measurement of deformation capacity. In addition, the definitions and procedures for measuring the bending angle, including the yield angle at which the yield moment is determined, play a significant role. Sandhaas and Blaß [83] also note that the increased yield moment in the smooth shank area of partially threaded screws should be taken into account. Together, these points indicate areas where experimental procedures and standards could be refined to improve the accuracy and consistency of test results.

Earlier findings of Blaß et al. [14] demonstrate that the bending capacity of dowel-type fasteners is a critical parameter for the load-bearing behaviour of dowel-type connections. They propose modified equations to account for diameter effects, particularly for large fasteners, which lead to lower effective bending strengths. These results align with the observations by Sandhaas [83] that the yield moment can vary significantly depending on material and manufacturing, and they highlight the importance of accurate measurement procedures.

Steilner [97] proposes a method to determine the plastic bending angle of dowel-type fasteners. This approach further supports the importance of consistent and precise measurement techniques, particularly for large-diameter fasteners or partially threaded screws. The method allows for more accurate determination of the yield moment and helps reduce variability in experimental results, which is crucial for predictive modelling and practical design.

Experimental results and predictive models should also be considered in the context of existing standards. These include EN ISO 10666 [123], which specifies mechanical and functional requirements for drilling screws with tapping screw threads; DIN EN 409 [120], focusing on bending and torsional tests; EN 14592 [121], providing general rules for mechanical timber joints; and the European Assessment Document EAD 130118-01-0603 [127], which defines assessed performance for screws in timber constructions. Together, these documents provide a normative framework for experimental data and highlights areas where testing methods could be refined to account for material-dependent variability and combined loading effects.

In conclusion, the tensile strength and bending behaviour of self-tapping screws are relatively well understood. Established experimental methods and predictive models provide a reliable basis for determining these properties, despite some variability due to material, manufacturing, or test procedure. In contrast, the shear capacity of screws has received comparatively little attention in European research. Some regulations in North America, e.g. AISI S904 [109] provide test setups for shear loading, but corresponding standardised procedures are still limited for European conditions. This highlights a clear gap in knowledge and motivates the investigation of combined loading conditions, which are commonly encountered in timber connections but have not yet been systematically studied. The following section addresses these combined resistances and the interaction of forces and moments within fasteners.

7.1.2.3 Combined Resistances

The interaction of steel parameters under combined loading represents a largely unexplored area in the context of timber fasteners. Different combinations of internal forces, normal N and shear force V, and moment M can occur within a fastener during service, raising questions about its resistance under such interaction loads. The most relevant combinations include:

- *MNV*, e.g. in the shear plane of a steel-to-timber connection,
- *MN* in plastic hinges,
- *MV* in shear pane for failure modes with straight fasteners in very high density timber products, rarely occurring in typical timber connections,
- *NV* in shear planes of timber-to-timber connections.

These scenarios are particularly important because the presence of multiple interacting forces can lead to failure modes that are not captured by single-resistance tests. The following sections will present a methodology and an experimental approach developed to investigate one of these combined loading conditions, aiming to quantify the resistance of fasteners.

7.2 Literature Study on Tension-Shear Interaction Tests

Fasteners behave differently under combined loading compared to single forces. In steel structures, the interaction of tension and shear forces in threaded rods or bolts has been investigated, while in timber connections, tension and bending have mostly been studied separately. Experimental data on fasteners under combined loading remain limited due to the complexity of testing. Nevertheless, relevant test setups from the literature are summarised and compared in the following.

An overview of previous interaction tests and their results is provided in the DASt research report [40]. Thus, this section highlights only key aspects, discusses further literature, and relates the findings to the current research question on timber fasteners.

In the 1970s and 1980s, experimental evidence was needed to assess the influence of combined forces. The first combined force test that served as a basis for the German DIN standard was conducted by Hassler [44]. A tensile force was applied up to a defined proportion of the fastener's tensile resistance using a tensile testing machine. Subsequently, a shear force was applied via three plates to create a double shear plane. These tests were performed on threaded rods of grade 4.6, which were the easiest to handle.

The test setup of Knobloch and Schmidt [55] was similar, see Fig. 7.2. Specimens were first preloaded by the horizontal load Z in tension to a certain proportion of their tensile capacity. In a second step, shear forces were applied vertically via three steel plates (load F), producing a combination of tensile and shear stresses in the cross-section. The results in Fig. 7.3 suggest a quadratic relationship between tensile and shear ratios.

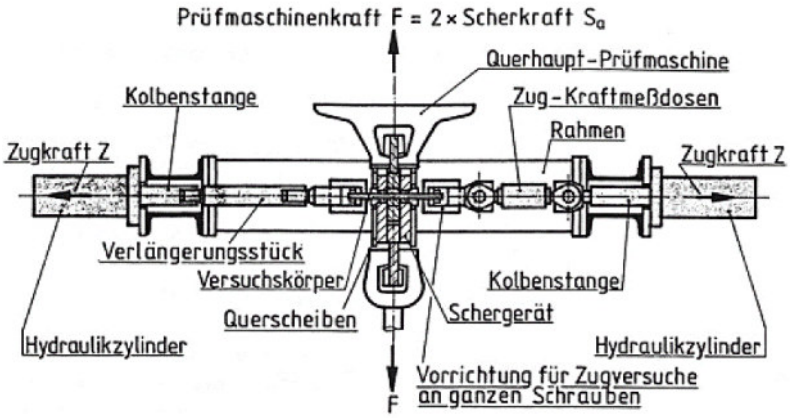

Fig. 7.2: Test setup from Knobloch and Schmidt [55].

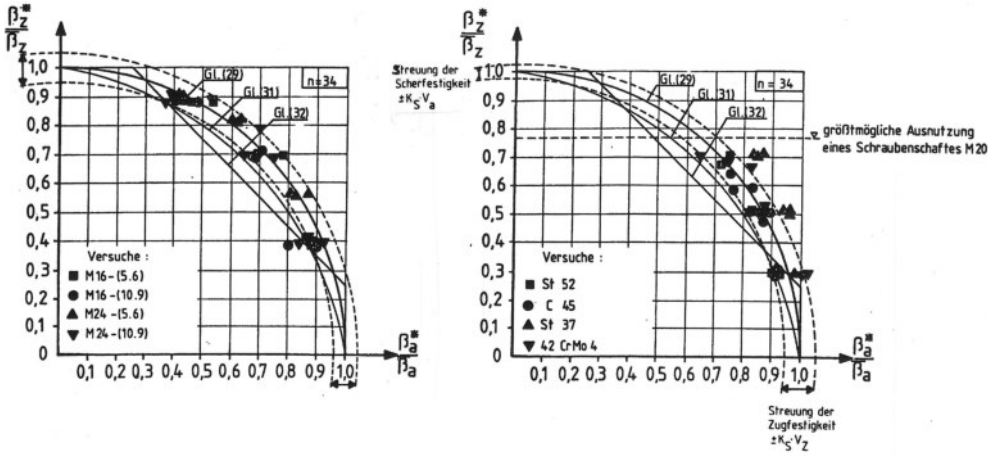

Fig. 7.3: Results from Knobloch and Schmidt [55]. Left: threaded rods, right: circular rods.

These tests included both unthreaded and threaded rods to distinguish shear plane effects in the shank and threaded part. Steel grades 4.6, 5.6, 8.8, and 10.9 were tested, yielding comparable results. Behaviour under combined tensile and shear loading was consistent with a quadratic correlation, which later informed standardisation, for example in DIN 18800-1:1990 [113].

$$\left(\frac{F_{\mathrm{t}}}{F_{\mathrm{td}}}\right)^2 + \left(\frac{F_{\mathrm{v}}}{F_{\mathrm{vd}}}\right)^2 \leq 1.0 \tag{7.1}$$

with

F_{t} Tensile force in kN
F_{td} Tensile resistance in kN
F_{v} Shear force in kN
F_{vd} Shear resistance in kN

Later on, the verification of simultaneously acting shear and tension forces in fasteners was adopted in Eurocode 3, Part 1-8 [117] as

$$\left(\frac{F_{\mathrm{t}}}{1.4 \cdot F_{\mathrm{td}}}\right)^2 + \left(\frac{F_{\mathrm{v}}}{F_{\mathrm{vd}}}\right)^2 \leq 1.0, \tag{7.2}$$

where F_{t} and F_{td} denote the applied and design tensile forces, and F_{v} and F_{vd} the applied and design shear forces, respectively.

Although some studies attempted to distinguish between load transfer via the shank and via the thread, Eurocode 3 provides only one interaction equation. In principle, the factor 1.4 could be increased to 1.8 for cases where the shear plane lies in the shank. However, the final equation. was chosen to represent the more critical case of the shear plane in the thread, making it the conservative option. This formulation, given in Eq. 7.2, remains unchanged in the current version of Eurocode 3 [117].

The statistical basis for Eq. 7.2 was provided by Snijder et al. [95], who evaluated available test results to derive strength functions and model factors for bolted connections. At the time, the database was limited, and concerns arose that a quadratic interaction curve might not be sufficiently conservative. Consequently, Eurocode 3 incorporated only the conservative formulation. In addition, the separate requirement $F_{\mathrm{t}} \leq F_{\mathrm{td}}$ must always be satisfied alongside Eq. 7.2. The applicability and transferability of the available test results to real installed bolts have since been questioned by

several authors [40, 72, 77]. These critical discussions highlight both the value of the conservative approach and the need for more representative experimental data.

A comparison of the Eurocode 3 formulation with other international standards, such as the British Standard [112], see Eq. 7.3, and the American National Standard [110], see Eq. 7.4, shows that similar approaches are adopted to describe the interaction of normal and shear forces in bolts or threaded rods. Both design codes include additional conditions, for example $F_\mathrm{t} \leq F_\mathrm{td}$ and $F_\mathrm{v} \leq F_\mathrm{vd}$ in [112]. They also neglect small amounts of one force component if the other is dominant, or apply additional safety and resistance factors [110].

Overall, while the mathematical formulations differ in detail, the underlying philosophy is consistent: conservative interaction equations are preferred, complemented by additional conditions to ensure robustness across different loading scenarios.

$$\frac{F_\mathrm{t}}{F_\mathrm{td}} + \frac{F_\mathrm{v}}{F_\mathrm{vd}} \leq 1.4 \tag{7.3}$$

$$\frac{F_\mathrm{t}}{F_\mathrm{td}} + \frac{F_\mathrm{v}}{F_\mathrm{vd}} \leq 1.3 \tag{7.4}$$

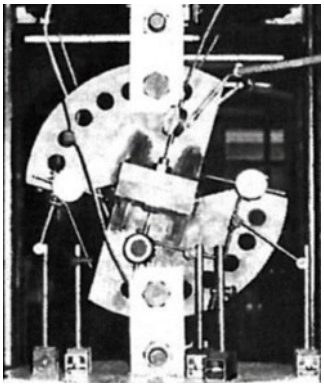

a. Shakir-Khalil and Ho [94].

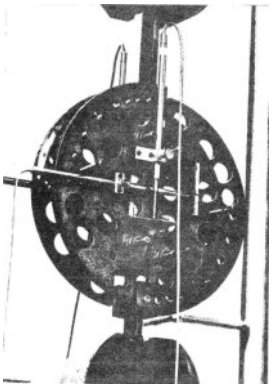

b. Ehlbeck and Siebert [31].

c. Steeve and Wingate [96].

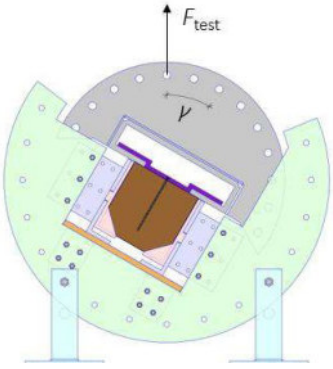

d. Ringhofer et al. [79].

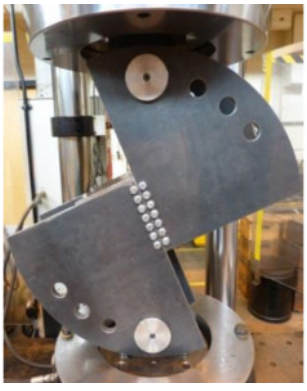

e. Pitrakkos et al. [72].

Fig. 7.4: Test setups for combined tension and shear forces from Shakir-Khalil and Ho [94] in 1979, Ehlbeck and Siebert [31] in 1984, Steeve and Wingate [96] in 2012, Ringhofer et al. [79] in 2021 and Pitrakkos et al. [72] in 2021.

Five test configurations using circular sector plates are shown in Fig. 7.4. Their common principle is to vary the angle between tension and shear force by rotating sector plates with prefabricated holes, ensuring that the load passes through the specimen centre. The main differences lie in the number of fasteners tested (two in Shakir-Khalil and Ho [94], one in Steeve and Wingate [96] and Pitrakkos et al. [72]), the specimen type (single fasteners in setups a and c, withdrawal-shear loading of nails in timber in b, and anchorage-type connections in d), and the evaluation (setup a averages over two specimens, potentially reducing scatter).

Shear and tension tests on 142 A325 and A490 bolts by Kulak et al. [60] confirmed an average shear-to-tensile strength ratio of 0.62 with a standard deviation of 0.03, independent of bolt grade. Results did not depend on bolt diameter or the position of the shear plane (thread or shank). Longer bolts showed slightly higher capacities due to bending and an increased effective shear area. The data aligned well with previous interaction curves, essentially equivalent to Eq. 7.1, thus supporting the quadratic formulation.

More recent studies by Renner and Lange [76, 77] addressed discrepancies between threaded and smooth-shank fasteners. Their test setup allowed six different loading angles in the range 0°–90°. Double shear tests are included in the test programme, reducing overestimation effects observed in single shear tests. Results showed that threaded parts in the shear plane conform to the quadratic interaction in DIN 18800-1 [113], whereas smooth-shank fasteners deviate significantly, especially for higher-strength, lower-ductility bolts. Based on these findings, a modified interaction criterion was proposed:

$$\left(\frac{F_{\mathrm{t}}}{F_{\mathrm{td}}}\right)^{1.5} + \left(\frac{F_{\mathrm{v}}}{F_{\mathrm{vd}}}\right)^{1.5} \leq 1.0 \tag{7.5}$$

This proposal, also adopted in the DASt research report [40], reflects the need for refined formulations to capture the behaviour of different bolt types under combined loading.

In order to identify a suitable test setup for fasteners typically used in timber engineering, several options are available. As previously described, the load can be applied at an angle to the fastener axis, allowing the resulting failure load to be vectorially split into tensile and shear components. Alternatively, the load components can be applied

sequentially, with tension applied first to reach a defined level of tensile utilisation, followed by shear loading to determine the remaining shear resistance. Reversing the order of load application is theoretically possible, but impractical, since an initial shear force would deform the specimen to such an extent that the subsequent application of a tensile load would no longer be feasible. One advantage of sequential loading with tension applied first is that different levels of tensile utilisation can be predefined and tested. However, this requires two shear planes and a biaxial loading device.

The test setups developed by Renner and Lange [76, 77] addressed this challenge with three different constructions, partly to reduce the weight of the apparatus. Earlier studies by Bilderbeek [8] and Chesson et al. [21] used large and complex devices to vary the load angle, but these setups were not well suited for practical testing of timber fasteners. Chesson demonstrated that for high-strength bolt materials the ratio of shear-to-tensile capacity decreases, with interaction curves lying below those of lower-strength bolts. Bilderbeek [8] showed that preload had no significant influence on load capacity, an effect that can be considered negligible in timber fasteners, as prestressing rarely occurs in practice. The interaction between tensile and shear forces has therefore been confirmed in numerous studies, though exclusively for bolts or threaded rods in steel applications. As shown by Chesson et al. [21], high-strength materials tend to amplify the interaction effect, suggesting that hardened screws are of particular interest.

Whether these findings can be transferred to timber fasteners remains uncertain. Their smaller diameters, different material properties, and more complex geometries, e.g. self-tapping screws, may lead to different interaction behaviour. To address this question, the following section introduces an experimental programme specifically developed for timber fasteners.

7.3 Tension-Shear Tests on Timber Fasteners

To investigate the tension-shear interaction of fasteners typically used in timber engineering, a dedicated experimental programme was developed. The aim is to determine how tensile and shear forces interact in timber fasteners, which are often thinner and have more complex cross-sectional shapes than the steel bolts studied in previous research. Existing test setups from steel construction were adapted to account for the lower expected loads, smaller diameters, and typical geometries of timber fasteners, ensuring meaningful and transferable results. Preliminary considerations based on

the experimental work of Renner and Lange [76, 77] and the DASt research report [40] are summarised in Tab. 7.1.

Table 7.1: Preliminary considerations for investigations, based on findings in [76].

Fasteners in steel design	**Fasteners in timber design**
Tensile and shear capacities of screws influence each other when occurring simultaneously	Valid
Decisive: thread or shank in the shear plane	Influence of geometry, screw
Diameter: no noticeable influence	Influence of hardened cross-sections of screws
No influence of steel strength of shear plates	Valid
No effect of preload on maximum load capacity under combined tensile and shear stress	Preload is irrelevant
Clamping length of the screw: very little influence	Valid
Influence of strength class: ratio of shear to tensile load-bearing capacity changes	Degree of hardness and differences between manufacturers
Influence of shear capacity: single- or double-shear	To be analysed

In general, the method of load application plays a decisive role when selecting the test setup. Various approaches have been explored in previous studies and are briefly illustrated in Fig. 7.5. One option applies a primary load to a defined level while gradually increasing a secondary load, as shown in Figs. 7.5a and b. Alternatively, the contributions of each load component can be varied flexibly (Fig. 7.5c), or both loads can be increased simultaneously (Fig. 7.5d). The chosen procedure corresponds to variant d, reflecting the simultaneous occurrence of normal and shear forces in practical applications. By synchronously and proportionally increasing both load components, the setup captures the full interaction behaviour and identifies the onset of failure across the entire envelope. The test rig is compact and lightweight, facilitating handling and minimising undesired effects, while its modular design adapts to different connector types. The angular position of the load can be systematically varied, enabling the assessment of multiple load combinations and their influence on capacity. Load transfer occurs through pinned, well-defined boundary conditions, ensuring a clear load path and high reproducibility of results.

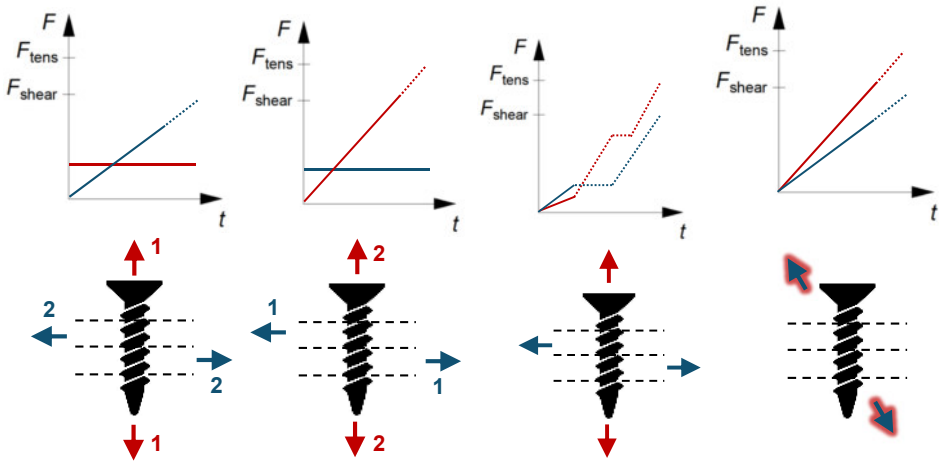

a. Tensile preload and secondary shear load.

b. Shear preload and secondary tensile load.

c. Flexible load application.

d. Simultaneous load increase.

Fig. 7.5: Load application variants for tension–shear interaction.

To accommodate the lower loads typical of timber fasteners and ensure flexibility across different fastener types, a variable test setup is developed (Figs. 7.6 and 7.7). Unlike the multi-component arrangements used by Renner and Lange [76] to test several angles simultaneously, this rig allows all load angles to be achieved on a single apparatus. The setup consists of four circular sector plates mounted in pairs on central steel blocks. Each plate features a hole pattern that enables variation of the load application angle. A single fastener is tested per experiment to provide accurate individual results rather than averages, as in Shakir-Khalil and Ho [94]. The load angle is varied from 0° to 90° in eight increments of 11.25°. This fine resolution ensures that differences in axial resistance between fastener types, such as screws versus dowels, are adequately captured. The design also minimises the influence of the rig on the measured results while allowing pure tensile and pure shear tests as needed.

A sleeve system is developed to enable testing of different fastener cross-sections within a single setup. The sleeves can be adjusted to match fasteners with outer diameters between 6 –16 mm. They transfer the shear load, particularly for screws, through an intermediate element that protects the test rig from damage. The intermediate element can be replaced if wear or deformation occurs, for example due to compression of the thread flanks. The sleeves are inserted into steel blocks, which are rigidly connected to the circular sector plates using a bolted, non-slip connection.

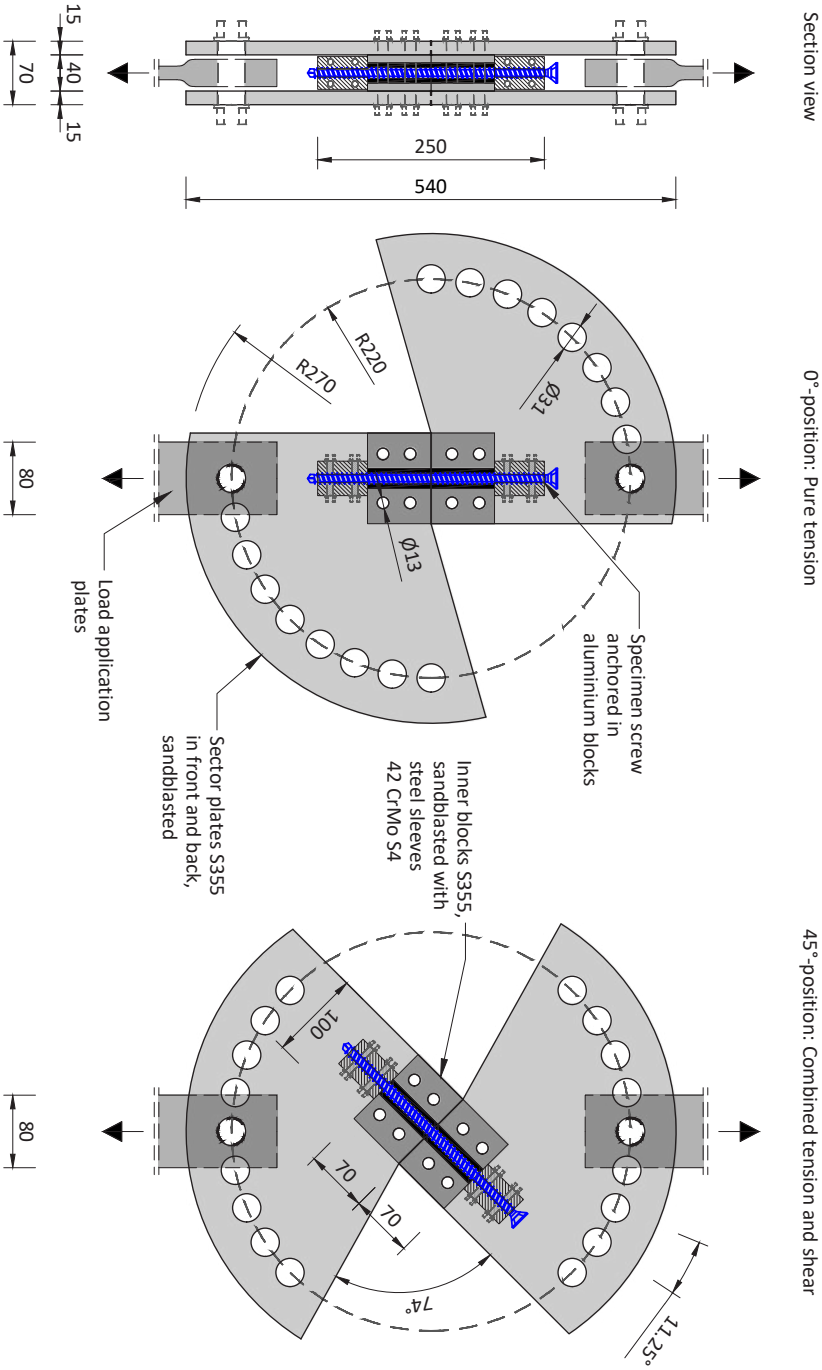

Fig. 7.6: Schematic test setup on an exemplary screw with $d = 12$ mm for tension, shear and combined tension and shear forces, in mm.

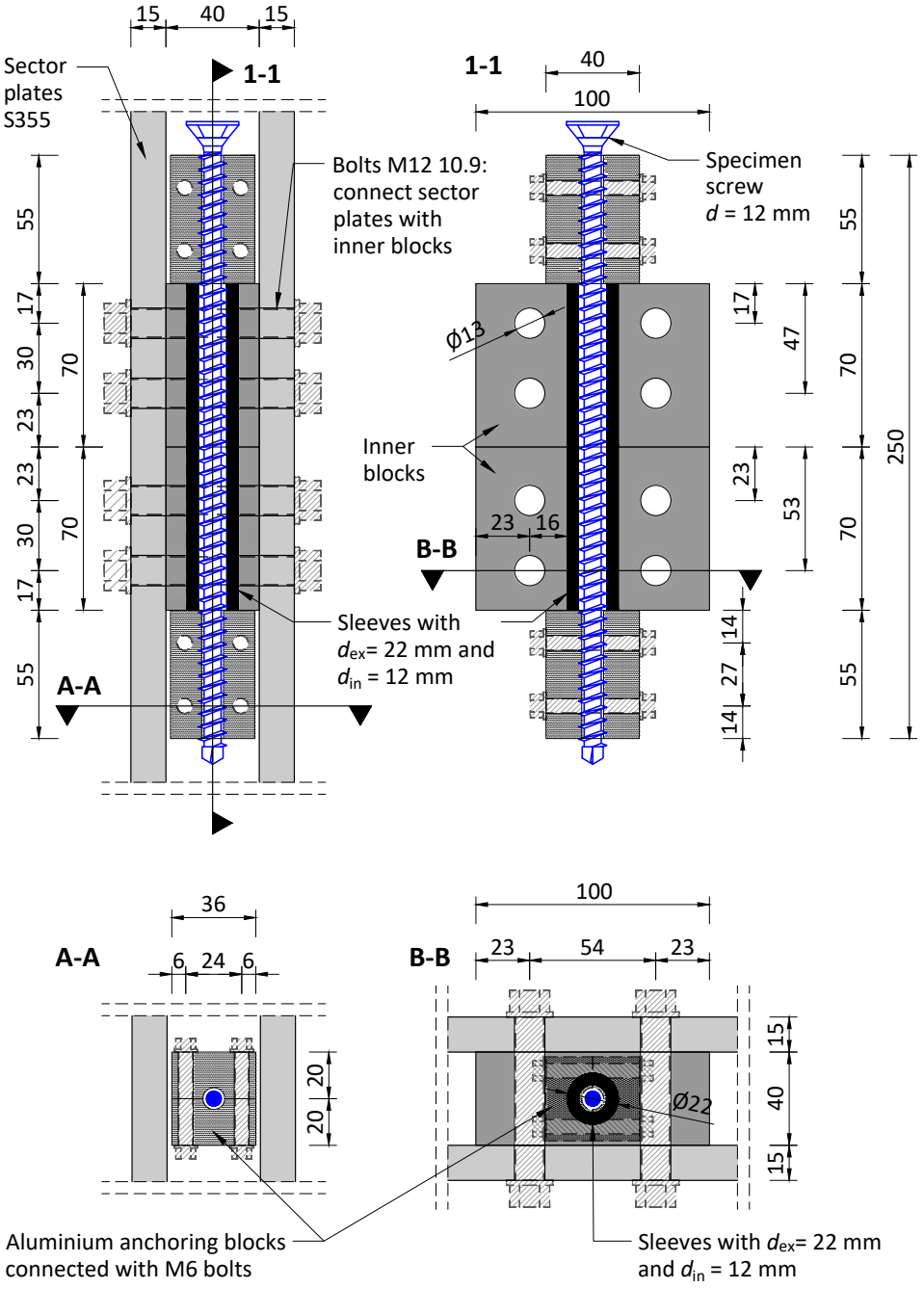

Fig. 7.7: Schematic test setup with detail in the centre on an exemplary screw with d = 12 mm for tension, shear and combined tension and shear forces, top views of bolts are not shown, in mm.

Fasteners are anchored to ensure reproducible and symmetric load application. Bolts are secured with washers, while screws require a system independent of the head shape. This is achieved using aluminium blocks with a prefabricated negative imprint of the screw thread, providing uniform grip. The blocks have a borehole pattern allowing two blocks to be connected, and a perpendicular half-hole is drilled at the contact surfaces, slightly larger than the core diameter of the screw. A dummy screw is inserted during assembly to create the imprint, which allows the subsequent insertion of the test screw of the same type with precise fit and alignment.

To ensure non-slip load transfer, the surfaces of both the sector plates and the inner aluminium blocks are sandblasted. The test rig is assembled by first mounting the central components (see Fig. 7.7) and ensuring a tight fit. These are then inserted between the sector plates and secured using M12 bolts to complete the non-slip connection.

Pretests on aluminium anchoring

Tensile tests ensure that the screws are securely anchored in the aluminium blocks. To achieve this, two aluminium blocks are first clamped together, holes are drilled for the clamping bolts, and a hole is drilled in the contact surfaces, creating a half-hole in each block. The hole diameter is adapted to the screw being anchored and lies between its core diameter and outer diameter, ultimately determining the proportion of thread flanks engaged in the aluminium. The test programme and selected diameters are listed in Tab. 7.2.

A screw is inserted into the hole, embedding its thread into the inner wall of the half-holes. The height of the aluminium blocks, and thus the anchoring length, is given in Tab. 7.2. The tests aim to achieve tensile failure of the screws in all cases. Fig. 7.8 shows the schematic test setup for a screw with diameter $d = 12$ mm. All dimensions follow the setup shown in Fig. 7.6 to reproduce the anchoring conditions in the final mounted configuration. The imprint of the screw thread in the aluminium blocks is illustrated in Fig. 7.9.

Several screws are required to successfully insert a screw through the full length of the aluminium block. Some screws fail due to reaching their torsional resistance, causing the head to tear off. After removing these screws, a new screw continues the imprint of the thread. When comparing the quality of the imprints, noticeable differences appear. For the 6 and 8 mm screws, the imprints show a clear and sharp pattern. However,

Table 7.2: Test parameters for tensile tests of screws anchored in aluminium blocks.

number of tests	nominal diameter d_{nom} in mm	core diameter d_{core} in mm	aluminium length l_{alu} in mm	hole diameter d_{hole} in mm
3	6	3.9	24	4.5
3	8	5.2	32	6.0
3	12	7.3	55	9.3

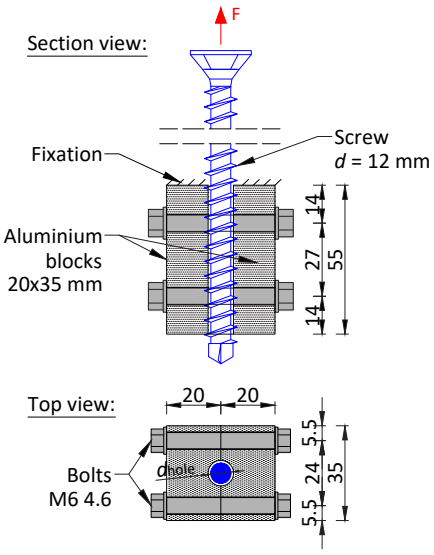

Fig. 7.8: Schematic test setup for pull-out tests on an exemplary screw with $d = 12$ mm, in mm.

in one case, a deviation of the borehole from the originally planned axis is observed (top left aluminium blocks in Fig. 7.9). Due to this inclination, the screw thread does not fully engage the flanks along the bottom part. For screws with a diameter of $d = 12$ mm, the borehole is enlarged from 8.5 mm to 9.3 mm during manufacturing due to high insertion resistance. The first attempt with the smaller borehole would have aligned with the ratio d_{hole}/d_{core} of the other screws, i.e., 1.15–1.16. Using the larger borehole diameter results in comparable ratios of d_{hole}/d_{nom}, i.e., 0.75–0.78, for all three screw sizes, leading to manageable insertion moments. Nevertheless, differences in imprint quality are remarkable when comparing the three manufactured anchoring block pairs for the 12 mm screws. The pair with the sharpest pattern in the middle is manufactured in multiple separate steps, with the borehole enlarged stepwise. In contrast, the other two block pairs are manufactured faster, resulting in a

blurred contour caused by thread parts deforming and tearing off during insertion. The test configuration shown schematically in Fig. 7.8 is realised using a manufactured steel U-profile, held in place by two additional profiles, see Fig. 7.10.

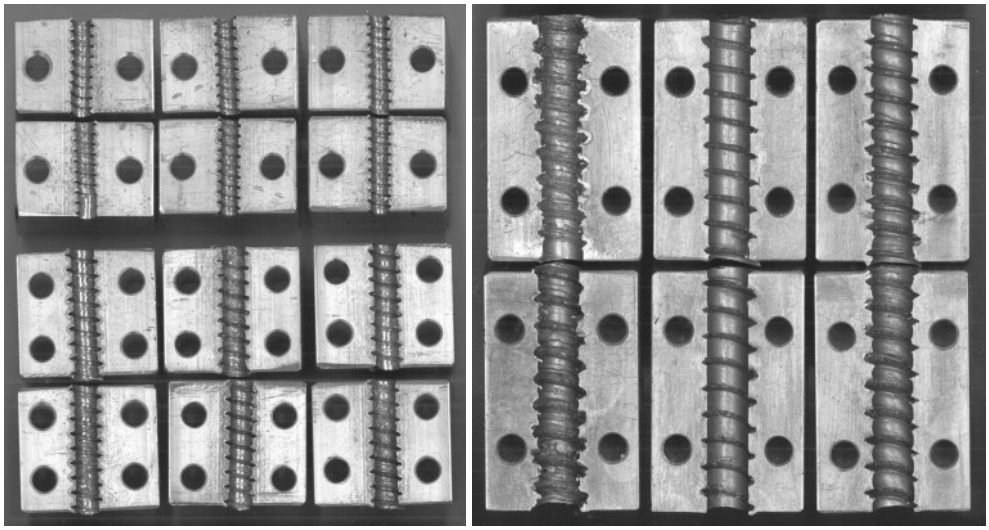

Fig. 7.9: Section views of manufactured aluminium anchoring blocks for screws with $d = 6$ mm (left top), 8 mm (left bottom) and 12 mm (right).

Results on aluminium anchoring

The aim is to reach the tensile capacity of the fasteners to ensure a secure anchoring of the screws. This is achieved in all cases. The maximum loads observed in the tests correspond to or reach the tensile capacity of the screws; results are summarised in Tab. 7.3 and Fig. 7.11. Since all screws fail due to tensile failure, the anchoring length is sufficient to guarantee a secure position of the screws within the interaction assembly. These pretests confirm that all fasteners are securely anchored, ensuring consistent load application in subsequent tension–shear tests.

7.3.1 Material and Methods

The fasteners examined primarily consist of fully threaded screws with diameters of 6, 8 and 12 mm, M12 4.8 bolts, and partially threaded screws with a nominal

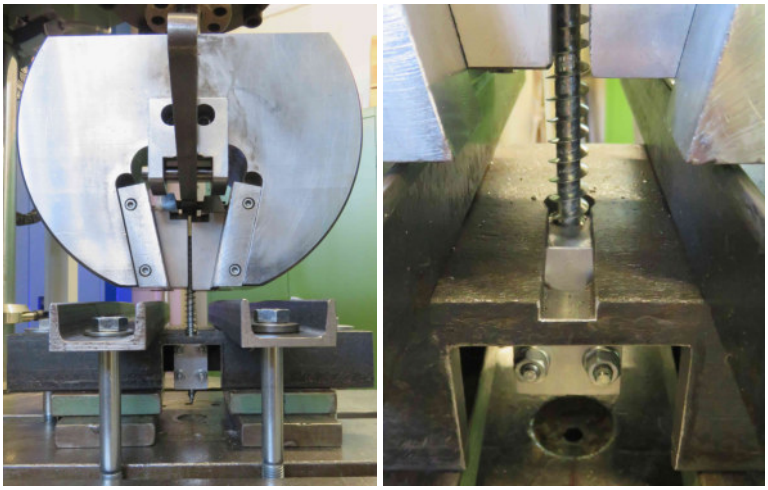

Fig. 7.10: Exemplary test setup for screw anchoring in aluminium blocks on the left and detail of manufactured steel U-profile on the right.

Table 7.3: Results of tension tests of screw anchoring in aluminium blocks.

Test name acc. to screw diameter	F_{max} in kN	Mean value in kN
6a	14.4	14.4
6b	14.5	
6c	14.3	
8a	25.7	25.6
8b	25.6	
8c	25.4	
12a	51.0	50.0
12b	50.2	
12c	48.8	

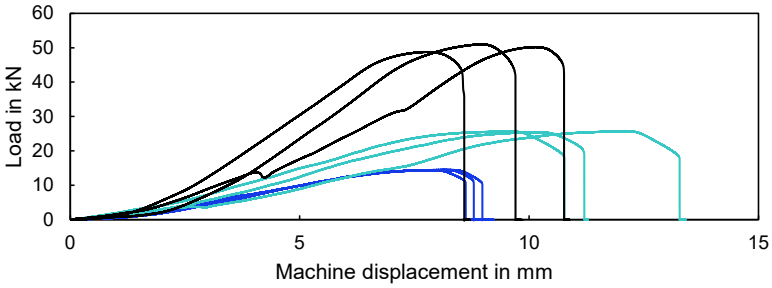

Fig. 7.11: Tension test results on screw anchoring in aluminium: 6 mm, 8 mm, 12 mm.

diameter of 8 mm. Examples of sections of the fully threaded screws, which constitute the majority of the tests, are shown in Fig. 7.12. The manufacturing process of the fully threaded screws differs depending on diameter. For smaller diameters (6 and 8 mm), threads are produced by *thread rolling*. In this process, a cylindrical screw blank passes between rolls with a negative profile of the desired thread. Material is displaced laterally, forming the thread on the blank without cutting. For the 12 mm screws, threads are produced by *thread forming by rolling*. Here, the blank passes through rolls with a positive thread profile, pressing the material into the desired shape. Like thread rolling, this is a chipless process that produces durable, high-quality threads. Both methods create threads through plastic deformation rather than cutting. The difference lies in the surface and formation: thread rolling “pushes up” the thread from a negative profile, whereas thread forming presses the material into a positive profile. This difference is visible on the thread surface, with thread forming leaving a smoother finish, as shown in Fig. 7.12c.

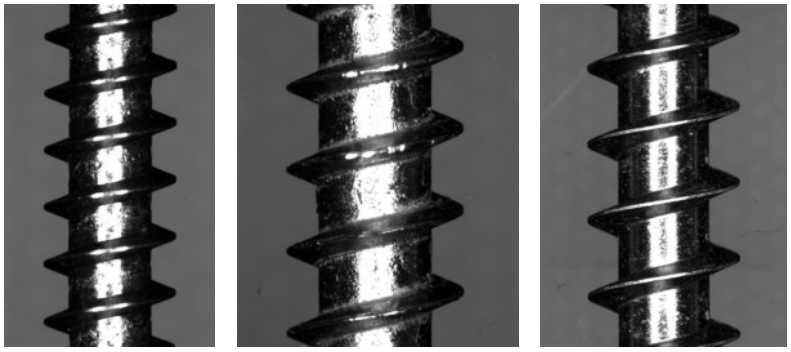

a. 6 mm. b. 8 mm. c. 12 mm.

Fig. 7.12: Sections of tested fully threaded screws.

The tests are conducted displacement controlled with a speed of 1 mm/min. During the test, the applied load is recorded and displacements in the area of the shear plane are measured. Cable displacement transducers are used to capture the relative movements of the circular sector plates at the shear plane. The measuring lengths are 500 mm. To ensure high accuracy, a minimum measuring length of 100 mm is maintained, and the transducers are mounted at the appropriate positions on the circular sector plates. Displacements measured perpendicular to the shear plane (*perp*) represent the opening of the shear plane, while displacements measured parallel to the shear plane (*para*) correspond to shear displacements along the plane, see the exemplary test setup and measuring devices in Fig. 7.13. It should

be noted that these displacement measurements do not directly reflect the actual deformation of the tested fasteners. Slip and elastic deformation from the test setup and the installation of the fastener are included in the readings. Nevertheless, the measurements allow for qualitative comparisons within the test series and enable the observation and description of deformation and rotation of the test setup.

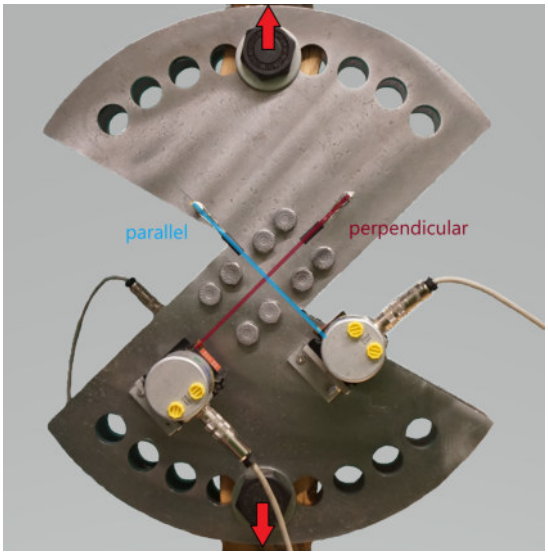

Fig. 7.13: Test setup and cable displacement transducers, mounted on both sides.

The focus of this study is on reproducing realistic boundary conditions rather than determining pure material properties of the fasteners. The following section therefore describes specimen preparation and the test configuration, with particular attention to screw diameters, manufacturing processes, and the load-transfer mechanism. The experimental programme with fully threaded screws includes diameters of 6 mm, 8 mm, and 12 mm. Special consideration is given to the manufacturing process, as thread rolling can influence mechanical behaviour through variations in surface hardness, residual stresses, and thread geometry. The screws are inserted into the sleeves such that the outer diameter of the screw matches the inner diameter of the sleeve. As a result, contact occurs exclusively between the thread flanks and the inner surface of the sleeve, meaning that shear forces are transmitted solely via the flanks. This configuration is chosen intentionally, as it reflects typical conditions in steel-to-timber connections, where similar or even greater hole clearances are present. Although fully embedding the screws in a negative mould would allow shear forces to also act on

the screw core, this approach is intentionally avoided, as it would not represent typical installation conditions. Consequently, the interaction test provides a configuration-dependent test parameter rather than a direct material property, characterising the combined behaviour of the partially supported screw and the surrounding sleeve under tension and shear. In this way, the experiment captures the load-transfer mechanism as it occurs in practice, ensuring high practical relevance and enabling the results to inform design model calibration and numerical validation.

7.3.1.1 Test Programme

To investigate different effects and influences, a test programme is carried out for fully threaded screws and additional tests are carried out with bolts and partially threaded screws. The aim here is to investigate geometric differences and also to investigate the influence of the hardened shank cross-section in comparison to bolts. The entire test programme is listed in Tab. 7.4.

Table 7.4: Test programme and number of tests for fully and partially threaded screws and bolts.

	Fully threaded screws			Partially threaded screws	Bolts 4.8
α / d	6	8	12	8	M12
0° (Tension)	3	5	3	2	2
11.25°	4	-	-	2	3
22.5°	5	8	5	3	3
45°	10	9	4	3	2
67.5°	8	5	3	3	3
90° (Shear)	8	16	5	3	3
$\sum$	38	43	20	16	16

7.3.2 Evaluation

In addition to the pure tensile stress (α= 0°) and shear stress (α= 90°), individual intermediate stages are also tested and evaluated. This means that the screw is subjected to an interaction stress from tensile and shear. To evaluate the two components, the shear force component parallel, F_V, and tensile force component perpendicular, F_N,

to the shear plane are used according to Fig. 7.14. The angle α describes the applied load angle.

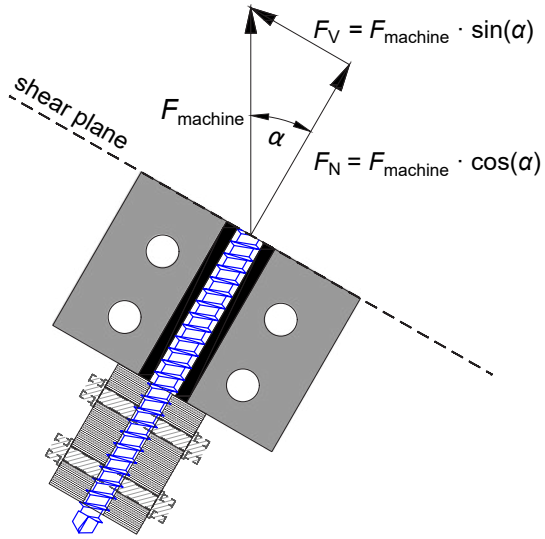

Fig. 7.14: Schematic illustration of force component distribution.

7.4 General Results and Discussion

7.4.1 Interaction Analysis

The capacities of fasteners subjected to combined normal force N and shear force V are analysed using a MATLAB routine. The input comprises force–displacement measurements from tests carried out at several prescribed loading angles α, each corresponding to a distinct combination of N and V. For each test, the maximum applied force F_{max} is taken directly from the experimental record and resolved into its normal and shear components:

$$F_N = F_{max} \cos \alpha, \qquad F_V = F_{max} \sin \alpha, \tag{7.6}$$

where α denotes the loading angle measured from the *N*-axis.

For each angle group, mean values of F_N and F_V are computed as

$$\overline{F_\mathrm{N}}(\alpha) = \frac{1}{n_\alpha} \sum_{i=1}^{n_\alpha} F_{\mathrm{N},i}(\alpha), \qquad \overline{F_\mathrm{V}}(\alpha) = \frac{1}{n_\alpha} \sum_{i=1}^{n_\alpha} F_{\mathrm{V},i}(\alpha), \tag{7.7}$$

where n_α denotes the number of tests performed at angle α.

The forces are then normalised with respect to the mean values under pure tension (0°) and pure shear (90°):

$$F_\mathrm{N} = \frac{F_\mathrm{N}(\alpha)}{\overline{F_\mathrm{N}}(0^\circ)}, \qquad F_\mathrm{V} = \frac{F_\mathrm{V}(\alpha)}{\overline{F_\mathrm{V}}(90^\circ)}. \tag{7.8}$$

This yields a dimensionless interaction diagram in the $(F_\mathrm{N}, F_\mathrm{V})$ plane, representing the ultimate load-bearing capacity under combined *N*-*V* loading. Several analytical interaction criteria are subsequently fitted to the normalised data:

Quadratic fit:

$$F_\mathrm{N} = a F_\mathrm{V}^2 + (-1 - a) F_\mathrm{V} + 1 \tag{7.9}$$

The quadratic model follows the general form

$$y = a\,x^2 + b\,x + c, \tag{7.10}$$

with boundary conditions enforced as

$$b = -1 - a, \qquad c = 1, \tag{7.11}$$

ensuring that the curve passes exactly through the point $(0, 1)$ corresponding to pure normal loading. In the MATLAB routine, only the curvature parameter *a* is optimised, while *b* is automatically determined by the boundary condition. This formulation allows the model to capture the interaction between normal and shear forces with a single degree of freedom.

Cubic fit:

$$F_{\mathrm{N}} = p_1 F_{\mathrm{V}}^3 + p_2 F_{\mathrm{V}}^2 + p_3 F_{\mathrm{V}} + 1 \tag{7.12}$$

The cubic model generalises the quadratic form by adding an additional degree of freedom, allowing for more flexibility in capturing non-linear interactions between normal and shear forces. The constant term is fixed at 1 to ensure the curve passes through pure normal loading, while the coefficients p_1, p_2, and p_3 are optimised based on the normalised test data.

Circular criterion:

$$F_{\mathrm{N}}^2 + F_{\mathrm{V}}^2 = 1 \tag{7.13}$$

The circular model represents a unit circle,

$$y = \sqrt{1 - x^2}, \tag{7.14}$$

which is suitable for distributions where the normalised forces maintain an approximately constant distance from the origin. This provides a geometrically intuitive interaction criterion between normal and shear forces.

Elliptical fit:

$$\left(\frac{F_{\mathrm{N}}}{a}\right)^2 + \left(\frac{F_{\mathrm{V}}}{b}\right)^2 = 1 \tag{7.15}$$

Here, *a* and *b* are free parameters defining the shape of the ellipse. The ellipse is centred at the origin and not rotated, allowing it to be stretched or compressed along the *x*- or *y*-axis as required. Typically, *a* and *b* are adjusted to best fit the normalised experimental forces. Only the upper-right quadrant of the ellipse is evaluated, considering positive values of F_{N} and F_{V}.

Superellipse fit:

$$|F_{\mathrm{N}}|^\beta + |F_{\mathrm{V}}|^\beta = 1 \tag{7.16}$$

The parameters are normalised such that *a*=*b*= 1. The exponent β controls the roundness or squareness of the curve: $\beta = 2$ corresponds to a circle, while $\beta > 2$ yields increasingly rectangular or pointed shapes. This model is particularly useful for capturing interactions that are neither purely circular nor purely elliptical. Note that the MATLAB implementation evaluates only the positive quadrant, i.e., $F_N \geq 0$ and $F_V \geq 0$, to simplify the computation.

The coefficient of determination R^2 is computed using orthogonal residuals for all model curves. Instead of measuring deviations only in the vertical (y) direction, the shortest Euclidean distance d_i from each data point (x_i, y_i) to the discretised curve is employed:

$$d_i = \min_t \sqrt{\big(x_i - x(t)\big)^2 + \big(y_i - y(t)\big)^2}, \tag{7.17}$$

where *x(t), y(t)* is a parametrisation of the curve, and *t* spans a sufficiently dense discretisation of the curve (e.g. $x(t) = a\cos(t),\ y(t) = b\sin(t)$ for an ellipse). This procedure approximates the true orthogonal projection numerically.

The R^2 value is then defined as

$$R^2 = 1 - \frac{\sum_{i=1}^{n} d_i^2}{\sum_{i=1}^{n} \left[(x_i - \bar{x})^2 + (y_i - \bar{y})^2\right]}, \tag{7.18}$$

with $\bar{x}, \bar{y}$ denoting the mean coordinates of all data points. The denominator represents the total variance around the centroid of the dataset.

This distance metric is applied consistently for all models, whether they are explicit functions *y(x)* (e.g. polynomial, exponential) or implicit curves (circle, ellipse, super ellipse). By using orthogonal distances, the R^2 values are directly comparable across different functional forms. For implicit curves, vertical deviations would be misleading since multiple *y* values may exist for some *x*. Even for *y(x)* curves, orthogonal distances provide a more accurate estimate of the fit error, particularly in steep regions.

Fig. 7.15 shows an exemplary dataset illustrating the normalisation procedure and the resulting fit for one of the regression models, including the corresponding R^2 value. This figure serves purely as a demonstration of the method and does not represent all experimental results.

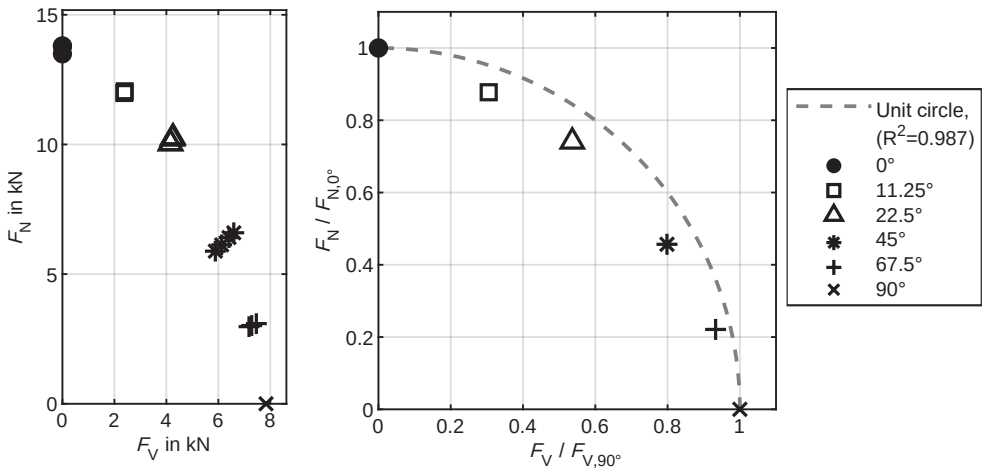

a. Force diagram.

b. Normalised force diagram with mean values per angle group.

Fig. 7.15: Exemplary regression visualisation of 6 mm screw with unit circle for comparison.

7.4.2 Tensile and Shear Capacities

As an initial evaluation and results, the well-known parameter, the tensile capacity at 0°, and the shear capacity at 90°, is addressed. These two parameters are used as reference values for the subsequent normalisation of the individual components at other intermediate angles. Results are listed in Tab. 7.5. Since screws (d_i = 6 and 8 mm) of different lengths, i.e. from different production batches, are used in the tests on the functionality of the aluminium anchoring, differences in tensile strength can be attributed to this, see Tab. 7.3. The 12 mm screws were all taken from the same screw package and the results are comparable. An initial conclusion from this is that no effects from friction or eccentricity influence the results of the test setup and that the setup itself is suitable for the intended investigations. In typical steel design, the ratio of shear to tensile stress is given as $1/\sqrt{3}$ (= 0.58) [116], which, however, refers to the yield strength. In this case, the maximum loads achieved and their ratio values are determined.

Table 7.5: Results for tension (0°) and shear tests (90°) on screws and bolts, pt = partially threaded.

d		6	8	12	8 pt	M12
$F_{V,mean}$	kN	7.84	14.2	32.8	17.6	38.3
$F_{N,mean}$	kN	13.7	23.3	50.3	20.9	51.8
$F_{V,mean}$ / $F_{N,mean}$	-	0.572	0.609	0.652	0.852	0.739

The results of the shear tests reveal some peculiarities, which are illustrated in Fig. 7.16. An overview with all shear tests shows several curve shapes and a scatter in maximum loads. For some of the tested fasteners, a load increase with a clearly detectable load maximum is observed, see Fig. 7.16c. Considering the other given examples, it is apparent that failure may occur differently. Kinks in the load-position-curves are observed, as well as late increases of load after reaching a first peak.

This raises questions as to whether the test rig is suitable to determine the shear capacity reliably and what are the reasons for the occurrence of different loads and curve shapes. Observations during the tests revealed a comparably wide opening in the shear plane, i.e. a gap, for some of tests. For these tests, kinks or late increases are determined. In order to investigate the cause, it is useful to examine the force transmission within the shear plane. The load is applied from the top and bottom and, under ideal conditions, passes precisely through the centre of the fastener within the shear plane. The inner blocks, including sleeves and the fastener, undergo a slight relative rotation assuming an angle $\alpha > 0°$. This deformation results from a combination of slip and the elastic elongation of the fastener over its free length of 140 mm under tensile loading. Due to the gap in the shear plane, the load transmission path is altered, as schematically illustrated in Fig. 7.17. Consequently, the line of action of the applied load is offset by an eccentricity *e*, which introduces a free transfer length of the fastener within the shear plane. As a result of this eccentricity, the fastener is also subjected to bending. This leads to an increased inclination of the fastener and an increased tensile force in the overall load transfer mechanism, which in turn results in higher total loads. Considering the extreme case of pure shear loading at 90°, it can be assumed that no elastic elongation due to tension is initially present. In this case, only slip and an additional geometric effect play a significant role. Initially, the fastener is fully embedded in the sleeve, i.e., the inner diameter of the sleeve corresponds to the outer diameter of the fastener. Under shear loading, the thread flanks closest to the shear plane are highly stressed and undergo local deformation or indentation. This causes a slight inclination of the fastener in the region of the shear plane, as illustrated

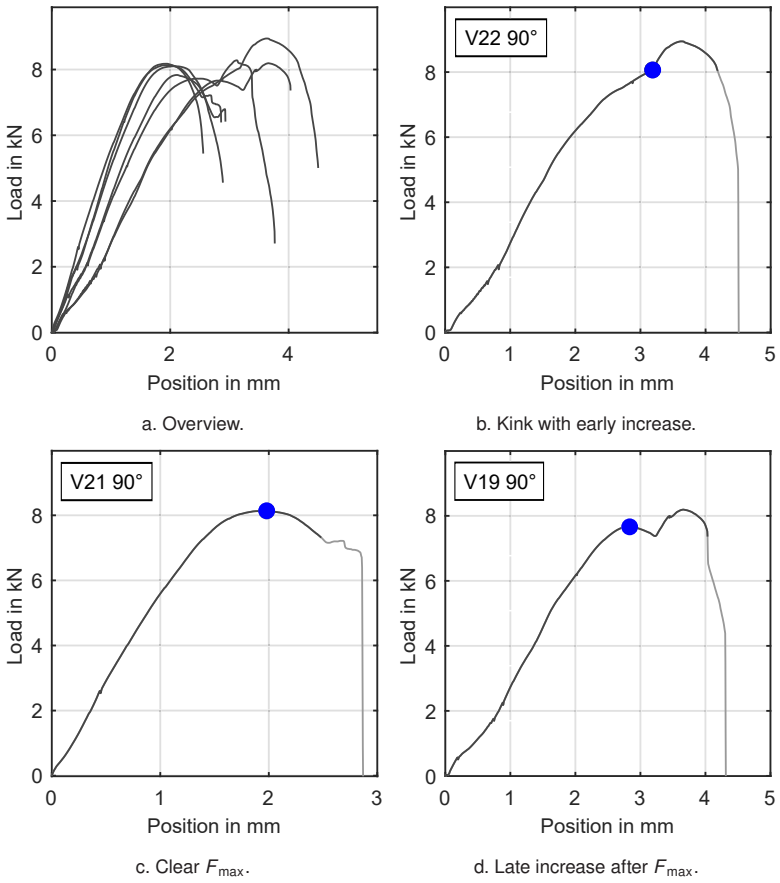

a. Overview.
b. Kink with early increase.
c. Clear F_{max}.
d. Late increase after F_{max}.

Fig. 7.16: Overview of shear test results (90°) for $d = 6$ mm and definition of exemplary evaluation points.

in Fig. 7.17c. The combined effects of the aforementioned deformations ultimately lead to a inclination of the fastener and the generation of additional tensile components. The extent of this phenomenon depends, among other factors, on the size of the gap in the shear plane. Therefore, the installation conditions of the fasteners are varied, with initial gaps intentionally predefined, in order to investigate their influence.

Exemplary results for $\alpha = 67.5°$ in Fig. 7.18 show that the effect of the subsequent load increase and the curve shape with kink can be reproduced if a gap is allowed in the shear plane in the beginning of the test. The dark curves are carried out with a gab, that varied between 0.5–2 mm. With larger gaps, the kink appears earlier, as it can be seen in Fig. 7.18a. After the kink, some of the curves reach a load that is comparable

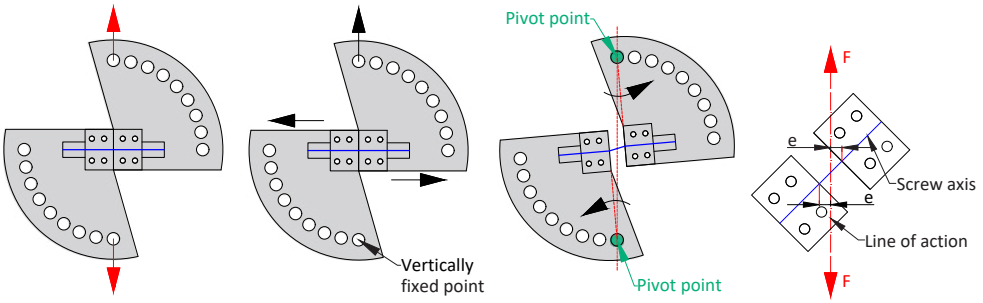

a. Load application. b. Direction of movement. c. Deformation and rotation. d. Gap and Eccentricity.

Fig. 7.17: Schematic illustration of movement and rotation of test setup under $\alpha > 0°$. Exaggerated and out-of-scale representation.

to the regular tests, but some of them reach lower loads. That means, that compared to the pure shear tests, it leads to lower capacities rather than an increase as observed for shear tests. Qualitatively, the trends of the curves can be reproduced; however, the effects differ. For predominantly or purely shear-dominated loading, e.g. at large angles such as 67.5° and 90°, and in combination with a interaction between tension and shear, an increasing tensile component leads to a temporary rise in load, but overall results in lower total loads. For angles of 45° or smaller, i.e., tension-dominated configurations, small initial gaps also result in reduced loads, whereas for large gaps of e.g. 5 mm, an increase in total load (compared to the regularly conducted tests) can occur. For larger gaps, a inclination occurs shortly after the onset, causing the additional normal force component to dominate and leading to higher loads. This approach with differing the gaps has two benefits. Firstly, it allows the identification of incorrect curve progressions. Secondly, it enables a targeted consideration and control of this effect, which is to ensure a very tight fit of the blocks before the start of the tests. For the evaluation, this finding also means that only results with undisturbed curve progressions are used.

7.5 Fully Threaded Screws

The number of successfully evaluated tests was lower than initially specified in the test programme. This means that only 15 test results can be used for 6 mm screws and 18 for 8 mm screws. For the 12 mm screws, all 20 tests carried out are included in the evaluation. Several results had to be excluded due to unexpected behaviour resulting from inaccurate assembly or faulty execution of the tests. Examples include

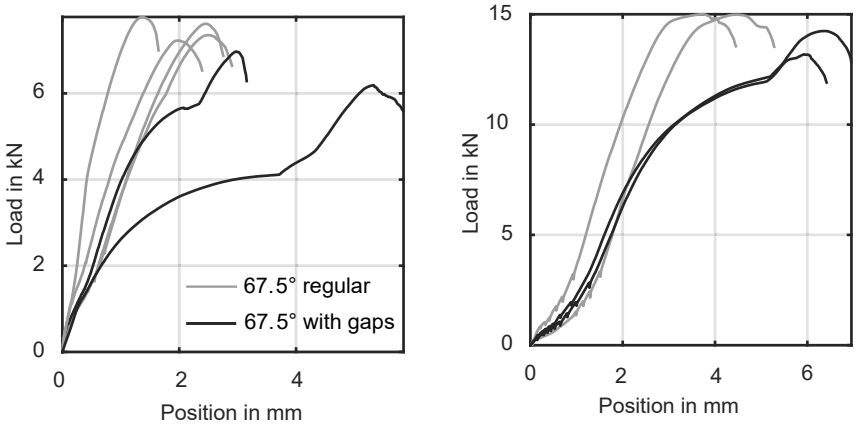

a. Fully threaded screws d = 6 mm.

b. Fully threaded screws d = 8 mm.

Fig. 7.18: Exemplary results for screws under 67.5°. with initial gaps in shear plane.

the loosening of insufficiently tightened bolts, slip, or gaps in the shear plane. The systematic identification and exclusion of such unreliable results formed part of an iterative validation process. This procedure was implemented to enhance both the reproducibility and the reliability of the final dataset.

A particularly meaningful representation of the interaction behaviour is achieved through normalised diagrams, with the two normalised parameters plotted on the x- and y-axes. In the normalisation procedure, the measured loads were first decomposed into their components F_N (normal force) and F_V (shear force) according to the inclination angle α. These components were then divided by their respective reference values: the pure tension load at 0° and the pure shear load at 90°. This procedure accounts for the angle dependence and enables direct comparison of all tests on a common scale.

Two approaches can be adopted for the derivation of approximations to describe the test results. One option is to include all individual test results, which leads to a higher weighting of angle groups with a greater number of tests. Alternatively, mean values can be calculated for each angle group prior to approximation, resulting in equal weighting of all angle groups regardless of sample size. In the present study, the latter approach was applied to ensure balanced representation of all inclination angles.

In the machine load-position diagrams in Fig. 7.19, differences can be observed both in the maximum load and in the onset of plastic behaviour, i.e. initiation of failure, as indicated by the regions at which the curves begin to flatten. Since these diagrams

provide an overview of the orders of magnitude but do not yet permit an interpretation of the behaviour of the individual angles, the results of the maximum loads are summarised in Fig. 7.20. The individual results in Fig. 7.20a exhibit a certain degree of scatter within the series; however, this scatter is not considered statistically meaningful owing to the small sample size.

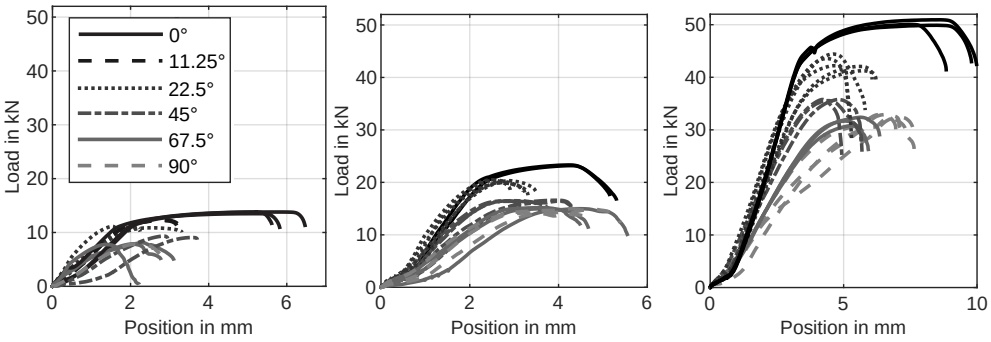

a. Tests with 6 mm screws. b. Tests with 8 mm screws. b. Tests with 12 mm screws.

Fig. 7.19: Machine load-position curves for fully threaded screws with diameters 6, 8 and 12 mm

For comparability, Fig. 7.20b presents the normalised loads, defined as the maximum load at a given angle divided by the maximum load at 0°. This representation enables a direct comparison between the three diameters. A pronounced decrease is observed for small angles, whereas the decrease becomes less pronounced at larger angles. The 6 mm screw series constitutes the lower limit, as it consistently exhibits the lowest normalised loads. Screws with diameters of 8 and 12 mm yield higher values, but no clear distinction between them is apparent. Moreover, the normalised mean values diverge more strongly at larger angles. It is noted that for the 6 and 8 mm screws, erroneous test results can be identified and excluded with confidence. For the 12 mm screws, however, particularly under pure shear, a renewed increase in load is observed after the flattening of the curves, which prevents a clear definition of the shear capacity. Consequently, the shear capacity of the 12 mm screws is likely overestimated. This effect is also evident in the load-position curves in Fig. 7.19c, where the maximum loads of the 90° curves (grey dashed) reach equal or even greater values compared with the 67.5° curves (grey solid).

When the maximum loads are plotted against the individual angle groups, trends in the relationship between load-bearing capacity and inclination angle can be identified. A reduction in maximum load is observed for inclination angles greater than 0°.

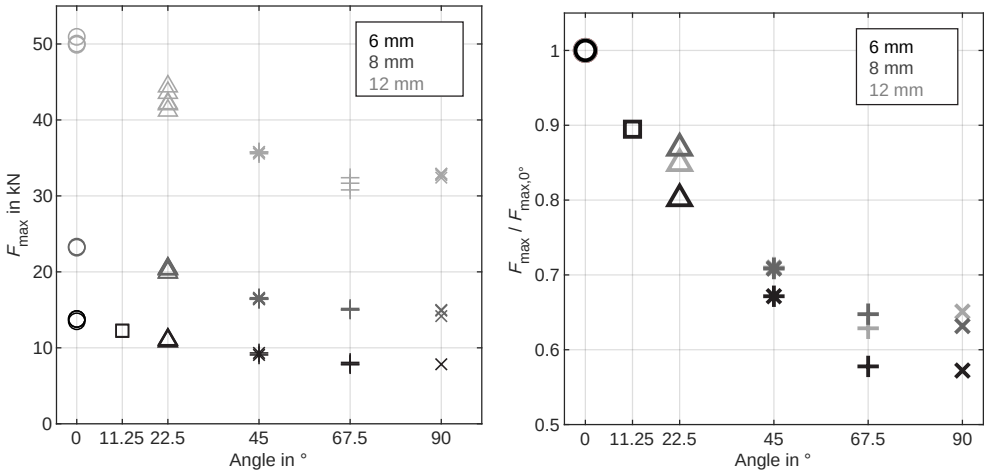

a. Load vs. angle.

b. Normalised load vs. angle, mean values per series.

Fig. 7.20: Maximum load F_{max} over angle for fully threaded screws with diameters 6, 8 and 12 mm.

However, the decrease in load with increasing angle is not equally pronounced for all screws tested. Notable exceptions occur at large angles, in particular at 67.5° and 90°. This behaviour can be attributed to inclination effects, such as opening of the shear plane and the late activation of a normal force component under pure or predominantly shear loading due to large deformation effects. In order to enable a clear and consistent comparison between the individual series, a normalisation of the data is applied. When the maximum loads are plotted against the individual angle groups, trends in the relationship between load-bearing capacity and inclination angle become apparent. A reduction in maximum load is observed for inclination angles greater than 0°. However, the decrease in load with increasing angle is not equally pronounced for all screws tested. Notable exceptions occur at large angles, in particular at 67.5° and 90°. This behaviour is attributed to inclination effects, such as the opening of the shear plane and the delayed activation of a normal force component under pure or predominantly shear loading, which becomes significant due to large deformation effects.

Since these diagrams provide an overview of the orders of magnitude but do not yet permit a precise comparison between the series, a normalisation of the maximum loads is applied. The results are summarised in Fig. 7.20. The individual results in Fig. 7.20a exhibit a certain degree of scatter within the series; however, this scatter

is not considered statistically meaningful owing to the small sample size. For comparability, Fig. 7.20b presents the normalised loads, defined as the maximum load at a given angle divided by the mean load at 0°. This representation enables a direct comparison between the three diameters. A pronounced decrease is observed for small angles, whereas the decrease becomes less pronounced at larger angles. The 6 mm screw series constitutes the lower limit, as it consistently exhibits the lowest normalised loads. Screws with diameters of 8 and 12 mm yield higher values, but no clear distinction between them is apparent. Moreover, the normalised mean values diverge more strongly at larger angles.

It is noted that for the 6 and 8 mm screws, erroneous test results can be identified and excluded with confidence. For the 12 mm screws, however, particularly under pure shear, a renewed increase in load is observed after the flattening of the curves, which prevents a clear definition of the shear capacity. Consequently, the shear capacity of the 12 mm screws is likely overestimated. This effect is also evident in the load-displacement curves in Fig. 7.19c, where the maximum loads of the 90° curves (grey dashed) reach equal or even greater values compared with the 67.5° curves (grey solid). Another influencing factor is that the ratio of pure tensile capacity to shear capacity does not have to be the same for all screw diameters. Reasons for this may include the manufacturing process and the hardened portion of the screw cross-section, but geometric factors such as the ratio of the outer diameter to the core diameter may also play a role. Since this illustration only shows the normalisation to the tensile capacity, this may lead to additional variation.

In order to derive the relationship between the shear and normal force components, the consideration of the normalised values is extended to the component-based representation according to the equations presented above. In this way, the resulting forces can again be visualised, and the normalisation enables a direct comparison between the different screw diameters. Fig. 7.21 illustrates both steps: first, the component decomposition in the F_N-F_V diagram, and second, the corresponding normalisation. After normalisation, the individual angle groups and screw diameters are arranged in an arc-shaped pattern around the origin.

This visualisation in Fig. 7.21b provides an illustrative representation for several reasons. First, the normalisation substantially reduces the apparent influence of screw diameter on the magnitude of the forces by scaling all series relative to their respective tensile and shear values. However, it does not completely remove differences in the relative effect of inclination, which can still vary slightly between diameters due to material properties and local stress distribution. Furthermore, the grouping of the

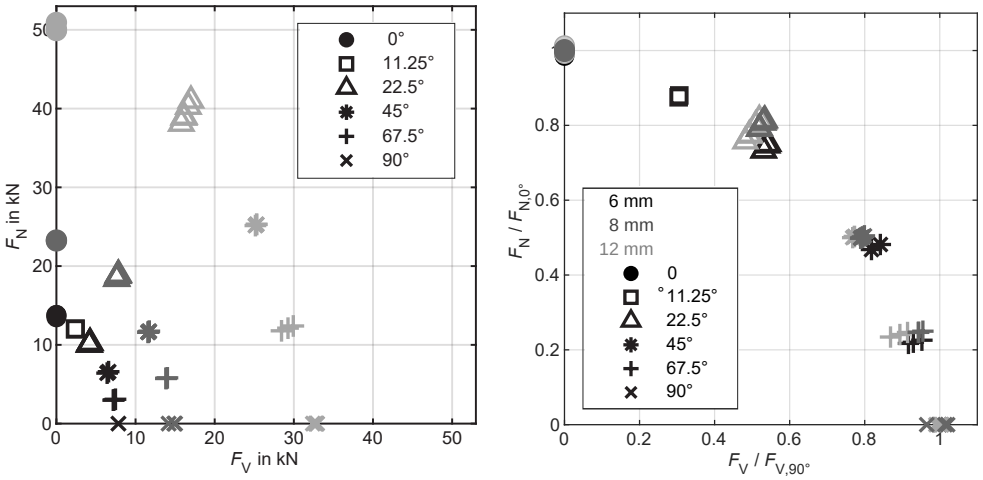

a. F_N vs. F_V.

b. Normalised F_N vs. F_V.

Fig. 7.21: Maximum load F_{max} over angle for fully threaded screws with diameters 6, 8 and 12 mm.

angle categories becomes apparent; however, the values for the individual series do not lie exactly along a line through the origin at a given angle to the x-axis. In the case of identical tension-to-shear ratios and perfectly uniform behaviour, the values would align along such lines. The observed scatter reflects small variations in material response, experimental inaccuracies, and deviations from idealised load conditions, rather than flaws in the normalisation procedure. Finally, the line analogy also emphasises the underlying physical principle: at constant tension-to-shear ratios, the normal and shear components are expected to follow a linear relationship. Deviations from this behaviour in the present data illustrate the combined effects of geometric, material, and experimental factors on the measured forces.

7.5.1 Approximation Models of Interaction Behaviour

From the previous analyses, approximation equations for the mean values of the individual angle groups can be derived, which describe the interaction behaviour. The different approaches for approximate solutions are restricted to three realistic ones, which are discussed below: a circular function, an ellipse with selectable semi-axes, and a super ellipse with fixed semi-axes (= 1). The fits are shown for the individual bolt diameters in Fig. 7.22. Associated and additionally investigated approximation curves are listed in Tab. 7.6.Quadratic and exponential approximations are excluded,

as they, although sometimes yielding favourable R^2 values, do not visually provide a good fit to the measured data points.

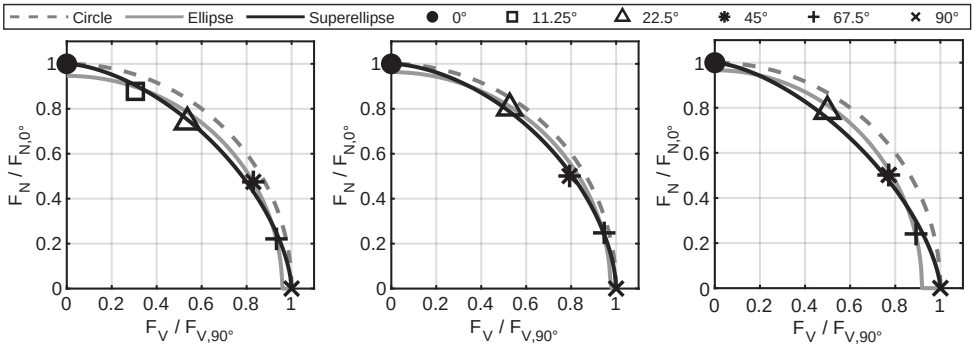

a. Tests with 6 mm screws. b. Tests with 8 mm screws. b. Tests with 12 mm screws.

Fig. 7.22: Interaction fittings for screws with 6, 8 and 12 mm.

Both the figures and the R^2 values in the table consistently indicate that all measured points lie well below the circular curve. Among the fitted approximations, the ellipse and super ellipse provide the closest representation of the interaction behaviour, both visually and according to R^2. Small differences are observed between the screw diameters: for the 6 mm and 8 mm screws, the super ellipse yields the best approximation, whereas for the 12 mm screws, the super ellipse exhibits an R^2 of 0.993, slightly below the ellipse value of 0.996. This discrepancy is associated with the overestimation of the shear capacity for the 12 mm screws, which affects both the reference value at 90° and the curve regions at larger angles. Given that the measurements are reproducible with the current experimental setup, no correction of the values or further assumptions regarding reduced shear capacity is applied. The exponents of the super ellipse fits for the smaller diameters are comparable, with values of 1.607 and 1.705 for the 6 mm and 8 mm screws, respectively. The 12 mm screws deviate slightly, exhibiting an exponent of 1.515. Overall, the ellipse and super ellipse approximations capture the interaction behaviour accurately across all screw diameters, with minor deviations observed for the largest diameter due to shear capacity effects.

Table 7.6: Coefficient of determination R^2 for different fits of screw diameters 6, 8 and 12 mm.

Diameter	Fit	Equation	R^2
6 mm	Quadr.	$y = -1.227x^2 + 0.227x + 1$	0.961
	Cubic	$y = -0.378x^3 - 0.551x^2 + 0.014x + 0.976$	0.982
	Circle	$x^2 + y^2 = 1$	0.944
	Ellipse	$\frac{x^2}{0.958^2} + \frac{y^2}{0.947^2} = 1$	0.993
	Sup.ell.	$\lvert x\rvert^{1.607} + \lvert y\rvert^{1.607} = 1$	0.996
8 mm	Quadr.	$y = -1.532x^2 + 0.532x + 1$	0.972
	Cubic	$y = -2.570x^3 + 2.743x^2 - 1.146x + 1.004$	0.992
	Circle	$x^2 + y^2 = 1$	0.971
	Ellipse	$\frac{x^2}{0.975^2} + \frac{y^2}{0.963^2} = 1$	0.992
	Sup.ell.	$\lvert x\rvert^{1.705} + \lvert y\rvert^{1.705} = 1$	0.999
12 mm	Quadr.	$y = -1.281x^2 + 0.281x + 1$	0.994
	Cubic	$y = -0.991x^3 + 0.305x^2 - 0.316x + 0.998$	0.999
	Circle	$x^2 + y^2 = 1$	0.893
	Ellipse	$\frac{x^2}{0.919^2} + \frac{y^2}{0.967^2} = 1$	0.996
	Sup.ell.	$\lvert x\rvert^{1.515} + \lvert y\rvert^{1.515} = 1$	0.993

7.5.2 Failure Surface Analysis

A look at the failure images of the screws, see Fig. 7.23, provides the missing pieces to understand the interaction and the corresponding fits. The images show, from left to right, increasing test angles, i.e. from tensile to shear loading, the fracture surfaces for the individual investigated angle groups. For the pure tensile tests, no particular anomalies are observed. However, proceeding towards higher angles, it becomes evident that two effects influence the failure pattern. Firstly, considering the thread flanks nearest to the fracture area, significant indentations are apparent, which increase towards the pure shear tests. This behaviour is consistent with expectations, as the shear force is transmitted in the shear plane, and it contributes increasingly as the angle rises. Due to these indentations of the thread flank, necessary for load transfer, the screw is no longer fully seated in the sleeve locally, resulting in a slight bending in the region of the first thread flank. This bending component is largest and

most visible for the pure shear test at 90°, where even the screw core up to the first thread flank is slightly inclined. This local deformation modifies the interaction between normal and shear forces. The reduced exponents of the fitted curves compared to the quadratic interaction reflect this effect, indicating a less-than-quadratic relationship due to the combined geometric and material behaviour of the fully threaded screws. Additional fracture surface images are included in Fig. A.132.

The exact circumferential position of the nearest thread flank relative to the shear plane is found to have no noticeable influence on the failure pattern and could not be correlated with the observed deformation or fracture behaviour; a dedicated study with controlled screw orientation would be required for a systematic investigation of this potential effect.

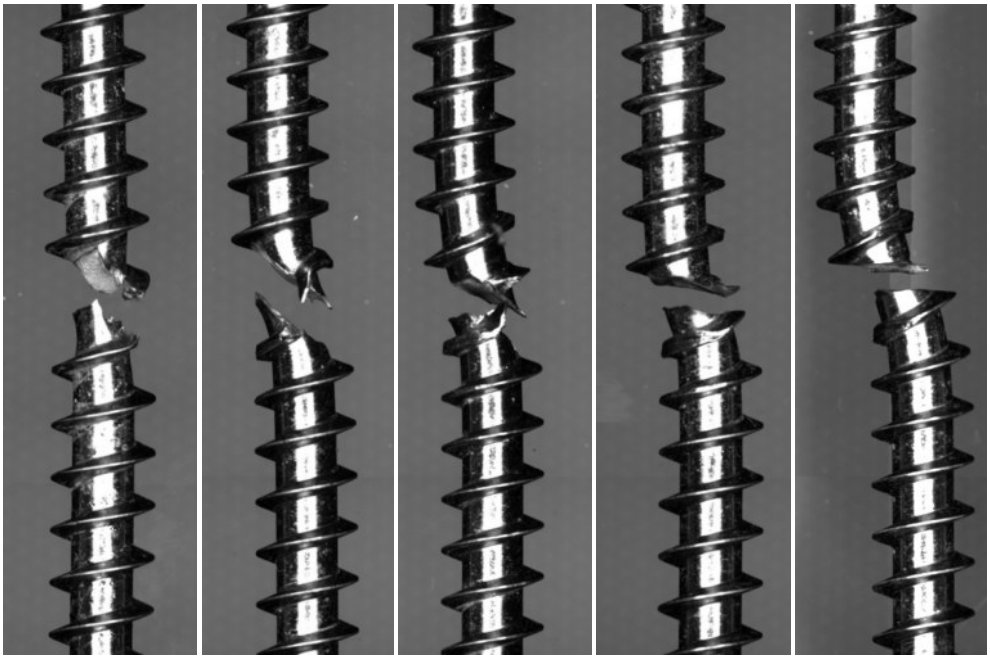

a. α = 0°. b. α = 22.5°. c. α = 45°. b. α = 67.5°. d. α = 90°.

Fig. 7.23: Failure surfaces for screws with diameter 12 mm.

The tested configuration, i.e. embedding the screw in the sleeve with contacting thread flanks (sleeve inner diameter = screw outer diameter), represents a realistic installation state. In typical timber-to-steel connections, screws have comparable or more clearance. Nonetheless, these tests do not clarify the potential influence of

hardening on the interaction. To further investigate geometric and material factors, additional experiments are conducted on shank sections of partially threaded screws ($d = 8$ mm) and standard M12 bolts of strength class 4.8.

7.5.3 Impact and Recommendation

The super elliptical fit with the highest average coefficient of determination can be interpreted as demonstrating that there is no direct dependency on the diameter. The lowest curve corresponds to a diameter of 12 mm, which may be related to the overestimation of the shear capacity. However, when all results from the single-shear test setup are taken into account, as is the case in the present study, the lower limit can be described by the Eq. 7.19. This description is therefore on the conservative side.

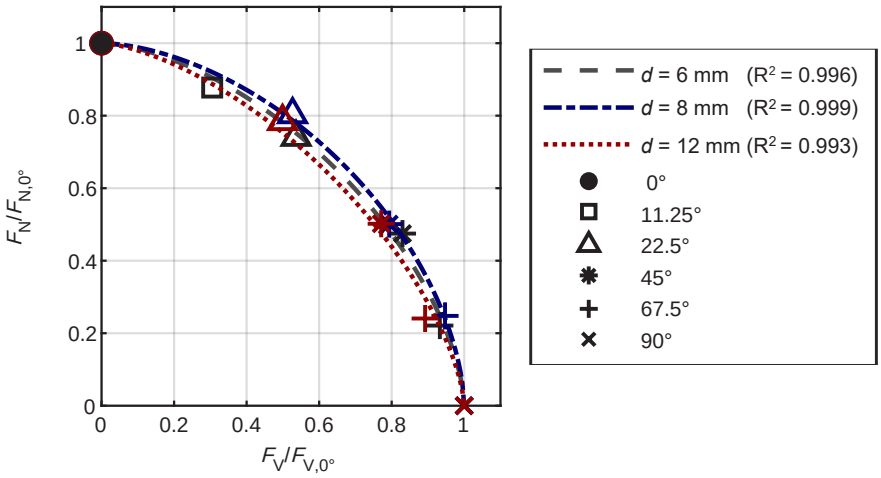

Fig. 7.24: Interaction curves of fully threaded screws with diameter 6 mm, 8 mm and 12 mm and super ellipse fits.

$$\left(\frac{F_\mathrm{t}}{F_\mathrm{td}}\right)^{1.5} + \left(\frac{F_\mathrm{v}}{F_\mathrm{vd}}\right)^{1.5} \leq 1.0 \tag{7.19}$$

It is important to note that, with knowledge or estimation of the acting N and V forces (see Section 4.4), it would be possible to predict screw failure in the shear plane. However, since these are generally not known, a reduction in the tensile capacity could be considered when calculating the rope effect, for example. In contrast to the utilisation of full tensile capacity, it is recommended that F_{tens} be reduced by the calculated load-bearing capacity, $F_{v,R}$, as proposed by Johansen, in accordance with the interaction equation provided in Eq. 7.19. Alternatively, the rope effect criterion could be modified so that the withdrawal capacity becomes decisive, rather than the tensile capacity in general. This may ensure a more ductile behaviour rather than a brittle cross-sectional failure of the screw.

Inclined screw investigations require separate consideration, as in this case, depending on the angle of inclination, high tensile forces already occur in the screws as planned, see Bejtka: Models with and without consideration of the shear component. Neglecting the shear component and solely applying the axial component at angles up to approximately 45° is discussed in [10, 11] Taking the shear component into account at larger angles is presented in [7]. Particularly with large embedment depths in hardwoods, tensile failure can become decisive before withdrawal failure is reached. To prevent this failure, Bejtka's design proposal could be expanded to include an additional adjustment of the normal and shear forces in the shear plane. Modified withdrawal values for hardwoods must be determined accordingly.

7.6 Partially Threaded Screws and Bolts

For the bolts and shank sections of the partially threaded screws, round cross-sections are tested in contrast to the previous investigations. Experiments are conducted at angles of 0°, 11.25°, 22.5°, 45°, 67.5°, and 90°. The partially threaded screws have a shank diameter of 5.8 mm, and a sleeve with an inner diameter of 6 mm is used. For the bolts, sleeves with an inner diameter of 12 mm are employed.

The partially threaded screws are placed with their shanks inserted into the sleeves on both sides. Anchorage is again achieved by aluminium blocks in the threaded section, whereby the shank cutter is also located within the aluminium anchorage, and the screw head is positioned by inserting the countersunk head into pre-formed conical recesses in the aluminium, see Fig. 7.25. The evaluated results are presented as load-position curves obtained from the testing machine and as F_N over F_V plots derived from component-based force decomposition, see Fig. 7.26. As expected,

the difference in dimensions becomes apparent in these representations, which is attributed to the different diameters.

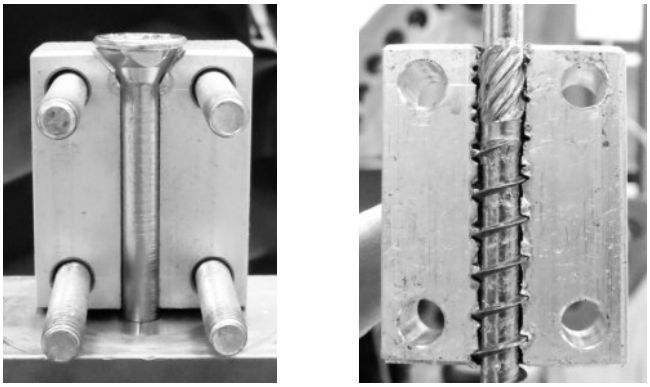

a. Head anchoring. b. Thread anchoring.

Fig. 7.25: Fracture surfaces for screws with diameter 12 mm.

However, the resulting curvature in the lower diagrams also differs from the previous investigations. The results for the 11.25° angle group lie within or above the tensile capacity range for both types of fastener examined; some of the 22.5° angle group results for the partially threaded screws also exhibit this behaviour. This effect is particularly evident in the load–displacement diagrams, where the highest load-bearing curves do not correspond to the 0° angle group. The reason for this observation is that, in this presentation, all tests are shown irrespective of their failure mode. However, in both the experiment and its evaluation, the varying geometry along the fastener axis must be taken into account. At small angles, where the normal force component is higher, failure of the weaker sections of the fastener, i.e. the thread and shank-cutter region of the screw, or the threaded section of the bolt, becomes more likely. Consequently, these angle groups exhibit premature tensile failure in these regions, preventing the maximum load transfer in the shear plane that would have led to interaction failure. Therefore, the results in the overall representation can only be discussed with this consideration in mind, or alternatively, separate representations and discussions are required. The different failure positions are included in Fig. A.133.

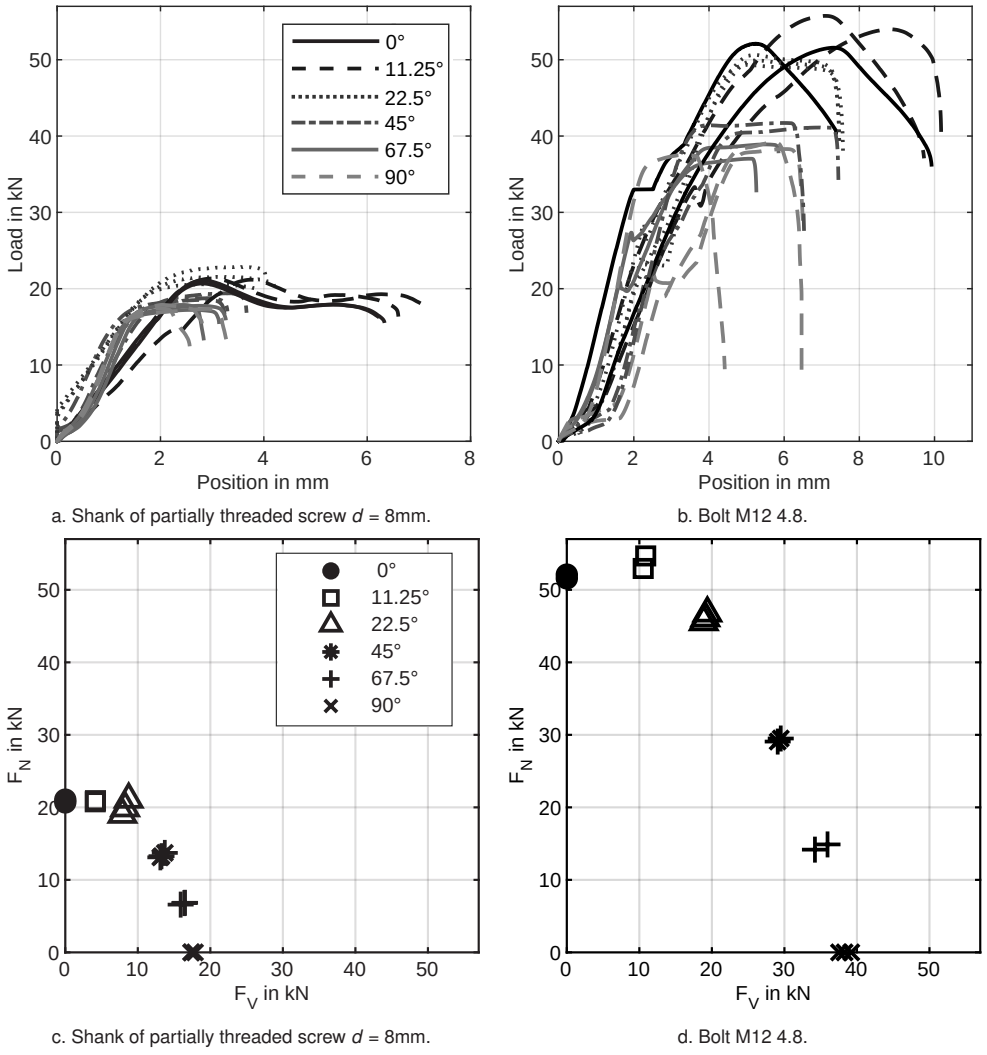

a. Shank of partially threaded screw d = 8mm.

b. Bolt M12 4.8.

c. Shank of partially threaded screw d = 8mm.

d. Bolt M12 4.8.

Fig. 7.26: Machine load-position curves on top and F_N vs. F_V visualisations on the bottom.

7.6.1 Discussion on Shanks of Partially Threaded Screws

For the shanks of the partially threaded screws, the normalised interaction plots shown in Fig. 7.27a are obtained. It becomes evident that the previously used fit equation provide an approximation but do not fully capture the distinct failure modes. Moreover, this approach does not yield a reliable global description across all angles, which

was the original hypothesis tested in this evaluation. The present analysis therefore investigates whether two separate models can better describe the different failure mechanisms. To this end, two fitting ranges are defined to reflect the fundamentally different failure behaviours observed in the two angle groups. In Fig. 7.27c, the fits are applied only to the angles that failed in the shank region (0°, 11.25°, and 22.5°), shown as grey curve sections, followed by an extrapolation towards larger angles (red curve sections). The counterpart, i.e., fitting across the angles exhibiting shear plane failure (45°, 67.5°, and 90°) and extrapolating towards the *y*-axis (blue curve sections), is shown in Fig. 7.27d. The corresponding equations and coefficients of determination are listed in Tab. 7.7. Negative R^2 values indicate that the fit performs worse than a simple mean-value approximation and are thus unsuitable for predictive purposes, as clearly visible in the plotted curves. It is evident that the grey fit curves closely match the measured data within their respective angle ranges, demonstrating that the split-fit method captures local behaviour more accurately. A key difference between the two extrapolations is that, for the leftward extrapolation (blue curve), the boundary conditions are adjusted. For the quadratic, cubic, and super elliptical approximations, the intersections with the y-axis are released and optimised, meaning that the boundary conditions are determined as accurately as possible through the modelling and curve fitting. For the circular fit, no modification of the boundary conditions is possible due to the nature of the function, whereas for the ellipse, the semi-axes are already defined as freely adjustable. This adjustment is necessary because the experimental results at small angles are underestimated or do not correspond to shank-region failure. The optimised y-axis intersections thus represent the theoretical tensile capacity predicted by the model. For the cubic model, it becomes evident that, even after adjusting the boundary conditions, a suitable extrapolation of the experimental data is not possible, or the dataset of the three angle groups is too small for adequate modelling. A similar limitation applies to the quadratic function. In contrast, the super ellipse fit and extrapolation provide a suitable approximation: the next data point of the 22.5° angle group is almost matched, resulting in an intersection at $y = 1.184$, which reflects the theoretical tensile capacity.

Using this factor to calculate a theoretical tensile capacity of the screw shank results in a value of 24.7 kN. What has not been considered in the previous investigation, however, is the fact that the shear capacity for single-shear tests is slightly overestimated. Since no double-shear tests were conducted, literature values are used instead, see [76], where a ratio of 0.955 between double- and single-shear capacity was determined for 4.6 bolts with a diameter of 20 mm.

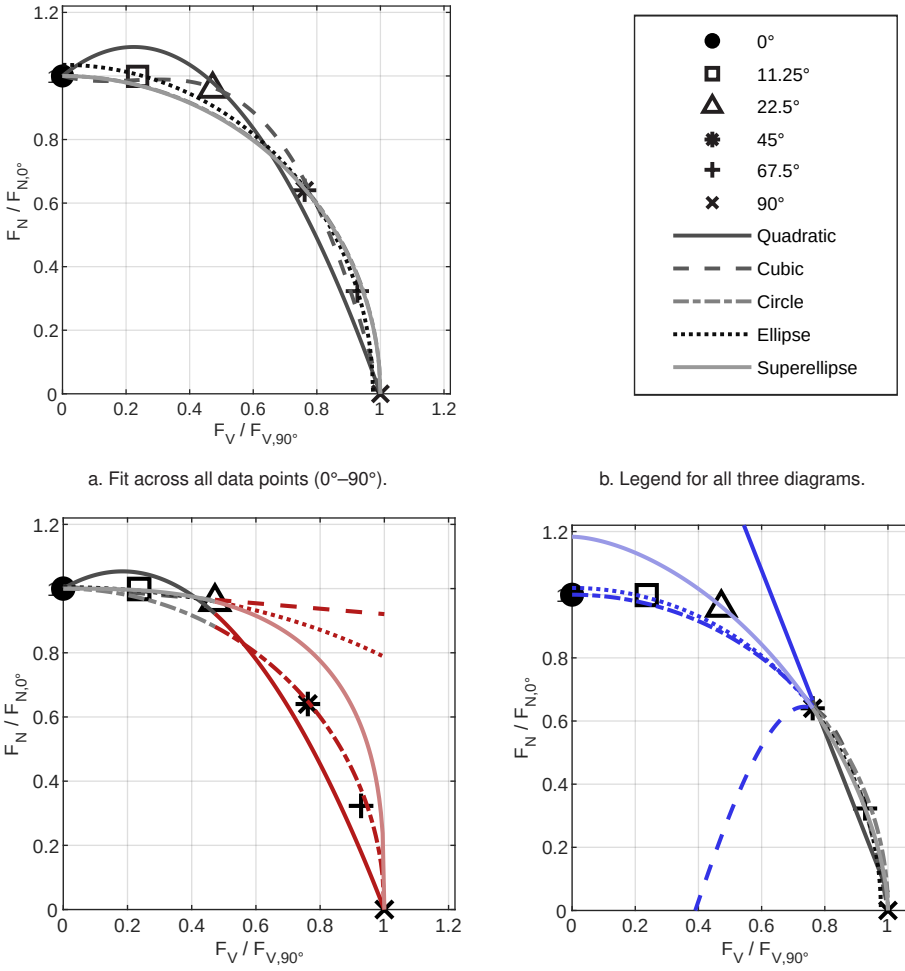

a. Fit across all data points (0°–90°).

b. Legend for all three diagrams.

c. Fit across 0°, 11.25° and 22.5° with extrapolation towards higher angles in red.

d. Fit across 45°, 67.5° and 90° with extrapolation towards the y-axis in blue.

Fig. 7.27: Normalised interaction plots for all angle groups for shanks of partially threaded screw. Grey curves are respective fits, red and blue curve sections are extrapolated.

In general, the question arises whether the use of a material parameter or a system parameter is more appropriate for timber fasteners. As screws are frequently used in single-shear configurations, it is controversial whether determining a double-shear capacity is meaningful in such cases. For other fasteners such as bolts or dowels, multiple-shear configurations are common. However, the stress state in the shear plane, i.e. where this type of interaction occurs, is influenced by deformations and

Table 7.7: Fit results and coefficient of determination R^2 for normalized mean forces.

Dataset	Fit	Equation	R^2
Fig. 7.27a: Fit across all	Quadr.	$y = -1.8135x^2 + 0.8135x + 1$	0.9645
	Cubic	$y = -2.1675x^3 + 1.4418x^2 - 0.2743x + 1$	0.9937
	Circle	$x^2 + y^2 = 1$	0.9893
	Ellipse	$\frac{x^2}{0.977^2} + \frac{y^2}{1.035^2} = 1$	0.9953
	Sup.ell.	$\lvert x\rvert^{1.9858} + \lvert y\rvert^{1.9858} = 1$	0.9893
Fig. 7.27c: Fit across 0° 11.25° 22.5°	Quadr.	$y = -1.5825x^2 + 0.5825x + 1$	-2.522
	Cubic	$y = -0.0015x^3 + 0.0051x^2 - 0.0897x + 1.0066$	0.7674
	Circle	$x^2 + y^2 = 1$	-5.059
	Ellipse	$\frac{x^2}{1.610^2} + \frac{y^2}{1.004^2} = 1$	0.9560
	Sup.ell.	$\lvert x\rvert^{2.9046} + \lvert y\rvert^{2.9046} = 1$	0.9851
Fig. 7.27d: Fit across 45° 67.5° 90°	Quadr.	$y = -0.0116x^2 - 2.5332x + 2.6014$	0.9492
	Cubic	$y = -6.4083x^3 + 6.5595x^2 + 0.7646x - 0.9158$	1.000
	Circle	$x^2 + y^2 = 1$	0.9872
	Ellipse	$\frac{x^2}{0.978^2} + \frac{y^2}{1.021^2} = 1$	1.000
	Sup.ell.	$\lvert x\rvert^{1.6527} + (\lvert y\rvert/1.1836)^{1.6527} = 1$	1.000

inclination, suggesting that a parameter derived from single-shear behaviour would be more suitable for describing failure at this location. Nevertheless, for the sake of completeness, an investigation with adjusted parameters is carried out. By reducing the shear capacity of the screw shanks by approximately 4% to 16.8 kN, the extrapolation yields different results. The tensile capacity of the shank is calculated based on the ratios of the cross-sectional areas. The inner shank cutter diameter is measured to be 5.35 mm on three sample screws. This leads to a cross-section ratio of shank to shank cutter of 1.18, neglecting the outer thread parts, which roughly corresponds to the tensile capacity obtained from the free elliptical extrapolation model. A fit across the newly normalised plot produces the plots shown in Fig. 7.28, with the exception of the 11.25° and 22.5° angle groups. The equations of the three fits, ellipses and circle, vary only slightly, and their coefficients of determination are consistently above 0.99. The outliers for the small angles remain unaccounted for due to geometric differences in the thread or shank cutter. When the tensile capacity of the shank cutter is taken into

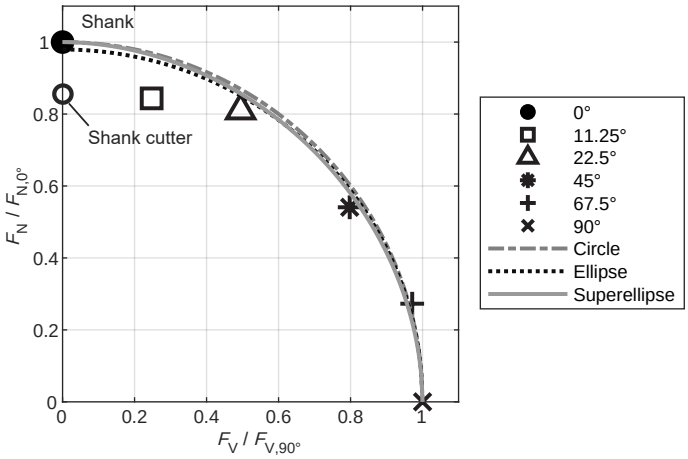

Fig. 7.28: Normalised interaction plot, fit for angles 0°, 45°, 67.5° and 90° for shanks of partially threaded screws. Adjusted $F_{N,0°}$ with extrapolation and reduced $F_{V,90°}$ for double-shear case.

account, the first three angle groups exhibit an almost horizontal or slightly inclined relationship. This yields results comparable to those reported in previous interaction tests [55, 76].

Nevertheless, the assumptions made within the scope of this investigation must be critically reviewed and verified. In particular, both the reduction and magnitude of the assumed shear capacity as well as the modelled tensile capacity of the shank region should be experimentally confirmed.

7.6.2 Discussion on Bolts

The main difference between the results of shanks of partially threaded screws and bolts is that, for bolts, the 22.5° angle actually failed in the shear plane. In contrast, for the partially threaded screws, although an increase in the measured load was observed for angles below 22.5° compared to tensile failure at 0° and 11.25°, the failure still occurred in the shank region.

Due to this difference, the results for the bolts are considered separately in the following analysis. Considering bolts for the full test range, the resulting interaction diagram is as follows. The bolts have a tensile strength of 400 N/mm^2 and a yield strength of 320 N/mm^2, corresponding to a slightly higher yield and lower plastic deformation compared to a typical 4.6-class screw. The cross-sectional areas according to ISO 898-1

[124] are listed in Tab. 7.8. Using this ratio of the areas, which also corresponds to the ratio of the tensile capacity of the thread to that of the shank [76], the tensile capacity and the normalised interaction diagram can likewise be adjusted.

Table 7.8: Cross-section areas for M12 bolts, $P = 1.75\,\text{mm}$.

Size	Formula	Result	Ratio
Shaft cross-section A_s	$A_s = \frac{\pi}{4} d^2$	113.1 mm^2	0.75
Nominal stress area A_t	$A_t \approx \frac{\pi}{4}\left(d - 0.9382\,P\right)^2$	84.3 mm^2	

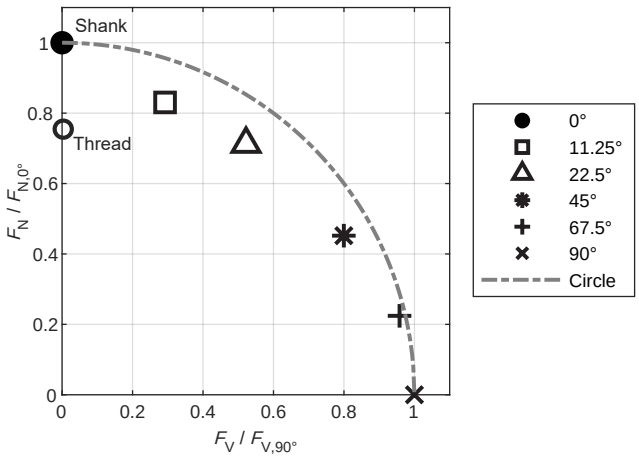

Fig. 7.29: Normalised interaction plot with circle curve for bolts. Adjusted $F_{N,0°}$ with extrapolation and reduced $F_{V,90°}$ for double-shear case.

The diagram highlights the challenge of providing a uniform description for round cross-sections, due to the differing failure modes at small and large angles. Here, failure in the threaded regions dominates the results at small angles, i.e., 0° and 11.25°, see additional fracture surfaces in Fig. A.134. It is also notable that the results lie significantly below the circular relationship and are therefore considerably lower than those for the partially threaded screws. In the latter, the circular and elliptical relationships could still reasonably describe the results for larger angles and higher shear contributions. This discrepancy may be attributed to the influence of material hardness, which affects the measured loads in the threaded region.

Based on these observations, a two-part description of the interaction is suggested for both types of round cross-sections examined, i.e. bolts and screw shanks: a constant or linear relationship for the regions dominated by thread failure, followed by a linear or elliptical function for larger angles.

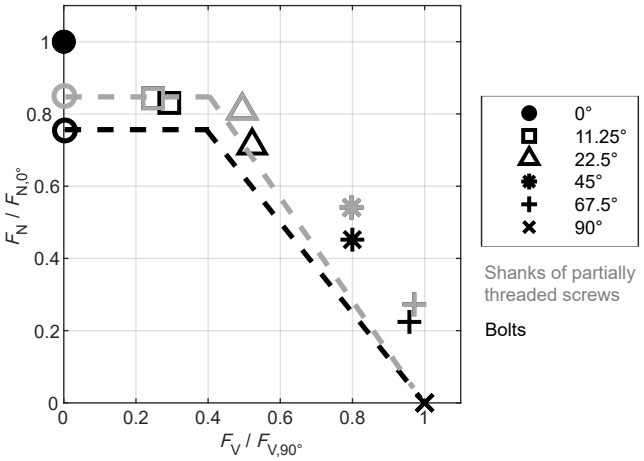

Fig. 7.30: Normalised interaction plot with bilinear conservative description, shanks of partially threaded screws and bolts.

7.7 Conclusion

This study investigated the interaction of normal and shear forces in fully threaded screws, shanks of partially threaded screws, and bolts under combined loading. The results indicate that design approaches which consider mainly the yield moment, and do not explicitly account for shear capacity or *NV* interaction, can underestimate the true failure risk and thus may lead to unsafe designs. This concern is particularly relevant for fasteners with circular cross-sections; fully threaded screws, show distinct behaviour and therefore require separate consideration.

The evaluation of fully threaded screws across three diameters (6, 8 and 12 mm) highlights the angle-dependent interaction behaviour between normal and shear forces. A pronounced reduction in maximum load was observed at small inclination angles, with the 6 mm screws consistently exhibiting the lowest normalised loads. The 8 and 12 mm screws reached higher normalised loads without a clear distinction

between them, although the pure-shear capacity of the 12 mm screws may be slightly overestimated. Normalisation and component-based decomposition revealed arc-shaped interaction curves that are best approximated by elliptical or super elliptical functions. Fracture observations indicate that local thread flank deformation and screw core bending at high angles lead to a less-than-quadratic interaction between normal and shear forces. It should be noted that the shear capacity is generally overestimated in single-shear tests and should ideally be evaluated in double-shear configurations. This effect becomes more pronounced for fasteners with profiled cross-sections, such as fully threaded screws. Due to thread flank indentation and slight bending, single-shear tests activate a significantly higher normal force component, due to inclination, which artificially increases the measured shear capacity. Because of the particularities in geometry, failure location, and failure mechanism highlighted above, these results should be regarded as indicative parameters rather than true material properties.

For fasteners with round cross-sections (e.g. shanks of partially threaded screws or bolts), it is necessary to consider the potential failure of the anchoring regions, i.e. the threaded sections, when evaluating smooth-shank areas. At small inclination angles, the tensile capacity of the threaded regions may be reached instead of the true interaction capacity in the smooth-shank region. Therefore, these results do not represent the actual interaction behaviour in the shear plane. In this context, two-part interaction models provide the most reliable description: a constant or linear relationship for regions with thread-dominated failure at small angles, and a linear, elliptical, or super elliptical interaction curve for shear-dominated regions at larger angles. This two-part fit should be interpreted as a conservative lower bound and is primarily valid for round cross-section fasteners; it does not universally transfer to fully threaded screws. When applicable, the two-part description reduces scatter between diameters and better represents the capacity under combined loading than single-limit approaches. The study only examined shank cross-sections at a sufficient distance from the shank cutter or thread transition. Due to the weak point and change in geometry located there, it is also recommended to test the interaction directly in that position. The shank cutter may also be located in the shear plane of a connection, where it would be exposed to combined shear and tensile stress.

Normalisation of force components enabled a consistent comparison across fastener types and revealed that diameter effects are less dominant than local stress distribution and manufacturing-related weaknesses (e.g. shank-to-thread transitions). These findings improve the understanding of *NV* interaction and support more reliable assessment of fastener behaviour under combined loading in timber connections.

8 Consequences and Impact on Connection Design

8.1 Introduction

A holistic approach to connection design is essential. All components must be considered in an adequate and consistent manner to ensure a realistic representation of the load-bearing behaviour. Generally, the continued use of previously established design equations is recommended; however, changes in material properties must be carefully evaluated. When transferring design concepts from softwood to hardwood, adjustments to parameters such as fastener slenderness, density, and embedment depth are necessary to account for differences in material behaviour.

The transfer of design concepts from softwood to hardwood is generally feasible and advisable, since the fundamental mechanical mechanisms and deformation behaviour, particularly regarding bending, do not change significantly. Nevertheless, the behaviour of the fasteners requires separate consideration, as implicit assumptions may no longer hold when basic parameters such as density are modified. Numerous studies have shown that density has a strong influence on almost all governing properties, which underlines the need to reassess established simplifications when moving to timber products or species with higher densities.

The potential for interdisciplinary learning becomes apparent in this context. Interaction phenomena are well known in steel construction, and with appropriate adaptation to the specific boundary conditions of timber connections, similar mechanisms can be applied to timber fasteners. Such transfer of knowledge contributes to a more complete understanding of the complex load interactions governing connection performance. The *MNV* interaction, which includes *NV* terms, can generally be applied to timber fasteners, provided that the specific characteristics of the connection are taken into account.

8.2 General Observations and Recommendations

An extended understanding of the relevant parameters affecting connection design is provided in the previous chapters. Several of the research questions could be addressed, in particular regarding the localisation of critical stress regions. For steel-to-timber connections, the shear plane is the most critical area due to the combined bending, normal, and shear (*MNV*) interaction. In timber-to-timber connections, critical regions occur both in the shear plane, governed by *NV* interaction, and at the formation of plastic hinges, governed by *MN* interaction.

While connection failure can occur in all types of connections, including those made from softwood, the probability of premature brittle failure of the fastener increases with higher density and more slender fasteners. Based on the investigations in Section 2.4 and Chapter 4, fasteners with a diameter of $d \leq 10\,\text{mm}$, tensile strength $f_u \leq 600\,\text{N/mm}^2$ and densities exceeding $800\,\text{kg/m}^3$, and especially combinations of them should be considered critical in terms of potential fastener failure. However, these values are for guidance only and are based on the material parameters used in the tests carried out.

In practice, there are already screw manufacturers who offer special hardwood screws. These have larger core diameters and a lower thread ratio. Even if this tendency to increase the cross-section is often due to the higher insertion moments, this geometric adaptation also helps when dealing with possible cross-section failure.

The question arises as to how these findings can be integrated into existing design models. Each failure mode according to Johansen implies a distinct internal force distribution and therefore requires separate consideration of the stress state in the shear plane. Although a yield criterion is generally suitable, plastic hinge formation requires progressive deformation, with additional forces developing that cannot be captured by a simple yield stress check. It may, however, be applied in cases with a straight fastener axis, corresponding to failure modes a, b, and c. For more complex cases (d, e, f), an extended formulation or a dedicated failure criterion can appropriately describe the observed behaviour.

The following sections illustrate how these general findings apply to specific fastener configurations and failure modes (Cases a–f), providing guidance for practical design and highlighting the influence of key parameters.

8.3 Reduction of Yield Moment

A general reduction of the yield moment for timber-to-timber connections can be introduced by applying the interaction relationship according to

$$M_{\mathrm{y}} \geq \frac{M}{1 - \left(\frac{N}{F_{\mathrm{tens}}} + \frac{V}{F_{\mathrm{shear}}}\right)^2} \tag{8.1}$$

This equation is based on the interaction relationship introduced in Section 2.2 and Section 2.3. This reduction, however, must be regarded as too imprecise at the current state of knowledge, since the actual magnitudes of the interacting internal forces are still insufficiently understood and require further research to describe a fastener failure.

Assuming that the yield moment in the plastic hinges is fully developed, as postulated in Johansen's yield theory, would correspond to a moment utilisation of 1.0. This implies that no, or only minimal, reserves remain for the influence of N and V, except for limited hardening effects of the material in the plastic range. Although, from a mechanical perspective, the shear force is zero at the points of maximum bending moment and only an additional normal force in the plastic hinge would need to be considered, even moderate normal force utilisations can noticeably reduce the available bending capacity.

For example, a tensile utilisation of $N/F_{\mathrm{tens}} = 0.2$ reduces the yield moment to approximately 96%, whereas a utilisation of 0.5 already decreases it to around 75%. In many screw connections with very slender fasteners, significant axial forces can be activated due to the threaded embedment depth or anchorage through the screw head (see Chapter 4). In these cases, axial force utilisations of about 30% with respect to the full screw cross-section were observed in the shear plane at a deformation of 7 mm, corresponding to a reduction of the yield moment to roughly 91%. This example illustrates that substantial normal force utilisations can indeed occur, although they strongly depend on connection geometry, material properties, and fastener type.

If the normal forces acting in the connection are known, this approach represents a way to account for the interaction. However, estimating the normal forces solely based on axial resistances is not recommended, as considerable uncertainties exist. These include, for instance, the variability in magnitude of head pull-through depth depending on the screw head shape, and the dependence of withdrawal or head pull-through resistance activation on the relative displacement in the shear plane. This

relationship is, in essence, heuristic, but parts of it have been investigated empirically; in particular, the *NV* interaction has been studied experimentally, contributing new insights into the actual behaviour and measured outcomes.

The quadratic interaction formulation can be applied in the following cases: for partially threaded screws and dowels, when the tensile capacity of the threaded section is considered even if the interaction is calculated in the shank region, and for fully threaded screws in timber-to-timber connections. In other cases, such as steel-to-timber connections, the exponent in the interaction term should be reduced to 1.5 to better reflect the observed behaviour. This can be expressed as

$$M_\mathrm{y} \geq \frac{M}{1 - \left(\frac{N}{F_\mathrm{tens}} + \frac{V}{F_\mathrm{shear}}\right)^\alpha} \tag{8.2}$$

with α = 1.5 for steel-to-timber connections.

8.4 Adjustment of the Rope Effect Limitation

Currently, the rope effect is calculated as the minimum of head pull-through, thread withdrawal, and the tensile capacity of the fastener (see Eq. 2.2). When the tensile capacity becomes governing, this implies that the embedment depth or timber thickness must be chosen such that the screw thread is securely anchored and/or the screw head is sufficiently large (e.g. washer-head screws), thereby potentially activating substantial normal forces.

An extension to the design criterion, such as

$$F_\mathrm{tens} > F_\mathrm{ax} \quad \text{and} \quad F_\mathrm{tens} > F_\mathrm{head}, \tag{8.3}$$

could provide additional safety. A positive side effect of this approach is that failure modes which allow a certain ductility of the connection may become controlling. This condition therefore implies that the tensile capacity should not act as the governing design variable. Depending on the desired level of safety, factors could be defined for different application scenarios with a further reduction for critical connection configurations. It should be noted that imposing a condition on F_ax and/or F_tens simultaneously constrains the timber thickness, which must therefore be considered already during the design and conceptual phase of the connection.

8.5 Consideration of Individual Interactions

Simplified formulas with $\beta = 1$, see Eq. 2.1, and reference to the force diagrams following are shown for timber-to-timber connections. The formulas without conversion factors can be applied for mean or measured values. In the following, the undeformed state is chosen.

$$F_{\mathrm{D}} = \min \begin{cases} f_{\mathrm{h},1}\, t_{\mathrm{h}1}\, d & \text{(a) } MV^{\mathrm{a}} \\ f_{\mathrm{h},2}\, t_{\mathrm{h}2}\, d & \text{(b) } MV^{\mathrm{a}} \\ \dfrac{f_{\mathrm{h},1}\, t_{\mathrm{h}1}\, d}{2} \left[\sqrt{3 + 2\dfrac{t_{\mathrm{h}2}}{t_{\mathrm{h}1}} + 3\left(\dfrac{t_{\mathrm{h}2}}{t_{\mathrm{h}1}}\right)^2} - \left(1 + \dfrac{t_{\mathrm{h}2}}{t_{\mathrm{h}1}}\right) \right] & \text{(c) } MNV^{\mathrm{b}} \\ \dfrac{f_{\mathrm{h},1}\, t_{\mathrm{h}1}\, d}{3} \left[\sqrt{4 + \dfrac{12\, M_{\mathrm{y}}}{f_{\mathrm{h},1}\, d\, t_{\mathrm{h}1}^2}} - 1 \right] & \text{(d) } MN^{\mathrm{c}},\ NV^{\mathrm{d}} \\ \dfrac{f_{\mathrm{h},1}\, t_{\mathrm{h}2}\, d}{3} \left[\sqrt{4 + \dfrac{12\, M_{\mathrm{y}}}{f_{\mathrm{h},1}\, d\, t_{\mathrm{h}2}^2}} - 1 \right] & \text{(e) } MN^{\mathrm{c}},\ NV^{\mathrm{d}} \\ \sqrt{2\, M_{\mathrm{y}}\, f_{\mathrm{h},1}\, d} & \text{(f) } MN^{\mathrm{c}},\ NV^{\mathrm{d}} \end{cases} \tag{8.4}$$

[a] Applicable only for steel-to-timber connections with very high timber densities $\rho > 800\,\mathrm{kg/m^3}$ in combination with soft fasteners $f_{\mathrm{u}} < 600\,\mathrm{N/mm^2}$

[b] Bending moment remains in the elastic range for case (c), providing sufficient reserve for *N* and *V*

[c] In plastic hinge

[d] In shear plane

A rope-effect contribution can be added for failure modes with inclined fastener sections (c–f):

$$F_{\mathrm{rp}} = \min \begin{cases} k_{\mathrm{rp},1}\, F_{\mathrm{ax,t}} \\ k_{\mathrm{rp},2}\, F_{\mathrm{D}} \end{cases} \tag{8.5}$$

$k_{\mathrm{rp},1}$ Factor for the rope effect (0.25 general)
$F_{\mathrm{ax,t}}$ Minimum of head pull-through, withdrawal, and tensile resistance
$k_{\mathrm{rp},2}$ Limitation factor for the rope effect (e.g. 0 for dowels, 1.0 for screws)
F_{D} Dowel-effect contribution determined with Eq. 8.4

8.5.1 General Considerations and Limitations

Knowledge of the acting internal forces allows for an individual design of fastener cross-sections. Recent advances in numerical modelling of connections [5, 6, 63, 101] have the potential to partially close the research gap concerning the determination of internal forces in laterally loaded fasteners. Comprehensive parameter studies could help quantify the magnitude of normal and shear forces for different types of fasteners, thereby providing a basis for more individualised designs.

Experimental approaches are also available for measuring forces in fasteners. In this thesis, measuring screws with embedded strain gauges were employed, and alternative methods such as Fibre Bragg Grating screws have been used by Claus et al. [23]. These systems determine local forces along the fastener by detecting strain-induced shifts in the reflected wavelength of embedded optical fibres. Such measurements are particularly valuable for validating numerical models and improving the reliability of connection design.

8.5.1.1 Quadratic *NV* Interaction

The experimentally investigated *NV* interaction can describe the failure of fasteners in the shear plane of timber-to-timber connections. The previously described magnitudes of normal forces in fully threaded screws, see Chapter 4 apply for a diameter of 8 mm. In the conducted tests, the connections were designed such that withdrawal in the side member governed, rather than the tensile capacity of the fastener. For greater timber thickness, higher normal forces would be expected. A ductility limit of 10 mm relative displacement in the shear plane according to the EAD 130118-01-0603 [127] can be taken as reference, whereas the tested connections reached only approximately 7.4 mm.

The assumption of the quadratic interaction relationship is valid when no thread flank indentation occurs, and therefore no additional bending components are present. While these observations are specific to timber-to-timber connections, the same relationship may be applied to other cases with care. For steel-to-timber connections, inclined fasteners, or cases with thin steel plates, potential reductions in the interaction parameters should be considered. It is necessary to investigate in such cases whether the governing interaction occurs in the plastic hinge (*MN*) or in the shear plane (*NV*), and whether thread flank indentation is present for thin steel plates.

8.5.2 Failure Modes a and b: Straight Fastener

For cases (a) and (b), the *MV* interaction in the shear plane is governing for steel-to-timber connections. If the fastener remains straight, F_{shear} applies and no reduction is necessary. For timber products with very high density, F_{shear} should be taken as the upper limit of the load per shear plane. In timber-to-timber connections, shear stresses are generally too low to cause fastener failure.

$$F_{\text{D}} \leq F_{\text{shear}} \tag{8.6}$$

8.5.3 Failure Mode c: Inclined Fastener

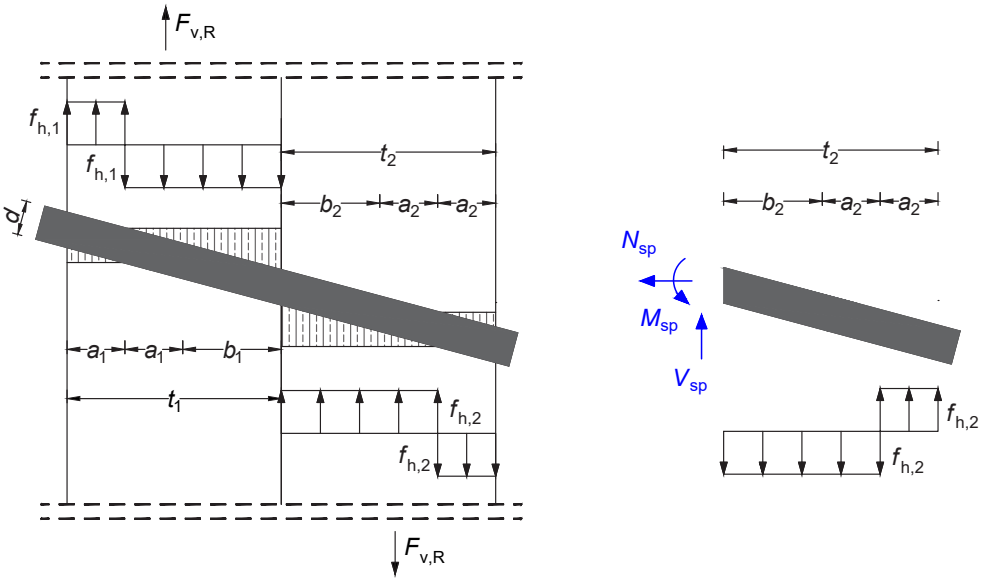

Fig. 8.1: Failure mode c with inclined fastener and force diagram.

In this case, as shown in Fig. 8.1, the fastener experiences a pure inclination and no plastic deformation. The moment in the shear plane stays in the elastic range and can be calculated following derivations in [13]:

$$M_{\text{sp,left}} = f_{\text{h,1}} \cdot d \cdot \left(\frac{b_1^2}{2} - a_1^2\right),$$
$$M_{\text{sp,right}} = f_{\text{h,2}} \cdot d \cdot \left(a_2^2 - \frac{b_2^2}{2}\right), \tag{8.7}$$

with

$$b_1 = \frac{t_1}{1+\beta}\left[\sqrt{\beta + 2\beta^2\left(1 + \frac{t_2}{t_1} + \left(\frac{t_2}{t_1}\right)^2\right) + \beta^3\left(\frac{t_2}{t_1}\right)^2} - \beta\left(1 + \frac{t_2}{t_1}\right)\right], \tag{8.8}$$

$$a_1 = \frac{t_1 - b_1}{2}, \quad a_2 = \frac{t_2 - b_2}{2} = \frac{\beta t_2 - b_1}{2\beta}. \tag{8.9}$$

The shear-plane moment approaches zero for $a_2/t_2 = 1\text{-}\sqrt{2}/2 \approx 0.3$. For smaller ratios, the tensile side is at the bottom, for larger ratios at the top of the fastener referring to the case and load direction in Fig. 8.1. Since the moment remains within the elastic range, the interaction of the internal forces can be neglected.

8.5.4 Failure Mode d: One Plastic Hinge

Cases d and e involve the formation of a single plastic hinge in the fastener, whereby case d is exemplarily shown in Fig. 8.2. Depending on geometry and load distribution, the interaction in the shear plane (*NV*) or in the plastic hinge (*MN*) may be governing. The design may consider the quadratic interaction of *N* and *V*, with appropriate adjustments based on the position of the hinge and measured or estimated internal forces. However, observations show that the location of the plastic hinge is more critical, e.g. [98].

8.5.5 Failure Mode f: Two Plastic Hinges

The force diagram indicates a consideration of two potential failure locations: the shear plane and the plastic hinge. For case f in the shear plane, the design may be based on a quadratic *NV* interaction relation. If *V* is unknown, the dowel contribution

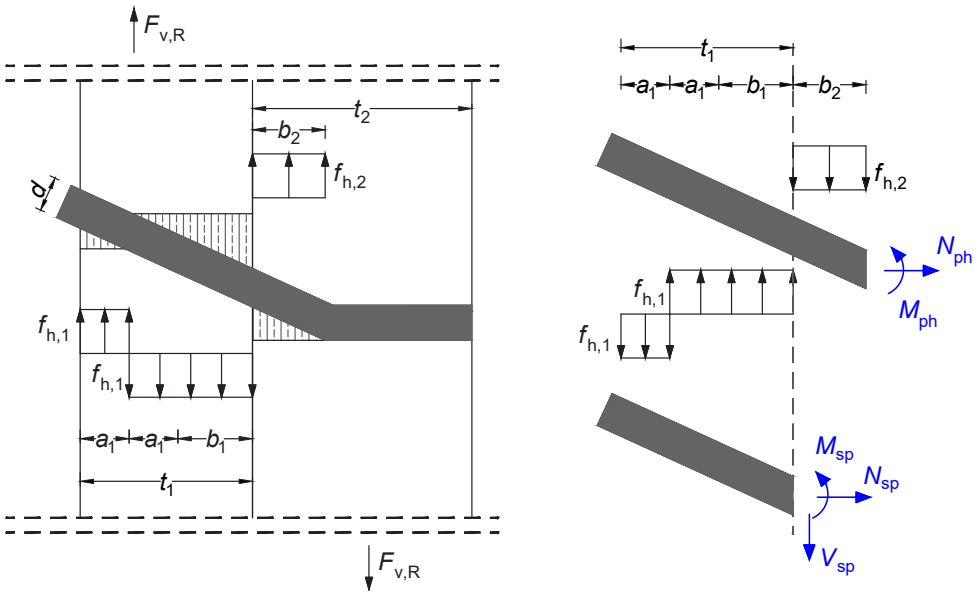

Fig. 8.2: Failure mode d with one plastic hinge and force diagram.

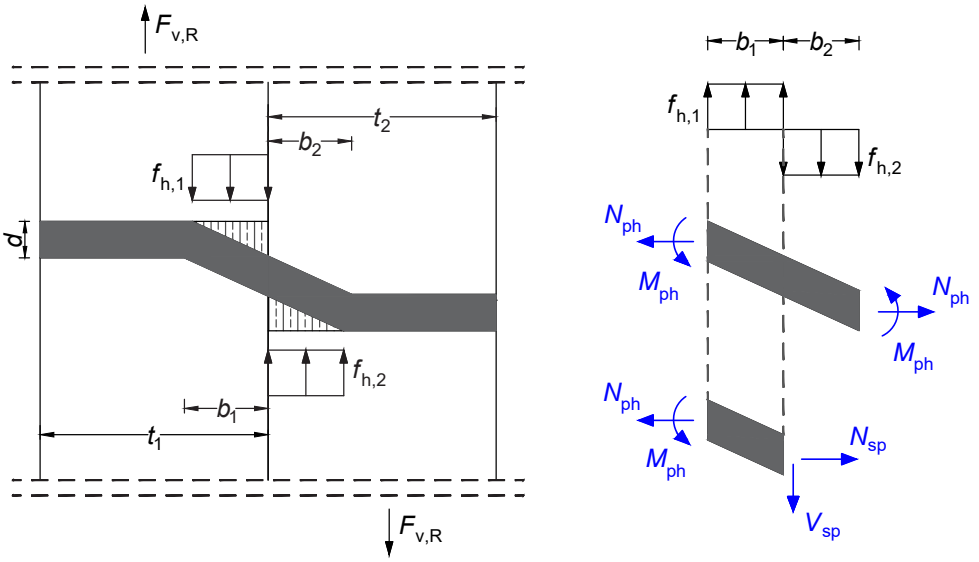

Fig. 8.3: Failure mode f with two plastic hinges and force diagram.

F_D can be used to approximate the shear effect. For the design in the plastic hinge, the reduction of the yield moment described above can be applied.

8.5.6 Steel-to-Timber Connections

For steel-to-timber connections, the new draft of Eurocode 5 [128] only provides a simplified case, namely with two plastic hinges per shear plane. All other steel-to-timber connections can be calculated using the formulas presented above. Since this is the most commonly used and also the most critical case, only this one is discussed here. Compared to the timber-to-timber connections discussed above, the calculation formula is multiplied by a factor of $\sqrt{2}$ and reads as follows:

$$F_D = 2\sqrt{M_y \, f_{h,1} \, d} \quad \text{(f)} \quad \textit{MNV} \text{ in shear plane} \tag{8.10}$$

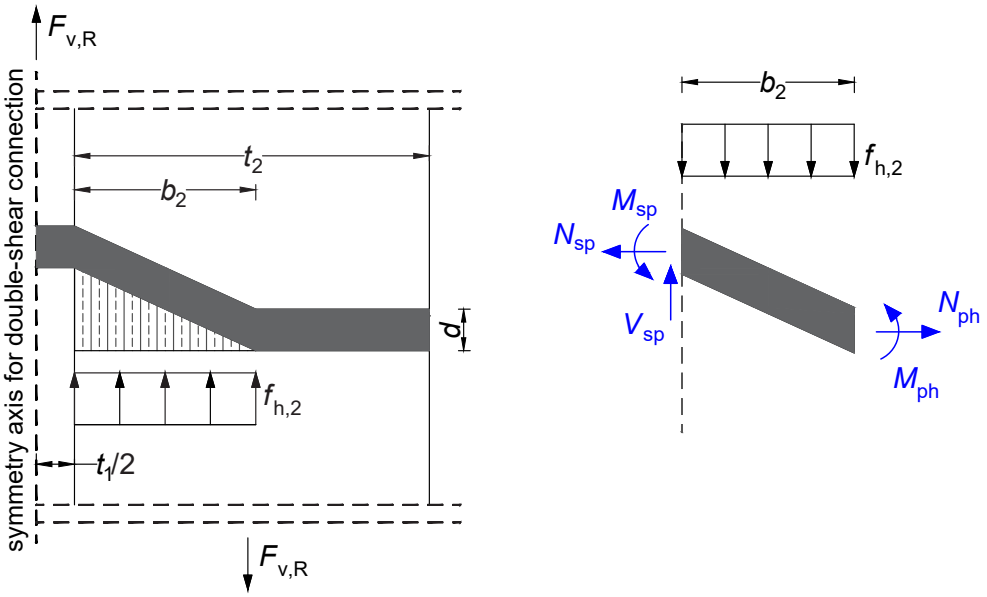

Fig. 8.4: Failure mode f in steel-to-timber connection with one or two plastic hinges.

For steel-to-timber connections, whether one or two plastic hinges form, the interaction in the shear plane is always governing. The plastic hinge may be simplified as located directly in the shear plane, even if in reality it occurs slightly in the steel plate section.

The linear *M* and quadratic *N* and *V* interaction relationship provides a generally suitable description for round fasteners. The consideration of the two different interactions in the plastic hinge and in the shear plane can be taken into account by Eq. 8.11.

$$
\begin{aligned}
F_{\mathrm{D}} &= \sqrt{2(M_{\mathrm{y,ph}} + M_{\mathrm{y,sp}})\, f_{\mathrm{h,1}}\, d} \\
\text{with } M_{\mathrm{y,ph}} &= M_{\mathrm{y}}\left(1 - \left(\frac{N}{F_{\mathrm{tens}}}\right)^{2}\right) \\
\text{and } M_{\mathrm{y,sp}} &= M_{\mathrm{y}}\left(1 - \left(\frac{N}{F_{\mathrm{tens}}} + \frac{V}{F_{\mathrm{shear}}}\right)^{\alpha}\right)
\end{aligned}
\tag{8.11}
$$

with

$M_{\mathrm{y,ph}}$	Yield moment in plastic hinge
$M_{\mathrm{y,sp}}$	Yield moment in shear plane
α	Factor 2 for round fasteners, 1.6 for profiled fasteners

Although these observations provide useful descriptions and delineations of critical cases, a comprehensive representation of connection behaviour is not yet possible. The present study has investigated a limited set of fastener types and configurations, often based on a few representative tests. Consequently, uncertainties regarding the full range of internal force distributions and the behaviour of other connection types remain. Nevertheless, there is no indication of a general risk of fastener failure; only specific cases have been investigated and may require separate consideration in design. Despite these limitations, the present work lays important foundations for further research and a more comprehensive understanding of timber connection performance.

8.5.7 Further Remarks

A general comparative analytical model based on experimental results is only feasible where the internal force distribution and load effects acting within the fastener are fully understood. Consequently, no universal statement can be made regarding the accuracy or applicability of the proposed model in its present form, and further measurements and experimental investigations are required for its validation. Nevertheless,

the model provides an indication of the potential reduction in load-bearing capacity for representative levels of force utilisation.

9 Summary and Outlook

9.1 Summary

Using hardwoods instead of softwoods in timber construction subjects fasteners to higher loads, resulting in multiaxial stress states that are not fully addressed by current design models. These stresses can cause brittle failure, including shear, tensile, bending, or combined loading failures, in both timber-to-timber and timber-to-steel connections. Understanding these stress states and their associated failure mechanisms is essential for a safe design of timber connections.

From a theoretical perspective, a comprehensive design approach requires knowledge of the forces and moments acting on the fastener and the fastener's capacity to resist them. Bending moments, normal forces, and shear forces, as well as their interactions, govern the behaviour of laterally loaded fasteners. Hardwood shifts the stress state from bending-dominated to shear-dominated, and, increases normal forces significantly, which makes normal forces critical in triggering cross-sectional failure. These theoretical considerations form the basis for the experimental investigations in this study. The investigation of novel aspects of fastener behaviour in hardwood connections required the development of new testing approaches, customised setups, and problem-specific measurements and analyses, with standard methods applied where applicable.

The test programme combines several approaches to quantify fastener behaviour in softwood and hardwood. Embedded strain gauges in fully threaded screws and digital image correlation on exposed fasteners provide detailed measurements of local strains, critical stress concentrations, and elastic re-deformation. Bending angles, plastic hinge positions, and strain distributions are determined for aluminium and steel fasteners, allowing the influence of fastener strength to be assessed across different connection configurations and timber densities. Timber-to-timber connections are dominated by plastic hinge formation, whereas timber-to-steel connections exhibit

more pronounced shear-plane yielding. These measurements provide essential reference values for modelling connection behaviour and highlight the strong influence of fastener material on local strain and ductility.

Furthermore, the study focuses on a selected interaction between normal and shear forces, one of several possible types that can lead to fastener failure in the shear plane. A dedicated experimental setup was developed for screws and bolts, allowing detailed observation under combined loading. Fully threaded screws show an angle-dependent reduction of maximum load, reflecting variations in the relative contributions of tensile and shear forces as the direction of the applied load is changed, with interaction curves best described by elliptical or super elliptical functions. Round fastener sections, such as smooth shanks of partially threaded screws and bolts, are effectively represented by a bilinear model: at small angles, failure is dominated by threaded regions and follows a constant or linear relationship, while at larger angles, the shear-dominated region can be conservatively described by a linear trend. Single-shear tests tend to overestimate shear capacity, particularly for profiled fasteners.

Through testing a variety of hardwood screw connections, several practical insights emerge. Correct installation, flush fitting, and predrilling improve on-site handling and help avoid early slip, ensuring the intended load-bearing behaviour. Loads and deformations are evaluated at service-relevant relative displacements ($F_{5\text{mm}}$, $F_{10\text{mm}}$, $F_{15\text{mm}}$), providing a consistent basis for comparing softwood and hardwood connections. Increasing screw spacing in grain direction, as demonstrated with a spacing of $a_1 = 8d$, enhances ductility, while overlapping screw tips prevent brittle failure perpendicular to the grain. These findings provide guidance for extended design and detailing of hardwood connections.

In addition, general limitations of fastener failure can be defined. Critical stress regions arise in the shear plane and at plastic hinge formation, where bending, normal, and shear interactions (*MNV*) govern. The risk of brittle failure increases for slender fasteners ($d \leq 10\,\text{mm}$) and timber densities above 750 kg/m^3. Modified hardwood screws with larger cores and lower thread ratios mitigate these effects and improve ductility. Limiting the rope effect by ensuring head pull-through or thread withdrawal governs prevents complete axial load mobilisation and is one way to control fastener interaction A complete understanding of internal force magnitudes and distributions, however, remains a subject for further research.

Overall, the study demonstrates that fastener type, cross-section, timber density, and connection configuration strongly influence failure mechanisms, load distribution, and ductility. Typical bending-dominated slender fasteners in timber-to-timber connections are governed by plastic hinge formation, whereas shear-plane yielding dominates in timber-to-steel and high-density timber connections. Strain measurements confirm that normal forces critically affect the interaction of internal forces and moments, influencing both load-bearing response and failure modes. These findings integrate theoretical understanding with experimental evidence, providing a basis for improved design, informed fastener selection, and optimised installation in hardwood construction, while highlighting areas requiring further validation.

9.2 Outlook

Further research is required to validate the assumptions made within the scope of the thesis. The magnitude of shear capacity reduction from single-shear to double-shear tests, shank tensile capacities, and normal force magnitudes along the fastener axis, particularly for fully threaded screws or other fastener types exhibiting high normal forces, need further investigations. Extension to other fastener and connection types is still pending. Although this work primarily focuses on *MV* and *NV* interaction, other interaction types, such as *MN* and *MNV*, are identified and briefly discussed but not separately investigated. Nevertheless, the study provides a solid basis for identifying critical locations in fasteners and connections under combined loadings. These two mentioned interaction types may occur in plastic hinges of timber-to-timber connections (*MN*) or in the shear plane of a timber-to-steel/steel-to-timber connections (*MNV*). Conceptual ideas and initial sketches for possible test setups are developed to investigate these additional interactions. These proposed setups are outlined in this outlook and can serve as inspiration for future experimental work. Overall, the present results provide a foundation for revising design rules and fastener approvals when building with hardwoods, explicitly incorporating multiaxial stress states in the fastener and local deformation behaviour.

Concepts for Further Experimental Investigations

As described above, additional interaction types are possible and require investigation. Ideas for a test setup for possible *MN* and *MNV* interactions are presented below. The

testing concepts are initially illustrated schematically and subsequently accompanied by potential setups or implementation suggestions, which, however, are not yet fully developed. These concepts can serve as inspiration for other studies.

The test setup illustrated schematically in Fig. 9.1 consists of the fastener to be investigated, or a substitute cross-section, which is anchored on both sides in a steel element. This steel element is equipped with a roller bearing to allow the rotation of the tested fastener at the support. For testing the variable *MN* or *MNV* interaction, flat steel specimens can initially be used. Similar to a tensile specimen, these elements have a bone-shaped geometry with local reductions in cross-section. In this way, the weakened cross-sectional area can be freely chosen, and failure within the anchorage can be avoided by appropriate dimensioning of the specimen. Flat or rectangular specimens are also easier to anchor in the support roller or beams. For rectangular cross-sections, reductions can be introduced in width and/or thickness. Rectangular profiles are recommended for reasons of handling, but they do not replace tests on round cross-sections, which are required to transfer the results to timber fasteners. Cross-sectional reductions in round specimens must therefore be designed carefully, and it must be ensured that, for hardened materials, the reduction of the outer region does not lead to unrepresentative results for the entire cross-section. If this risk exists, cross-sectional reductions should be avoided, and alternative approaches need to be considered. The applied normal force can be introduced by prestressing. However, due to the large deformations that may occur during testing, continuous monitoring or measurement of the normal force is recommended. This can be achieved, for example, by applying, controlling, and measuring the normal force through a horizontal actuator, or alternatively by using load cells placed beneath the specimen head or anchorage, e.g. force measuring rings. This test setup remained at the conceptual stage. One potential advantage of this setup would be that multiple types of interaction could be investigated within a single configuration. However, due to the high level of complexity, no experiments or detailed planning towards its realisation were undertaken.

The realisation and execution of the test setup illustrated schematically in Fig. 9.2 were planned, but not carried out within the scope of this thesis. The test setup and its function are nevertheless briefly introduced here based on its main components. The test setup is illustrated in detail in Fig. 9.3 consists of an upper and a lower part, which are connected solely by the fastener, in this case a screw. The load is introduced via a bolt passing through two outer steel plates that enclose a rectangular hollow section (RHS). Inside the RHS, steel blocks are welded in, each containing a hole with an inner diameter corresponding to the outer diameter of the inserted sleeves. The fastener is to

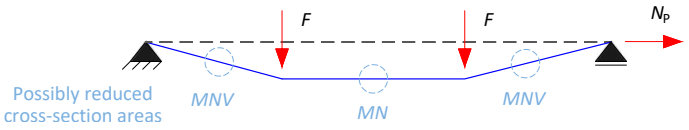

a. Test setup comparable to four-point-bending test.

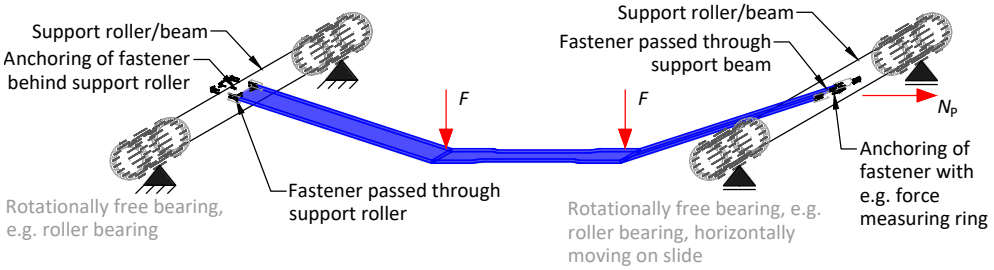

b. Description of the test setup components with exemplary cross-section reduction in centre area.

Fig. 9.1: Test setup concepts to test *MN* and *MNV* interaction behaviour with one test rig. Simplified deformation sketches.

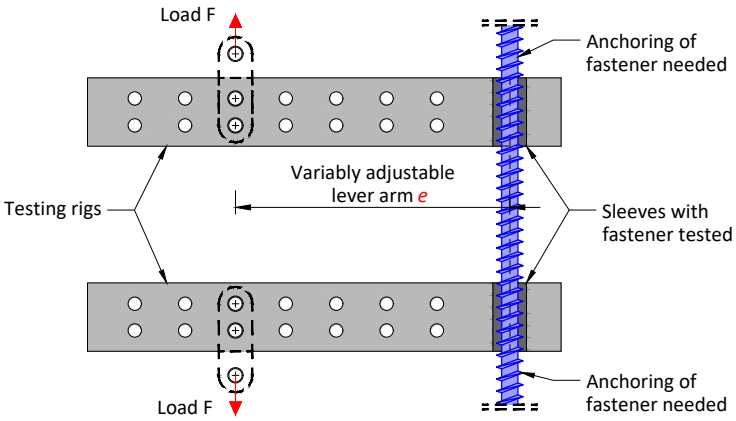

Fig. 9.2: *MN* scheme with transmitted forces F and $M = F \cdot e$.

be anchored accordingly, for example by screwing it into aluminium blocks as applied in the realised setup described in Chapter 7. The combined *MN* loading is generated by shifting the RHS eccentrically relative to the line of action of the applied load. In analytical terms, the resulting eccentricities remain small, as bending soon governs the overall response. To adjust the eccentricity and fix the RHS position, spacer plates of varying thickness and a fixing block are provided and assembled with bolts. The

fixing block ensures the distance between the RHS and the edge plate. Using only the fixing block corresponds to a pure tension test configuration, see section view A-A. Increasing the eccentricity is achieved by inserting additional spacers on the inner side, while the bolt length can remain the same, with any remaining spacers placed on the outer side. Sufficient space between the upper and lower parts must be ensured, as significant rotations are expected during testing.

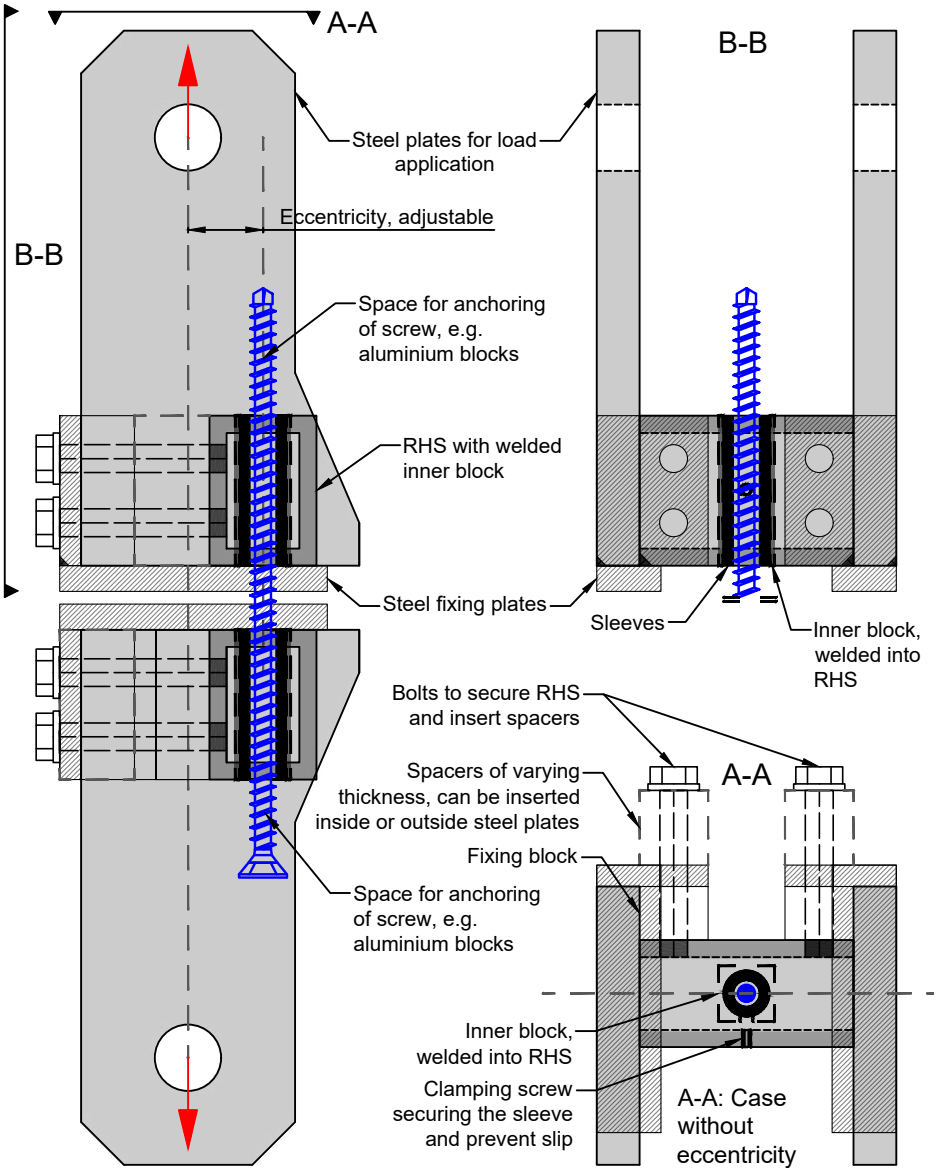

Fig. 9.3: Schematic illustration of a possible test setup with individual components for combined bending moment and normal force in a screw. Side view on the left exemplarily with maximum eccentricity, section view A-A shows setup without eccentricity.

Own Publications

Journal Articles

[1] E. Kuck and C. Sandhaas. Load-bearing behaviour of partially threaded screws in hardwood. *Wood Material Science & Engineering*, pages 283–298, 2022. doi: 10.1080/17480272.2022.2084453.

Conference Articles

[2] E. Kuck. Studie zum Tragverhalten von Teilgewindeschrauben in Buchenfurnierschichtholz. In Prof. Dr.-Ing. Ulrike Kuhlmann, editor, *9. Doktorandenkolloquium Holzbau Forschung + Praxis*, pages 195–202, 2022.

[3] E. Kuck. Studie zu auftretenden Normalkräften in auf Abscheren beanspruchten Schrauben. In Prof. Dr.-Ing. Ulrike Kuhlmann, editor, *10. Doktorandenkolloquium Holzbau Forschung + Praxis*, pages 73–80, March 2024.

[4] E. Kuck, C. Sandhaas, and H. J. Blaß. How Interaction of Internal Forces and Moments influence the Load-Bearing Capacity of Dowels. In *Proceedings of WCTE*, pages 2834–2840, Brisbane, Australia, 2025.

References

[5] T. K. Bader, M. Schweigler, E. Serrano, M. Dorn, B. Enquist, and G. Hochreiner. Integrative experimental characterization and engineering modeling of single-dowel connections in LVL. *Construction and Building Materials*, 107:235–246, 2016.

[6] T. K. Bader, J. F. Bocquet, M. Schweigler, and R. Lemaître. Numerical modeling of the load distribution in multiple fastener joints. International Conference on Connections in Timber Engineering – From Research to Standards: COST Action FP1402, 2017. Graz, Austria.

[7] I. Bejtka and H. J. Blaß. Joints with inclined screws: Paper 35-7-4. CIB-W18 Meeting 35, 2002. Kyoto, Japan.

[8] D. W. Bilderbeek. Voorspannbouten en handelsbouten op trek en afschuiving, 1971. Stevin-Laboratorium, Delft, The Netherlands.

[9] H. J. Blaß. Moment-Normalkraft-Querkraft Interaktion in stiftförmigen Verbindungsmitteln von Stahlblech-Holz-Verbindungen. In *Karlsruher Tage HOLZBAU Forschung für die Praxis*, pages 17–26. KIT Scientific Publishing, October 2018.

[10] H. J. Blaß and I. Bejtka. Selbstbohrende Holzbauschrauben und ihre Anwendungsmöglichkeiten. Technical report, Bruderverlag Karlsruhe, 2003.

[11] H. J. Blaß and I. Bejtka. Verbindungen mit geneigt angeordneten Schrauben. *Bauen mit Holz Fachzeitschrift für konstruktioven Holzbau und Ausbau*, (Oktober):28–36, 2003.

[12] H. J. Blaß and F. Colling. Load-carrying capacity of dowelled connections, 48-7-3. In *INTER Proceedings Meeting 48*, pages 115–129, Sibenik, Croatia, 2015.

[13] H. J. Blaß and C. Sandhaas. *Ingenieurholzbau. Grundlagen der Bemessung*. KIT Scientific Publishing, Karlsruhe, 2016.

[14] H. J. Blaß, A. Bienhaus, and V. Krämer. Effective bending capacity of dowel-type fasteners. In *Proceedings of CIB-W18 Meeting 33*, Delft, The Netherlands, 2000.

[15] H. J. Blaß, C. Sandhaas, and N. Meyer. Steel-to-timber connections: Failure of laterally loaded dowel-type fasteners, 50-7-1. In *INTER Proceedings Meeting 50*, pages 67–79, Kyoto, 2017.

[16] R. Brandner. Properties of axially loaded self-tapping screws with focus on application in hardwood. *Wood Material Science and Engineering*, 14(5):254–268, 2019.

[17] R. Brandner, A. Ringhofer, and T. Reichinger. Performance of axially-loaded self-tapping screws in hardwood: Properties and design. *Engineering Structures*, 188:677–699, 2019.

[18] B. V. Burzlaff. Experimentelle und Analytische Untersuchung der Verbindungsmittelverformung bei Beanspruchung auf Abscheren. Master thesis, unpublished, KIT, 2024.

[19] W. D. Callister and D. G. Rethwisch. *Materialwissenschaften und Werkstofftechnik: eine Einführung*. Wiley-VCH, Weinheim, 1. edition, 2013.

[20] W. F. Chen and D. J. Han. *Plasticity for Structural Engineers*. Springer Verlag, 1988.

[21] E. Jr. Chesson, N. L. Faustino, and W. H. Munse. High-Strength Bolts Subjected to Tension and Shear. *Journal of the Structural Division*, 91(5), 1965.

[22] J. Choquette. Évaluation d'une nouvelle méthode de calcul des assemblages de bois à l'aide de connecteurs de petits diamètres. Master thesis, Université Laval, Québec, 2016.

[23] T. Claus, W. Seim, and J. Küllmer. Force distribution in self-tapping screws: experimental investigations with fibre Bragg grating measurement screws. *European Journal of Wood and Wood Products*, 80(1):183–197, February 2022.

[24] Correlated Solutions. Speckle Pattern Generator. URL `https://www.correlatedsolutions.com/downloads`. accessed on June 2025.

[25] Dantec Dynamics. ISTRA 4D, April 2017. Software Manual, Q-400 System. Manual: 4.4.6 v2, Software: 4.4.6.160.

[26] D. Dinkler. Traglastverfahren mit M–N–Q–Interaktion. In *Grundlagen der Baustatik: Modelle und Berechnungsmethoden für ebene Stabtragwerke*, pages 388–398. Springer Fachmedien, Wiesbaden, 2022.

[27] E. Dobrowolska, P. Wroniszewska, and A. Jankowska. Density Distribution in Wood of European Birch (Betula pendula Roth.). *Forests*, 11(4), 2020.

[28] D. C. Drucker. The Effect of Shear on the Plastic Bending of Beams. *Journal of Applied Mechanics*, pages 509–514, 1956.

[29] D. C. Drucker and W. Prager. Soil mechanics and plastic analysis or limit design. *Quarterly of Applied Mathematics*, 10(2):157–165, 1952.

[30] D. C. Drucker, W. Prager, and H. J. Greenberg. Extended limit design theorems for continuous media. *Quarterly of Applied Mathematics*, 9(4):381–389, January 1952.

[31] J. Ehlbeck and W. Siebert. Tragverhalten von Nagelverbindungen bei gleichzeitiger Beanspruchung auf Abscheren und Ausziehen. Forschungsbericht, Versuchsanstalt für Stahl, Holz und Steine, Abt. Ingenieurholzbau, Universität Fridericiana Karlsruhe, 1984.

[32] J. Ehlbeck and H. Werner. Softwood and hardwood embedding strength for dowel-type fasteners: Paper 25-7-2. In *Proceedings of CIB-W18 Meeting 25*, Ahus, Sweden, 1992.

[33] M. Enders-Comberg. *Leistungsfähige Verbindungen des Ingenieurholzbaus - Einsatzmöglichkeiten für Nadel- und Laubholz*. PhD thesis, Karlsruhe Institute for Technology (KIT), 2015.

[34] F. Engesser. Die Knickfestigkeit gerader Stäbe. *Centralblatt der Bauverwaltung*, 11(49):483–486, 1891.

[35] S. Franke and B. Franke. Bemessung von Stabdübelverbindungen in Buchen-Brettschichtholz. *Bautechnik*, 97(S1), 2020.

[36] S. Franke and N. Magnière. Discussion of testing and evaluation methods for the embedment behaviour of connections. 47-7-1. In *INTER Proceedings Meeting 47*, pages 93–102, Bath, UK, 2014.

[37] M. Frese. Density variations in beech LVL: influence on insertion moment and withdrawal capacity of screws. In *Proceedings of INTER Meeting 52*, Tacoma, USA., 2019.

[38] M. Frese, P. Fellmoser, and H. J. Blaß. Modelle für die Berechnung der Ausziehtragfähigkeit von selbstbohrenden Holzschrauben. *European Journal of Wood and Wood Products*, 68(4):373–384, 2010. doi: 10.1007/s00107-009-0378-1.

[39] K. Fukazawa. Juvenile wood of hardwoods judged by density variation. *IAWA Bulletin n.s.*, 5(1):65–73, 1984.

[40] DASt Deutscher Ausschuß für Stahlbau e.V. Forschungsbericht 2/2017, IGF-Nummer 18095 N: Untersuchungen zum Tragverhalten von hochfesten Schrauben unter kombinierter Zug- und Scherbeanspruchung. Technical report, Technische Universität Darmstadt Institut für Stahlbau und Werkstoffmechanik, Fachgebiet Stahlbau, Prof. Dr.-Ing. Jörg Lange, 2021.

[41] K. Goossens. M-N-V Interaktion in stiftförmigen Verbindungsmitteln für Stahlblech-Holzverbindungen. Master thesis, unpublished, KIT, 2017.

[42] Y. H. Guu, H. Hocheng, C. Y. Chou, and C. S. Deng. Effect of electrical discharge machining on surface characteristics and machining damage of AISI D2 tool steel. *Materials Science and Engineering: A*, 358(1):37–43, October 2003. doi: 10.1016/S0921-5093(03)00272-7.

[43] A. Hassanieh, H. R. Valipour, and M. A. Bradford. Load-slip behaviour of steel-cross laminated timber (CLT) composite connections. *Journal of Constructional Steel Research*, 122:110–121, 2016.

[44] M. Hassler. Versuche mit Schrauben bei kombinierter Zug-und Scherbeanspruchung. Technical Report 1, Universität Stuttgart, 1973.

[45] R. Hill. A theory of the yielding and plastic flow of anisotropic metals. *Proceedings Royal Society (London), Series A*, 193:281–297, 1948.

[46] R. Hill. *The mathematical theory of plasticity*. Oxford University Press, 1950.

[47] M. R. Horne. The Plastic Theory of Bending of Mild Steel Beams with Particular Reference to the Effect of Shear Forces. In *Proceedings of the Royal Society of London*, volume 1089, pages 216–228, 1951.

[48] U. Hübner, T. Bogensperger, and G. Schickhofer. Embedding strength of European hardwoods: Paper 41-7-5. In *CIB-W18 Meeting 41*, St. Andrews by-the-Sea, Canada, 2008.

[49] G. Jeitler, M. Augustin, and G. Schickhofer. Birch – GLT&CLT: Mechanical properties of glued laminated timber and cross laminated timber produced with the wood species Birch. In *In Proceedings of WCTE 2016, Vienna, Austria*, 2016.

[50] K. W. Johansen. Theory of Timber Connections. *IABSE: International Association of Bridge and Structural Engineering, Basel, Switzerland.*, 9:249-262, 1949.

[51] A. Jorissen. *Double-shear timber connections with dowel-type fasteners*. PhD Thesis, Delft University of Technology, 1998.

[52] S. Kaliszky, I. Sajtos, B. A. Lógó, J. M. Lógó, and Z. Szabó. Gábor Kazinczy and His Legacy in Structural Engineering. *Periodica Polytechnica Civil Engineering*, 59(1):3–7, 2015.

[53] G. v. Kazinczy. Kritische Betrachtungen zur Plastizitätstheorie. *IVBH Kongressbericht*, 2, 1936.

[54] R. Kindmann and J. Frickel. *Elastische und plastische Querschnittstragfähigkeit: Grundlagen, Methoden, Berechnungsverfahren, Beispiele: Online-Auflage*. Online-Auflage, 2017.

[55] M. Knobloch and H. Schmidt. *Tragfähigkeit und Tragverhalten stahlbauüblicher Schrauben unter reiner Scherbeanspruchung und unter kombinierter Scher-Zugbeanspruchung*. Forschungsberichte aus dem Fachbereich Bauwesen. Universität Essen, 1987.

[56] P. Kobel. *Dowel-Type Connections in Beech LVL*. PhD thesis, ETH Zurich, 2019.

[57] P. Kobel, R. Steiger, and A. Frangi. Experimental analysis on the structural behaviour of connections with LVL made of beech wood. *Materials and joints in timber structures. Recent developments in technology*, pages 211–220, 2014.

[58] H. Krenn. Der Einfluss der Gruppenwirkung von Schraubenverbindungen auf das Nachweisverfahren. In *Proceedings of 16. Internationales Holzbau-Forum*, Garmisch, 2010.

[59] H. Krenn. *Ein Beitrag zur Stahlblech-Holz-Zuglaschenverbindung mit geneigt angeordneten selbstbohrenden Holzschrauben.* PhD thesis, TU Graz, 2017.

[60] G. L. Kulak, J. W. Fisher, and J. H. A. Struik. Guide to Design Criteria for Bolted and Riveted Joints. Technical Report second edition, John Wiley & Sons, 1987. published by American Institute of Steel Construction.

[61] H. J. Larsen. Determination of Load-Slip Curves for Bolts and Nails. In *Proceedings of IUFRO, International Union of Forestry Research Organisation*, Delft, The Netherlands, April 1975.

[62] J. Laumann, M. Feldmann, J. Frickel, M. Krahwinkel, M. Kraus, N. Stranghöner, and T. Ummenhofer. *Petersen Stahlbau - Grundlagen der Berechnung und baulichen Ausbildung von Stahlbauten*. Springer Vieweg, 5 edition, 2020.

[63] R. Lemaître, J. F. Bocquet, M. Schweigler, and T. K. Bader. Beam-on-foundation (BOF) modelling as an alternative design method for timber joints with dowel-type fasteners – Part 1: Strength and stiffness per shear plane of single-fastener joints. Paper 51-7-13. INTER Meeting 51, 2018. Tallinn, Estonia.

[64] U. Mahlknecht, R. Brandner, and A. Ringhofer. Minimum geometric and execution requirements for axially loaded groups of screws in hardwood, 54-7-6. In Rainer Görlacher, editor, *INTER Proceedings Meeting 54*, Online, 2021. Timber Scientific Publishing, KIT Holzbau und Baukonstruktionen, Karlsruhe, Deutschland.

[65] C. Meiertoberend. Ermittlung von Bemessungsparametern von Teilgewindeschrauben in Laubholz. Bachelor thesis, unpublished, KIT, 2021.

[66] A. Meyer. Die Tragfähigkeit von Nagelverbindungen bei statischer Belastung. *Holz als Roh- und Werkstoff: European Journal of Wood and Wood Industries*, 15(2), 1957.

[67] N. Meyer. *Tragfähigkeit mechanischer und geklebter Verbindungsmittel in Buchenfurnierschichtholz*. PhD thesis, Karlsruhe Institute for Technology (KIT), 2020.

[68] M. A. Meyers and K. K. Chawla. *Mechanical behavior of materials*. Cambridge University Press, Cambridge, 2. edition, 2010.

[69] A. Misconel, M. Ballerini, and J. W. van de Kuilen. Steel-to-timber joints of beech-LVL with very high strength steel dowels. In *Proceedings of 14th WCTE*, Vienna, Austria, 2016.

[70] K. Ogawa and K. Kobayashi. Difference in Mechanical Properties due to Inhibition Techniques of Friction Applied to Lateral Tests of Timber Joints. In *Proceedings of WCTE*, pages 1494–1499, Brisbane, Australia, 2025.

[71] B. Pan, Z. Lu, and H. Xie. Mean intensity gradient: An effective global parameter for quality assessment of the speckle patterns used in digital image correlation. *Optics and Lasers in Engineering*, 48(4):469–477, April 2010.

[72] T. Pitrakkos, W. Tizani, M. Cabrera, and N. Faqe. Blind Bolts with Headed Anchors Under Combined Tension and Shear. *Journal of Constructional Steel Research*, 179(106546), 2021.

[73] W. Prager and B. G. Neal. Introduction to Plasticity. *Journal of Applied Mechanics*, 27:221–221, 1960.

[74] J. Pyykkö and S. Svensson. Load-bearing capacity of slender dowel-type fasteners in Timber-Concrete Composite connections. *Engineering Structures*, 316, 2024.

[75] G. Quino, Y. Chen, K. R. Ramakrishnan, F. Martínez-Hergueta, G. Zumpano, A. Pellegrino, and N. Petrinic. Speckle patterns for DIC in challenging scenarios: rapid application and impact endurance. *Measurement Science and Technology*, 32(1):015203, October 2020.

[76] A. Renner and J. Lange. Versuche zur Zug-Abscher-Interaktionstragwirkung von Schrauben. *Stahlbau*, 83(4):265–272, 2014.

[77] A. Renner and J. Lange. Zum Tragverhalten und zur Bemessung von Schrauben unter kombinierter Zug-Abscher-Belastung. *Stahlbau*, 88(4):324–330, 2019.

[78] A. Ringhofer. *Axially Loaded Self-Tapping Screws Axially Loaded Self-Tapping Screws in Solid Timber and Laminated Timber Products: TET 5*. PhD thesis, TU Graz, 2017.

[79] A. Ringhofer, M. Burtscher, R. Sieder, and M. Gstettner. Self-tapping Timber Screws Subjected to Combined Axial and Lateral Loading, 54-7-2. In Rainer Görlacher, editor, *INTER Proceedings Meeting 54*, Online, 2021. Timber Scientific Publishing, KIT Holzbau und Baukonstruktionen, Karlsruhe, Deutschland.

[80] J.W. Roderick. LXV. Theory of plasticity—elements of simple theory. *The London, Edinburgh, and Dublin Philosophical Magazine and Journal of Science*, 7(39:294):529–539, 1948.

[81] C. Sandhaas. *Mechanical behaviour of timber joints with slotted-in steel plates*. PhD thesis, Delft University of Technology, 2012.

[82] C. Sandhaas. *Timber fasteners: a study on input parameters for the design of timber joints*. Habilitation, Karlsruhe Institute for Technology (KIT), 2024.

[83] C. Sandhaas and H. J. Blaß. Steel properties of self-tapping screws. In *INTER Proceedings Meeting 54*, online, 2021.

[84] C. Sandhaas and H. J. Blaß. Head pull-through properties of self-tapping screws. In *INTER Proceedings Meeting 55*, Bad Aibling, 2022.

[85] C. Sandhaas and H.J. Blaß. Withdrawal properties of self-tapping screws. In *INTER Proceedings Meeting 55*, Biel, 2023.

[86] C. Sandhaas, G. Ravenshorst, H. J. Blaß, and J. W. G. van de Kuilen. Embedment tests parallel-to-grain and ductility aspects using various wood species. *European Journal of Wood and Wood Products*, 71(5):599–608, 2013. ISSN 0018-3768. doi: 10.1007/s00107-013-0718-z.

[87] C. Sandhaas, J. Munch-Andersen, and P. Dietsch. Design of Connections in Timber Structures: A state-of-the-art report by COST Action FP1402 / WG3. A state-of-the-art report by COST Action FP1402 / WG3, Shaker Verlag Aachen, 2018.

[88] K. Sawata and M. Yasumura. Determination of embedding strength of wood for dowel-type fasteners. *Journal of Wood Science*, 48(2):138–146, 2002. ISSN 1435-0211. doi: 10.1007/BF00767291.

[89] G. Schiro, I. Giongo, W. Sebastian, D. Riccadonna, and M. Piazza. Testing of timber-to-timber screw-connections in hybrid configurations. *Construction and Building Materials*, 171:170–186, May 2018.

[90] E. Schwab, M. Liesebach, and B. R. Stephan. Holzeigenschaften der japanischen Maximowicz-Birke von einem norddeutschen Standort. *Holz als Roh- und Werkstoff*, 54(5):301–306, 1996.

[91] M. Schweigler, T. K. Bader, G. Hochreiner, G. Unger, and J. Eberhardsteiner. Load-to-grain angle dependence of the embedment behavior of dowel-type fasteners in laminated veneer lumber. *Construction and Building Materials*, 126: 1020–1033, 2016. ISSN 0950-0618. doi: 10.1016/j.conbuildmat.2016.09.051.

[92] M. Schweigler, T. K. Bader, J.-F. Bocquet, R. Lemaître, and C. Sandhaas. Embedment test analysis and data in the context of phenomenological modeling for dowelled timber joint design: 52-07-8. In *INTER Proceedings Meeting 52*, pages 155–172. Timber Scientific Publishing, 2019.

[93] M. Schweigler, M. Vedovelli, R. Lemaître, J.-F. Bocquet, C. Sandhaas, and T. K. Bader. Beam-on-Foundation Modeling as an Alternative Design Method for Timber Joints with Dowel-Type Fasteners – Part 3: Second Order Theory Effects for Considering the Rope Effect. In *INTER Proceedings Meeting 54*, pages 209–225, online, 2021.

[94] H. Shakir-Khalil and C. M. Ho. Black Bolts under Combined Tension and Shear. *The Structural Engineer*, Volume 57B(16), 1979.

[95] H. H. Snijder, D. Ungermann, J. W. B. Stark, G. Sedlacek, F. S. K. Bijlaard, and A. Hemmert-Halswick. Evaluation of Test Results on Bolted Connections in order to obtain Strength Functions and Suitable Model Factors. *Netherlands organization for applied scientific research*, 1989.

[96] B. E. Steeve and R. J. Wingate. Aerospace Threaded Fastener Strength in Combined Shear and Tension Loading. Technical report, NASA Marshall Space Flight Center, Huntsville, AL, United States, 2012.

[97] M. Steilner and H. J. Blaß. A method to determine the plastic bending angle of dowel-type fasteners. *Materials and joints in timber structures. Recent developments in technology*, pages 603–613, 2014.

[98] S. Strübel and H. J. Blaß. Study of steel-to-timber connections with very thin steel plates. In *Proceedings ICEM20 - Experimental Mechanics in Engineering and Biomechanics. Ed.: J.F. Silva Gome*, pages 959–970. NEGI-Instituto de Ciência e Inovação em Engenharia Mecânica e Gestão Industrial, 2023.

[99] M. A. Sutton. Digital Image Correlation for Shape and Deformation Measurements. In W. N. Sharpe, editor, *Springer Handbook of Experimental Solid Mechanics*, pages 565–600. Springer US, Boston, MA, 2008.

[100] S. Timoshenko. On the Correction for Shear of the Differential Equation for Transverse Vibrations of Prismatic Bars. *The London, Edinburgh, and Dublin Philosophical Magazine and Journal of Science*, 41:744–746, 1921.

[101] J. Töpler, M. Schweigler, R. Lemaître, P. Palma, M. Schenk, P. Grönquist, C. Tapia Camú, G. Hochreiner, and U. Kuhlmann. Finite element based design of timber structures, 56-102-1. In *Proceedings of INTER 2023, 10th meeting*, Biel, 2023.

[102] I. Vayas. Interaktion der plastischen Grenzschnittgrößen doppelsymmetrischer I-Querschnitte. *Stahlbau*, 69(9):693–706, 2000.

[103] M. Vedovelli. Untersuchungen zu Zugscherverbindungen in Laubholz. In *8. Doktorandenkolloquium Holzbau Forschung + Praxis*, pages 127–134, 2020.

[104] R. von Mises. Mechanik der festen Körper im plastisch- deformablen Zustand. *Nachrichten von der Gesellschaft der Wissenschaften zu Göttingen (Mathematisch-physikalische Klasse)*, pages 582–592, 1913.

[105] Y. Wang, T. Wang, R. Crocetti, M. Schweigler, and M. Wålinder. Embedment behavior of dowel-type fasteners in birch plywood: Influence of load-to-face grain angle, test set-up, fastener diameter, and acetylation. *Construction and Building Materials*, 384, 2023.

[106] M. Westermayr and J. W. van de Kuilen. A conceptual model to predict the withdrawal capacity of screws inserted parallel to grain in beech, ash and spruce. In *INTER Proceedings Meeting 53*, Online, 2020.

[107] L. R. J. Whale and I. Smith. A method for measuring the embedding characteristics of wood and wood-based materials. *Materials and Structures*, 22(6): 403–410, 1989. doi: 10.1007/BF02472217.

[108] Schlussbericht zum Vorhaben 22026818. Innovative Verbindungen unter Verwendung von Laubhölzern. Technical report, Holzbau und Baukonstruktion, KIT, 2023. URL www.fnr.de/index.php?id=11150&fkz=22026818.

Standards and Approvals

[109] AISI S904-17. Test Standard for Determining the Tensile and Shear Strengths of Steel Screws, 2017. American Iron and Steel Institute.

[110] ANSI/AISC 360-16. Specification for Structural Steel Buildings, 2016. American Institute of Steel Construction.

[111] ASTM D5764-97a. Standard test method for evaluating dowel-bearing strength of wood and wood-based products, 2013. West Conshohocken, United States.

[112] BS 5950-1:2000. Structural use of steelwork in building. Code of practice for design. Rolled and welded sections, 2000. British Standards Institution, London, United Kingdom.

[113] DIN 18800-1:1990-11. Stahlbauten; Bemessung und Konstruktion, 1990. DIN Deutsches Institut für Normung e.V., Berlin.

[114] DIN EN 1382:2016-07. Holzbauwerke - Prüfverfahren - Ausziehtragfähigkeit von Holzverbindungsmitteln, 2016. DIN Deutsches Institut für Normung e.V., Berlin.

[115] DIN EN 1383:2016-07. Holzbauwerke - Prüfverfahren - Prüfung von Holzverbindungsmitteln auf Kopfdurchziehen, 2016. DIN Deutsches Institut für Normung e.V., Berlin.

[116] DIN EN 1993-1-1:2010. Eurocode 3: Bemessung und Konstruktion von Stahlbauten – Teil 1-1: Allgemeine Bemessungsregeln und Regeln für den Hochbau, 2010. DIN Deutsches Institut für Normung e.V., Berlin.

[117] DIN EN 1993-1-8:2010. Eurocode 3. Bemessung und Konstruktion von Stahlbauten - Teil 1-8: Bemessung von Anschlüssen, 2010. DIN Deutsches Institut für Normung e.V., Berlin.

[118] DIN EN 1995-1-1:2010-12. Eurocode 5: Bemessung und Konstruktion von Holzbauten - Teil 1-1: Allgemeines - Allgemeine Regeln und Regeln für den Hochbau, 2010. DIN Deutsches Institut für Normung e.V., Berlin.

[119] DIN EN 383:2007-03. Holzbauwerke - Prüfverfahren - Bestimmung der Lochleibungsfestigkeit und Bettungswerte für stiftförmige Verbindungsmittel, 2007. DIN Deutsches Institut für Normung e.V., Berlin.

[120] DIN EN 409:2009. Holzbauwerke - Prüfverfahren – Bestimmung des Fließmoments von stiftförmigen Verbindungsmitteln, 2009. DIN Deutsches Institut für Normung e.V., Berlin.

[121] EN 14592:2012. Timber structures – Dowel-type fasteners – Requirements, 2012. Comité Européen de Normalisation (CEN), Brussels, Belgium.

[122] EN 26891. Timber structures – Joints made with mechanical fasteners – General principles for the determination of strength and deformation characteristics (ISO 6891), 1991.

[123] EN ISO 10666:2010. Drilling screws with tapping screw thread – Mechanical and functional properties, 2010. Comité Européen de Normalisation (CEN), Brussels, Belgium.

[124] EN ISO 898-1:2013. Mechanical properties of fasteners made of carbon steel and alloy steel. Bolts, screws and studs with specified property classes. Coarse thread and fine pitch thread, 2013. British Standards Institution, London, United Kingdom.

[125] ETA-14/0354 vom 11. Juli 2018. Brettschichtholz aus Laubholz - Buchenfurnierschichtholz für tragende Zwecke; Österreichisches Institut für Bautechnik (OiB), 2018.

[126] ETA-19/0031 from 12. August 2021. Glued laminated timber (GLT) made of solid hardwood; Austrian Institute of Construction Engineering (OIB), 2021.

[127] European Assessment Document EAD 130118-01-0603. Screws and threaded rods for use in timber constructions, February 2019. EOTA.

[128] FprEN 1995-1-1:2024. Eurocode 5: Design of timber structures - Part 1-1: General rules and rules for buildings, 2024. Version 3d, CEN/TC 250.

[129] ISO/DIS 10984-2. Timber structures – Dowel type fasteners – Part 2: Determination of embedding strength and foundation values, 2008. International Organization for Standardization, Geneva.

A Appendices

A.1 Results on Basic Input Parameters

Table A.1: Results of embedment tests, density ρ in kg/m^3, moisture content u in %, embedment strength f_h in N/mm^2, CoV in %.

Wood species			Screw type 1 np			Screw type 2 p		
			ρ	u	f_h	ρ	u	f_h
Beech LVL type S	Shank	Mean	812	7.06	58.6	816	7.11	55.5
		CoV	5.25	6.45	10.3	2.13	2.39	6.46
	Thread	Mean	823	9.64	72.4	818	7.14	63.1
		CoV	2.98	8.35	7.86	2.97	3.67	6.51
Birch solid wood	Shank	Mean	599	11.6	23.7	601	11.3	27.4
		CoV	6.90	2.90	11.5	9.18	2.67	13.9
	Thread	Mean	625	11.3	31.7	615	11.4	32.5
		CoV	9.93	3.18	16.9	7.70	2.44	13.9

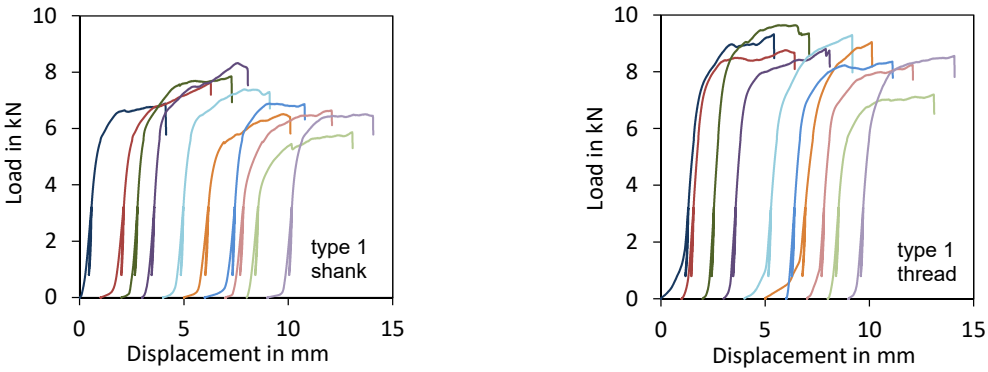

Fig. A.1: Embedment test results in beech LVL for screw type 1, non-predrilled, in shank and threaded screw sections.

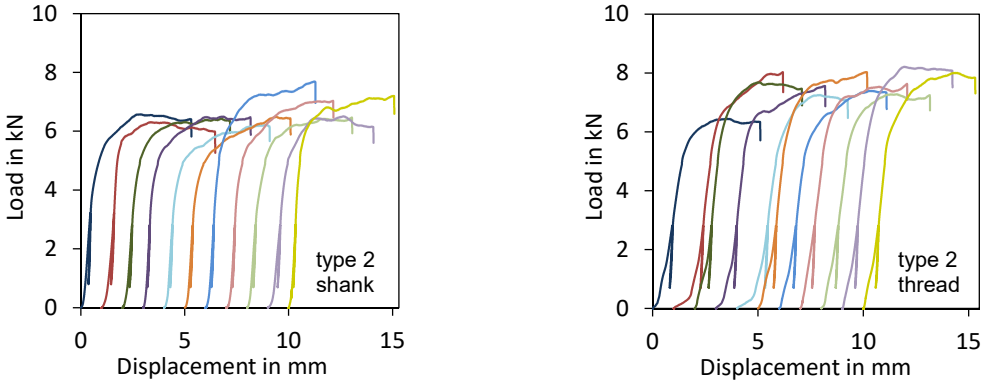

Fig. A.2: Embedment test results in beech LVL for screw type 2, predrilled, in shank and threaded screw sections.

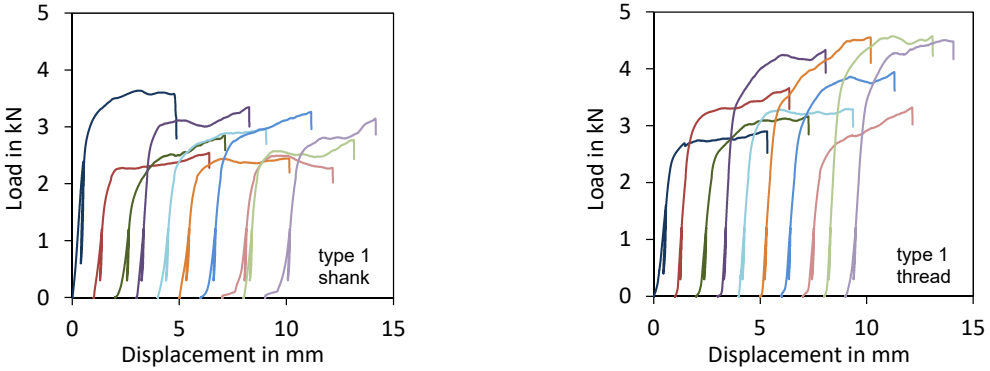

Fig. A.3: Embedment test results in birch solid wood for screw type 1, non-predrilled, in shank and threaded screw sections.

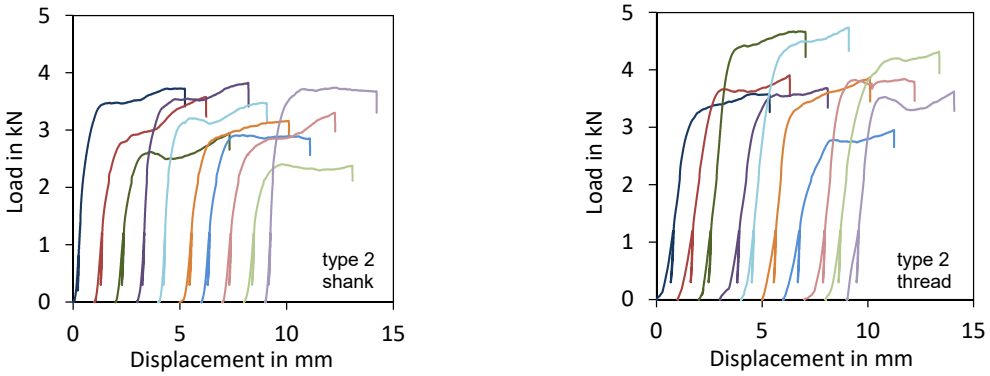

Fig. A.4: Embedment test results in birch solid wood for screw type 2, predrilled, in shank and threaded screw sections.

Table A.2: Results of withdrawal tests, density ρ in kg/m^3, moisture content u in %, withdrawal parameter f_{ax} in N/mm^2, CoV in %, r.. radial, t.. tangential.

		Screw type 1 np			Screw type 2 p		
Wood species		ρ	u	f_{ax}	ρ	u	f_{ax}
Beech LVL	Mean	816	7.58	51.6	822	7.46	39.3
type S	CoV	1.56	3.17	4.96	1.50	3.85	4.02
Birch glulam	Mean	616	10.6	26.5r / 30.1t	630	10.6	22.0r / 27.1t
	CoV	7.49	2.49	15.3r / 11.2t	6.64	1.94	19.5r / 17.3t

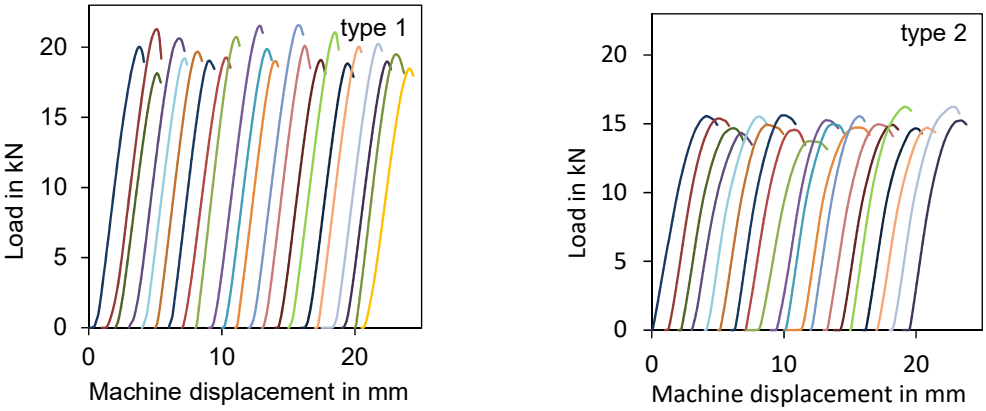

Fig. A.5: Withdrawal test results in beech LVL for both screw types.

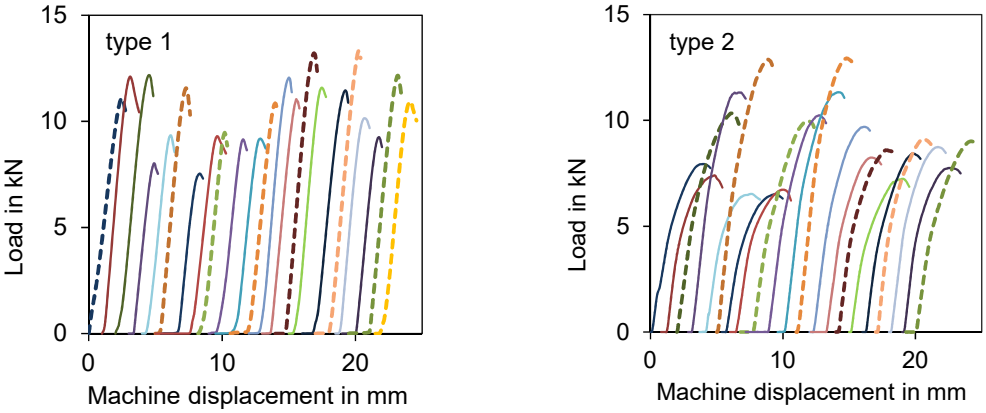

Fig. A.6: Withdrawal test results in birch glulam for both screw types. Dotted lines mark predominantly tangential direction, solid lines mark predominantly radial direction of annual rings.

Table A.3: Results of head pull-through tests, density ρ in kg/m^3, moisture content u in %, head pull-through parameter f_{head} in N/mm^2, CoV in %.

		Screw type 1 np			Screw type 2 p		
Wood species		ρ	u	f_{head}	ρ	u	f_{head}
Beech LVL type S	Mean	796	7.42	53.4	812	7.38	68.6
	CoV	2.38	2.16	6.47	2.31	1.62	7.28
Birch solid wood	Mean	587	10.7	27.2	576	10.8	28.6
	CoV	7.53	4.33	15.9	8.43	4.09	15.4

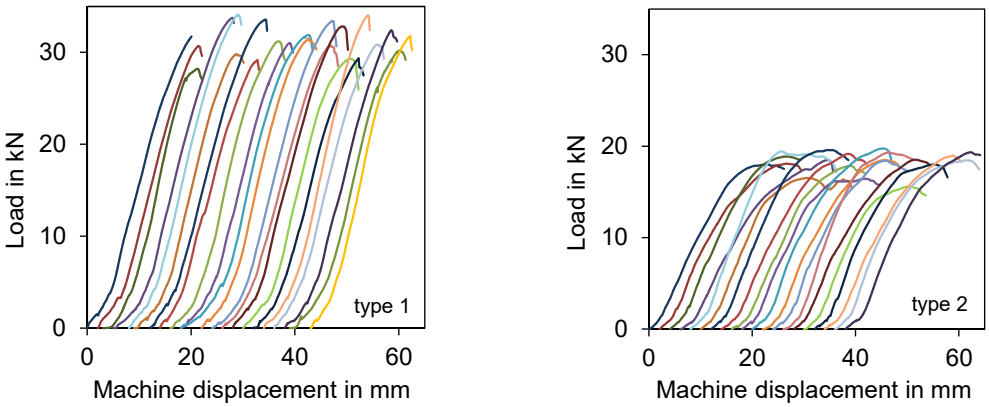

Fig. A.7: Head pull-through test results in beech LVL for both screw types.

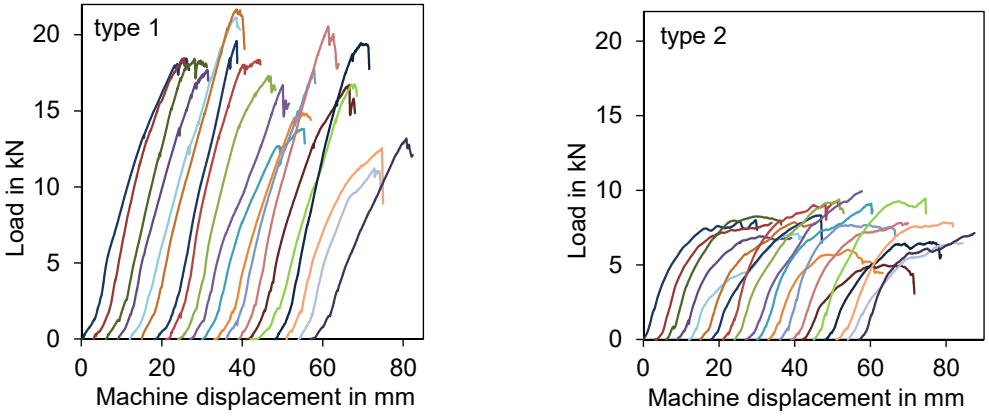

Fig. A.8: Head pull-through test results in birch solid wood for both screw types.

A.2 Results on Connection Tests with Birch Glulam

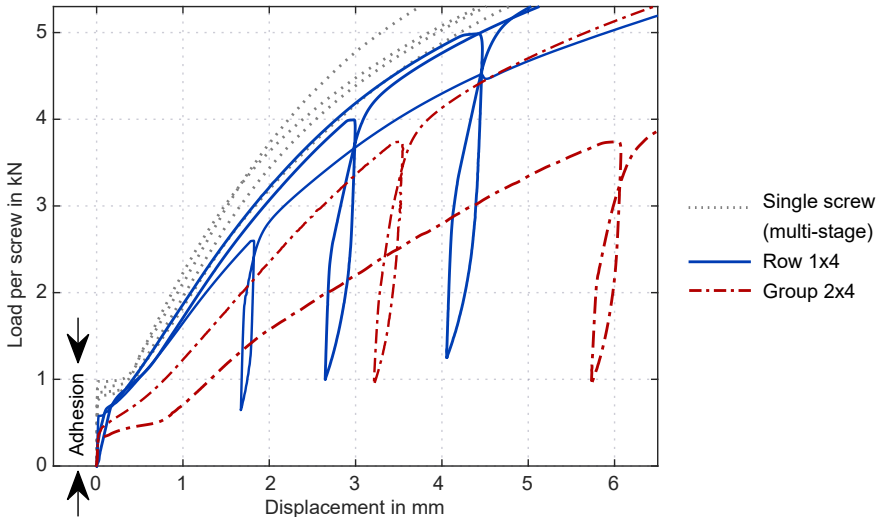

Fig. A.9: Initial range of load-displacement curves of predrilled type 2 screws in birch glulam.

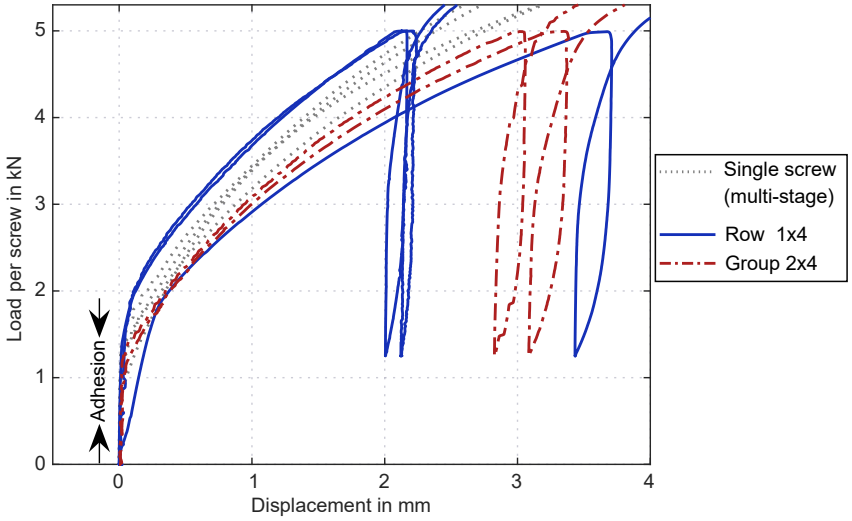

Fig. A.10: Initial range of load-displacement curves of non predrilled type 1 screws in birch glulam.

Table A.4: Results of measured geometries on opened specimens including two exemplary evaluations of Screw A8_1 and A8_2.

Specimen	image no.	u_{max} in mm	u_{remain} in mm	Axis angle* in °		b_l in mm		Radius in mm		Bending angle in °	
				shank	thread	shank	thread	shank	thread	shank	thread
A4_1	DSC08324	5	1.86	0	-1	11.2	9.49	276	195	5	6
A4_2	DSC08326		1.82	0	0	18.9	10.8	355	131	3	3
A3_1	DSC08319	10	5.76	0	-1	14.6	11.6	57.2	41.8	13	14
A3_2	DSC08321		7.3	1	1	17.3	11.8	82.5	71.9	14	14
A8_1	DSC08289	25	19.5	0	0	13.8	11.3	36.8	25.1	38	38
A8_2	DSC08291		18.4	1	1	20	11.2	48.6	38.6	30	29
A2_1	DSC08329	42	32.1	-2	-1	21.4	13.8	57.5	28.6	45	44
A2_2	DSC08331		32.2	1	2	16.1	14.6	47.6	26.2	46	44

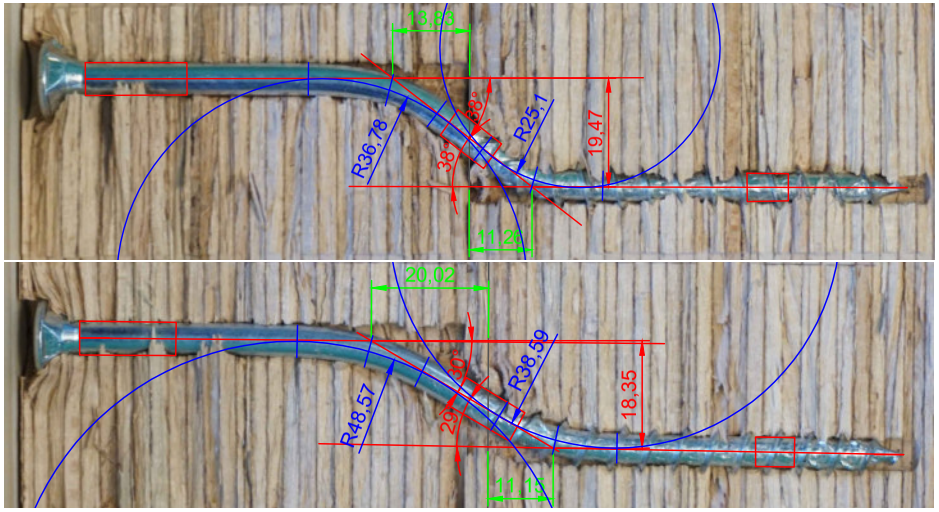

Axis angle is angle to horizontal axis in image, given as a positive value in clockwise direction

u	Beech LVL	Birch glulam	Spruce glulam
5 mm		-	-
10 mm			
25 mm			
Failure			
	u_{Fail} = 35 - 40 mm	u_{Fail} = 53 - 58 mm	u_{Fail} = 40 - 50 mm

Fig. A.11: Overview of tested configurations and deformation stages in multi-stage tests with predrilled screws.

u	Beech LVL	Birch glulam	Spruce glulam
5 mm		-	-
10 mm			
25 mm			
Failure			
	u_{Fail} = 12 - 36 mm	u_{Fail} = 53 - 59 mm	u_{Fail} = 47 mm

Fig. A.12: Overview of tested configurations and deformation stages in multi-stage tests with nonpredrilled screws.

A.3 Results for Strains in Fully Threaded Screws

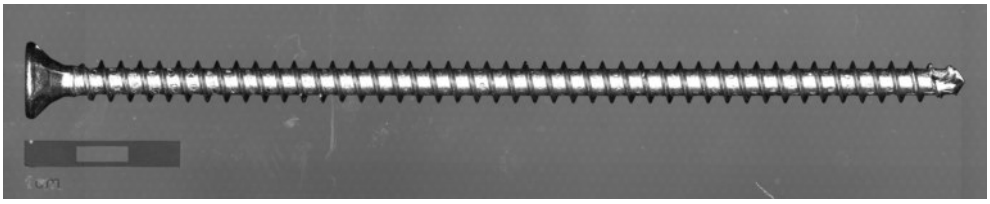

Fig. A.13: Exemplary fully threaded screw.

Table A.5: Dimensions of fully threaded screws used, in mm.

Dimension	1	2	3	4	5	Mean	Deviation from mean in %
d_h	15.0	14.8	14.9	15.0	14.8	14.9	+0.50 / -0.53
L	180	180	180	181	180	180	+0.30 / -0.12
d	8.18	8.17	8.18	8.21	8.18	8.19	+0.33 / -0.15
d_1	4.97	5.04	4.98	4.96	5.02	4.99	+1.00 / -0.78
h	3.68	3.71	3.68	3.70	3.71	3.70	+0.41 / -0.56

Table A.6: Results of bending tests on weakened screws. Moment in Nm.

Sample	M_y	$M_{y,45°}$	Max M_y
1	22.8	23.8	23.8
2	23.4	7.92	23.6
3	23.1	5.38	23.2
4	24.2	9.57	24.5
Mean	23.4	11.7	23.7
SD	0.583	8.25	0.558
COV in %	2.50	70.8	2.35

Table A.7: Results of bending tests on intact screws. Moment in Nm.

Sample	M_y	$M_{y,45°}$	Max M_y
1	24.9	26.6	27.0
2	23.3	25.1	25.7
3	25.9	27.0	27.3
4	26.1	26.9	26.9
5	25.3	26.5	26.6
6	24.7	25.7	26.1
7	26.0	27.0	27.1
8	25.2	26.5	26.8
9	25.4	26.8	27.1
10	26.2	27.6	28.5
Mean	25.3	26.6	26.9
SD	0.856	0.701	0.745
COV in %	3.38	2.64	2.77

A.4 Correlation Parameters for DIC Evaluation

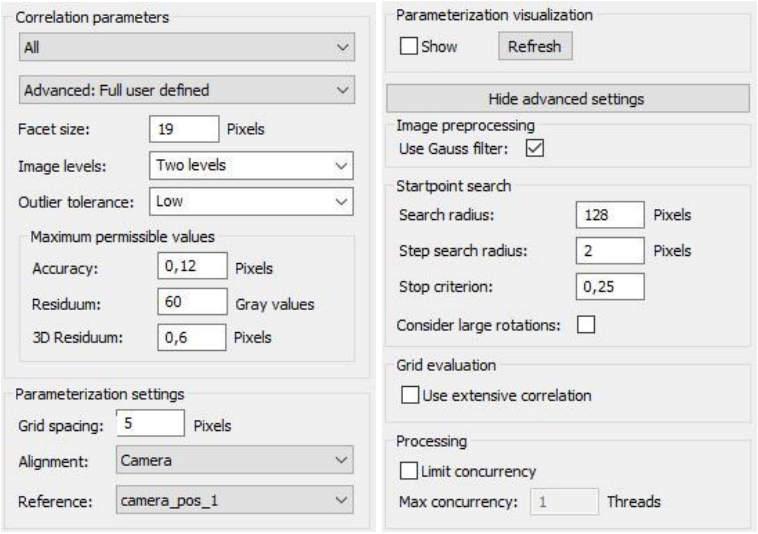

Fig. A.14: Correlation parameters for DIC evaluation in ISTRA 4D.

A.5 Results on Rectangular Fasteners

Embedment Test Results

Table A.8: Embedment results for series 1 in spruce.

Specimen	F_{max} kN	v (F_{max}) mm	F_{5mm} kN	$k_{i,0\text{-}40}$ kN/mm	$k_{s,20\text{-}40}$ kN/mm	$k_{s,10\text{-}40}$ kN/mm	ρ kg/m^3	u %	f_h N/mm^2
Spr_Alu1	16.6	0.403	11.7	46.3	90.9	83.2	465	11.5	43.3
Spr_Alu2	18.3	0.796	13.6	49.6	108	81.2	465	10.9	47.7
Spr_Alu3	18.5	0.463	6.58	70.1*	447*	317*	496	10.5	48.1
Spr_Steel1	19.5	0.687	14.7	19.9	46.6	32.2	441	10.6	50.7
Spr_Steel2	19.0	1.09	11.2	10.13	35.2	18.7	448	11.1	49.5
Spr_Steel3	18.5	1.10	12.7	16.51	41.9	35.5	470	10.9	48.2
$Mean_{Alu}$	**17.8**	**0.554**	**10.6**	**47.9**	**99.3**	**82.2**	**475**	**11.0**	**46.4**
SD_{Alu}	1.03	0.212	3.62	12.9	12.0	1.38	17.6	0.503	2.69
COV_{Alu}	5.80	38.2	34.1	27.0	12.0	1.68	3.69	4.59	5.80
$Mean_{Steel}$	**19.0**	**0.958**	**12.9**	**15.5**	**41.2**	**28.8**	**453**	**10.9**	**49.5**
SD_{Steel}	0.476	0.235	1.79	4.96	5.70	8.88	15.3	0.252	1.24
COV_{Steel}	2.51	24.5	13.9	32.0	13.8	30.8	3.37	2.32	2.51

*excluded because of initial negative displacements.

Table A.9: Embedment results for series 1 in beech LVL.

Specimen	F_{max} kN	v (F_{max}) mm	F_{5mm} kN	$k_{i,0\text{-}40}$ kN/mm	$k_{s,20\text{-}40}$ kN/mm	$k_{s,10\text{-}40}$ kN/mm	ρ kg/m^3	u %	f_h N/mm^2
BB_Alu1	26.4	0.447	12.4	79.2	134	117	789	7.30	68.7
BB_Alu2	27.1	0.505	11.0	72.3	167	151	776	7.10	70.7
BB_Alu3	27.9	0.625	22.6	82.4	164	156	853	7.20	72.7
BB_Alu4	32.5	0.419	14.5	94.0	157	148	868	6.90	84.6
BB_Steel1	34.5	0.570	16.5	43.2	101	89.0	838	6.50	89.8
BB_Steel2	33.2	0.580	7.89	40.5	80.9	72.3	827	6.50	86.5
BB_Steel3	32.0	0.654	15.6	56.8	98.6	88.1	820	6.70	83.4
$Mean_{Alu}$	**28.5**	**0.499**	**15.1**	**82.0**	**155**	**143**	**821**	**7.13**	**74.2**
SD_{Alu}	2.74	0.091	5.19	9.039	15.0	17.7	45.8	0.171	7.13
COV_{Alu}	9.62	18.2	34.4	11.0	9.6	12.4	5.57	2.40	9.62
$Mean_{Steel}$	**33.2**	**0.602**	**13.3**	**46.8**	**93.4**	**83.1**	**828**	**6.57**	**86.6**
SD_{Steel}	1.23	0.0458	4.73	8.76	10.9	9.42	8.71	0.115	3.21
COV_{Steel}	3.70	7.62	35.5	18.71	11.7	11.3	1.05	1.76	3.70

Table A.10: Embedment results for series 1 in DVW.

Specimen	F_{max} kN	v (F_{max}) mm	F_{5mm} kN	$k_{i,0\text{-}40}$ kN/mm	$k_{s,20\text{-}40}$ kN/mm	$k_{s,10\text{-}40}$ kN/mm	ρ kg/m^3	u %	f_h N/mm^2
DVW_Steel1	83.2	1.29	55.4	178	237	236	1309	1.60	217
DVW_Steel2	87.5	1.31	60.8	169	230	231	1329	1.50	228
DVW_Steel3	90.8	1.37	40.2	165	244	230	1327	1.40	236
DVW_Steel4	91.5	1.40	59.9	180	261	248	1346	1.20	238
DVW_Steel5	86.0	1.37	56.9	181	239	250	1345	1.30	224
$Mean_{DVW}$	**87.8**	**1.35**	**54.6**	**175**	**242**	**239**	**1331**	**1.40**	**229**
SD_{DVW}	3.44	0.0454	8.37	7.05	11.7	9.45	15.2	0.158	8.95
COV_{DVW}	3.91	3.36	15.3	4.04	4.83	3.95	1.14	11.3	3.91

Table A.11: Embedment results for series 2 in spruce.

Specimen	F_{max} kN	v (F_{max}) mm	F_{5mm} kN	$k_{i,0\text{-}40}$ kN/mm	$k_{s,20\text{-}40}$ kN/mm	$k_{s,10\text{-}40}$ kN/mm	ρ kg/m^3	u %	f_h N/mm^2
Spr_Alu1	15.6	1.89	13.2	13.4	16.0	15.7	446	11.4	40.7
Spr_Alu2	18.3	2.62	16.8	13.8	15.6	15.0	449	11.0	47.5
Spr_Alu3	14.8	1.82	13.7	17.9	23.5	22.4	424	11.4	38.6
Spr_Steel1	16.8	2.13	13.4	19.3	23.4	23.0	448	11.1	43.9
Spr_Steel2	16.1	2.03	13.8	20.6	21.8	22.5	443	11.2	41.9
Spr_Steel3	14.6	1.71	12.4	20.1	23.8	23.4	420	11.2	37.9
$Mean_{Alu}$	**16.2**	**2.11**	**14.6**	**15.0**	**15.8**	**15.3**	**440**	**11.3**	**42.3**
SD_{Alu}	1.80	0.443	1.95	2.47	0.268	0.499	13.7	0.231	4.68
COV_{Alu}	11.1	21.0	13.4	16.5	1.70	3.25	3.12	2.05	11.1
$Mean_{Steel}$	**15.8**	**1.96**	**13.2**	**20.0**	**23.0**	**23.0**	**437**	**11.2**	**41.2**
SD_{Steel}	1.16	0.222	0.728	0.656	1.04	0.425	15.0	0.0577	3.03
COV_{Steel}	7.34	11.4	5.53	3.28	4.52	1.85	3.43	0.517	7.34

Table A.12: Embedment results for series 2 in beech LVL.

Specimen	F_{max} kN	v (F_{max}) mm	F_{5mm} kN	$k_{i,0\text{-}40}$ kN/mm	$k_{s,20\text{-}40}$ kN/mm	$k_{s,10\text{-}40}$ kN/mm	ρ kg/m^3	u %	f_h N/mm^2
BB_Alu1	30.6	1.24	20.6	27.5	37.4	33..8	841	6,70	80.6
BB_Alu2	34.5	1.43	26.6	28.7	39.5	35.1	885	6.50	89.9
BB_Alu3	30.8	1.81	27.4	16.7	22.9	19.2	849	6.50	80.3
BB_Alu4	32.5	0.42	14.5	94.0	157	148	849	6.70	84.6
BB_Steel1	34.0	1.15	27.4	27.2	39.7	37.2	883	6.70	88.4
BB_Steel2	31.4	1.66	27.7	27.1	38.2	36.6	811	6.60	81.8
BB_Steel3	31.9	1.65	27.5	25.6	26.4	27.5	806	6.60	83.1
$Mean_{Alu}$	**32.0**	**1.49**	**24.9**	**24.3**	**33.3**	**29.3**	**858**	**6.57**	**83.6**
SD_{Alu}	2.20	0.293	3.72	6.63	9.03	8.83	23.6	0.115	5.49
COV_{Alu}	6.88	19.6	15.0	27.2	27.1	30.1	2.75	1.76	6.56
$Mean_{Steel}$	**32.4**	**1.49**	**27.5**	**26.6**	**34.7**	**33.8**	**833**	**6.63**	**84.4**
SD_{Steel}	1.35	0.290	0.154	0.920	7.30	5.42	43.1	0.058	3.52
COV_{Steel}	4.17	19.5	0.56	3.45	21.0	16.1	5.18	0.870	4.17

Table A.13: Embedment results for series 2 in DVW.

Specimen	F_{max} kN	v (F_{max}) mm	F_{5mm} kN	$k_{i,0\text{-}40}$ kN/mm	$k_{s,20\text{-}40}$ kN/mm	$k_{s,10\text{-}40}$ kN/mm	ρ kg/m^3	u %	f_h N/mm^2
DVW_Steel1	81.0	3.45	60.4	31.8	32.7	32.2	1321	1.50	211
DVW_Steel2	80.8	3.00	55.1	49.5	53.3	53.7	1327	1.50	210
DVW_Steel3	78.0	2.98	51.4	42.7	51.7	49.1	1320	1.70	203
$Mean_{DVW}$	**79.9**	**3.14**	**55.6**	**41.3**	**45.9**	**45.0**	**1323**	**1.57**	**208**
SD_{DVW}	1.72	0.26	4.48	8.92	11.4	11.3	3.95	0.115	4.47
COV_{DVW}	2.15	8.39	8.05	21.6	24.9	25.2	0.298	7.37	2.15

Table A.14: Embedment results for series 3 in spruce.

Specimen	F_{max} kN	v (F_{max}) mm	F_{5mm} kN	$k_{i,0\text{-}40}$ kN/mm	$k_{s,20\text{-}40}$ kN/mm	$k_{s,10\text{-}40}$ kN/mm	ρ kg/m^3	u %	f_h N/mm^2
Spr_Steel1	98.7	1.22	71.6	155	325	305	406	10.7	45.6
Spr_Steel2	85.1	1.14	64.3	209	275	272	442	10.2	39.3
Spr_Steel3	96.6	0.719	63.8	245	387	358	487	11.8	44.6
Spr_Steel4	88.5	0.908	64.2	214	345	352	400	11.0	40.8
Spr_Steel5	83.5	1.31	76.1	218	315	332	487	11.4	38.6
Spr_Steel6	88.2	0.898	59.9	315	366	362	466	10.5	40.7
$Mean_{Steel}$	**90.1**	**1.03**	**66.7**	**226**	**336**	**330**	**448**	**10.9**	**41.6**
SD_{Steel}	6.17	0.227	5.96	52.3	39.7	35.4	38.8	0.592	2.85
COV_{Steel}	6.84	21.9	8.94	23.1	11.8	10.7	8.67	5.42	6.84

Table A.15: Embedment results for series 3 in beech LVL.

Specimen	F_{max} kN	v (F_{max}) mm	F_{5mm} kN	$k_{i,0\text{-}40}$ kN/mm	$k_{s,20\text{-}40}$ kN/mm	$k_{s,10\text{-}40}$ kN/mm	ρ kg/m^3	u %	f_h N/mm^2
BB_Steel1	168	0.716	68.7	372	547	536	789	6.70	77.6
BB_Steel2	171	0.729	86.6	389	453	494	837	7.20	78.7
BB_Steel3	168	0.735	71.0	352	425	446	804	7.20	77.7
BB_Steel4	175	0.757	83.3	439	434	506	838	6.50	80.6
$Mean_{Steel}$	**170**	**0.734**	**77.4**	**388**	**465**	**495**	**817**	**6.90**	**78.7**
SD_{Steel}	3.02	0.0172	8.89	37.1	56.2	37.1	24.7	0.356	1.40
COV_{Steel}	1.77	2.34	11.5	9.55	12.1	7.49	3.02	5.16	1.77

Density and Moisture Content of Beech LVL and Spruce Glulam Specimens

Table A.16: Density ρ and moisture content u of beech LVL and spruce glulam specimens.

Timber-to-timber	u in %	ρ in kg/m^3	Timber-to-steel	u in %	ρ in kg/m^3
1_Fi_Alu_oK_Rs_V1	11.4	428	2_Fi_Alu_oK_Rs	12.2	451
1_Fi_Alu_oK_Mi_V1	11.5	420	2_Fi_Alu_oK_Ls	11.7	445
1_Fi_Alu_oK_Ls_V1	11.2	433	2_Fi_Alu_mK_Rs	11.8	433
1_Fi_Alu_mK_Rs	11.7	447	2_Fi_Alu_mK_Ls	11.8	436
1_Fi_Alu_mK_Mi	11.6	439	2_Fi_St_oK_Rs	11.6	435
1_Fi_Alu_mK_Ls	11.5	445	2_Fi_St_oK_Ls	11.5	435
1_Fi_St_oK_Rs	11.5	435	2_Fi_St_mK_Rs	11.6	416
1_Fi_St_oK_Mi	11.5	425	2_Fi_St_mK_Ls	11.3	414
1_Fi_St_oK_Ls	11.5	452	2_BB_Alu_oK_Rs	7.8	795
1_Fi_St_mK_Rs	11.5	449	2_BB_Alu_oK_Ls	7.9	805
1_Fi_St_mK_Mi	11.8	445	2_BB_Alu_mK_Rs	7.5	827
1_Fi_St_mK_Ls	11.4	455	2_BB_Alu_mK_Ls	7.6	837
1_BB_Alu_oK_Rs	7.4	810	2_BB_St_oK_Rs	8.1	787
1_BB_Alu_oK_Mi	7.5	824	2_BB_St_oK_Ls	7.8	783
1_BB_Alu_oK_Ls	7.4	814	2_BB_St_mK_Rs	8.1	809
1_BB_Alu_mK_Rs	7.5	837	2_BB_St_mK_Ls	7.9	775
1_BB_Alu_mK_Mi	7.6	803	**Mean Spruce glulam**	**11.7**	**433**
1_BB_Alu_mK_Ls	7.4	834	SD Spruce	0.264	12.8
1_BB_St_oK_Rs_V1	7.5	849	**Mean BB**	**7.84**	**802**
1_BB_St_oK_Mi_V1	7.6	839	SD BB	0.213	21.5
1_BB_St_oK_Ls_V1	7.6	825			
1_BB_St_oK_Rs_V2	8.3	790			
1_BB_St_oK_Mi_V2	8.4	810			
1_BB_St_oK_Ls_V2	8.5	795			
1_BB_St_mK_Rs	7.7	830			
1_BB_St_mK_Mi	7.7	849			
1_BB_St_mK_Ls	7.6	837			
Mean Spruce glulam	**11.5**	**440**			
SD Spruce	0.151	11.3			
Mean BB	**7.71**	**823**			
SD BB	0.370	18.7			

Fi = spruce glulam, BB = Beech LVL, St = Steel, oK = no head, mK = with head

Deformations and Strains

The results for deformations and strains along the neutral axis of the fasteners are listed below. In addition, the results of the glued-on strain gauges are illustrated together with the evaluated DIC results of circles with $d = 2$ mm (mean over surface) in the remaining shear planes (timber-to-timber) or in a distance to shear planes (timber-to-steel). If not mentioned separately, the second diagram shows the strain gauge results, which can also be distinguished as the curve is smoother than the DIC results. The order of the specimens' results is as follows:

Timber-to-timber connections:

Timber-to-steel connections:

Abbreviations in the following:

Spr	Spruce glulam
BB	Beech LVL
DVW	Densified Veneer Wood
mk	with head
S_	Timber-to-steel connection

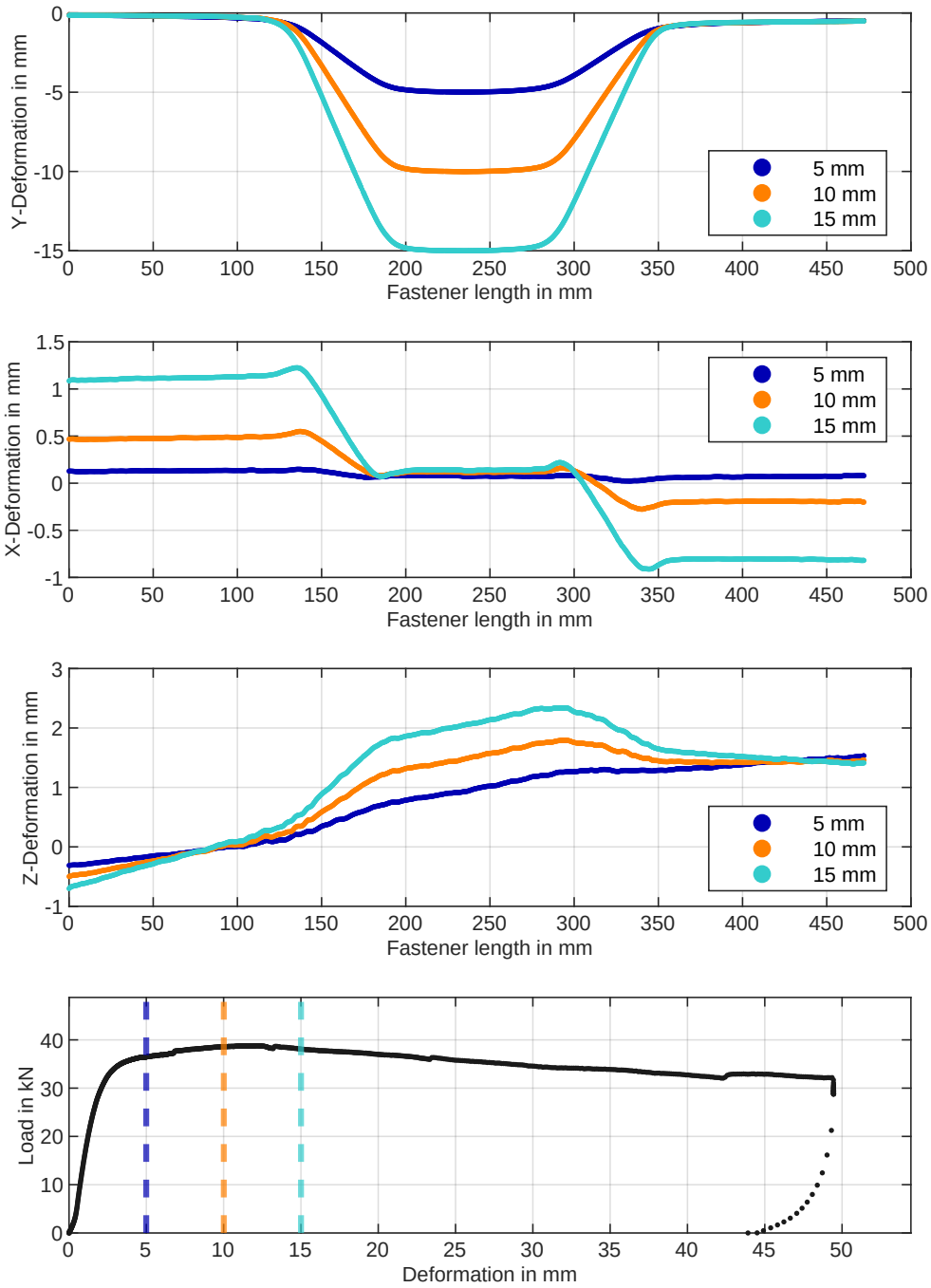

Fig. A.15: Spr_Alu deformation results, front side.

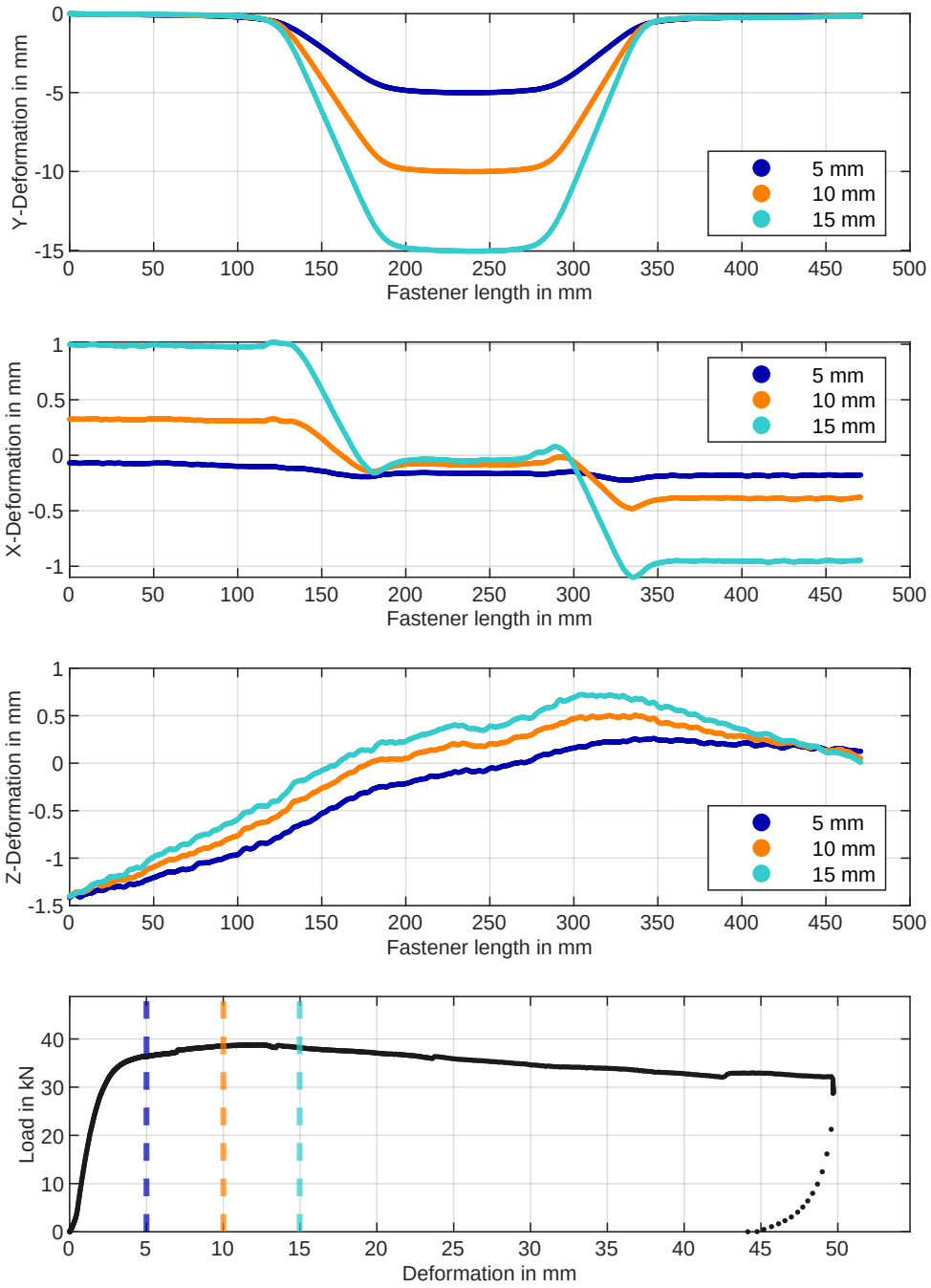

Fig. A.16: Spr_Alu deformation results, rear side.

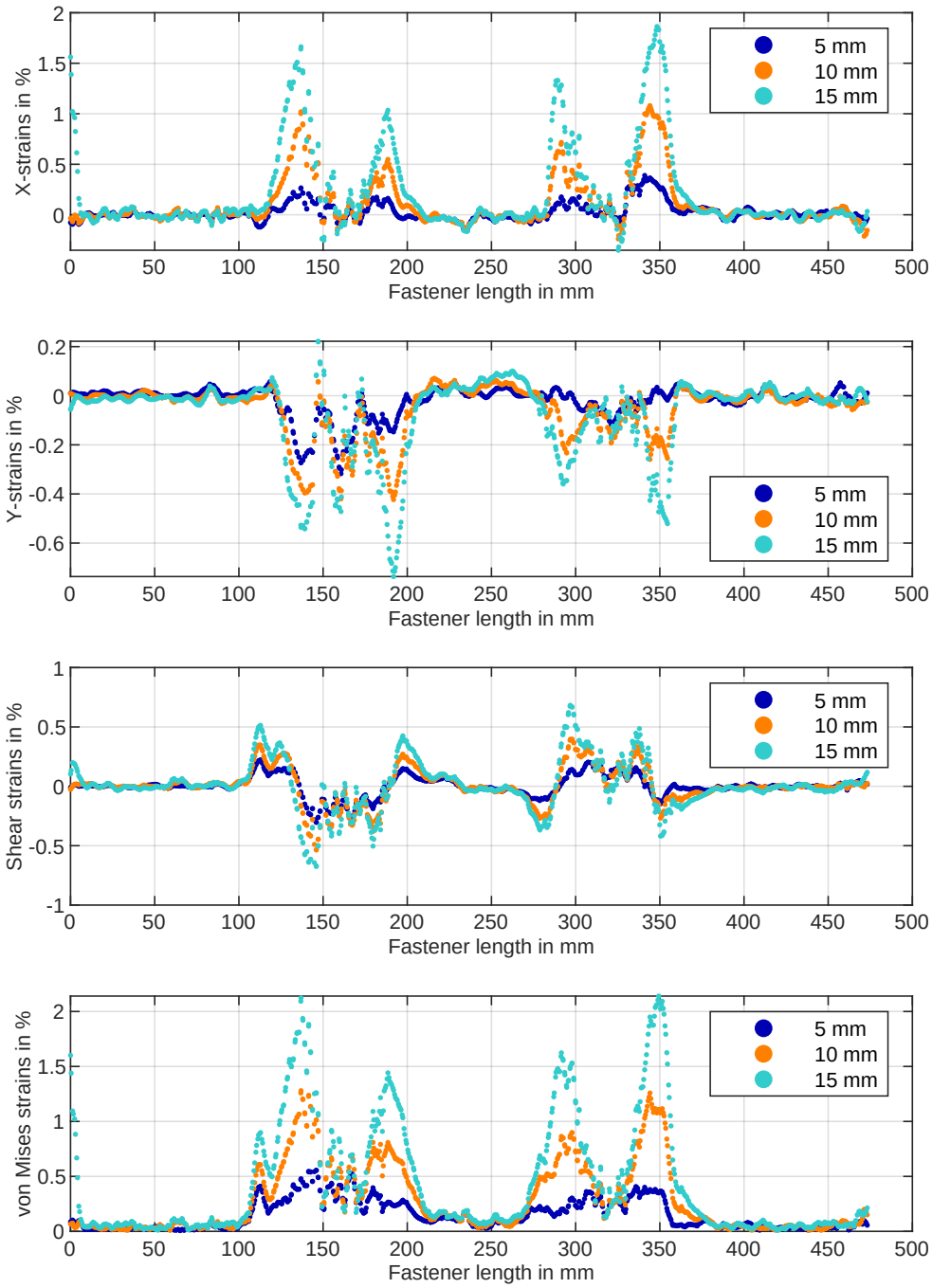

Fig. A.17: Spr_Alu strain results, front side. Strain gauge at 320 mm.

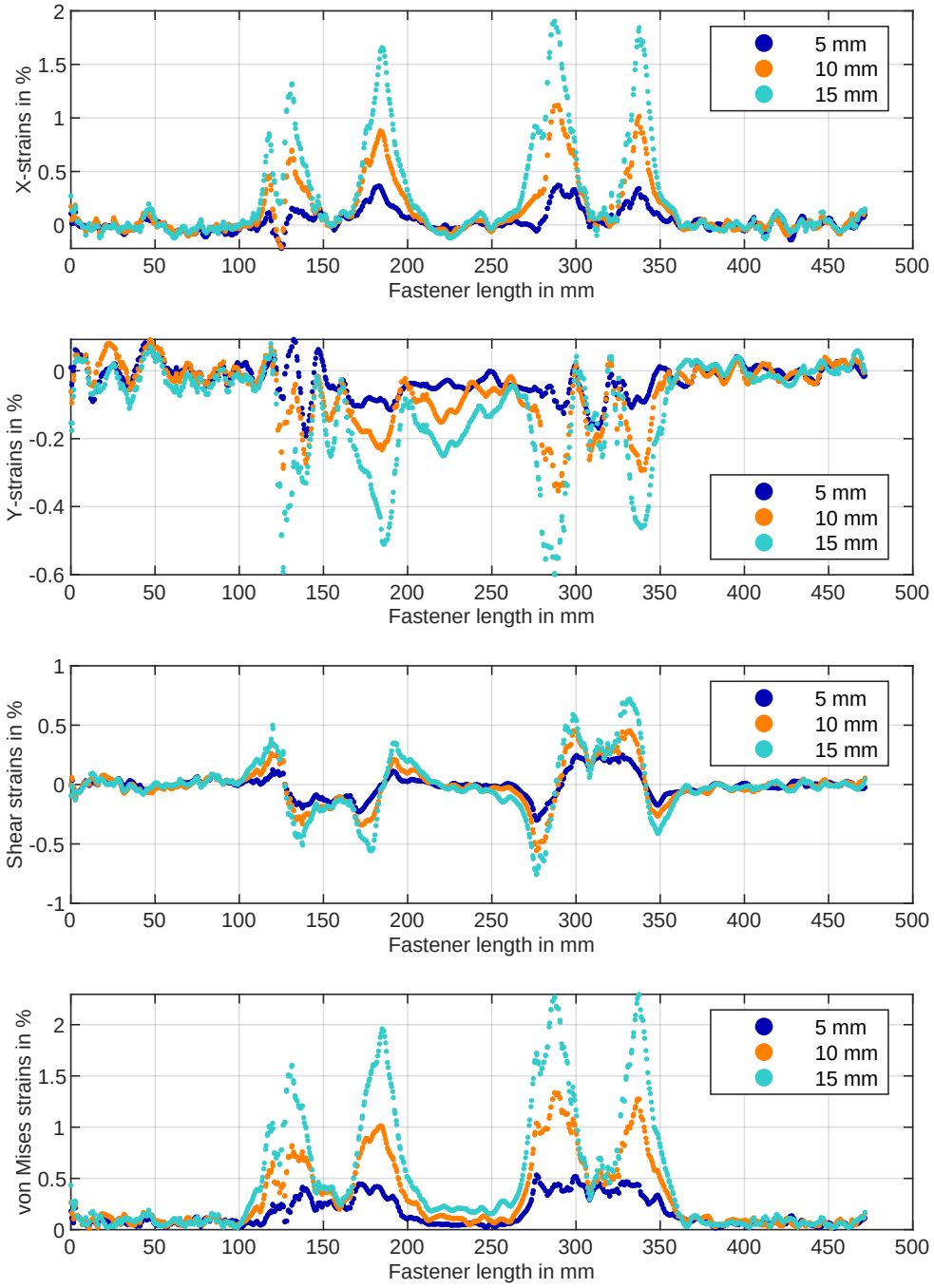

Fig. A.18: Spr_Alu strain results, rear side.

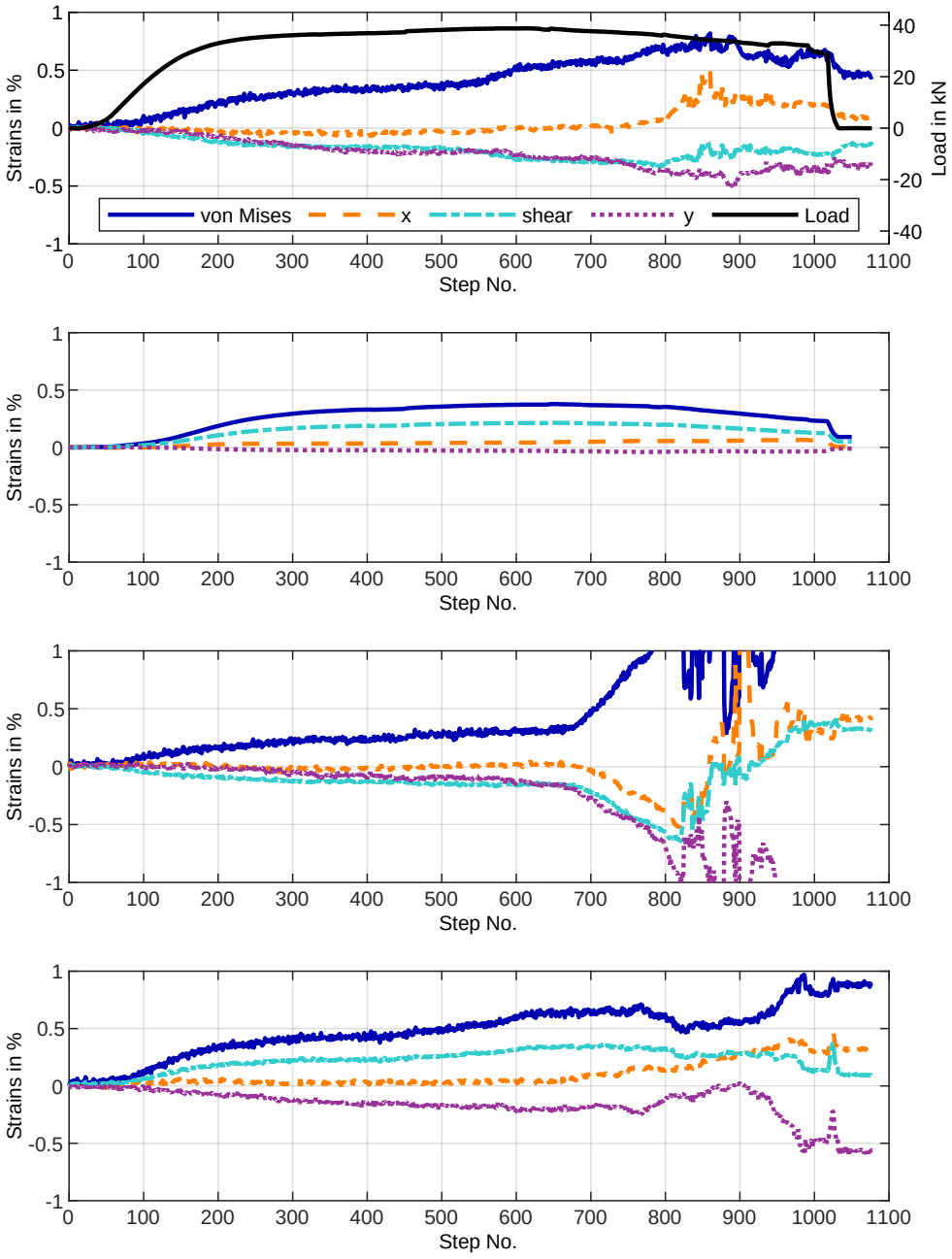

Fig. A.19: Spr_Alu strain results of DIC or strain gauge in shear planes.

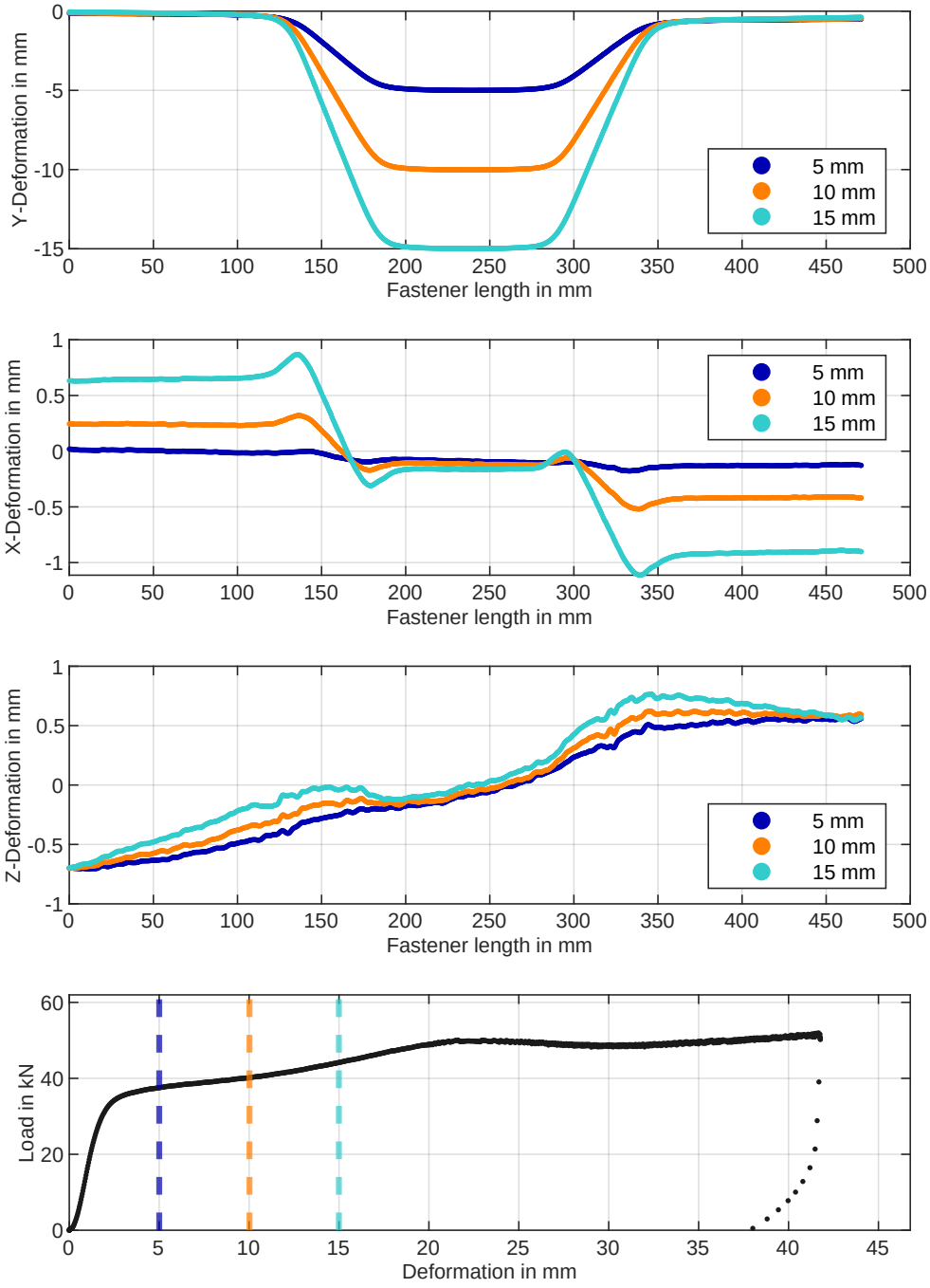

Fig. A.20: Spr_Alu_mk deformation results, front side.

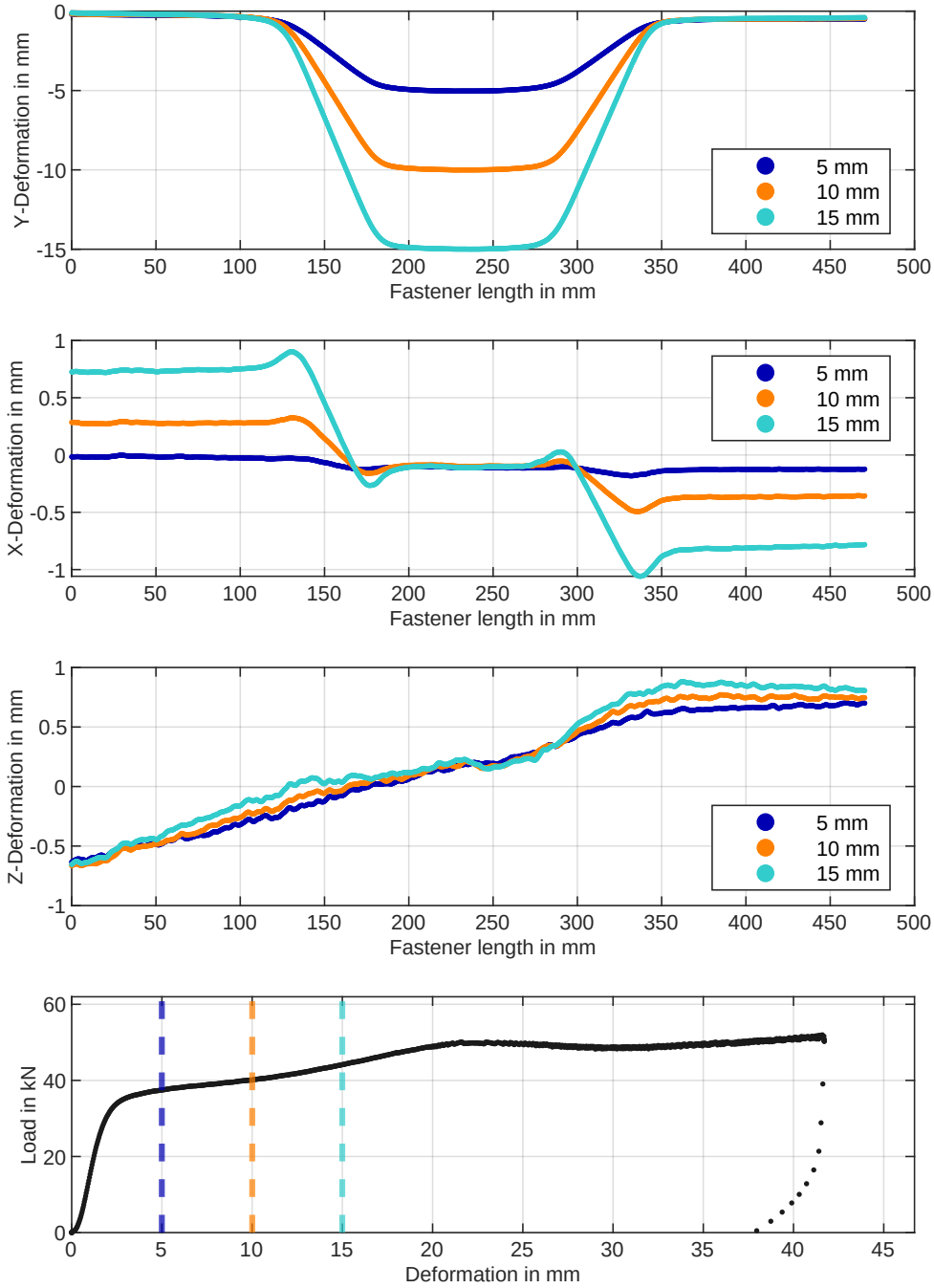

Fig. A.21: Spr_Alu_mk deformation results, rear side.

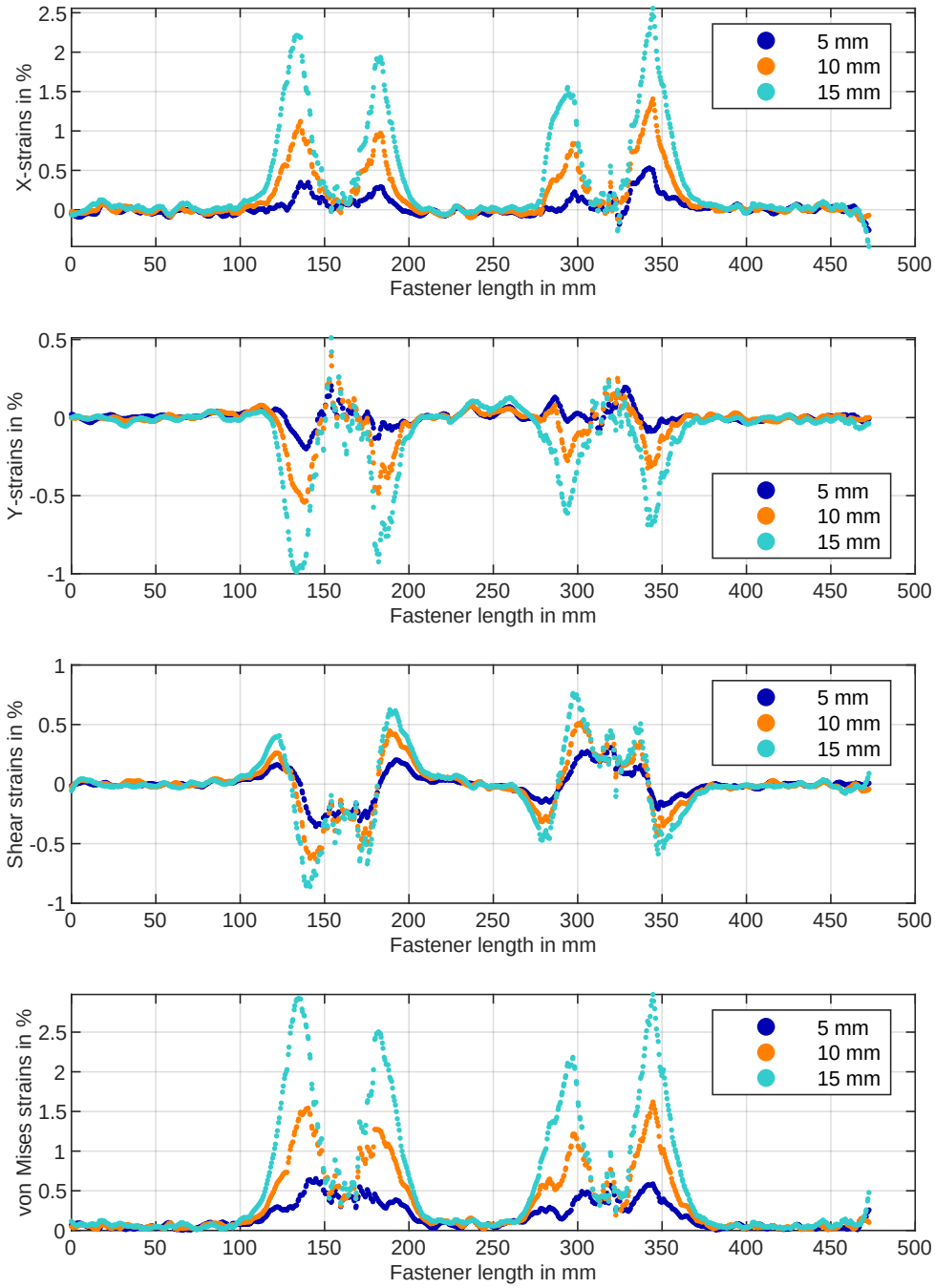

Fig. A.22: Spr_Alu_mk strain results, front side. Strain gauge at 320 mm.

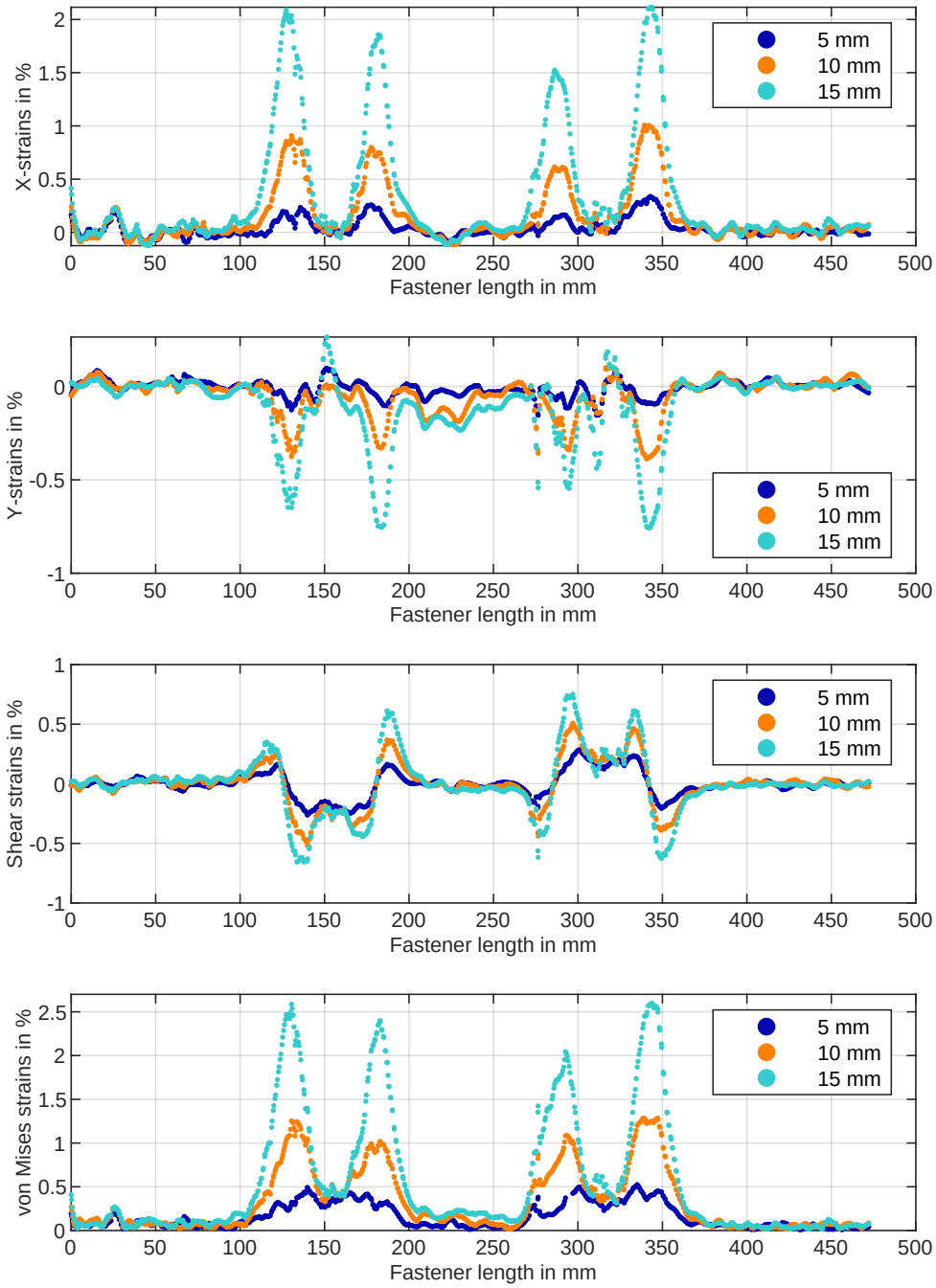

Fig. A.23: Spr_Alu_mk strain results, rear side.

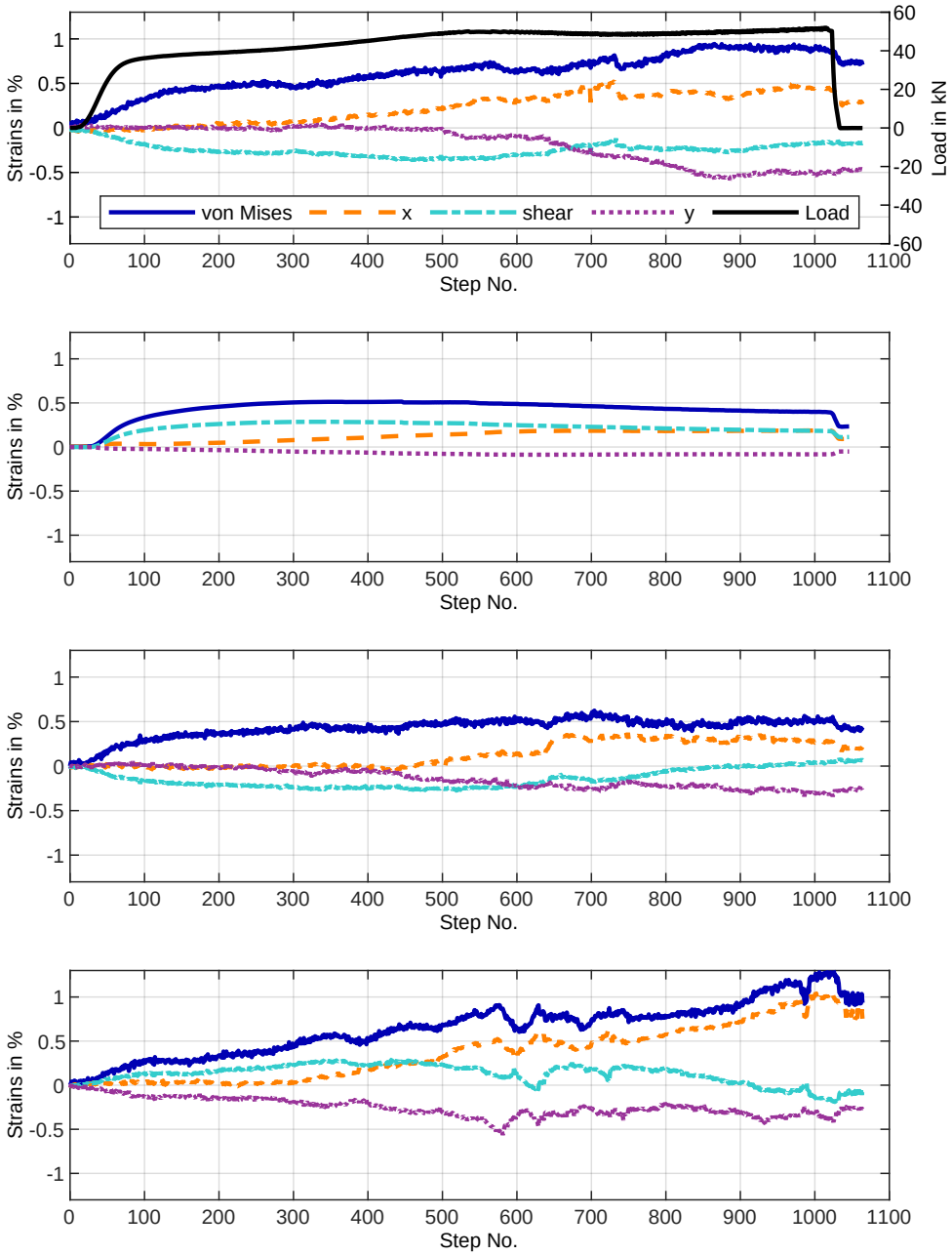

Fig. A.24: Spr_Alu_mk strain results of DIC or strain gauge in shear planes.

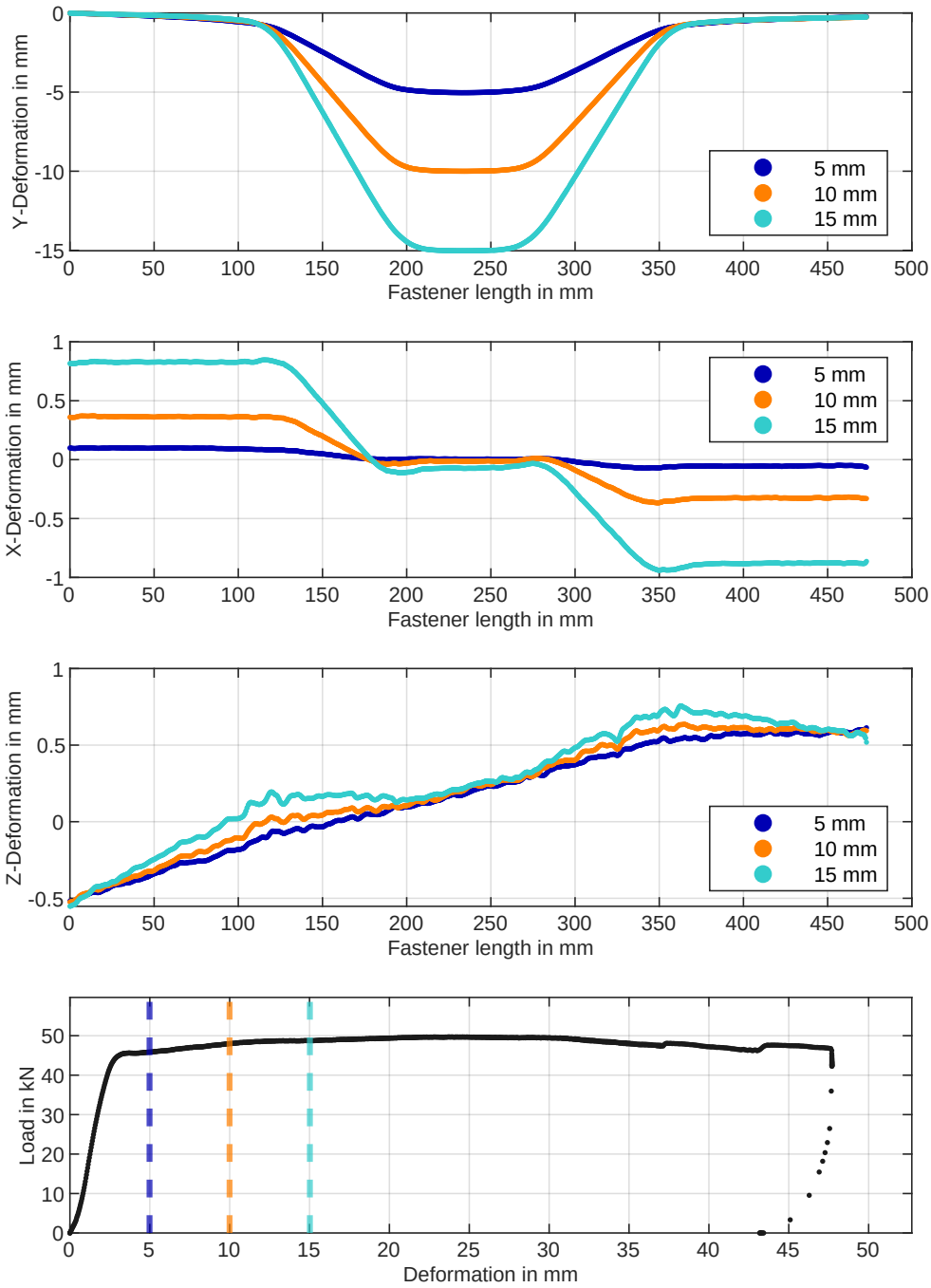

Fig. A.25: Spr_Steel deformation results, front side.

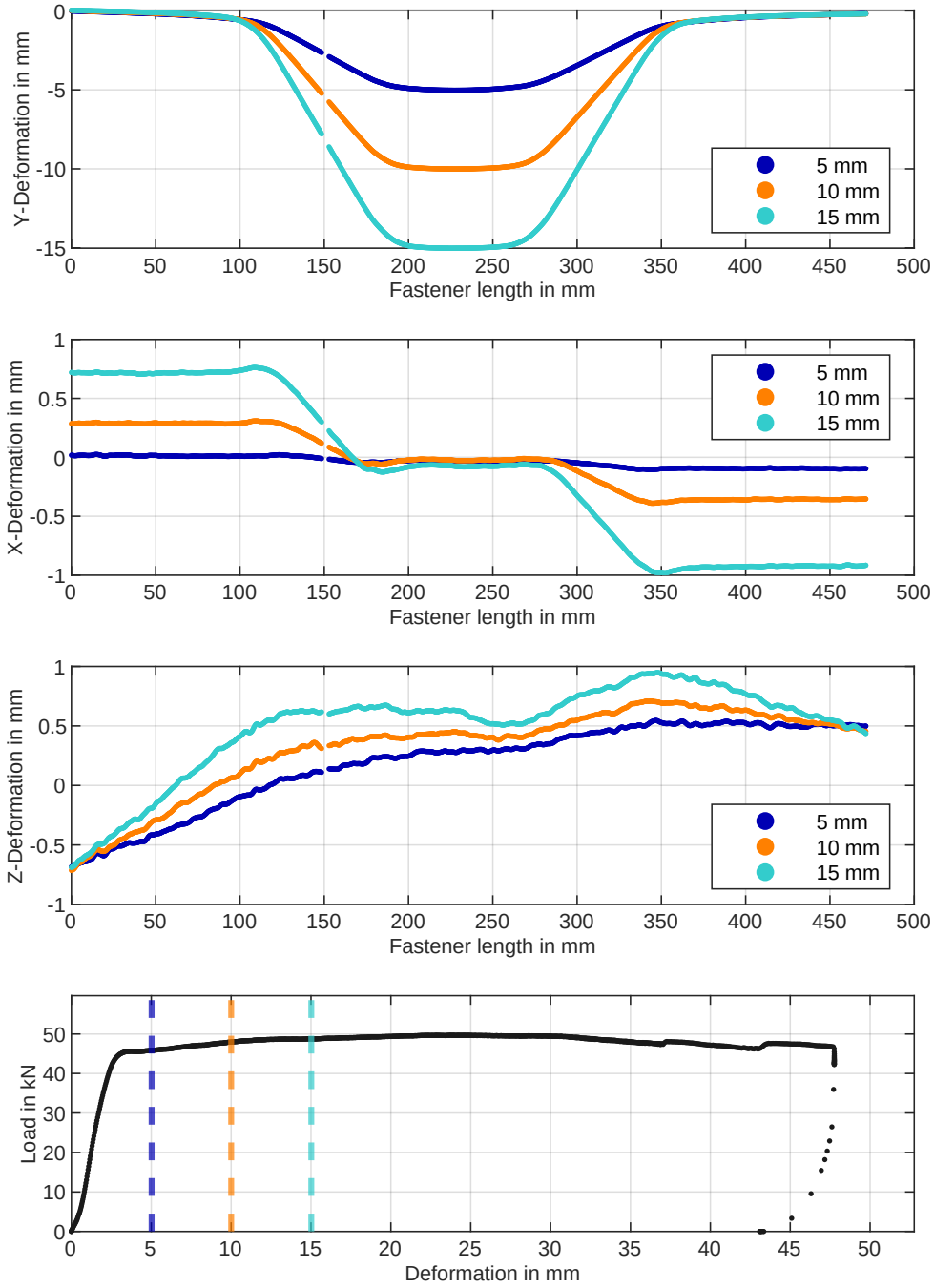

Fig. A.26: Spr_Steel deformation results, rear side.

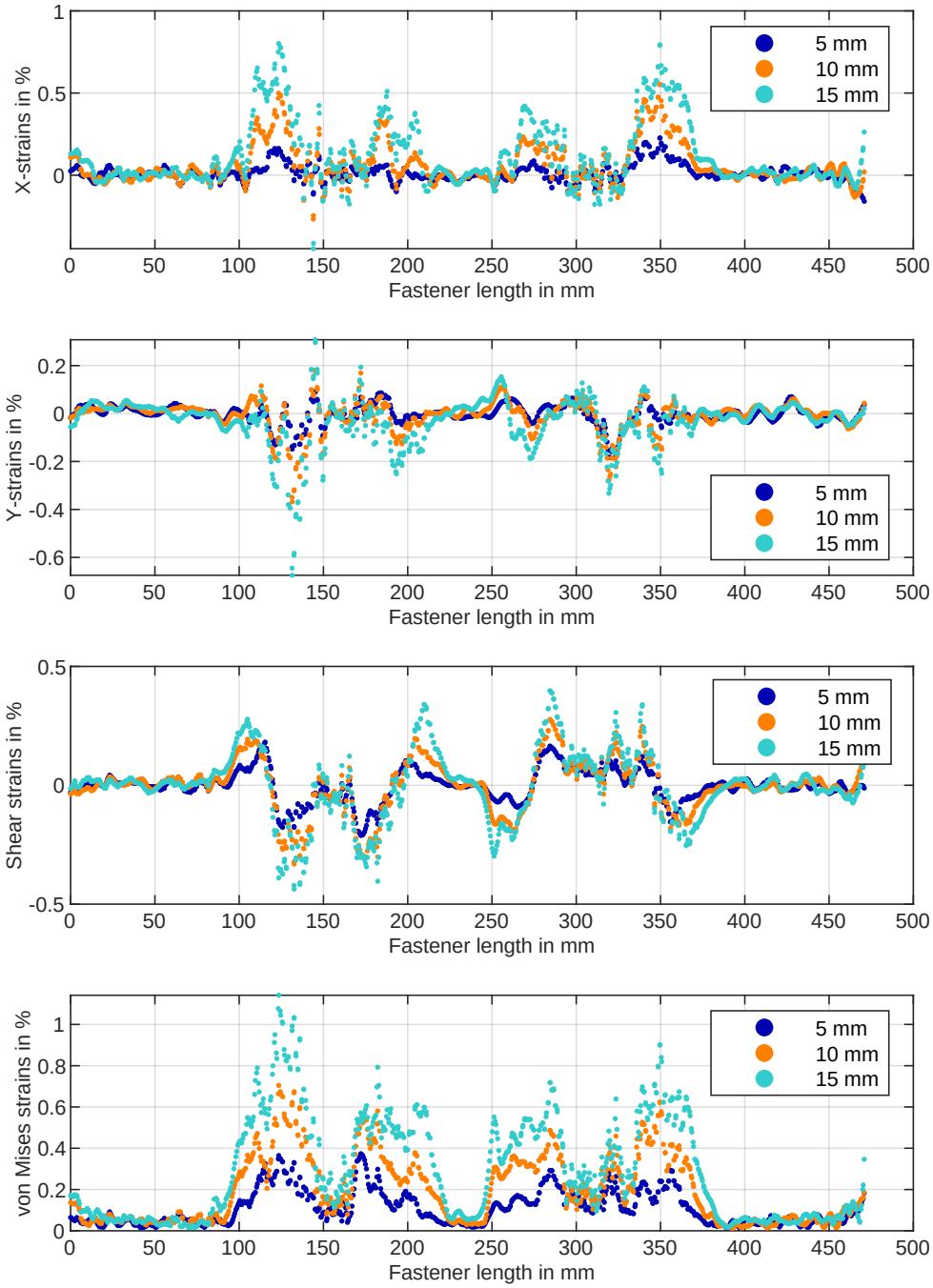

Fig. A.27: Spr_Steel strain results, front side. Strain gauge at 320 mm.

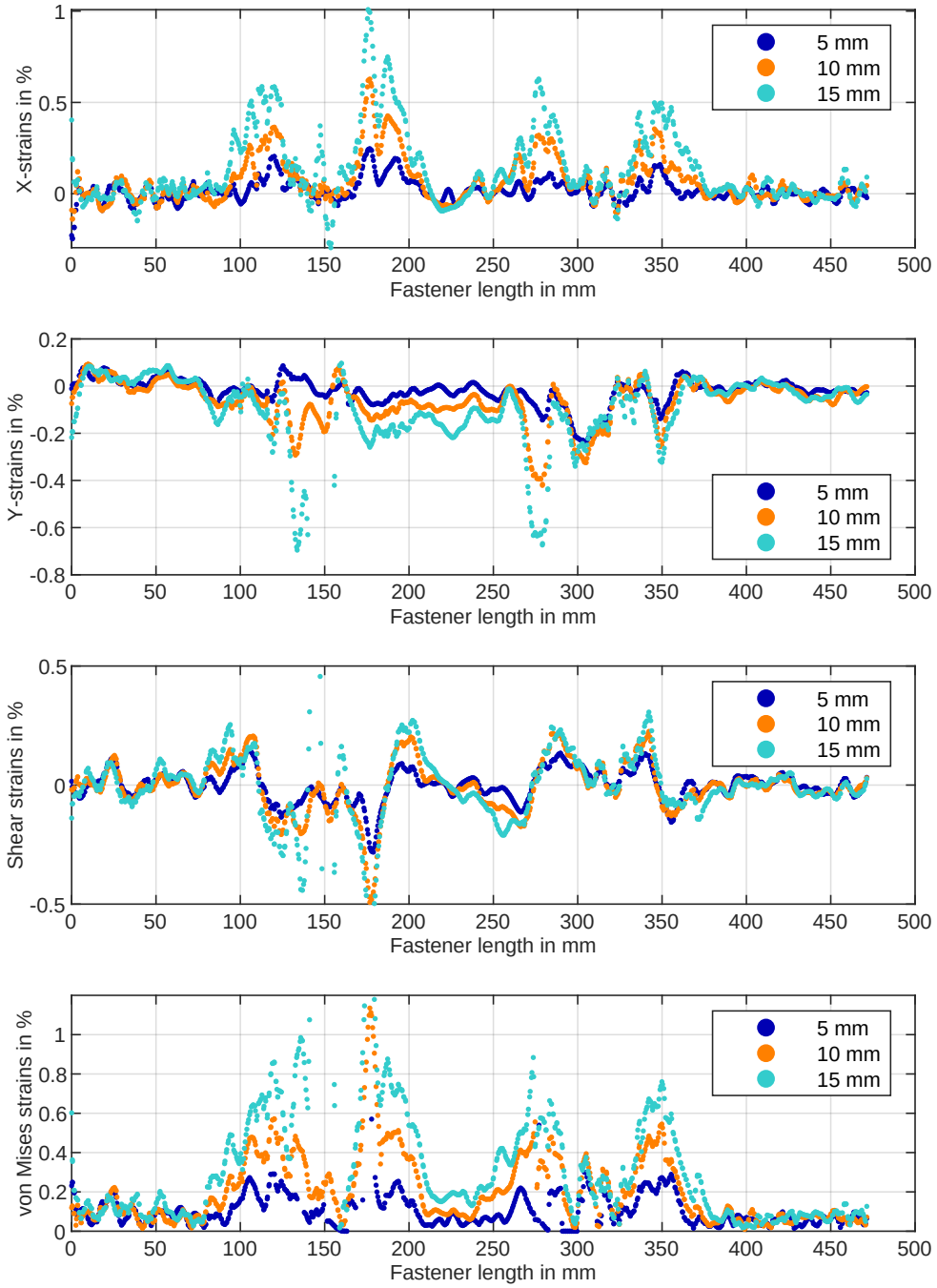

Fig. A.28: Spr_Steel strain results, rear side.

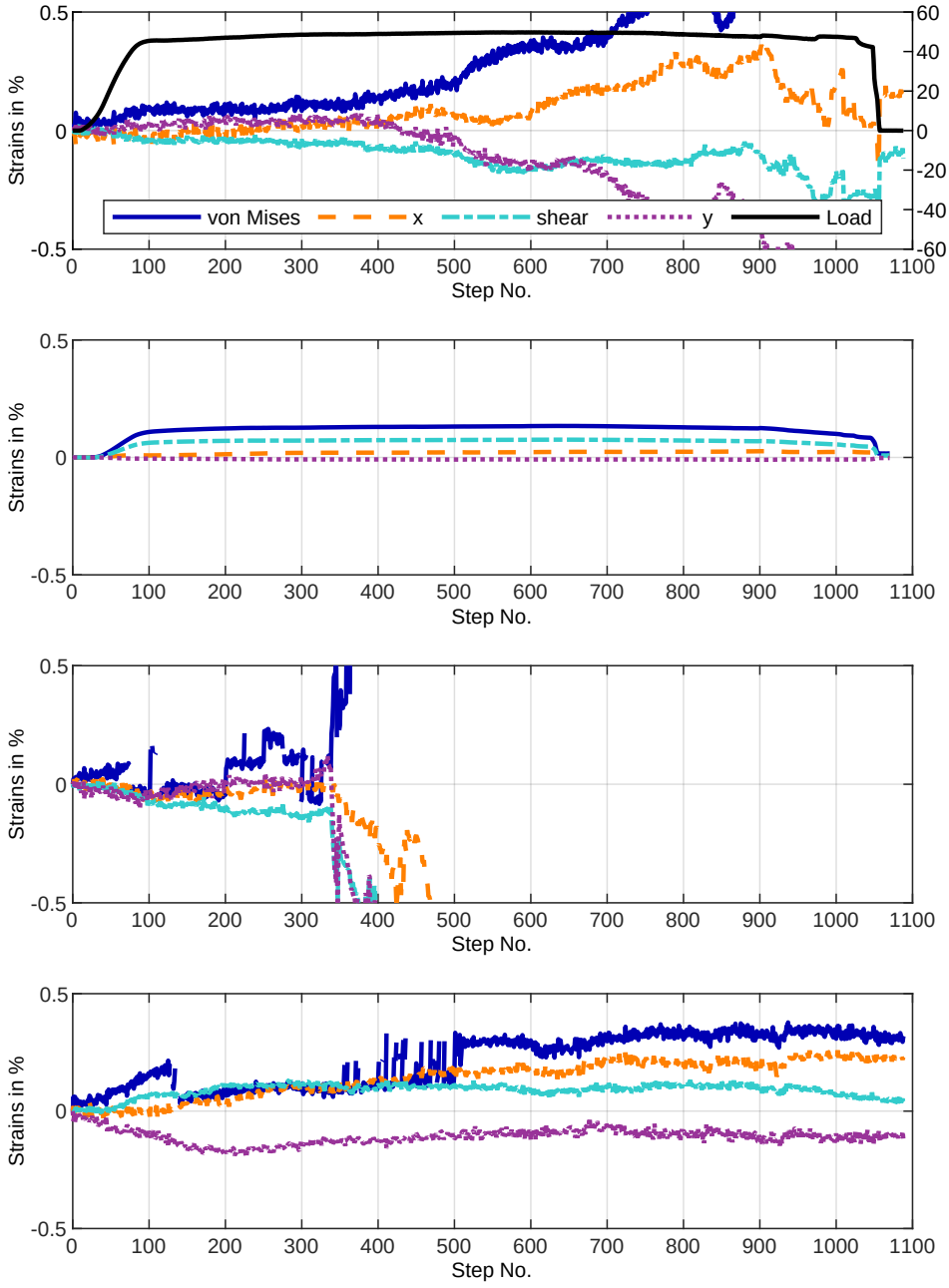

Fig. A.29: Spr_Steel strain results of DIC or strain gauge in shear planes.

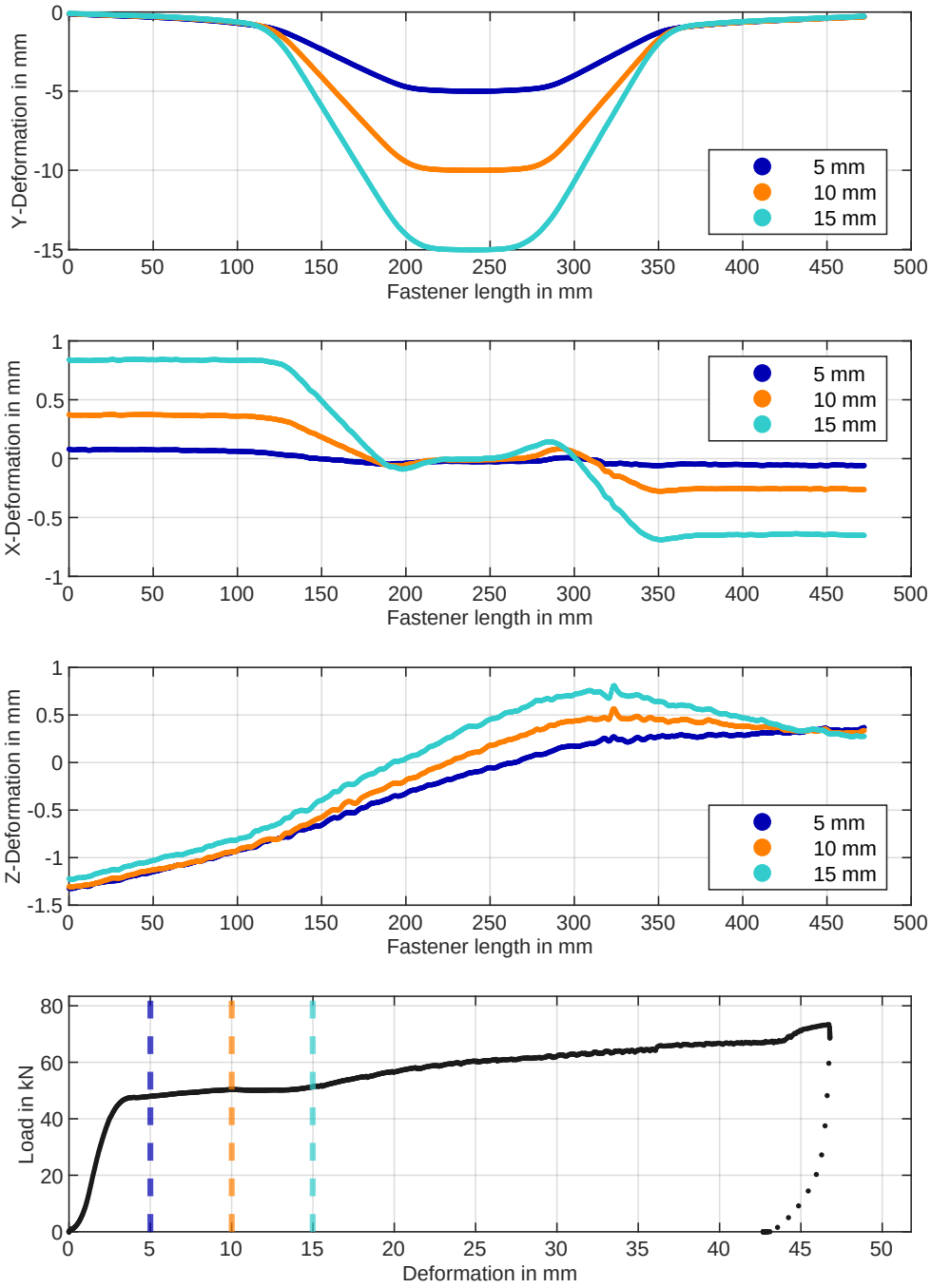

Fig. A.30: Spr_Steel_mk deformation results, front side.

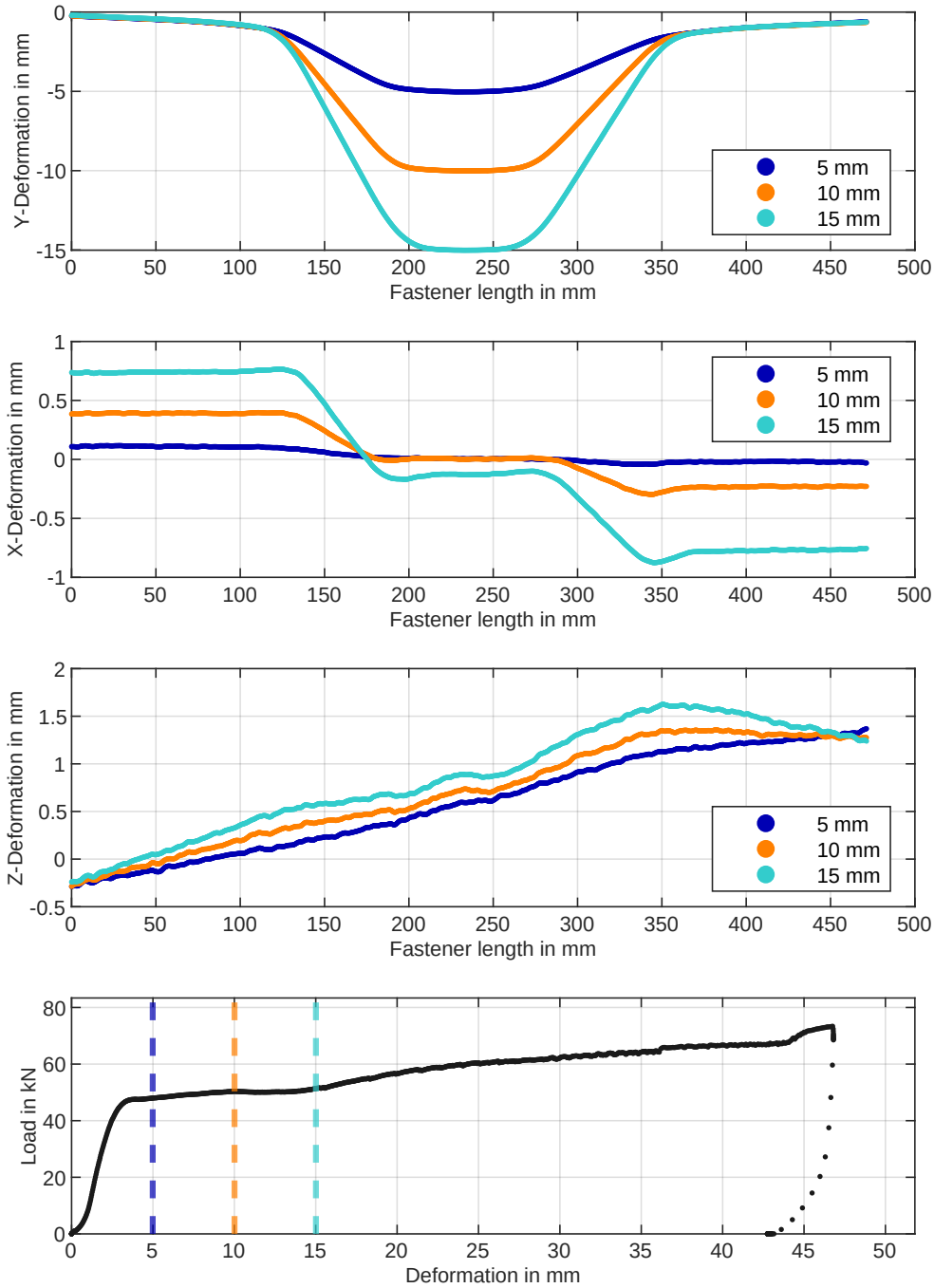

Fig. A.31: Spr_Steel_mk deformation results, rear side.

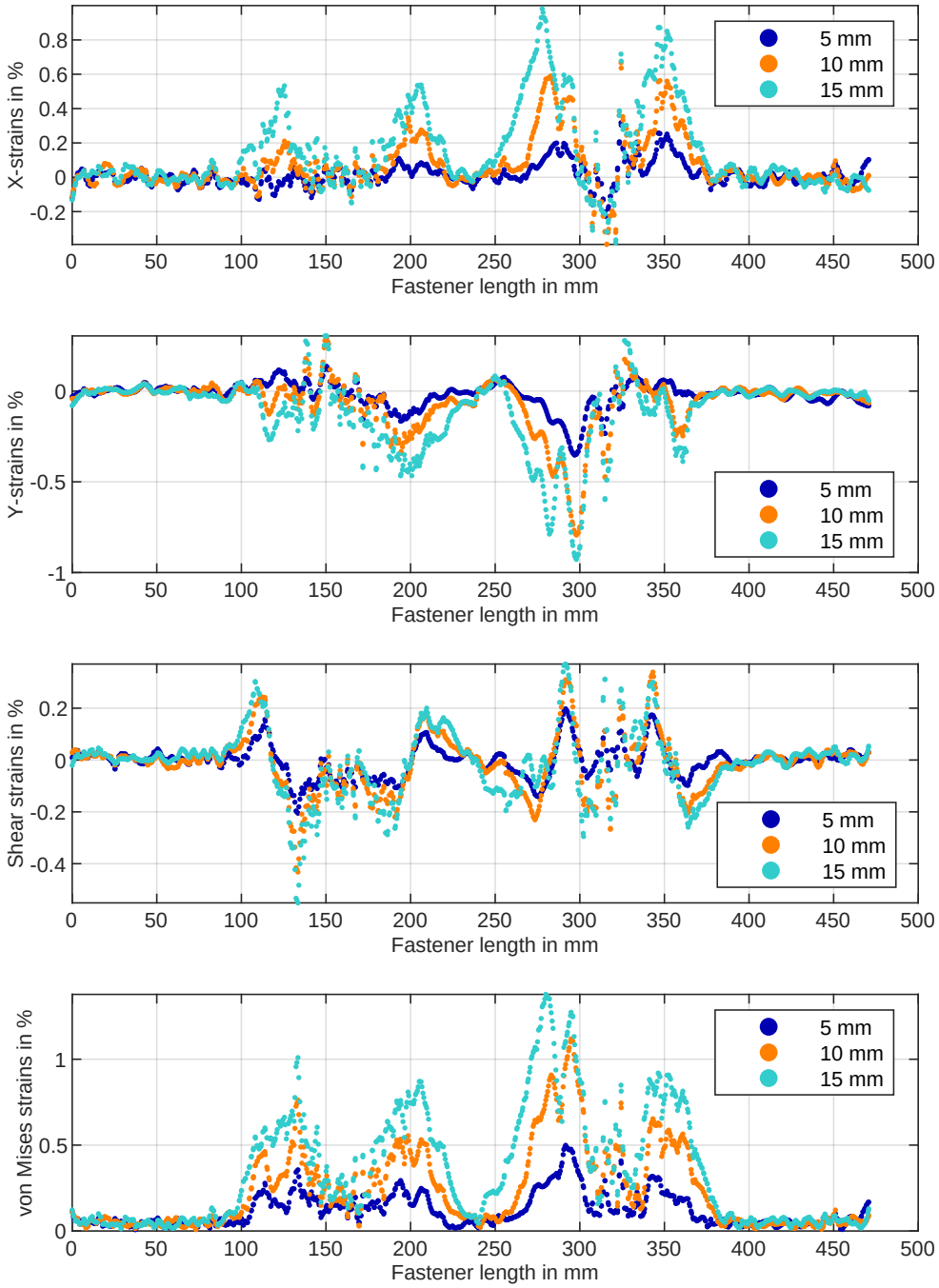

Fig. A.32: Spr_Steel_mk strain results, front side. Strain gauge at 320 mm.

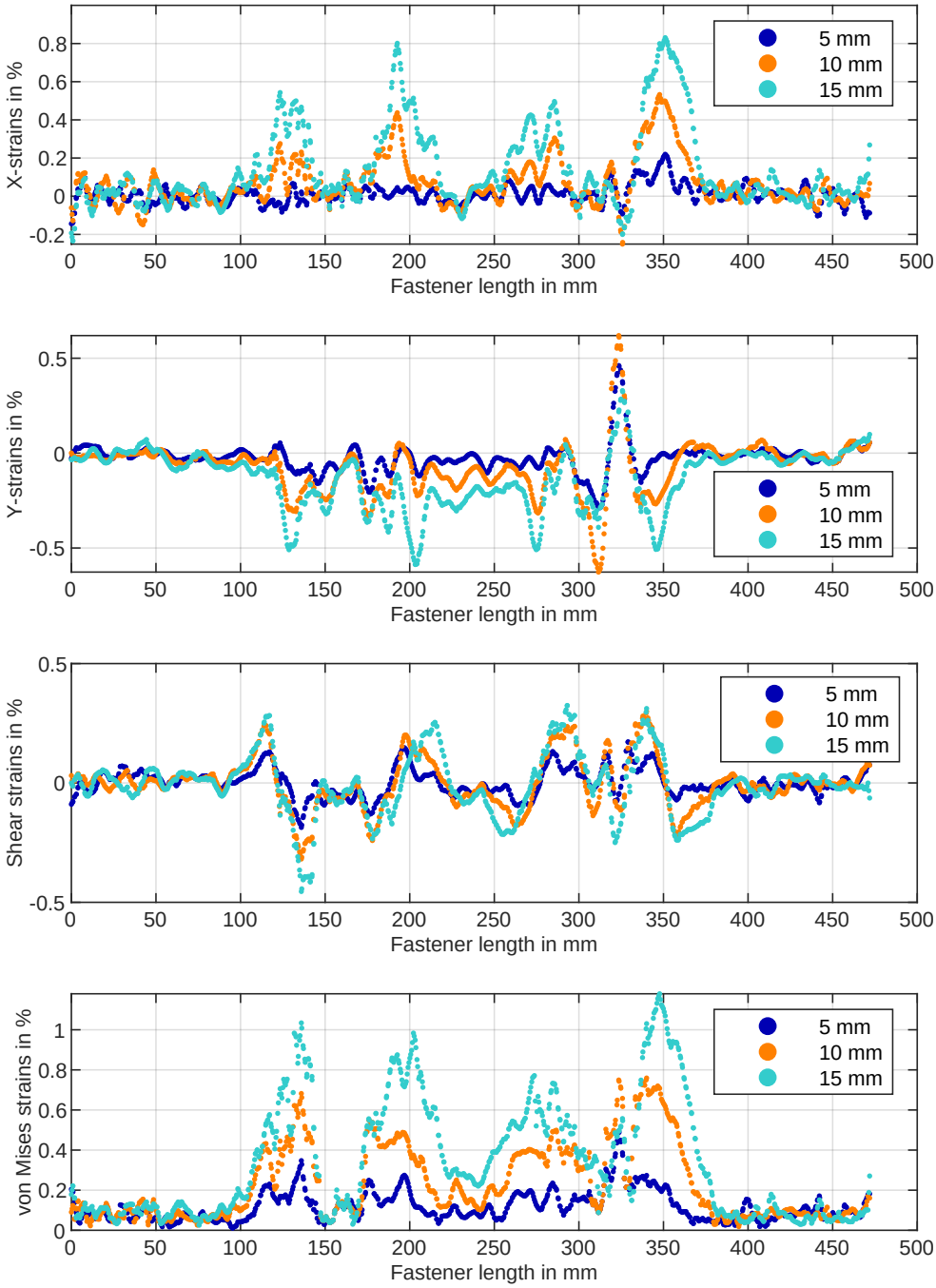

Fig. A.33: Spr_Steel_mk strain results, rear side.

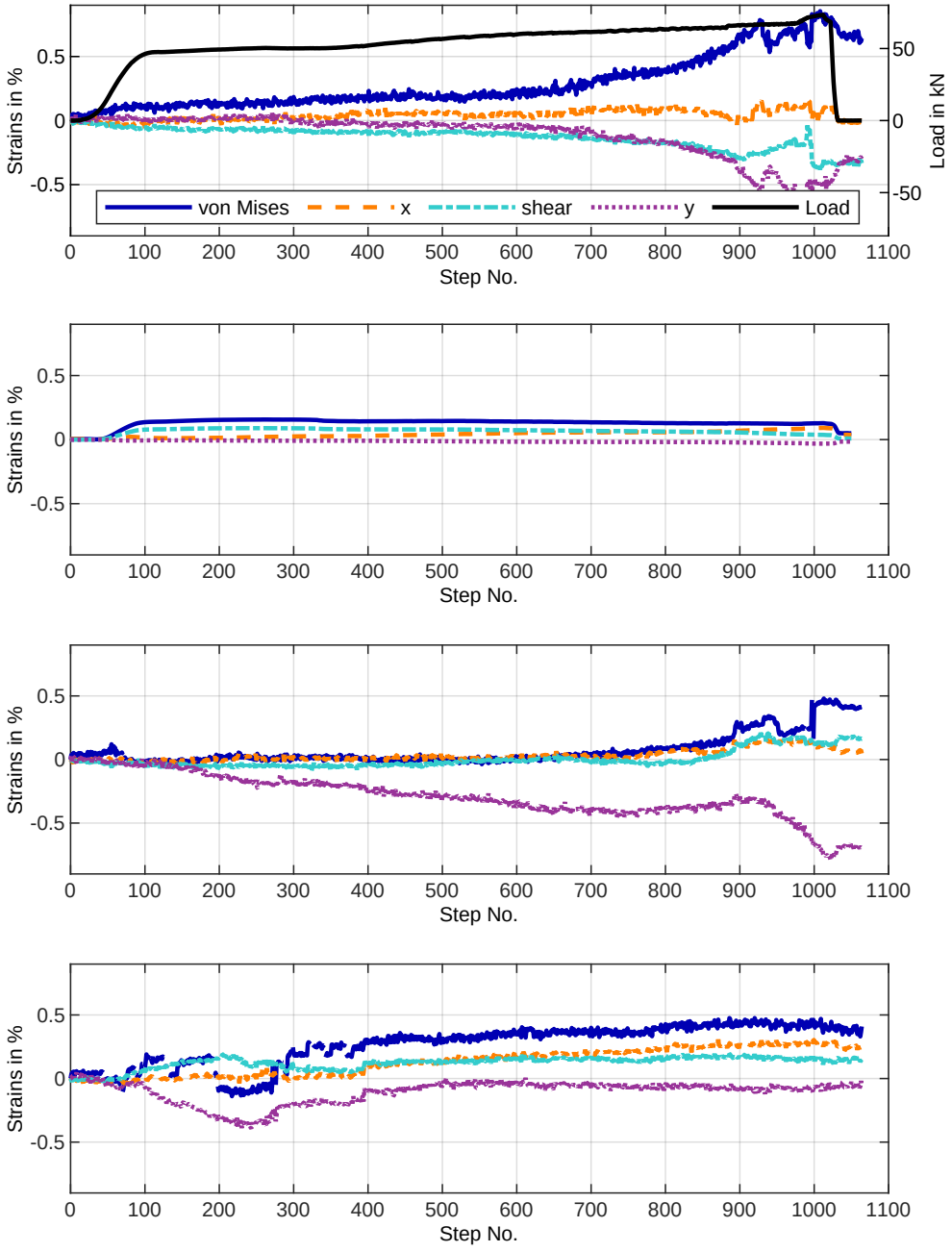

Fig. A.34: Spr_Steel_mk strain results of DIC or strain gauge in shear planes.

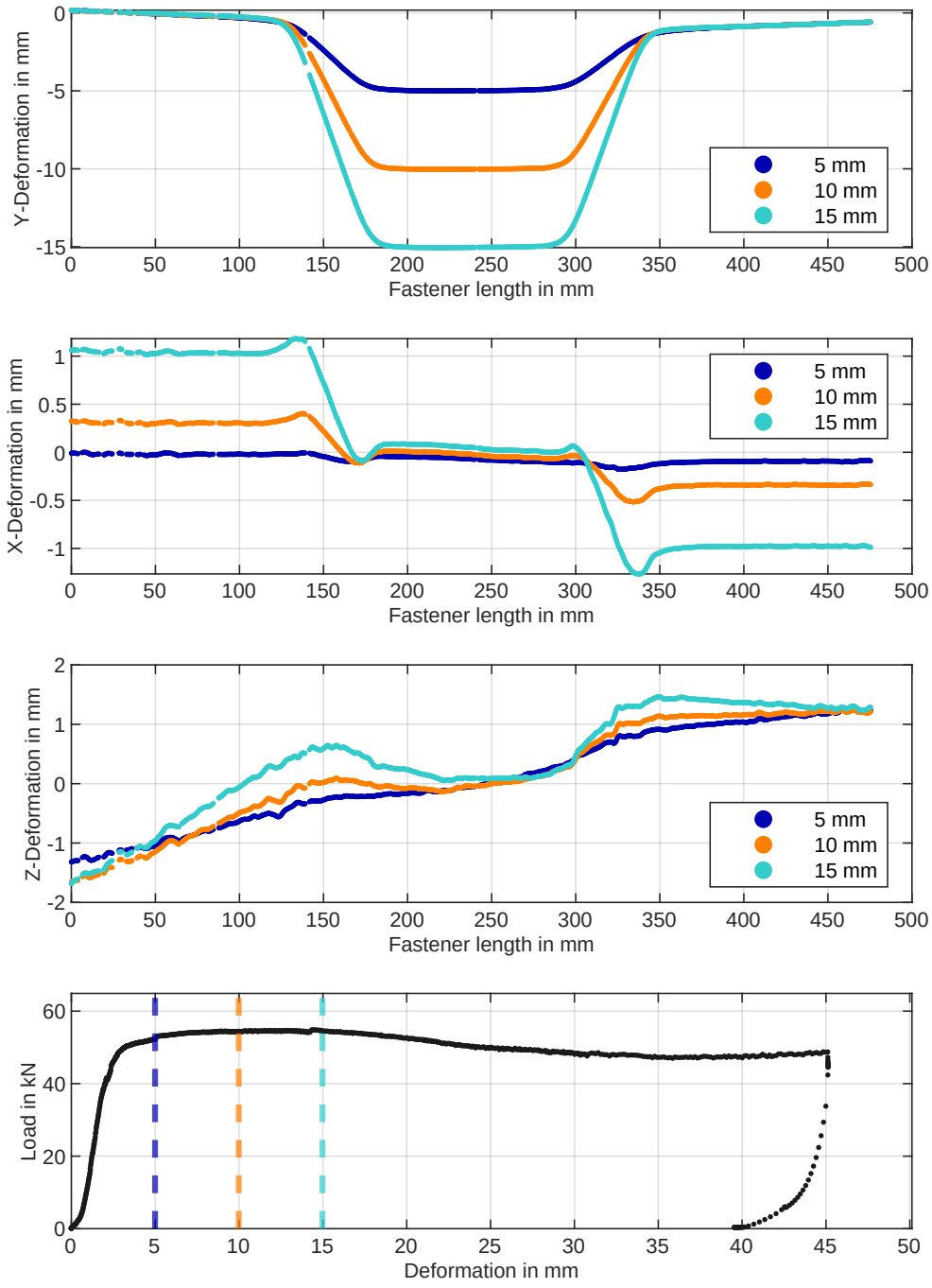

Fig. A.35: BB_Alu deformation results, front side.

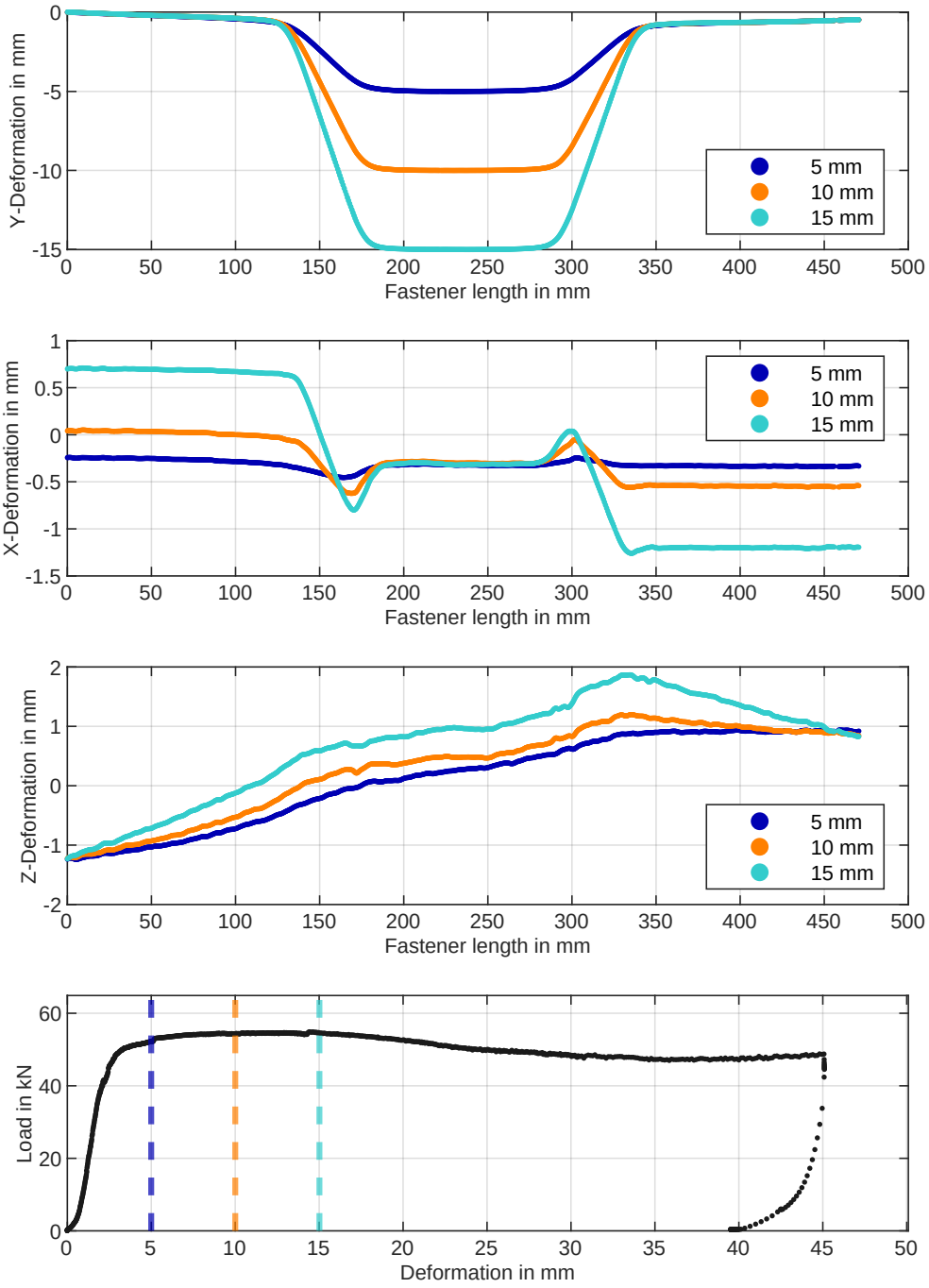

Fig. A.36: BB_Alu deformation results, rear side.

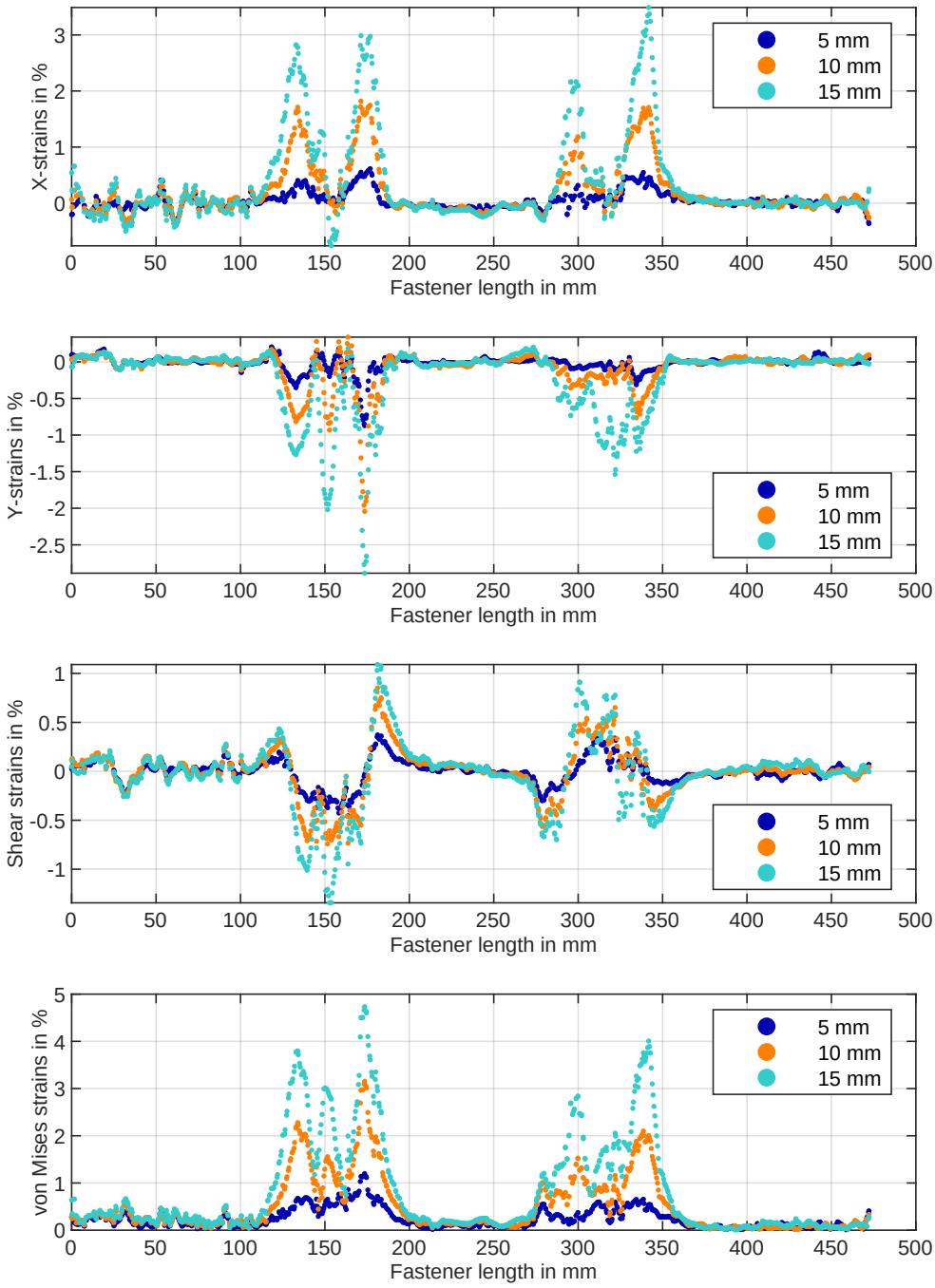

Fig. A.37: BB_Alu strain results, front side. Strain gauge at 320 mm.

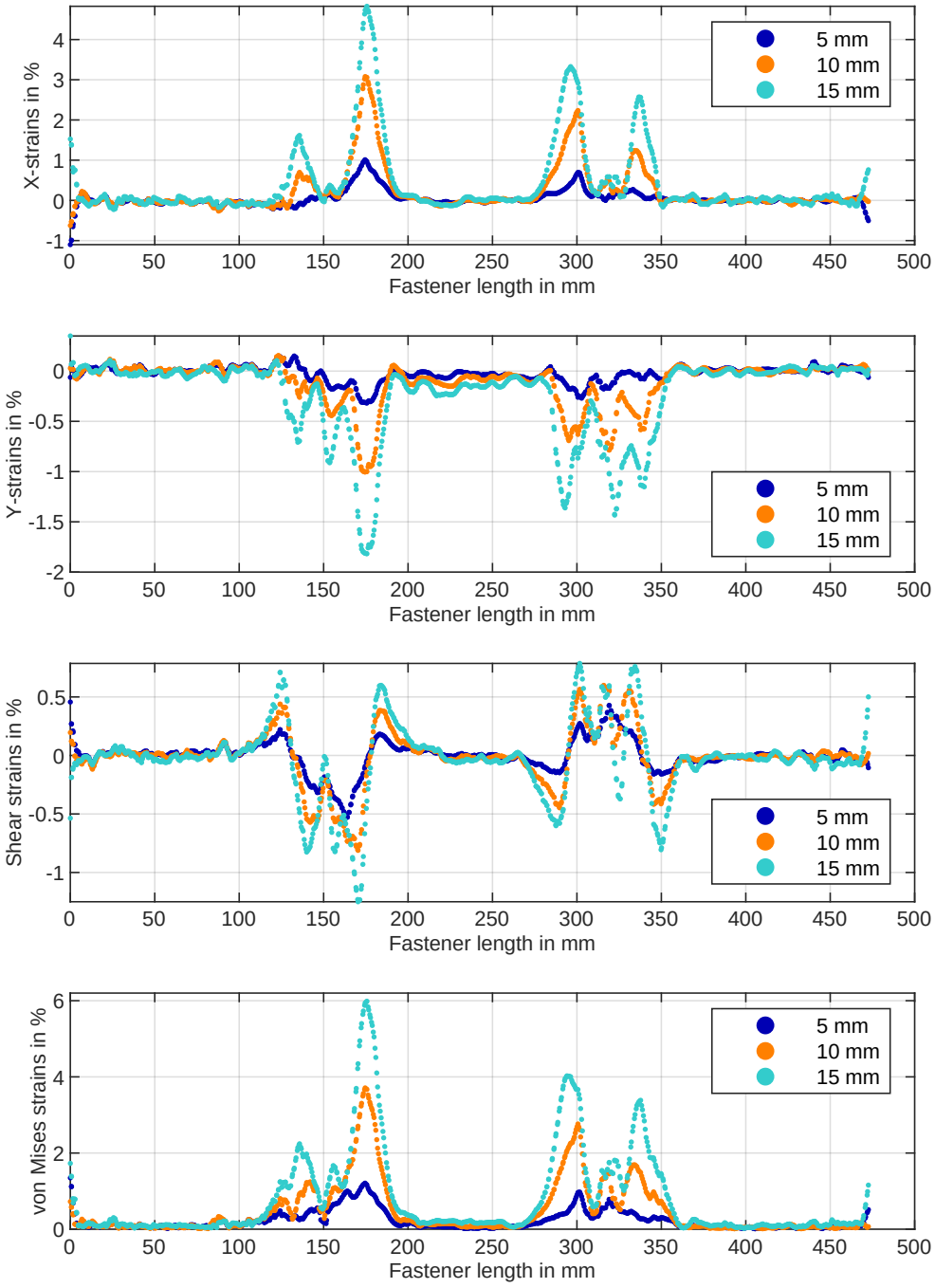

Fig. A.38: BB_Alu strain results, rear side.

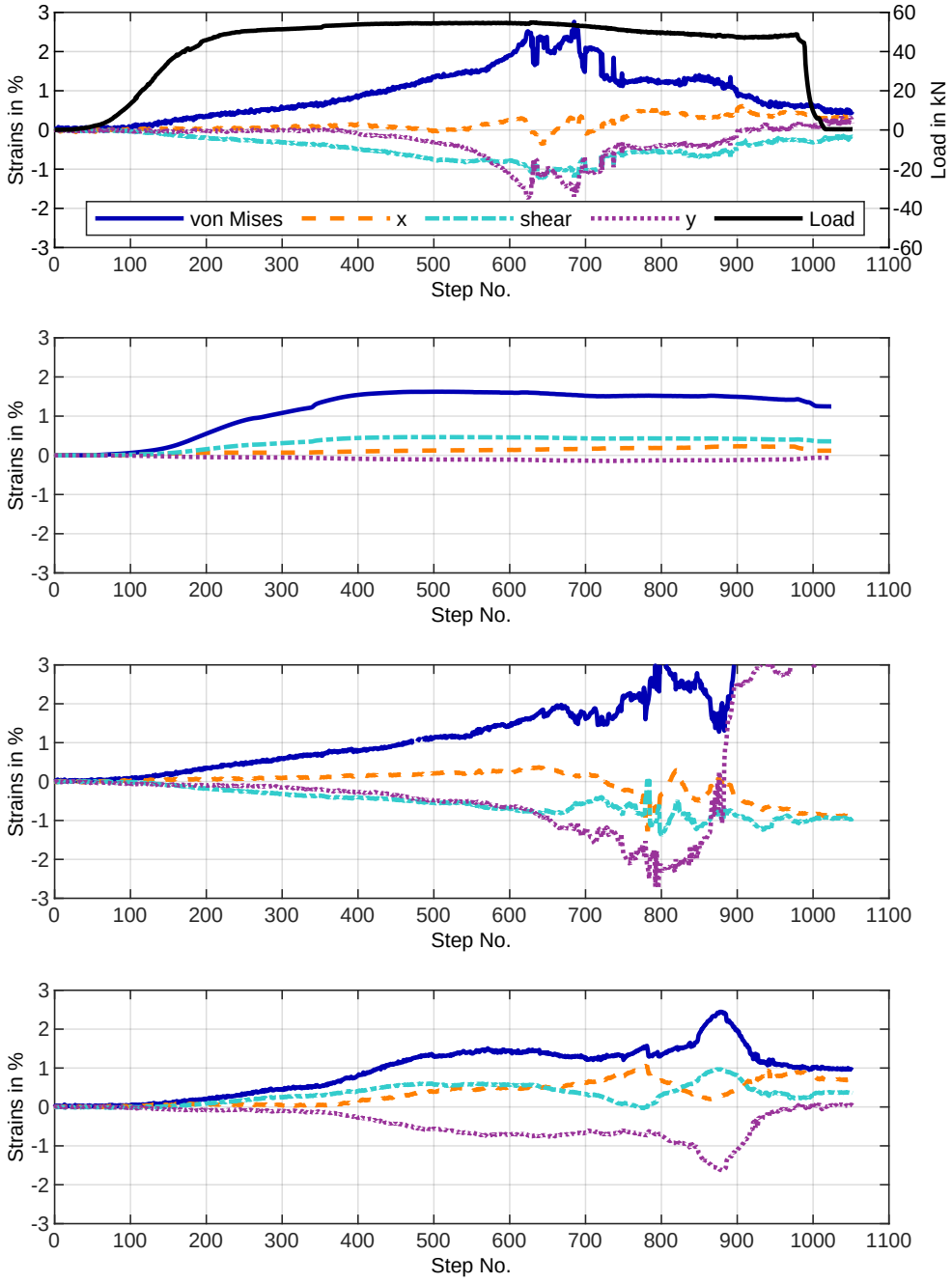

Fig. A.39: BB_Alu strain results of DIC or strain gauge in shear planes.

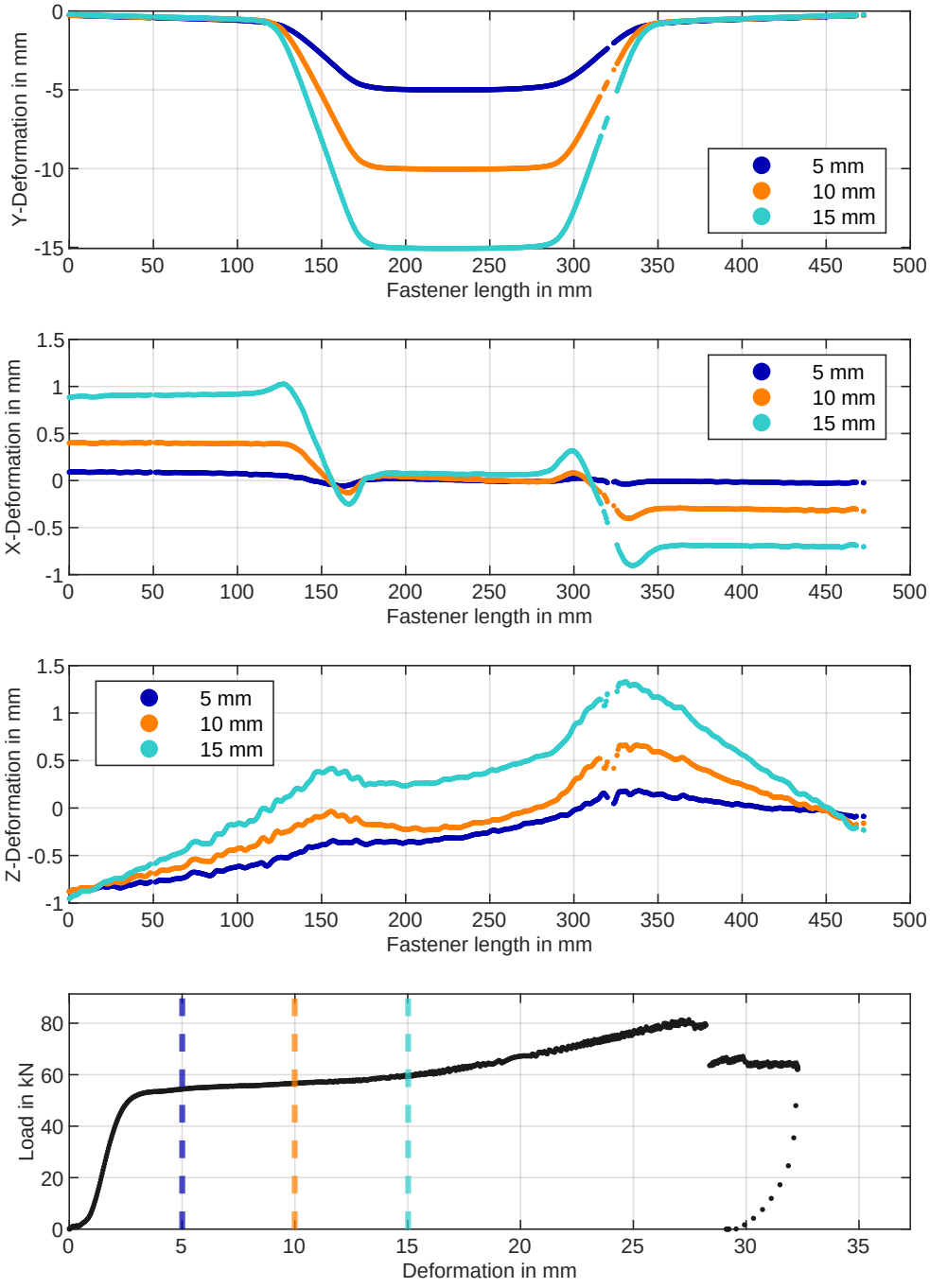

Fig. A.40: BB_Alu_mk deformation results, front side.

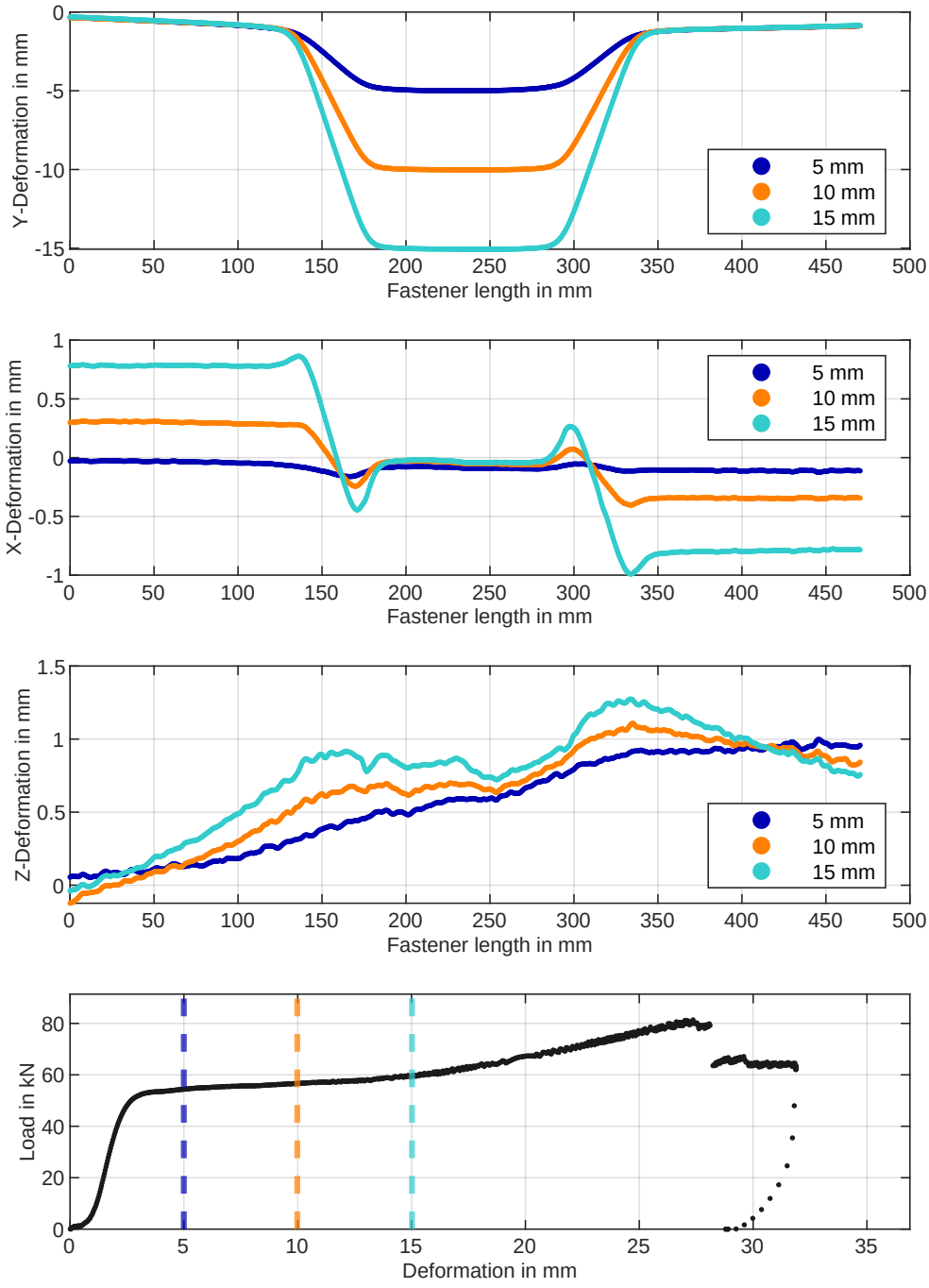

Fig. A.41: BB_Alu_mk deformation results, rear side.

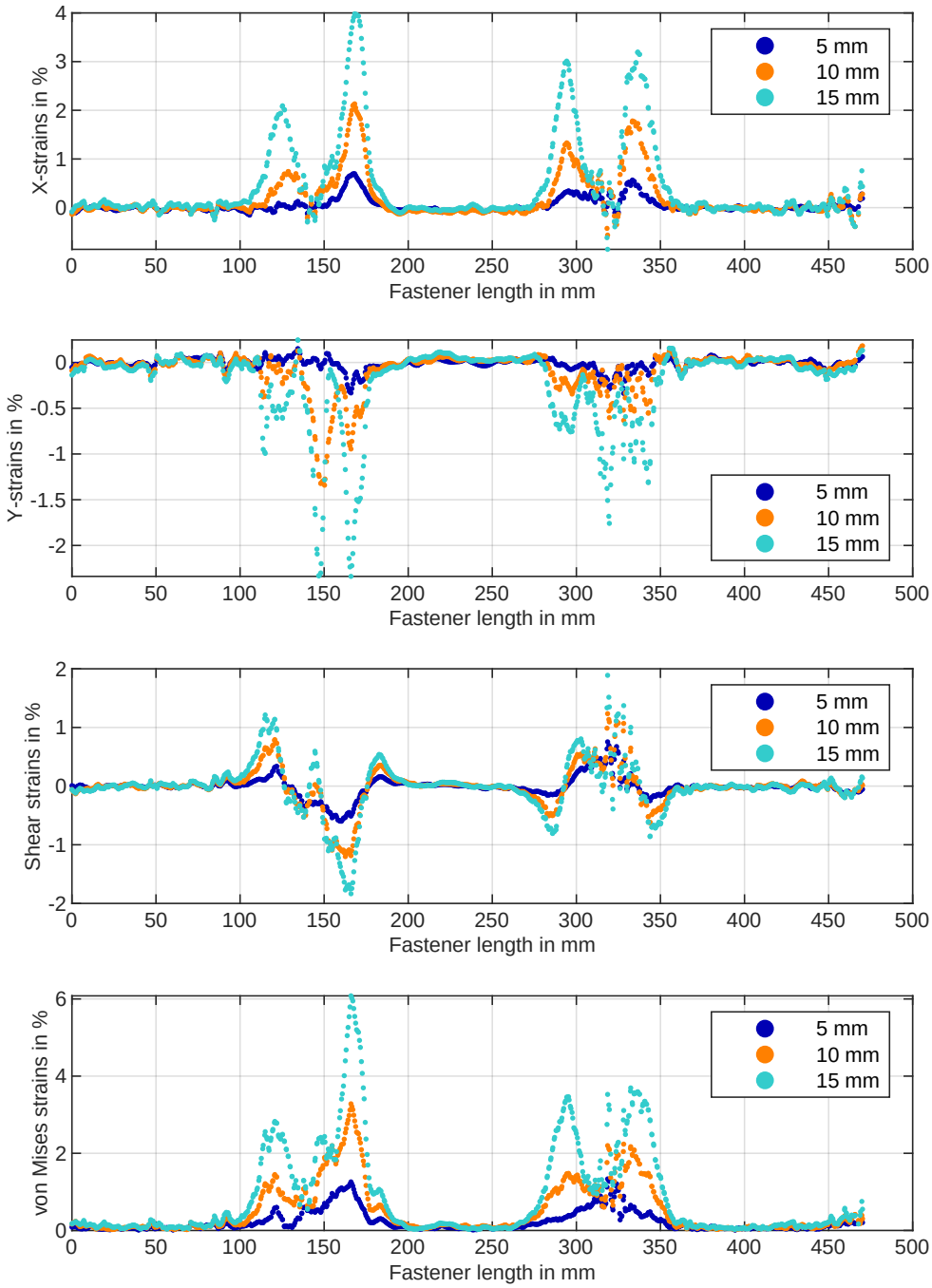

Fig. A.42: BB_Alu_mk strain results, front side.

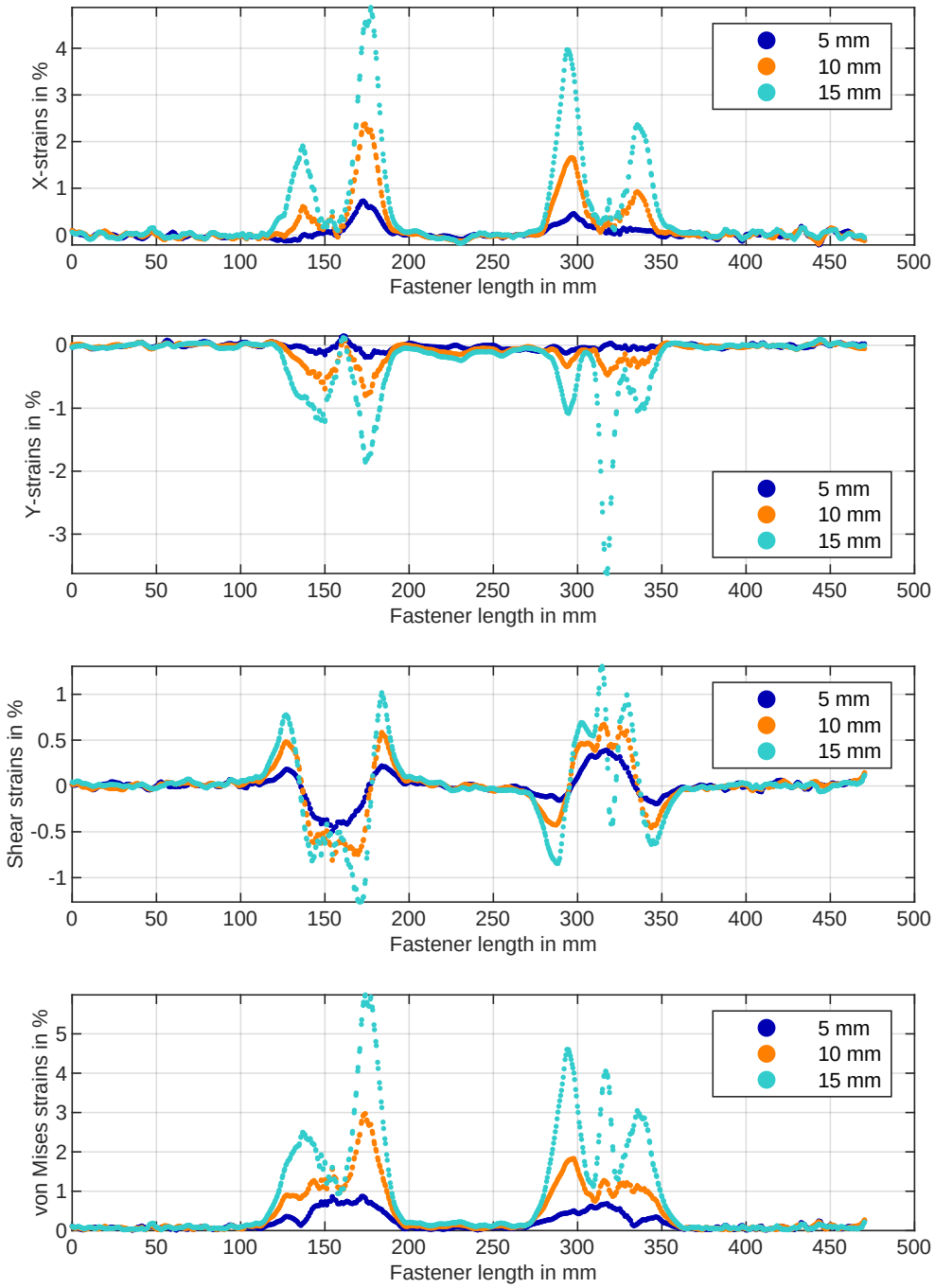

Fig. A.43: BB_Alu_mk strain results, rear side.

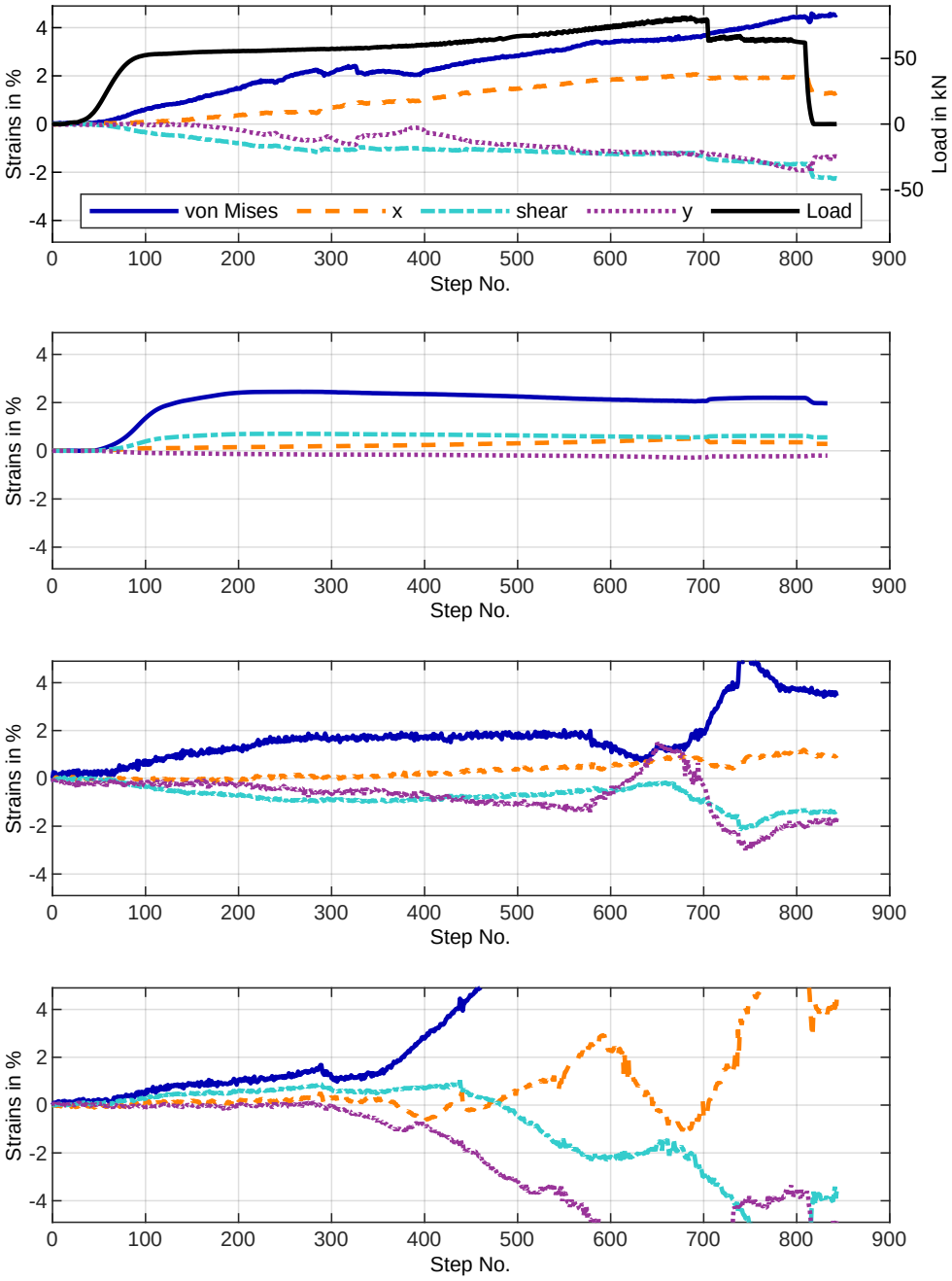

Fig. A.44: BB_Alu_mk strain results of DIC or strain gauge in shear planes.

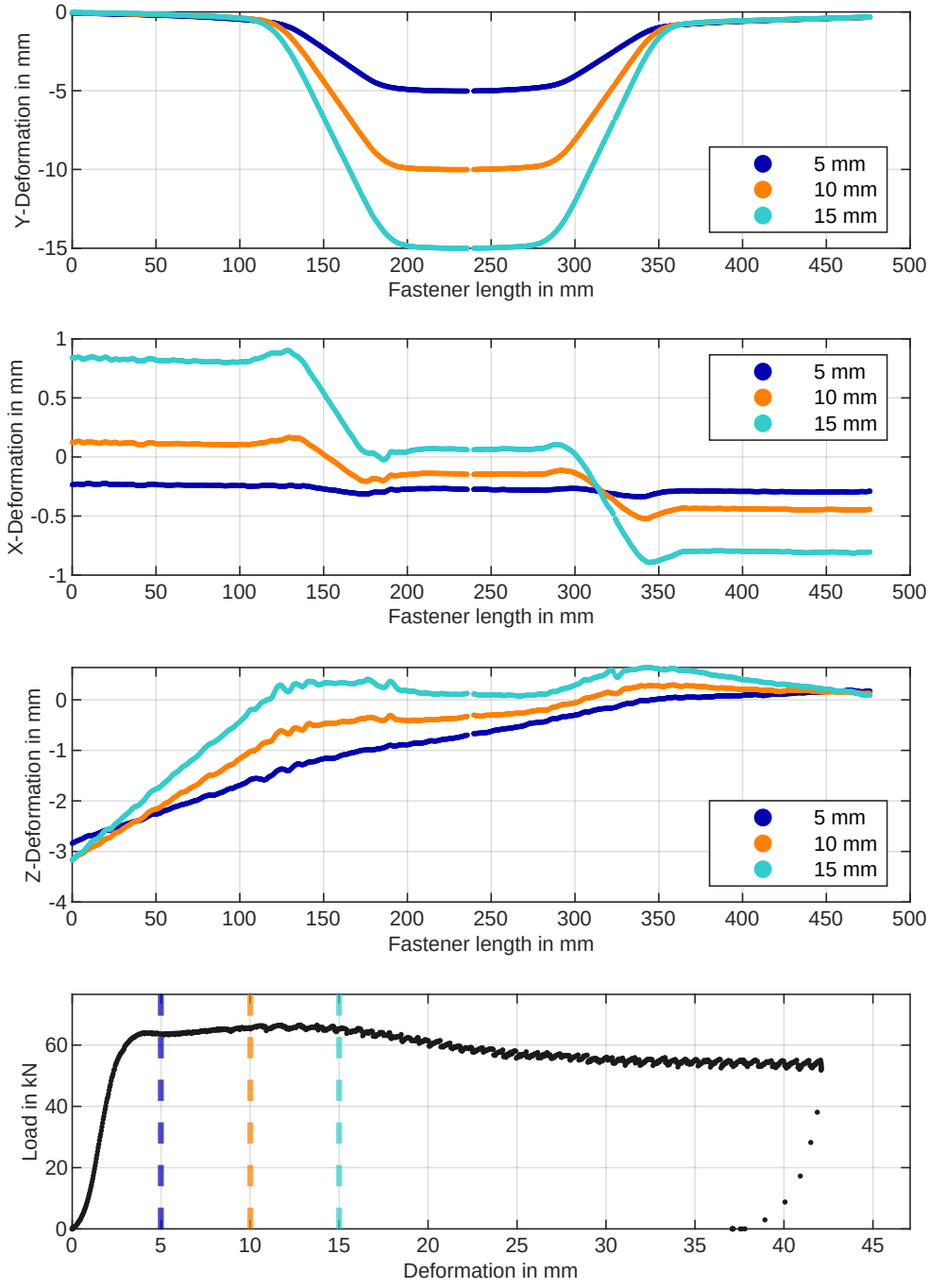

Fig. A.45: BB_Steel deformation results, front side.

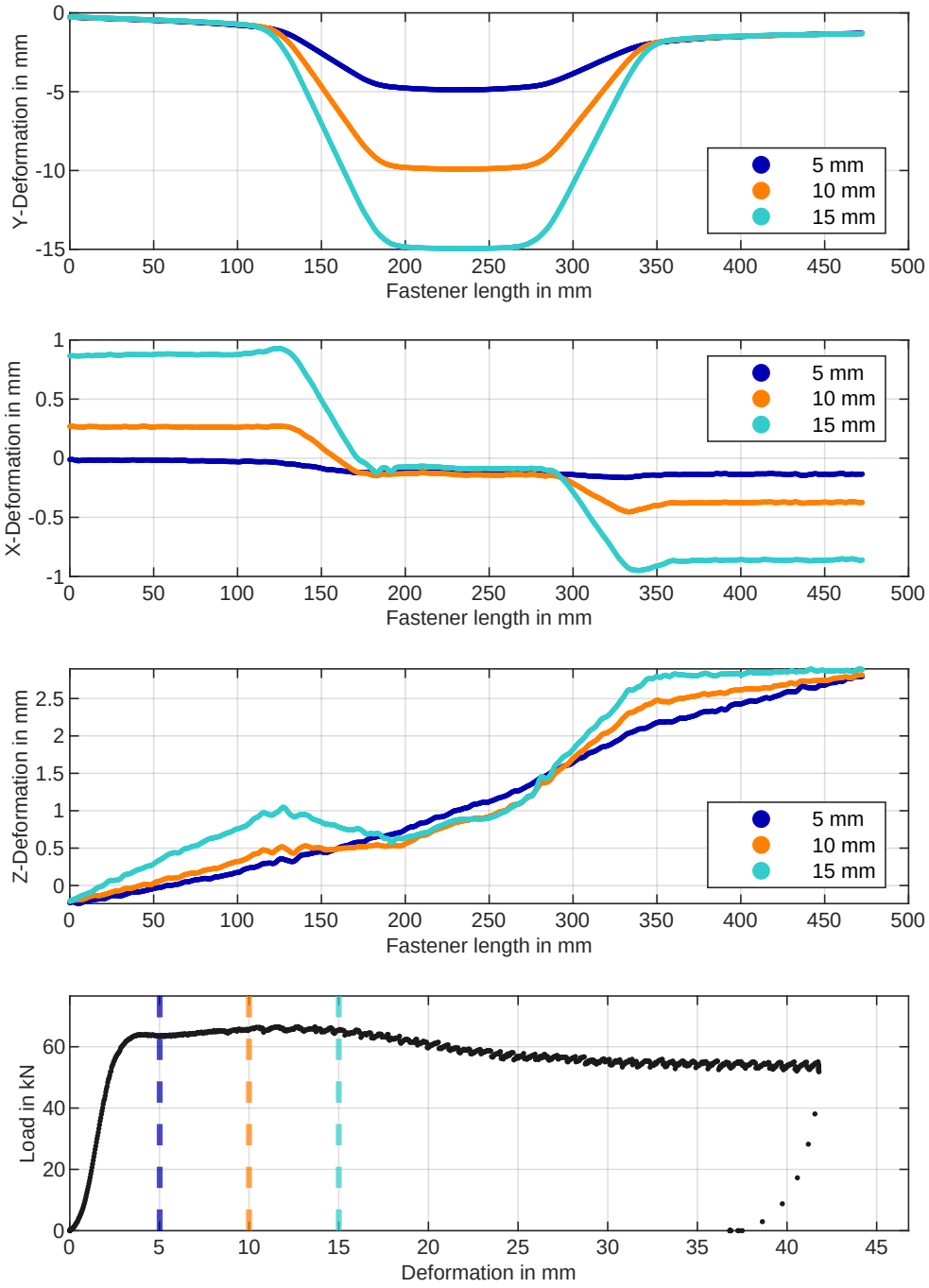

Fig. A.46: BB_Steel deformation results, rear side.

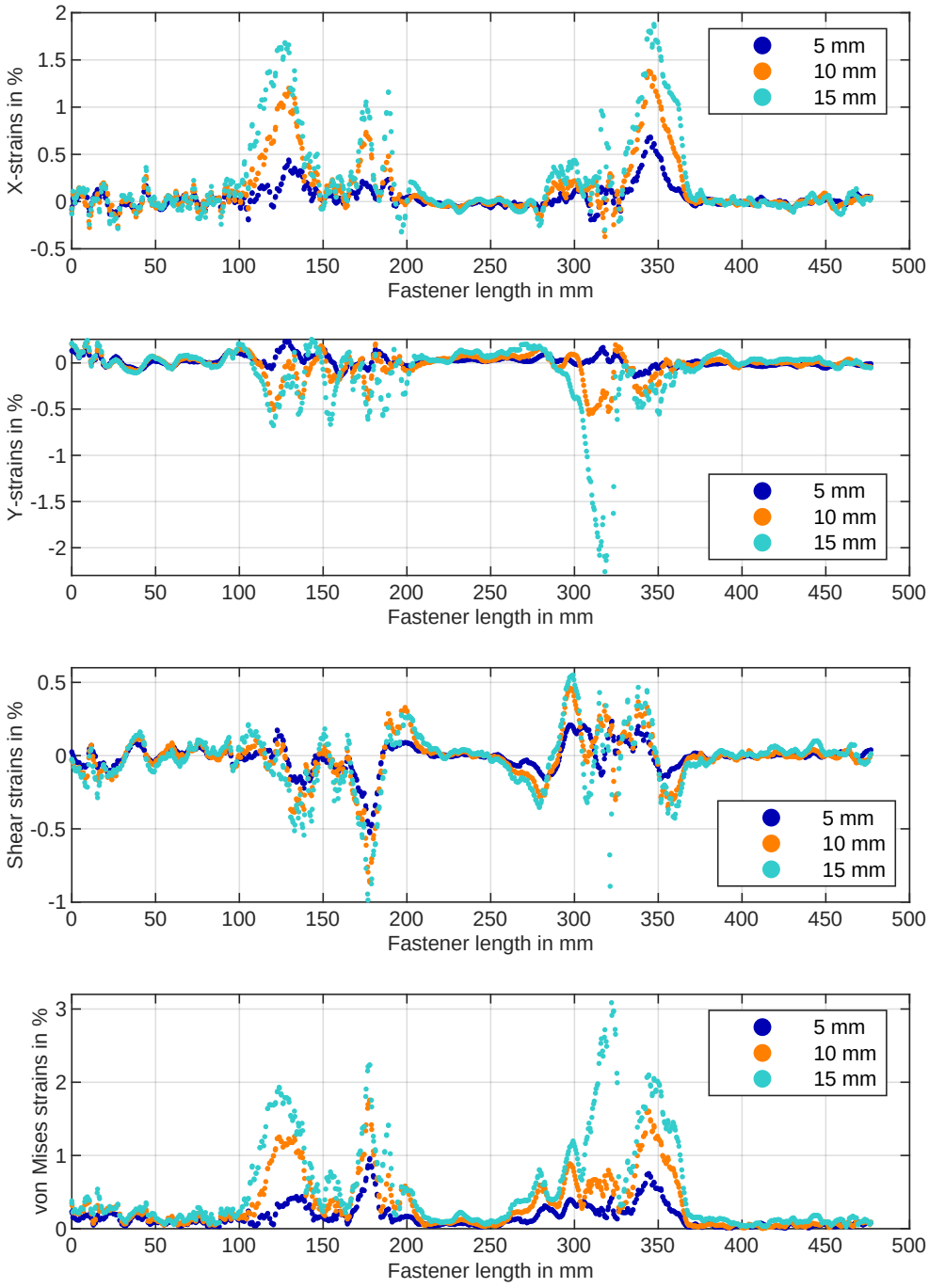

Fig. A.47: BB_Steel strain results, front side. Tinder layer has not been removed. Strain gauge at 320 mm.

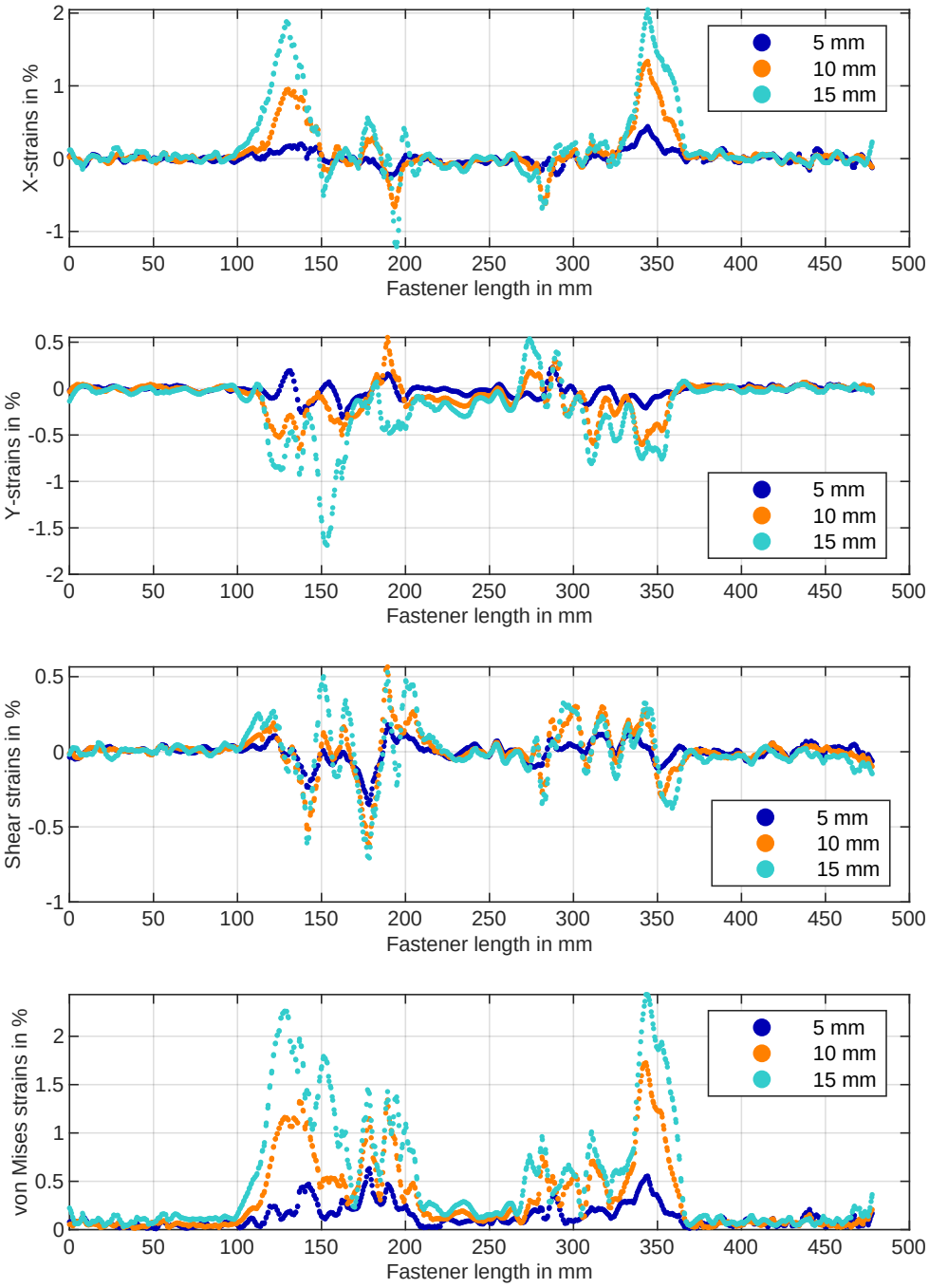

Fig. A.48: BB_Steel strain results, rear side. Tinder layer has not been removed.

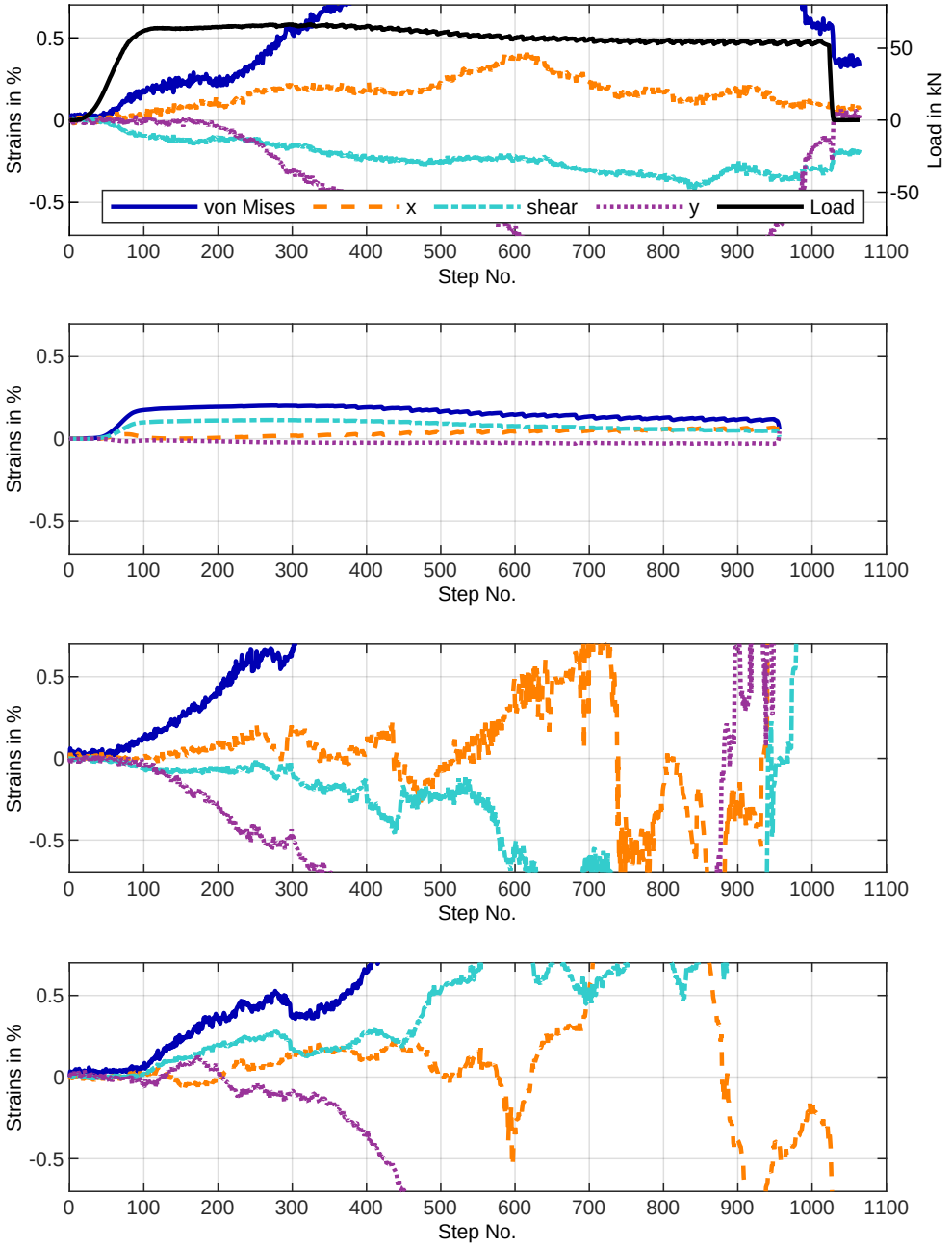

Fig. A.49: BB_Steel strain results of DIC or strain gauge in shear planes. Tinder layer has not been removed.

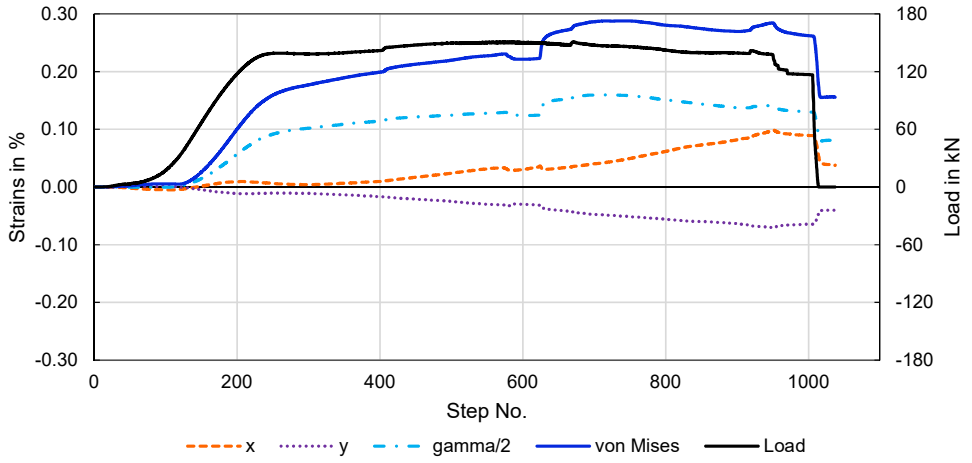

Fig. A.50: Additional specimen BB_Steel_2: Strain results of strain gauge in shear plane. The visual measurement via DIC was interrupted due to technical problems and could not be saved. Only data for the load and the values of the strain gauges are available.

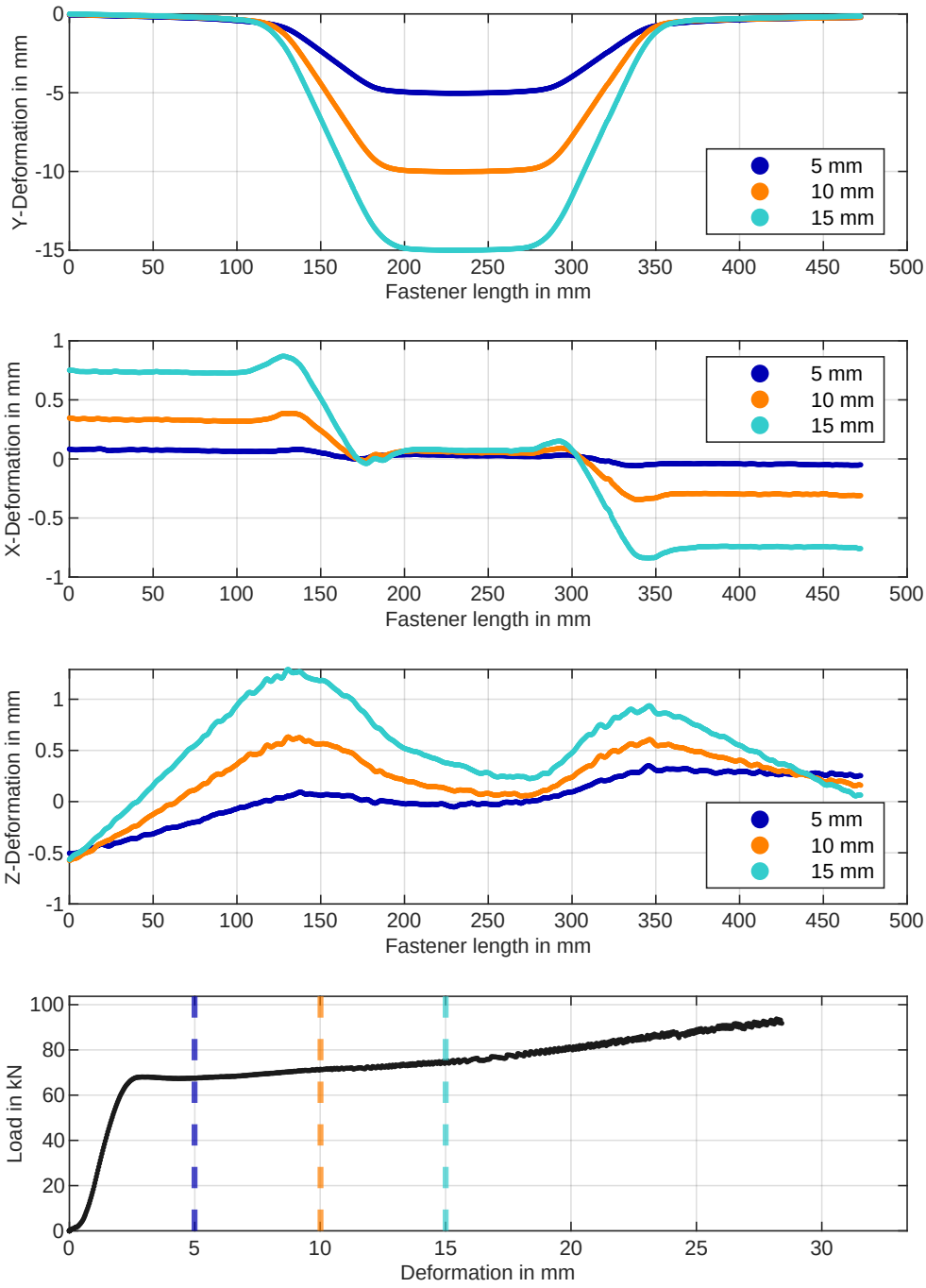

Fig. A.51: BB_Steel_mk deformation results, front side.

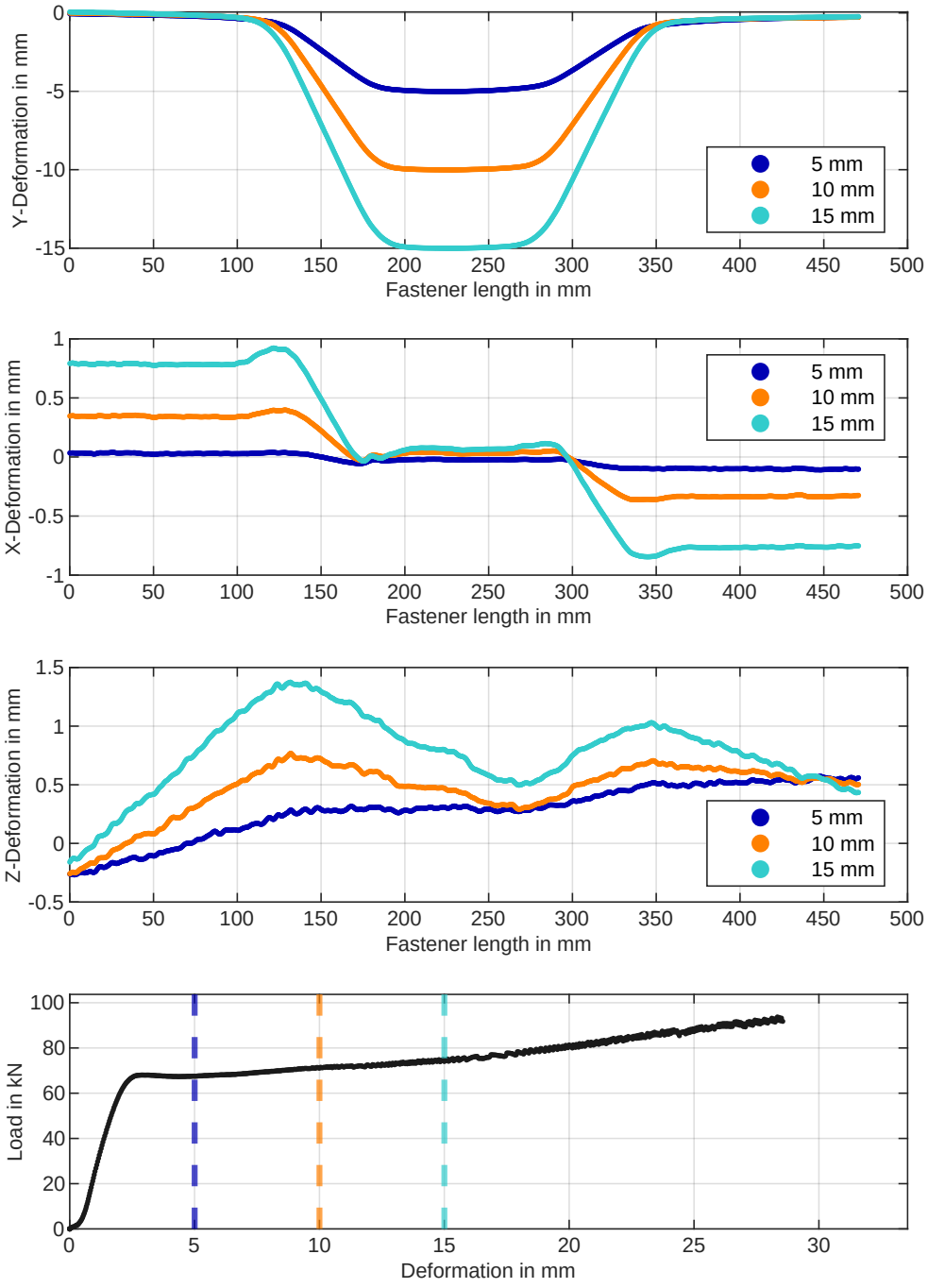

Fig. A.52: BB_Steel_mk deformation results, rear side.

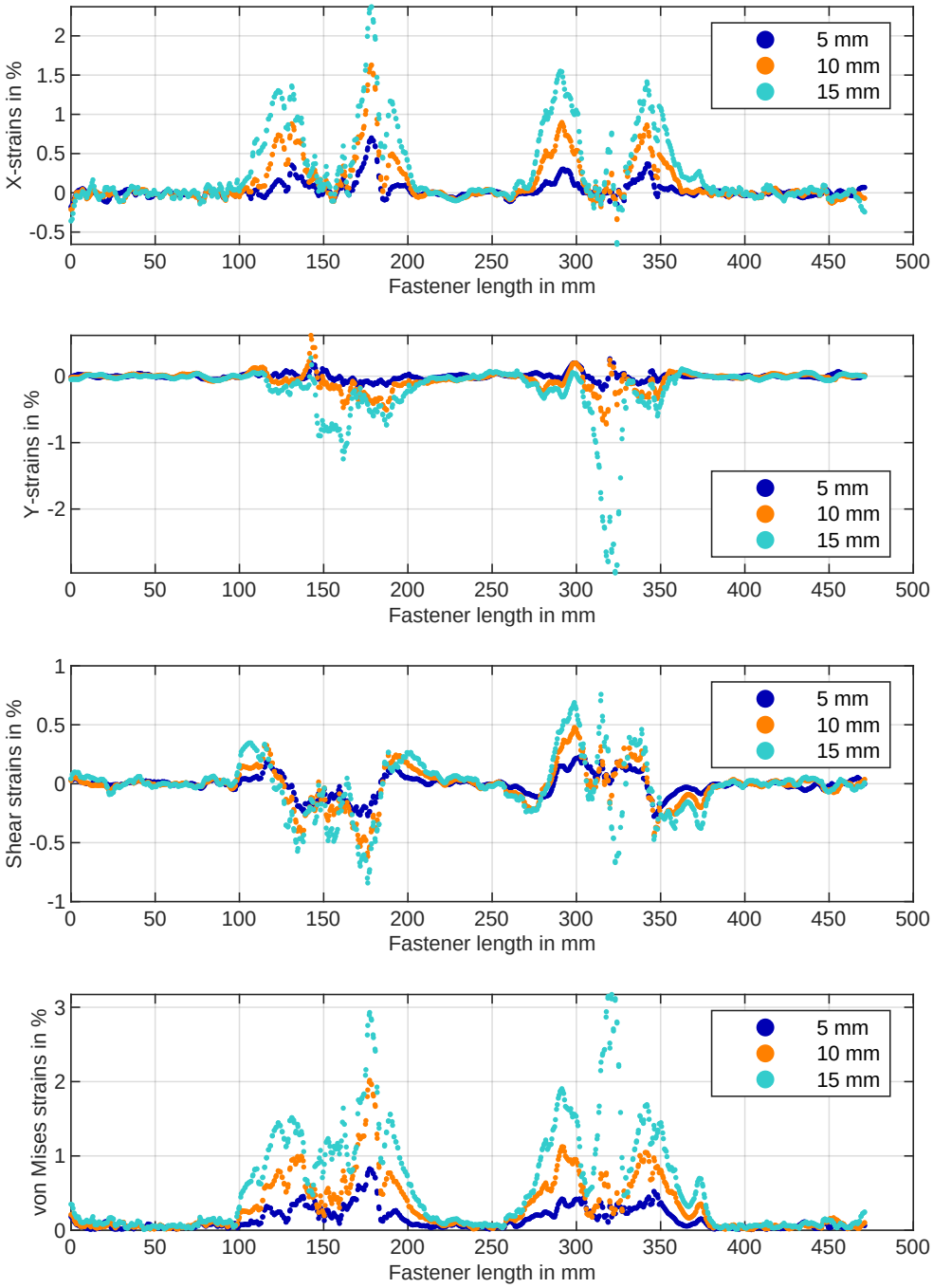

Fig. A.53: BB_Steel_mk strain results, front side. Strain gauge at 320 mm.

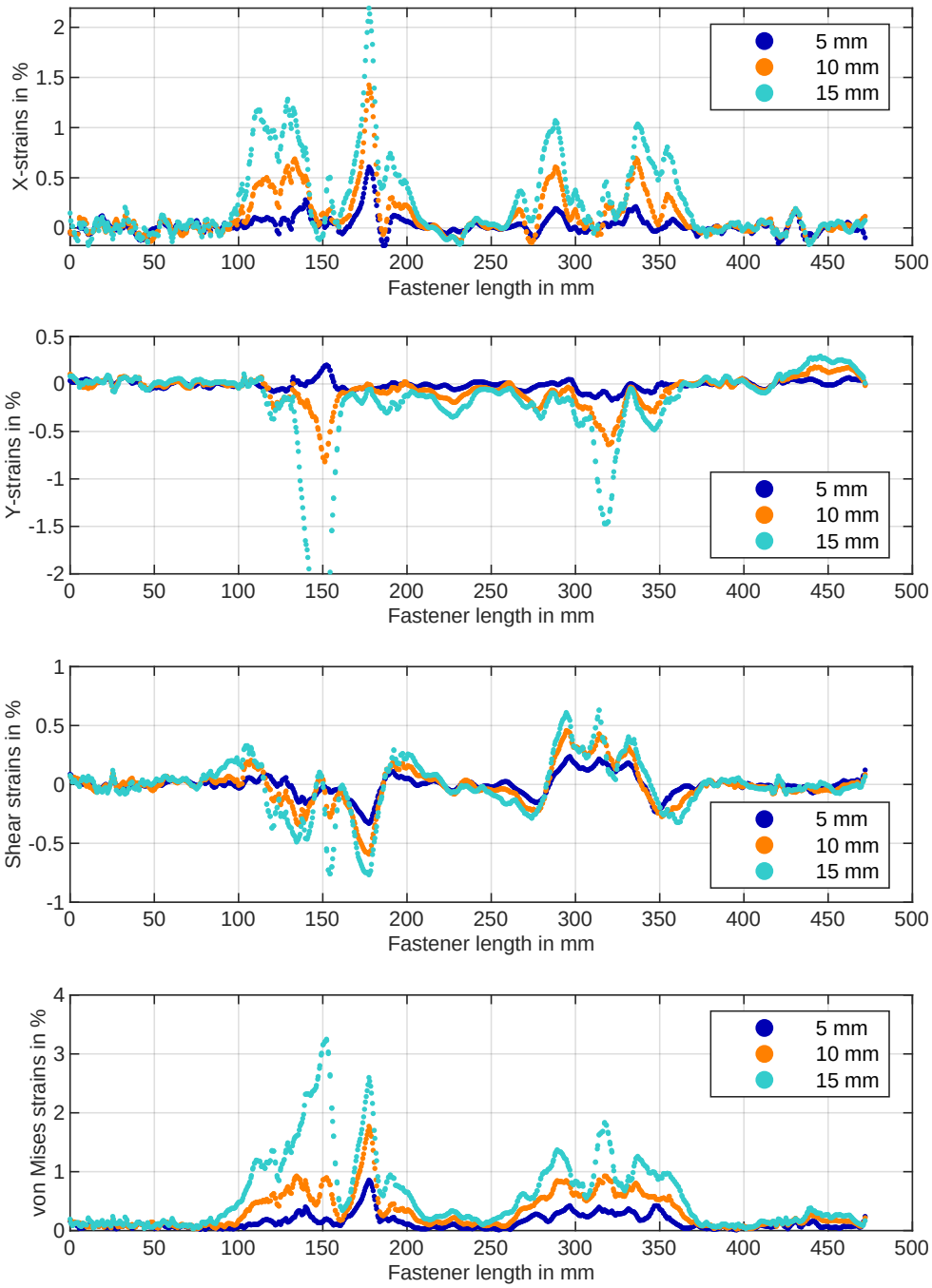

Fig. A.54: BB_Steel_mk strain results, rear side.

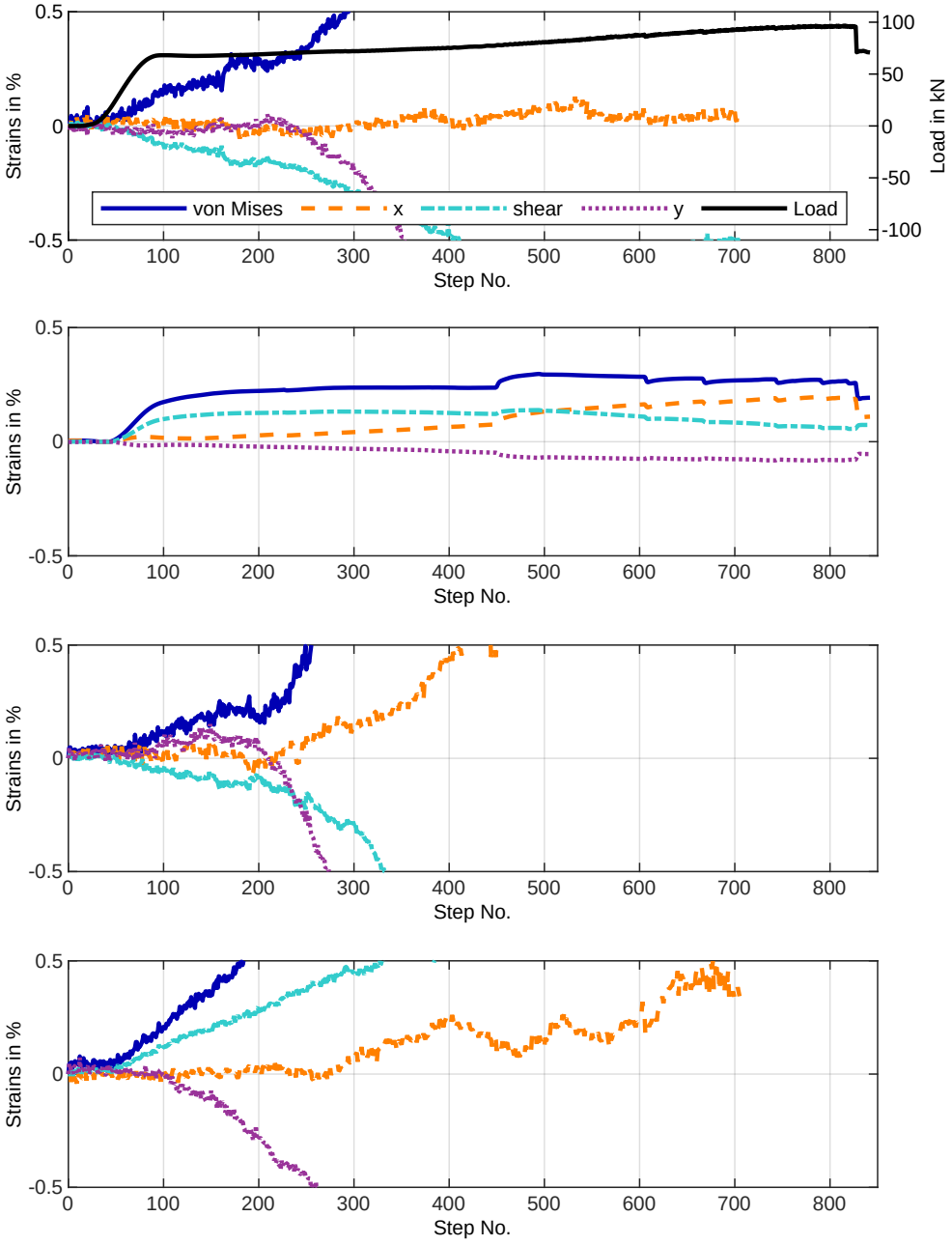

Fig. A.55: BB_Steel_mk strain results of DIC or strain gauge in shear planes.

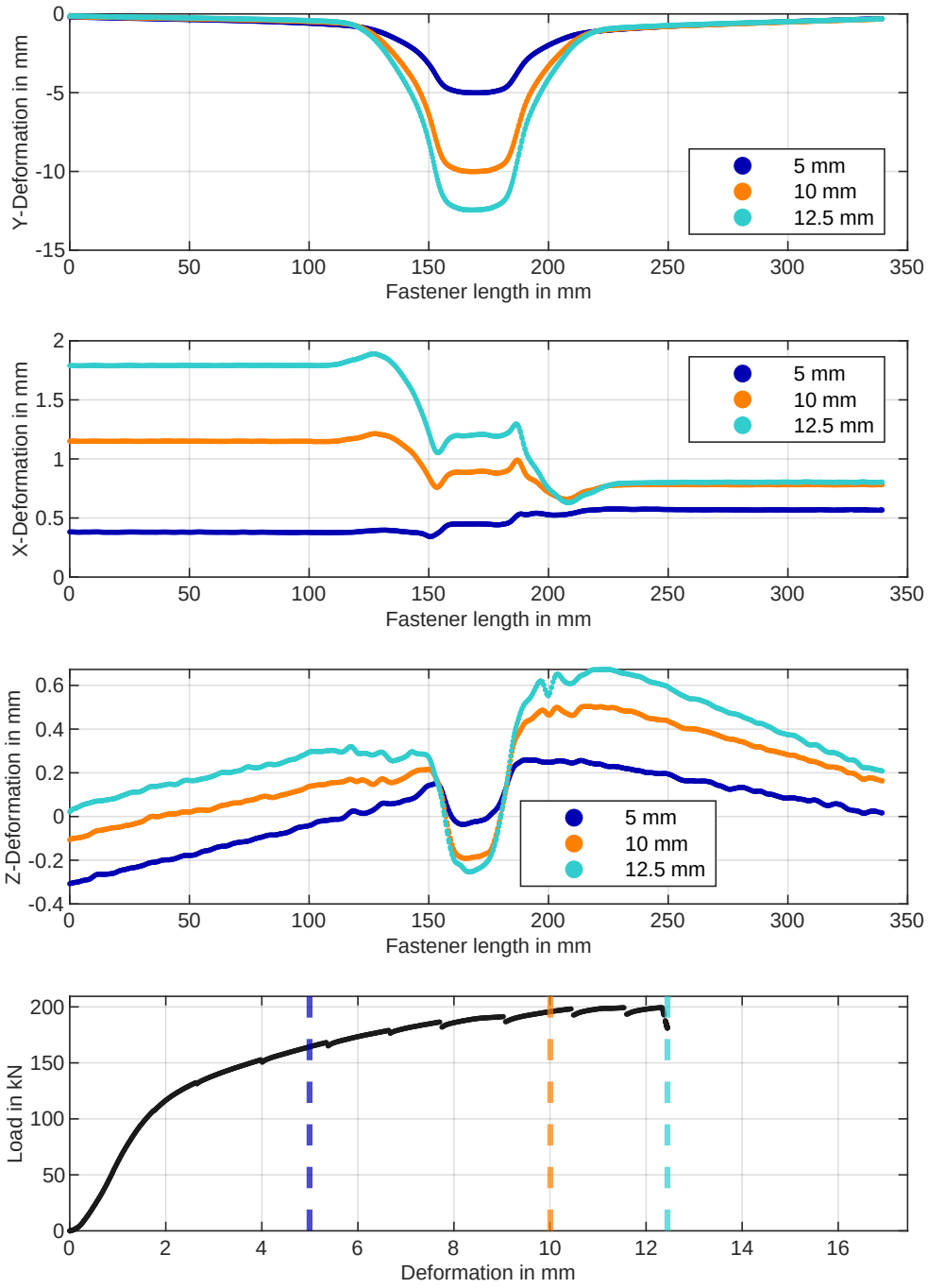

Fig. A.56: DVW_Steel deformation results, front side.

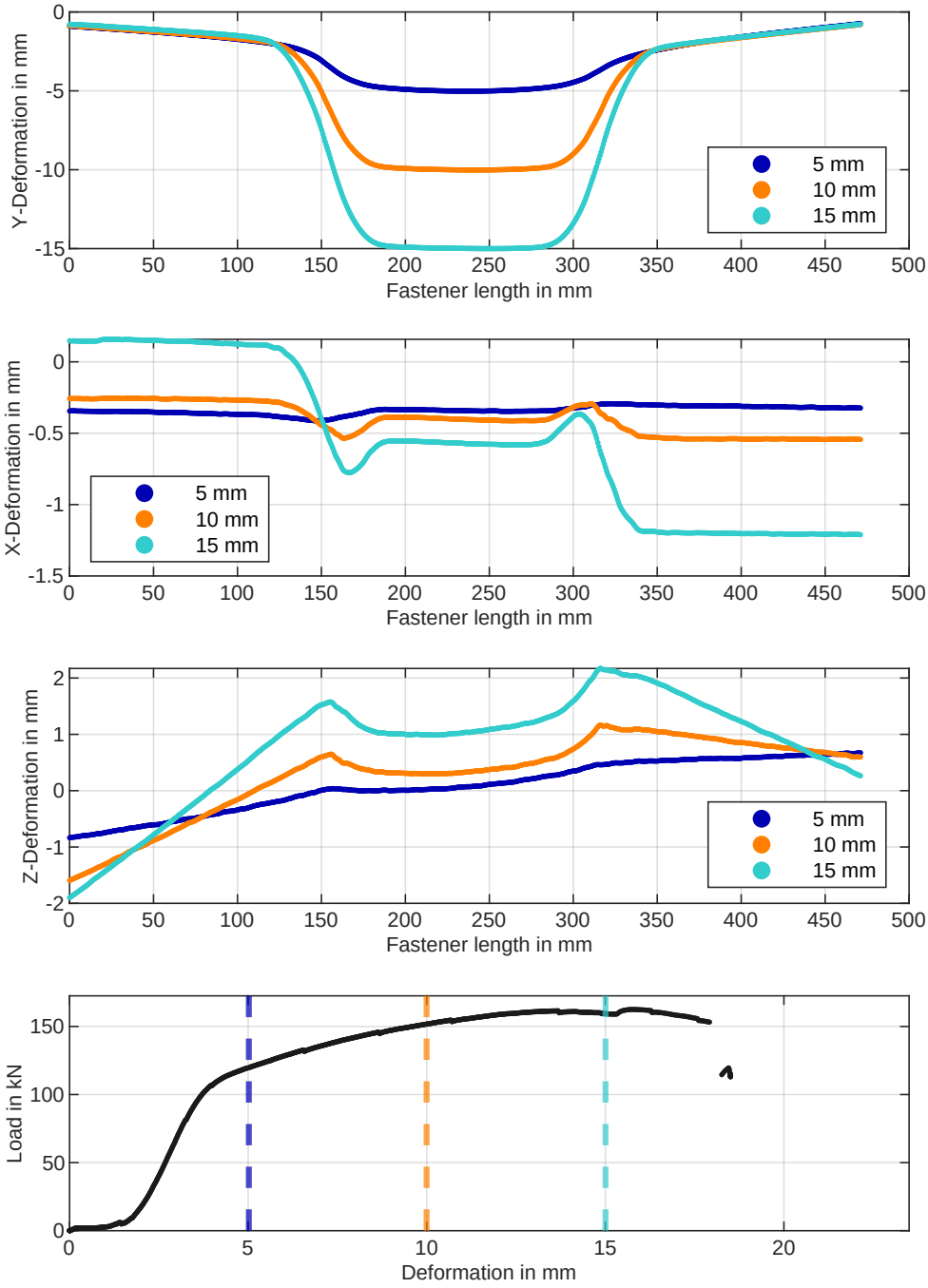

Fig. A.57: DVW_Steel deformation results, rear side.

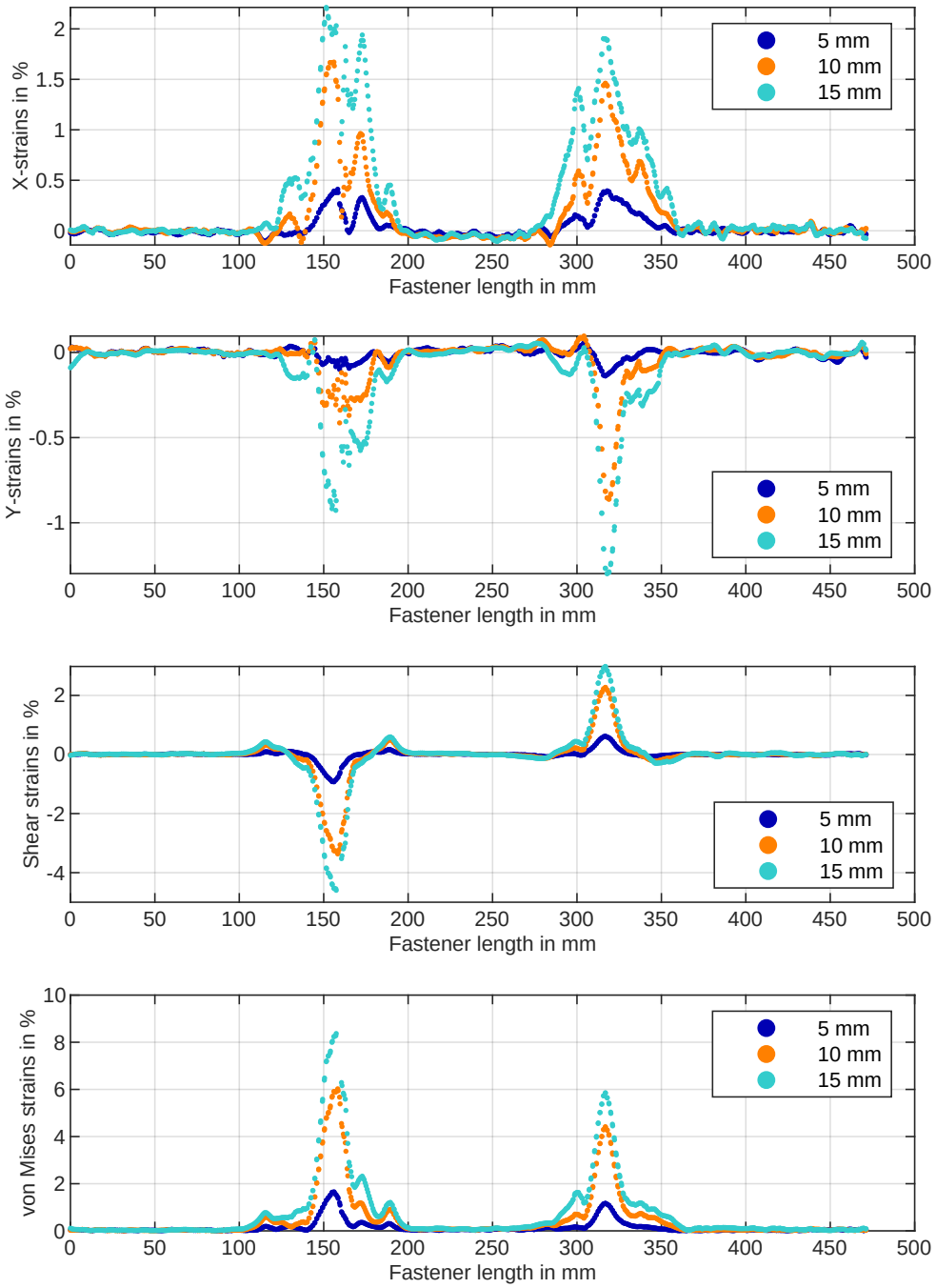

Fig. A.58: DVW_Steel strain results, front side. Strain gauge at 320 mm.

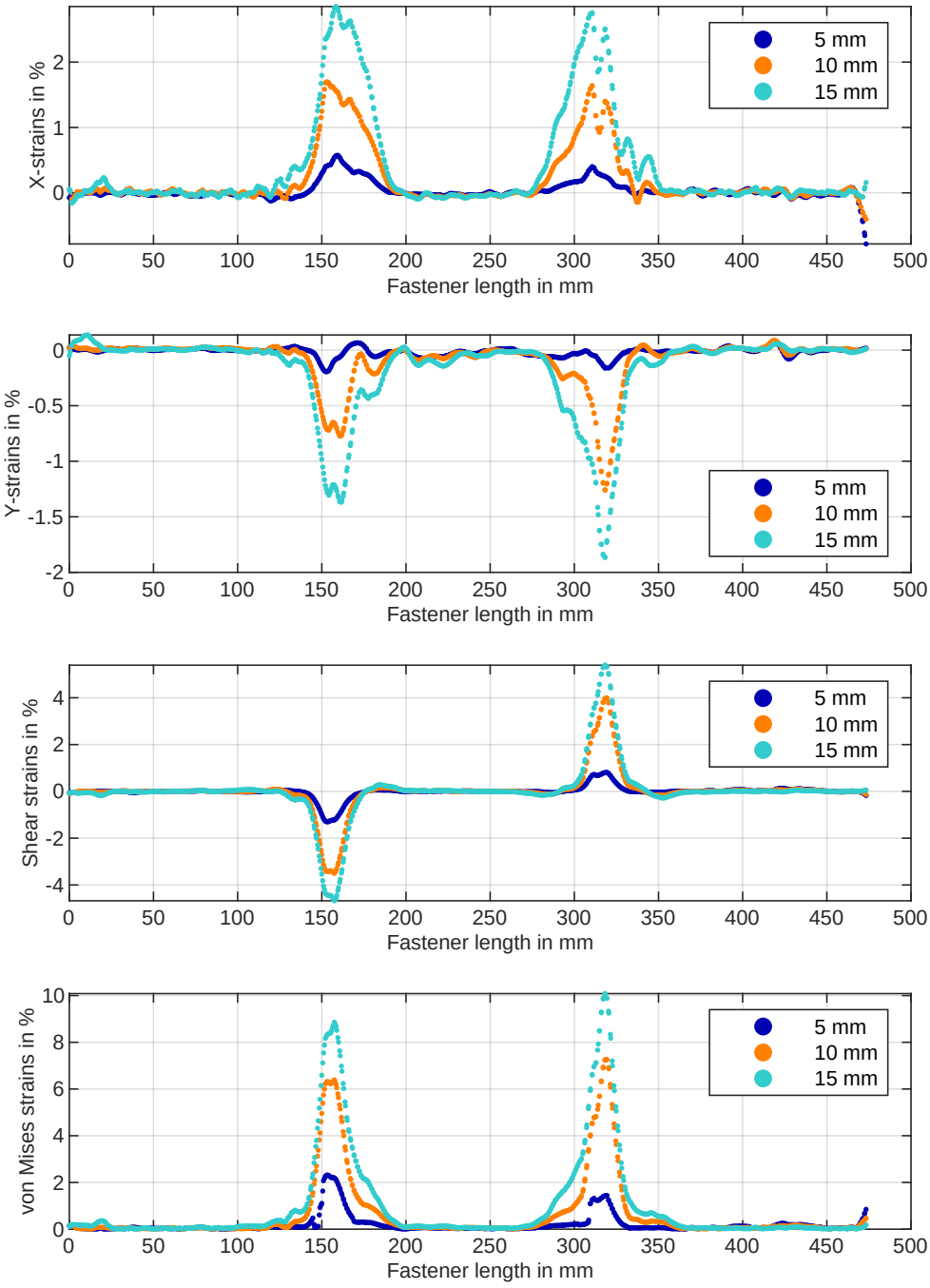

Fig. A.59: DVW_Steel strain results, rear side.

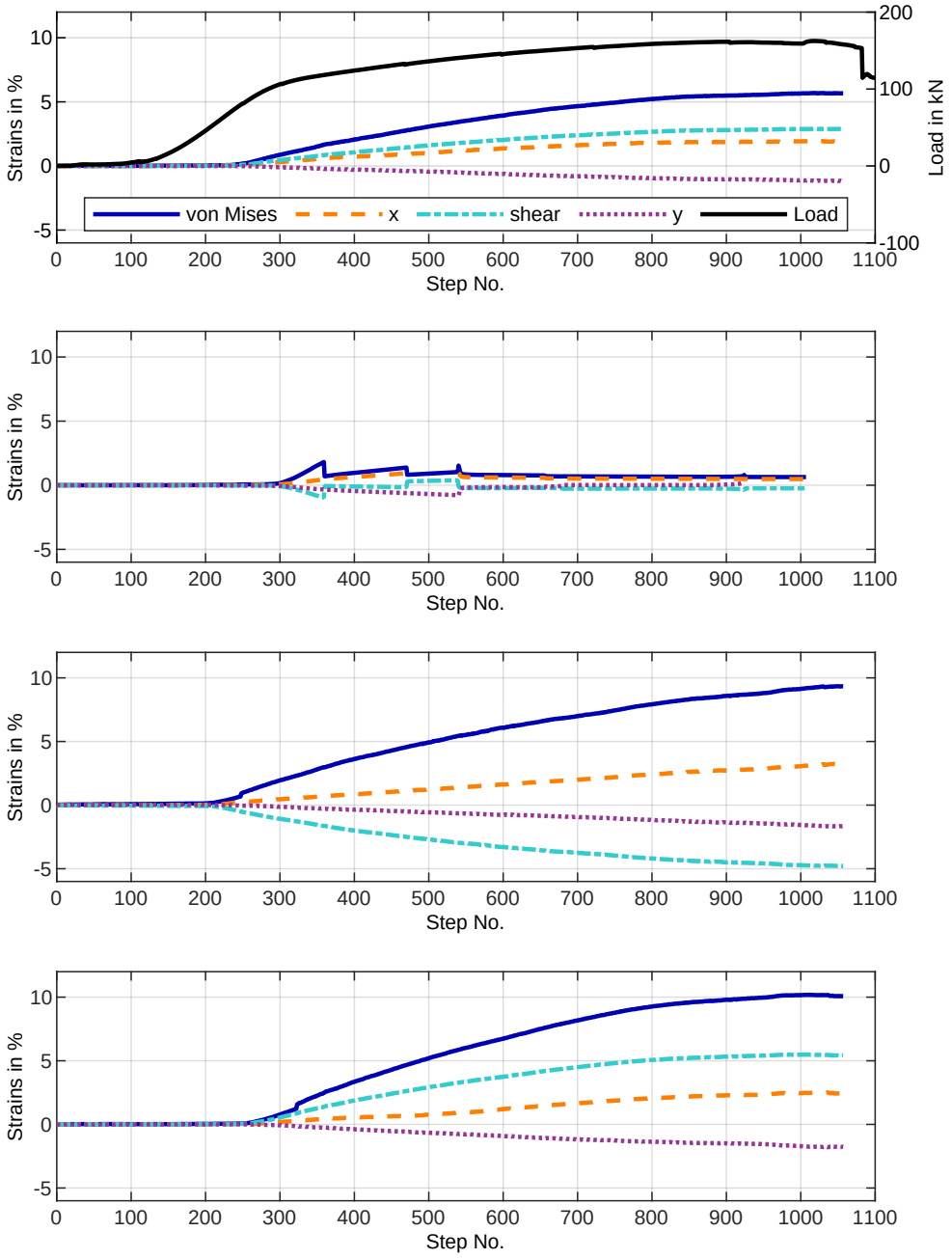

Fig. A.60: DVW_Steel strain results of DIC or strain gauge in shear planes.

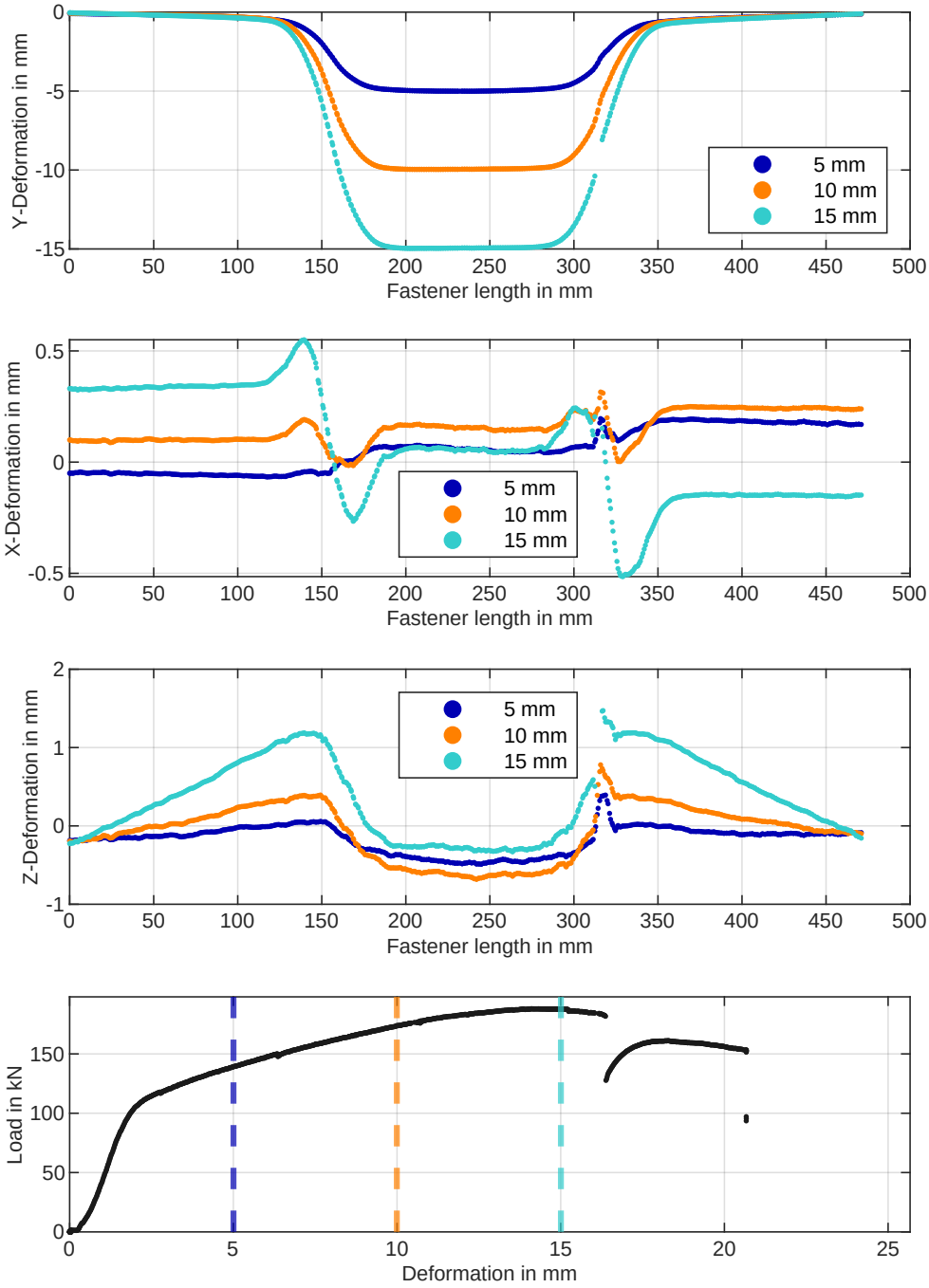

Fig. A.61: DVW_Steel_mk deformation results, front side.

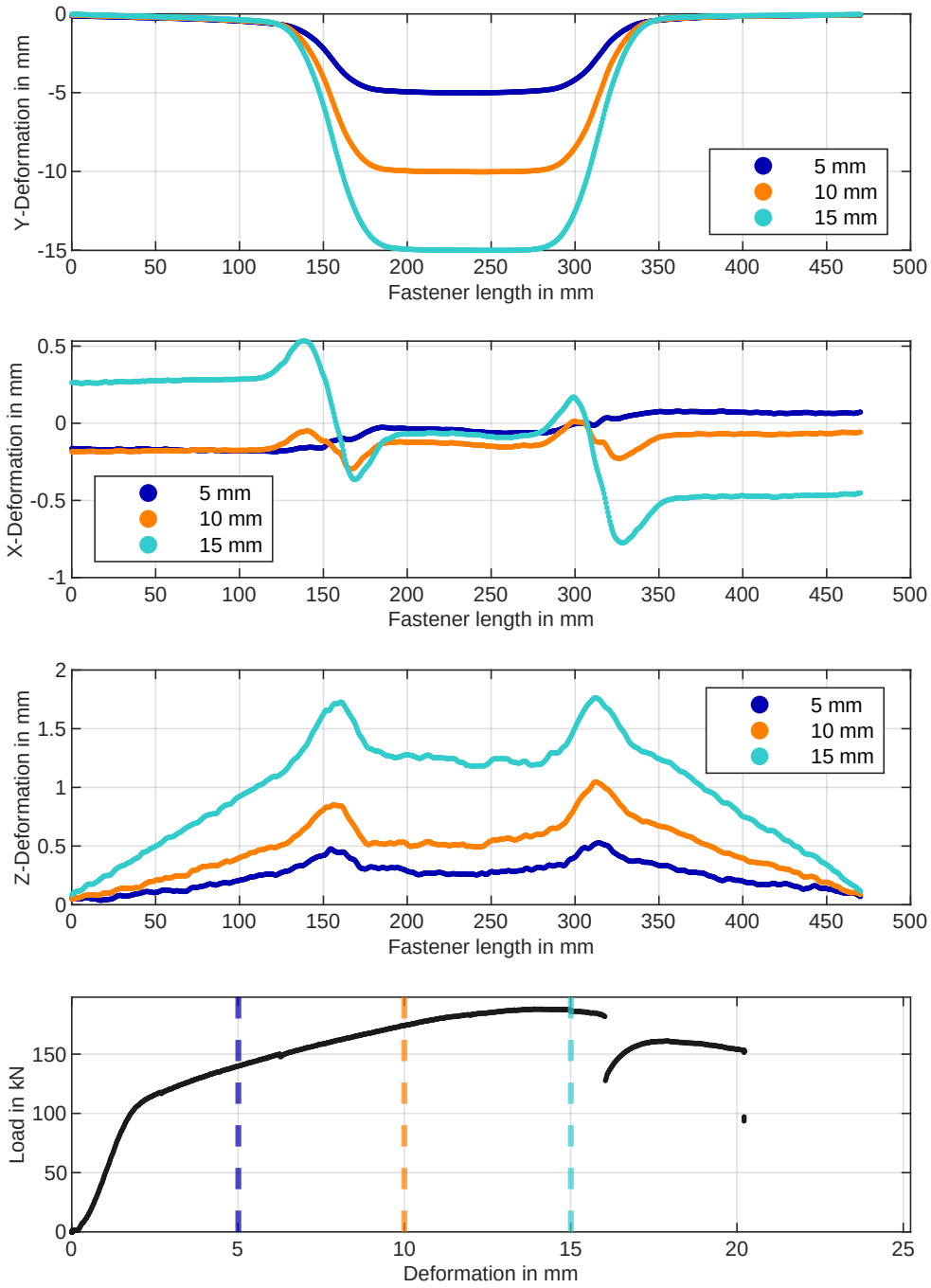

Fig. A.62: DVW_Steel_mk deformation results, rear side.

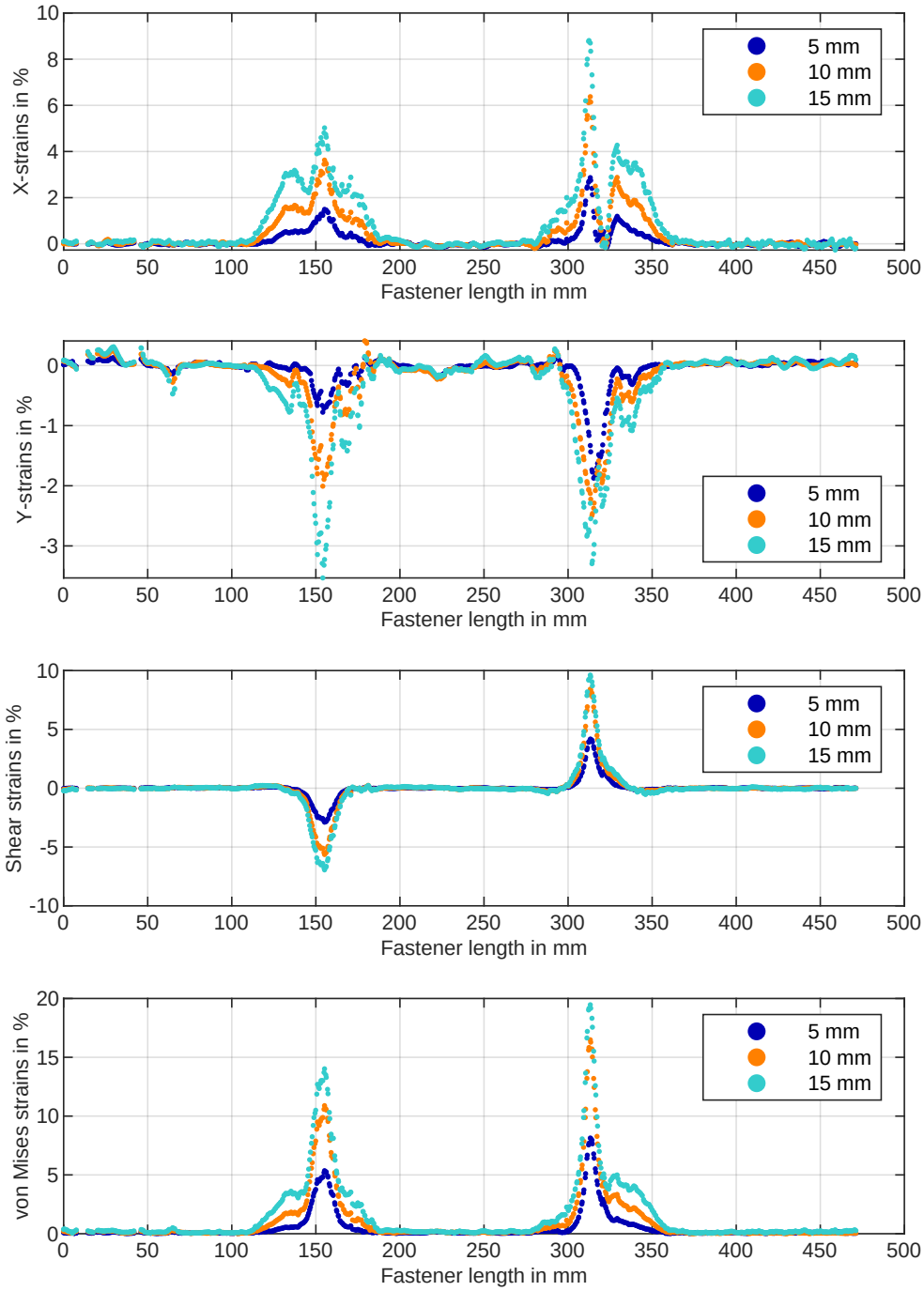

Fig. A.63: DVW_Steel_mk strain results, front side. Strain gauge at 320 mm.

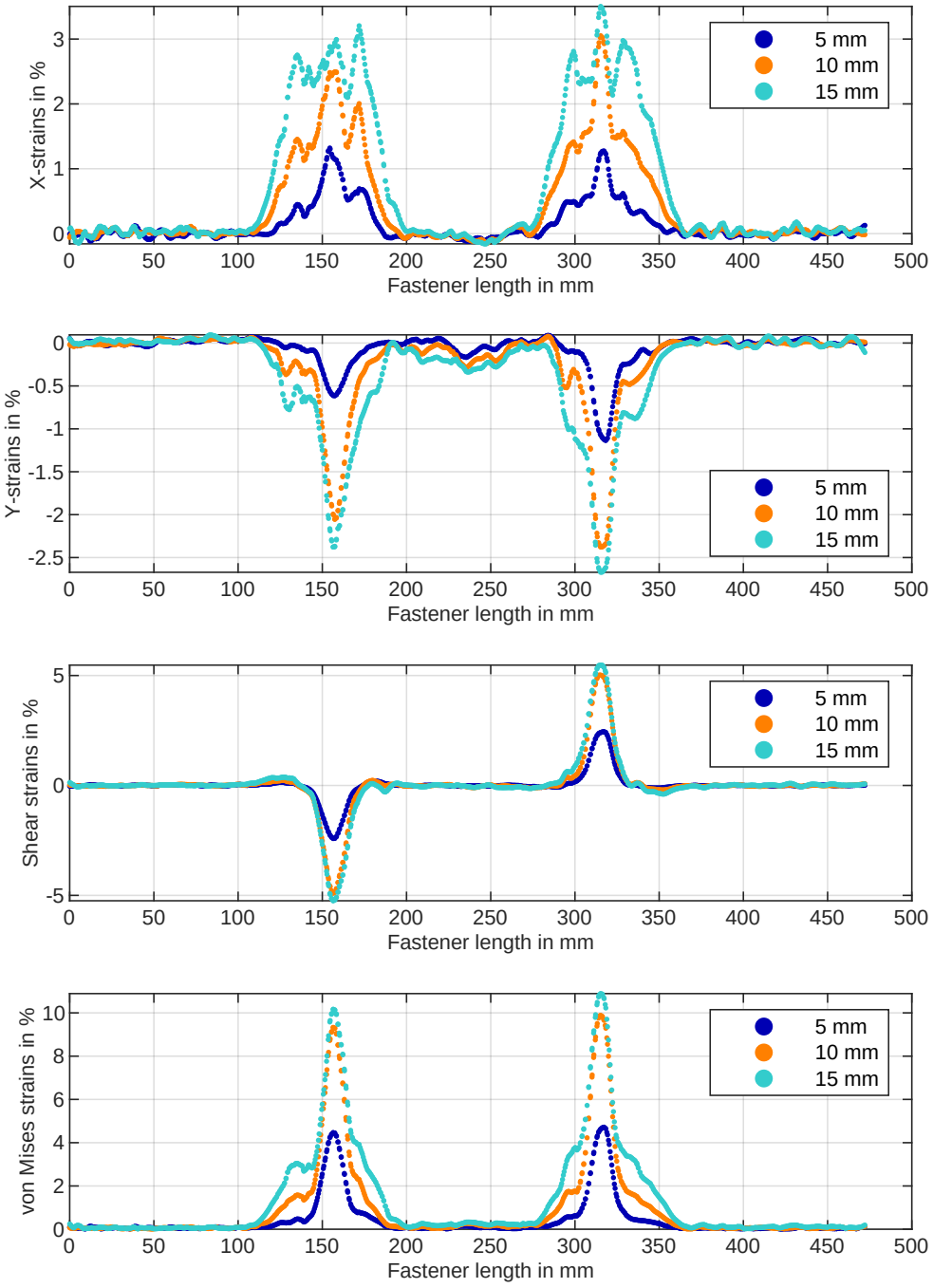

Fig. A.64: DVW_Steel_mk strain results, rear side.

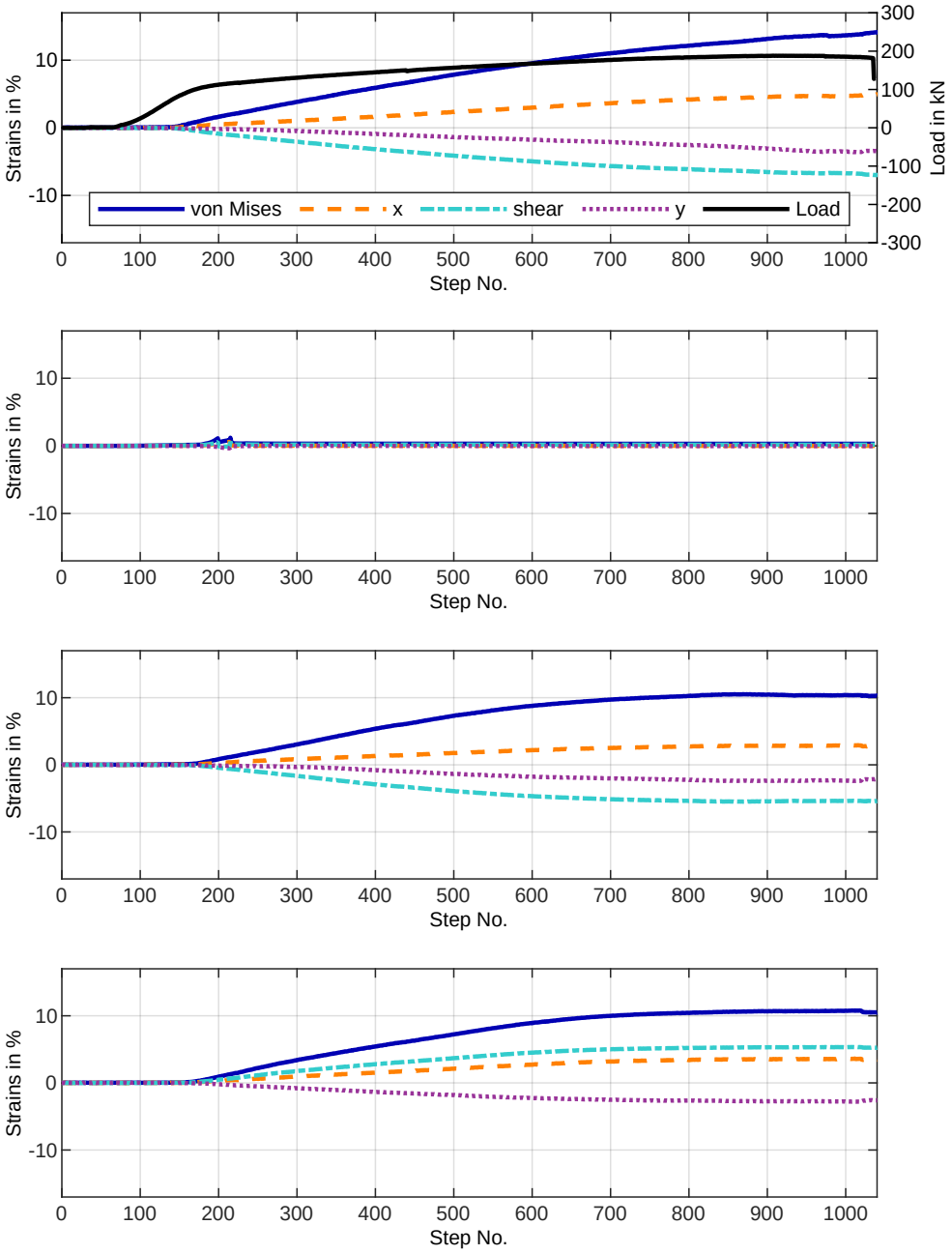

Fig. A.65: DVW_Steel_mk strain results of DIC or strain gauge in shear planes.

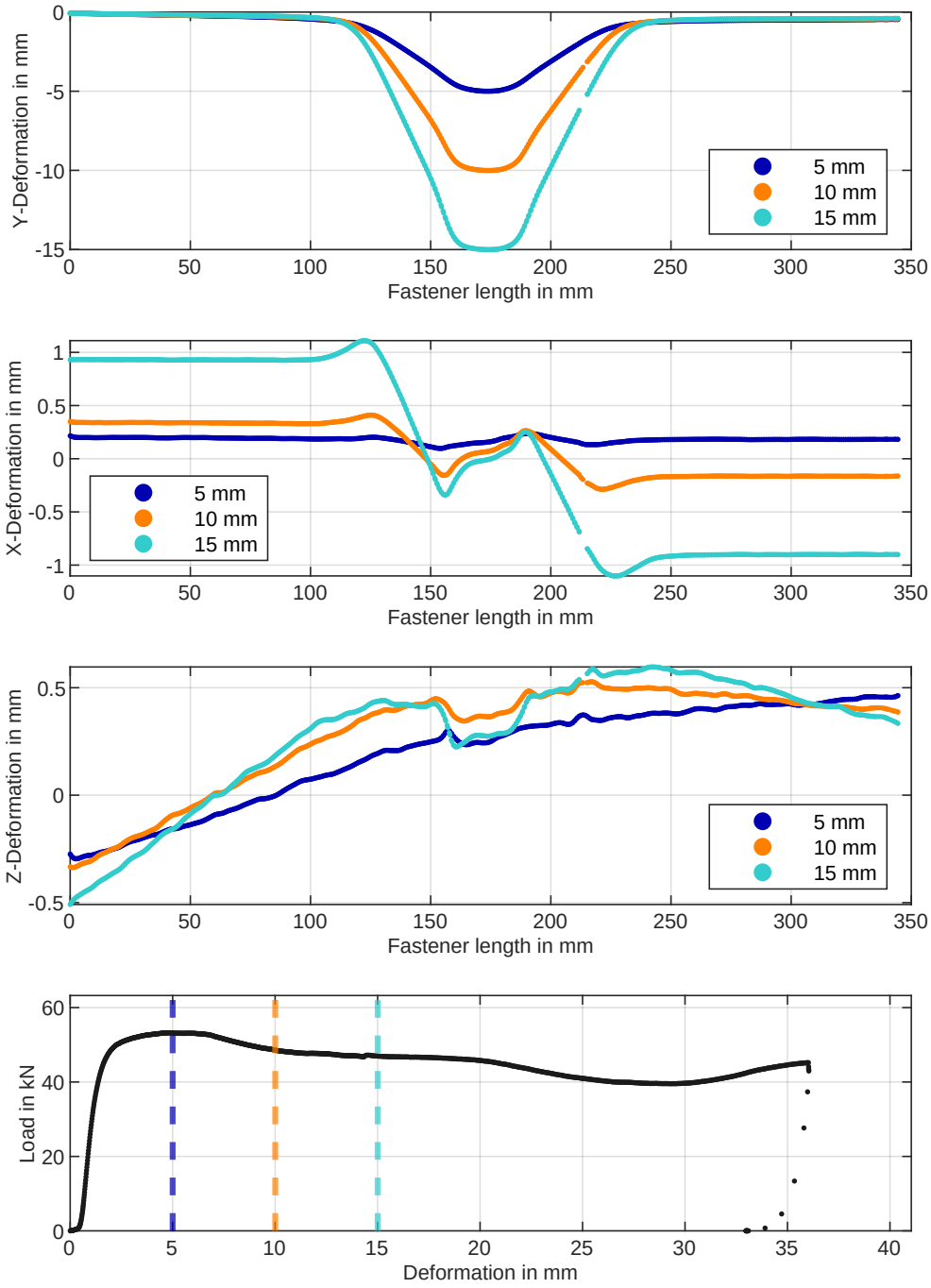

Fig. A.66: S_Spruce_Alu deformation results, front side.

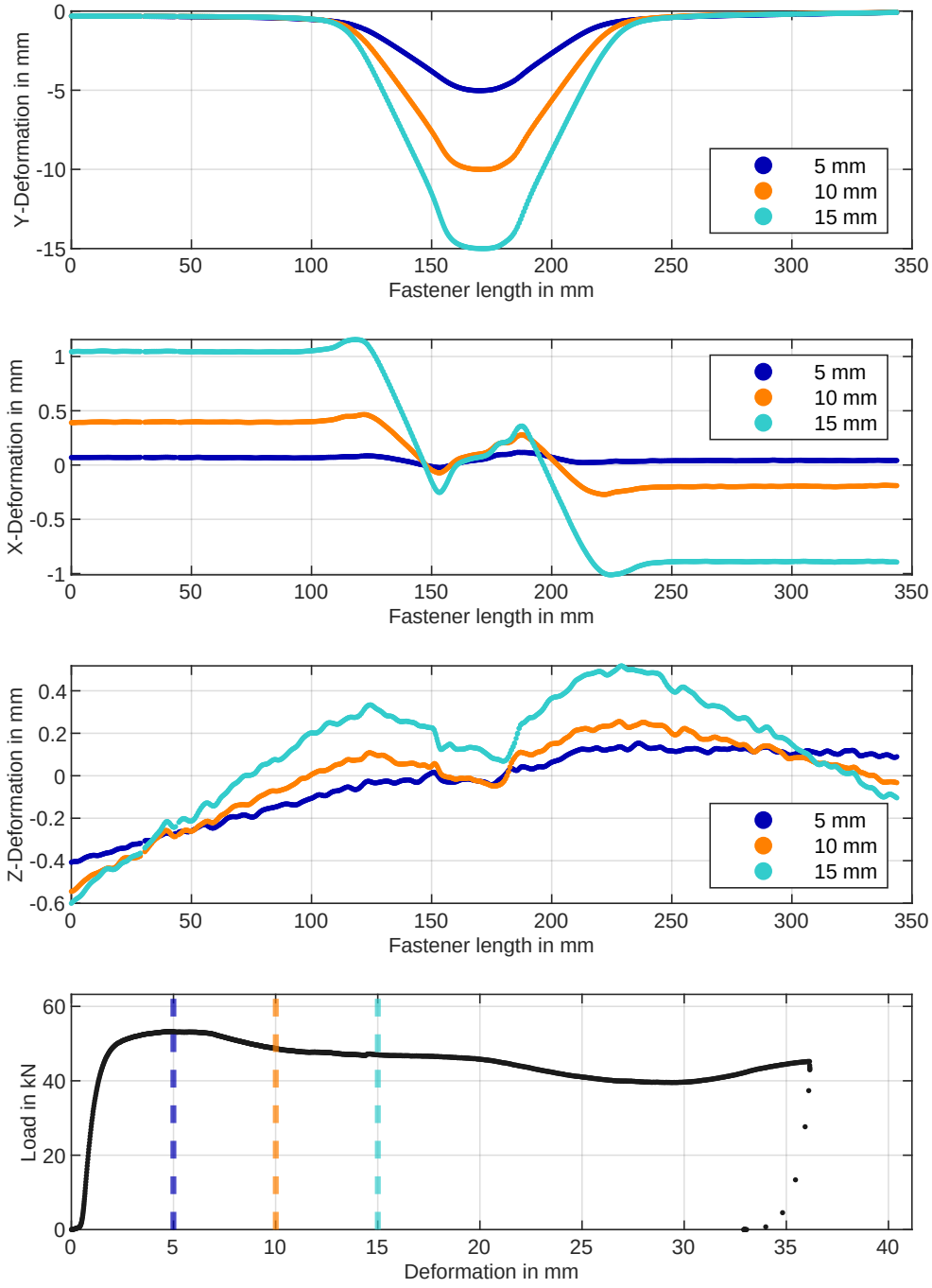

Fig. A.67: S_Spruce_Alu deformation results, rear side.

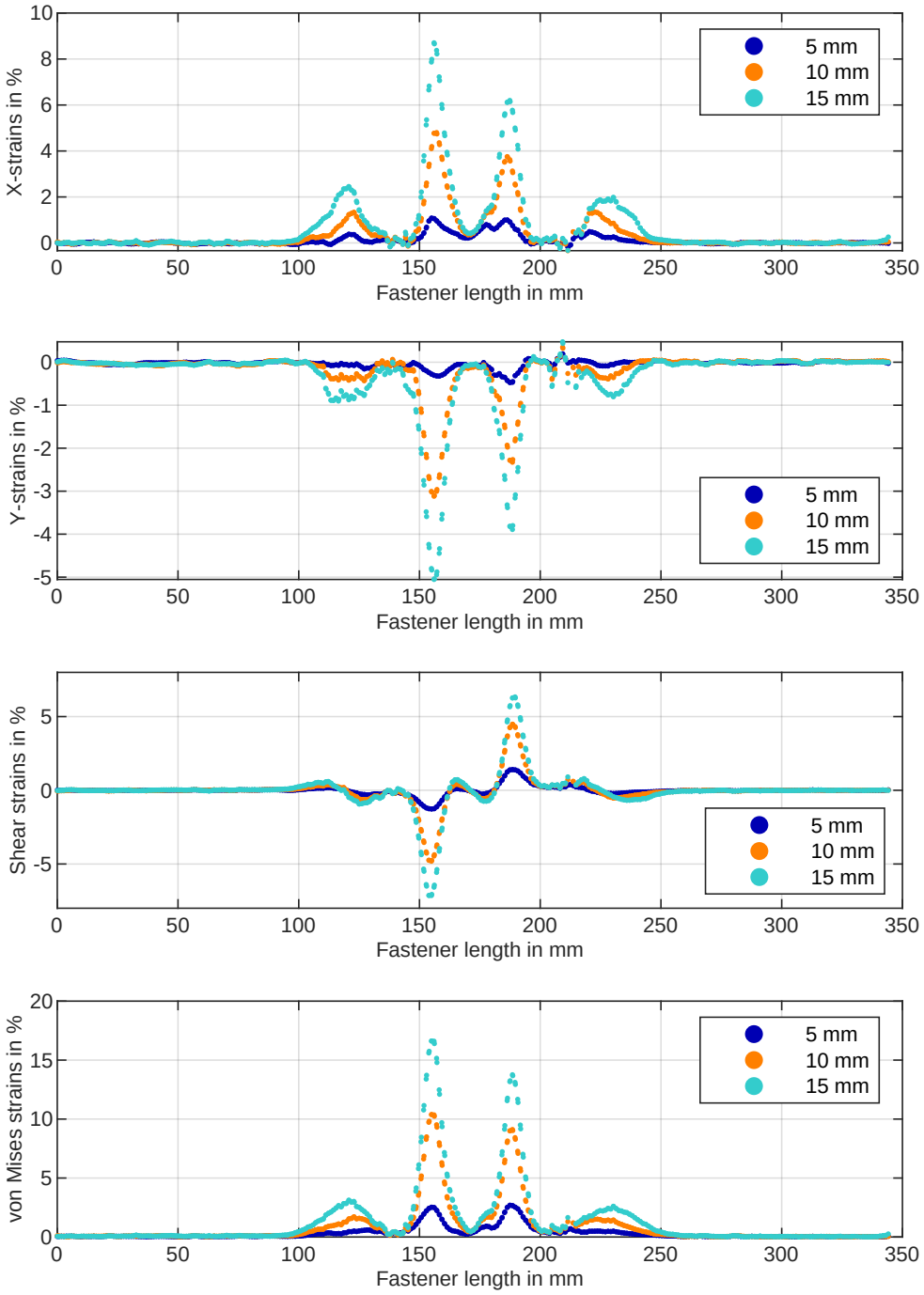

Fig. A.68: S_Spruce_Alu strain results, front side.

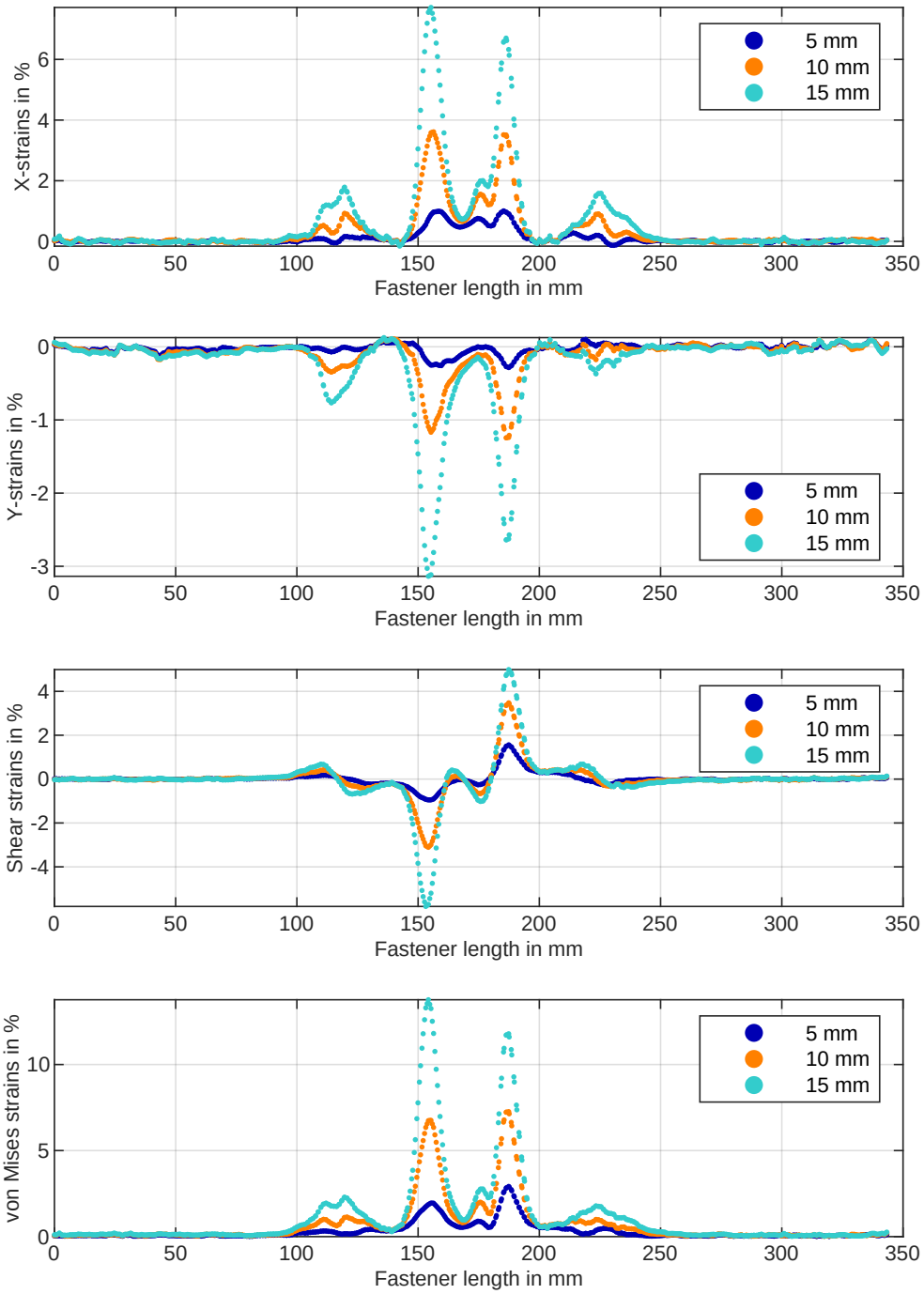

Fig. A.69: S_Spruce_Alu strain results, rear side.

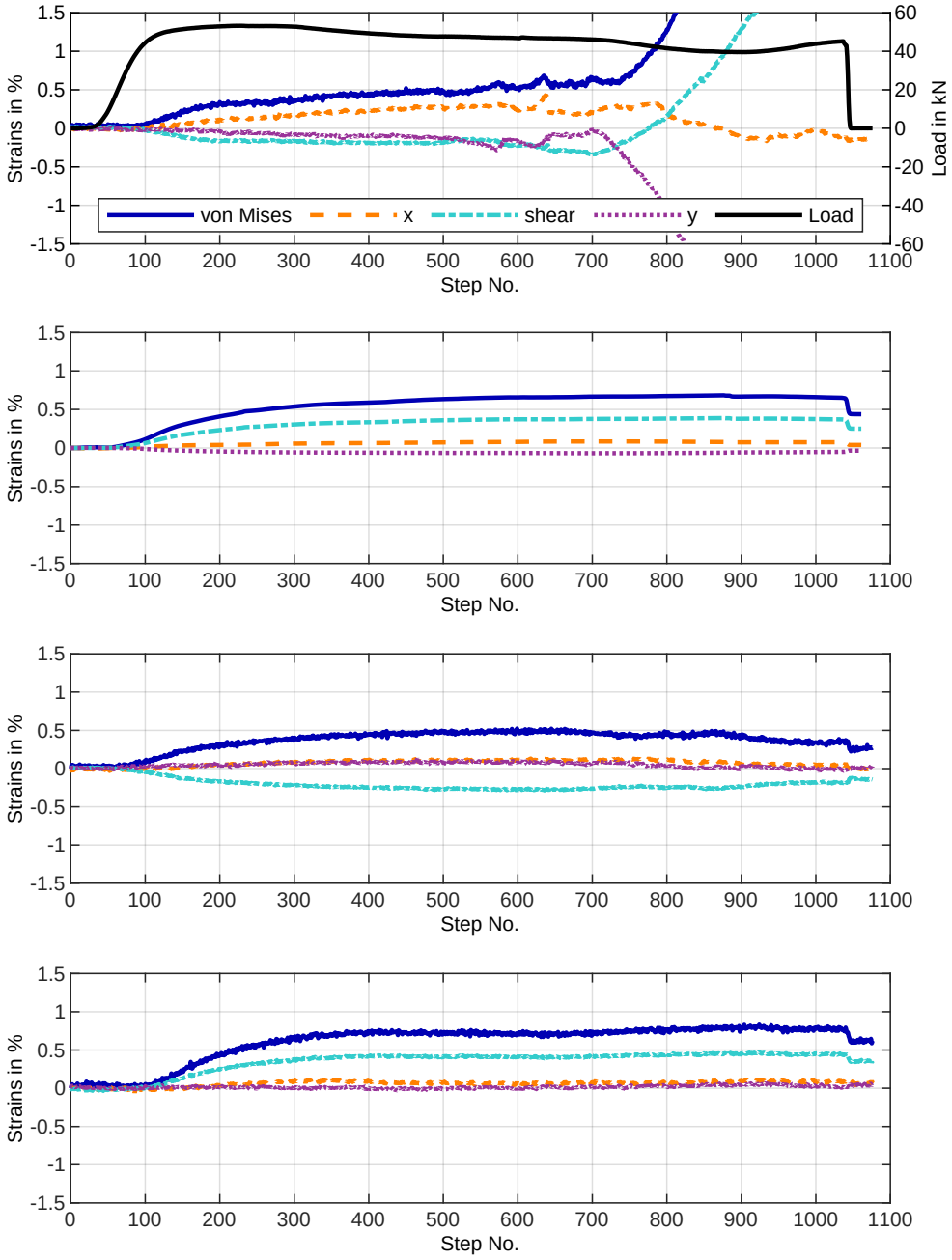

Fig. A.70: S_Spruce_Alu strain results of DIC or strain gauge in distance *a* to shear planes.

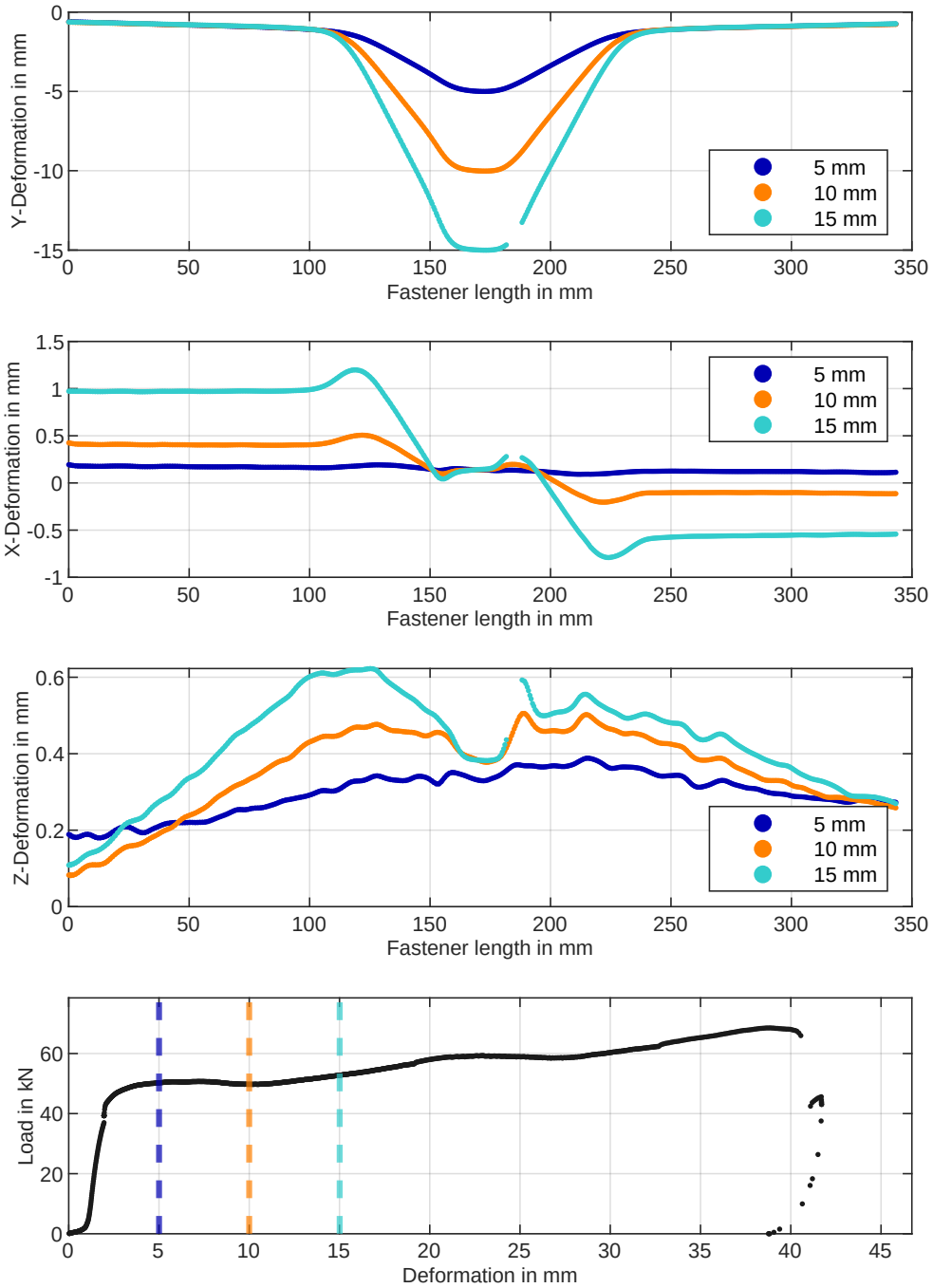

Fig. A.71: S_Spruce_Alu_mk deformation results, front side.

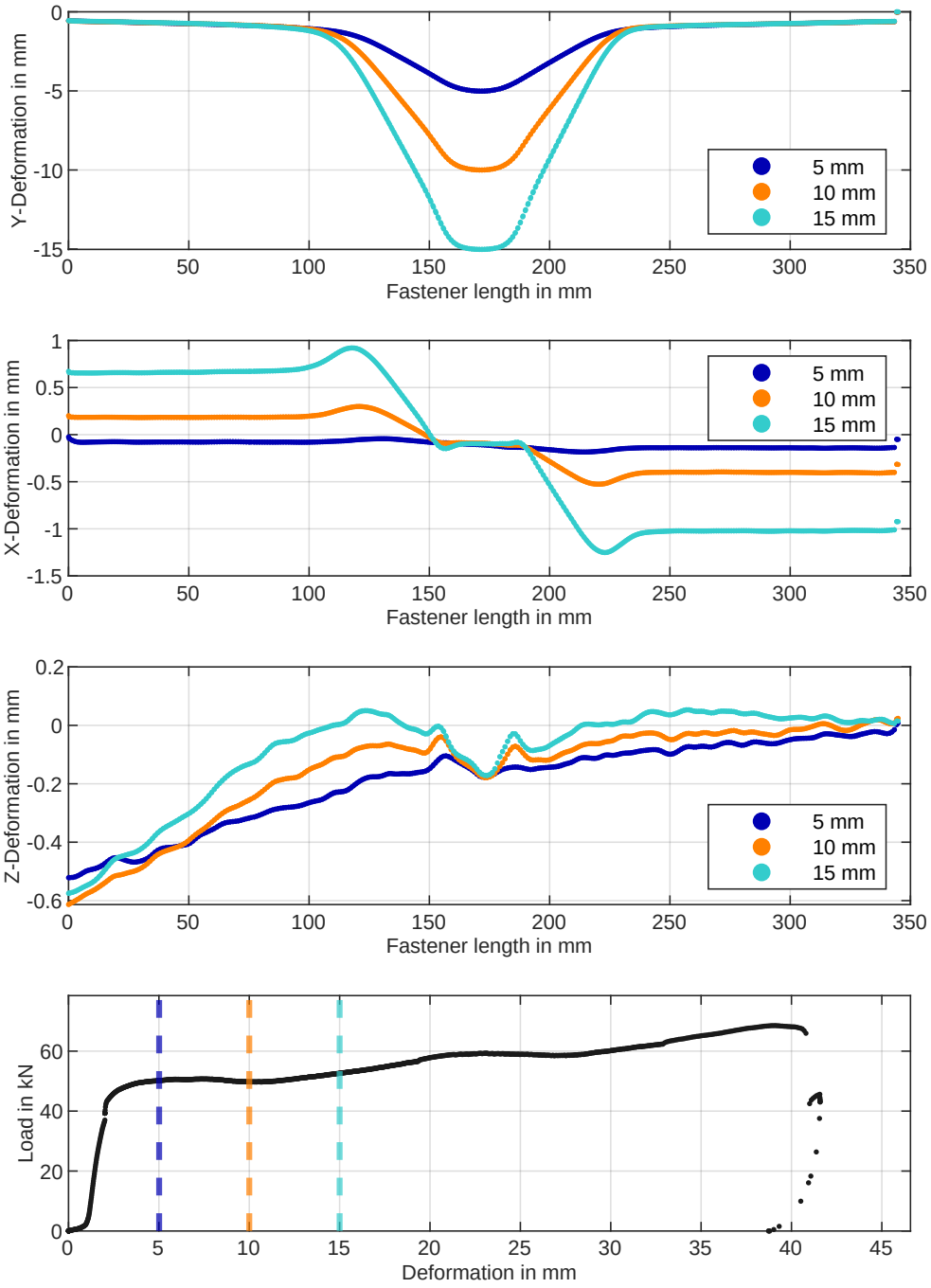

Fig. A.72: S_Spruce_Alu_mk deformation results, rear side.

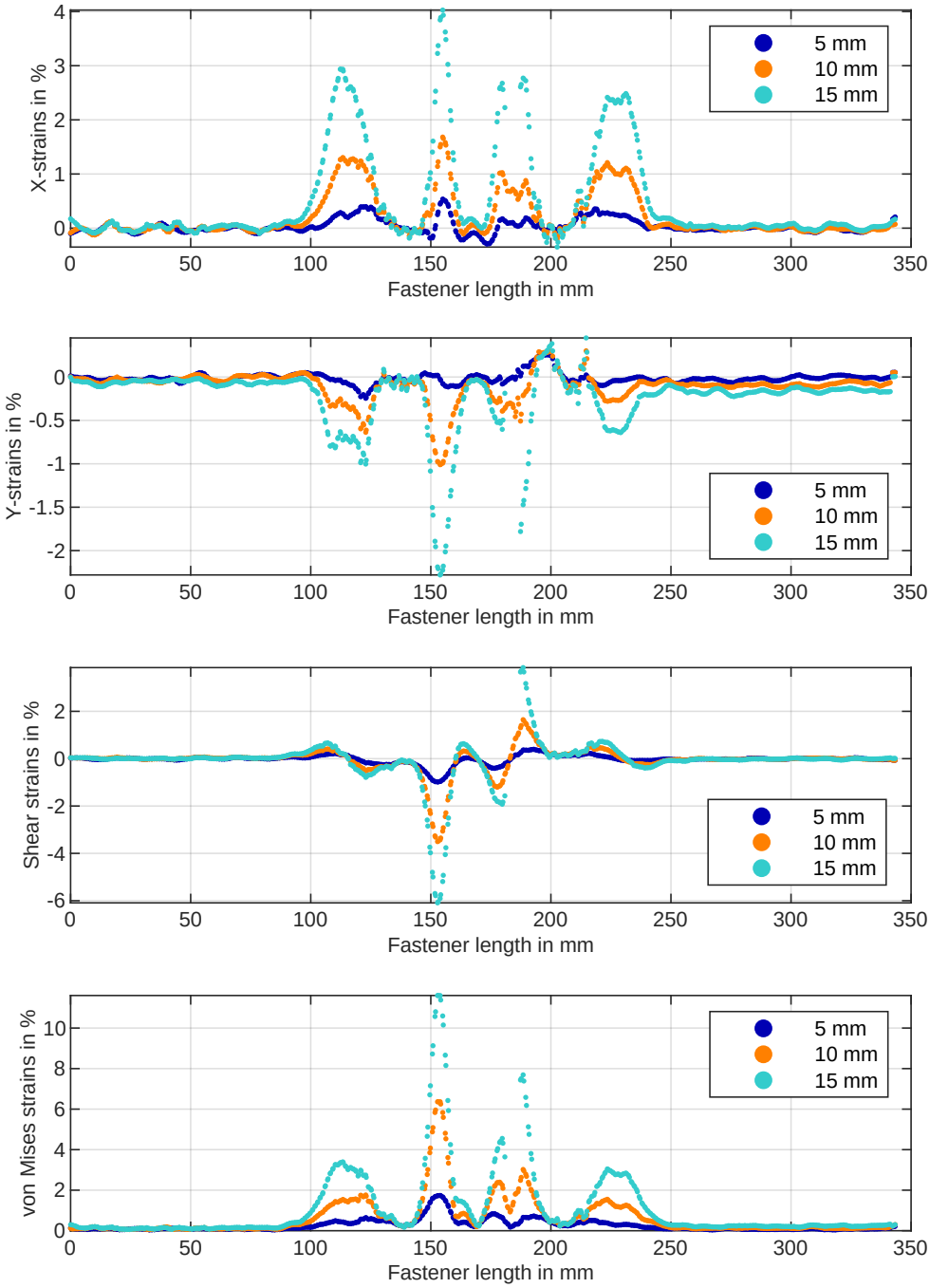

Fig. A.73: S_Spruce_Alu_mk strain results, front side.

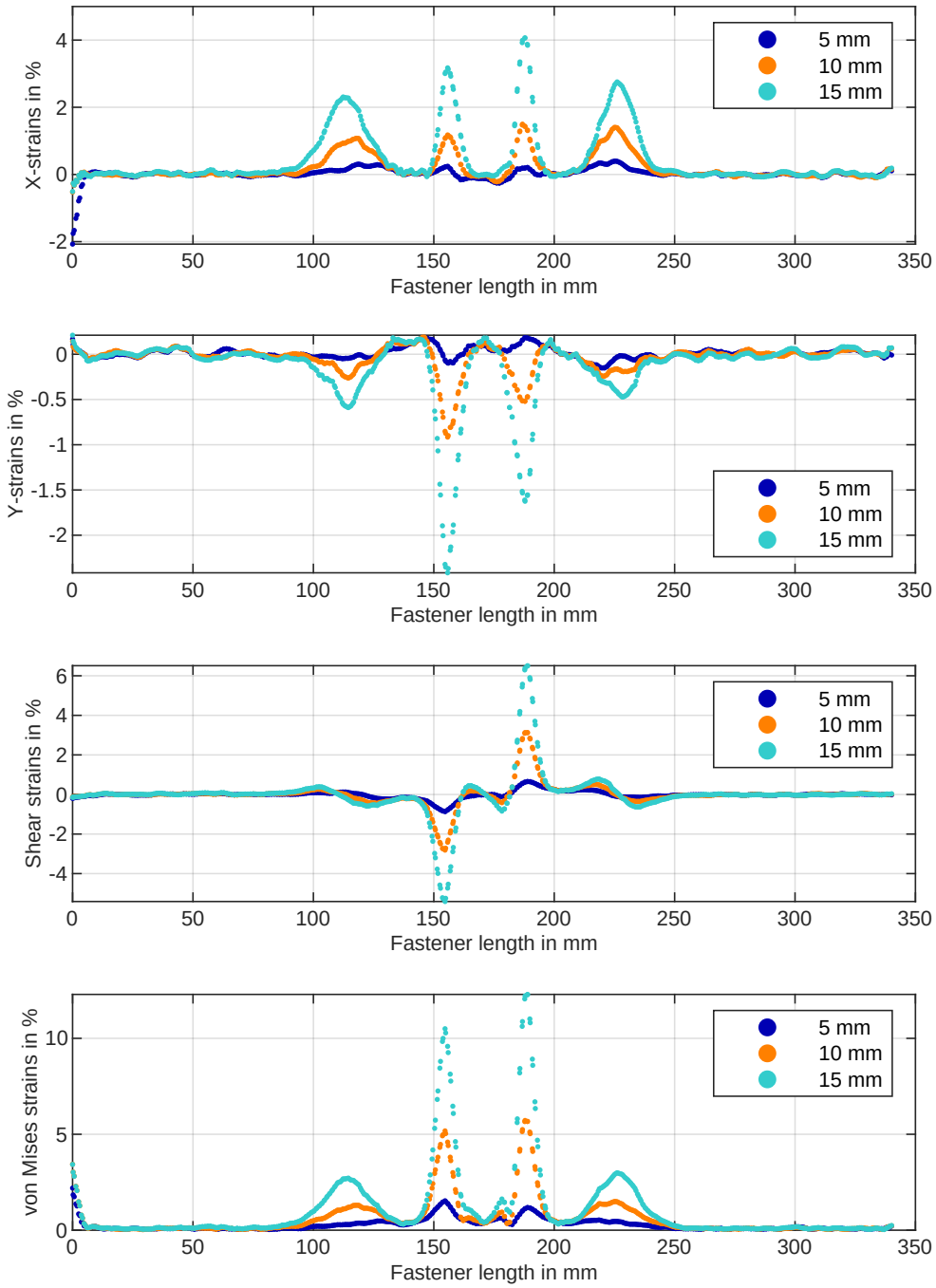

Fig. A.74: S_Spruce_Alu_mk strain results, rear side.

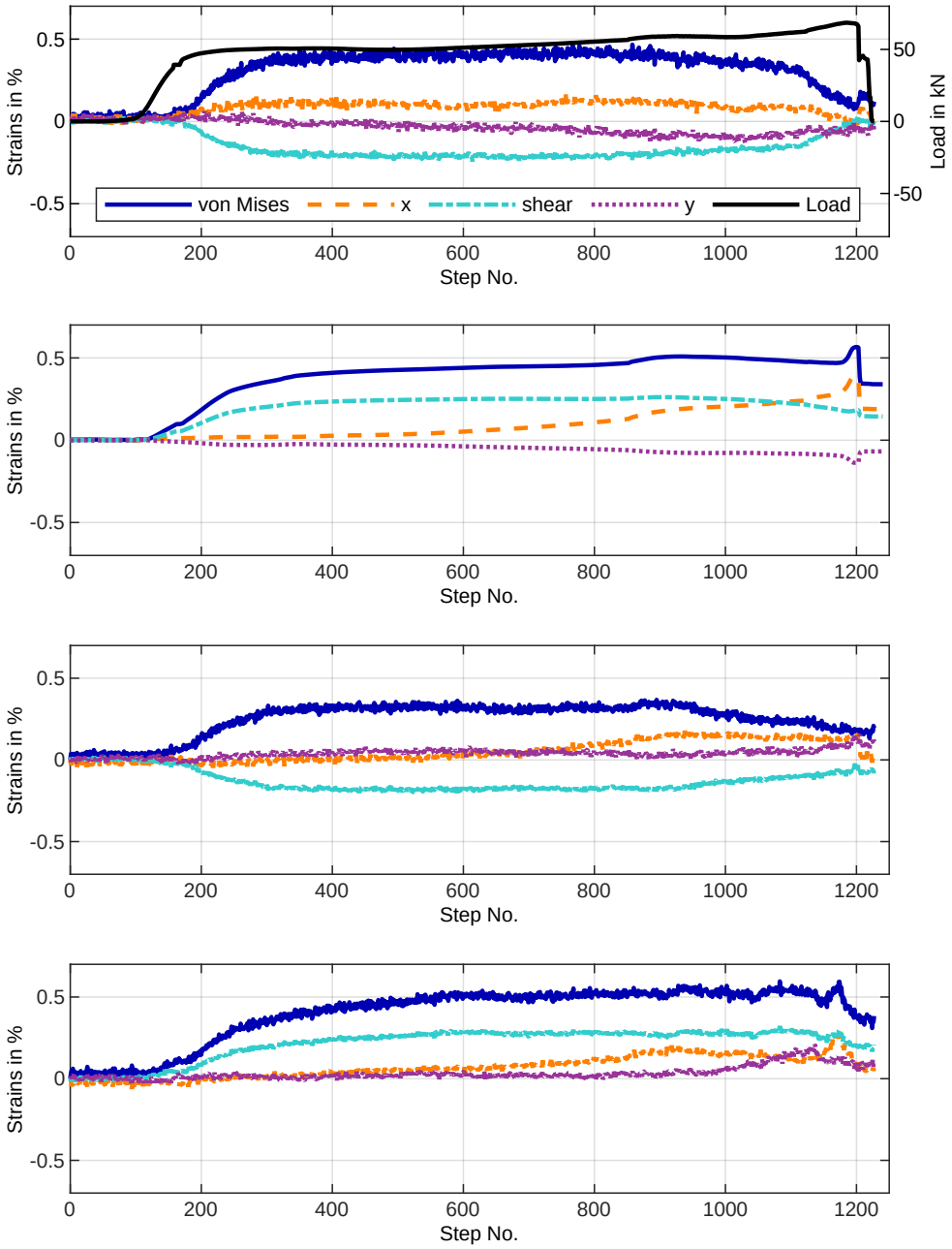

Fig. A.75: S_Spruce_Alu_mk strain results of DIC or strain gauge in distance *a* to shear planes.

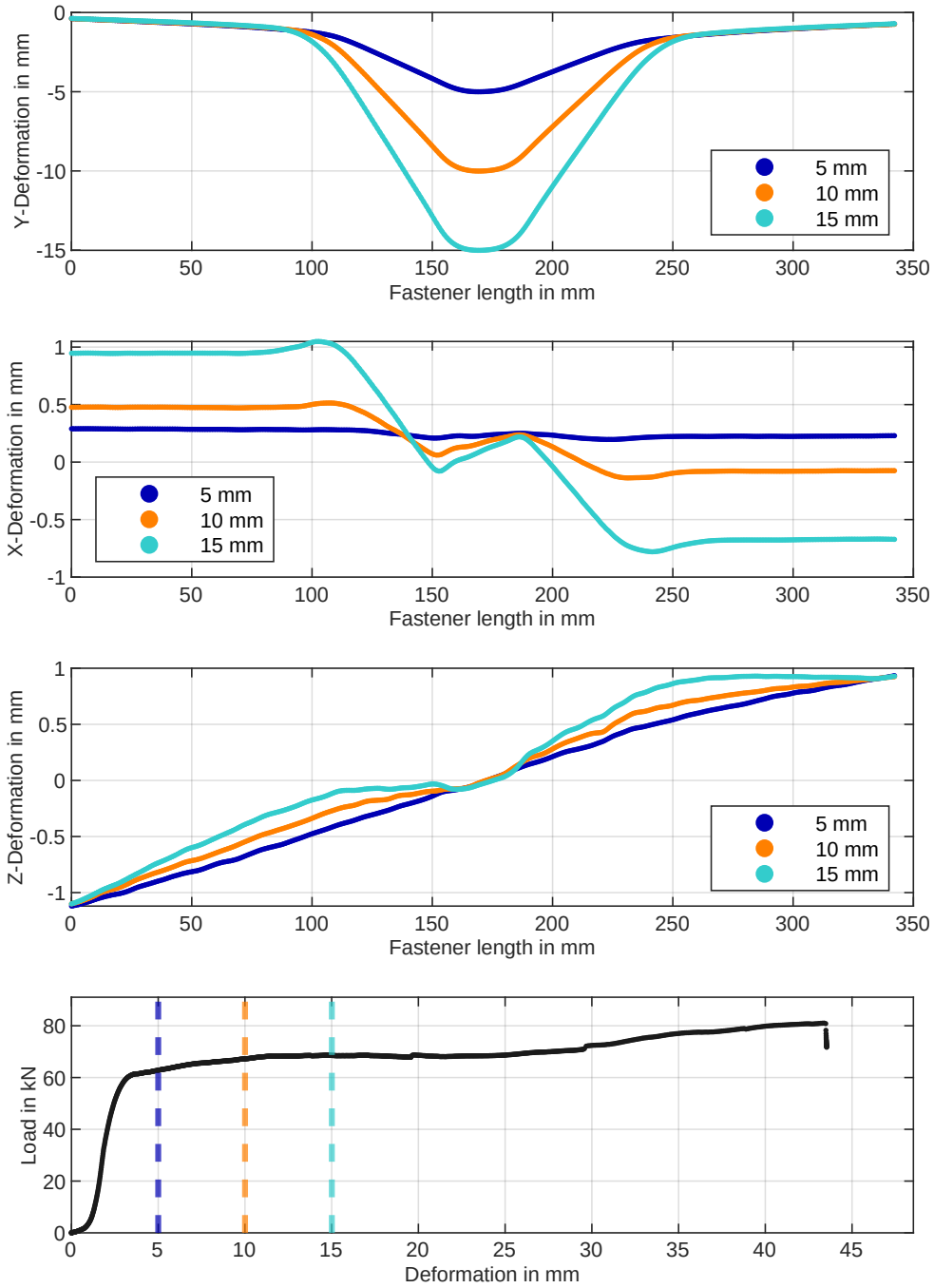

Fig. A.76: S_Spruce_Steel deformation results, front side.

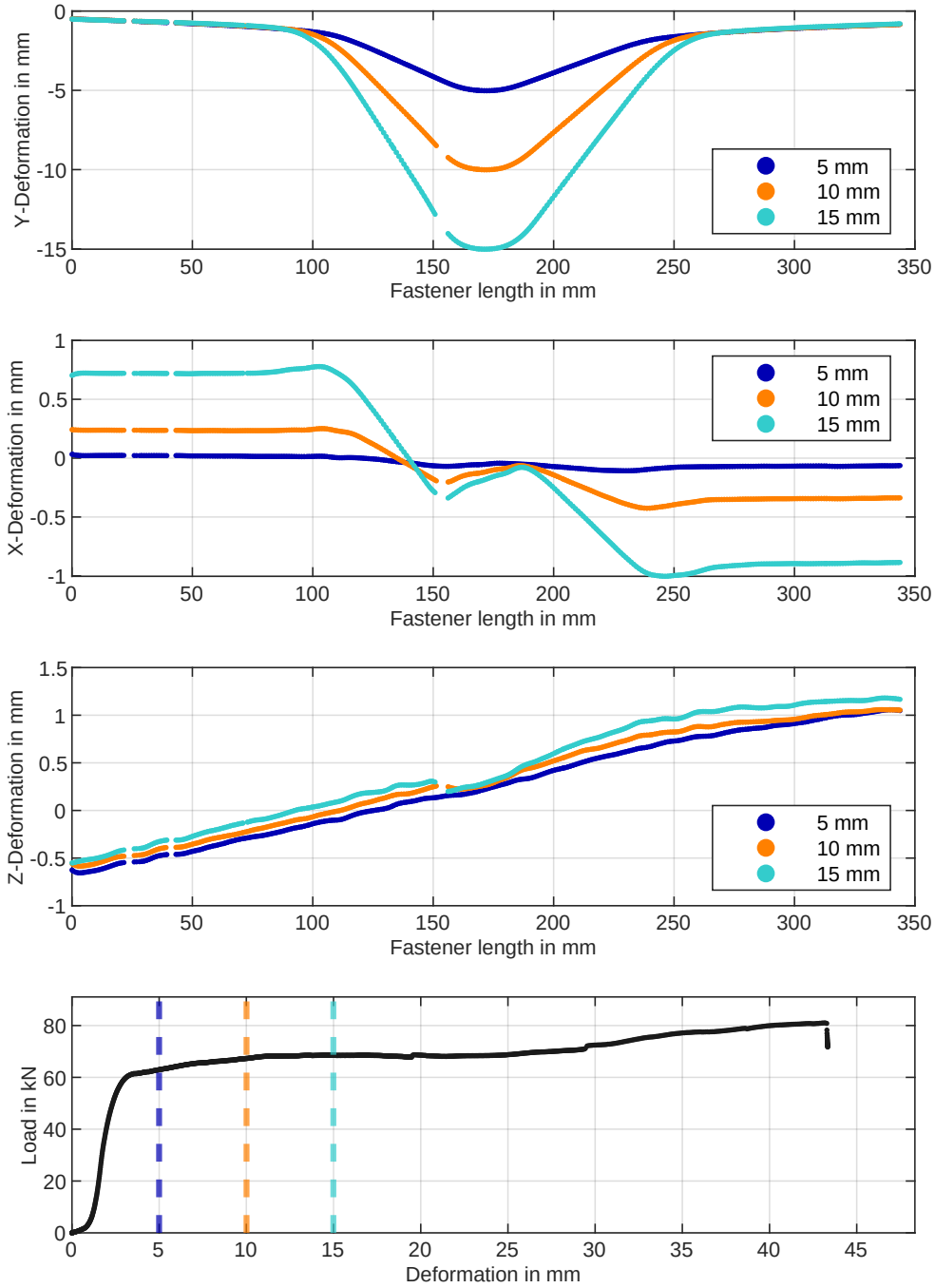

Fig. A.77: S_Spruce_Steel deformation results, rear side.

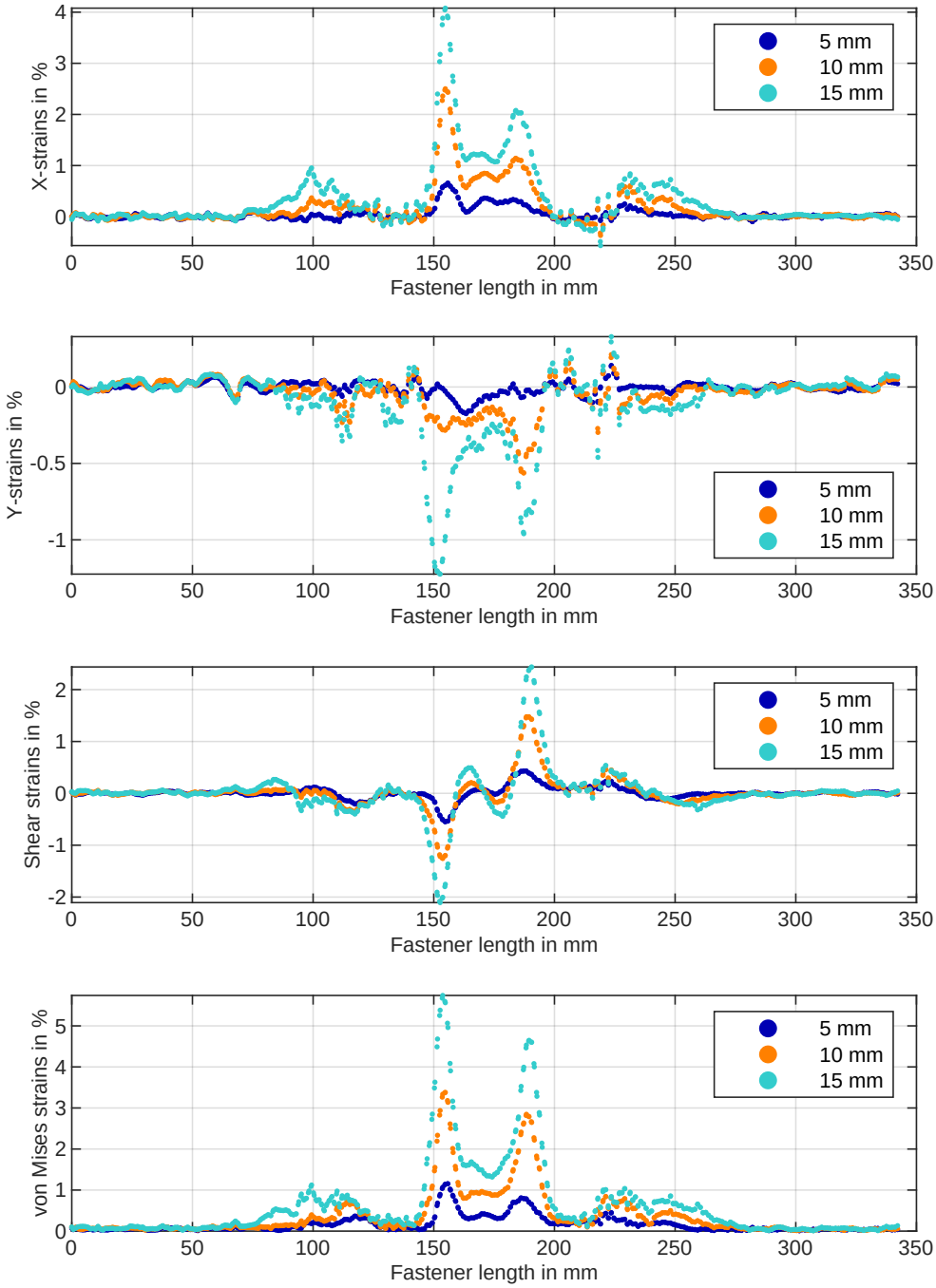

Fig. A.78: S_Spruce_Steel strain results, front side.

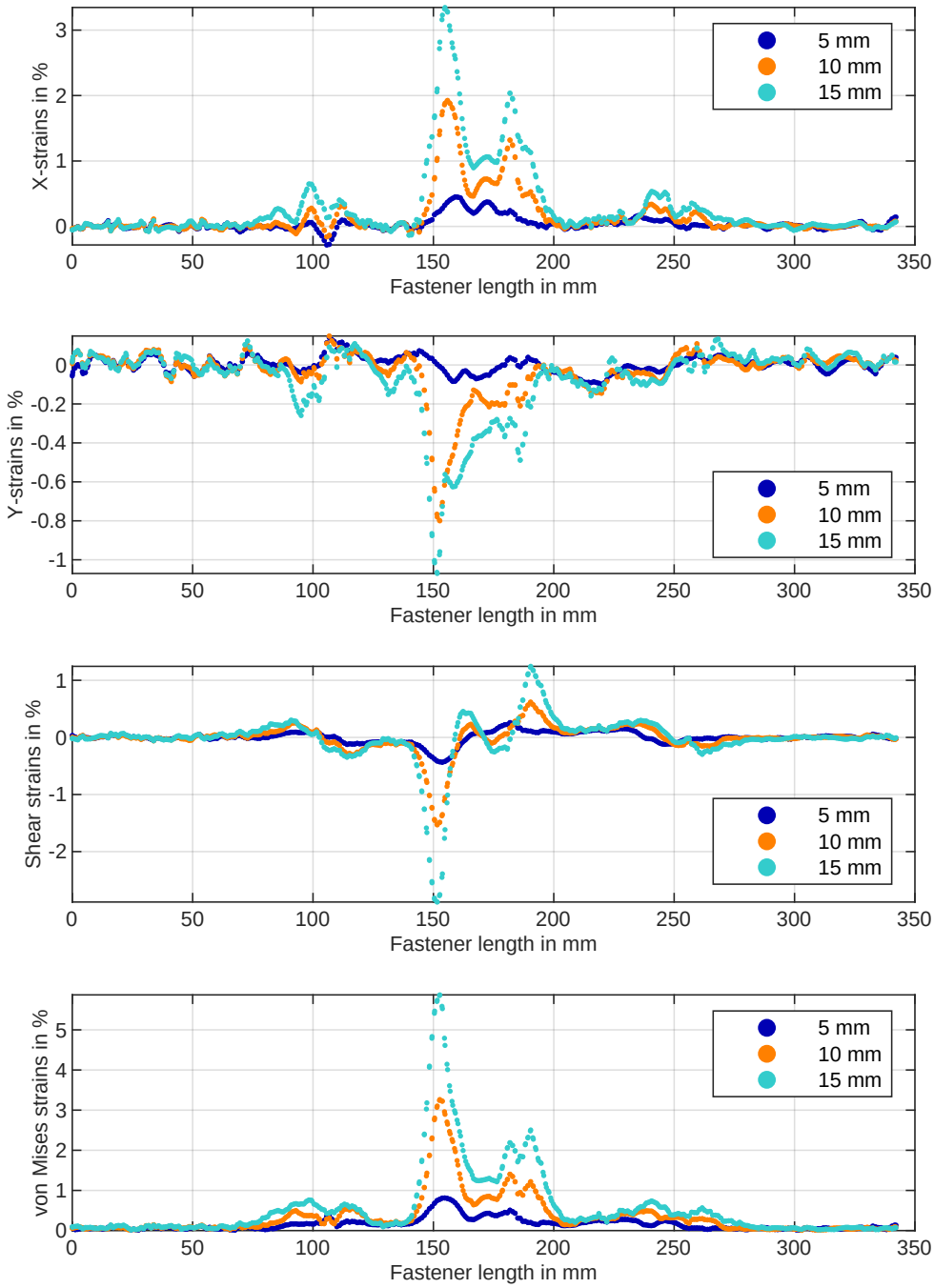

Fig. A.79: S_Spruce_Steel strain results, rear side.

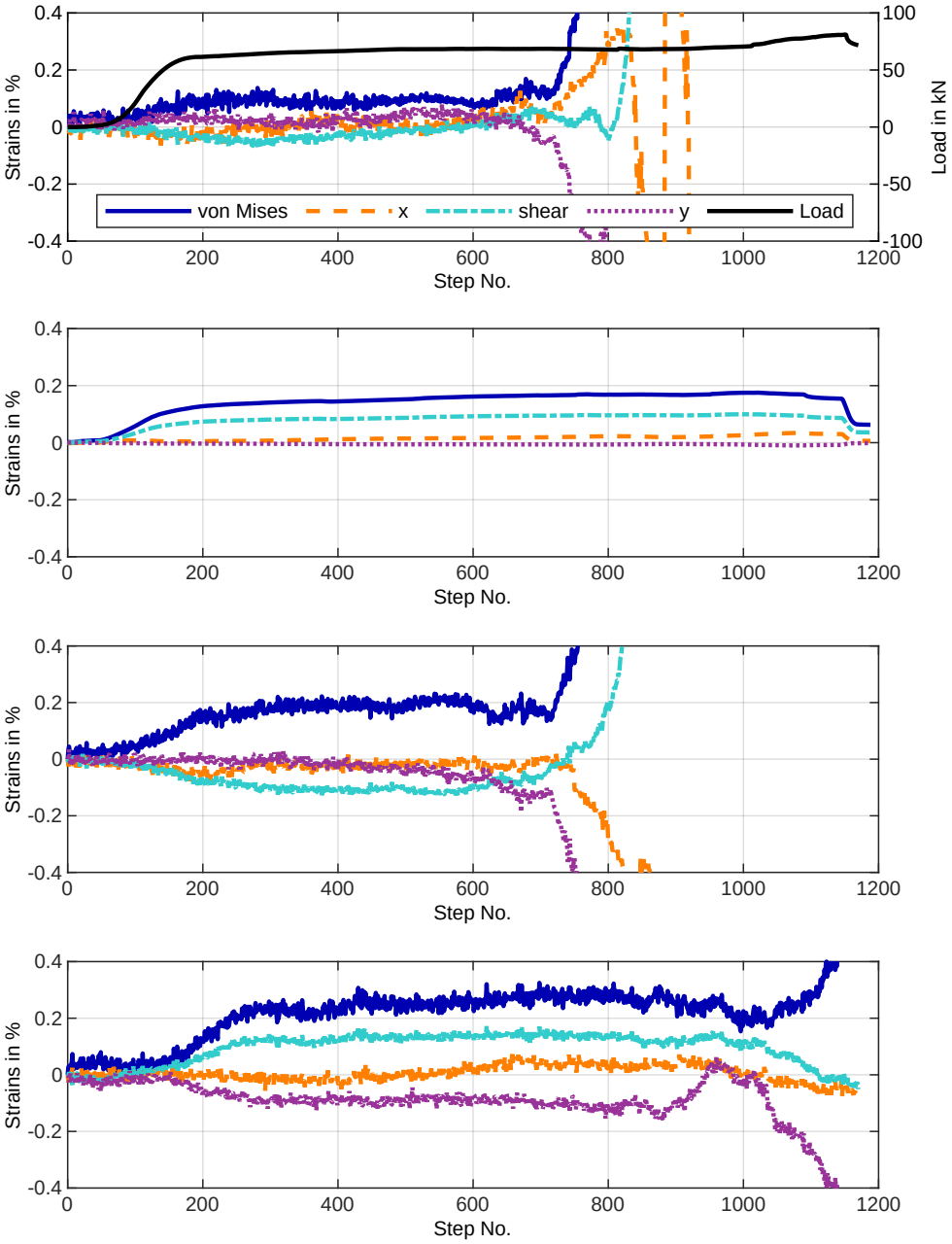

Fig. A.80: S_Spruce_Steel strain results of DIC or strain gauge in distance *a* to shear planes.

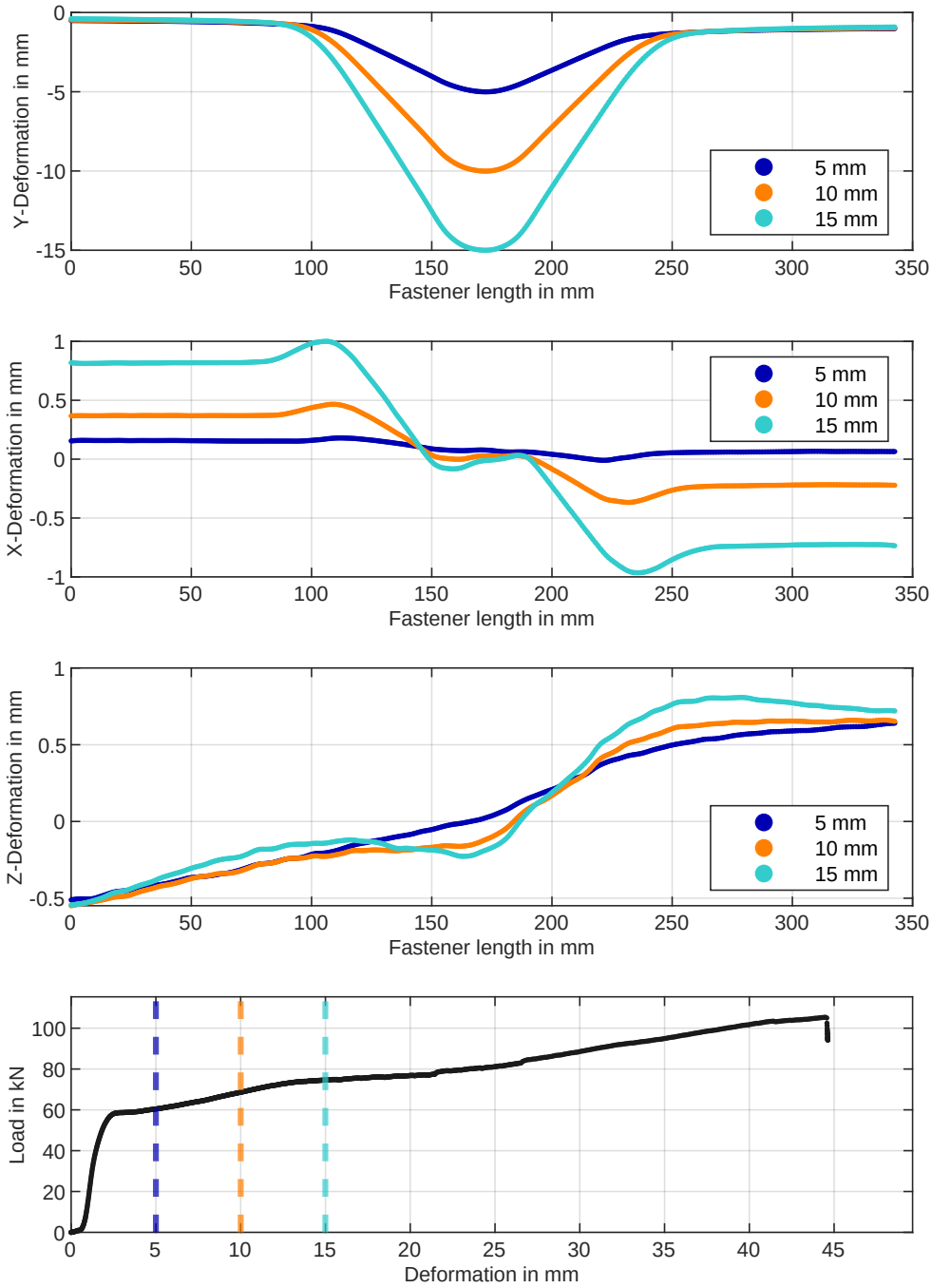

Fig. A.81: S_Spruce_Steel_mk deformation results, front side.

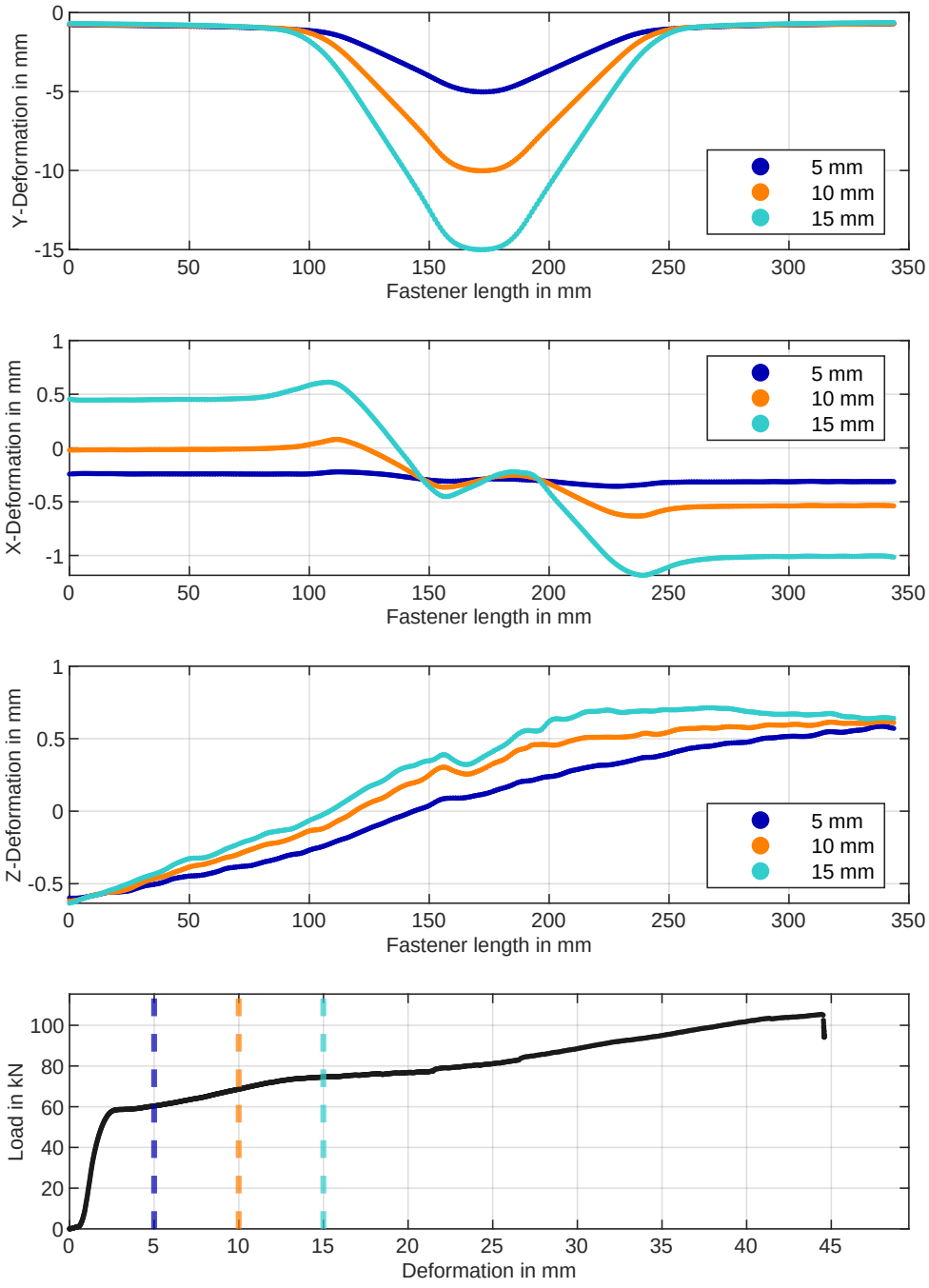

Fig. A.82: S_Spruce_Steel_mk deformation results, rear side.

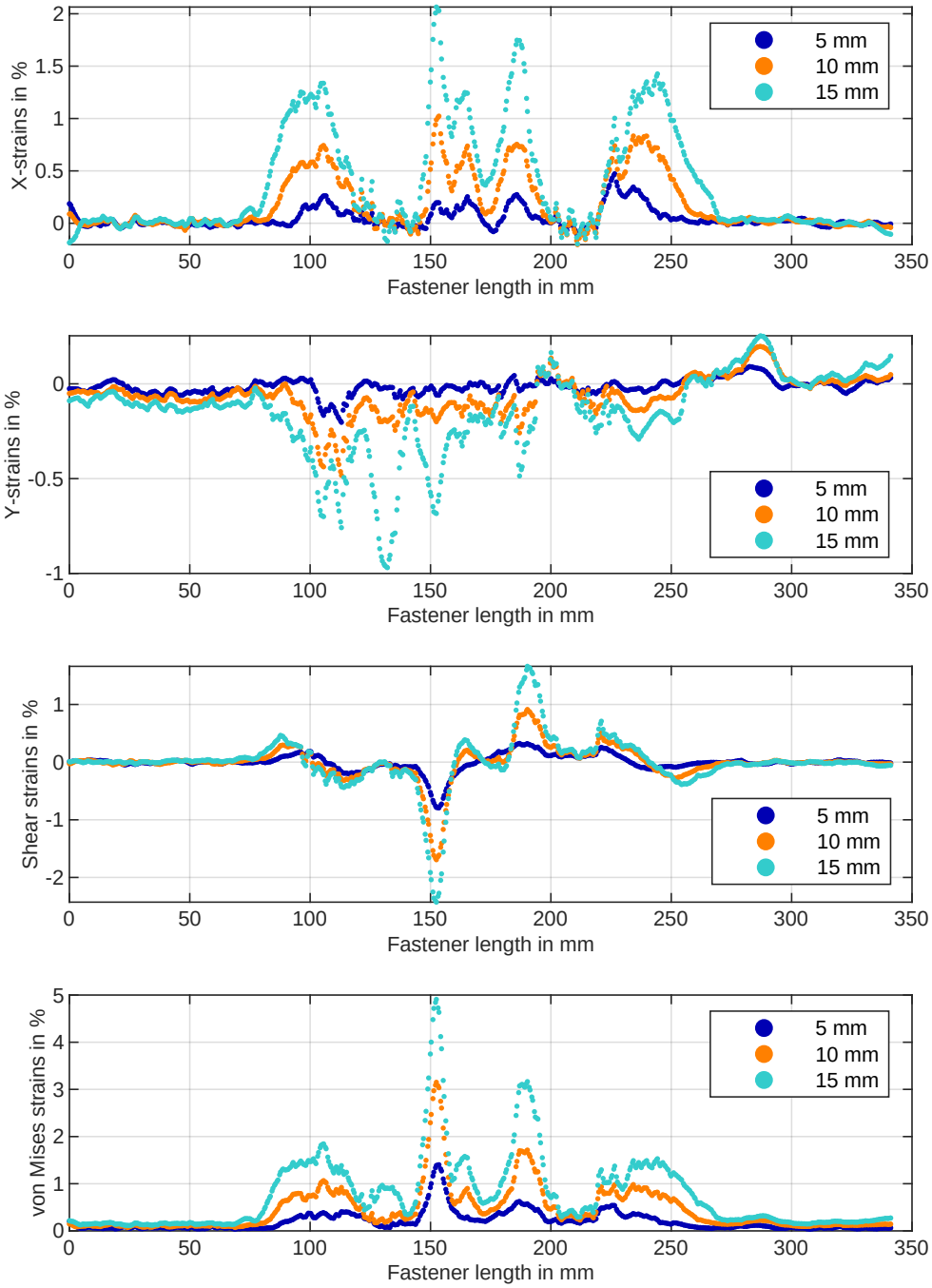

Fig. A.83: S_Spruce_Steel_mk strain results, front side.

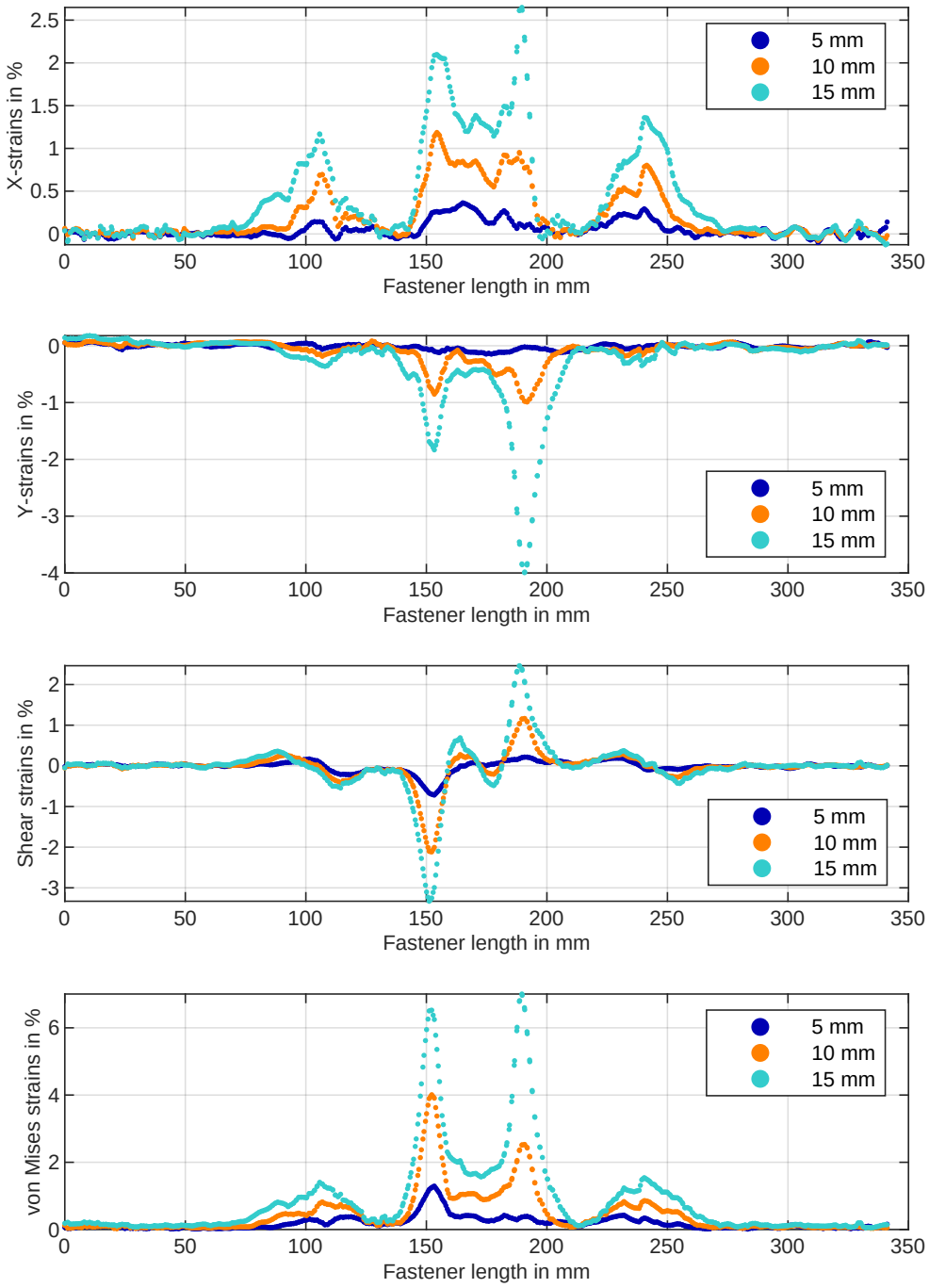

Fig. A.84: S_Spruce_Steel_mk strain results, rear side.

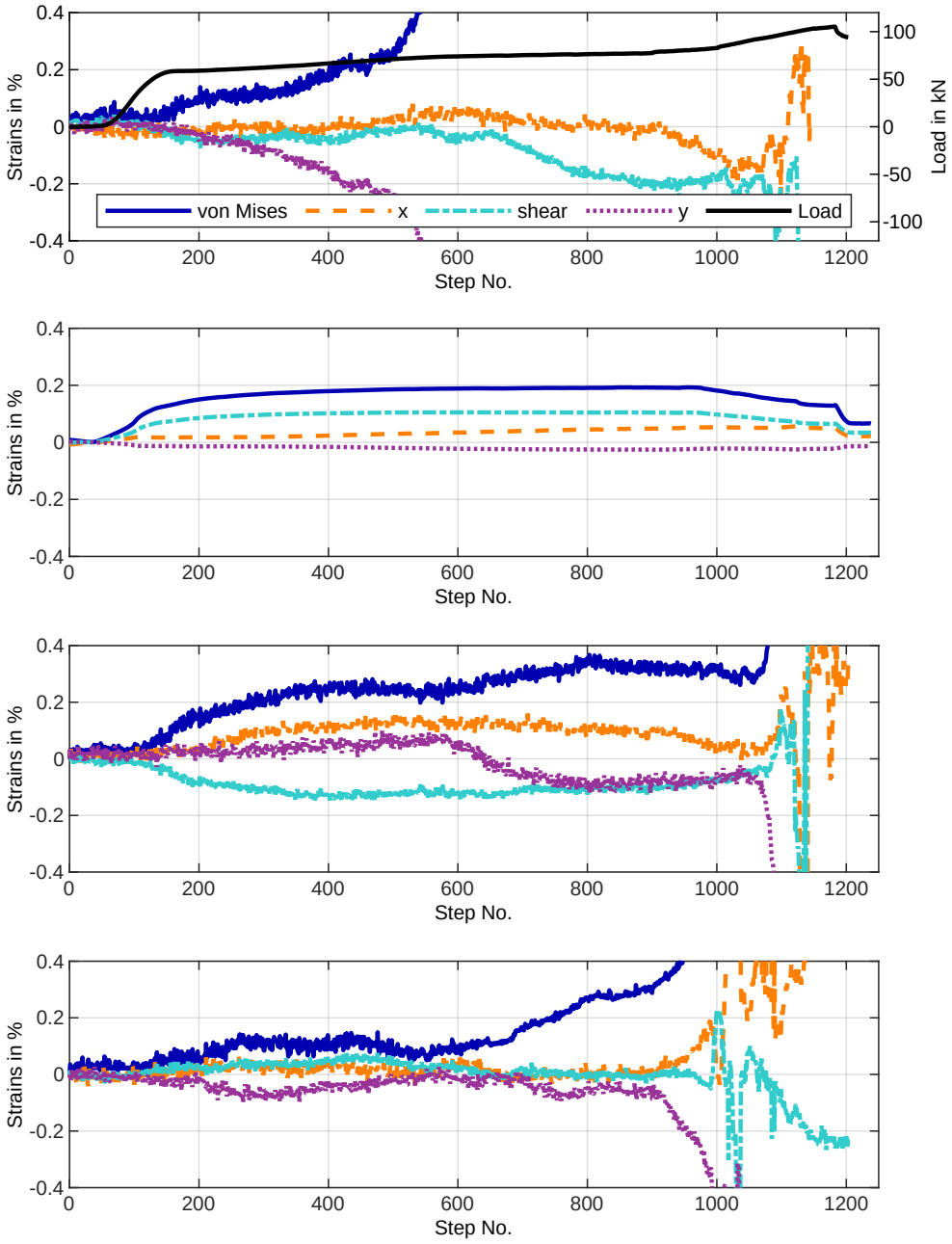

Fig. A.85: S_Spruce_Steel_mk strain results of DIC or strain gauge in distance *a* to shear planes.

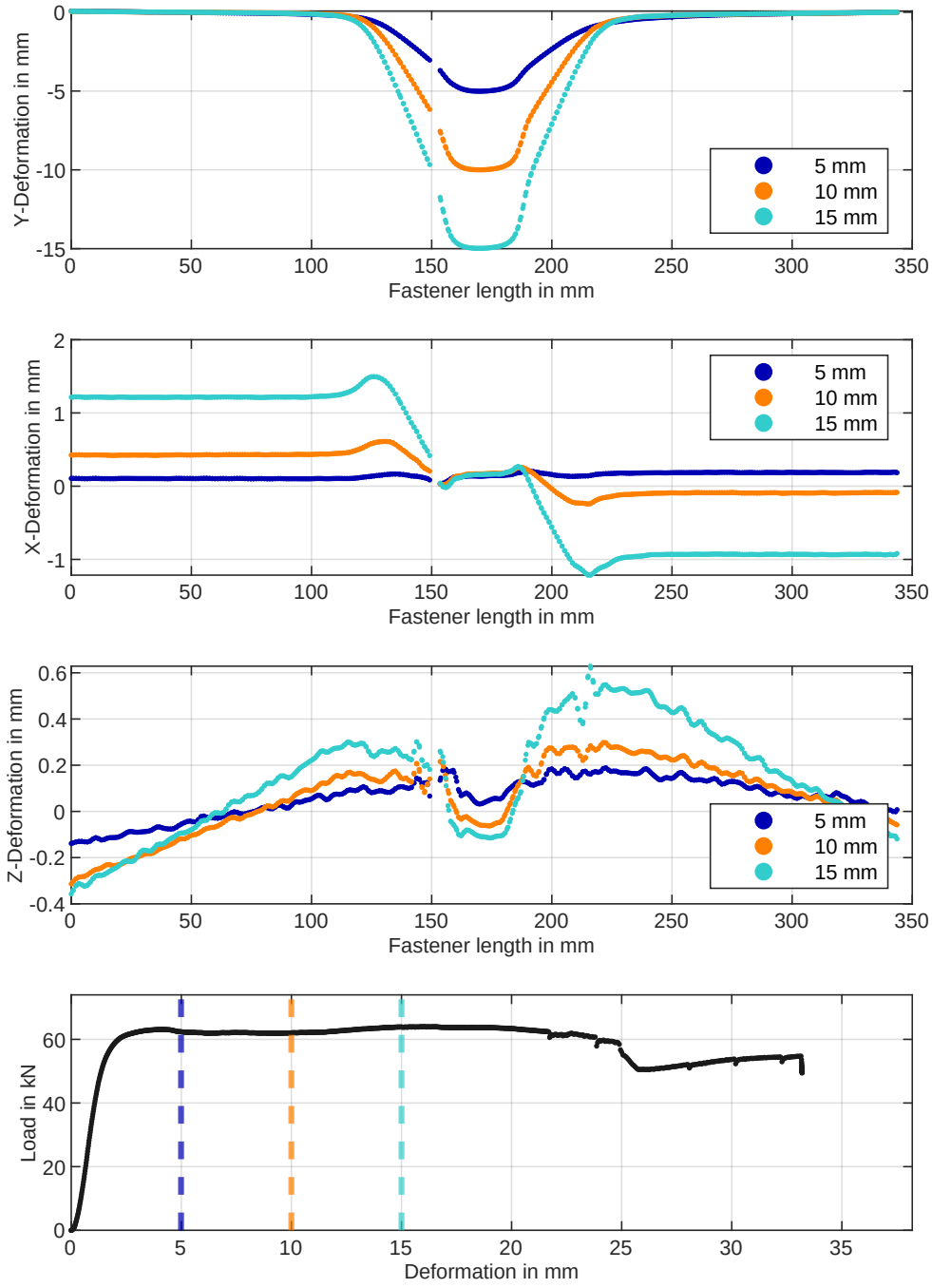

Fig. A.86: S_BB_Alu deformation results, front side.

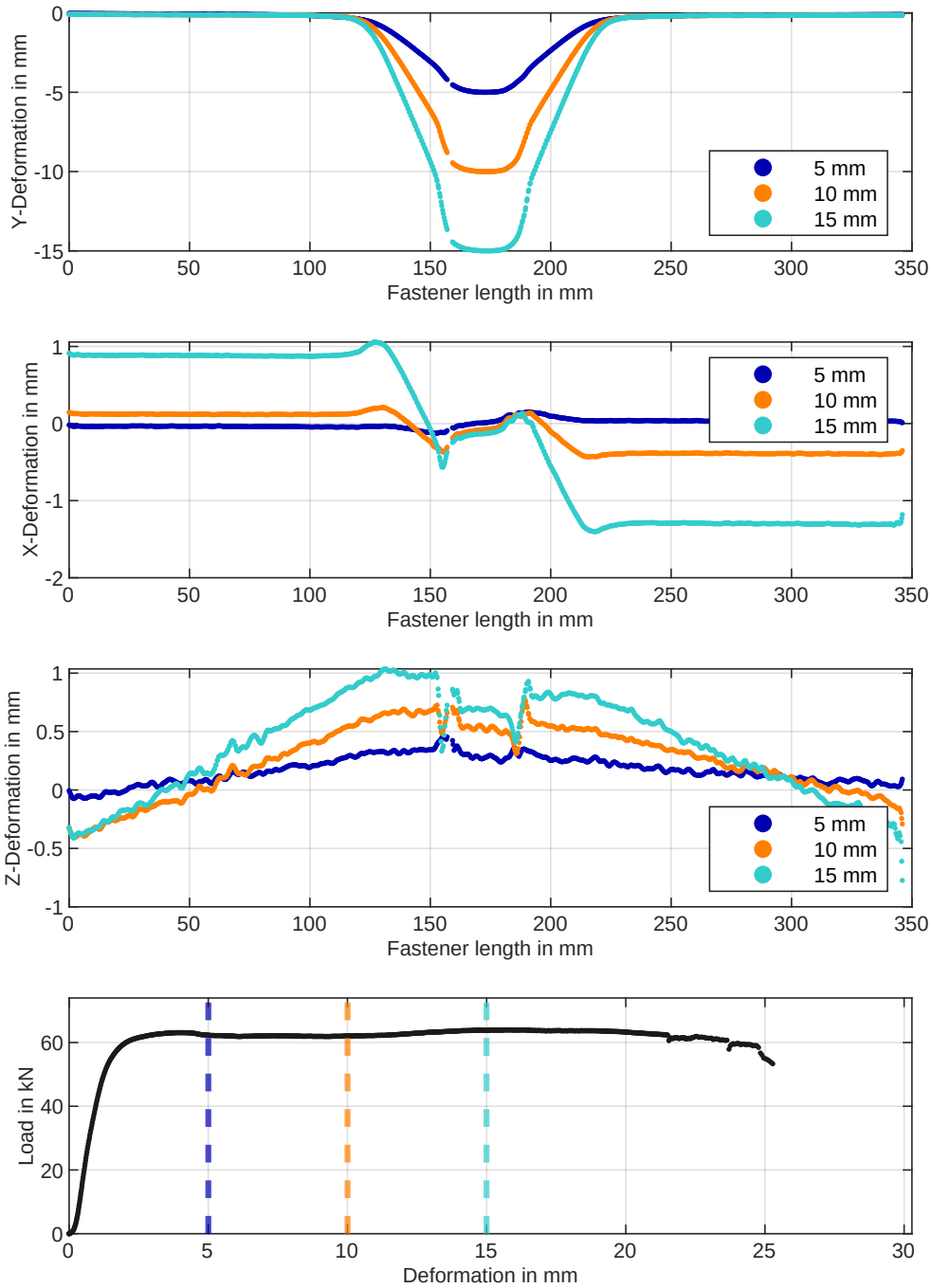

Fig. A.87: S_BB_Alu deformation results, rear side.

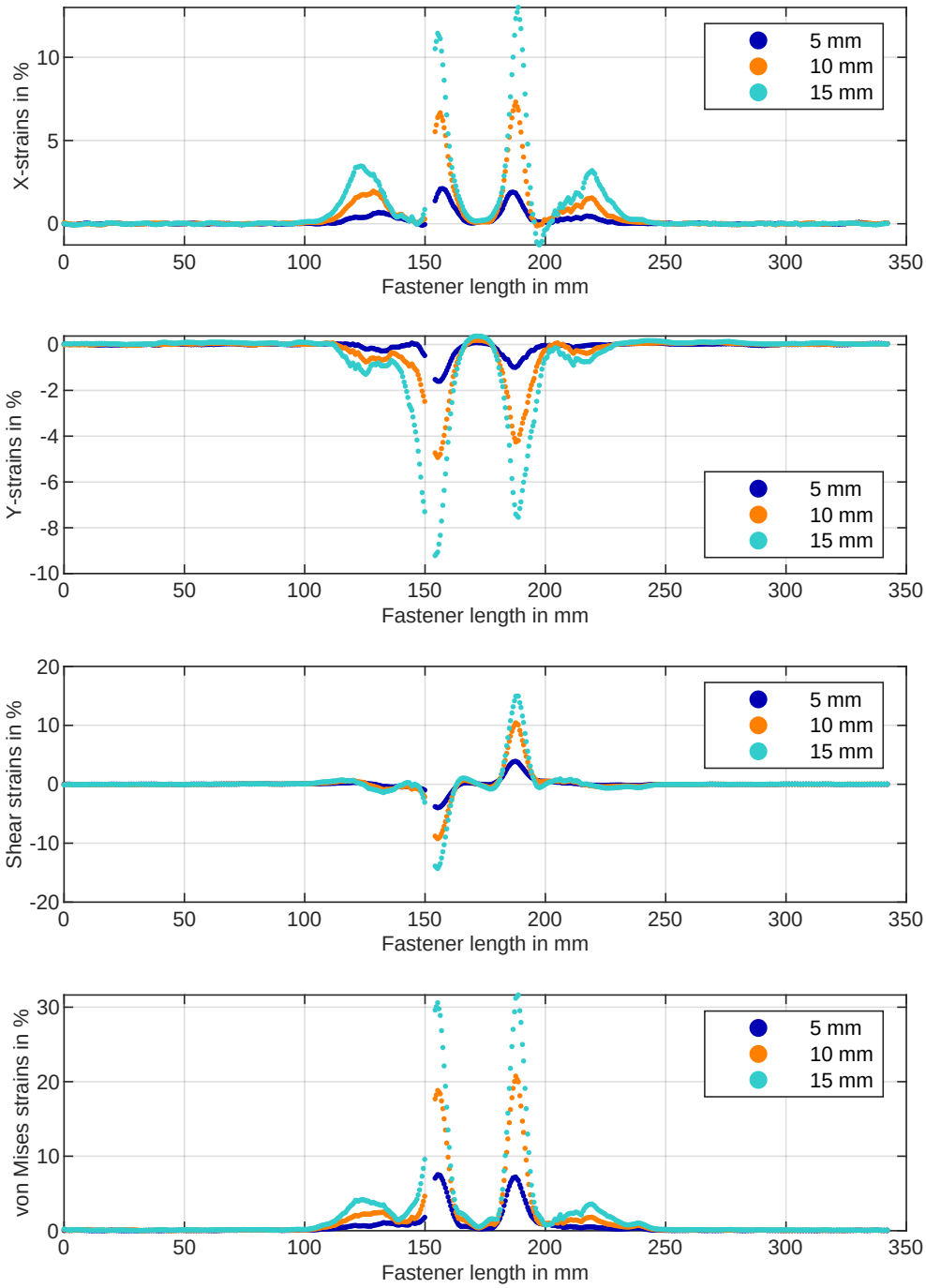

Fig. A.88: S_BB_Alu strain results, front side.

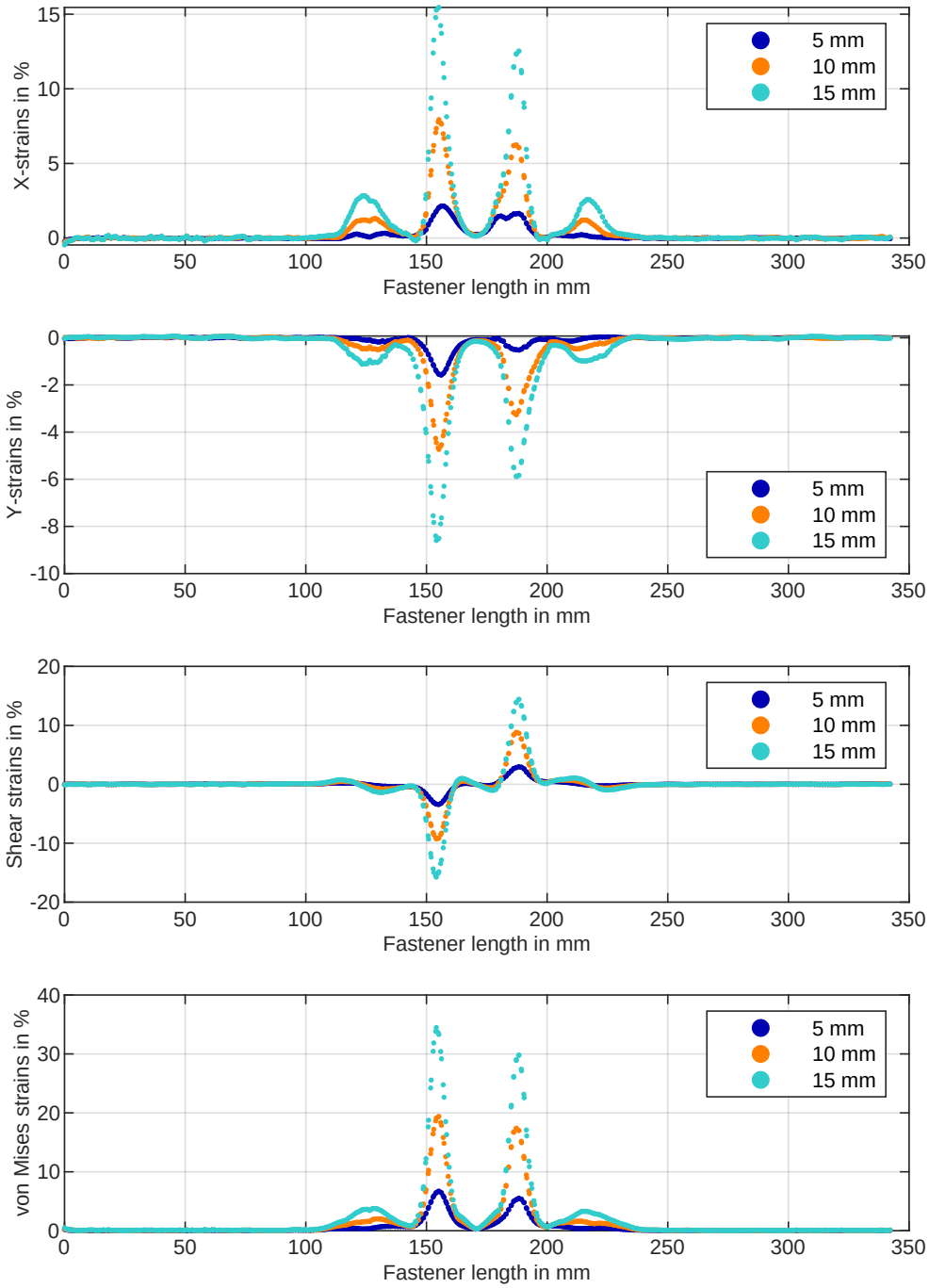

Fig. A.89: S_BB_Alu strain results, rear side.

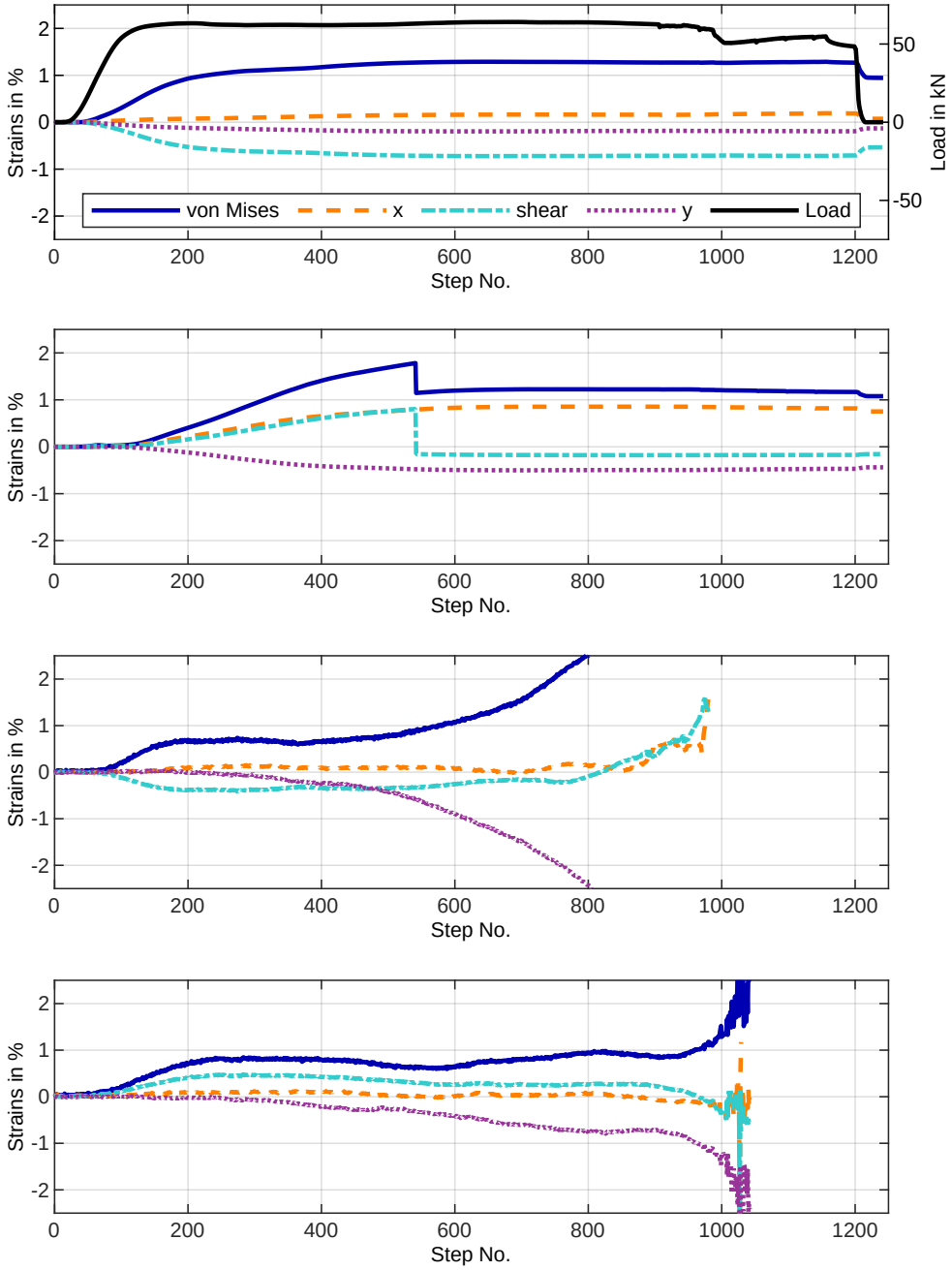

Fig. A.90: S_BB_Alu strain results of DIC or strain gauge in distance *a* to shear plane. Strain gauge 1 at $a = 14$ mm, strain gauge 2 at $a = 21$ mm, DIC results at $a = 14$ mm.

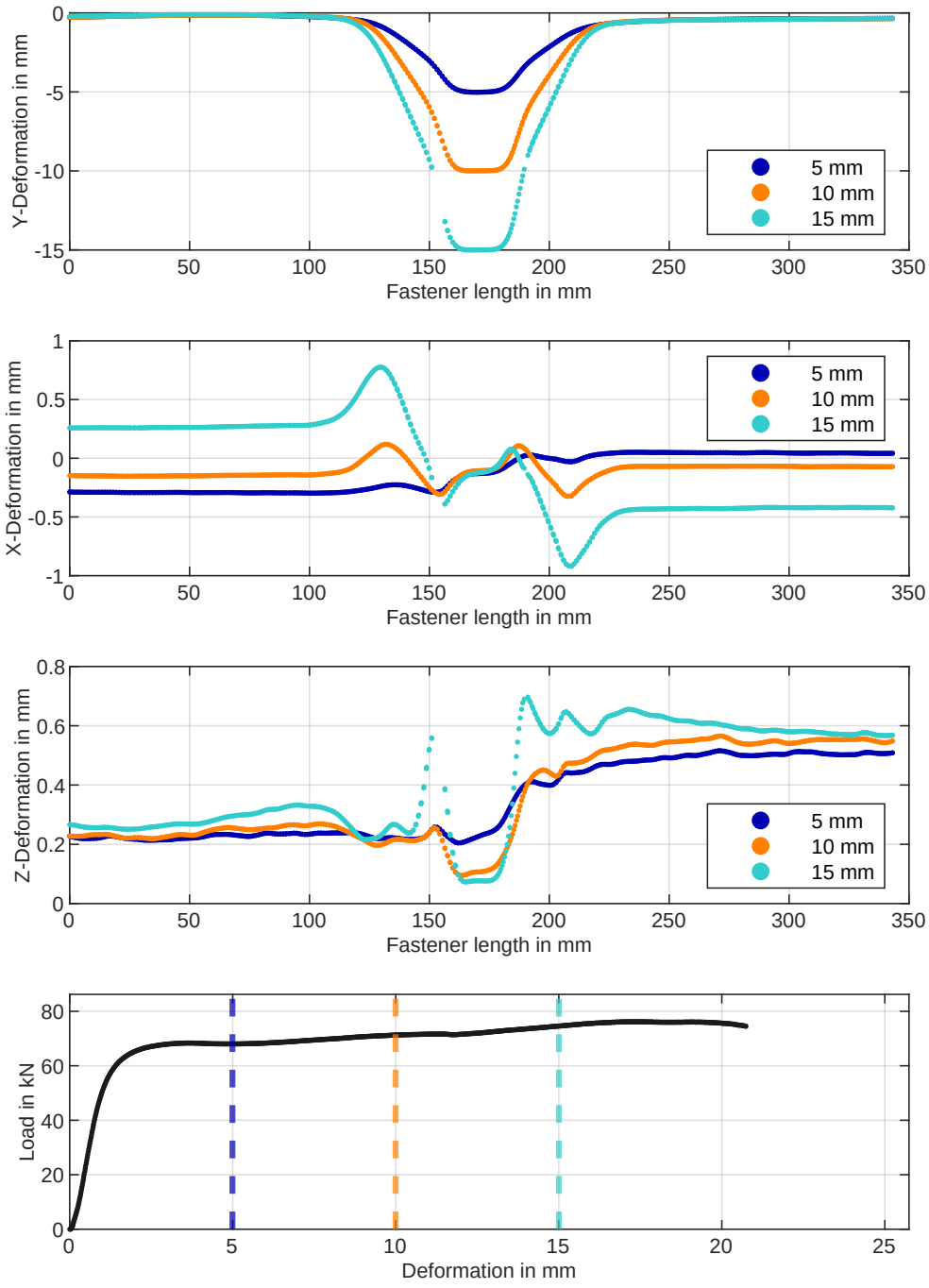

Fig. A.91: S_BB_Alu_mk deformation results, front side.

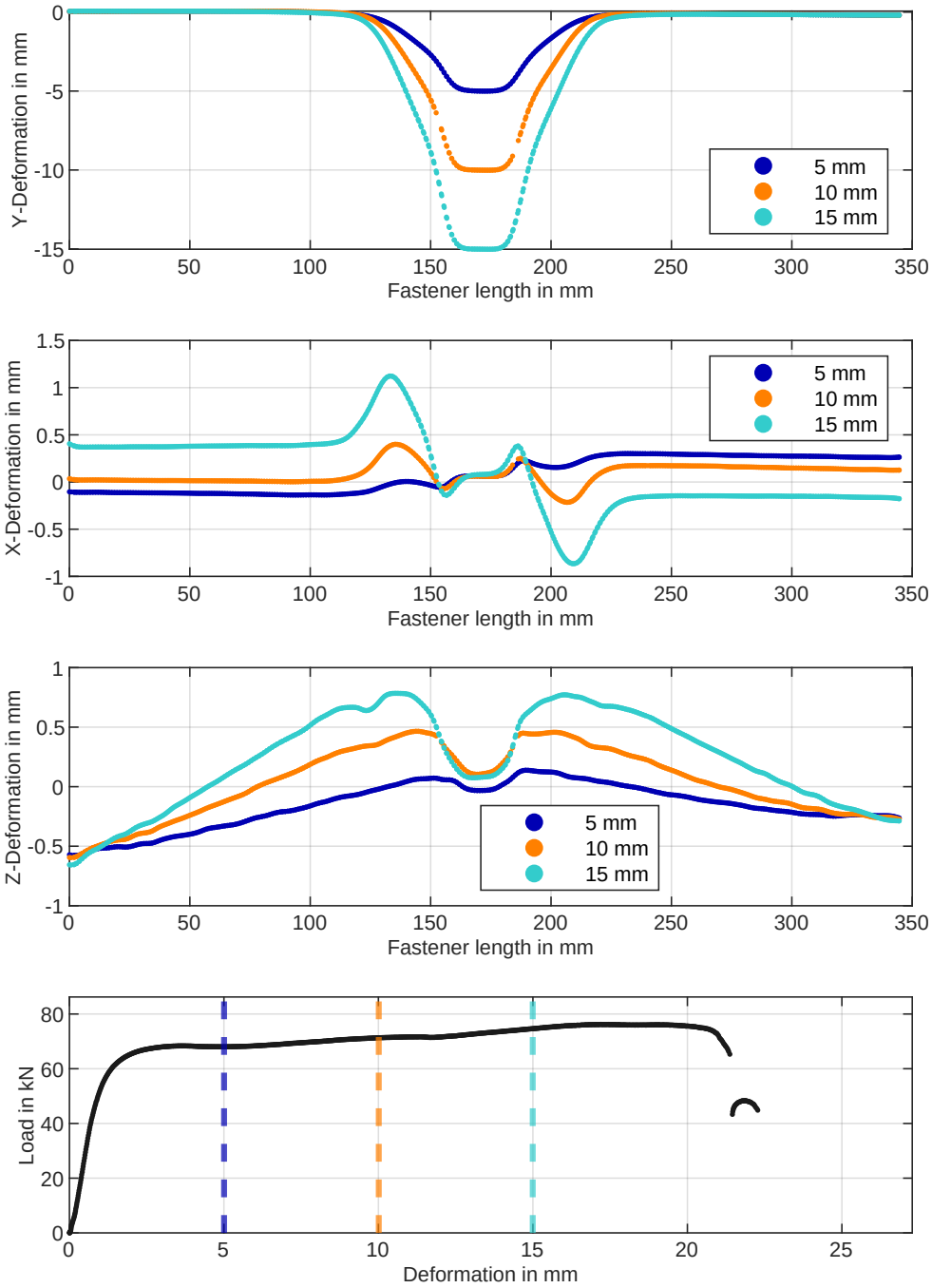

Fig. A.92: S_BB_Alu_mk deformation results, rear side.

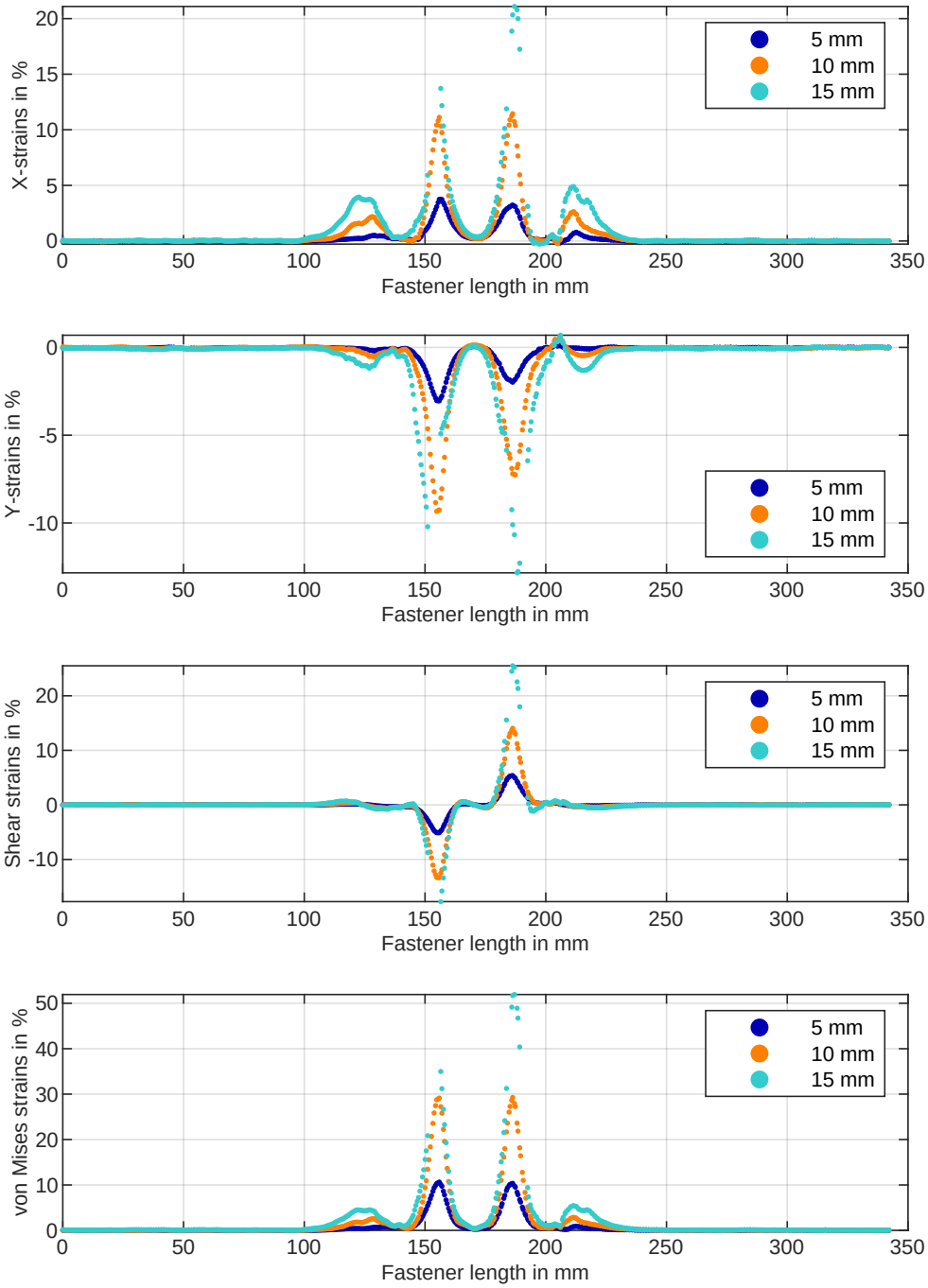

Fig. A.93: S_BB_Alu_mk strain results, front side.

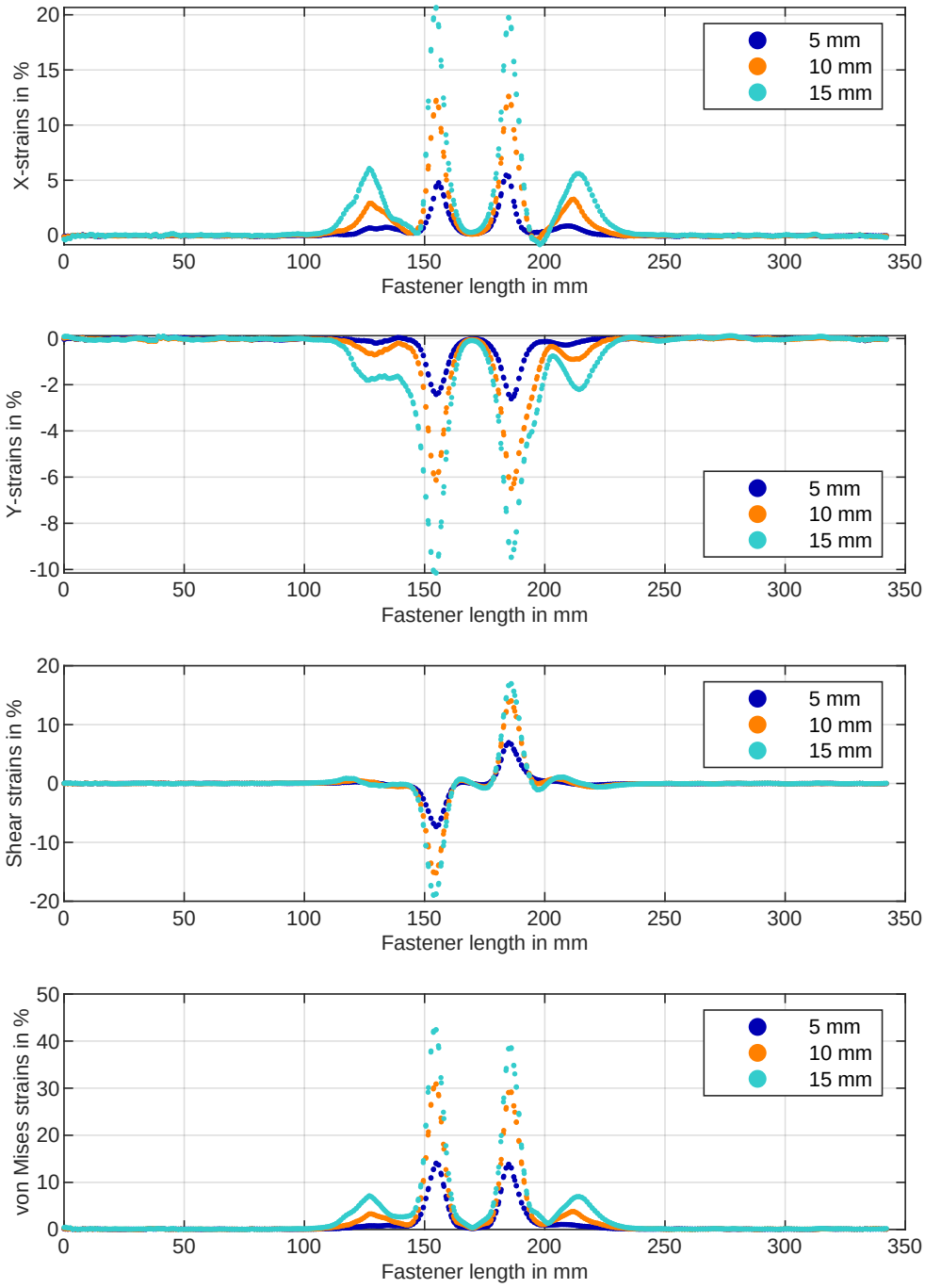

Fig. A.94: S_BB_Alu_mk strain results, rear side.

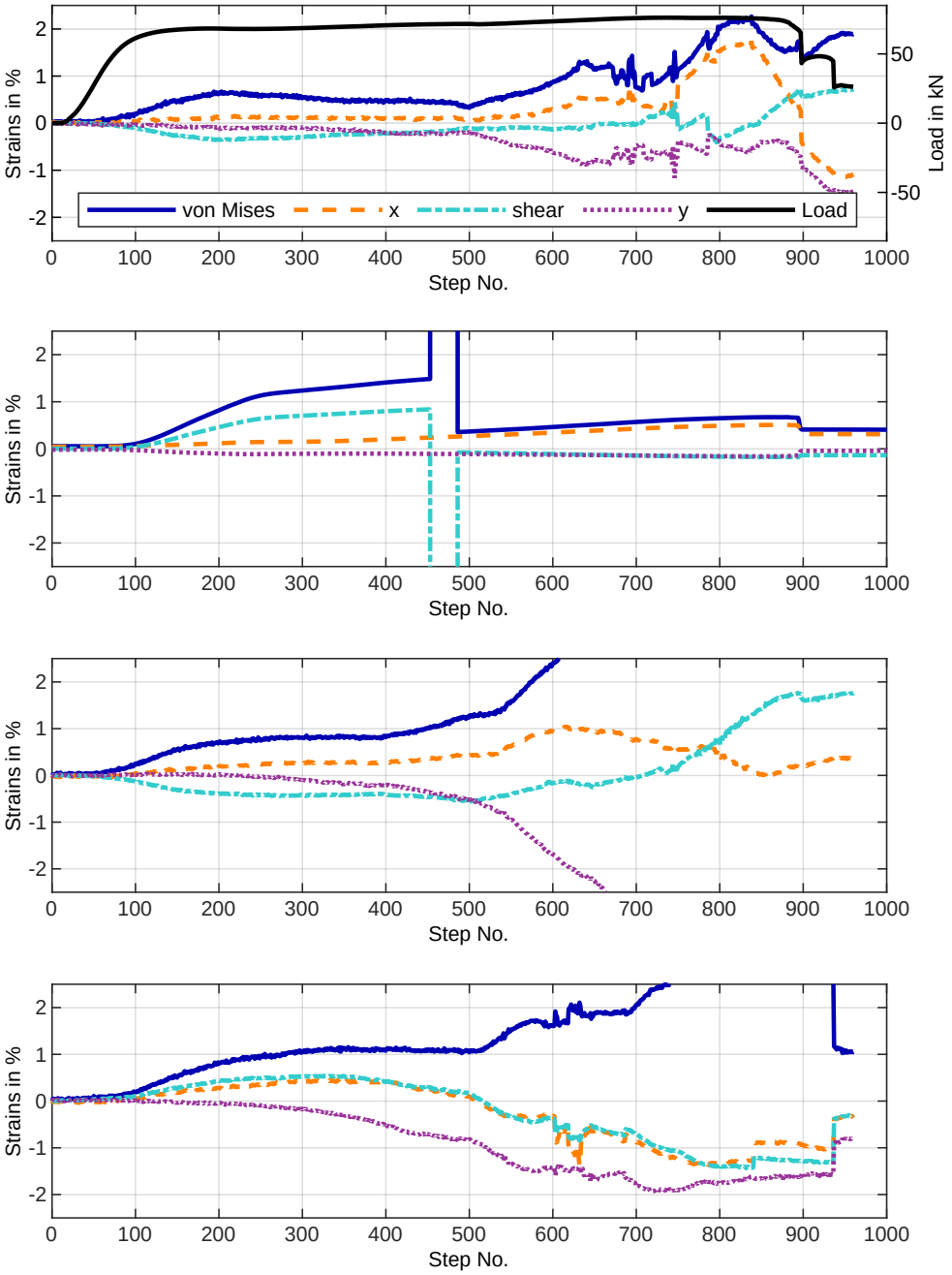

Fig. A.95: S_BB_Alu_mk strain results of DIC or strain gauge in distance *a* to shear planes.

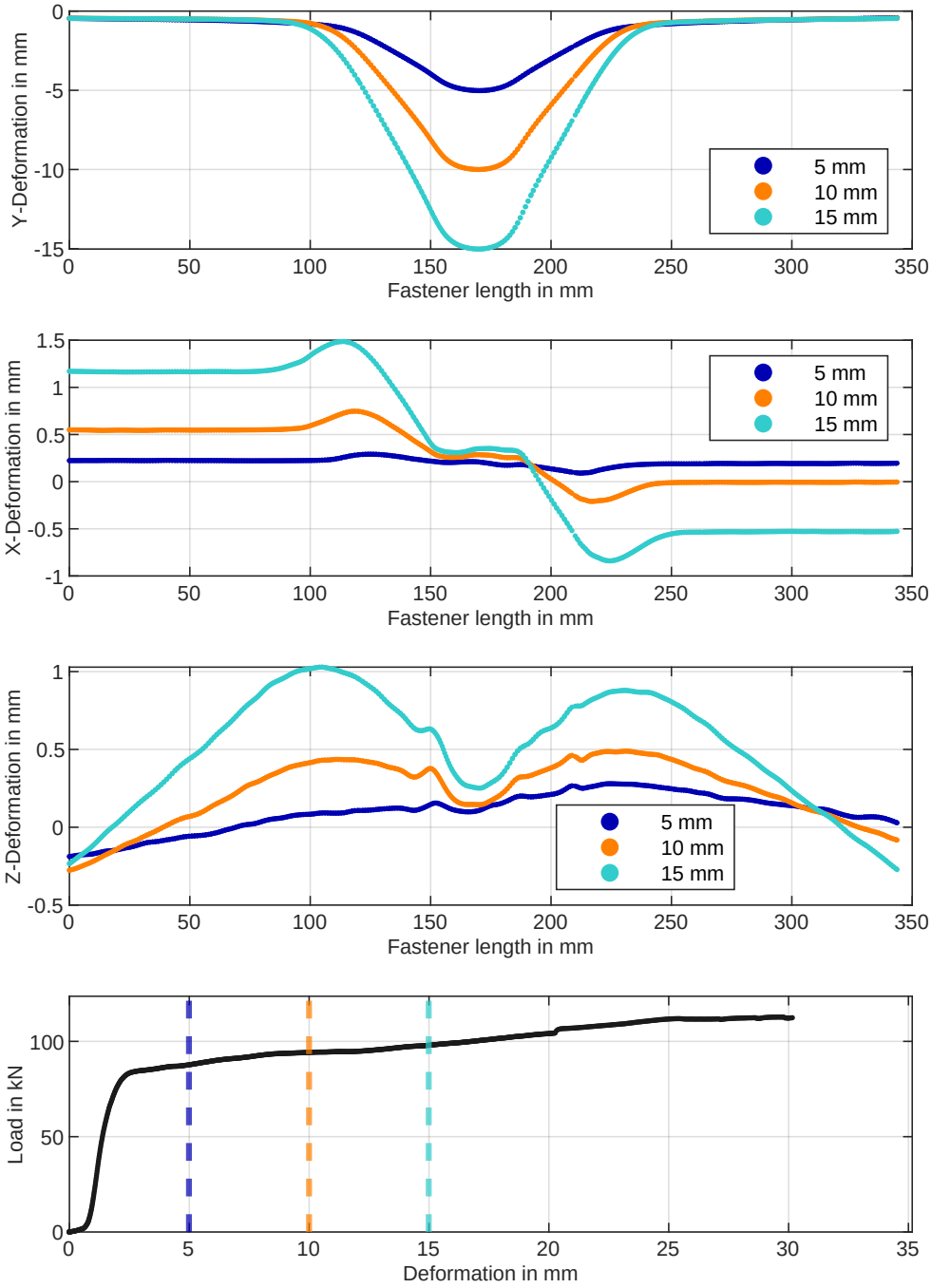

Fig. A.96: S_BB_Steel deformation results, front side.

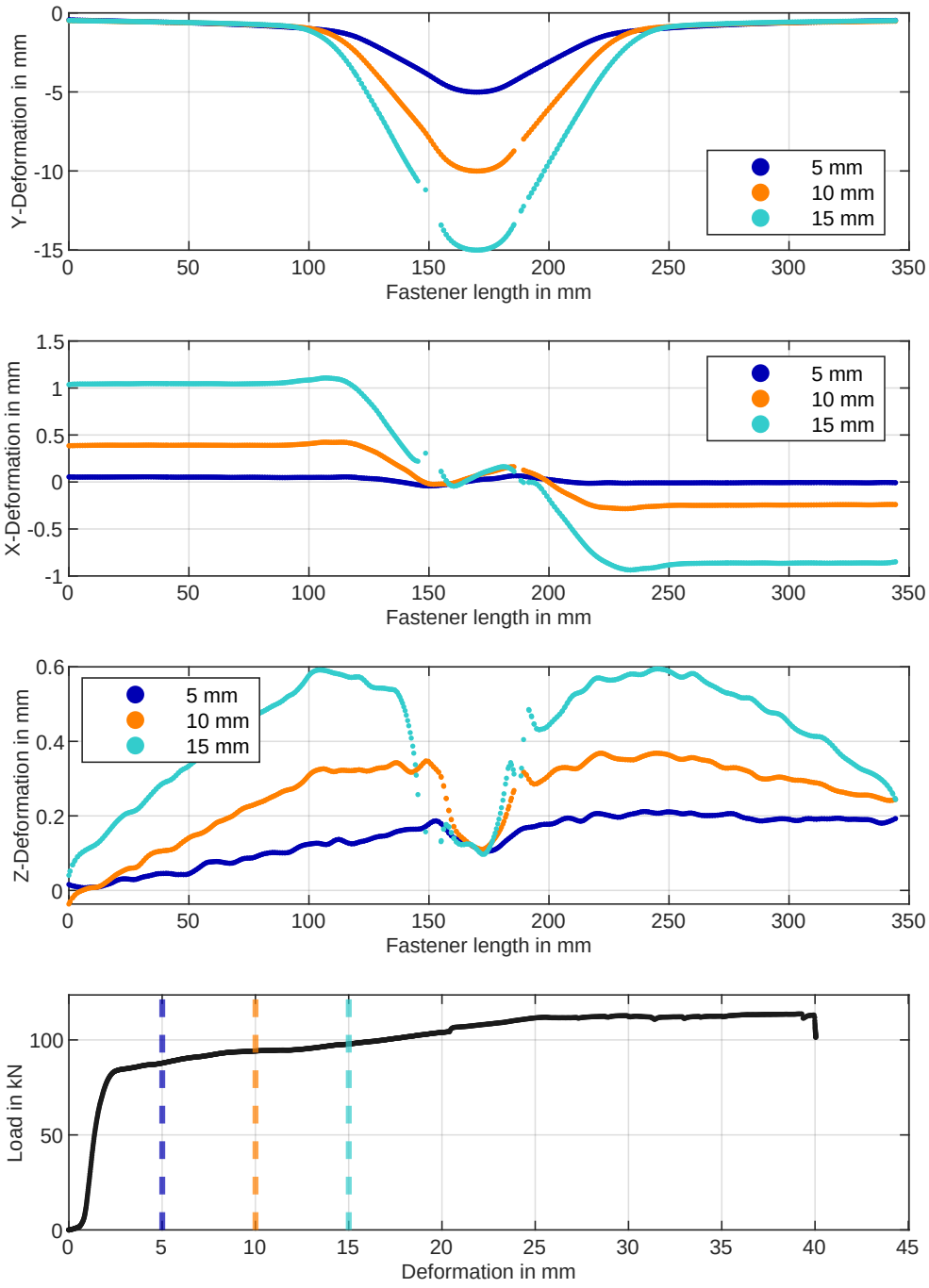

Fig. A.97: S_BB_Steel deformation results, rear side.

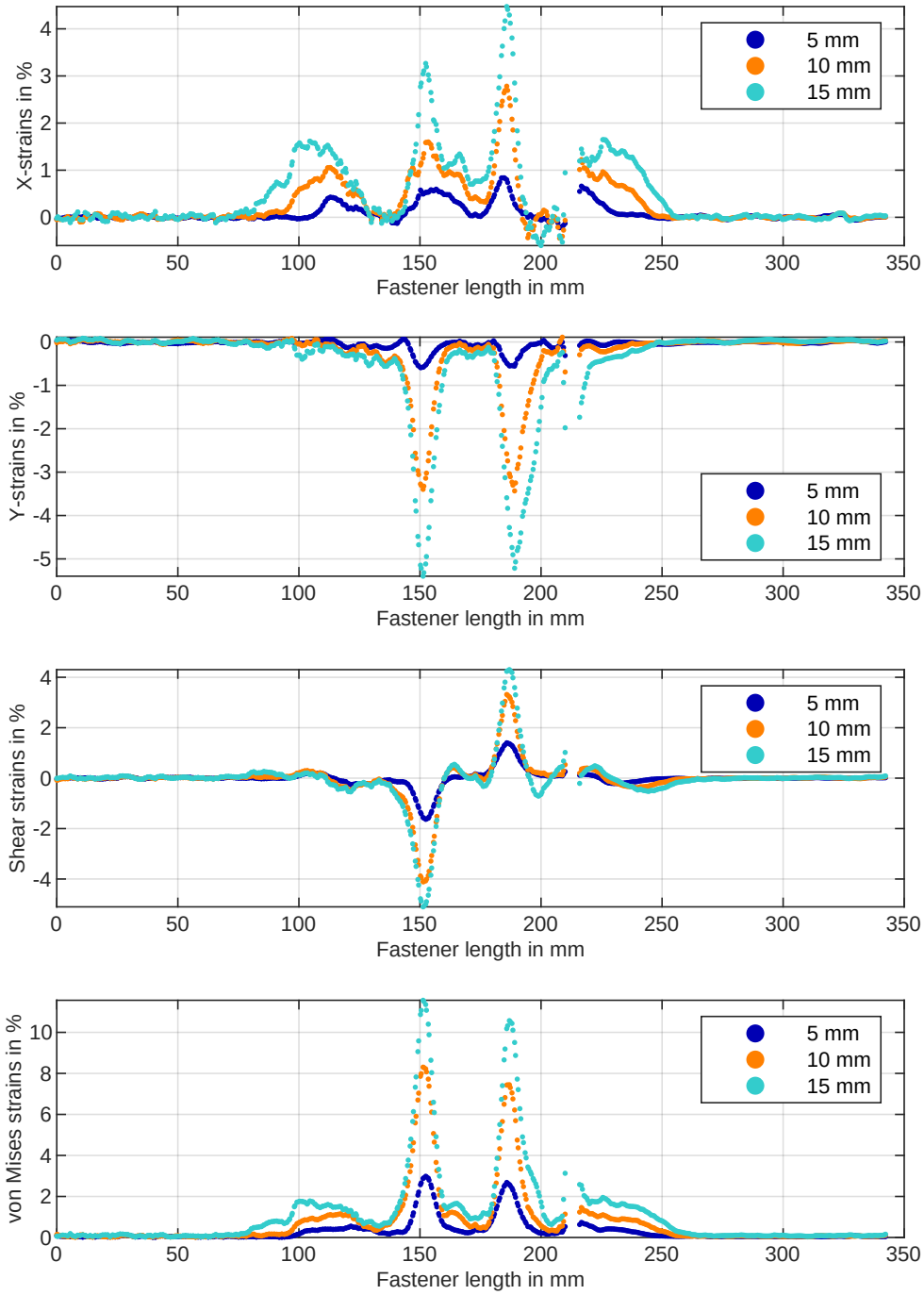

Fig. A.98: S_BB_Steel strain results, front side.

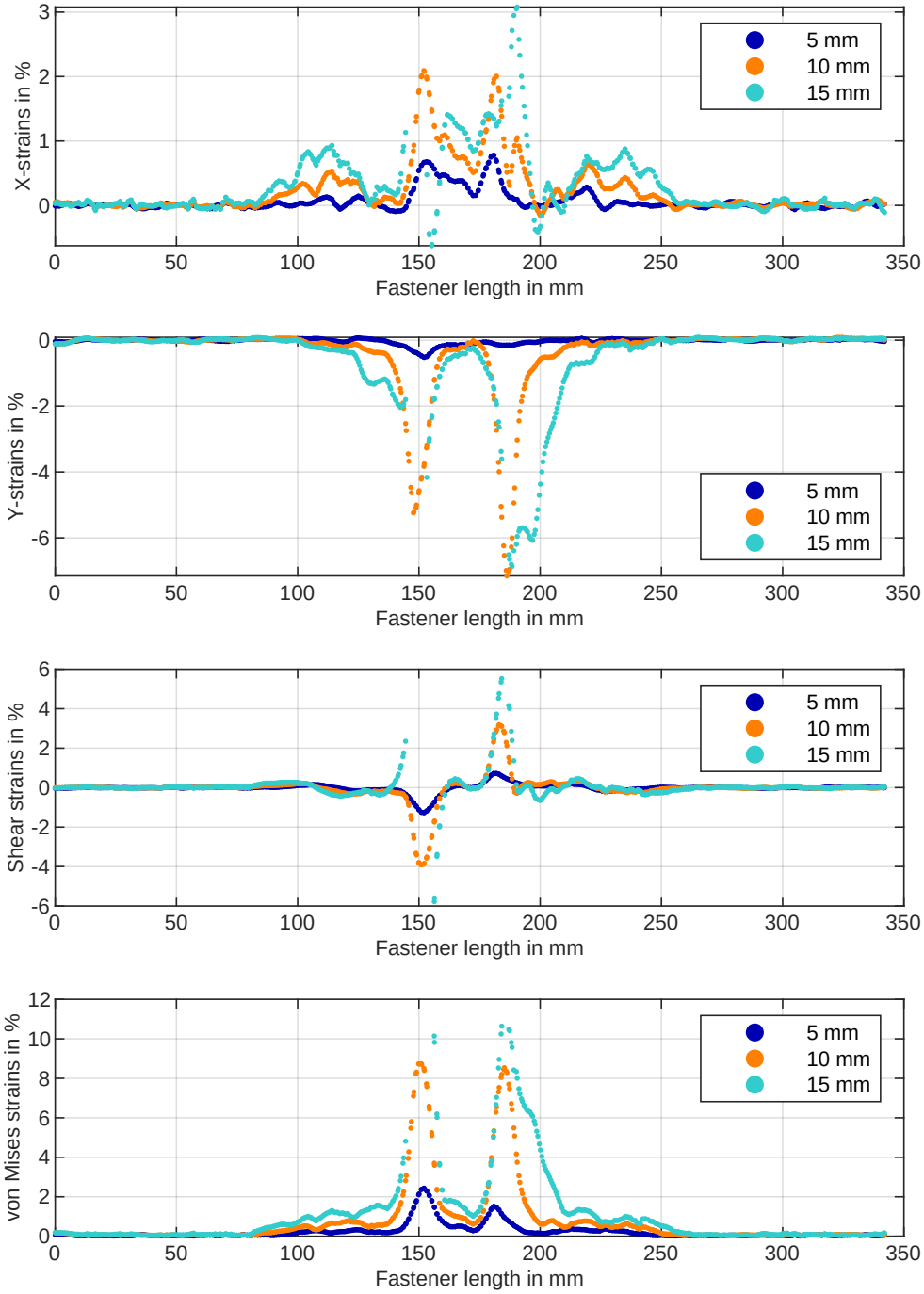

Fig. A.99: S_BB_Steel strain results, rear side.

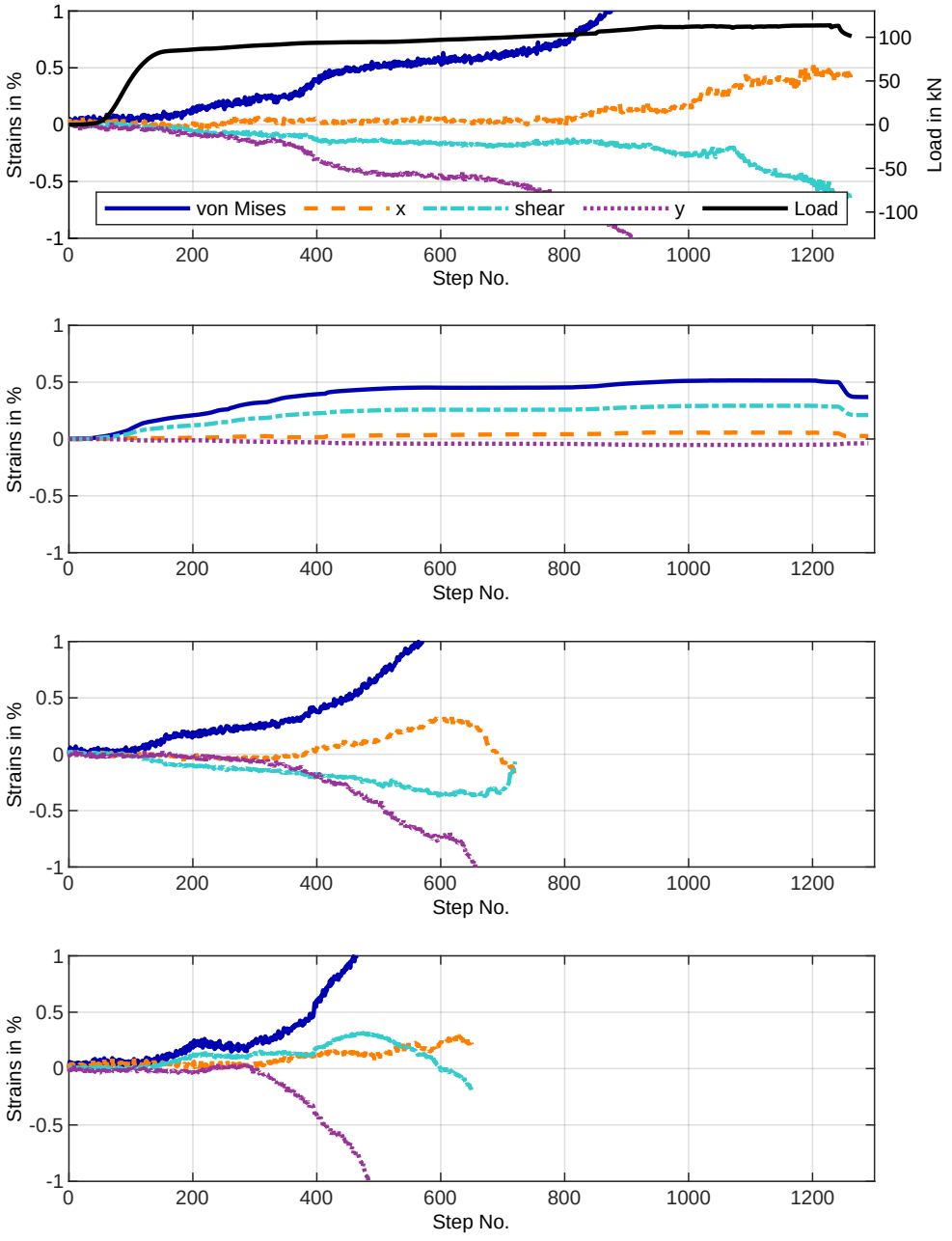

Fig. A.100: S_BB_Steel strain results of DIC or strain gauge in distance *a* to shear planes.

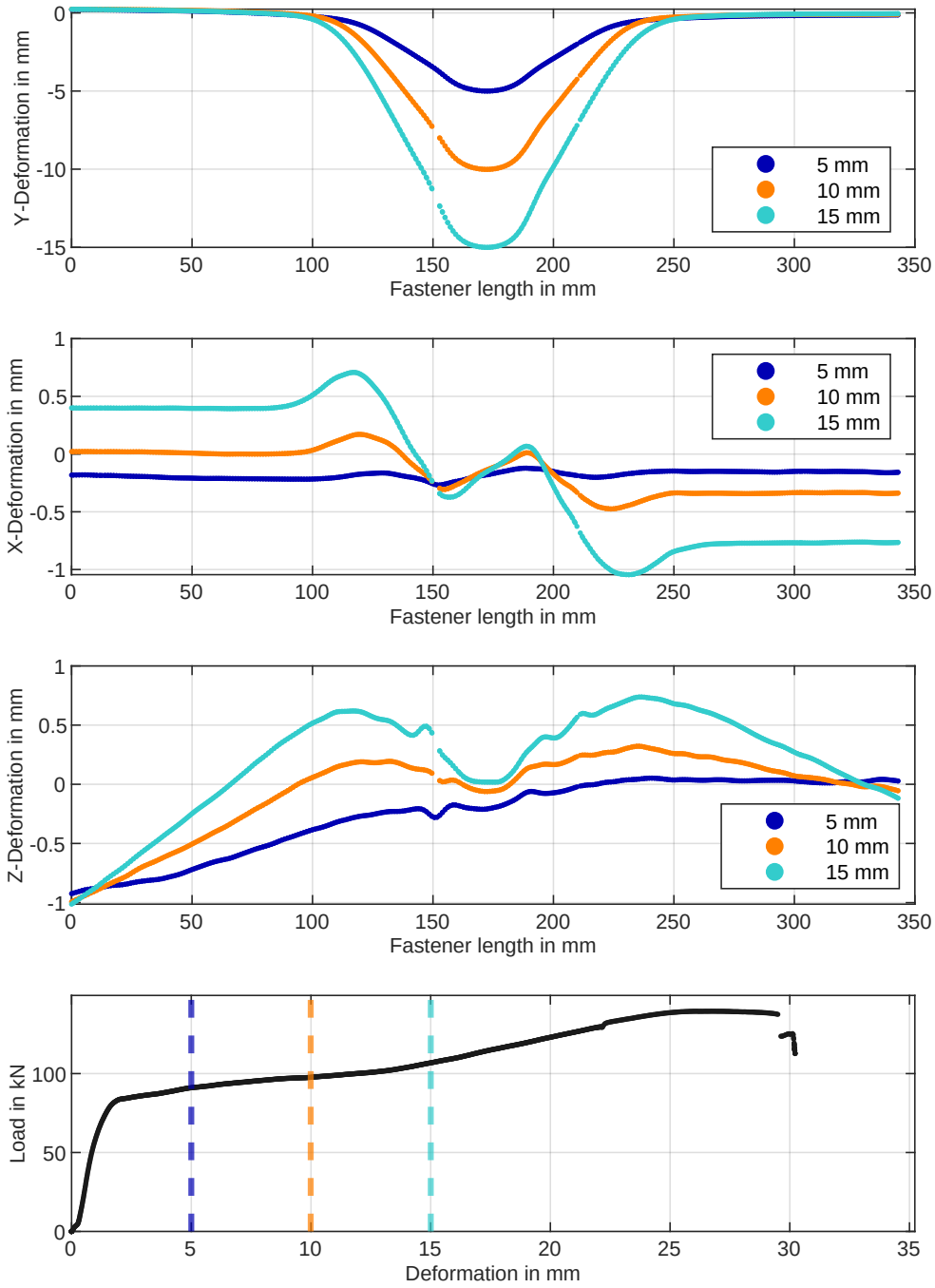

Fig. A.101: S_BB_Steel_mk deformation results, front side.

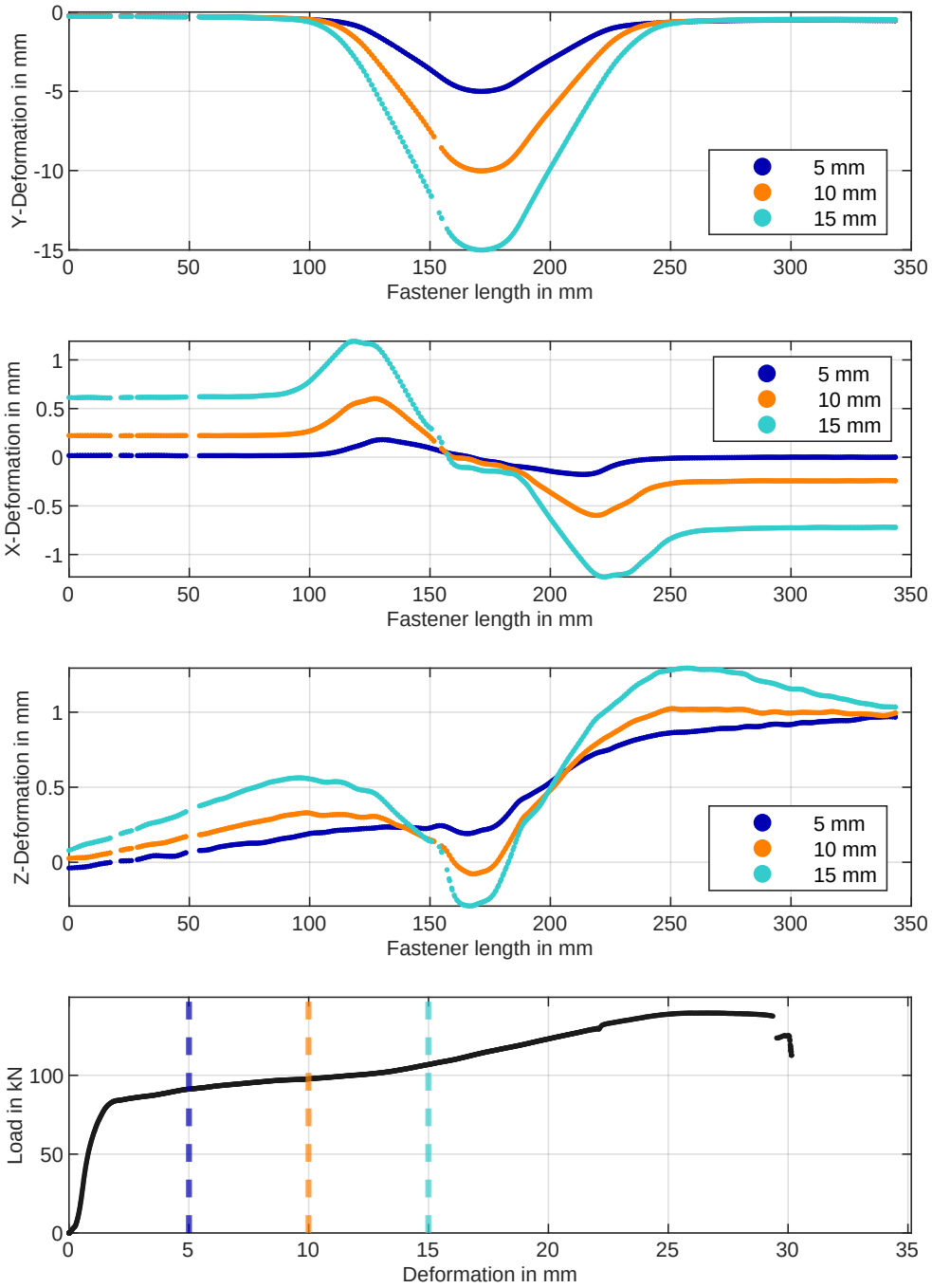

Fig. A.102: S_BB_Steel_mk deformation results, rear side.

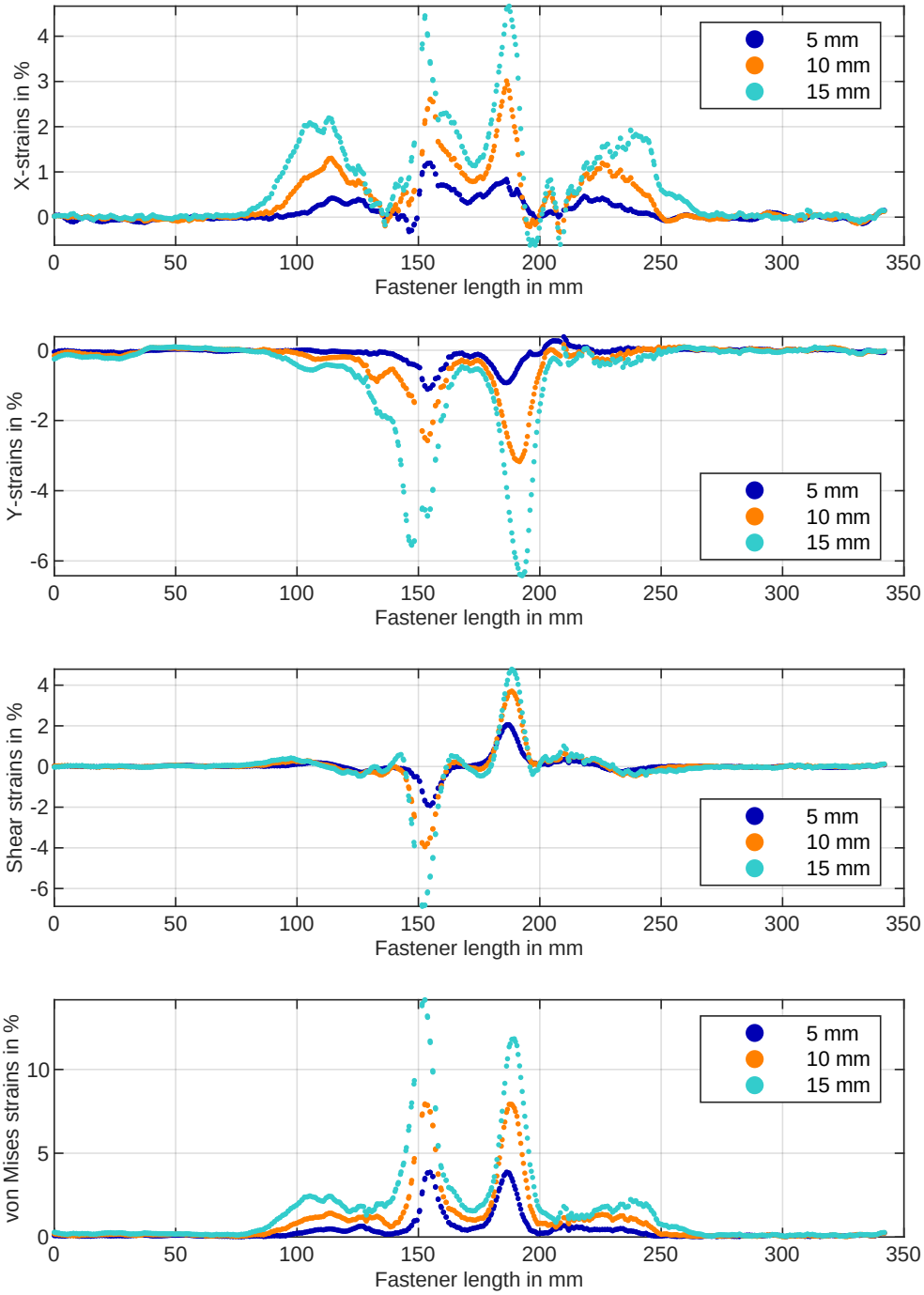

Fig. A.103: S_BB_Steel_mk strain results, front side.

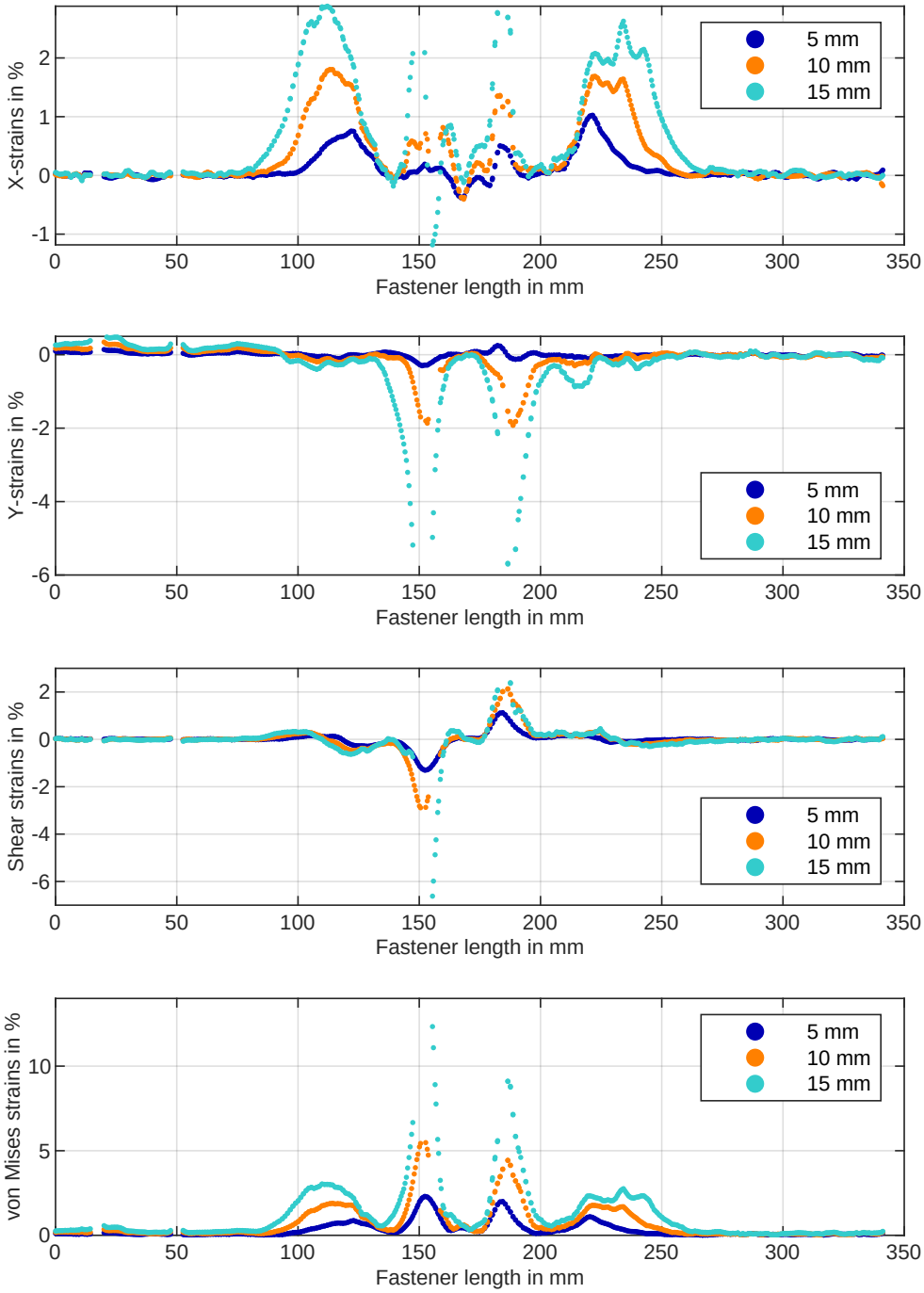

Fig. A.104: S_BB_Steel_mk strain results, rear side.

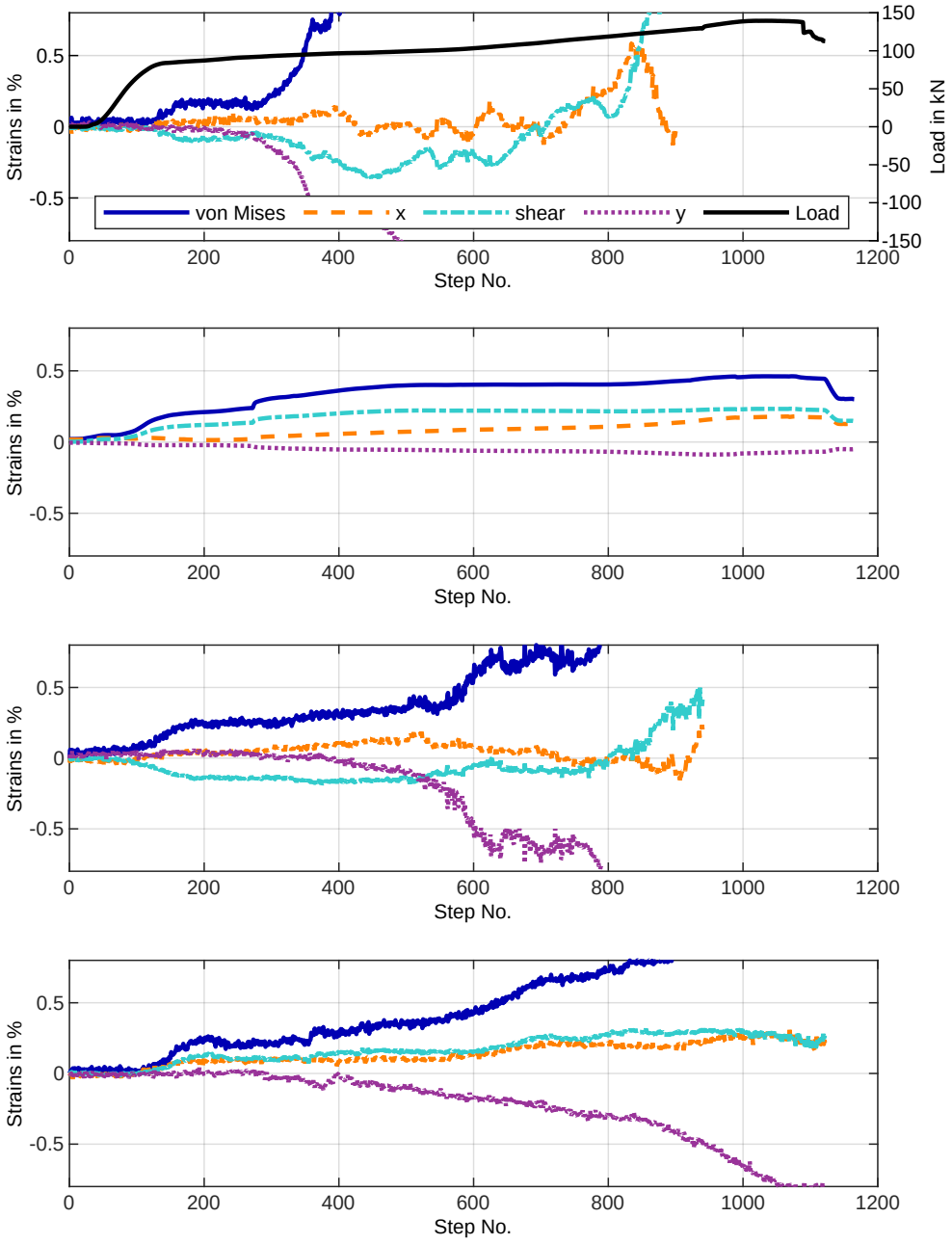

Fig. A.105: S_BB_Steel_mk strain results of DIC or strain gauge in distance *a* to shear planes.

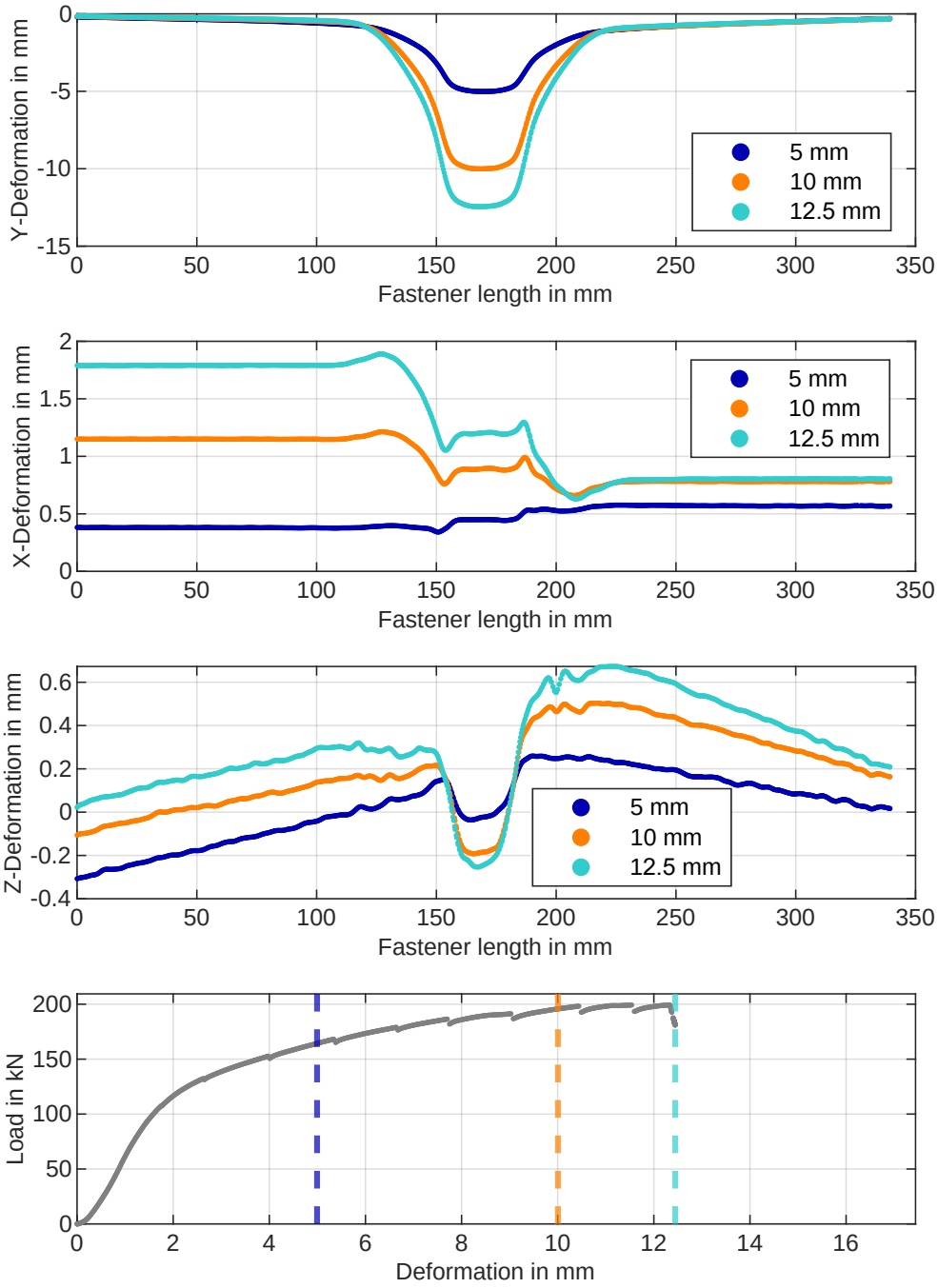

Fig. A.106: S_DVW_Steel deformation results, front side.

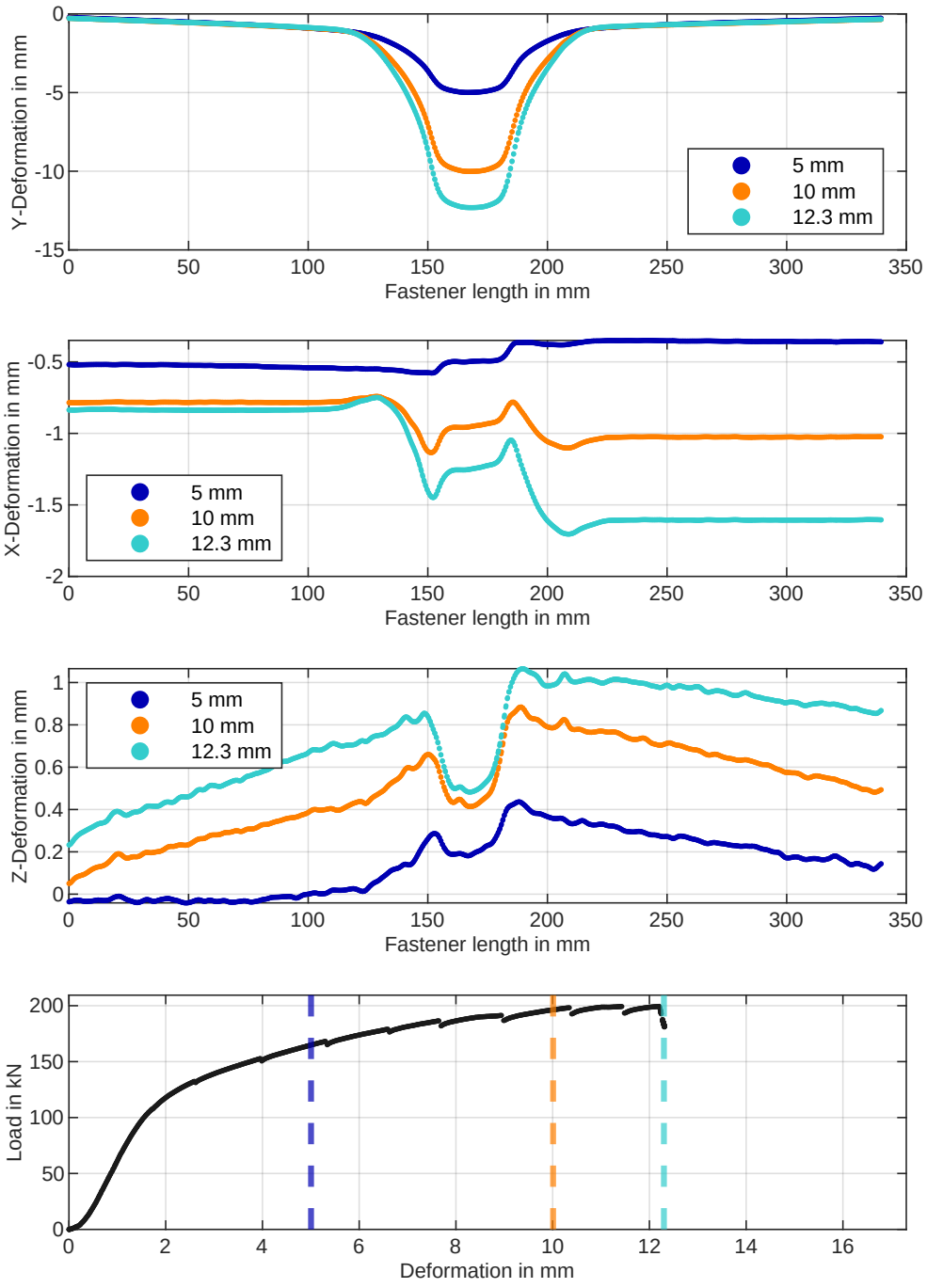

Fig. A.107: S_DVW_Steel deformation results, rear side.

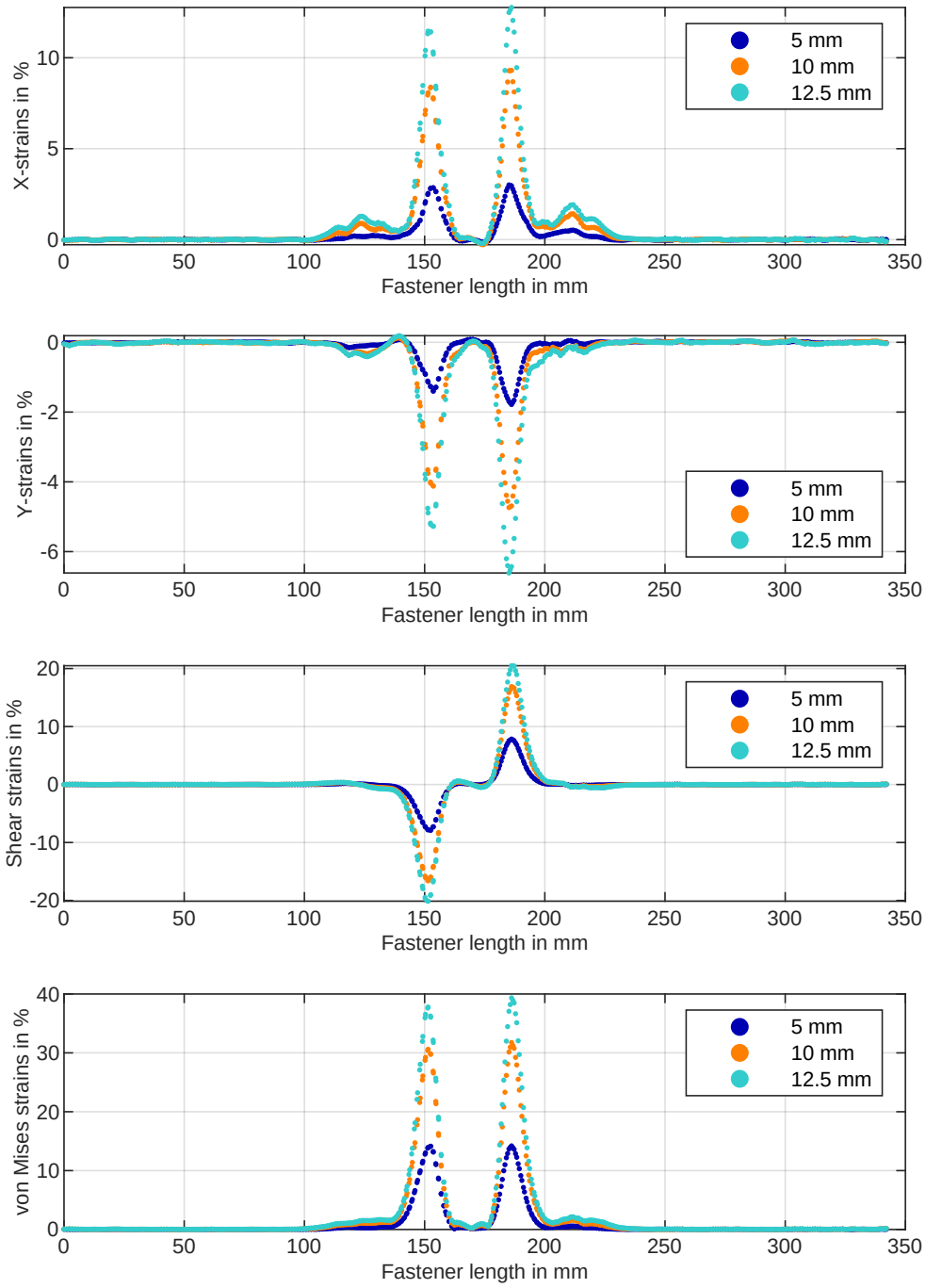

Fig. A.108: S_DVW_Steel strain results, front side.

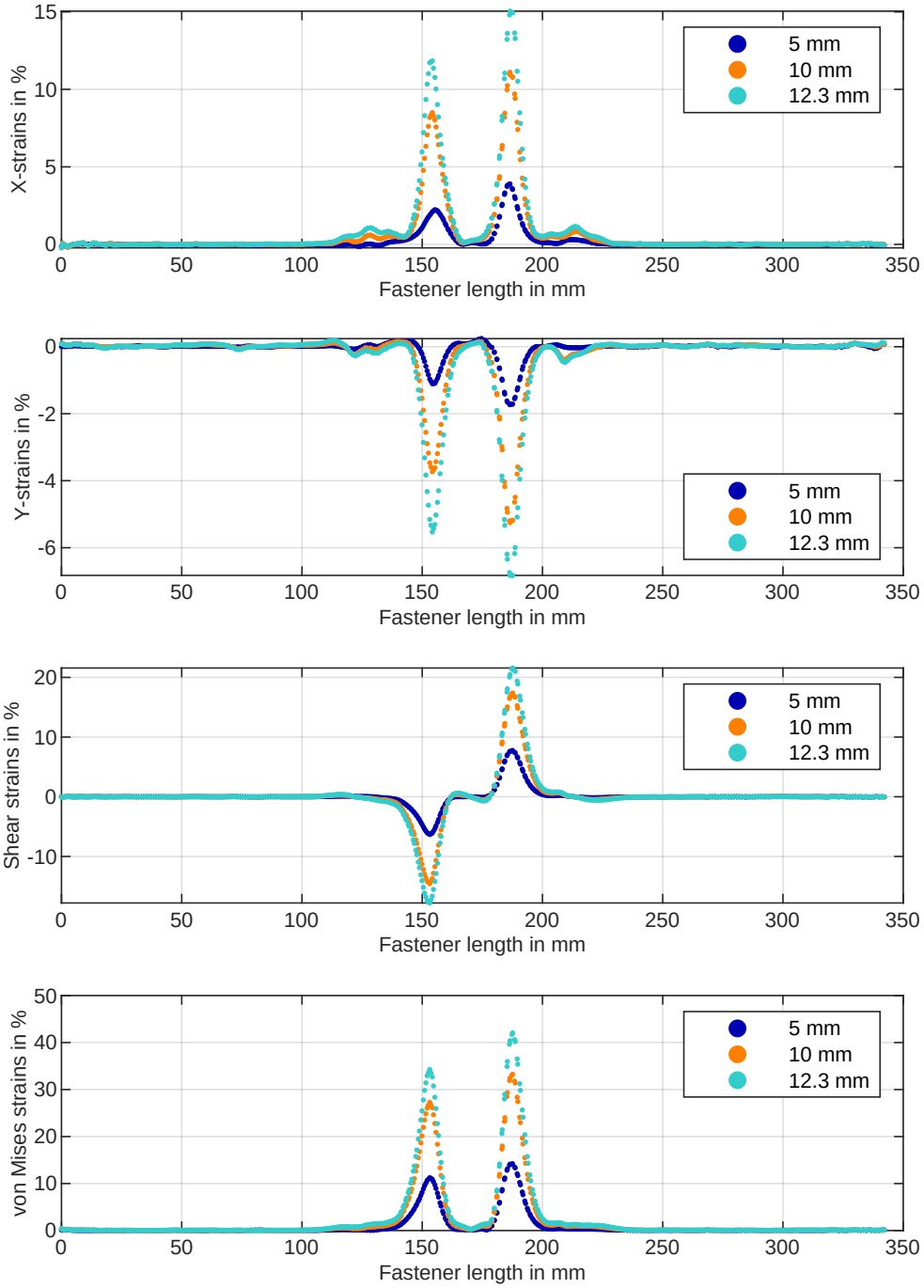

Fig. A.109: S_DVW_Steel strain results, rear side.

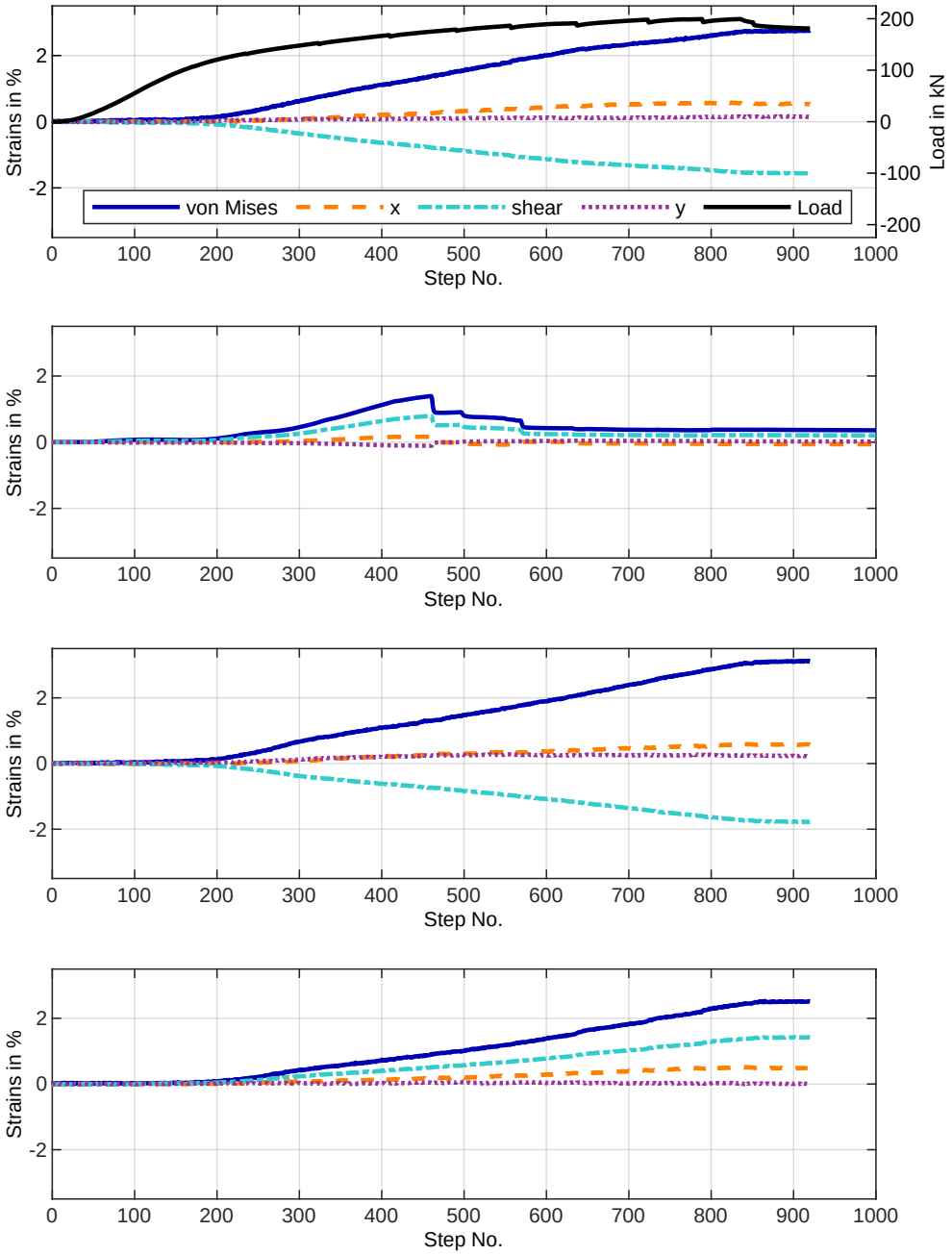

Fig. A.110: S_DVW_Steel strain results of DIC or strain gauge in distance *a* to shear planes.

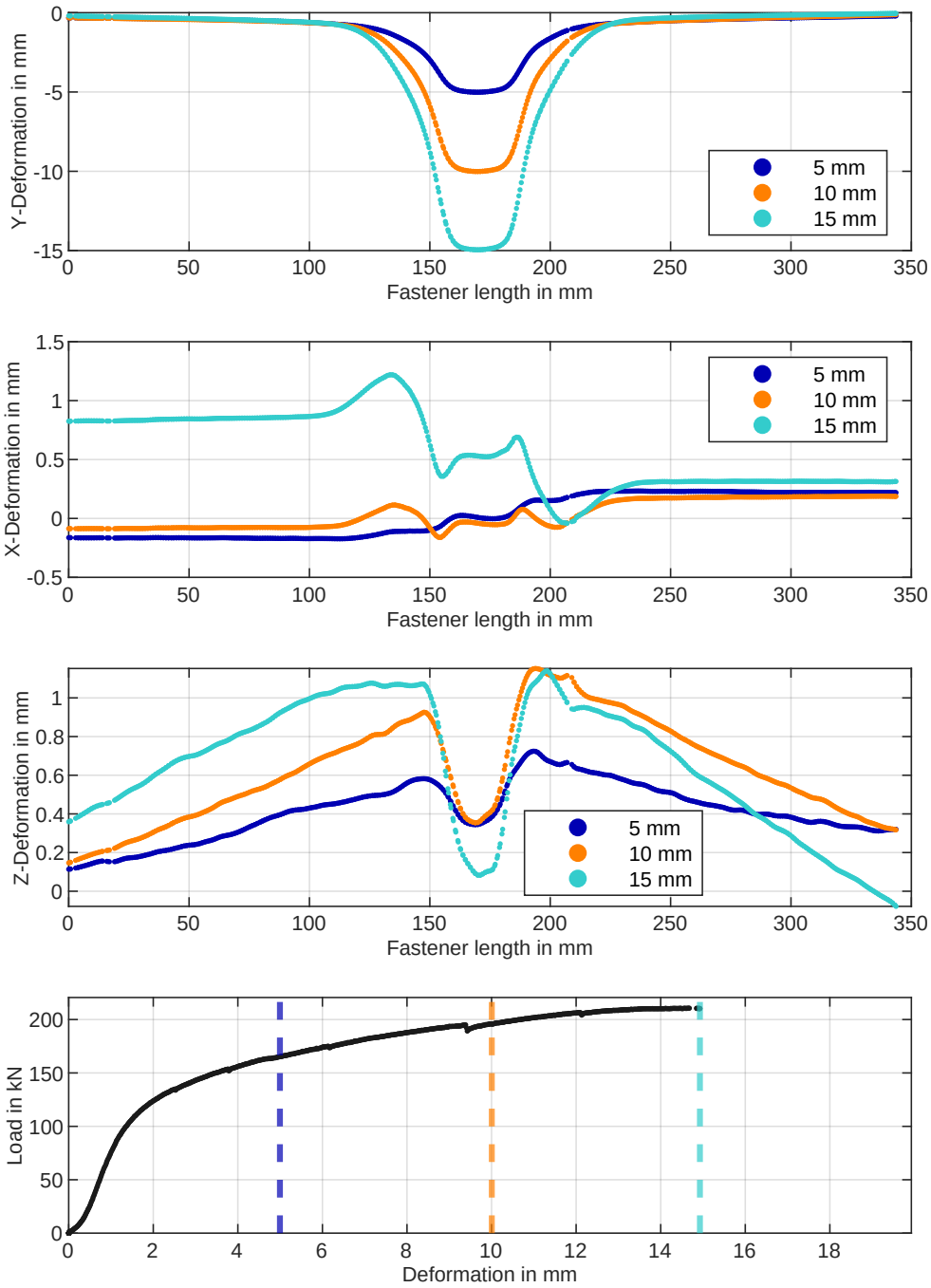

Fig. A.111: S_DVW_Steel_mk deformation results, front side.

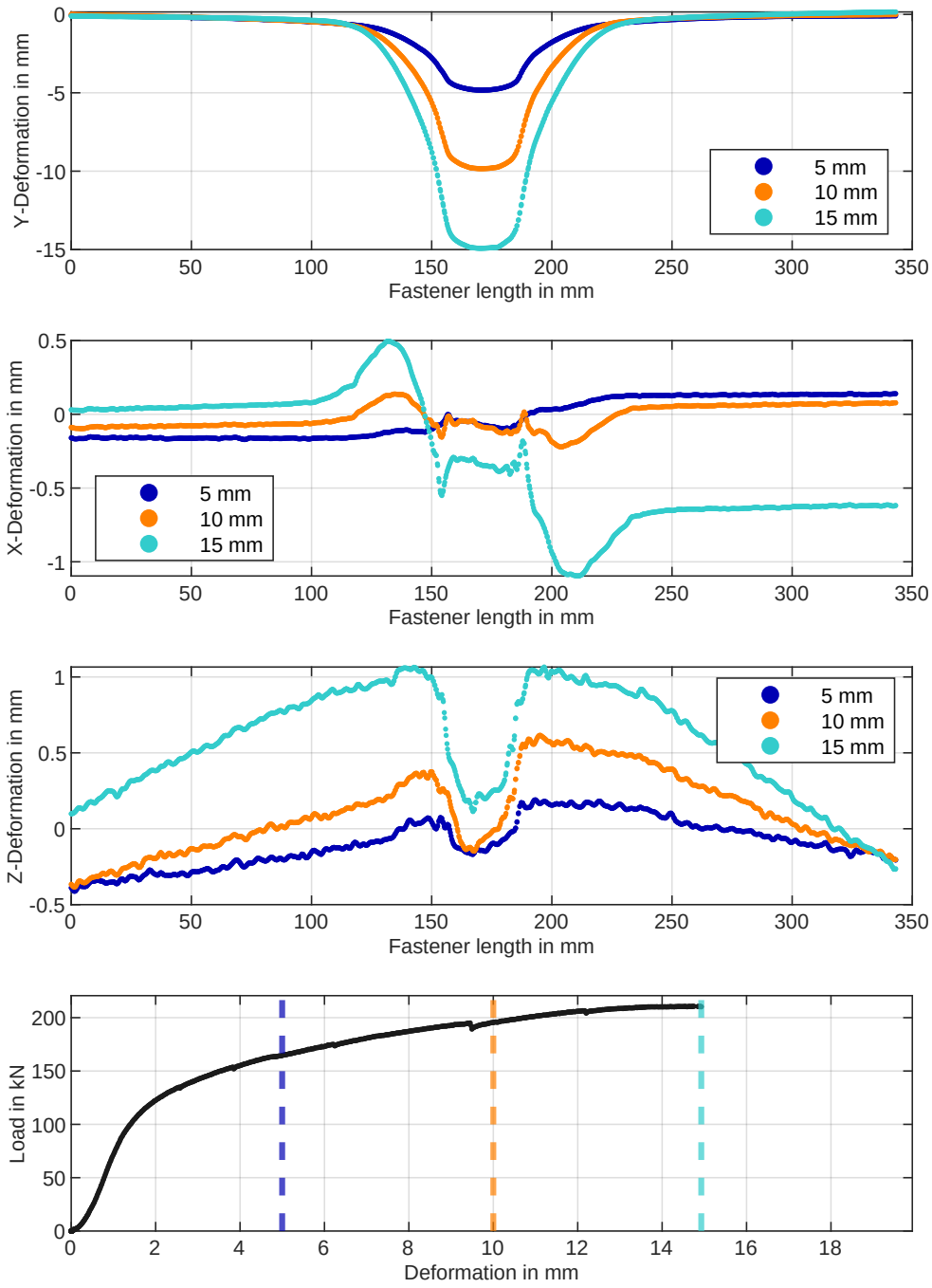

Fig. A.112: S_DVW_Steel_mk deformation results, rear side.

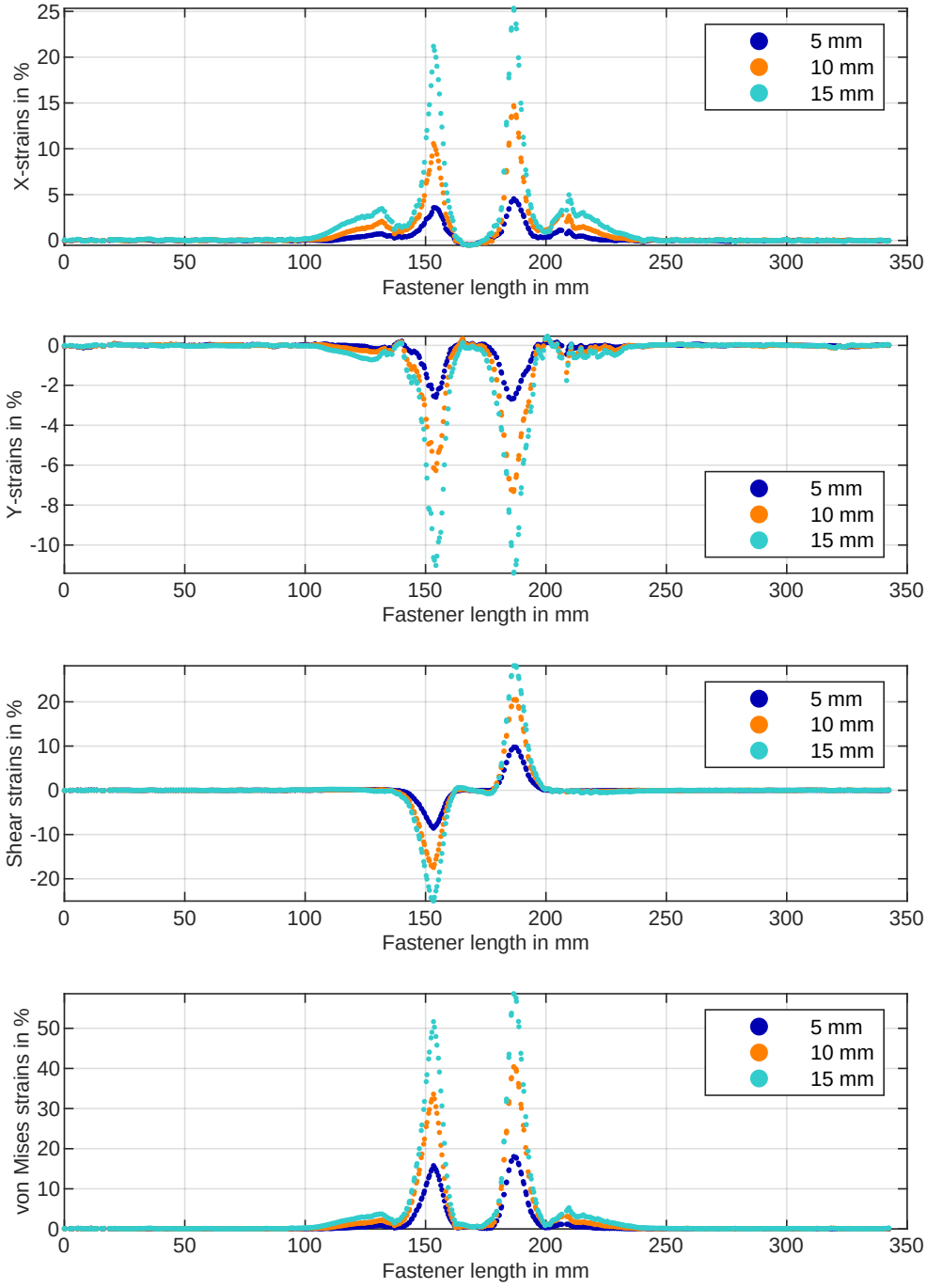

Fig. A.113: S_DVW_Steel_mk deformation results, front side.

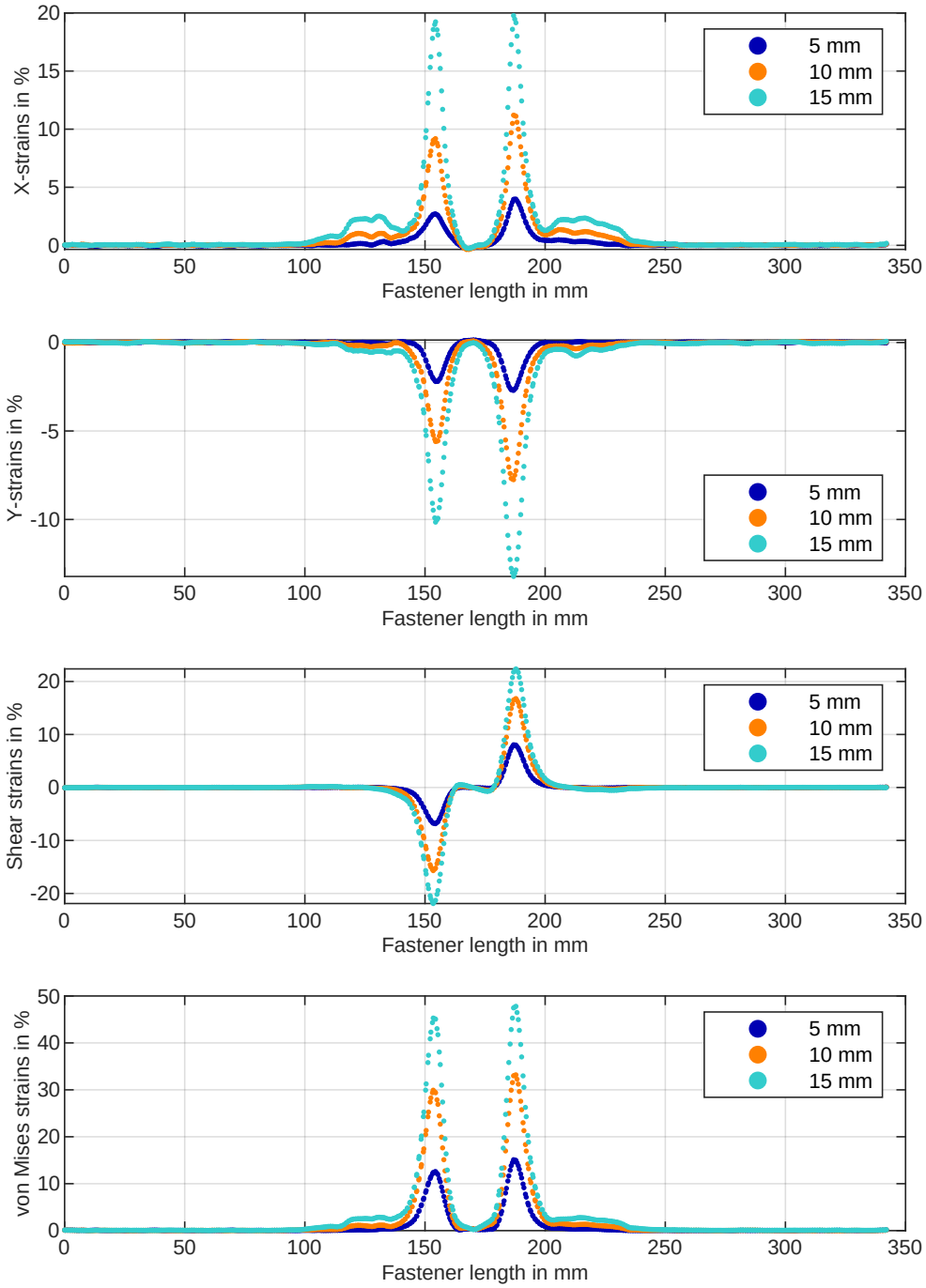

Fig. A.114: S_DVW_Steel_mk deformation results, rear side.

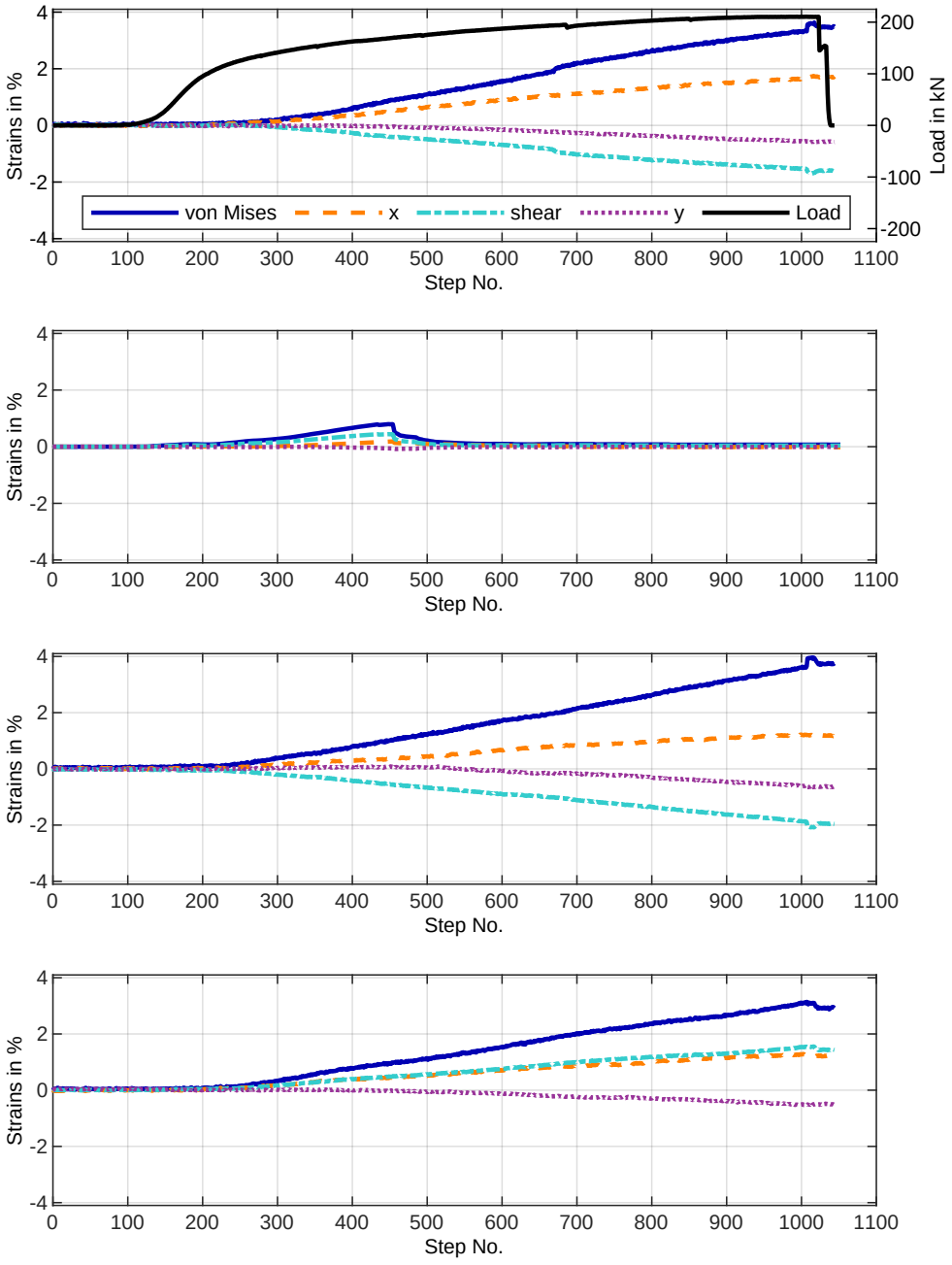

Fig. A.115: S_DVW_Steel_mk deformation results of DIC or strain gauge in distance *a* to shear planes.

Rectangular Fasteners: Scans of Fasteners' Back Sides

The fasteners of connections with spruce glulam and beech LVL were removed and scanned after the tests. Thus, the scans show a visualisation of plastic zones and different failure modes.

a. Front fastener.

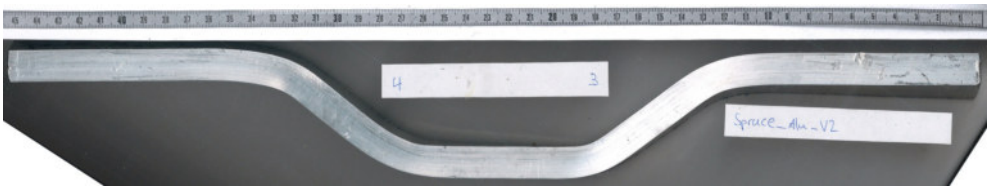

b. Rear fastener.

Fig. A.116: Aluminium fasteners taken out of timber-to-timber connection with spruce glulam.

a. Front fastener.

b. Rear fastener.

Fig. A.117: Aluminium fasteners with head taken out of timber-to-timber connection with spruce glulam.

a. Front fastener.

b. Rear fastener.

Fig. A.118: Aluminium fasteners taken out of timber-to-timber connection with beech LVL.

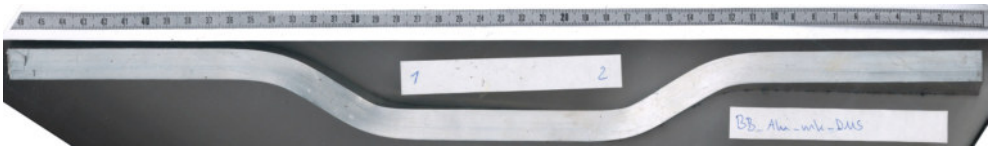

a. Front fastener.

b. Rear fastener.

Fig. A.119: Aluminium fasteners with head taken out of timber-to-timber connection with beech LVL.

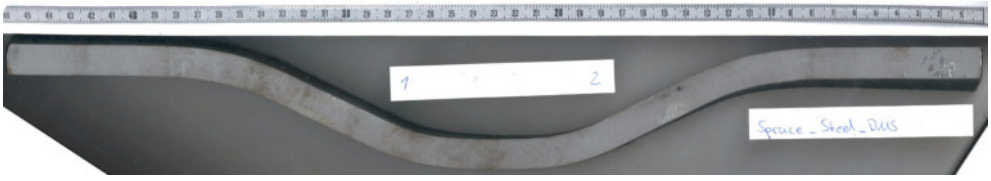

a. Front fastener.

b. Rear fastener.

Fig. A.120: Steel fasteners taken out of timber-to-timber connection with spruce glulam.

a. Front fastener.

b. Rear fastener.

Fig. A.121: Steel fasteners with head taken out of timber-to-timber connection with spruce glulam.

a. Front fastener.

b. Rear fastener.

Fig. A.122: Steel fasteners taken out of timber-to-timber connection with beech LVL.

a. Front fastener.

b. Rear fastener.

Fig. A.123: Steel fasteners with head taken out of timber-to-timber connection with beech LVL.

a. Front fastener.

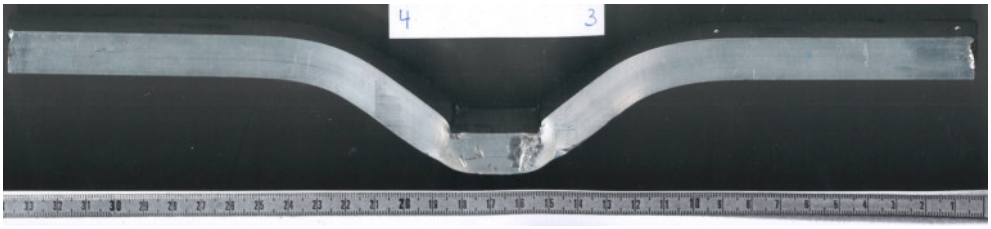

b. Rear fastener.

Fig. A.124: Aluminium fasteners taken out of timber-to-steel connection with spruce glulam.

a. Front fastener.

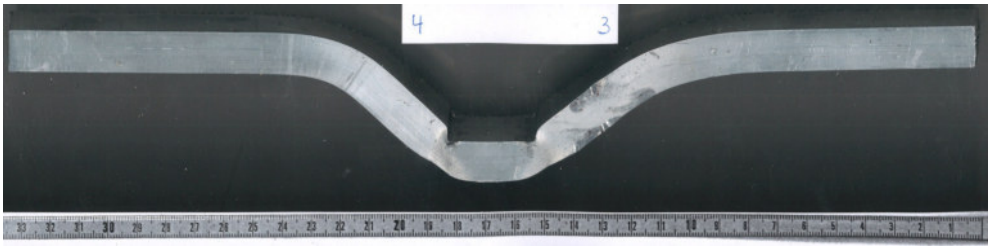

b. Rear fastener.

Fig. A.125: Aluminium fasteners with head taken out of timber-to-steel connection with spruce glulam.

a. Front fastener.

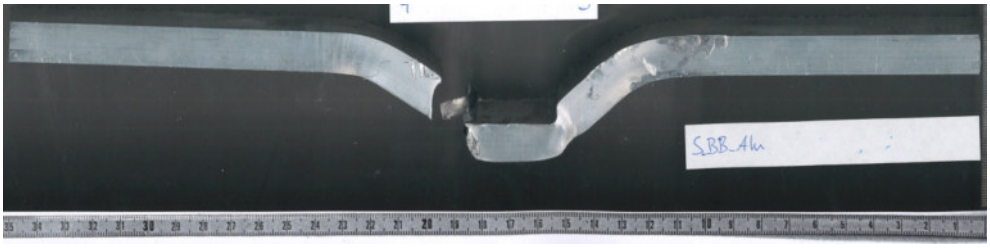

b. Rear fastener.

Fig. A.126: Aluminium fasteners taken out of timber-to-steel connection with beech LVL.

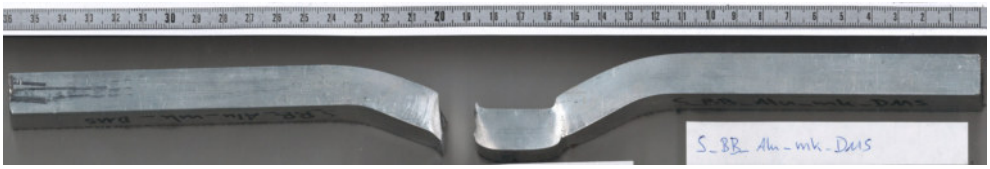

a. Front fastener.

b. Rear fastener.

Fig. A.127: Aluminium fasteners with head taken out of timber-to-steel connection with beech LVL.

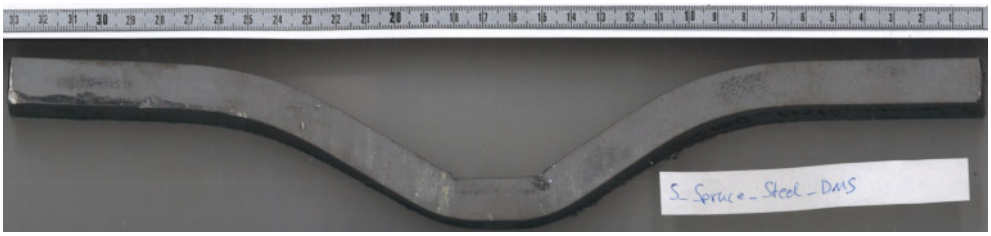

a. Front fastener.

b. Rear fastener.

Fig. A.128: Steel fasteners taken out of timber-to-steel connection with spruce glulam.

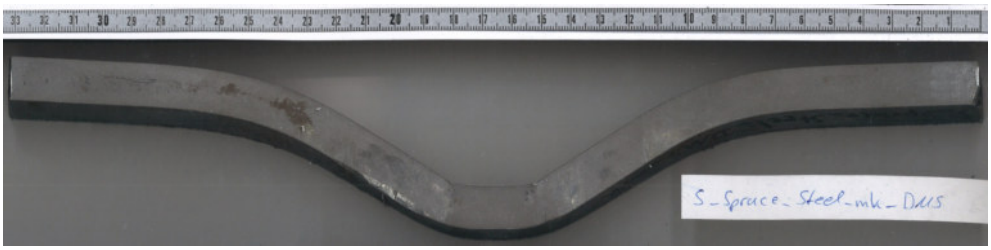

a. Front fastener.

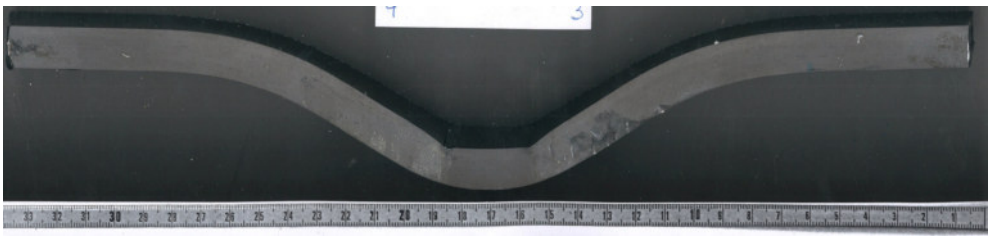

b. Rear fastener.

Fig. A.129: Steel fasteners with head taken out of timber-to-steel connection with spruce glulam.

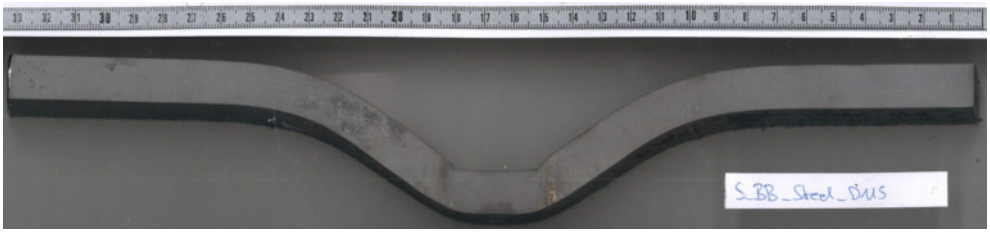

a. Front fastener.

b. Rear fastener.

Fig. A.130: Steel fasteners taken out of timber-to-steel connection with beech LVL.

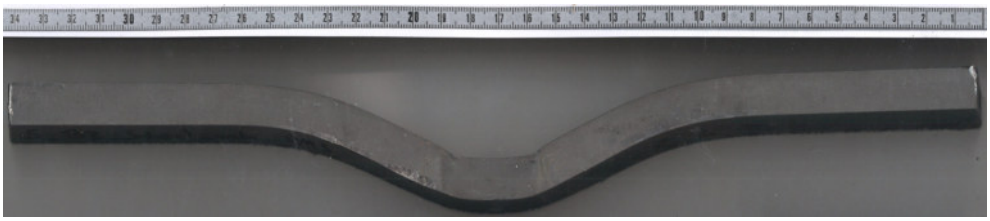

a. Front fastener.

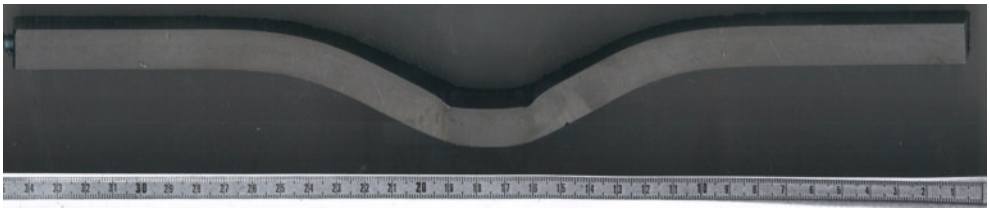

b. Rear fastener.

Fig. A.131: Steel fasteners with head taken out of timber-to-steel connection with beech LVL.

Rectangular Fasteners: Regression Results

Timber-to-Timber Connections (TT)

The following tables include the evaluated regression parameters *m* and *b*, bending angles α_i and coordinates for intersection points of the regression lines and the location of the plastic hinges (nextpoint).

Table A.17: TT connection with aluminium fastener in spruce glulam, front side, $y_{def} = 15$ mm. Evaluation ranges: [20 65], [150 169], [215 259], [309 330], [410 454], in mm.

Regression	*m*	*b*	Angle	in °	x_{intsec}	y_{intsec}	$x_{nextpoint}$	$y_{nextpoint}$
Reg1	-0.00066	-0.142	α_{12}	13.8	129.7	-0.2	129.3	-1.1
Reg2	-0.24713	31.83	α_{23}	13.9	189.6	-15.0	189.6	-14.2
Reg3	0.00056	-15.12	α_{34}	13.1	286.9	-15.0	287.1	-14.2
Reg4	0.23375	-82.03	α_{45}	13.1	348.2	-0.6	348.4	-1.4
Reg5	0.00098	-0.976						

Table A.18: TT connection with aluminium fastener in spruce glulam, rear side, $y_{def} = 15$ mm. Evaluation ranges: [20 65], [145 165], [216 256], [304 323], [410 454], in mm.

Regression	*m*	*b*	Angle	in °	x_{intsec}	y_{intsec}	$x_{nextpoint}$	$y_{nextpoint}$
Reg1	-0.00086	-0.010	α_{12}	13.5	124.9	-0.1	124.7	-0.9
Reg2	-0.24108	30.00	α_{23}	13.5	186.6	-15.0	186.9	-14.2
Reg3	-0.00084	-14.83	α_{34}	14.5	283.6	-15.1	283.4	-14.1
Reg4	0.25828	-88.32	α_{45}	14.4	340.9	-0.3	340.8	-1.0
Reg5	0.00089	-0.591						

Table A.19: TT connection with aluminium fastener with head in spruce glulam, front side, $y_{def} = 15$ mm. Evaluation ranges: [20 65], [147 166], [215 259], [308 328], [410 454], in mm.

Regression	*m*	*b*	Angle	in °	x_{intsec}	y_{intsec}	$x_{nextpoint}$	$y_{nextpoint}$
Reg1	-0.00129	-0.047	α_{12}	14.8	129.1	-0.2	128.9	-1.0
Reg2	-0.26543	34.04	α_{23}	14.9	184.7	-15.0	185.0	-14.2
Reg3	-0.00006	-14.97	α_{34}	14.1	288.1	-15.0	287.9	-14.3
Reg4	0.25128	-87.39	α_{45}	14.0	345.4	-0.6	345.4	-1.5
Reg5	0.00173	-1.205						

Table A.20: TT connection with aluminium fastener with head in spruce glulam, rear side, $y_{def} = 15$ mm. Evaluation ranges: [20 65], [143 163], [212 255], [305 325], [410 454], in mm.

Regression	*m*	*b*	Angle	in °	x_{intsec}	y_{intsec}	$x_{nextpoint}$	$y_{nextpoint}$
Reg1	-0.00153	-0.115	α_{12}	14.2	124.9	-0.3	124.8	-1.2
Reg2	-0.25483	31.52	α_{23}	14.3	182.4	-15.0	182.3	-14.2
Reg3	-0.00020	-14.93	α_{34}	13.7	284.6	-15.0	284.4	-14.2
Reg4	0.24438	-84.54	α_{45}	13.7	343.8	-0.5	343.8	-1.2
Reg5	0.00085	-0.805						

Table A.21: TT connection with steel fastener in spruce glulam, front side, $y_{def} = 15$ mm. Evaluation ranges: [20 65], [143 171], [221 249], [302 331], [410 454], in mm.

Regression	*m*	*b*	Angle	in °	x_{intsec}	y_{intsec}	$x_{nextpoint}$	$y_{nextpoint}$
Reg1	-0.00289	-0.007	α_{12}	10.3	118.0	-0.3	117.9	-1.1
Reg2	-0.18479	21.46	α_{23}	10.5	197.5	-15.0	197.6	-14.2
Reg3	0.00032	-15.09	α_{34}	9.8	273.2	-15.0	273.1	-14.3
Reg4	0.17379	-62.50	α_{45}	9.7	356.5	-0.5	356.4	-1.3
Reg5	0.00256	-1.457						

Table A.22: TT connection with steel fastener in spruce glulam, rear side, $y_{def} = 15$ mm. Evaluation ranges: [20 65], [133 160], [215 245], [300 328], [410 454], in mm.

Regression	m	b	Angle	in °	x_{intsec}	y_{intsec}	$x_{nextpoint}$	$y_{nextpoint}$
Reg1	-0.00367	0.070	α_{12}	10.2	107.6	-0.3	107.5	-1.1
Reg2	-0.18307	19.37	α_{23}	10.4	187.9	-15.0	187.9	-14.2
Reg3	0.00050	-15.13	α_{34}	10.2	272.7	-15.0	272.7	-14.2
Reg4	0.18033	-64.16	α_{45}	10.1	353.1	-0.5	353.1	-1.3
Reg5	0.00267	-1.438						

Table A.23: TT connection with steel fastener with head in spruce glulam, front side, $y_{def} = 15$ mm. Evaluation ranges: [20 65], [145 173], [225 252], [304 331], [410 454], in mm.

Regression	m	b	Angle	in °	x_{intsec}	y_{intsec}	$x_{nextpoint}$	$y_{nextpoint}$
Reg1	-0.00397	-0.067	α_{12}	9.6	118.8	-0.5	118.6	-1.3
Reg2	-0.17303	20.01	α_{23}	9.8	202.4	-15.0	202.3	-14.3
Reg3	-0.00020	-14.97	α_{34}	10.4	276.2	-15.0	275.8	-14.2
Reg4	0.18253	-65.44	α_{45}	10.1	354.2	-0.8	354.4	-1.5
Reg5	0.00450	-2.388						

Table A.24: TT connection with steel fastener with head in spruce glulam, rear side, $y_{def} = 15$ mm. Evaluation ranges: [20 65], [145 171], [220 250], [302 331], [410 454], in mm.

Regression	m	b	Angle	in °	x_{intsec}	y_{intsec}	$x_{nextpoint}$	$y_{nextpoint}$
Reg1	-0.00482	-0.192	α_{12}	10.8	123.3	-0.8	123.2	-1.6
Reg2	-0.19569	23.34	α_{23}	11.1	196.0	-15.0	196.0	-14.1
Reg3	0.00008	-15.02	α_{34}	9.6	272.1	-15.0	272.0	-14.2
Reg4	0.16919	-61.05	α_{45}	9.3	353.9	-1.2	353.9	-1.9
Reg5	0.00473	-2.850						

Table A.25: TT connection with aluminium fastener in beech LVL, front side, $y_{def} = 15$ mm. Evaluation ranges: [20 65], [140 165], [220 255], [307 332], [410 455], in mm.

Regression	*m*	*b*	Angle	in °	x_{intsec}	y_{intsec}	$x_{nextpoint}$	$y_{nextpoint}$
Reg1	-0.00392	0.158	α_{12}	16.7	129.9	-0.4	129.6	-1.1
Reg2	-0.30425	39.17	α_{23}	17.0	178.3	-15.1	178.3	-14.3
Reg3	0.00079	-15.23	α_{34}	16.6	295.1	-15.0	295.1	-14.2
Reg4	0.29884	-103.2	α_{45}	16.4	341.6	-1.1	341.5	-1.9
Reg5	0.00378	-2.391						

Table A.26: TT connection with aluminium fastener in beech LVL, rear side, $y_{def} = 15$ mm. Evaluation ranges: [20 65], [140 165], [219 253], [305 330], [410 455], in mm.

Regression	*m*	*b*	Angle	in °	x_{intsec}	y_{intsec}	$x_{nextpoint}$	$y_{nextpoint}$
Reg1	-0.00391	0.019	α_{12}	17.2	130.7	-0.5	130.7	-1.3
Reg2	-0.31391	40.54	α_{23}	17.4	176.9	-15.0	177.0	-14.2
Reg3	-0.00010	-14.99	α_{34}	17.1	292.1	-15.0	292.1	-14.2
Reg4	0.30704	-104.7	α_{45}	16.9	338.5	-0.8	338.6	-1.5
Reg5	0.00233	-1.573						

Table A.27: TT connection with aluminium fastener with head in beech LVL, front side, $y_{def} = 15$ mm. Evaluation ranges: [20 65], [149 165], [210 255], [301 316], [410 455], in mm.

Regression	*m*	*b*	Angle	in °	x_{intsec}	y_{intsec}	$x_{nextpoint}$	$y_{nextpoint}$
Reg1	-0.00276	-0.223	α_{12}	16.7	125.0	-0.6	124.9	-1.4
Reg2	-0.30355	37.38	α_{23}	16.9	172.8	-15.1	173.1	-14.4
Reg3	0.00034	-15.14	α_{34}	16.6	292.3	-15.0	292.0	-14.3
Reg4	0.29797	-102.1	α_{45}	16.4	340.4	-0.7	340.5	-1.5
Reg5	0.00359	-1.917						

Table A.28: TT connection with aluminium fastener with head in beech LVL, rear side, $y_{def} = 15$ mm. Evaluation ranges: [20 65], [145 167], [212 257], [304 326], [410 455], in mm.

Regression	m	b	Angle	in °	x_{intsec}	y_{intsec}	$x_{nextpoint}$	$y_{nextpoint}$
Reg1	-0.00497	-0.293	α_{12}	17.4	133.3	-1.0	133.1	-1.8
Reg2	-0.31876	41.53	α_{23}	17.7	177.4	-15.0	177.8	-14.4
Reg3	-0.00050	-14.94	α_{34}	17.0	292.4	-15.1	292.4	-14.3
Reg4	0.30603	-104.6	α_{45}	16.9	337.7	-1.2	337.7	-2.0
Reg5	0.00259	-2.078						

Table A.29: TT connection with steel fastener in beech LVL, front side, $y_{def} = 15$ mm. Evaluation ranges: [20 65], [138 168], [218 258], [306 336], [410 455], in mm.

Regression	m	b	Angle	in °	x_{intsec}	y_{intsec}	$x_{nextpoint}$	$y_{nextpoint}$
Reg1	-0.00267	-0.004	α_{12}	12.1	120.6	-0.3	120.5	-1.2
Reg2	-0.21631	25.75	α_{23}	12.3	188.5	-15.0	188.5	-14.2
Reg3	0.00080	-15.18	α_{34}	12.4	286.8	-14.9	286.7	-14.1
Reg4	0.22029	-78.14	α_{45}	12.3	351.6	-0.7	351.7	-1.5
Reg5	0.00298	-1.743						

Table A.30: TT connection with steel fastener in beech LVL, rear side, $y_{def} = 15$ mm. Evaluation ranges: [20 65], [138 168], [213 252], [299 330], [410 455], in mm.

Regression	m	b	Angle	in °	x_{intsec}	y_{intsec}	$x_{nextpoint}$	$y_{nextpoint}$
Reg1	-0.00399	-0.245	α_{12}	12.4	122.0	-0.7	121.9	-1.5
Reg2	-0.22436	26.64	α_{23}	12.6	185.3	-14.9	185.3	-14.2
Reg3	-0.00026	-14.89	α_{34}	11.7	280.2	-15.0	280.2	-14.2
Reg4	0.20770	-73.15	α_{45}	11.6	344.6	-1.6	344.9	-2.3
Reg5	0.00203	-2.272						

Table A.31: TT connection with steel fastener with head in beech LVL, front side, $y_{def} = 15$ mm. Evaluation ranges: [20 65], [138 168], [217 257], [304 334], [410 455], in mm.

Regression	*m*	*b*	Angle	in °	x_{intsec}	y_{intsec}	$x_{nextpoint}$	$y_{nextpoint}$
Reg1	-0.00254	0.019	α_{12}	12.7	122.0	-0.3	122.2	-1.3
Reg2	-0.22758	27.48	α_{23}	12.9	186.8	-15.0	187.0	-14.2
Reg3	0.00076	-15.17	α_{34}	12.7	285.0	-15.0	285.1	-14.1
Reg4	0.22625	-79.44	α_{45}	12.6	349.4	-0.4	349.7	-1.2
Reg5	0.00207	-1.099						

Table A.32: TT connection with steel fastener with head in beech LVL, rear side, $y_{def} = 15$ mm. Evaluation ranges: [20 65], [138 168], [213 253], [298 328], [410 455], in mm.

Regression	*m*	*b*	Angle	in °	x_{intsec}	y_{intsec}	$x_{nextpoint}$	$y_{nextpoint}$
Reg1	-0.00263	0.074	α_{12}	12.7	119.9	-0.2	119.8	-1.2
Reg2	-0.22778	27.07	α_{23}	12.9	184.9	-15.1	184.9	-14.2
Reg3	0.00119	-15.27	α_{34}	12.3	280.3	-14.9	280.4	-14.1
Reg4	0.21879	-76.27	α_{45}	12.3	346.7	-0.4	346.7	-1.3
Reg5	0.00159	-0.981						

Table A.33: TT connection with steel fastener in DVW, front side, $y_{def} = 15$ mm. Evaluation ranges: [20 65], [147 158], [210 260], [314 327], [410 455], in mm.

Regression	*m*	*b*	Angle	in °	x_{intsec}	y_{intsec}	$x_{nextpoint}$	$y_{nextpoint}$
Reg1	-0.01011	-0.611	α_{12}	17.6	135.3	-2.0	135.1	-3.3
Reg2	-0.32763	42.35	α_{23}	18.3	175.3	-15.1	175.3	-13.7
Reg3	0.00217	-15.48	α_{34}	16.3	295.9	-14.8	295.9	-13.6
Reg4	0.29523	-102.2	α_{45}	16.0	338.8	-2.2	339.2	-3.3
Reg5	0.00770	-4.776						

Table A.34: TT connection with steel fastener in DVW, rear side, $y_{def} = 15$ mm. Evaluation ranges: [20 65], [147 158], [210 260], [313 323], [410 455], in mm.

Regression	m	b	Angle	in °	x_{intsec}	y_{intsec}	$x_{nextpoint}$	$y_{nextpoint}$
Reg1	-0.00693	-0.761	α_{12}	18.5	133.1	-1.7	132.8	-3.3
Reg2	-0.34250	43.91	α_{23}	18.8	171.7	-14.9	171.9	-13.6
Reg3	-0.00111	-14.72	α_{34}	19.3	298.8	-15.1	298.5	-13.6
Reg4	0.34891	-119.3	α_{45}	18.6	335.3	-2.3	335.3	-3.8
Reg5	0.01138	-6.133						

Table A.35: TT connection with steel fastener with head in DVW, front side, $y_{def} = 15$ mm. Evaluation ranges: [20 65], [147 158], [215 260], [317 327], [410 455], in mm.

Regression	m	b	Angle	in °	x_{intsec}	y_{intsec}	$x_{nextpoint}$	$y_{nextpoint}$
Reg1	-0.00301	-0.035	α_{12}	22.0	137.0	-0.4	136.7	-2.1
Reg2	-0.40845	55.51	α_{23}	22.3	172.6	-15.0	172.9	-13.4
Reg3	0.00076	-15.12	α_{34}	18.5	296.5	-14.9	296.5	-14.0
Reg4	0.33548	-114.4	α_{45}	18.3	338.8	-0.7	338.9	-2.0
Reg5	0.00438	-2.167						

Table A.36: TT connection with steel fastener with head in DVW, rear side, $y_{def} = 15$ mm. Evaluation ranges: [20 65], [150 160], [215 255], [309 318], [410 454], in mm.

Regression	m	b	Angle	in °	x_{intsec}	y_{intsec}	$x_{nextpoint}$	$y_{nextpoint}$
Reg1	-0.00307	-0.022	α_{12}	21.4	136.6	-0.4	136.3	-2.1
Reg2	-0.39488	53.49	α_{23}	21.5	173.4	-15.0	173.6	-13.4
Reg3	-0.00062	-14.86	α_{34}	22.3	296.0	-15.0	295.5	-13.5
Reg4	0.40908	-136.1	α_{45}	22.2	332.3	-0.2	332.5	-1.9
Reg5	0.00113	-0.570						

Timber-to-Steel Connections (TS)

Table A.37: TS connection with aluminium fastener in spruce glulam, front side, $y_{def} = 15$ mm. Evaluation ranges: [20 65], [134 148], [171 177], [199 212], [280 325], in mm.

Regression	*m*	*b*	Angle	in °	x_{intsec}	y_{intsec}	$x_{nextpoint}$	$y_{nextpoint}$
Reg1	-0.00183	-0.087	α_{12}	17.8	118.6	-0.3	118.4	-1.2
Reg2	-0.32374	38.10	α_{23}	18.0	164.0	-15.0	164.0	-14.8
Reg3	0.00106	-15.18	α_{34}	16.8	182.8	-15.0	182.8	-14.8
Reg4	0.30221	-70.22	α_{45}	16.8	230.9	-0.4	231.2	-1.4
Reg5	0.00035	-0.528						

Table A.38: TS connection with aluminium fastener in spruce glulam, rear side, $y_{def} = 15$ mm. Evaluation ranges: [20 65], [130 147], [169 174], [195 212], [280 325], in mm.

Regression	*m*	*b*	Angle	in °	x_{intsec}	y_{intsec}	$x_{nextpoint}$	$y_{nextpoint}$
Reg1	-0.00068	-0.309	α_{12}	17.4	115.0	-0.4	114.8	-1.3
Reg2	-0.31489	35.81	α_{23}	17.5	161.4	-15.0	161.5	-14.8
Reg3	0.00074	-15.13	α_{34}	16.9	179.9	-15.0	180.1	-14.7
Reg4	0.30473	-69.81	α_{45}	16.8	227.9	-0.4	228.0	-1.4
Reg5	0.00228	-0.871						

Table A.39: TS connection with aluminium fastener with head in spruce glulam, front side, $y_{def} = 15$ mm. Evaluation ranges: [20 65], [130 148], [169 176], [195 214], [280 325], in mm.

Regression	m	b	Angle	in °	x_{intsec}	y_{intsec}	$x_{nextpoint}$	$y_{nextpoint}$
Reg1	-0.00354	-0.622	α_{12}	16.1	113.6	-1.0	113.5	-1.9
Reg2	-0.29268	32.22	α_{23}	16.3	161.3	-15.0	161.2	-14.8
Reg3	-0.00079	-14.87	α_{34}	15.9	181.3	-15.0	181.1	-14.7
Reg4	0.28438	-66.58	α_{45}	15.7	230.3	-1.1	230.4	-2.0
Reg5	0.00318	-1.832						

Table A.40: TS connection with aluminium fastener with head in spruce glulam, rear side, $y_{def} = 15$ mm. Evaluation ranges: [20 65], [127 148], [168 175], [194 214], [280 325], in mm.

Regression	m	b	Angle	in °	x_{intsec}	y_{intsec}	$x_{nextpoint}$	$y_{nextpoint}$
Reg1	-0.00364	-0.552	α_{12}	15.3	111.3	-1.0	111.3	-2.0
Reg2	-0.27790	29.98	α_{23}	15.5	161.9	-15.0	162.2	-14.8
Reg3	-0.00052	-14.93	α_{34}	16.7	180.9	-15.0	180.4	-14.8
Reg4	0.29988	-69.26	α_{45}	16.5	227.8	-0.9	227.7	-1.8
Reg5	0.00299	-1.630						

Table A.41: TS connection with steel fastener in spruce glulam, front side, $y_{def} = 15$ mm. Evaluation ranges: [20 65], [115 146], [167 172], [196 231], [280 325], in mm.

Regression	m	b	Angle	in °	x_{intsec}	y_{intsec}	$x_{nextpoint}$	$y_{nextpoint}$
Reg1	-0.00621	-0.349	α_{12}	13.1	100.8	-1.0	100.8	-1.9
Reg2	-0.24012	23.22	α_{23}	13.5	159.2	-15.0	159.1	-14.6
Reg3	-0.00035	-14.95	α_{34}	12.2	181.1	-15.0	181.3	-14.6
Reg4	0.21496	-53.95	α_{45}	11.7	244.5	-1.4	244.8	-2.3
Reg5	0.00734	-3.195						

Table A.42: TS connection with steel fastener in spruce glulam, rear side, $y_{def} = 15$ mm. Evaluation ranges: [20 65], [120 147], [169 175], [200 232], [280 325], in mm.

Regression	*m*	*b*	Angle	in °	x_{intsec}	y_{intsec}	$x_{nextpoint}$	$y_{nextpoint}$
Reg1	-0.00555	-0.486	α_{12}	12.9	101.3	-1.0	101.6	-2.1
Reg2	-0.23543	22.79	α_{23}	13.3	160.6	-15.0	160.7	-14.6
Reg3	0.00099	-15.18	α_{34}	11.1	183.3	-15.0	183.1	-14.6
Reg4	0.19804	-51.31	α_{45}	10.8	252.0	-1.4	251.9	-2.3
Reg5	0.00705	-3.178						

Table A.43: TS connection with steel fastener with head in spruce glulam, front side, $y_{def} = 15$ mm. Evaluation ranges: [20 65], [117 146], [168 176], [198 228], [280 325], in mm.

Regression	*m*	*b*	Angle	in °	x_{intsec}	y_{intsec}	$x_{nextpoint}$	$y_{nextpoint}$
Reg1	-0.00230	-0.375	α_{12}	13.2	99.8	-0.6	99.5	-1.5
Reg2	-0.23681	23.03	α_{23}	13.3	160.4	-15.0	160.7	-14.5
Reg3	-0.00122	-14.77	α_{34}	12.8	182.3	-15.0	182.3	-14.6
Reg4	0.22569	-56.13	α_{45}	12.5	243.4	-1.2	243.4	-2.2
Reg5	0.00335	-2.024						

Table A.44: TS connection with steel fastener with head in spruce glulam, rear side, $y_{def} = 15$ mm. Evaluation ranges: [20 65], [117 146], [166 177], [198 228], [280 325], in mm.

Regression	*m*	*b*	Angle	in °	x_{intsec}	y_{intsec}	$x_{nextpoint}$	$y_{nextpoint}$
Reg1	-0.00281	-0.656	α_{12}	13.0	101.2	-0.9	101.1	-1.9
Reg2	-0.23405	22.74	α_{23}	13.1	161.2	-15.0	161.0	-14.6
Reg3	-0.00104	-14.81	α_{34}	12.8	182.0	-15.0	182.2	-14.6
Reg4	0.22582	-56.10	α_{45}	12.6	244.6	-0.9	244.7	-1.8
Reg5	0.00272	-1.531						

Table A.45: TS connection with aluminium fastener in beech LVL, front side, $y_{def} = 15$ mm. Evaluation ranges: [20 70], [130 148], [154 157], [168 172], [185 188], [195 212], [275 325], in mm.

Regression	m	b	Angle	in °	x_{intsec}	y_{intsec}	$x_{nextpoint}$	$y_{nextpoint}$
Reg1	-0.00122	0.054	α_{12}	19.1	121.8	-0.1	121.6	-1.0
Reg2a	-0.34821	42.32						
Reg2b	-0.58630	78.13	α_{23}	30.4	158.8	-15.0	159.0	-14.4
Reg3	-0.00005	-14.97	α_{34}	30.8	183.7	-15.0	183.5	-14.4
Reg4a	0.59654	-124.6						
Reg4b	0.34295	-75.68	α_{45}	18.8	220.1	-0.2	220.3	-1.2
Reg5	0.00170	-0.587						

Table A.46: TS connection with aluminium fastener in beech LVL, rear side, $y_{def} = 15$ mm. Evaluation ranges: [20 70], [133 149], [153 156], [170 175], [188 191], [195 212], [275 325], in mm.

Regression	m	b	Angle	in °	x_{intsec}	y_{intsec}	$x_{nextpoint}$	$y_{nextpoint}$
Reg1	-0.00037	-0.096	α_{12}	19.5	124.1	-0.1	124.0	-1.0
Reg2a	-0.35401	43.78						
Reg2b	-0.82756	116.0	α_{23}	39.5	158.2	-15.0	159.2	-14.4
Reg3	-0.00192	-14.66	α_{34}	37.6	185.9	-15.0	185.8	-14.2
Reg4a	0.76652	-157.5						
Reg4b	0.35588	-78.66	α_{45}	19.6	220.5	-0.2	220.6	-1.0
Reg5	0.00027	-0.235						

Table A.47: TS connection with aluminium fastener with head in beech LVL, front side, $y_{def} = 15$ mm. Evaluation ranges: [20 70], [130 148], [156 158], [168 172], [184 187], [192 210], [275 325], in mm.

Regression	m	b	Angle	in °	x_{intsec}	y_{intsec}	$x_{nextpoint}$	$y_{nextpoint}$
Reg1	0.00099	-0.163	α_{12}	18.3	122.4	0.0	122.5	-1.1
Reg2a	-0.32992	40.33						
Reg2b	-0.51891	67.99	α_{23}	27.5	160.0	-15.0	159.8	-14.5
Reg3	0.00174	-15.30	α_{34}	33.1	182.2	-15.0	181.9	-14.5
Reg4a	0.65342	-134.0						
Reg4b	0.32549	-71.03	α_{45}	18.0	216.7	-0.5	216.8	-1.3
Reg5	0.00108	-0.717						

Table A.48: TS connection with aluminium fastener with head in beech LVL, rear side, $y_{def} = 15$ mm. Evaluation ranges: [20 70], [133 146], [154 157], [168 174], [185 188], [197 210], [275 325], in mm.

Regression	m	b	Angle	in °	x_{intsec}	y_{intsec}	$x_{nextpoint}$	$y_{nextpoint}$
Reg1	-0.00020	0.063	α_{12}	19.1	125.1	0.0	124.9	-0.9
Reg2a	-0.34566	43.27						
Reg2b	-0.68250	93.87	α_{23}	34.2	159.5	-15.0	159.8	-14.4
Reg3	-0.00171	-14.72	α_{34}	31.8	182.4	-15.0	182.1	-14.5
Reg4a	0.61847	-127.8						
Reg4b	0.33751	-73.61	α_{45}	18.7	217.8	-0.1	218.1	-1.0
Reg5	-0.00092	0.117						

Table A.49: TS connection with steel fastener in beech LVL, front side, $y_{def} = 15$ mm. Evaluation ranges: [20 65], [116 150], [168 171], [188 222], [280 325], in mm.

Regression	m	b	Angle	in °	x_{intsec}	y_{intsec}	$x_{nextpoint}$	$y_{nextpoint}$
Reg1	-0.00116	-0.447	α_{12}	14.9	105.8	-0.6	106.0	-1.7
Reg2	-0.26691	27.67	α_{23}	14.8	159.9	-15.0	159.7	-14.6
Reg3	-0.00232	-14.62	α_{34}	15.3	179.0	-15.0	178.6	-14.7
Reg4	0.27153	-63.63	α_{45}	15.1	231.9	-0.7	232.1	-1.7
Reg5	0.00186	-1.099						

Table A.50: TS connection with steel fastener in beech LVL, rear side, $y_{def} = 15$ mm. Evaluation ranges: [20 65], [120 142], [168 171], [199 222], [280 325], in mm.

Regression	m	b	Angle	in °	x_{intsec}	y_{intsec}	$x_{nextpoint}$	$y_{nextpoint}$
Reg1	-0.00284	-0.471	α_{12}	14.8	108.2	-0.8	108.1	-1.8
Reg2	-0.26739	28.15	α_{23}	14.9	161.4	-15.0	161.4	-14.7
Reg3	-0.00182	-14.70	α_{34}	14.3	178.0	-15.0	178.1	-14.7
Reg4	0.25273	-60.00	α_{45}	14.0	234.4	-0.8	235.0	-1.8
Reg5	0.00265	-1.378						

Table A.51: TS connection with steel fastener with head in beech LVL, front side, $y_{def} = 15$ mm. Evaluation ranges: [20 65], [122 149], [171 174], [196 223], [280 325], in mm.

Regression	m	b	Angle	in °	x_{intsec}	y_{intsec}	$x_{nextpoint}$	$y_{nextpoint}$
Reg1	-0.00298	0.274	α_{12}	15.2	109.2	-0.1	109.0	-1.2
Reg2	-0.27499	29.97	α_{23}	15.5	163.6	-15.0	163.8	-14.7
Reg3	0.00158	-15.27	α_{34}	14.8	180.6	-15.0	180.3	-14.7
Reg4	0.26611	-63.05	α_{45}	14.8	236.3	-0.2	236.6	-1.4
Reg5	0.00136	-0.492						

Table A.52: TS connection with steel fastener with head in beech LVL, rear side, $y_{def} = 15$ mm. Evaluation ranges: [20 65], [122 149], [169 173], [195 224], [280 325], in mm.

Regression	m	b	Angle	in °	x_{intsec}	y_{intsec}	$x_{nextpoint}$	$y_{nextpoint}$
Reg1	-0.00123	-0.252	α_{12}	15.6	110.8	-0.4	110.7	-1.5
Reg2	-0.28058	30.70	α_{23}	15.6	162.9	-15.0	163.3	-14.7
Reg3	-0.00169	-14.72	α_{34}	14.5	179.8	-15.0	179.6	-14.7
Reg4	0.25631	-61.11	α_{45}	14.3	236.5	-0.5	236.9	-1.7
Reg5	0.00062	-0.651						

Table A.53: TS connection with steel fastener in DVW, front side, $y_{def} = 10$ mm. Evaluation ranges: [20 65], [135 145], [151 153], [166 171], [186 188], [195 205], [280 325], in mm.

Regression	m	b	Angle	in °	x_{intsec}	y_{intsec}	$x_{nextpoint}$	$y_{nextpoint}$
Reg1	-0.00280	-0.163	α_{12}	11.6	125.9	-0.5	126.0	-1.2
Reg2a	-0.20768	25.63	α_{23}	29.3	156.6	-10.0	156.9	-9.4
Reg2b	-0.56024	77.73	α_{34}	28.4	182.2	-10.0	182.2	-9.4
Reg3	0.00017	-10.03	α_{45}	10.3	212.8	-1.0	212.8	-1.5
Reg4a	0.53988	-108.4						
Reg4b	0.18774	-40.90						
Reg5	0.00501	-2.020						

Table A.54: TS connection with steel fastener in DVW, rear side, $y_{def} = 10$ mm. Evaluation ranges: [20 65], [134 142], [150 153], [166 171], [183 186], [193 201], [280 325], in mm.

Regression	m	b	Angle	in °	x_{intsec}	y_{intsec}	$x_{nextpoint}$	$y_{nextpoint}$
Reg1	-0.00576	-0.272	α_{12}	10.7	125.0	-1.0	124.7	-1.6
Reg2a	-0.19560	23.46						
Reg2b	-0.50402	68.56	α_{23}	26.9	156.0	-10.0	156.1	-9.4
Reg3	0.00312	-10.53	α_{34}	28.7	180.7	-10.0	180.6	-9.4
Reg4a	0.55134	-109.6						
Reg4b	0.19699	-42.27	α_{45}	10.9	210.2	-0.9	210.1	-1.5
Reg5	0.00396	-1.691						

Table A.55: TS connection with steel fastener with head in DVW, front side, $y_{def} = 10$ mm. Evaluation ranges: [20 65], [136 144], [151 154], [167 172], [186 189], [195 203], [280 325], in mm.

Regression	m	b	Angle	in °	x_{intsec}	y_{intsec}	$x_{nextpoint}$	$y_{nextpoint}$
Reg1	-0.00231	-0.314	α_{12}	10.3	126.2	-0.6	126.2	-1.3
Reg2a	-0.18463	22.70						
Reg2b	-0.49198	68.00	α_{23}	26.3	158.6	-10.0	158.8	-9.5
Reg3	0.00150	-10.26	α_{34}	29.3	182.5	-10.0	182.3	-9.3
Reg4a	0.56370	-112.9						
Reg4b	0.19486	-41.90	α_{45}	10.8	211.8	-0.6	212.0	-1.3
Reg5	0.00384	-1.442						

Table A.56: TS connection, steel fastener with head in DVW, rear side, $y_{def} = 10$ mm. Evaluation ranges: [20 65], [136 144], [152 155], [167 175], [187 190], [198 206], [280 325], in mm.

Regression	m	b	Angle	in °	x_{intsec}	y_{intsec}	$x_{nextpoint}$	$y_{nextpoint}$
Reg1	-0.00375	0.007	α_{12}	10.6	126.0	-0.5	125.8	-1.2
Reg2a	-0.19063	23.55						
Reg2b	-0.52739	73.77	α_{23}	27.8	158.5	-9.8	158.6	-9.2
Reg3	0.00020	-9.86	α_{34}	29.9	183.7	-9.8	183.7	-9.2
Reg4a	0.57478	-115.4						
Reg4b	0.18453	-40.26	α_{45}	10.3	216.9	-0.2	217.1	-1.0
Reg5	0.00185	-0.632						

A.6 Results for *NV* Interaction Tests

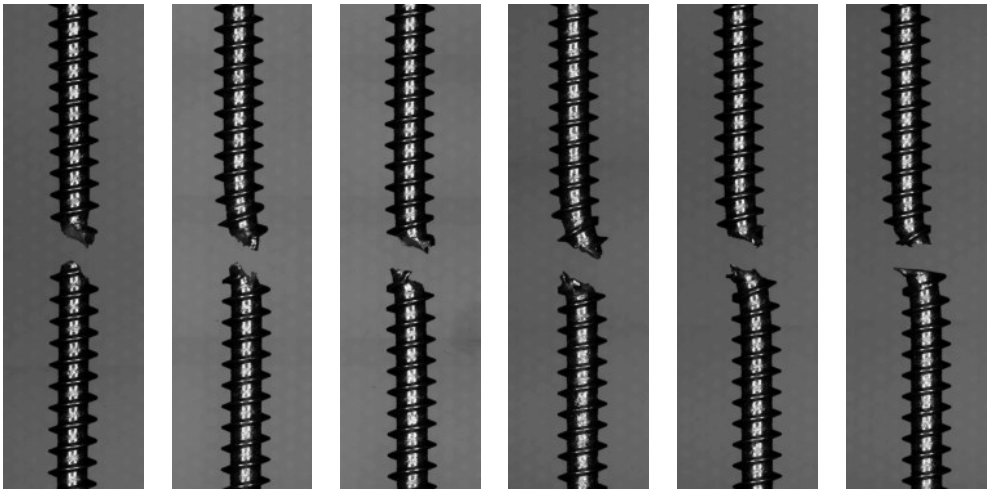

a. 0° b. 11.25° c. 22.5° d. 45° e. 67.5° f. 90°

Fig. A.132: Fracture surfaces for fully threaded screws d = 6 mm.

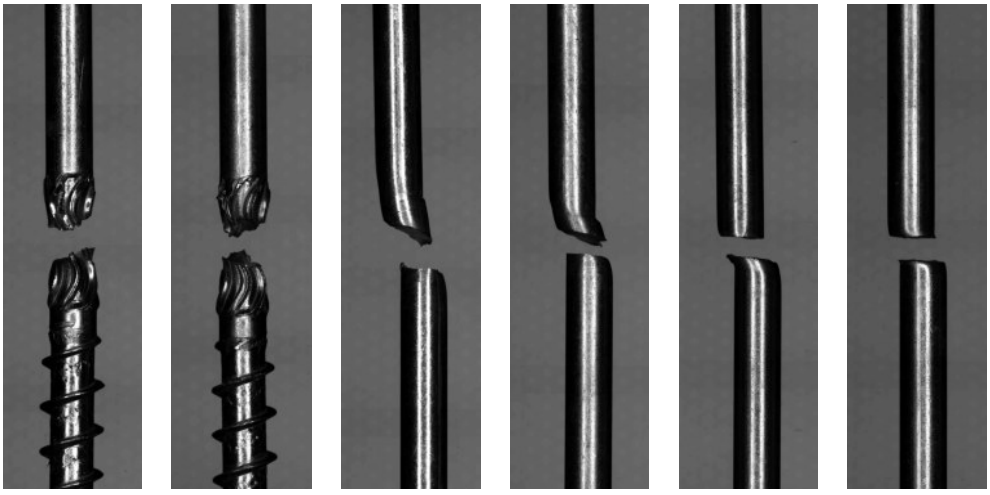

a. 0° b. 11.25° c. 22.5° d. 45° e. 67.5° f. 90°

Fig. A.133: Fracture surfaces for partially threaded screws d = 8 mm.

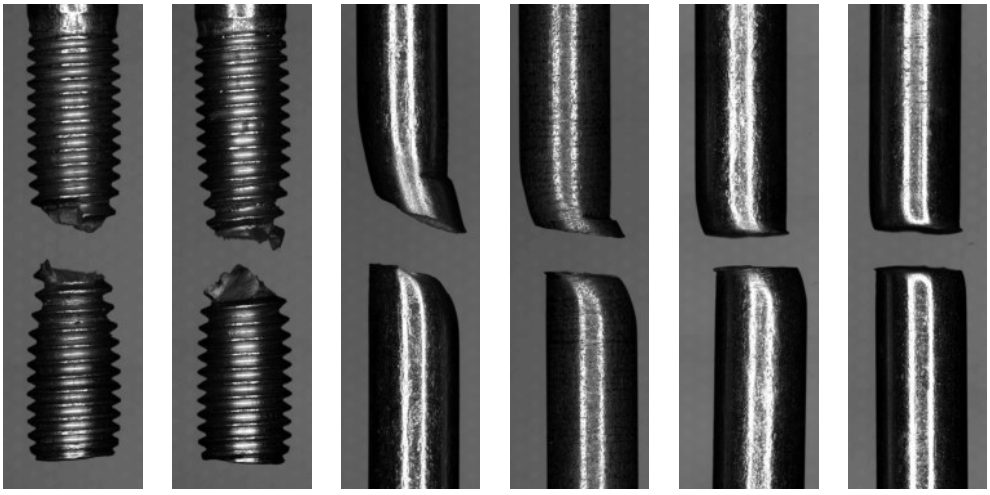

a. 0° b. 11.25° c. 22.5° d. 45° e. 67.5° f. 90°

Fig. A.134: Fracture surfaces for bolts M12 4.8.